Liposomal delivery of glucoCEST and 2-deoxyglucoCEST reagents

Harriet Story

Supervisors: Prof Alethea Tabor, Prof Xavier Golay, Prof Helen Hailes and Prof Tony Ng

Department of Chemistry UCL; UCL institute of Neurology; UCL Oncology

PhD in Chemistry

I, Harriet Story, confirm that the work presented in this thesis is my own. Where information has been derived from other sources, I confirm that this has been indicated in the thesis.

Acknowledgements

Firstly, I would like to thank Professor Alethea Tabor for her support and guidance. I would also like to thank Dr. Robin Bofinger for showing me the ropes when I started and providing invaluable advice and positivity throughout. I am grateful to the entire Hailes/Tabor group for creating such an amicable working environment. A special thanks to Dr. Richard Fitzmaurice for proof reading.

Many thanks to Professor Xavier Golay for his integral input and supervision and to his PhD student, Dr. Eleni Demetriou, for conducting CEST MRI experiments and taking time out of her busy schedule to discuss the outcomes.

Thank you to Lim Win Gel for providing the novel glucose-lipid GlcEGSL and the isothiocyanate intermediate **10**.

It has been fantastic to collaborate with Professor Ricki Sharma, Dr. Rebecca Carter and Adam Westhorpe at the UCL Cancer Institute and I thank them for all the time and effort they invested in the radiosensitisation and cytotoxicity cell-based assays.

I am grateful to Professor Jayne Lawrence, Dr. Hisham Al-Obaidi and Dr. Fabrizia Foglia for being my points of contact at King's College London, for introducing me to their lab in the Franklin Wilkins building and allowing me to use the extruder.

Finally, I would like to thank Kersti Karu and Abil Aliev for providing the departmental mass spectrometry and NMR services, respectively.

Abbreviations

Δω – frequency difference between the chemical shift of bulk water and exchangeable protons

2-DG – 2-deoxy-D-glucose

2-DG-CEST – 2-deoxyglucoCEST

5-FC – 5-fluorocytosine

5-FU – 5-fluorouracil

anti-EGFR-IL-DOX – anti-epidermal growth factor receptor immunoliposomal doxorubicin

APT – amide proton transfer

ATP – adenosine triphosphate

BA – barbituric acid

2-DG – 2-deoxy-D-glucose

2-DG6P – 2-deoxy-D-glucose-6-phosphate

Boc – *tert*-butoxycarbonyl

BW – body weight

CA – contrast agent

CESL – chemical exchange spin lock

CEST – chemical exchange saturation transfer

CHEMS – cholesteryl hemisuccinate

CRC – colorectal cancer

CT – computerized tomography

DCC – *N,N'*-dicyclohexylcarbodiimide

DCE – dynamic contrast enhanced

DEPC – dierucoylphosphatidylcholine

DI - deionised

DIBAL-H – diisobutylaluminium hydride

DIPEA – diisopropylethylamine

DLS – dynamic light scattering

DMPE-PEG2000 – 1,2-dimyristoyl-*sn*-glycero-3-phosphoethanolamine-*N*-[methoxy(polyethylene glycol)-2000]

DNA – deoxyribonucleic acid

DODEG4 – DiOleylDimethyl Ethylene Glycol 4

DOPE – 1,2-dioleoyl-sn-glycero-3-phosphoethanolamine

DOTA – 1,4,7,10- tetraazacyclododecane-1,4,7,10-tetraacetic acid

DOTAM – 1,4,7,10- tetraazacyclododecane-1,4,7,10-tetraamide

dotma – α,α’,α’’,α’’’-tetramethyl-1,4,7,10-tetraacetic acid

DOTMA – (*N*-[1-(2,3-dioleyloxy) propyl])-*N*,*N*,*N*-trimethylammonium chloride

DOX – doxorubicin

DPPC – dipalmitoyl phosphatidylcholine

DPPE-PEG2000 – 1,2-dipalmitoyl-*sn*-glycero-3-phosphoethanolamine-*N*-[methoxy(polyethylene glycol)-2000]

DPPG – 1,2-dipalmitoyl-*sn*-glycero-3-phosphoglycerol

DSPC -–1,2-distearoyl-*sn*-glycero-3-phosphocholine

DSPE-PEG2000 – 1,2-distearoyl-*sn*-glycero-3-phosphoethanolamine-*N*-[methoxy(polyethylene glycol)-2000]

DSPS – 1,2-distearoyl-*sn*-glycero-3-phosphoserine

DSS – 4,4-dimethyl-4-silapentane-1-sulfonic acid

DTPA – diethylene triamine pentaacetic acid

EGF – epidermal growth factor

EGFR – epidermal growth factor receptor

EPR – enhanced permeability and retention

eq. – equivalents

FCC – flash column chromatography

FDG – 2-deoxy-2-[^{18}F]-fluoro-D-glucose

FDG-PET – [^{18}F]-fluorodeoxyglucose positron emission tomography

gagCEST – glycosaminoglycan chemical exchange saturation transfer

GBCA – gadolinium-based contrast agent

GCE – glucoCEST enhancement

Glc - glucose

gluCEST – glutamate chemical exchange saturation transfer

glucoCEST – glucose chemical exchange saturation transfer

G6PDH – glucose-6-phosphate dehydrogenase

GLUT – glucose transporter

glycoCEST – glycogen chemical exchange saturation transfer

HBTU – *N,N,N′,N′*-Tetramethyl-*O*-(1*H*-benzotriazol-1-yl)uronium hexafluorophosphate, *O*-(Benzotriazol-1-yl)-*N,N,N′,N′*-tetramethyluronium hexafluorophosphate

H_{II} – inverted hexagonal phase

HK – hexokinase

HOBt – 1-hydroxybenzotriazole

HPDO3A – 10-(2-hydroxypropyl)-1,4,7,10-tetraazacyclododecane-1,4,7-triacetato

HRMS – high resolution mass spectrometry

IARC – International Agency for Research on Cancer

i.v. – intravenous injection

k_{ex} – exchange rate between solute protons and bulk water protons

LC-MS – liquid chromatography-mass spectrometry

Ln - lanthanide

LRMS – low resolution mass spectrometry

MP – melting point

MPS – mononuclear phagocytic system

MRI – magnetic resonance imaging

MRS - magnetic resonance spectroscopy

MSPC – 1-myristoyl-2-stearoyl-*sn*-glycero-3-phosphocholine

MTR_{asym} – magnetisation transfer ratio asymmetry

MUC1 – mucin-1

MucCEST – mucin chemical exchange saturation transfer

EG – ethylene glycol

NMR – nuclear magnetic resonance

OXPHOS – mitochondrial oxidative phosphorylation

PBS – phosphate-buffered saline

PC – phosphatidylcholine

PdI – polydispersity index

PE – phosphatidylethanolamine

PEG – polyethylene glycol

RF – radio frequency

RGD – arginylglycylaspartic acid

RT – room temperature

SAR – specific absorption rate

siRNA – small interfering ribonucleic acid

SPECT – single-photon emission computed tomography

SR – shift reagent

TFA – trifluoroacetic acid

T_m – melting transition temperature

TNF-α – tumor necrosis factor

Triton – Triton X-100

uMUC1 – underglycosylated mucin-1

Z-Ave – mean diameter

Abstract

Chemical Exchange Saturation Transfer (CEST) is an emerging MRI contrast mechanism that detects the presence of exchangeable protons, enabling natural sugars such as glucose to be used as contrast agents (glucoCEST). GlucoCEST offers a cheaper, safer and higher resolution alternative for the visualisation and staging of tumors than the current standard method, FDG-PET. Section 2 demonstrates that high concentrations of glucose can be encapsulated inside 1,2-dipalmitoyl-sn-glycero-3-phosphocholine (DPPC) liposomes to produce vesicular CEST contrast agents, from which the generated signal was concentration, temperature and pH dependent.

The use of paramagnetic metal ions to create paraCEST agents can result in superior imaging sensitivity compared to diaCEST agents. Thus, Section 3 describes work carried out on the incorporation of lanthanide ions into liposomal glucoCEST reagents in an attempt to produce paraCEST signals. The results were largely unsuccessful due to the finding that co-solvation of glucose and lanthanide-DOTA complexes in water does not cause an significantly enhanced shift difference between the hydroxyl proton resonances and the water resonance.

The *in vivo* CEST signal arising from the glucose analogue, 2-DG, is enhanced and prolonged in comparison to glucose due to its poor metabolism. Additionally, 2-DG is a glycolytic inhibitor and is thereby cytotoxic to cancer cells. Section 4 reports the encapsulation of 2-DG inside DPPC liposomes and the characterisation of both lipo-glucose and lipo-2-DG agents when exposed to a number of variables: 0-20% PBS buffer was found to have a negligiable effect on CEST signal generation; lipo-2-DG and lipo-glucose CEST signal gradually increased across the temperature range 25-37 °C; monosaccharide encapsulating DSPC liposomes were found to generate inferior signal to analogous DPPC liposomes; and smaller 2-DG liposomes appeared to give slightly greater CEST signal but this was offset by the higher internal volume and encapsulation efficiency of larger liposomes, if not corrected for.

The advantages of liposomal encapsulation of monosaccharides include prolonged *in vivo* circulation and the potential for both passive and active tumor targeting. In Section 5, an active EGFR-targeting strategy was constructed which included the synthesis of EGFR-targeting peptides, two novel maleimide lipids and several novel short-chain PEG lipids, with the hydroxyl-capped analogue proving most promising. In addition, 2-DG was found to be a poor radiosensitiser in CRC cell lines as well as in a lung cancer cell line when a successful literature procedure was followed.

Impact Statement

This research was carried out with a view to develop an improved imaging method for the diagnosis, staging and restaging of cancer to ultimately improve clinical outcomes. CEST MRI has the potential to offer a safer and cheaper alternative to the current gold standard for *in vivo* cancer imaging; FDG-PET. Clinical translation would eliminate the radiation exposure that is unavoidable for PET and/or CT techniques, enabling risk-free imaging of susceptible patient populations (young children, elderly people and pregnant women), as well as oncologic patients who require frequent imaging as part of their treatment management. Patient MRI scanning is generally cheaper than PET and does not require the expensive synthesis and handling of short-lived radiotracers, thus, the translation of glucoCEST or 2-DG-CEST could allow for dramatic reductions in the overall cost. MRI offers higher spatial resolution in comparison to PET (a decrease in voxel size by approximately a factor of 40), therefore, CEST MRI could allow smaller tumor masses to be evaluated for earlier diagnoses, more immediate monitoring of response to therapy and more effective characterisation of intratumor heterogeneity. Crucially, more hospitals are equip to carry out MRI in comparison to PET, enabling more patients to be scanned in a timely manner and creating the potential for application in developing countries as access to MRI increases.

If un-labelled natural D-glucose were to be used as the CEST contrast generating species, the logistics and infrastructure necessary to acquire and handle the contrast agent would be significantly simplified compared to the use of FDG and translation would be fast since D-glucose is already approved for human use. If 2-DG were to be employed as the CEST contrast generating species, additional signal intensity or chemotherapeutic benefits could be realised due to 2-DG's metabolic profile and glycolytic inhibition properties, respectively.

A patent application has been filed surrounding the novel sugar-encapsulating liposomal CEST contrast agents described herein, for diagnostic and theranostic purposes. If the work were to attract the attention of a company already in this space, that entity could license the IP from UCLB to further develop, obtain approval and commercialise the CEST contrast agents for clinical use.

Within academia, researchers working in a variety of different fields could benefit from the findings reported in this thesis, for example those engaging in research including: CEST signal generated by sugars or other hydroxyl group-bearing small molecules; encapsulation of high concentrations of sugars or similar small molecules inside liposomes; CEST signal generated by liposomally encapsulated species; or research requiring the quantification of glucose or 2-DG concentrations within liposomal samples by utilising the reported procedures adapted for the Glucose HK Assay® and Glucose GO Assay®.

Synthetic routes to and characterisation of novel short chain PEG lipids (DPPE-EG4-NH_2, DPPE-EG4-OH, and DPPE-EG6-OH) and novel maleimide lipids (Mal1 and Mal2) have been established and these lipids may find use in future liposome formations with various *in vivo* applications.

Finally, the finding that 2-DG did not appear to radiosensitise any of the tested CRC cell lines, nor a lung cancer cell line when repeating a literature procedure, raises concerns over the validity of previous literature and is a particularly relevant outcome to anyone interested in 2-DG as a radiosensitiser.

Contents

1 Introduction

1.1 Cancer imaging

Cancer constitutes a colossal burden on society which is increasing due to the growth and aging of the population, as well as the prevalence of established risk factors such as smoking (lung, colorectal, stomach, and liver cancer), obesity and physical inactivity (breast and colorectal cancer) and infection (liver, stomach, and cervical cancer).[1] Recently, the burden has shifted to less economically developed countries, which currently account for approximately 57% of cancer cases and 65% of cancer deaths worldwide.[1] This is due to the adoption of behaviours and lifestyles that are known to cause cancer, in combination with reduced availability of detection practices and treatments. According to estimates from the International Agency for Research on Cancer (IARC), in 2012 there were 14.1 million new cases of cancer and 8.2 million cancer related deaths worldwide.[1,2] By 2030 these figures are predicted to rise to 21 million (50% increase) and 13 million (60% increase), respectively.[2,3]

In 2000, Hanahan and Weinberg published a highly cited review describing the hallmarks of cancer.[4] The six hallmarks they identified include: uncontrolled proliferative signalling, insensitivity to growth suppressors, evasion of apoptosis, limitless replicative potential, induction of angiogenesis, and tissue invasion and metastasis.[4] Due to the continuous progression of cancer research over the following decade, in 2011, Hanahan and Weinberg extended their list to include two additional traits; reprogramming of energy metabolism and evasion of immune destruction.[5] They suggest that most, if not all, cancers share these common alterations to cell physiology, albeit *via* a myriad of different mechanisms. Arguably the most fundamental characteristic of cancer cells is their ability to sustain chronic proliferation. In their more recent review, Hanahan and Weinberg consider that chronic proliferation is not just the product of deregulated control over cell division, but that it is also governed by corresponding adjustments in energy metabolism. Under aerobic conditions, normal cells rely primarily on mitochondrial oxidative phosphorylation (OXPHOS) to generate adenosine triphosphate (ATP) for energy, whereas under anaerobic conditions, glycolysis is favoured. The efficiency of ATP production *via* glycolysis is 18-fold lower than for OXPHOS.[5] Cancer cells utilise glucose at enhanced rates compared to normal cells to generate ATP for rapid cell growth. This manifests in a seemingly unlikely enhanced dependence on glycolysis (even in the presence of oxygen) for the production of ATP, a phenomenon called the “Warburg effect” that was first described by Otto Warburg in the 1920s.[6] To facilitate enhanced glucose uptake, malignant tumors typically have elevated levels of glucose transporters

(GLUTs), as well as hexokinases (HKs).[7] GLUT dysregulation is an obvious target for cancer because the influx of glucose to cells is the first step in the glucose metabolism process. Upregulation of HKs provides cancer cells with an advantage because the first step of glucose metabolism is phosphorylation by hexokinase to produce glucose 6-phosphate. Once glucose is converted to glucose 6-phosphate, it becomes trapped inside the cell due to increased polarity, preventing it from exiting the cell and maintaining its transmembrane gradient.[8] The advantages of the metabolic switch to glycolysis for cancer cells are not fully understood but theories include the ability to sustain high growth rates in hypoxia,[9] and that high glycolysis enables the diversion of glycolytic intermediates into biosynthetic pathways such as those generating nucleosides, amino acids and lipids, which in turn facilitate the biosynthesis of macromolecules and organelles required for the assembly of new cells.[10] Supporting this theory is the finding that a Warburg-like metabolism is present in embryonic tissue and other rapidly dividing cell populations.[11] It is beyond the scope of this thesis to review the major hallmarks of cancer in more detail, for in depth summaries please see publications by Hanahan and Weinberg.[4,5]

Cancer treatment and outcome depend largely on imaging techniques to provide accurate diagnosis, staging and restaging of the disease. Early detection *via* imaging is one of the major ways in which cancer mortality and management costs can be reduced. There are multiple biomedical imaging techniques that can be employed throughout all phases of cancer management to provide morphological, structural, metabolic and functional information. Additionally, hybrid imaging techniques can be used to provide complementary information and further improve staging and therapeutic strategy selection.

1.1.1 FDG-PET

The current standard method for imaging tumors *in vivo* is [^{18}F]-fluorodeoxyglucose positron emission tomography (FDG-PET). Positron emission tomography (PET) imaging detects positrons originating from the decay of systemically administered radiotracers containing isotopes such as ^{11}C, ^{13}N, ^{15}O or ^{18}F.[12,13] A considerable number of cancer-relevant metabolic substrates, drugs, and antibodies have been radiolabelled for use as PET imaging agents.[13] A benefit of PET is that naturally occurring C, N or O atoms in biomolecules can be substituted with their radionuclide counterparts to label them without impacting their biological activity or pharmacokinetics. Fluorine is not a normal element in biological systems, but it can often replace either a hydrogen atom or a hydroxyl moiety.[14] This differentiates PET from other techniques where relatively large imaging "handles" are attached to target molecules to label them, such as biotin, leading to significant modification of their *in vivo* behaviour. The most important advantage of PET is that *via* this labelling mechanism it can generate information about metabolism, receptor or enzyme function and biochemical mechanisms within living tissue, which is in contrast to techniques that mainly provide detailed anatomical images (computed tomography, X-ray, ultrasound). Additionally, PET is one of the most sensitive clinical imaging techniques with radiolabelled probes that can be detected at picomolar concentrations.[15]

When PET radionuclides undergo beta decay in the body they emit a positron, which is a subatomic particle that is equal in mass but opposite in charge to an electron.[16] Emitted positrons travel a certain distance (the annihilation distance) before colliding with an electron, producing two 511 keV photons that travel away from each other at an angle of 180°.[13,17] The PET scanner surrounding the patient encases a circular ring of scintillation crystals which are used to detect photons. Only when two antiparallel photons are coincidentally detected by a pair of opposing crystals is a signal counted. The spatial resolution of PET is partially governed by the annihilation distance because the position where the annihilation photons are created is different to the exact location of the parent nucleus. Therefore the maximal resolution of clinical PET scanners ranges between 5-8 mm^3.[16] The annihilation distance is known to be affected by the specific radionuclide used and the tissue type, for example less dense tissues such as the lungs have longer annihilation distances, resulting in lower resolution.[16,18] The body attenuates 511 keV photons, with only 10% successfully penetrating through 25 cm of solid tissue.[16] Thus, it is estimated that approximately 1 in 2000 photons produced at the cancer site are detected by PET and that current PET technology is only capable of detecting solid tumors ≥ 10^9 cells in size.[16]

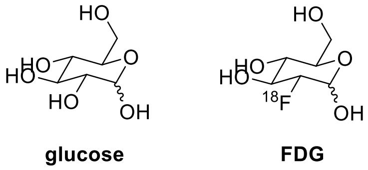

Figure 1. The structure of the naturally occurring sugar, D-glucose (left) and the radiolabelled probe, [^{18}F]-fluorodeoxyglucose (right), which is used in FDG-PET imaging.

FDG-PET requires the administration of a radioactively labelled glucose analogue, 2-deoxy-2-[^{18}F]-fluoro-D-glucose (FDG) (Figure 1). FDG-PET exploits the previously described high glucose avidity of tumors, known as the Warburg effect. At the molecular level, FDG enters cells *via* GLUTs and becomes phosphorylated by HKs. The product of this, FDG-6-phosphate, cannot be further metabolized *via* any metabolic pathway, including glycolysis, therefore it accumulates inside cells.[7] The abnormally high glucose uptake by tumors forms the basis of the ability of FDG-PET to distinguish between cancerous and benign tissue, as well as enabling identification of metabolic abnormalities before morphological alterations occur to achieve early diagnoses.[19]

90 years on from the discovery of the Warburg effect it is known that it is not consistent across all types of cancer, with various tumor populations relying on different bioenergetic alternations to fulfil their high energy requirement.[6] Likewise, the dysregulation in expression of GLUTs (predominantly GLUT1 and GLUT3) and HKs (I and II) differs greatly between tumor types.[7,8] It follows that the utility of FDG-PET is reduced for tumors with low overall glucose metabolic rate or relatively low GLUT expression. For example, prostate cancer and renal clear cell carcinoma cannot be reliably detected using FDG-PET.[17,20] Radiotracers other than FDG have shown more promising results with several of these non–FDG-avid tumors, but these are still in the early stages of development.[17] Conversely, not all FDG-avid tissue is malignant; the brain and sometimes myocardial or inflamed tissue can produce intense PET signals. It is a common problem that FDG-PET can overestimate the size of a tumor.[6] A potential explanation for this could be the presence of a phenomenon called the reverse Warburg effect. The reverse Warburg effect, first proposed by Pavlides *et al.*,[21] describes how epithelial cancer cells can induce the Warburg effect (aerobic glycolysis) in neighbouring stromal fibroblasts. The cancer-associated fibroblasts then secrete metabolites formed during glycolysis such as lactate and pyruvate, which are taken up by epithelial cancer cells and recruited by mitochondria to enable ATP production *via* more efficient OXPHOS, helping to fuel cancer cell replication.[21] The glycolytic surroundings of the tumor is what could lead to overestimation of tumor size by FDG-PET.

Nevertheless, the shortcomings discussed thus far are minor and FDG-PET is undeniably an extremely useful technique that works well for most clinically important malignant tumors. Furthermore, the integration of PET and computed tomography (CT) (PET/CT) offers major interpretive advantages by allowing accurate anatomical localisation of the lesions detected by FDG-PET.[19] However conjugation with CT does not solve the major drawbacks of FDG-PET, such as the administration of a radioactive dose to patients and high expense. Even small doses of radiation can increase an individual's risk of malignancy and this risk is further increased in childhood and early adult exposure.[22] PET typically delivers a radiation dose of 3 to 5 times the amount a person would receive in one year due to naturally occurring background radiation, whereas PET/CT delivers a dose of 5 to 10 times the average annual background radiation.[17] PET is a very expensive modality, requiring not only a million-dollar-plus PET scanner but also expensive equipment and highly trained personnel. A challenge of PET for chemists is the rapid syntheses that are required for radiotracers due to the introduction of short-lived positron-emitting isotopes. Of the four isotopes discussed, ^{15}O has the shortest half-life of 2 minutes and ^{18}F has the longest at 110 minutes.[13] Therefore the probes must be synthesised, purified, analysed, transported and used in quick succession. Due to short half-lives of the isotopes, radiotracers are often prepared in close proximity to cyclotrons (which are used to produce radioisotopes). As a result of this, modern PET facilities often house PET scanners, cyclotrons and radiosynthesis laboratories all under one roof, further increasing the cost of the technique. Nevertheless, thousands of PET scanners are in service around the world.

1.1.2 MRI

Magnetic resonance imaging (MRI) is one of the most important diagnostic imaging tools available in clinical medicine today, producing high resolution images of soft tissue anatomy by measuring the relaxation processes of protons largely belonging to water molecules in biological systems. The spinning of a ^{1}H nucleus creates a weak magnetic dipole. In a thermodynamic state, all the nuclear dipoles are randomly oriented giving rise to a net magnetic moment (M) of zero. During an MRI scan an external magnetic field, B_0, is applied which causes the magnetic dipoles of ^{1}H nuclei to align with the field in two separate, quantised energy states. Subsequently, a resonant radio frequency (RF) transverse pulse (B_1) is applied perpendicular to B_0. This causes resonant excitation of the magnetic moment precession into the perpendicular plane, i.e. M tilts away from B_0.[23] Once the RF pulse is removed, the dipoles return to their previous position prior to RF disruption causing M to be parallel with B_0 again, a process referred to as relaxation. The relaxation of the dipoles takes place *via* two unique and co-dependent relaxation processes termed T1 (longitudinal relaxation parallel to B_0) and T2 (transverse relaxation along an axis perpendicular to B_0).[12] The relaxation of ^{1}H nuclei back to the resting state produces a loss of energy in the form of an emitted RF signal, this signal referred to as the *free-induction decay* (FID) response signal. FIDs are detected by receiver coils surrounding the patient and must be encoded for each dimension to construct an MRI image.[23] The inherent contrast in an MR image is predominantly due to regional differences in the relaxation rates, T1 and T2. Conventional MRI contrasts are based on the differences in T1 and T2 belonging to different body tissues under a static magnetic field and various RF pulses.

There are no known biological hazards of MRI, unlike PET, X-ray and CT which deliver a dose of ionising radiation to patients, MRI uses radiation in the radiofrequency range which is ubiquitous in everyday life and does no damage as it passes through tissue. However, the use of MRI can be limited in patients with metal implants such as pacemakers, internal defibrillators or other magnetic implants. RF radiation can cause slight tissue heating (1-2 °C) but the amount of energy absorbed per mass of tissue, defined as the specific absorption rate (SAR), is monitored and strictly controlled in the clinic.[24] A major advantage of MRI is the ability to provide three-dimensional images with exquisite spatial resolution; the maximal resolution is approximately 1 mm^3.[16]

Since the observation that nuclear magnetic relaxation times differ between normal tissue and tumor tissue,[25] MRI has played an important role in the visualisation of cancer. Over the years, higher field strengths, optimised pulse sequences and better coil design have facilitated tumor imaging.[12] In addition, contrast agents have been developed to further enhance image contrast and enable more accurate detection, diagnosis and monitoring of response to treatment.

1.1.2.1 MRI contrast agents

The intrinsic contrast produced by variations in T1 and T2 and the alterations induced by pathology are often too subtle to enable sensitive and specific diagnosis of disease.[26] Therefore, for most clinical applications it is common to administer an exogenous contrast agent (CA) either intravenously, orally or intra-articularly, to increase the contrast of specific tissue regions. MRI CAs can be classified as T1 or T2 modifying, depending on their relative effect on the two relaxation rates belonging to the surrounding water protons. The majority of clinically used CAs for MRI imaging of tumors are low molecular weight gadolinium(III) (Gd) chelates that reduce the T1 relaxation time and generate positive image contrast.[27] Gadolinium has 7 unpaired f electrons, giving rise to a large magnetic susceptibility, long electronic relaxation times and a relatively rapid water exchange rate, all of which are desirable qualities for a T1 contrast agent.[28] Various superparamagnetic iron oxide nanoparticles have been approved as T2 altering MRI contrast agents, however they were not well received by radiologists and several have now been discontinued, potentially due to undesirable negative contrast generation or prolonged *in vivo* contrast (up to several months).[27,29]

It is estimated that more than 200 million doses of gadolinium-based contrast agents (GBCAs) have been administered worldwide.[29] Small molecule GBCAs can be categorised into linear and macrocyclic chelates. In both cases the ligands are based on a polyaminocarboxylate motif, for example, linear diethylene triamine pentaacetic acid (DTPA) and cyclic 1,4,7,10-tetraazacyclododecane-1,4,7,10-tetraacetic acid (DOTA), the structures of which are shown in Figure 2.

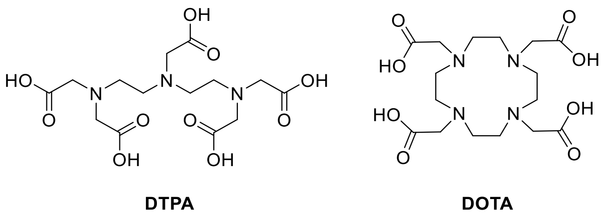

Figure 2. The structures of linear chelator diethylene triamine pentaacetic acid (DTPA) and cyclic chelator 1,4,7,10-tetraazacyclododecane-1,4,7,10-tetraacetic acid (DOTA).

Macrocyclic chelates have demonstrated greater kinetic and thermodynamic stability than linear alternatives.[27,29] High kinetic and thermodynamic stability is crucial for these complexes as free Gd^{3+} ions, as well as other trivalent lanthanide cations, are highly toxic due to acute interference with calcium channels and protein binding sites.[30] Consequently, patient doses of GBCAs are limited, which can lead to issues with sensitivity. Studies have shown that linear and charge-neutral GBCAs having a higher propensity to liberate Gd *in vivo*, relative to macrocyclic GBCAs, which correlates with the incidence of nephrogenic systemic fibrosis in patients with renal insufficiency.[27,29] Thus, the use of linear GBCAs has been discouraged in this patient group which has almost completely eliminated the incidence of nephrogenic systemic fibrosis.[29] A more recent concern is the discovery of Gd accumulation in the brain associated with multiple GBCA injections.[29] It is currently unclear whether the Gd is free or bound and no pathological consequences have been documented thus far. Nonetheless, long-term sequestration of any toxic metal in a sensitive structure such as the brain is concerning. As a result of this, in 2017 the European Medicines Agency (EMA) unauthorised the use of three multipurpose linear GBCAs (Magnevist®, Omniscan® and OptiMark®) and restricted the use of the other two previous approved linear GBCAs, Primovist® and MultiHance®, to liver imaging only.[31] The structures of GBCAs currently approved for use in Europe are shown in Figure 3.

Small molecule GBCAs have relatively low relaxivity, fast renal clearance and extravasate from the blood into both normal and tumor tissue in a non-discriminatory manor.[27,32] Relaxivity is defined as the ability of magnetic compounds to increase the relaxation rates of the surrounding water proton spins.[27,33] Attempts have been made to design small molecule GBCAs with enhanced relaxivity by enabling coordination of more than one inner sphere water molecule, however, reducing the number of donor atoms in the chelating ligands decreases the thermodynamic and kinetic stability and raises concerns over toxicity.[32] Instead, attention has been turned to the development of a variety of macromolecular GBCAs, the majority of which are produced by conjugating

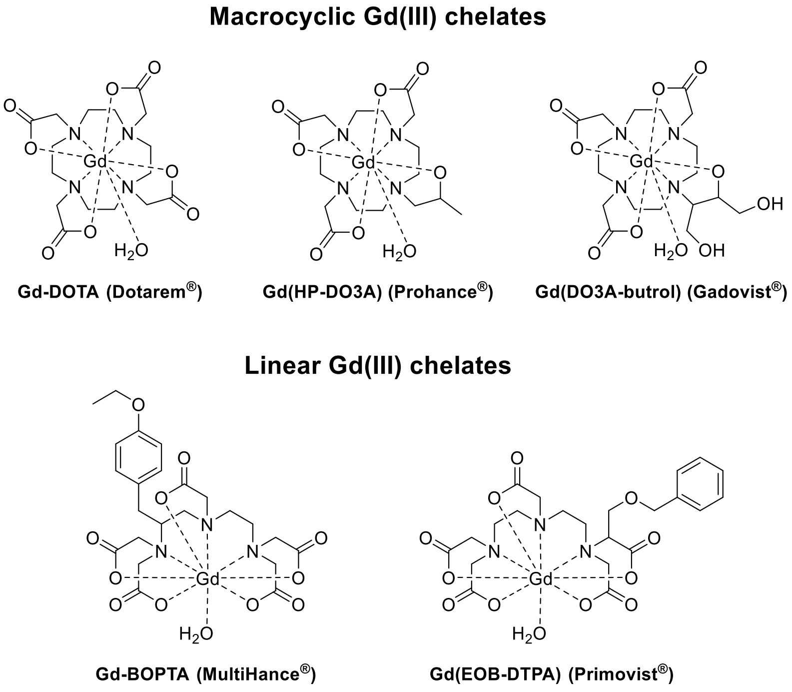

Figure 3. Structures of MRI GBCAs approved by the EMA for clinical use in Europe.

Gd-DOTA or Gd-DTPA to biocompatible macromolecules such as polymers, proteins, dendrimers and liposomes.[27,32] Examples of macromolecular GBCAs include; polylysine-(Gd-DTPA), Dextran-(Gd-DOTA) and Vistarem® (Figure 4).[27]

In general, attaching Gd chelates to larger macromolecules slows down the rotational motion of the complex, thereby enhancing relaxivity.[34] The increased size of the macromolecular systems enhances blood circulation time and produces passive, preferential accumulation at the tumor site due to leaky vasculature and poor lymphatic drainage, a phenomenon called the enhanced permeability and retention effect (the EPR effect, see Section 1.4.1.1).[35] In addition, the tumor retention time is increased, giving rise to superior tumor-to-background contrast over time.[35] Active targeting of GBCAs could be achieved by conjugating Gd complexes directly to targeting moieties such as antibodies or peptides, or by including them in a larger structure.[27] Importantly, macromolecular structures can be heavily loaded with Gd to significantly enhance sensitivity. For example, a typical synthesis of Gd-labelled human serum albumin protein yields 20-35 Gd per molecule *via* chemical conjugation to lysine residues, whereas polyaminoacids such as polylysine exhibit more than 500 available sites for Gd conjugation when synthesised to a similar molecular weight as albumin.[27,32] Even greater improvements in Gd loading can be achieved with nanoparticles, for example liposomes can either encapsulate chelated Gd or Gd chelates can be covalently anchored to the liposome bilayer. Encapsulating Gd complexes in the aqueous interior of liposomes

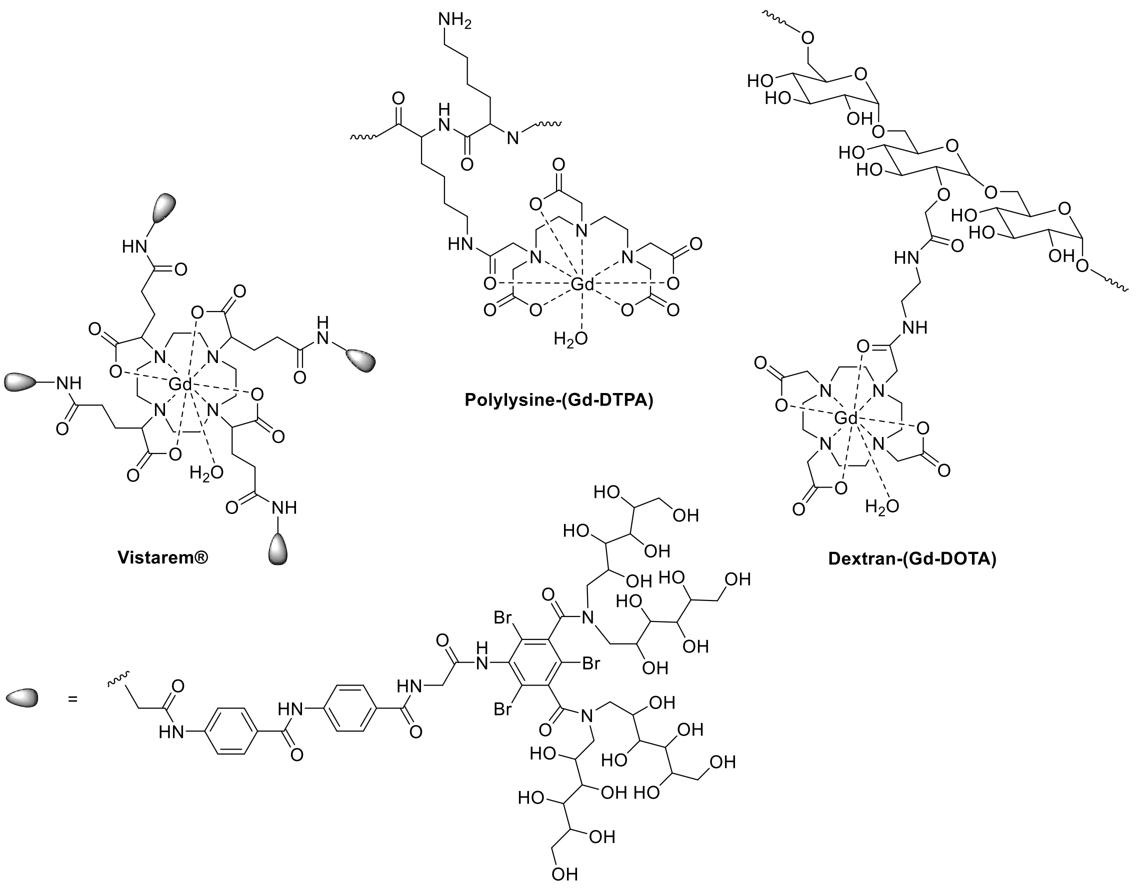

Figure 4. The chemical structure of some examples of reported macromolecular GBCAs.

enables exquisitely high loading capacity, however relaxivity has been found to decrease due to impaired exchange of water with Gd, a consequence of the physical barrier imposed by the bilayer.[32,36] This can be partially overcome by increasing the surface-to-volume ratio (i.e. decreasing the liposome diameter), although even liposomes with a 100 nm diameter exhibit a relaxivity (per Gd) that is 62% lower than free chelated Gd in solution.[32,37] Decoration of the liposome surface with Gd chelates gives easy access to bulk water and increases relaxivity (per Gd) due to slowed rotational correlation time, however loading capacity is less extensive.[32] Not surprisingly, dual mode liposomal GBCAs with core-encapsulated and membrane-bound Gd chelates demonstrate higher particle-based T1 relaxivity *in vitro* and *in vivo* compared to liposomes exhibiting a single Gd loading technique.[38] The high Gd concentration per unit liposome could allow administration of lower doses and produce increased contrast sensitivity. However, the discussed macromolecular Gd-based MRI probes have generally only been employed *in vitro* or, at most, in preliminary animal studies.

More recently, there has been a growing interest in paramagnetic CAs employing other lanthanide ions (see Section 1.2.1.3.1) in an attempt to overcome some of the shortcomings of Gd-based CAs. For example, dysprosium(III) (Dy) has been used in MRI to produce negative contrast *via* shortening of the T2 relaxation times of surrounding ^{1}H nuclei.[39] Clinical MRI is moving towards higher magnetic field strengths and under these conditions, commercial Gd(III) CAs demonstrate poor water relaxivity. In some Dy(III) complexes water molecules have long residence times and exhibit efficient T2 relaxivity, therefore these Dy complexes may produce CAs that perform better at higher magnetic field strengths.[39]

1.1.2.2 Magnetic resonance spectroscopy

While traditional MRI can elucidate the exact location and dimensions of a tumor with great precision, it is unable to convey any biochemical information. To evaluate disease progression or response to treatment based on just tumor volume has been shown to be inadequate, as this can only portray delayed responses to therapy with no indication of molecular changes, such as those involved with metabolism. To overcome this, magnetic resonance spectroscopy (MRS) was developed which utilises novel MR methods to detect molecular signatures at the cellular and gene expression levels.[40] MRS techniques are based on the principle that it is possible to detect RF signals generated by the magnetic nuclear spins of MR active nuclei such as ^{1}H, ^{31}P, ^{13}C, and ^{19}F, when they precess in an external magnetic field B_0.[41] Detection is possible after excitation with an RF pulse transmitted at the correct magnetic resonance frequency (which is linearly dependent on B_0 and on the gyromagnetic ratio of the nucleus).[41]

The most widely available MRS method is ^{1}H MRS, it is FDA-approved and does not require additional hardware beyond what is already required for MRI.[42] Furthermore, the ^{1}H is abundant in most biomolecules and the nucleus offers almost 100% availability of the isotope. Unlike MRI, which maps the distribution and interaction of hydrogen atoms in water molecules with the surrounding tissue, ^{1}H MRS can analyse signal from proton nuclei belonging to other molecules (water and fat suppression techniques must be employed), which can be identified by their characteristic resonance frequencies.[41] Thus, the output of MRS is a spectrum arraying the types and quantity of chemical environments present.[41,43] When MRS is carried out over a large volume which is divided into multiple smaller voxels, with each giving rise to a spectrum, a spatial distribution map of various biomolecules can be constructed. This technique is referred to as magnetic resonance spectroscopy imaging (MRSI).

^{1}H MRS has been widely applied to detect metabolic changes in various cancers as well as for other applications such as investigating metabolic disorders and neurobiology.[40,43] The main diagnostic value of ^{1}H-MRS in cancer has been the detection of elevated levels of choline-containing compounds or total choline.[40] ^{1}H MRS signals from water-soluble choline metabolites arise between 3.2 and 3.3 ppm due to the nine chemically equivalent protons in the trimethyl ammonium groups (Figure 5).[24,41] Choline and choline-containing compounds are involved in the formation of phosphatidylcholine (PC), the primary phospholipid of cell membranes, thus an increased total choline signal is indicative of increased membrane turnover.[15,24] The ^{1}H signal from total choline is significantly elevated in almost every tumor type investigated, which has been shown to correlate with malignancy.[24,44,45] Choline ratios in comparison to other MRS detectable metabolites have been used to classify cancer aggressiveness, for example, choline:N-acetylaspartate ratios have been used to differentiate low and high grade astrocytomas.[46]

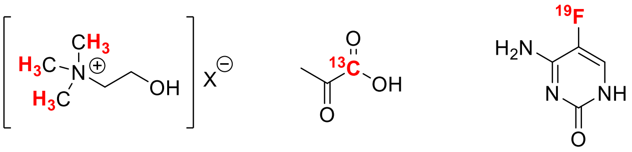

Choline **^{13}C-pyruvate** **^{19}F-fluorocytosine**

Figure 5. Chemical structures of molecules used in MRS imaging. The nuclei used for MRS detection are highlighted in red.

^{31}P MRS can be used to visualise phosphorylated compounds *in vivo* which are present at greater than roughly 100 µM concentration,[47] such as phosphocreatine, nucleotide triphosphates (including ATP), phosphomonoesters (including phosphocholine) and phosphodiesters (such as various PCs).[40] For example, ^{31}P MRS has visualised increased phosphomonoester concentrations in breast cancer tissue compared to healthy breast tissue, which decreases in response to chemotherapy.[47,48] However, the clinical utility of ^{31}P MRS is hampered by low signal intensity due to the low concentrations of phosphorous containing molecules *in vivo* and the need for long acquisition times.[15]

Since the isotopic abundance of ^{13}C is low (1.1% of natural carbon on Earth), ^{13}C MRS is typically used to detect exogenously administered hyperpolarised ^{13}C-laballed substrates, increasing the sensitivity of the technique up to 10,000-fold.[24,41] Biomolecules involved in metabolism can be ^{13}C-labelled, for example glucose, pyruvate and lactate, have been used to image metabolic fluxes in real-time.[41,49] To date, ^{13}C-labelled pyruvate has been most widely used in preclinical and clinical studies (Figure 5).[40] One of the main biochemical consequences of the Warburg effect is increased conversion of pyruvate to lactate. The signal arising from ^{13}C-labelled lactate following administration of ^{13}C-

labelled pyruvate has been shown to increase with cancer progression and reduce in response to therapy in a number of cancer models including lymphoma, breast cancer, prostate cancer and glioma.[40,49–51] Clinical translation of this technique would allow diagnoses to be made quickly whilst avoiding invasive biopsies, thus, early clinical trials have been carried out with ^{13}C-labelled pyruvate on prostate cancer patients and brain tumor patients.[51,52]

^{19}F MRS has found use in investigating the pharmacokinetic properties of drugs as the ^{19}F nucleus provides relatively high sensitivity combined with the absence of background signal. For example, the ^{19}F-labelled chemotherapeutic prodrug, 5-fluorocytosine (Figure 5), has been extensively studied *via* ^{19}F MRS to determine the pharmacokinetic profile and *in vivo* conversion to the active drug, 5-fluorouracil.[53,54]

MRS techniques employing nuclei other than ^{1}H have failed to find clinical utility thus far due to being cost-inefficient and technically difficult, for example, standard MRI coils cannot be used and special coils tuned to the desired nucleus must be installed instead.[24] Although ^{1}H MRS is approved and can be carried out on conventional MR systems, its use is still far from routine. The primary drawback is the low sensitivity that arises as a result of low concentrations of target molecules *in vivo* and spectral overlap of signals from different nuclei, making most biomolecules difficult to image at clinical field strengths (the frequency difference between signals from protons with different chemical shift increases with the magnetic field strength).[15,42] This manifests in the need for long acquisition times as many averages are required to achieve sufficient signal-to-noise ratio.[42] Additionally, low sensitivity restricts MRS to the analysis of regions of interest that are much larger than those used in MRI, therefore the spatial resolution of MRS is in the range 1-10 cm^3, which is approximately 1000 times larger than what is typically achieved by MRI (1-10 mm^3).[55]

1.2 CEST MRI

Chemical exchange saturation transfer (CEST) is an emerging MR technique that enables the imaging of certain compounds at concentrations that are too low to impact the contrast of typical MRI and too low to be detected *via* MRS at typical imaging resolution.[42] CEST enables indirect detection of compounds with exchangeable protons at millimolar to micromolar concentrations *via* the water signal utilised in MRI.[56,57] In MR, saturation is a temporary state in which a tissue exhibits no net magnetization. This can be exploited to produce image contrast by exciting the sample in a way that causes only certain tissue types to become saturated, resulting in decreased signal or total absence from the image. For example, this is how fat suppression techniques are carried out, by saturating at the resonance frequency of the methylene protons in triglyceride molecules.[42] In CEST imaging, magnetisation is transferred from target molecules to water molecules *via* chemical exchange and the resultant reduction in water signal can be conveniently detected by standard MR imaging sequences.[42] Thus, it is required that CEST contrast agents possess ^{1}H nuclei that are able to exchange with water, such as hydroxyl, amine or amide protons.

The first condition for CEST signal generation is that the exchangeable protons belonging to an endogenous or exogenous target solute must resonate at a distinct frequency to the bulk water protons in an applied magnetic field. Figure 6 shows the basic principles of CEST signal generation, using a single hydroxyl proton on glucose as an example of a target exchangeable proton. Figure 6a depicts a simplified ^{1}H NMR spectrum displaying a large water peak at 4.7 ppm and a single glucose hydroxyl resonance at 6.7 ppm (in reality the 5 hydroxyl protons have five distinct resonances). The chemical shift difference ($\Delta\omega$) of 2 ppm allows the hydroxyl proton to be selectively saturated by a narrow band with radiofrequency pulse centered at its resonance frequency. In a ^{1}H NMR spectrum this causes a complete loss or a near complete loss of the exchangeable proton signal that was previously visible (Figure 6b).

The saturated hydroxyl protons undergo chemical exchange with bulk water protons, thereby transferring their saturated magnetisation to water, giving rise to a small reduction in the large water signal (Figure 6c). Given the low solute concentration (µM-mM range) comparative to the water protons (approximately 110 M), in reality a single exchange is too insignificant to produce any measurable effect on the water signal.[58] However, during chemical exchange each saturated hydroxyl proton is replaced by a non-saturated proton from water, this new hydroxyl proton is then saturated by the narrow bandwidth RF pulse and exchanged, leading to further reductions in the water signal amplitude (Figure 6d-e). Thus, prolonged saturation periods provide an amplification process for the small solute signal and give rise to measurable decreases in the water signal.[58] If this exchange takes places 100 times, then the detectability of the solute (through the reduction of water signal) is amplified by a factor of 100 compared to other methods. This is the crux of CEST, the continuous process of re-saturation and exchange enables detection of target molecules with sensitivity that is increased by two orders of magnitude or more, when compared to techniques such as MRS which have no inbuilt amplification process.[42]

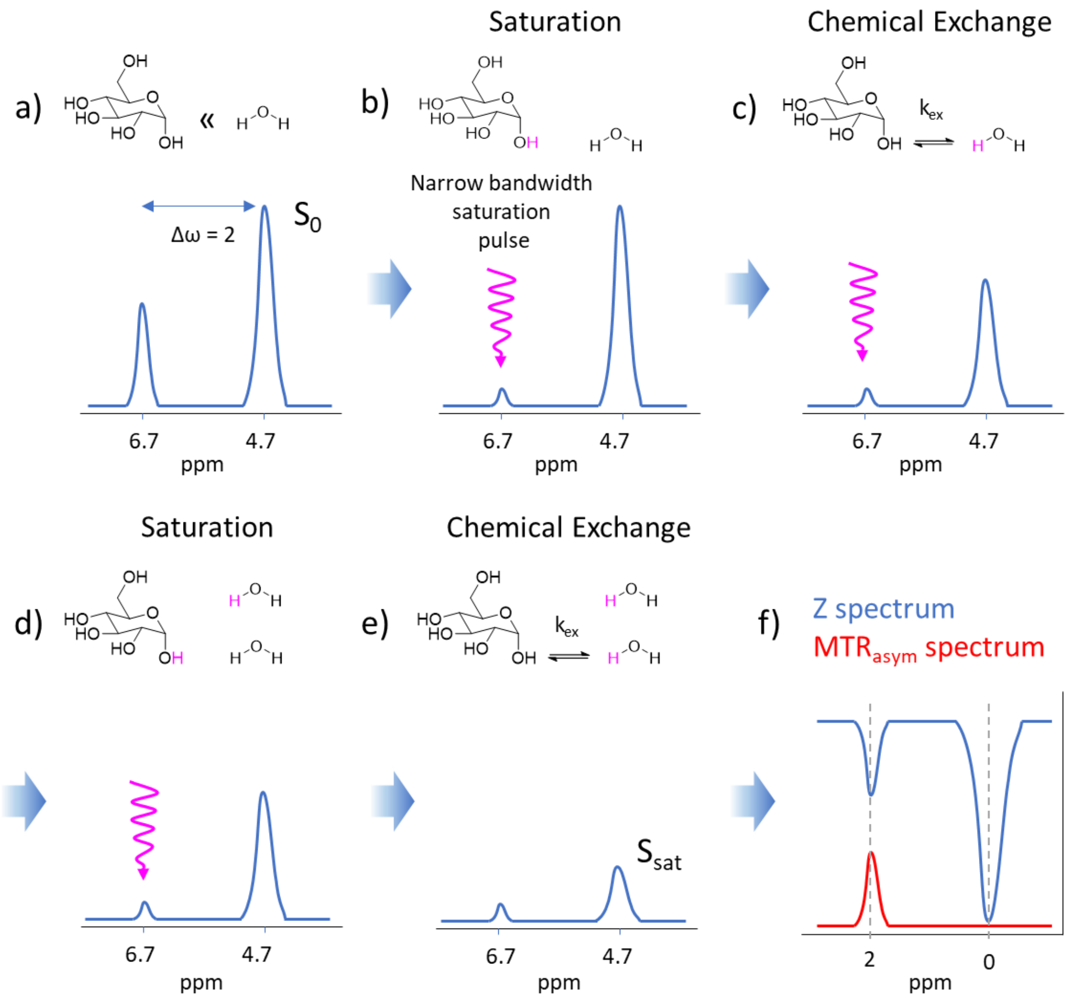

Figure 6. The basic principles of CEST, using a single glucose hydroxyl signal at 6.7 ppm as an example. S_0 is the magnitude of the water peak prior to the application of a narrow bandwidth RF pulse centred at the hydroxyl proton resonance frequency, whereas S_{sat} is the magnitude of the water peak at the end of the saturation period.

The results of CEST experiments are presented in a so-called Z or CEST spectrum. To obtain a Z spectrum a series of narrow bandwidth RF pulses are applied across a certain range of ppm values and the resultant amplitude of the water peak (S_{sat}, obtained after RF saturation) normalised as a proportion of the water signal prior to irradiation (S_0, obtained before RF saturation) is plotted as a function of the RF saturation pulse frequency (Figure 6f, blue).[58] This creates what looks like an upside down spectrum in which the large water signal is centered at 0 ppm. There are peaks at the resonance frequencies (with respect to water) at which exchangeable protons participating in the CEST mechanism are present. The magnitude of these peaks represents the extent to which that exchangeable environment was able to transfer saturation to the bulk water.

In CEST techniques, asymmetry analysis is carried out which converts a Z spectrum into a magnetisation transfer ratio asymmetry (MTR_{asym}) spectrum. The MTR_{asym} is plotted as the difference in signal on either side of the water peak, which is centred at 0 ppm (Figure 6f, red). MTR_{asym} analysis effectively removes the large water peak from the spectrum, enabling facile identification of CEST environments. Thus, MTR_{asym} analysis provides a clearer representation of the frequencies at which exchangeable protons resonate with respect to water, the magnitude of which changes in a concentration dependent manner.[58]

When RF saturation pulses are applied, two additional processes can decrease water signal magnitude aside from the transfer of saturation from target solutes to water; magnetisation transfer contrast and direct water saturation.[42] Magnetisation transfer contrast describes a phenomenon in which off-resonance RF pulses can partially saturate proton pools in semi-solid macromolecules (e.g. membranes or myelin sheets) that have large dipolar couplings and very short T2.[59] The width of these resonances are so broad that they can even be irradiated at frequencies extending beyond the normal proton NMR spectral range (0-10 ppm where water is approximately 4.75 ppm).[59] The saturation can be transferred rapidly through the semi-solid matrix *via* fast intramolecular dipolar transfer and is eventually transferred to water protons.[58,59] Direct water saturation refers to the fact that RF irradiation centered at a specific metabolite resonance frequency is never perfect and has side lobes, so there is an inevitable effect on the water proton magnetisation to some degree.[42] This effect is more prominent when the solute protons resonate close to the water frequency or when using a strong B_1.[59] For the most part, the MTR asymmetry analysis removes the effects of these two non-CEST contributions. However, it is not perfect because the assumption that their contributions are perfectly symmetrical about the water peak is not always correct, particularly *in vivo* but also *in vitro*.[58]

In order to generate successful CEST contrast the exchange process between solute protons and water protons must be in the slow to intermediate regime on the NMR time scale.[42,58,60] This requirement can be roughly described by $k_{ex} < \Delta\omega$, where the exchange rate K_{ex} must be smaller than the difference in chemical shift between the solute ^1H nuclei and water ($\Delta\omega$) to enable the two groups to be distinguished between.[42] Thus the contrast produced by an agent depends on the exchangeable proton concentration of the agent and the rate of exchange of those protons with water.[58]

1.2.1 CEST contrast agents

A wide variety of low molecular weight molecules, macromolecules and nanoparticles can be used as CEST CAs. Any compound with exchangeable protons can be used providing the slow to intermediate exchange regime is obeyed. CEST CAs can be grouped as diaCEST or paraCEST agents, a classification that relates mostly to the size of their chemical shift difference with water. For diaCEST compounds this range is typically 0-7 ppm away from the water peak (hydroxyl, amine, amide and imino groups), but this can be extended up to 19 ppm through hydrogen bonding.[58] Whereas, paraCEST agents have much larger frequency differences with respect to water, often lying more than 100 ppm from bulk water.[60] ParaCEST agents are exogenous and have to be administered, whereas many diaCEST agents can be endogenous.

1.2.1.1 DiaCEST

In 2000, Ward *et al.* were the first to demonstrate that exchangeable protons belonging to a series of naturally occurring biomolecules and small diamagnetic molecules could be selectively saturated and undergo subsequent exchange with bulk water protons to allow their indirect detection *via* measurable decreases in the water signal of an MRI.[61] They proposed that this new class of CEST-based CAs can be selectively “turned on” and “turned off” by presaturation pulses and could offer advantages over conventional metal-based CAs that operate *via* relaxivity-based contrast mechanisms. A series of sugars, amino acids, metabolites and other small diamagnetic molecules were evaluated using a technique that has become the standard method of investigating the CEST capabilities of a compound.

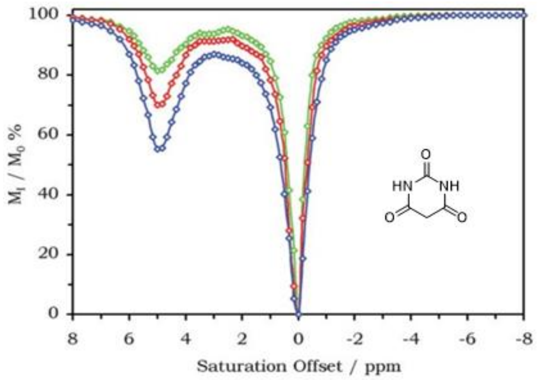

Figure 7. Z spectra of barbituric acid solutions at concentrations of 31.25 mM (green), 62.5 mM (red) and 125 mM (blue). Spectra were measured at 300 MHz, 37 °C and pH 7.0. Adapted from Woods *et al.*[62]

The Z spectra obtained by Ward *et al*. for barbituric acid (BA) at varying concentrations are shown in Figure 7.[61] The direct consequence of bulk water proton saturation can be seen at 0 ppm and the CEST effect arising from saturation and subsequent exchange of the –NH protons of BA can be observed at +5 ppm. Figure 7 demonstrates the ability of this kind of diamagnetic agent to modify the signal from bulk water and thereby act as a contrast media for MRI. However, it also demonstrates the primary challenge of exploiting diaCEST contrast produced by low molecular weight compounds; the concentration of agent required to produce a significant decrease in the water signal is relatively large. BA concentrations as high as 15 mM only reduce the intensity of the water signal by 5%.[61] This is equivalent to approximately 100 times the concentration of conventional gadolinium agents currently administered to create contrast in MRI.[62] Nonetheless, a plethora of endogenous and exogenous low molecular weight molecules have been imaged using CEST techniques including glutamate and creatine (*via* -NH_2 protons),[42,63,64] glycosaminoglycan, myo-inositol, glycogen and glucose (*via* -OH protons),[42,65] and peptides and proteins (*via* amide -NH protons).[66] The nomenclature for CEST contrast generated by a specific biomolecule is as follows; gluCEST for the detection of glutamate,[63] gagCEST for glycosaminoglicans,[67] glycoCEST for glycogen,[68] and so on.

CEST contrast can be generated by large groups of compounds rather than a specific biomolecule to achieve greater sensitivity, an extreme example of this is a CEST technique called amide proton transfer (APT). Amide protons have a chemical shift that is approximately 3.5 ppm downfield of water, which corresponds to the amide resonance around 8.3 ppm in an NMR spectrum.[69] APT detects the signal from all endogenous amide protons, the major contributors to which are proteins and peptides.[69,70] The exchange rate between the amide protons of mobile peptides and bulk water protons *in vivo* is suitably low for CEST detection (approximately 20-30 Hz).[69,71] This enables APT imaging to be carried out with low powers and at clinical field strength (3 T).[71] The main clinical indications are for cancer detection and ischemic stroke. APT exploits the elevated protein concentrations found in tumor regions compared to the surrounding tissue and has thus been demonstrated for human brain tumor grading,[71,72] distinction between tumor tissue and peritumoral edema in brain cancer patients,[73] and differentiation of malignant and benign thoracic lesions.[74] Although the majority of APT imaging in humans has been carried out on the brain, it has demonstrated utility in monitoring response to neoadjuvant chemotherapy in breast cancer patients,[75] and applications are emerging in studies of other types of cancer such as prostate cancer and lung cancer.[40,76] The utility of APT in ischemic stroke is based on the fact that the amide proton exchange is highly dependent on pH; base catalysis is present above pH 5, so higher pH values give rise to faster exchange rates.[65] This difference in exchange rate can be used to probe pH because the magnitude of CEST is heavily influenced by exchange rate, thus, regions of ischemia arising due to reduced tissue oxygenation and aerobic metabolism can be clearly identified by APT imaging.[65]

Specific biomarkers of tumors can be exploited by diaCEST, as Song *et al.* have demonstrated for the altered glycosylation of mucins.[77] Mucins are a family of high molecular weight and heavily glycosylated proteins that constitute the mucous barrier of epithelial surfaces.[78] Mucin-1 (MUC1) is a cell-surface-associated mucin encoded by the MUC1 gene, the expression of which is dysregulated in 900,000 of the 1.4 million tumors diagnosed annually in the USA.[78] In healthy epithelial cells, MUC1 is extensively glycosylated, whereas cancerous cells are often underglycosylated giving rise to the tumor-associated underglycosylated MUC1 antigen (uMUC1).[77] Most malignant adenocarcinomas of epithelial origin (breast, ovarian and colon cancers) overexpress uMUC1. The multitude of -OH protons belonging to the vast glycan chains bound to MUC1 can be readily detected by CEST MRI, with a signal peak at approximately 1 ppm.[77] Song *et al.* have shown that the deglycosylation of MUC1 can result in reductions in CEST signal of greater than 75%. MucCEST was able to distinguish between uMUC1-positive and uMUC1-negative tumors *in vivo*. Their results suggest that mucCEST would provide a label-free and non-invasive method to assess mucin glycosylation and therefore tumor malignancy.

DiaCEST can also be used to monitor intracellular cancerous alterations at the molecular level. Recently, Haris *et al*. used a gluCEST method to map cathepsin protease activity, which is highly associated with tumor malignancy.[79] Cathepsin cleaves poly-L-glutamate into smaller fragments, exposing glutamate amine protons and thereby generating an increased gluCEST signal that can be noninvasively detected to assess tumor malignancy.[79] Furthermore, poly-L-glutamate has been employed as a drug carrier for targeted delivery to tumors,[80] thus, gluCEST could be developed to evaluate drug delivery and the evoked efficacy on cancer cells.

Additionally, pharmaceuticals with exchangeable proton groups can be directly imaged using CEST. This technique is limited by the low concentrations of drugs found *in vivo*, however, it has been successfully carried out for a few small molecule pharmaceuticals. For example, the delivery of the neuroprotective agent, citicoline, to ischemic brain regions has been imaged *via* CEST MRI in a rat model of transient focal cerebral ischemia.[81] Citicoline (Figure 8) contains cytosine, which has previously been shown to elicit a CEST signal.[82] Citicoline has two distinct CEST signals at +1 and +2 ppm away from the water peak, attributed to the hydroxyl protons and amine protons belonging to cytosine, respectively.[81] Similarly, the tumor uptake of gemcitabine has been shown *via* CEST contrast generated by the amine protons.[83] At pH 7.4, gemcitabine has two CEST signals at +1 and +2.3 ppm, attributed to the -OH and -NH_2 protons respectively (Figure 8).[83] However at lower pH, the CEST contrast of -OH completely disappears while that of -NH_2 is shifted as much as 3.4 ppm away from the water peak.[83] CEST signal from tumor bearing mice was measured at 3.2 ppm, showing a conspicuous elevation at the tumor site following administration of the drug.[83] CEST imaging of drugs allows their tracking without inclusion of an imaging probe, avoiding inevitable concerns over modified efficacy and pharmacokinetics. Notably, both the discussed drugs, citicoline and gemcitabine, were encapsulated inside liposomes to produce high enough concentrations for CEST detection at the site of interest.[81,83] Issues with sensitivity restrict the CEST tracking of pharmaceuticals to agents with extensive safety profiles, for example 200-500 mg of citicoline can be intravenously administered daily, which is much higher than most clinically used drugs.[82]

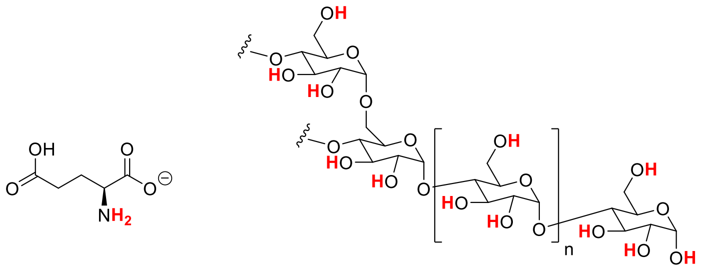

Glutamate

Glycogen

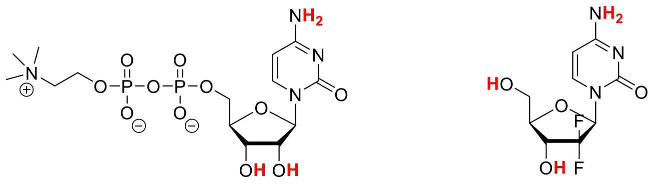

Citicoline

Gemcitabine

Figure 8. The structures of some examples of molecules that have been used to generate CEST contrast, exchangeable protons are highlighted in red.

1.2.1.2 GlucoCEST

GlucoCEST is a form of diaCEST where the exchangeable protons participating in the CEST mechanism are the hydroxyl protons belonging to the natural sugar, D-glucose. As glucose is biocompatible, exhibits 5 exchangeable protons and its increased uptake into tumors has been previously exploited by FDG-PET imaging, it is a promising candidate to develop as a diaCEST CA for cancer imaging.

Glucose is a ubiquitous energy source found in the human body, however, due to limited intrinsic concentrations and the small spectral separation between glucose hydroxyl proton resonances and the bulk water resonance, direct mapping of endogenous glucose distribution *in vivo* has been challenging at clinical field strengths.[42] However, natural, non-radiolabelled D-glucose has been exogenously administered at physiologically acceptable quantities to image glucose accumulation in tumor xenografts and even successfully discriminate between distinct tumor phenotypes using CEST techniques.[56,84] Walker-Samuel *et al.* described a new parameter to reduce the contributions of endogenous exchangeable protons in glucoCEST measurements; the glucoCEST enhancement (GCE), defined as the change in area under the MTR_{asym} curve from baseline following glucose administration.[84] Using mouse xenograft models they found that GCE was significantly increased in tumor tissue compared to muscle following intraperitoneal bolus glucose injection, giving rise to an increase in blood glucose concentration of approximately 5 mM.[84] The generated glucoCEST images clearly visualised the tumors and created good contrast between tumor tissue and muscle (Figure 9a). A statistically significant positive correlation was found between the measured median tumor GCE and FDG-PET signal, supporting the reliability of glucoCEST imaging (Figure 9b). Furthermore, measured GCE enabled them to distinguish between two distinct subcutaneous human colorectal tumor mouse xenograft models employed in the study. Additionally, Chan *et al*. used glucoCEST to image breast cancer mouse xenografts, showing significant glucoCEST signal enhancement during systemic glucose infusion. Similarly, they too could distinguish between two well-known breast cancer cell lines (highly malignant MDA-MB-231 and less aggressive MCF-7) due to the differences in the generated glucoCEST contrast, which were not possible to detect by FDG-PET or contrast enhanced MRI employing Gd-DTPA.[56] The animal experiments conducted by Walker-Samuel *et al.* and Chan *et al.* were carried out at ultrahigh field strengths; 9.4 T and 11.7 T, respectively.

Recently, glucoCEST has been used to image the uptake of unlabelled glucose in head and neck cancer patients using a clinical 3 T MRI scanner. The CEST contrast between tumor and normal tissue can be seen prior to administration of glucose (5.06% in the 1-5 ppm range and 7.58% in the 3-4 ppm range), an effect that has been previously documented.[85] It is speculated that the contrast at 3-4 ppm may be heavily contributed to by APT (Section 1.2.1.1). In the study, a 20 mL glucose bolus was administered to patients intravenously and a second CEST scan was carried out after 10 minutes, the sequence took 5 minutes to complete, thus this acquisition timing should encompass the peak glucose uptake.[56,84,86–88] MTR_{asym} analysis was carried out on both

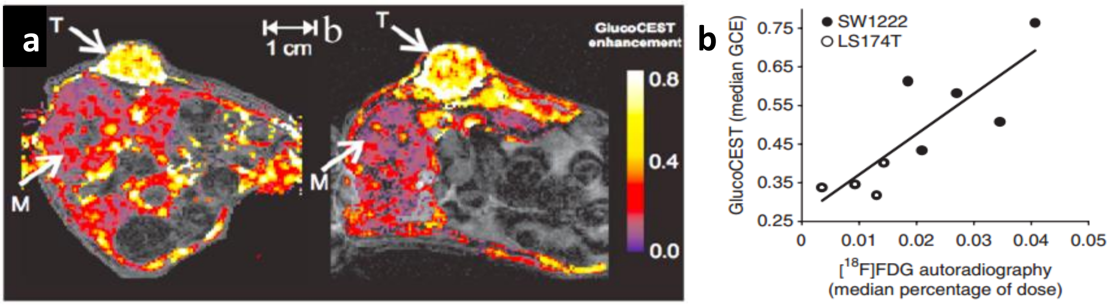

Figure 9. a) GCE maps from cross-sections through two mouse xenografts, the colour scale represents the extent of GCE measured. GlucoCEST imaging creates good contrast between tumor (T) and muscle (M) regions. b) Scatter plot of median tumor FDG and GCE signal showing a significant positive correlation ($P < 0.01$, Spearman's ρ). Figures were adapted from Walker-Samuel *et al.*[84]

sets of CEST data (before and after glucose infusion) and the GCE was defined as the difference in area between the two MTR_{asym} curves (1-5 ppm),[85] as has been done in previous animal studies.[84] Following injection of glucose, elevated CEST signal in head and neck tumors relative to surrounding tissue was clearly visualised, especially around 1 ppm and in the 3-4 ppm range.[85] The avid uptake of glucose by tumors produced greater GCE for tumor regions compared to muscle regions (4.98% GCE for tumor *vs.* 1.28% GCE for muscle).[85] Most previous glucoCEST imaging studies were performed at ultrahigh field strengths (7 T or higher), so to obtain this level of contrast at a clinical field strength is promising.

Additionally, glucoCEST has been used to measure signal change as a function of time, termed dynamic glucose enhanced MRI.[88,89] Similar dynamic contrast enhanced (DCE) methods employing CT and MRI (DCE-CT and DCE-MRI) are used in the clinic to assess tumor blood volume and permeability, although their use is not yet routine.[89] The principle is to administer a bolus of contrast agent intravenously and measure the signal change over time employing rapid sequential imaging. The DCE-MRI response curve also contains information about the intravascular volume and the extravascular extracellular space in tumors.[88] Compartmental modelling approaches are becoming available to extract these parameters. Dynamic glucose enhanced MRI has been demonstrated to visualise the effects of angiogenesis and blood-brain barrier breakdown in the brains of mice bearing human gliomas.[89] The results were similar to those obtained by DCE-MRI, supporting the validity.[89] Furthermore, dynamic glucose enhanced MRI has been used to image three glioma patients at 7 T, showing strong signal enhancement of the blood vessels and varied spatial enhancement across tumors.[88] These preliminary results suggest that dynamic glucose enhanced MRI is feasible to study glucose uptake in humans, with the potential to provide time-specific information regarding tissue perfusion, glucose metabolism and glucose transport across the blood-brain barrier and cell membranes.[88]

Dysregulated uptake and metabolism of glucose is a feature of many other afflictions as well as cancer. Thus, glucoCEST has the potential for more widespread clinical use, for example the technique could find utility in the management of stroke, various psychiatric disorders and neurodegenerative diseases such as Alzheimer's. Recently, glucoCEST MRI has been used to assess acute cellular allograft rejection, which frequently occurs after kidney transplantations, in a rat model.[90] This study used the MTR_{asym} contrast ratio between the renal cortex and the renal medulla to differentiate allograft rejection from other important forms of acute kidney injury and monitor the success of immunosuppressive treatment at a very early stage.[90] The findings show that glucoCEST could have a significant impact on the management of patients suffering from acute cellular allograft rejection.

1.2.1.2.1 GlucoCESL

Chemical exchange spin lock (CESL) is an alternative technique to CEST that encodes the exchange process between water and labile protons using an RF preparation period, however the labelling approaches vary. In the on-resonance CESL technique, water proton spins are excited, then spin lock irradiation is applied at that same water resonance frequency.[87] In the spin lock period, water protons undergo exchange with labile protons (such as the hydroxyl protons of glucose). When the water proton magnetisations return to the longitudinal plane, differences in magnetisation evoked by chemical exchange can be detected and quantified. GlucoCESL has been carried out on healthy rat brains and showed dose-dependent linear responses in the range of 0.25-1 g/kg glucose administration.[87] The CESL technique offers some advantages over CEST including the ability to use high RF powers whilst avoiding increased levels of direct water saturation and enhanced sensitivity to faster exchanging species with smaller chemical shifts.[42,87] Thus CESL may present a suitable alternative to CEST for glucose mapping *in vivo*.

1.2.1.2.2 GlucoCEST as an alternative to FDG-PET

GlucoCEST presents an exciting potential alternative to FDG-PET for the diagnosis and monitoring of cancer. Translation of glucoCEST into the clinic would eliminate the radiation exposure that is unavoidable for PET and/or CT techniques, enabling risk-free imaging of susceptible patient populations (young children, elderly people and pregnant women),[84] as well as oncologic patients who require frequent imaging as part of their treatment management. As un-labelled natural D-glucose is used, the logistics and

Table 1. Comparative summary of glucoCEST versus FDG-PET.

	GlucoCEST	**FDG-PET**
Safety considerations	• SAR caused by excessive RF irradiation can lead to tissue heating, however this is prevented by built-in software safety measures • Deep vein thrombosis development due to large glucose bolus injection • Hyperglycaemia in diabetic patients	• Dose of ionizing radiation is delivered to the patient, both by the radiotracer and the transmission scan used for attenuation correction purposes, approximately equal to 3-5 times an annual dose of background radiation • Often carried out alongside a CT scan to allow accurate anatomical localisation of detected lesions, increasing radiation dose to 5-10 times an annual dose of background radiation
Spatial resolution	• In the order of 1–2 mm^3 depending on the hardware and pulse sequence • There is no inherent limit, it’s generally a trade-off with acquisition time	• ~ 5 mm^3 • Intrinsically limited by positron range
Sensitivity	• Generally micro- to millimolar concentrations, although nanomolar concentrations have been reported for supramolecular structures	• Can detect picomolar concentrations of FDG
Cost	• MRI scan varies from \$1000 to over \$4000	• Generally considered more expensive than MRI, varies from \$3000 and up
CA preparation	• Very simple	• Requires ^{18}F labelling, a cyclotron, radiation shielding and specialised personnel
Selectivity	• GlucoCEST signal could be from exogenous or endogenous glucose and its metabolites • Additional contributing factors to signal magnitude such as pH and temperature	• Only FDG and its metabolic products
Field of view/ acquisition time	• Relatively slow imaging technique • Same output as MR: typically a single slice or a few 2D slices • Limited potential for whole body and 3D image acquisition	• A 15-60 min delay is required after radiotracer injection for redistribution and uptake purposes, after this period whole body FDG-PET can be performed in 10–15 min on modern systems • 3D image reconstruction and inherently quantitative output

infrastructure necessary to acquire and handle the contrast agent are significantly simplified compared to the use of FDG. D-glucose is already approved for human use, for example in the glucose tolerance test for diabetic patients, so clinical translation as a contrast agent is expected to be fast since basic safety testing has been previously completed.[56,84,88,89] MRI as an imaging modality is cheaper than PET, this factor in combination with avoidance of expensive synthesis and handling of short-lived radiotracers would allow for dramatic reductions in the overall cost. MRI offers higher spatial resolution in comparison to PET; approximately 5 mm^3 for PET versus 1 mm × 1 mm × 3 mm for MRI, which is a decrease in voxel size by a factor of 40.[16,55,84] The considerable improvements in resolution offered by CEST MRI would allow smaller tumor masses to be evaluated for earlier diagnoses, more immediate monitoring of response to therapy and more effective characterisation of intratumor heterogeneity.

However, there are differences in the information that would be conveyed by glucoCEST versus FDG-PET. For instance, FDG-PET detects intracellularly accumulated FDG-6-phosphate, whereas, the glucoCEST signal is mainly derived from unmetabolized glucose and therefore detects intracellular, extracellular and vascular glucose alike.[42,56] It is possible that other glucose metabolism intermediates contribute to glucoCEST signal, whereas FDG-PET specificity is much more absolute. Based on well-established knowledge of solid tumor metabolism, little signal is thought to arise from intracellular or phosphorylated glucose derivatives because these have been shown to be rapidly converted to lactate.[91] Additionally, a small contribution is thought to be made by blood glucose transiently passing through voxels in the vasculature, leaving the majority of glucoCEST signal attributed to glucose in the extravascular extracellular space.[56] As a result, perfusion related properties such as blood volume and vascular leakage will modify the glucoCEST signal as well as metabolic abnormalities.[90] In addition, the extracellular space surrounding tumors is generally increased in size and more acidic,[56,92] both of which will alter CEST signal magnitude (Section 1.2.2). GlucoCEST output is pH responsive which is not the case for FDG-PET.

1.2.1.2.3 Limitations of glucoCEST in its current form

There are practical issues to overcome before glucoCEST can offer a viable alternative to FDG-PET in the clinic. A primary drawback is the large quantity of glucose that must be administered to patients to generate sufficient contrast, raising concerns over hyperglycaemia, especially in diabetic patients. FDG-PET requires administration of micrograms of FDG and picomolar concentrations can be detected due to its exquisite sensitivity, whereas, the first in-man glucoCEST study required intravenous infusion of 25 g of D-glucose over approximately 1 minute.[42,88] In addition to potential hyperglycaemic adverse side effects and contraindications for diabetic patients, large doses of glucose could disrupt tumor metabolism, meaning glucoCEST may depict altered metabolic processes, whereas FDG is present in such small quantities that it is believed to have no effect on the biological processes on which it reports. Detailed *in vivo* studies are required to validate or disprove these concerns. Another major obstacle is the short duration of glucoCEST contrast. In a study conducted by Xu *et al.* on 4 healthy volunteers and 3 glioma patients, the peak blood glucose concentration occurred 2-4 minutes post-infusion.[88] These values did not correlate with the weight of the participant and glucose response curves are most likely to be determined by the individuals insulin response. Golay *et al*. have shown vastly different responses in blood glucose curves following glucose bolus infusion, with peaks ranging from 5-100 min after infusion and large variations in the time taken to return to baseline.[93] One volunteer was withdrawn from the study due to development of superficial vein thrombosis in the infusion arm, a potential side effect that has been previously documented for dextrose infusion, and which may pose another complication for glucoCEST tranlation.[94] These results highlight the large inter-person differences in insulin response, which poses a substantial obstacle for glucoCEST imaging to overcome because the ideal glucose dose and timepoint for imaging will vary between patients.

1.2.1.3 ParaCEST

1.2.1.3.1 Lanthanide shift reagents

The lanthanides (Ln) are a series of elements containing the fifteen metallic chemical elements with atomic numbers between 57 and 71; from lanthanum through to lutetium. They comprise the first row of f-block elements in the periodic table; the 4f subshell is progressively filled with electrons as atomic number increases across the series. All lanthanides form trivalent cations (Ln^{3+}), the chemistry of which is mainly determined by ionic radius, which steadily decreases across the series. Lanthanides have been employed in NMR spectroscopy for several decades to separate superimposed signals in ^1H NMR spectra and allow more accurate structural analysis. The addition of lanthanide complexes (referred to as shift reagents (SRs) in this context) to a solution of a compound possessing a suitable lone pair of electrons causes the proton resonances of the compound to spread out, a greater effect is exerted on the resonances of protons closest to the coordination site.[95] Coupling constants are observed to be largely unaffected.[95,96] Lanthanide-induced shifts are thought to be primarily due to pseudocontact interactions and can be both upfield and downfield, depending on the lanthanide ion and ligand system in question.[95] The magnitude of a lanthanide-induced shift expands with increasing lanthanide concentration relative to the sample compound, however, the majority of lanthanide complexes produce substantial line broadening at higher concentrations.[95,97] NMR spectroscopy can be used to predict how a lanthanide SR will alter the appearance of a CEST spectrum.

1.2.1.3.2 ParaCEST agents

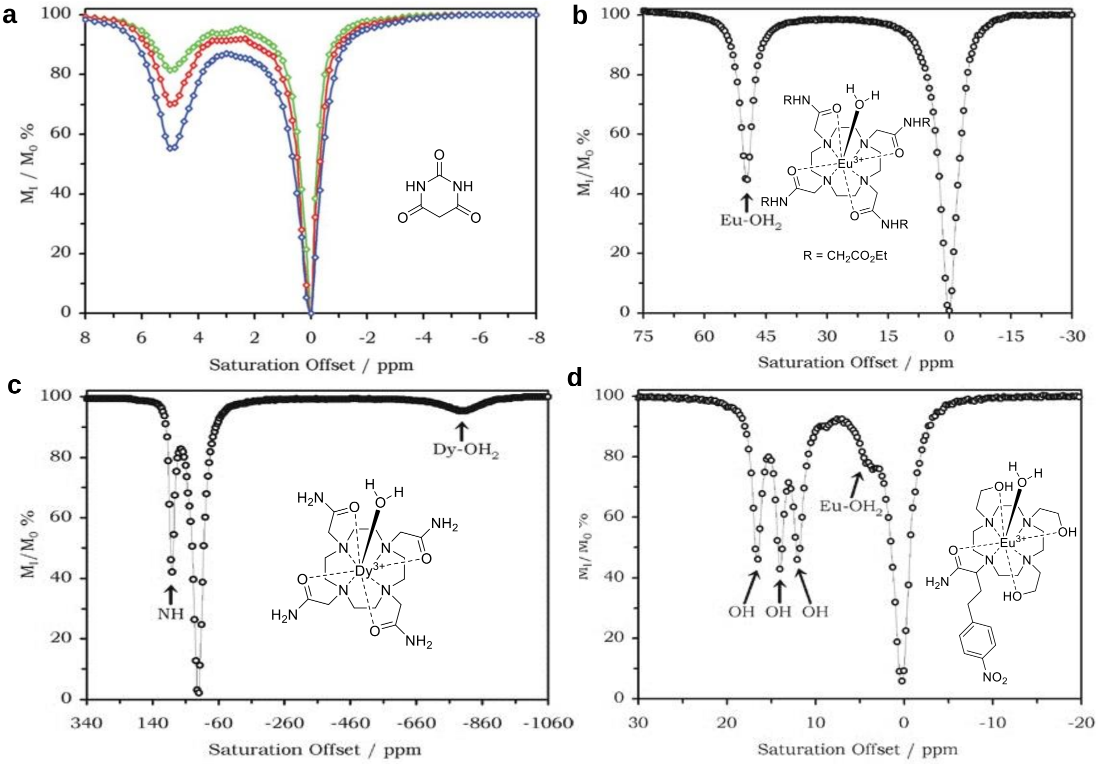

Figure 10. Z spectra and structures for: a) Solutions of barbituric acid at concentrations of 125 mM (blue), 62.5 mM (red) and 31.25 mM (green), spectra were recorded at 300 MHz, 37 °C and pH 7.0, b) Eu-DOTA-4AmCE^{3+} (30 mM) recorded at 270 MHz and 25 °C, c) Dy-DOTAM^{3+} (30 mM) recorded at 400 MHz and 25 °C, d) Eu-CNPHC^{3+} (35 mM) recorded at 270 MHz and 25 °C. Figures were adapted from Woods *et al.*[62]

ParaCEST agents incorporate a paramagnetic lanthanide ion or a transition metal ion with a short electronic relaxation time (e.g. Fe(II) or Co(II)),[28] and thereby exhibit certain advantages over diaCEST agents. Ideal chemical exchange sites on CEST CAs have large chemical shift differences to bulk water (Δω), allowing a high exchange rate (k_{ex}) without approaching the fast exchange limit at physiological temperature (37°C) and pH (6.5–7.6), as well as avoiding complications arising from magnetic field susceptibility.[61] By incorporating lanthanides into complexes with exchangeable protons such as alcohols, amines and amides, the chemical shift difference with respect to water can typically be increased up to ±50 ppm.[98] Furthermore, the chelated metal ions can coordinate water molecules with sufficient strength and proximity to slow down the exchange of protons between this water molecule and the surrounding water molecules to a rate capable of producing CEST contrast, generating huge shifts of up to 720 ppm.[62] This large frequency difference with bulk water enables the use of relatively fast exchanging species for CEST contrast whilst still adhering to the slow to intermediate exchange regime (CEST requirement defined in Section 1.2).[58,60] In addition, the large spectral gap facilitates selective RF saturation of the paramagnetically shifted protons without saturation of endogenous exchangeable protons or indirect partial saturation of bulk water magnetisation, reducing the need to perform asymmetry analysis.[60,98] The effectiveness of a CEST agent can therefore be optimised by the inclusion of various lanthanide ions to increase $\Delta\omega$, allow faster K_{ex} and reduce the necessary concentration of CA required to create sufficient contrast.

For traditional T1 shortening GBCAs the exchange rate between coordinated water and bulk water is too fast to allow CEST detection.[62] However, the exchange of Eu-coordinated water protons in various Eu(III)-DOTA-tetraamine chelates such as Eu-DOTA-4AmCE^{3+} is slow enough that these protons create a distinct environment in NMR spectroscopy that is shifted significantly downfield of the bulk water peak.[99] Similarly, these coordinated water molecules can be observed at approximately +50 ppm in a CEST spectrum (Figure 10b).[100] The Z spectrum of Eu-DOTA-4AmCE^{3+} demonstrates that a sizable decrease in the water peak intensity can be accomplished by application of a presaturation pulse 50 ppm away from the bulk water resonance frequency. The exchangeable amide protons displayed by this complex are not visible in the Z spectrum but can be readily detected in other related DOTA-tetraamide (DOTAM) chelates, such as Dy-DOTAM^{3+} (Figure 10c).[62] The exchange of the eight amide protons in Dy-DOTAM^{3+} can be clearly observed at +80 ppm whereas a less intense CEST signal can be seen for the Dy^{3+}-coordinated water protons at -720 ppm. Interestingly, the hydroxylethyl groups of Eu-CNPHC^{3+} retain their hydroxyl protons upon coordination and therefore provide chemical exchange sites for CEST which are clearly resolved for the three magnetically distinct sites, with resonances in the range of 10-20 ppm downfield of water in a Z spectrum (Figure 10d).[62] An additional advantage of employing lanthanides in paraCEST agents is that their coordination chemistry is virtually identical across the series, therefore, the relaxation characteristics and hyperfine shift properties can be tuned by selecting particular combinations of lanthanide ions and ligand systems.[62] Disadvantages include power deposition due to the high presaturation powers required to visualise the fast exchange of paraCEST agents with water, and the potential toxicity of un-chelated lanthanide ions.[58,62]

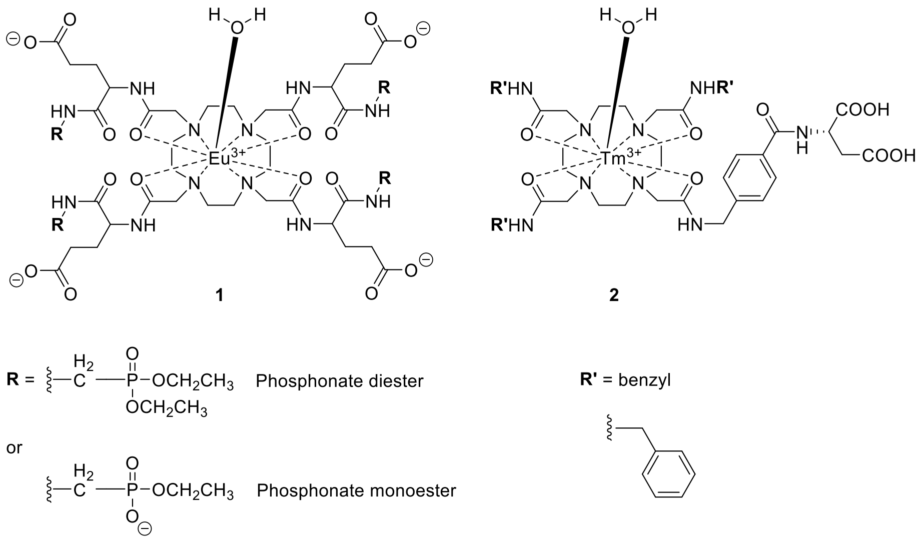

Figure 11. The structures of two recently reported paraCEST agents. Glutamyl-phosphonate substituted Eu^{3+}-DOTAM complexes with enhanced water-bound lifetimes reported by Fernando *et al.*[101] (**1**) and a single aspartate modified Tm^{3+}-DOTAM complex with improved biocompatibility reported by Suchý *et al.*[102] (**2**).

Recently, Fernando *et al.* published the design of two Eu(III)-DOTAM complexes with glutamyl-phosphonate side arms that exhibit the slowest water exchange rates of any paraCEST agent reported to date (Figure 11, **1**).[101] The bound water lifetime of the phosphonate diester analogue was the longest at 735 µs, which is optimal for CEST signal generation at the low RF powers required for *in vivo* use.[101] The authors demonstrated that this complex can be detected in the kidneys of mice following administration of a 0.4 mmol/kg dose. The CEST signal generated by the phosphonate diester analogue *in vivo* was detected at +42 ppm downfield of the water peak and varied between 6-14% in water suppression magnitude at the 8-minute time point following administration. These results are promising because very few *in vivo* studies on water-based paraCEST agents have been successfully carried out due to the extensive line broadening caused by the complexes.[101] Another study by Suchý *et al.* reported the derivatisation of Tm(III)-DOTAM complexes.[102] Tm(III)-DOTAM-alkyl complexes are acutely toxic, which is thought to be a result of their tri-cationic charge.[103] Suchý *et al.* have shown that by modifying one arm of Tm(III)-DOTAM complexes with an aspartate residue to reduce the charge from +3 to +1 (for fully ionised species), the biocompatibility can be markedly improved without elimination of CEST signal from the amide protons.[102] For example, the single aspartate substituted, benzyl decorated Tm(III)-DOTAM (Figure 11, **2**) exhibits a CEST signal of 10% at -50 ppm at a concentration of 10 mM (37 °C, pH 7 and B_1 = 15 µT). This was the only complex out of the four trialled to elicit a modest but detectable *in vivo* CEST signal, however, all four complexes were well tolerated by mice. This method of aspartate substitution or the use of similar charge modifying side arms may aid in combating the toxicity issues currently surrounding paraCEST agents.

1.2.1.4 LipoCEST

More pronounced improvements in sensitivity can be made by extending CEST CA design to supramolecular structures, predominantly because these larger assemblies can incorporate a higher number of exchangeable protons. Encapsulating lanthanide SRs inside liposomes has given rise to new and more sensitive CAs, termed lipoCEST agents. Due to the slow exchange rate across the lipid bilayer, a large number of exchangeable water protons can be compartmentalised inside liposomes. Depending on the size of the liposomes (typically 50–300 nm in diameter), the number of exchangeable protons per liposome can be as high as 10^6-10^8.[60,104] Encapsulation of a paramagnetic agent shifts the resonance of the entrapped water protons away from the exterior bulk water resonance to an extent that depends on the properties and concentration of the encapsulated SR.[60,62,104–108] As the paramagnetic complex coordinated water molecule and the intraliposomal water molecules are in fast exchange, the intraliposomal pool yields a single distinct resonance that is separate from that of bulk water (Figure 12a).[104]

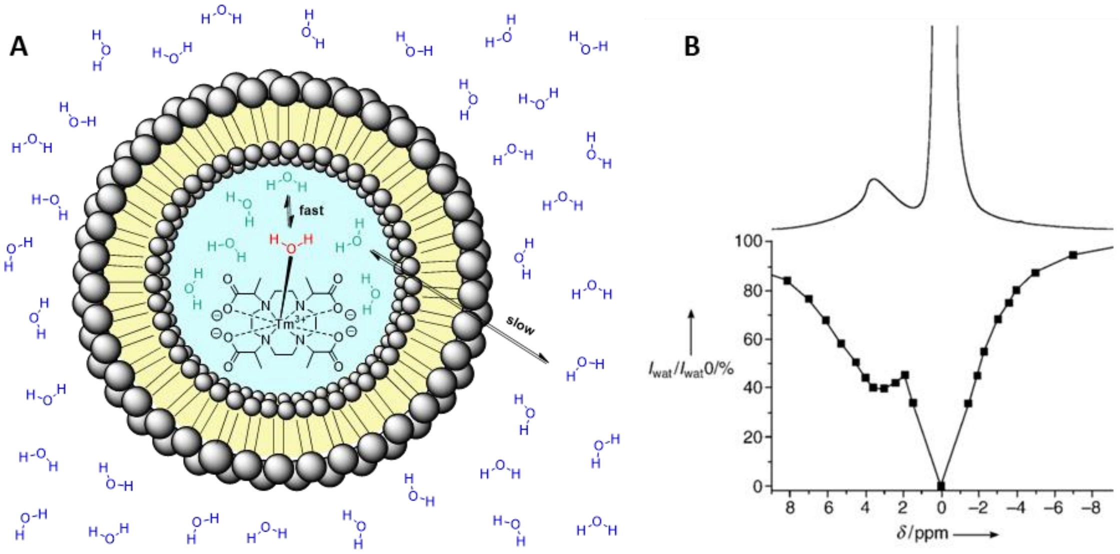

Figure 12. A) LipoCEST schematic. The exchange rate for Tm-dotma$^-$ is too fast to be used as a paraCEST agent however it if is encapsulated inside a liposome it can act as a SR by altering the chemical shift of the water molecules that are also encapsulated. Water exchange across the lipid bilayer is slow allowing the entire liposome to be used as a paraCEST agent. B) Top: ^{1}H NMR spectrum of a suspension of liposomes encapsulating 0.1 M Tm-dotma$^-$. The signal at +3.1 ppm away from the water peak which is centred at 0 ppm is due to the entrapped water which is supported by the Z spectrum (lower), which shows that a presaturation pulse at 3.1 ppm results in significant reduction of the water signal. The ^{1}H NMR spectrum was recorded at 14.1 T and the Z spectrum at 7 T. Both were recorded at 37 °C. Figure B was obtained from Aime *et al.*[109]

For example, Aime *et al.* found that liposomal encapsulation of Tm(III)-α,α',α'',α'''-tetramethyl-1,4,7,10-tetraacetic acid (dotma) chelates shifted the internal water resonance downfield by 3.1 ppm (Figure 12b).[109] Presaturation at this frequency resulted in a decrease of the bulk water peak intensity by 5% at a lipoCEST agent concentration of 90 pM. The picomolar sensitivity of this lipoCEST agent is exceptionally high relative to any other MRI CA.[62]

The main problem with first-generation lipoCEST agents is the small chemical shift difference between the intraliposomal water resonance and bulk water signal (generally up to ±4 ppm depending on the lanthanide complex employed and the concentration).[60,104,110] Hence lipoCEST agents offer a large sensitivity advantage over diaCEST agents but are similarly hampered by the resonance frequency overlap with endogenous exchangeable protons. Larger chemical shift variation can be achieved by altering the liposome shape.[105,106] Terreno *et al.* showed that by increasing the osmotic pressure of the extra-liposomal solution (thereby shrinking the liposomes), the chemical shift difference between the intra- and extra-liposomal signals increased for their lipoCEST agent, which comprised Tm-(10-(2-hydroxypropyl)-1,4,7,10-tetraazacyclododecane-1,4,7-triacetato) (HPDO3A) encapsulated inside DPPC:Tm-1:DSPE-PEG2000 (65:30:5 mol%) liposomes.[105] With an intraliposomal Tm-HPDO3A concentration of 40 mM and isotonic extra-liposomal solution of NaCl, the offset from water achieved by the liposomal CA in a CEST spectrum was only +0.4 ppm. Upon addition of NaCl to the exterior medium to increase the osmolarity to 300 mOsm, the offset increased by over +20 ppm. Additionally, the offset from the water signal could also be improved by approximately 3 ppm by increasing the internal Tm-HPDO3A concentration from 40 mM to 250 mM.

Another property of lipoCEST agents that can be tuned for optimal contrast is the water exchange rate across the lipid bilayer. The water permeability of liposomes can be somewhat controlled by altering the lipid composition, for example, exchange is faster across unsaturated chain bilayers (with or without cholesterol) in comparison to solely saturated chain lipid bilayers.[33,109] A study by Fossheim *et al.* on liposomal formulations of Gd-HPDO3A measured greater relaxivity for DPPC/1,2-dipalmitoyl-*sn*-glycero-3-phosphoglycerol (DPPG) liposomes compared to 1,2-distearoyl-*sn*-glycero-3-phosphocholine (DSPC)/1,2-Distearoyl-*sn*-glycero-3-phosphoserine (DSPS) liposomes (relaxivity is defined as the ability of magnetic compounds to increase the relaxation rates of the surrounding water proton spins, which usually improves the contrast of an image).[33] This was attributed to more efficient water exchange across the membrane for DPPC/DPPG bilayers, which are less rigid and have a melting transition temperature

(T_m) that is approximately 10 °C lower than that of DSPC/DSPS bilayers.[33]

A major advantage of CEST MRI methodology is that it is theoretically possible to visualise multiple probes within the same MR image, and even within the same image voxel, providing that the resonance frequencies of the labile protons of the two agents are distinct and associated with sufficient sensitivity. Therefore, inherent “frequency coding” of multiple CEST probes offers the possibility of simultaneous visualisation of several biomarkers in the same anatomical region, which could offer synergistic information for the diagnosis and staging of disease. Terreno *et al.* were the first to demonstrate the *ex vivo* co-localisation of two lipoCEST agents, with intraliposomal water proton frequencies of +3 ppm and +15 ppm, imaged in mouse muscle.[111] The signal from the two agents did not interfere with each other, enabling simultaneous visualisation of lipoCEST agents present at nanomolar concentrations. This is promising for future dual imaging technique development using highly sensitive lipoCEST agents.

1.2.1.4.1 Environmentally responsive lipoCEST agents

Recently, there has been a focus on the development of CAs that are capable of responding to their local biochemical environment, where a switch in image contrast is triggered by a specific stimulus or biochemical variable. This feature could strengthen diagnosis, provide unique disease-specific biochemical information and even stimulate release of drug cargo at the site of interest. There are a variety of environmentally responsive liposomes reported in the literature (see Section 1.4.4), thus one can envisage the development of stimuli response lipoCEST agents. Indeed, Langereis *et al.* reported a temperature responsive liposome formulation that can be used for both ^{1}H CEST and ^{19}F MRI.[112] The liposomes encapsulate a fluorine compound (NH_4PF_6) for ^{19}F detection and a SR (Tm-HPDO3A) for lipoCEST detection. The ^{19}F MRI signal is very broad when NH_4PF_6 is held inside the liposomes due to the fast relaxation induced by proximity to a paramagnetic complex. In response to mild hyperthermic treatment (39-42 °C), temperature-sensitive liposomes are known to release their contents due to the lipid membrane approaching its T_m.[60,112–114] Once the liposome reaches its T_m, the contents are released, resulting in total loss of the lipoCEST signal and simultaneous appearance of ^{19}F MRI contrast. It is suggested that a system such as this could be used to quantify drug release from liposomes (using the ^{19}F signal) as well as to measure the local liposome concentration immediately preceding payload delivery (using the lipoCEST signal).

Opina *et al.* have reported their design for a pH sensitive lipoCEST agent by encapsulating a thulium complex of the DOTA-tetraglycinate ligand which possesses four equivalent amide protons capable of generating CEST contrast.[108] Encapsulation of the complex generated CEST contrast with 10^4-fold higher sensitivity than the free agent. pH dependent CEST curves were obtained for the lipoCEST agent and it was found that the amine proton CEST intensity was reduced with increasing acidity. This observation was mostly attributed to a change in membrane permeability of the lipid bilayer at the varying pH, which had been previously reported for PC bilayers.[115] Nano-carriers such as these could be valuable for pH mapping using liposomes targeted to tumors. However, future development of these agents is required to enable determination of pH without knowing the exact agent concentration. This could be made possible by ratiometric imaging. One could imagine the co-encapsulation of two distinct CEST agents (with different exchange frequencies and pH dependencies) inside liposomes and using the ratio of two CEST spectra to obtain a direct readout of pH. Liposomal entrapment would also eliminate concerns over potential differences in tissue biodistribution for the two pH-sensitive agents.

Another advantage of employing liposomes is that bioactive molecules can be anchored to the exterior liposome surface, enabling active targeting of liposomes to disease regions such as tumors. Flament *et al.* have developed a Tm(III) complex-incorporating lipoCEST agent functionalised with the tripeptide Arg-Gly-Asp (RGD) which is known to target a common biomarker for tumor angiogenesis, the integrin $\alpha_v\beta_3$ receptor.[107] RGD-bearing and untargeted variations of the lipoCEST agent were compared in their ability to image brain tumors in a murine model of U87 glioma. The targeted lipoCEST agent, the first of its kind to be reported, produced slightly higher tumor contrast and this contrast persisted for a much longer time period compared to the untargeted lipoCEST vesicle. These results demonstrate the feasibility of *in vivo* detection of targeted lipoCEST agents.

1.2.1.5 DiaCEST liposomes

To avoid the inclusion of metal ions in lipoCEST agents, compounds with diaCEST properties can be encapsulated inside liposomes at high concentrations to give rise to diaCEST liposomes. Liu *et al.* encapsulated simple bioorganic and biodegradable compounds (glycogen, L-arginine, and poly-L-lysine) into separate liposomes to generate unique “multicolour” MR images.[116] Three artificial colours were assigned for the hydroxyl protons of glycogen (0.8 ppm), the amino protons of L-arginine (1.8-2.2 ppm) and the backbone amide protons of poly-L-lysine (3.6 ppm). The liposomes were injected intradermally to mice and their homing to draining lymph nodes was visualised. Using frequency-dependent acquisition processes, Liu *et al.* demonstrated that it is possible to differentiate between different diaCEST liposomes *in vivo* employing multicolour MRI.

Chan *et al.* proposed the potential utility of diaCEST liposomes to monitor the efficiency of nanocarrier delivery of therapeutics to tumors.[117] Nanocarriers have been shown to improve the efficacy of some cancer treatments however a lack of methods to evaluate the pharmacological fate of the nanocarrier systems has slowed their clinical translation. Chan *et al.* created diaCEST liposomes based on the clinically approved doxorubicin (DOX) formulation, Doxil®, by co-encapsulating DOX and BA.[117] BA exhibits excellent CEST contrast at an offset of +5 ppm away from the water signal (Figure 10a), which was used to detect and track the liposomes.[61] The liposomes were used to assess the effect of tumor necrosis factor (TNF-α), an agent in clinical trials for increasing the vascular permeability and thus the uptake of nanocarriers to tumors, in CT26 tumor bearing mice. The CEST contrast of tumors following liposome administration was 0.4% at the BA frequency (+5 ppm) which increased to 1.5% upon co-administration with TNF-α. Subsequently, the same group demonstrated that BA encapsulating liposomes can be used to successfully monitor liposomal delivery to mucosal membranes *via* CEST MRI.[118]

Theranostic nanoparticles are particles containing both imaging agents and therapeutics. Theranostic liposomes loaded with chemotherapeutic drugs can generate CEST contrast utilising the labile protons belonging to a co-incorporated compound (as above) or the labile protons of the drug itself. A recent study by Li *et al.* characterised the CEST properties of several chemotherapeutic agents belonging to three major structural categories; pyrimidine analogs, purine analogs, and antifolates.[83] Subsequently, gemcitabine (Figure 8, Section 1.2.1.1), a chemotherapeutic with a favourable CEST profile, was selected to be encapsulated inside liposomes and used to image a CT26 tumor-bearing mouse model. A bilayer composition of DPPC:cholesterol:DPPE-PEG2000 (55:45:5 mol%) and hydrodynamic size of 80 nm were selected to optimise gemcitabine encapsulation and liposomal biodistribution. The mice were administered with 20 mg lipid/kg of body weight (BW), which equates to approximately 80 mg gemcitabine/kg BW, and TNF-α (1 μg) to give rise to CEST signal in tumor regions 5 hours after tail vein injection. Citicoline (Figure 8, Section 1.2.1.1) is another drug whose CEST properties have been exploited to create diaCEST theranostic liposomes used for the imaging and treatment of ischemic brain regions in rats.[81]

In summary, the diaCEST liposome strategy presents a non-radioactive, non-metallic, biocompatible, semi-quantitative and clinically translatable approach to assess the tumor targeting of stealth liposome formations *in vivo*, which may find practice in personalised medicine procedures. Due to the increasing interest in nanocarrier delivery of drugs to sites of interest, in particular chemotherapeutic drugs to tumors, diaCEST liposomes lend themselves to the field of theranostics.

1.2.2 Factors affecting Z spectra

CEST detection of exchangeable protons is mediated by magnetic field strength B_0, RF saturation power B_1, the exchange rate of the labile protons with water protons, concentration, pH, temperature and solvent.[56–58,68] To discuss the way various parameters affect the generated CEST signal it is easiest to pick an example molecule, for which the most relevant choice is glucose. Chan *et al.* found that CEST detection of glucose solutions can be achieved at millimolar concentrations, giving rise to asymmetry in the Z spectrum towards higher frequency, producing a robust MTR_{asym} signal between +0.5-2.2 ppm at pH 7.3.[56] As glucose concentration is increased, the line shape broadens and there is an apparent shift in the MTR_{asym} curve maximum to higher frequencies (Figure 13a). The MTR_{asym} curve is asymmetric but featureless at pH 7.3, which is no longer the case as the pH is decreased. Several resonances corresponding to the chemically distinct –OH groups of glucose become visible at 1.2, 2.2 and 2.8 ppm as the solution is acidified (Figure 13b).[56] The CEST contributions of the five –OH groups are not proportional because the signal magnitude generated by each hydroxyl group depends on each of the individual proton exchange rates with water. The maximum MTR_{asym} signal was observed to move slightly further away from the water signal with increasing acidity, a property which should aid *in vivo* detection. The relationship between pH and the signal generated by a CEST agent depends on the type of exchangeable protons belonging to the agent (-OH, $-NH_2$, -NH) and the mechanism of exchange catalysis (acid, base).[58] Hydroxyl proton exchange is base catalysed so when the pH is reduced below neutral, the exchange rates of the hydroxyl protons are reduced so that they are more in line with the slow-intermediate exchange regime, that is known to be favourable for CEST signal generation.[56]

The CEST characteristics of glucose do not considerably change when higher saturation fields are applied however the sensitivity rapidly increases with increasing B_1 (Figure 13c and d).[56] This is expected because higher saturation fields give rise to greater saturation efficiency before exchange occurs. However, as B_1 is increased the peak corresponding to direct saturation of bulk water broadens and will compete with glucoCEST detection.[56,58] Importantly, as previously mentioned in Section 1.1.2, B_1 can only be increased up to a certain point before the energy deposition causes tissue heating, i.e. the SAR is too high.

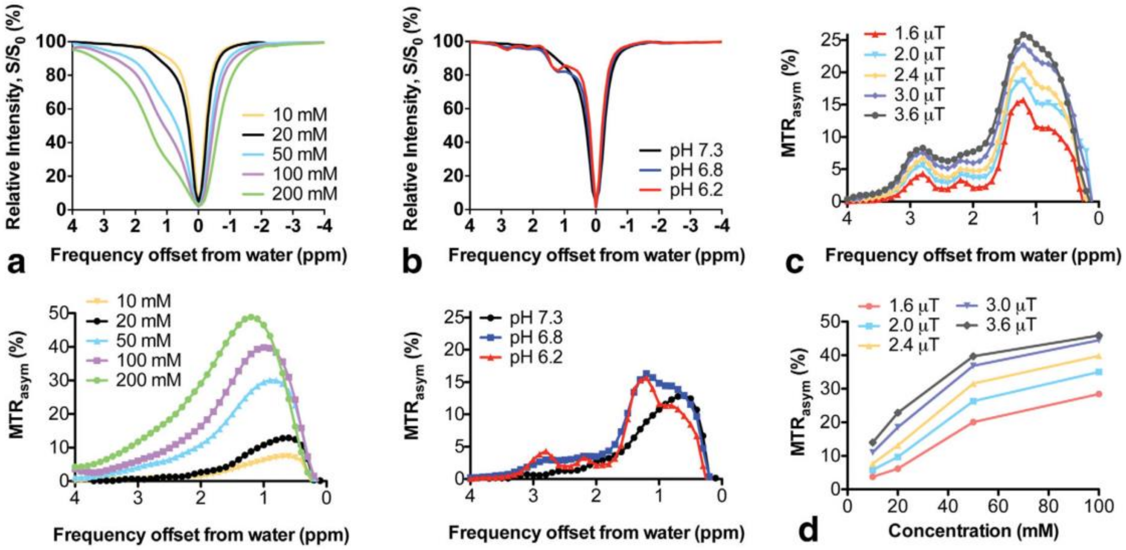

Figure 13. The effect of concentration, pH and RF saturation field on glucoCEST signal from D-glucose in PBS recorded at 11.7 T and 37 °C. a) Z spectra (top) and MTR_{asym} curves (bottom) for varying glucose concentrations at pH 7.3 and B_1 = 1.6 μT. b) Z spectra (top) and MTR_{asym} curves (bottom) for 20 mM glucose at varying pH and B_1 = 1.6 μT. c) MTR_{asym} spectra for 20 mM glucose at varying B_1 and pH 6.2. d) GlucoCEST signal (averaged MTR_{asym} value over 0.8-2.2 ppm) as a function of concentration at varying B_1. Figure was obtained from Chan *et al.*[56]

An example utilising glucose could not be found in the literature for every parameter affecting the acquisition of Z spectra. Glycogen is a multibranched polysaccharide of glucose (structure shown in Figure 8). Van Zijl *et al.* showed that the CEST signal generated by the hydroxyl protons on glycogen becomes increasingly intense when raising the temperature from 4 °C to 25 °C and from 25 °C to 37 °C (Figure 14a).[68] This is due to the temperature-induced increase in -OH exchange and the dependency of the CEST effect on proton exchange rates. Increasing the temperature will increase the exchange rate of labile protons, but whether this will enhance or reduce resultant CEST signal will depend on whether the CEST agent has an original exchange regime (K_{ex}) that is slower or quicker than optimal.

The magnetic field strength, B_0, also influences CEST detection. Figure 14b, published by van Zijl *et al.,* shows that as B_0 is increased, the CEST signal produced by glycogen is more readily observed.[68] Increasing B_0 results in enhanced frequency separation between the exchangeable protons on glycogen and the water peak, which reduces the overlap with regions of direct water saturation and thereby allows more selective irradiation. For this reason, the phenomenon of stronger B_0 generating more prominent Z spectra is consistent across CEST agents.[58]

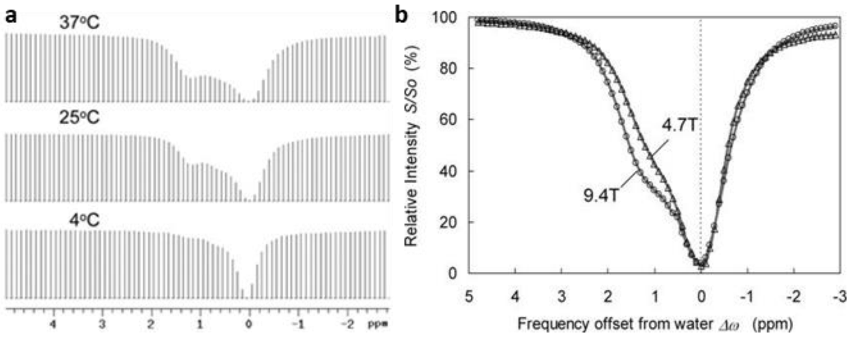

Figure 14. Z spectra of 200 mM glycogen a) acquired at 9.4 T in unbuffered H_2O at pH 7.0 at varying temperatures (4, 25 and 37 °C), b) acquired at 37 °C and pH 7.4 with varying B_0 (4.7 T and 9.4 T) and a saturation pulse of 10 s and B_1 = 1.9 μT. Figures were adapted from van Zijl *et al.*[68]

1.3 Properties of 2-DG

2-Deoxy-D-glucose (2-DG) is an analogue of glucose in which the 2-hydroxyl group is replaced by hydrogen (Figure 15), resulting in several interesting biological consequences.

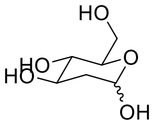

Figure 15. Structure of 2-deoxy-D-glucose

1.3.1 2-DG as a chemotherapeutic agent

2-DG acts as a competitive inhibitor of aerobic glycolysis,[119,120] and is thereby cytotoxic to mammalian cancer cells *in vitro* and has been shown to inhibit tumor growth *in vivo*.[121–124] Because of this mechanism of action, the cytotoxic effects of 2-DG are more pronounced in cancer cells versus normal cells due to cancer cells generally having a higher dependency on glycolysis for ATP production (the Warburg effect, Section 1.1). In concordance with this, tumors with higher glycolytic capacity appear to be more susceptible.[122,123] Additionally, 2-DG is reported to enhance the therapeutic effectiveness or reduce resistance to a number of established chemotherapeutic agents such as DOX,[122] trastuzumab,[125] adriamycin and paclitaxel.[126] For example Ahmad *et al.* showed that 27% of rapidly dividing, highly glycolytic, T47D breast cancer cells were killed after a 24 h exposure to 2-DG whilst no effect was observed on the slowly growing MCF-7 cells.[123] When a combination of 2-DG/DOX was used, the cell kill increased to 37% in T47D cells, while still no effect was seen on MCF-7 cells. 2-DG is tolerated in reasonably high doses of 0.5 g/kg in animals and doses up to 0.3 g/kg have been administered in humans without severe adverse side effects.[127] Although, there are currently no ongoing clinical trials employing 2-DG as a single agent due to the toxicity that arises at the large doses required to significantly inhibit tumor growth *in vivo*.[128] However, a phase I clinical trial has been completed for the use of 2-DG in combination with docetaxel to treat patients with advanced solid tumors, the outcome was that further phase II studies are justified in several solid tumors.[129] At the 2-DG doses employed in clinical trials thus far, non-serious transient side effects similar to hypoglycaemia have been recorded such as restlessness, nausea, and vomiting.[130,131] However, the main dose-limiting effect of 2-DG is its cardiotoxicity, with some patients exhibiting grade 3 asymptomatic QTc prolongation.[129,130]

1.3.2 2-DG as a radiosensitiser

1.3.2.1 Radiation therapy

Radiotherapy is the use of ionising radiation to kill malignant cells in cancer treatment. It can be employed as a single curative therapy or as part of adjuvant therapy. Radiation therapy is an extremely important component of cancer management; approximately 50% of cancer patients receive it and 40% of curative treatment strategies incorporate it.[132] Ionising radiation is usually delivered by a linear accelerator and carefully positioned beams are aimed from several different angles to intersect at the tumor, providing a much larger absorbed dose in the tumor than in the surrounding normal tissue. Radiotherapy is synergistic with chemotherapy, and has been used before, during, and after chemotherapy in susceptible cancers. It is well known that tumors differ in their sensitivity to radiation treatment. Cancers that can be cured by radiotherapy alone if they are detected early enough include: skin cancers (squamous and basal cell), prostate cancer, lung cancer (non-small cell), cervical cancer, lymphomas (Hodgkin's and low grade non-Hodgkin's) and head and neck carcinomas.[132]

Ionising radiation is believed to cause injury to cancer cells *via* the production of reactive free radicals, induction of oxidative damage and irreparable alterations to DNA.[121] Radiation can interact with DNA either directly, or indirectly *via* free radicals, both of which can elicit a variety of DNA lesions including base modifications, single-strand breaks and double-strand breaks.[132] Cells have mechanisms to repair DNA damage but some alterations will be left unrepaired or be repaired incorrectly, leading to impaired ability to divide and proliferate or even cell death.[132] Double-strand breaks in particular are closely linked with cell death.[122,132,133] Although radiation damages healthy cells as well, the objective of radiotherapy is to maximise damage to cancer cells whilst minimising damage to the healthy cells that lie adjacent to the tumor or in the path of radiation beams. In general, cancer cells are not as efficient as normal cells in repairing damage caused by radiation, resulting in differential cancer cell destruction.[132]

In addition, many compounds are able to modify the ability of ionising radiation to kill cells. There is interest in radiosensitisers and radioprotectors, which are capable of enhancing the cancer cell-killing efficacy or mitigating damage to surrounding non-malignant tissue, respectively. There are several mechanisms by which radiomodifiers are believed to sensitise tumor cells to radiation. One theory is based on the fact that the cellular processes required for error-free repair of DNA lesions require a continuous flow of metabolic energy,[122] which is often supplied by a high glycolytic rate in cancer cells, whereas normal cells rely more heavily on OXPHOS.[6] Therefore, modulation of energy supply using glycolytic inhibitors could sensitise cancer cells to radiation damage by inhibiting DNA repair processes. Another related theory is that radiation-induced cell injury is believed to be caused by the generation of free radicals which cause oxidative damage. Thus, it has been proposed that agents capable of enhancing oxidative stress could sensitise cells to the cytotoxic effects of radiation.

1.3.2.2 Evidence of 2-DG acting as a radiosensitiser

It has been demonstrated that 2-DG can be used to sensitise tumors to radiotherapy. *In vitro* studies have shown the radiosensitisation properties of 2-DG on a variety of cell types with high glycolytic rates, such as various murine and human cancer cell lines, as well as respiratory deficient mutants of yeast.[122,134–137] Some of these studies demonstrated that the presence of 2-DG for a few hours after irradiation was able to selectively inhibit the post-irradiation DNA repair process.[122,134,136] The rate of DNA repair appears to be strongly dependent on the rate of glycolysis,[136] thus, a proposed mechanism by which 2-DG radiosensitises cells is by inhibiting glycolysis and thereby preventing repair of potentially lethal DNA lesions. Additionally, a study by Lin *et al.* provided strong evidence that 2-DG-induced radiosensitisation is dependent on enhanced oxidative stress *via* disruptions to thiol metabolism.[121] They did this by showing that simultaneous treatment with a thiol antioxidant, N-acetyl-cysteine, protected HeLa cells from the otherwise radiosensitising effects of 2-DG, while N-acetyl-cysteine causes no alterations to radiosensitivity in the absence of 2-DG. Sinthupibulyakit *et al.* suggested that 2-DG radiosensitisation of cancer cells is p53-dependent by showing that p53-deficient lung cancer cells (H358) were more sensitive than p53 wild-type lung cancer cells (A549) to 2-DG-induced radiosensitisation.[137]

Interestingly, under similar conditions (the presence of 2-DG for a few hours after irradiation), 2-DG has been shown to acts as a radioprotector in non-cancerous, healthy cells such as human peripheral blood lymphocytes.[138] Dwarakanath *et al.* have shown that a significant increase in radiation-induced cell death due to the presence of 2-DG is only observed in cells if the rate of glucose utilisation is beyond a certain threshold (> 0.5 pmol/cell/h).[122] Since cancer cells are characterised as having much higher glucose avidity than normal cells, this can explain why healthy cells are not radiosensitised by 2-DG. The mechanism for radioprotection is yet to be elucidated but it is hypothesised that it could be due to reduced misrepair and fixation of DNA lesions.[122,136]

Importantly, these *in vitro* studies highlighted that the radiation-modifying effects of 2-DG are dependent on the cell type, the energy metabolism profile and the molar concentration ratio of 2-DG versus glucose. The ratio of glucose and 2-DG is important because 2-DG inhibits glycolysis in a competitive manor, which means the inhibition can be reversed by increased glucose concentrations.[120] For this reason, prior to radiosensitisation studies on 2-DG, the glucose concentration of cell media is reduced for *in vitro* studies and animals or patients are often glucose fasted from the night before.

Animal studies have confirmed that the radiomodification properties of 2-DG observed *in vitro* can be reproduced *in vivo*. Murine tumor models show increased tumor cell loss, tumor regression and enhanced animal survival when 2-DG (≥ 1g/kg BW) is administered immediately before or after irradiation.[139,140] Comparatively, similar doses of 2-DG in whole-body irradiated mice have demonstrated radioprotection of normal tissues such a bone marrow and spleen.[141,142]

These promising preclinical results instigated clinical trials to evaluate the potential for 2-DG to improve radiotherapy outcomes. Phase I/II trials have demonstrated that a 0.2-0.3 g/kg dose of 2-DG (20 min before irradiation, orally administered after overnight fasting) selectively enhances radiation-induced damage to glioma tumor cells whilst protecting normal cells.[131,133] A large weekly fraction of gamma radiation (5 Gy/fraction) was used in the studies and the combination with 2-DG was well tolerated by glioma patients without any acute toxicity or late radiation damage to normal brain tissue.[127] However, at the largest dose of 0.3 g/kg BW, two patients were too restless to complete treatment, although significant changes in the vital parameters were not observed even at this high dose.[133]

1.3.3 2-DG as a CEST agent

Previously, 2-DG has been isotopically labelled and utilised to elucidate glucose uptake and metabolism. Radiolabelled [^{14}C]-2-DG was first applied in *ex vivo* imaging of the rat brain *via* high-resolution autoradiography.[143] Labelled 2-DG has been used in preference to glucose due to its slower metabolism, offering a more convenient time scale to preform imaging techniques. 2-DG enters cells *via* the same transporters as glucose, mainly GLUT1 and GLUT3 in the brain.[144] Once inside the cell it is phosphorylated by hexokinase to form 2-DG-6-phosphate (2-DG6P) which is only minimally accepted as a substrate by glucose-6-phosphate dehydrogenase (G6PDH) and glucose-6-phosphate isomerase, preventing metabolism *via* both the oxidative pentose phosphate pathway and the glycolytic pathway, respectively.[144] 2-DG6P and its metabolites have poor cell permeability and thereby become trapped and accumulate intracellularly, much like FDG and its metabolic products.[86] FDG is another (extremely successful) example of a radiolabelled analogue of 2-DG that is used to investigate glucose metabolism *via* FDG-PET imaging. Additionally, ^{13}C-labelled 2-DG can be detected by nuclear magnetic resonance (NMR), however the current low detection sensitivity of *in vivo* NMR prohibits feasible imaging.

Recently, non-radiolabelled 2-DG has been employed in imaging studies as a CEST CA owing to its 4 hydroxyl groups that are able to transfer saturation to bulk water *via* chemical exchange with water protons.[86,144] The CEST signal arising from 2-DG and its metabolic product, 2-DG6P, have been characterised and *in vitro* studies have revealed that 2-DG6P produces a 20-30% higher CEST effect than 2-DG (depending on the temperature and pH) and a new resonance in the 'sugar-phosphate' chemical shift region.[86,144] Nasrallah *et al.* carried out an experiment on healthy rats to compare the CEST signal generated by 2-DG versus glucose *in vivo*.[144] CEST signal was calculated from the integral of the MTR_{asym} curve at 1.00 ±0.25 ppm. When a 1 g/kg bolus injection of either glucose or 2-DG was administered, the peak CEST contrast generated in the rat brain was 2.4 times greater for 2-DG than it was for glucose.[144] Furthermore, the 2-DG-CEST signal was sustained for 40 minutes and then slowly declined over more than 1 hour (Figure 16a), whereas, the glucoCEST signal was not discernible from baseline immediately after the initial surge in signal (Figure 16b, red line). These results reflect the rapid glucose-induced secretion of insulin and hence swift depletion of both extracellular and intracellular glucose. Additionally, glucose is broken down into metabolites that do not arbour a CEST effect, whereas the main metabolic product of 2-DG is 2-DG6P which heavily contributes to 2-DG-CEST signal.[86,144] The MTR_{asym} spectra of 2-DG and 2-DG6P were very similar, restricting the ability to deconvolute signal from the two saccharide compounds *in vivo*. Therefore, ^{31}P MRS was employed to compare changes in 2-DG-CEST signal with 2-DG6P levels.[144] Consistent with previous literature,[145] ^{31}P MRS showed that the 2-DG6P resonance reached a maximum between 30 and 40 minutes, then slowly decreased. This is in agreement with their finding that the 2-DG-CEST signal remained at a high level for the first 30-40 minutes which then began to decrease as the 2-DG6P concentrations declined. To help determine whether the majority of CEST signal was generated from extracellular or intracellular compartments, the blood glucose concentration of healthy rats was clamped above the peak level achieved with 1 g/kg BW 2-DG *via* continuous infusion of D-glucose. The results showed that even with the huge concentrations of extracellular D-glucose, the glucoCEST signal was still only 50% of that achieved by 2-DG bolus injection.[144] Thus, it is believed that the greater CEST signal achieved by 2-DG in comparison to glucose is largely due the 2-DG and 2-DG6P that accumulates intracellularly, whereas the vast majority of the glucoCEST signal is of extracellular origin since glucose is rapidly metabolised once it is internalised by cells.[144,146]

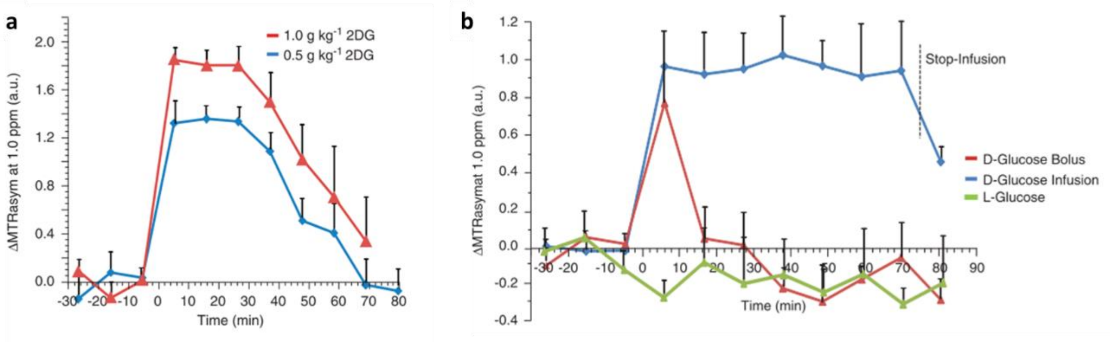

Figure 16. MTR$_{asym}$ in the rat brain at 1 ppm ±0.25 ppm as a function of time, generated by a) a 0.5 or 1 kg/g bolus of 2-DG, b) a 1 kg/g bolus of glucose (red) or L-glucose (green), or continuous infusion of glucose (blue). Figures were adapted from Nasrallah *et al.*[144]

Rivlin *et al.* investigated the ability of 2-DG, as well as FDG, to create CEST contrast in orthotopic mammary tumors implanted in mice.[86] Following a 2 g/kg BW injection of 2-DG there was a rapid increase in tumor CEST contrast measured at 1.2 ppm for the first 30 min, followed by a steady state of CEST signal that persisted for over an hour at a level of 22% water signal reduction. In the same study, they compared these results to tumor CEST enhancement following a 1.5 g/kg BW bolus injection of glucose. The maximum CEST enhancement by glucose was 10% and there was a sharp decline in signal after 20 minutes. The long persistence of the 2-DG-CEST signal from tumors is consistent with a previous study in which ^{13}C NMR was used to monitor 2-DG and 2-DG6P levels in implanted MCF-7 tumors in mice following intraperitoneal injection of 2-DG labelled at the 6th position.[147] In this study, they found that 2-DG6P reached the same concentration as 2-DG after approximately 90 minutes and after 250 minutes most of the 2-DG had disappeared while the 2-DG6P retained about half of its maximal value. The short duration of glucoCEST signal due to rapid metabolism *in vivo* is consistent with a number of studies in both animal models,[56,84,144] and in humans.[85,88,89] Rivlin *et al.* demonstrated that 2-DG can be used to create tumor contrast in mice at 7 T.[86] Clinical translation of 2-DG-CEST MRI would allow detection of tumors, provide information on metabolic alterations and enable monitoring of tumor response to therapy in a non-invasive manor and without the need for radiolabelled species. The technique could offer greater sensitivity and superior time frames for image acquisition in comparison to glucoCEST.

Additionally, a number of studies have been carried out on rat brains employing 2-DG as an imaging CA using a CESL MRI approach.[87,148,149] Findings from CESL experiments were similar to those from CEST experiments. For instance, following a 1 g/kg BW injection, generated CESL signal from 2-DG was 2.2 times higher at its maximum and persisted for a much longer duration when compared to CESL signal generated by glucose bolus injection.[87] One study obtained 2-DG-CESL results with exquisite $0.33 \times 0.33 \times 1.50$ mm^3 resolution.[148] Another study compared 2-DG-CEST and 2-DG-CESL techniques and reported better sensitivity and more specificity for 2-DG-water exchange effects for CESL than for CEST.[149] Thus, 2-DG-CESL imaging may provide a novel approach for inference of glucose uptake and metabolism in the brain.

1.4 Liposomes

Liposomes are artificially prepared spherical vesicles that are comprised of a lipid bilayer and encapsulate an aqueous interior. The components can include phospholipids, synthetic amphiphiles, and sterols such as cholesterol that are often employed to modify membrane permeability. Thin-film hydration is the most popular method of liposome preparation, in which lipids are dissolved in organic solvent, evaporated to dryness to create a thin film and hydrated with an aqueous solution (Figure 17).[150] Other methods include reverse-phase evaporation, freeze-drying and ethanol or ether injection to aqueous media.[151] Techniques such as extrusion, sonication and freeze-thaw cycling can then be employed to modify liposome diameter and size distribution.[151] Additional liposome characteristics that can be controlled include lamellarity and charge.

Liposomes have the capacity for covalent and non-covalent association with both hydrophilic and hydrophobic cargo, such as therapeutics or imaging agents. The surface charge, size and mechanical properties of the liposome itself can be fine-tuned to optimise pharmacokinetics, biodistribution and encourage accumulation in tissues of interest, such as tumor tissue.[152]

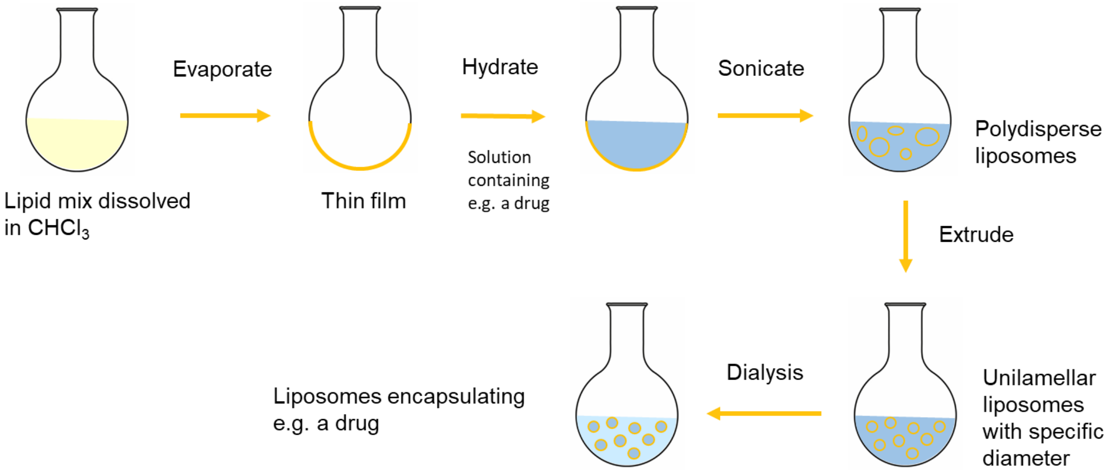

Figure 17. Schematic showing how liposomes can be prepared *via* thin-film hydration.

1.4.1 PEGylation of liposomes

Polyethylene glycol (PEG) coating of liposomes is often carried out resulting in several clinical advantages. Surface modification of liposomes with PEG can be achieved in several ways, by: physically adsorbing a PEG polymer onto the surface of the liposomes; incorporating a PEG-lipid conjugate into the bilayer during liposome formulation; or covalently attaching reactive PEG moieties onto the surface of pre-prepared liposomes.[153] Most commonly, PEG coating is achieved by formulating liposomes with a small molar percentage (typically 2-10 mol%) of PEG-lipid conjugates with PEG sizes in the range of 1000-5000 Da, such as 1,2-distearoyl-*sn*-glycero-3-phosphoethanolamine-*N*-[methoxy(polyethylene glycol)-2000] (DSPE-PEG2000, Figure 18).[154]

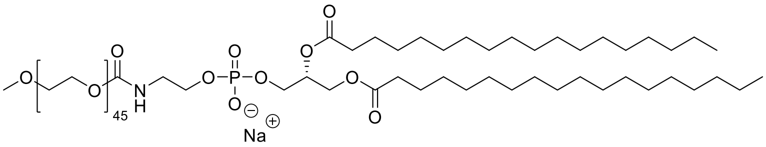

DSPE-PEG2000

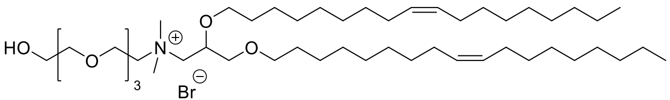

DODEG4

Figure 18. Chemical structures of the commercially available lipid, DSPE-PEG2000 and a short-chain PEG lipid developed by Hurley *et al.*,[154] DODEG4.

Uncharged nanoparticles rapidly aggregate due to attractive Van der Waals forces, and charged particles can undergo electrostatic interactions with counterions that neutralise their surface charge, rendering the surface amenable to aggregation.[155] In addition, prolonged exposure to circulating serum proteins increases the likelihood of liposome aggregation.[155] PEG coating of liposomes can be employed to overcome attractive forces between liposomes and neighbouring nanoparticles and/or blood components.[153,155–157] Firstly, due to the highly hydrophilic nature, each ethylene glycol (EG) subunit is surrounded by a minimum of 2–3 water molecules.[157] Thus, PEG grafted on the liposome surface creates a hydrated cloud with a large excluded volume that sterically precludes interaction with neighbouring liposomes or biomacromolecules.[155,157] Needham *et al.* performed X-ray analysis on liposomes containing 4 mol% PEG1900-lipid, the results showed that the PEG layer extends about 50 Å away from the lipid surface, giving rise to inter-liposome repulsive forces.[153,156] Secondly, the large conformational freedom provided by the highly flexible PEG chains renders interpenetration of foreign matter into the PEG corona thermodynamically unfavourable.[155,157] Together, these features greatly suppress interactions between PEGylated systems and the surrounding environment.

Importantly, PEG coating of liposomes decreases the rate of removal from the blood by reducing uptake into the mononuclear phagocytic system (MPS), thereby substantially lengthening the biological half-life.[157–159] PEG-coating has this effect because it reduces interaction with opsonins, which are biomolecules that bind to foreign material to label them for phagocytosis.[160] For example, using mice peritoneal macrophages *in vitro*, Doxil® liposomes showed 60% less MPS uptake compared to liposomes of identical size distribution and lipid composition except for the omission of 5 mol% DSPE-PEG2000.[161] Impressively, PEG coating of Doxil® liposomes with 5 mol% DSPE-PEG2000 achieves an *in vivo* circulation half-life of 3-4 days in humans, increasing the bioavailability compared to the free drug nearly 90-fold.[155,161]

The effectiveness of PEG coating to shield liposomes from the MPS is critically dependent on the density and conformations assumed by conjugated PEG chains.[155,157] When neighbouring PEG chains are sparsely packed and do not overlap, PEG occupies a diffuse volume referred to as a “mushroom” conformation. When the surface PEG density is increased such that adjacent PEG chains overlap, the excluded volume and repulsion between PEG chains causes them to stretch away from the liposome surface to form a “brush” layer, eventually reaching a dense “brush” regime. The mushroom-to-brush transition has long been considered as critical threshold at which PEG begins to exhibit stealth polymer functions. The dense brush conformation has been demonstrated as necessary for sustained *in vivo* circulation *via* evasion of serum protein adsorption and MPS uptake.[155,157]

To observe the effect of PEG molecular weight *in vivo*, Allen *et al.* monitored the blood concentration of liposomes with differential PEG-shielding.[162] The liposomes incorporated a small molar percentage of lipids conjugated to PEG chains with average molecular masses of 120, 750, 1900 and 5000 Daltons. Liposomes with longer molecular weight PEG (PEG-1900 and PEG-5000) retained higher blood levels than liposomes containing shorter chain PEG-lipids (PEG-750 and PEG-120), even when the molar percentage of short-chain PEG-lipid was increased to saturating levels. They concluded that the ability of PEG coating to extend *in vivo* circulation depends on both the amount of grafted PEG and the length of the chains.

The PEG-2000 chain is long, neutral and hydrophilic, which masks the charge of the liposome as well as decreasing the absorption of serum proteins and opsonins.[155] Cells have been shown to preferentially take up charged particles, and the absorption of serum proteins and opsonins to the liposome surface has been demonstrated to stimulate interaction with cell walls.[160] Thus, the advantages of liposome PEGylation can be at the expense of cellular uptake, which is especially problematic when the liposomal contents need to be delivered intracellularly (e.g. DNA, siRNA).[163,164] Therefore, there is a balancing act between employing increased PEGylation in attempts to optimise the pharmacokinetics and *in vivo* circulation, versus using less PEGylation to enhance uptake to the target tissue. In 2013, Mitchell *et al.* demonstrated that replacing DSPE-PEG2000 with higher molar portions of lipids exhibiting short EG shielding units was able to significantly enhance liposome internalisation in a range of tumor cells *in vitro*, whilst maintaining similar clearance rates to PEG-2000-stabilised liposomes *in vivo*.[164] Their short-chain PEG lipid, *N*-(2-(2-(2-(2-hydroxyethoxy)ethoxy)ethoxy)ethyl)-*N*,*N*-dimethyl-2,3- bis((Z)-octadec-9-enyloxy)propan-1-aminium (DODEG4), is derived from the structure of (*N*-[1-(2,3-dioleyloxy) propyl])-*N*,*N*,*N*-trimethylammonium chloride (DOTMA) and exhibits 4 EG units covalently attached at the hydrophilic end *via* a quaternary amine moiety (Figure 18).[154] Further work is required to determine the complicated relationship between the nature of EG-shielding and the extent of EPR liposome deposition in tumor tissue.

1.4.1.1 The EPR effect

Advantageously, PEG coating assists passive targeting of tumors.[153,155,160,161,164] Tumor vasculature is characterised by poorly aligned endothelial cells with wide fenestrations (up to 4 µm), allowing liposomes to pass from the blood into the interstitial spaces of tumor tissue.[155,165] Thus, liposome diameter should be smaller than 400 nm to enable efficient extravasation. On the other hand, to avoid filtration by the kidneys, nanocarriers must to be larger than 10 nm.[92,155] Small PEG-coated liposomes with a diameter of 10-

200 nm have been shown to be optimal for EPR delivery of imaging or therapeutic cargo to tumors.[164,166] Selecting a size within this range involves a compromise between the fact that smaller particles can perfuse more deeply and homogeneously into the tumor, however conversely, smaller particles have reduced capacity to carry a payload. The extended blood half-life produced by PEGylation enables the deposition of larger quantities of liposomes in the tumor over time. Additional defective lymphatic drainage from solid tumor tissue results in abundant accumulation of liposomes at the tumor site.[153,155,161] The combined outcome of these processes is termed the EPR effect (Figure 19).

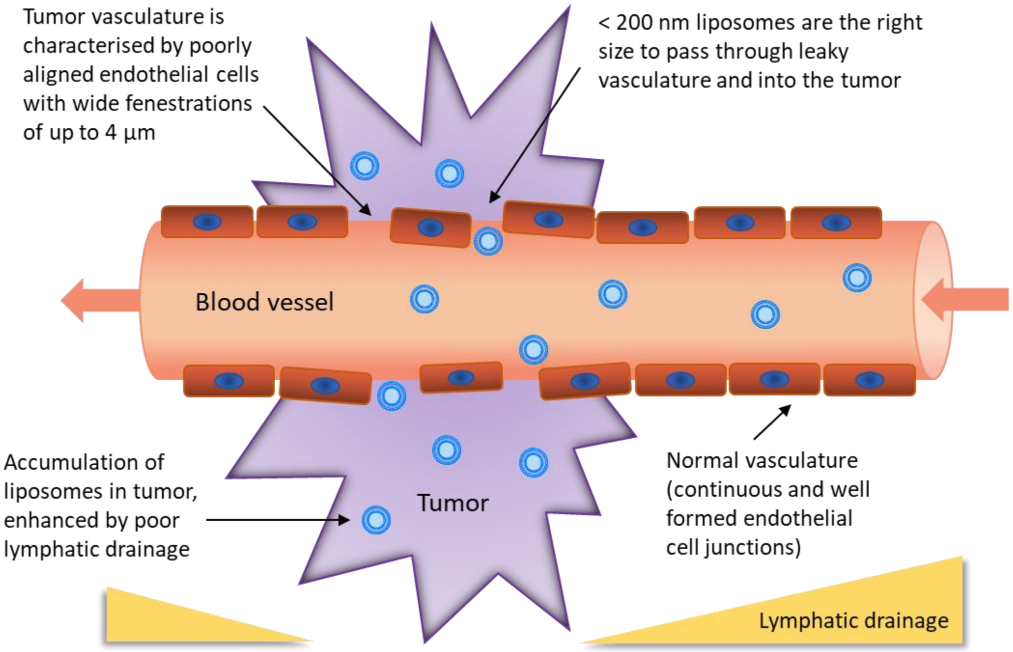

Figure 19. Diagram showing how liposomes accumulate in tumors *via* the EPR effect.

However, despite the vast success of nanoparticles exploting the EPR effect in animal models, recently it has become apparent that this effect often does not translate into humans when an agent reaches clinical trials.[167,168] Problems with the murine models in use have been indentified that may exadgerate the EPR effect, such as the much larger tumor-to-body weight ratio in mice compared to humans, and the time taken for murine tumors to grow (weeks *vs*. years) giving rise to rapid angiogenesis and therefore blood vessel structures that are particularly disorganized, hyperpermeable, and amenable to EPR.[167] Therefore, it is now thought that the EPR effect should only be invoked on a case-by-case basis, when clinical evidence suggests the tumor type is susceptible.

1.4.2 Liposomes as macromolecular imaging agents

Medical imaging requires a sufficiently intense signal to be generated by a contrast agent in order to differentiate a region of interest from the surrounding tissues. To facilitate the amassing of contrast at a required site, various microparticulates have been proposed as carriers for contrast agents. Amongst which, liposomes are one of the most popular candidates, due to their easily manipulated properties and useful pharmacological characteristics. Liposomes have been adapted to carry Gd(III) chelates and to thereby act as nanoscale MRI CAs for imaging tumors (Section 1.1.2.1).[27] Gd chelates have been both encapsulated in the aqueous interior and covalently linked to the bilayer surface, allowing high loading which can significantly enhance the sensitivity of these supramolecular CAs.[27] Liposomes internally loaded with Gd chelates exhibit decreasing relaxivity with increasing particle size, presumably due to a reduced surface-area-to-volume ratio.[36,37] As expected, liposomal CAs incorporating both core-encapsulated and surface-conjugated Gd chelates were found to have better relaxivity than liposomal CAs exhibiting only one method of Gd chelate loading.[38] Additionally, the whole internal aqueous cavity of liposomes has been utilised as CEST MRI contrast media *via* encapsulation of paramagnetic chelates in lipoCEST agent formulation (Section 1.2.1.4).

The radiolabelling of vesicles has been used for many years in preclinical studies to evaluate the performance of liposomes *in vivo*, providing an important tool in the development of liposomal drug formulations.[169] For example, radionuclides such as ^{111}In and ^{99m}Tc have been used for single-photon emission computed tomography (SPECT) imaging of liposomes and the relatively long living positron emitter, ^{64}Cu, has been employed in PET imaging of liposomes *in vivo*.[169]

1.4.3 Actively targeted liposomes

Another advantage of liposomes is that antibodies, endogenous ligands or short-chain peptides with a high affinity for biomarkers expressed by tumor cells can be anchored to the liposome surface to achieve highly specific targeting.[160] The aim of using targeting molecules in diagnostic applications is to increase the imaging agent concentration in diseased tissue relative to healthy organs and tissue. In the case of cancer imaging, active targeting can work in synergy with passive targeting *via* the EPR effect to enhance accumulation in tumors. This strategy has been applied to a variety of liposomal CAs, for example lipoCEST agents (an example of an RGD-targeted formulation is described in Section 1.2.1.4.1).[107] Targeted ligands have also been incorporated on the surface of Gd chelate-bearing liposomes, such as folic acid, peptides and antibodies.[27] Kamaly *et al.* prepared folate-targeted bimodal liposomes for MRI of tumors by incorporating a folic acid-conjugated lipid with a medial PEG spacer, a Gd chelate-conjugated lipid and a rhodamine-B-functionalised lipid, enabling both MR and florescent imaging.[170] The liposomal CAs were tested in a mouse model of human ovarian carcinoma, which overexpresses the folate receptor. Successful tumor targeting was confirmed by a histological study using fluorescence microscopy. The novel bimodal CAs generated a 4-fold tumor contrast enhancement in T1-weighted MRI 2 hours after liposome administration. This was a combined result of the active folate-mediated tumor targeting as well as passive tumor accumulation *via* the EPR effect. The non-targeted liposomes elicited similar contrast enhancement 24 hours post-injection, attribute to the EPR effect alone.

There is a wealth of research encompassing ligand-targeted strategies for cancer nano-therapeutics. Approaches for liposome targeting to cancer cells and tumor tissue have so far included ligands for a number of receptors, such as folate, integrin, transferrin, epidermal growth factor (EGFR), somatostatin and membrane matrix metalloprotease.[92,169] Whilst many preclinical studies have reported on nanomedicines exhibiting targeting ligands, none have been approved thus far. Several PEGylated liposomes decorated with active targeting agents are currently under clinical investigation.[171]

For example, a liposomal formulation of DOX targeted to EGFR-overexpressing tumors *via* coupling of antigen binding fragments from cetuximab, an inhibitory anti-EGFR monoclonal antibody, has progressed to clinical trials. *In vitro* studies showed superior cell association and internalisation of anti-EGFR immunoliposomal DOX (anti-EGFR-IL-DOX) compared to ligand-lacking control liposomes.[171] Experiments in rats showed similar pharmacokinetics of ligand-targeted and ligand-lacking liposomal DOX, indicating that conjugation of antibody fragments does not alter liposomal stability or circulation time.[172] In two EGFR-overexpressing tumor xenograft models, anti-EGFR-IL-DOX significantly inhibited tumor growth when compared to untargeted PEGylated liposomal DOX.[172] Quantitative flow cytometry analysis demonstrated that cellular accumulation of anti-EGFR liposomes was 6-fold higher when compared to ligand-lacking liposomes in tumor cells derived from mice, however, biodistribution studies in mice showed no differences in tumor accumulation for EGFR-targeted versus untargeted formulations.[172] In a recently completed Phase I trial containing 26 patients with EGFR-overexpressing advanced solid tumors, one patient showed complete response, one showed partial response and ten patients had stable disease lasting 2–12 months.[171] Anti-EGFR-IL-DOX showed signs of efficacy with very little toxicity in Phase I trials so it has progressed to Phase II trials to determine its efficacy as a first-line treatment in patients with advanced triple negative EGFR-positive breast cancer.[173]

The main emerging conclusions from preclinical and clinical studies on actively targeted liposomes are: 1) ligand-targeted liposomes appear to be safe and efficacious, 2) the vast majority of ligand-targeted liposomes are for applications in cancer therapy, 3) targeting ligands do not appear to enhance localisation within cancer tissue but rather provide benefits in terms of target cell internalisation and tumor retention once liposomes have already accumulated predominantly due to the EPR effect.[169,171]

1.4.4 Environmentally responsive liposomes

The observation that pathological tumor tissue exhibits a more acidic microenvironment than healthy tissue, as well as the known acidity of the endosomal lumen that liposomes become exposed to upon endocytosis, has provoked interest in pH-sensitive liposomes for the delivery of chemotherapeutic agents.[92] Such liposomes are designed to be stable at pH 7.4 but undergo destabilisation or acquire fusogenic properties when exposed to lower pH, resulting in the release of their encapsulated content. There are a number of methods for introducing this pH trigger into liposome formulations. The most established technique is to form the lipid bilayer with phosphatidylethanolamine (PE) derivatives

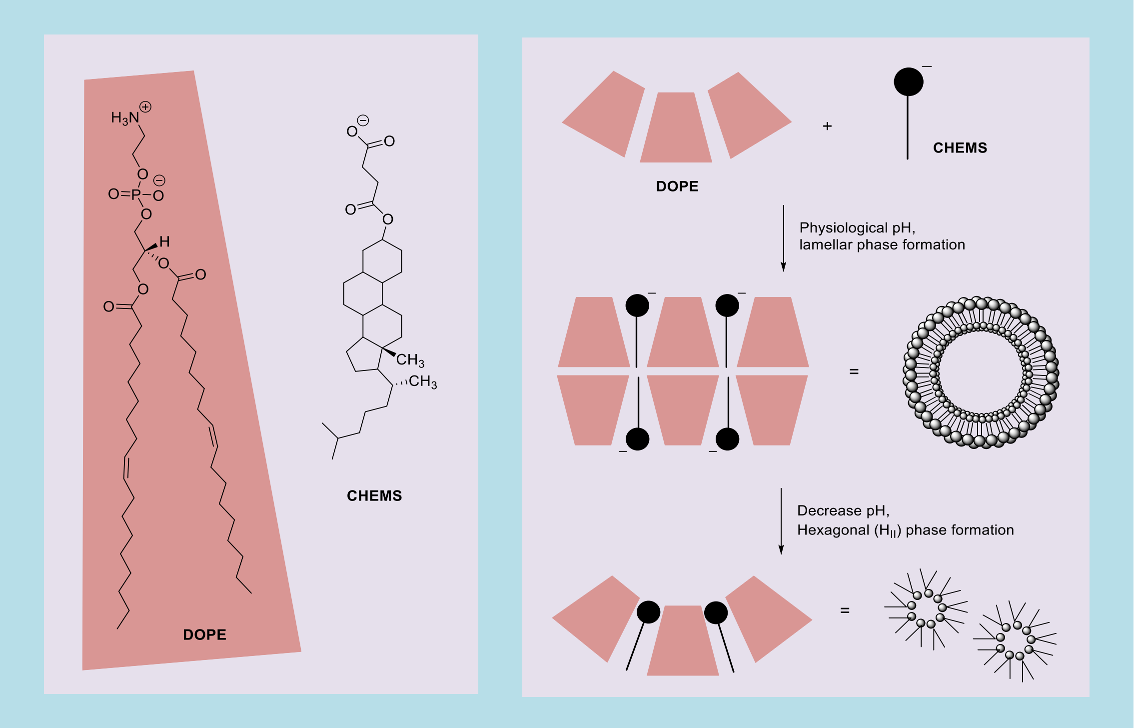

Figure 20. Left: chemical structure of the conic lipid DOPE and the stabilising acid CHEMS. Right: Pure DOPE assembles into an inverted hexagonal phase. At neutral pH, CHEMS enables the formation of bilayers (lamellar phase) by introducing charge repulsion and increasing the volume of the polar head region. Acidic pH induces protonation of CHEMS and liposome destabilisation resulting in reversion to the hexagonal phase.

(such as 1,2-dioleoyl-sn-glycero-3-phosphoethanolamine (DOPE), Figure 20) and intercalated amphiphilic molecules containing an acidic group that is negatively charged at physiological pH, but becomes protonated at lower pH.[174,175] In contrast to the majority of phospholipids, PE-derived lipids exhibit a small, minimally hydrated head group that occupies a smaller area compared to the hydrocarbon chains, resulting in a cone shape (as opposed to the cylindrical structure usually formed by phospholipids), thereby preventing formation of the lamellar phase.[176] The cone shape formed by PE and its derivatives favours strong intermolecular interactions between the charged amine and phosphate moieties of the polar head groups, resulting in a tendency for these lipids to assemble in the inverted hexagonal phase (H_{II}) when above the phase transition temperature T_m, which is 10 °C for DOPE (Figure 20).[175] The incorporation of amphiphilic molecules containing negatively charged acid groups at physiological pH such as oleic acid (OA) or cholesteryl hemisuccinate (CHEMS) generate electrostatic repulsion with the phosphate groups of PE, reducing the close interactions between PE polar head groups and effectively increasing the volume of the polar region, allowing organisation into the lamellar phase (Figure 20).[174,177,178] Protonation of the stabilising acids at lower pH removes this charge repulsion, resulting in reversion of PE lipids to H_{II}, inducing liposome destabilisation and endosome fusion with a final consequence of encapsulated content release.[179]

Another approach for introducing pH-sensitivity to liposomes involves the design and synthesis of novel lipids that contain acid-cleavable moieties, usually located between the polar head and fatty tail regions of the molecule. Thus, when these lipids are subjected to low pH they are cleaved, resulting in the liberation of membrane destabilising compounds.[175] While some groups have successfully employed highly acid-sensitive diortho ester moieties as cleavable linkers,[180] others have synthesised pH-labile *N*-acetylated aminophospholipid derivatives (including DOPE) which lose the stabilising group at low pH, increasing the concentration of the destabilising PE component and thereby inducing transition into the H_{II} phase.[181] Additionally, because PEG-coating can act as a barrier to intracellular delivery or drug release, environmentally responsive liposomes have been formulated with labile linkages between the PEG and lipid moieties, which can be cleaved upon exposure to the relatively acidic conditions of endocytic vacuoles or the acidotic tumor mass.[114,182]

Other stimuli inherent to the tumour microenvironment have been exploited to trigger release of encapsulated contents from nanocarriers. For example, Banerjee *et al.* reported liposomal release in response to a cancer-associated enzyme, matrix metalloproteinase-9. This was achieved by incorporation of a lipopeptide that was synthesised by conjugating a matrix metalloproteinase-9 substrate peptide to a fatty acid chain for insertion into the membrane. Metastatic cancer cells (MCF7) secreting high levels of the enzyme were found to induce rapid release of the encapsulated contents from liposomes incorporating the lipopeptide.

Although many pathological areas, such as inflamed tissues and tumors, exhibit intrinsic hyperthermia compared to normal tissues,[114] most temperature sensitive liposome strategies involve local heating of the tumor site (to approximately 39.5-42 °C).[113,114] Methods to achieving this local hyperthermia include high-intensity focused ultrasound and radio-frequency ablation.[92,113,183] This is an attractive strategy in cancer therapy since hyperthermia is associated with increased tumor permeability and enhanced drug uptake.[114] Lipids with a specific T_m are used to prepare these liposomes, for example the most commonly used lipid is dipalmitoyl phosphatidylcholine (DPPC) due to its phase transition around 41 °C, which is just higher than normal physiological temperature.[114,184] A thermo-responsive DOX formulation is currently undergoing Phase III clinical trials for the treatment of various solid tumours (see Section 1.4.5.1).[183]

In addition, external stimuli such as magnetic fields and light (typically UV and near-infrared) have been applied to encourage site-specific release of content from liposomes. Liposomes can be magnetised by incorporation of magnetites such as Fe_3O_4. These magnetic nanoparticles experience significantly elevated temperatures during exposure to a high-frequency alternating magnetic field, which can rupture the liposome membrane and selectively release the encapsulated cargo.[185] Alternatively, various light-sensitive lipids have been developed to facilitate photo-triggered structural and conformational changes such as photo-isomerism, photo-fragmentation, photo-polymerisation or direct interaction of liposomes with the target cells *via* membrane fusion.[114]

1.4.5 Liposome formulations approved for the treatment of cancer

Liposomes are the first nano-scale delivery systems to be successfully translated into the clinic. The first liposomal product to be introduced was Doxil® to the US market in 1995 (called Caelyx® in Europe), which is a liposomal formulation of DOX used for the treatment of ovarian cancer, multiple myeloma and AIDS-related Kaposi's sarcoma.[161] It is now marketed in over 80 countries and has been extremely successful due to the large reduction in cardiotoxicity and improved pharmacokinetics, in comparison to non-liposomal DOX.[186,161] Doxil®'s superior pharmacokinetic profile boasts nearly 90-fold greater DOX bioavailability at 1 week after injection versus the free drug.[155] DOX is entrapped inside liposomes *via* an active loading process first developed by

Barenholz.[161] Liposomes are formulated in the presence of ammonium sulfate, then once they are formed, ammonium sulfate is removed from the extra-liposomal media and replaced with DOX HCl. Ammonium sulfate dissociates into two ammonium cations and a single sulfate anion. Ammonia is able to freely permeate the lipid bilayer, whereas the sulfate anions cannot, thereby establishing a pH gradient across the membrane. DOX in its uncharged form can cross the membrane and under the acidic intra-liposomal conditions, it accumulates as a sulfate salt precipitate, ultimately resulting in greater than 90% encapsulation efficiency.[161] Doxil® was closely followed by the liposomal formulation of daunorubicin, DaunoXome®, which was approved for the management of advanced HIV-associated Kaposi's sarcoma in 1996. DaunoXome® alters the pharmacokinetics of daunorubicin to enhance circulation time, diminish toxicity including cardiotoxicity and allow administration of higher doses of the encapsulated drug.[187]

Table 2. Clinically approved liposome formulations for the treatment of cancers, adapted from Bulbake *et al.*[183]

Liposome product	Approved	Active agent	Lipid composition (molar ratio)	Mean diameter	Administration	Indication
Doxil®/ Caelyx®	1995	Doxorubicin	HSPC:Chol: DSPE-PEG2000 (56:39:5)	80-100 nm	i.v.	Ovarian, breast cancer, Kaposi's sarcoma
DaunoXome®	1996	Daunorubicin	DSPC:Chol (2:1)	45 nm	i.v.	AIDS-related Kaposi's sarcoma
Depocyt®	1999	Cytarabine/ Ara-C	DOPC, DPPG, Chol and Triolein	3–30 µm	spinal	Neoplastic meningitis
Myocet®	2000	Doxorubicin	EPC:Chol (55:45)	150-250 nm	i.v.	Metastatic breast cancer (with cyclophosphamide combination therapy)
Mepact®	2004	Mifamurtide	DOPS: POPC (3:7)	< 100 nm	i.v.	High-grade, resectable, non-metastatic osteosarcoma
Marqibo®	2012	Vincristine	SM:Chol (3:2)	100 nm	i.v.	Acute lymphoblastic leukaemia
Onivyde™	2015	Irinotecan	DSPC:Chol: DSPE-PEG2000 (3:2:0.015)	110 nm	i.v.	Metastatic adenocarcinoma of the pancreas (combination therapy with fluorouracil and leucovorin)

Abbreviations: hydrogenated soy phosphatidylcholine (HSPC); cholesterol (Chol); 1,2-dioleoyl-*sn*-glycero-3-phosphocholine (DOPC); Egg phosphatidylcholine (EPC); 1,2-dioleoyl-*sn*-glycero-3-phospho-L-serine (DOPS); 1-palmitoyl-2-oleoyl-*sn*-glycero-3-phosphocholine (POPC); sphingomyelin (SM).

Subsequently, the chemotherapeutic liposomal formulations Depocyt® (for neoplastic meningitis), Myocet® (for metastatic breast cancer in combination with cyclophosphamide) and Mepact® (for high-grade, resectable, non-metastatic osteosarcoma) were approved in 1999, 2000 and 2004, respectively.[183] Depocyt® is a multivesicular liposome formulation of cytarabine/Ara-C with a granular structure known as DepoFoam™.[188,189] DepoFoam™ formulations consist of spheroids (10-20 µM) with numerous internal aqueous chambers separated by a single lipid bilayer that are ideal for encapsulating hydrophilic drugs and give rise to extended-release profiles ranging from hours to several weeks. [188,189] This technology could provide marked improvements over traditional liposome formulations for medicines that require multiple and frequent administration due to short time of action or side effects. Myocet® is a non-PEGylated liposome formulation of DOX that offers the benefits of Doxil® without dose-limiting toxicity such as hand-foot-syndrome, which is caused by accumulation in the skin.[190] The clearance is much slower than conventional free DOX, but not as slow as PEGylated Doxil® due to enhanced uptake by phagocytic cells.[190]

More recently, in 2012 the FDA approved Marqibo®, a liposomal formulation of vincristine for the treatment of acute lymphoblastic leukaemia and in 2015 Onivyde™ was approved, which is used to manage metastatic adenocarcinoma of the pancreas.[183] Onivyde™ encapsulates the topoisomerase inhibitor, irinotecan, in an impressively high drug:lipid ratio (more than 800 g agent per mole of phospholipid).[191] This is achieved by a modified gradient loading method where highly charged anions such as sucrose octasulfate are trapped inside liposomes to stabilise internal irinotecan as a precipitated octasulfate salt, giving rise to unprecedented loading efficiency and *in vivo* drug retention with a drug release half-life of 56.8 h.[191]

Although the majority of interest in liposome-based products revolves around the management of cancer, it is worth noting that several have been developed for fungal infections; Abelcet®, Amphotec® and Ambisome® which were introduced in 1995, 1996 and 1997, respectively.[183] There has been interest in liposomes as vaccination delivery vectors since the approval of Epaxal® and Inflexal® V for inoculation against hepatitis and influenza, respectively.[192] Both formulations boast improved tolerability compared to their conventional vaccine alternatives.[192] Two pain relief formulations have received approval; DepoDur™ in 2004 and Exparel® in 2011. DepoDur™ exhibits the same DepoFoam™ structure as Depocyt®, whereas, the lipid structure of Exparel® is almost identical apart from the inclusion of a novel phospholipid component, dierucoylphosphatidylcholine (DEPC).[188,193] DepoDur™ and Exparel® were designed to create desirable sustained-release profiles for the analgesic drugs, morphine sulfate and bupivacaine, respectively, and are intended for use in combination with various surgical procedures.[188] Finally, Visudyne® is a unilamellar liposome formulation containing a photosensitising agent, verteporfin, that is employed in photodynamic therapy. The use of Visudyne® in combination with photodynamic therapy was approved in 2000 to remove abnormal bloods vessels in the eye, linked to conditions like age-related macular degeneration. The liposomal segmentation of verteporfin was developed to prevent the self-aggregation that readily occurs in aqueous media, a process that would otherwise severely limit the pharmacokinetics, biodistribution and photosensitising properties.[194]

1.4.5.1 Liposomes formulations in late stage clinical trials for cancer therapy

In additional to the several lipid-based products that have already been approved (Table 2), there are numerous liposome formulations currently undergoing clinical trials for various cancer applications.[183] Amongst those that have reached phase III trials is a temperature sensitive liposomal formulation of DOX, called ThermoDox®. The liposomes, which are comprised of DPPC, 1-myristoyl-2-stearoyl-*sn*-glycero-3-phosphocholine (MSPC) and DSPE-PEG2000, undergo a rapid onset of membrane permeability to release DOX when exposed to local hypothermia (39.5-42 °C), which can be achieved *via* radio frequency ablation.[183] This technique yields targeted tumor drug concentrations that are 25-fold higher than regular intravenous injection (i.v.) of DOX and 5-fold higher than the approved Doxil® formulation.[183] However, the free DOX concentration in the circulation is significantly higher compared to other liposomal DOX formulations.

A liposomal formulation of the classic DNA cross-linking agent, cisplatin, known as Lipoplatin™, is in Phase III clinical trials for non-small cell lung cancer. It is also in phase I trials for malignant pleural effusion, phase II for breast and gastric cancer and phase II/III for pancreatic cancer.[183] It offers remarkable improvements compared to the free drug such as longer circulation time, the ability to penetrate cell membranes, preferential accumulation in tumor tissue and significantly reduced adverse effects including renal toxicity, peripheral neuropathy, ototoxicity and myelotoxicity.[195] Bulbake *et al.* provide an excellent review of the plentiful lipid-based chemotherapies currently undergoing clinical trials alongside those with indications outside of cancer.[183]

In summary, due to a wealth of liposome formulations that have passed and are currently undergoing clinical trials, it can be confidently said that liposomes present extremely promising nanoscale carriers for CAs and/or therapeutics employed in cancer management.

Aims of the project

A CEST MRI technique that enables the visualisation of natural, non-radioactive glucose has recently been developed, termed glucoCEST.[84] Development of this technique could offer a higher resolution and more affordable alternative for oncologic imaging whilst evading the use of undesirable radioactive compounds and thereby allow vulnerable patient groups such as pregnant women and children to be scanned more regularly. GlucoCEST in its current form is hindered by low sensitivity, short duration of signal *in vivo* and problems arising from injection of a large glucose bolus, such as hyperglycaemia in diabetic patients and risk of developing deep vein thrombosis.

We propose that liposomes encapsulating, or covalently linked with, glucose and other saccharides could solve these issues and improve glucoCEST imaging. Encapsulation of glucose inside PEGylated liposomes could significantly enhance the circulation time and protect against rapid metabolism, processes that would enhance the duration and detectability of generated CEST signal. Sensitivity could be further increased if liposomal encapsulation reduces the apparent exchange rate between glucose hydroxyl protons and bulk water, to bring the exchange regime closer to the slow-intermediate range that is ideal for CEST (Figure 21).

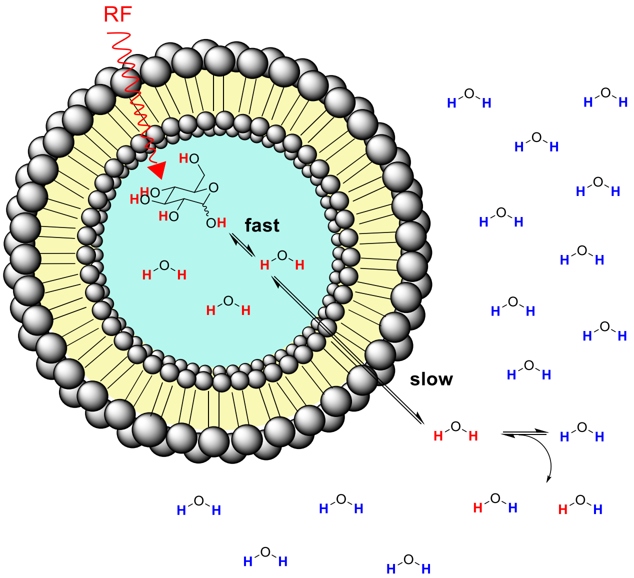

Figure 21. Schematic for CEST contrast generated by diaCEST liposomes encapsulating glucose. RF pulses saturate hydroxyl protons of encapsulated glucose. Saturated glucose hydroxyl protons exchange with internal liposomal water protons, this water molecule must then permeate the lipid membrane before it is able to transfer saturation to the bulk water pool. The magnitude of generated CEST contrast will depend on several variables such as internal glucose concentration, lipid composition, pH, temperature and irradiation power.

Additionally, liposomal encapsulation enables optimisation of desirable release-over time characteristics to keep blood glucose levels low and protect from the effects associated with large glucose bolus injection.

In previous work, Lim Win Gel formulated liposomes with a 7:2:1 molar ratio of DPPC:GlcEG3SL:DODEG4, GlcEG3SL being a glucose-lipid and DODEG4 being a short-chain PEG-lipid (Liposome **A**, Figure 22).[196] A glucoCEST measurement of the sample was taken but no signal from the glucose hydroxyl protons could be detected in the Z spectrum. Thus, our first objective was to observe a glucoCEST signal from a glucose liposome formulation. Methods to achieve this include; 1) increasing the liposome concentration, 2) encapsulating glucose in the aqueous interior (Liposome **B**) and 3) increasing the molar proportion of glucose-lipid in the bilayer (Liposome **C**). Additionally, we planned to investigate the pH and temperature dependency of glucoCEST signal from liposomal preparations.

Once liposome parameters and conditions that produce a robust glucoCEST signal have been established, our second aim was to investigate whether a lanthanide shift reagent could be incorporated into the liposomes to create a paraCEST signal. It was proposed that the shift reagent could create a greater shift difference between the resonances of the glucose hydroxyl protons and the bulk water protons to enable highly selective and sensitive saturation during paraCEST measurement. The shift reagent can be incorporated into the liposomes in two ways; 1) co-encapsulation with glucose in the aqueous interior (Liposome **D**) and 2) chelation to the surface of the liposomes *via* incorporation of a DOTA-lipid in the bilayer (Liposome **E**).

Due to the slower metabolism and the reported chemotherapeutic and radio-sensitisation properties of 2-DG, our third aim was to investigate the substitution of glucose with 2-DG in the aqueous interior of our liposomal CAs for the development of theragnostic agents to simultaneously image and treat tumors (Liposome **F**).

An advantage of encapsulation of monosaccharides inside liposomes is that liposomes can passively target tumors *via* the EPR effect. Liposomes must be PEGylated to give rise to effective *in vivo* half-lives and EPR accumulation. Finally, we aimed to formulate PEGylated and actively targeted liposomes encapsulating monosaccharides by covalently attaching EGFR-targeting peptides to the bilayer surface (Liposome **G**). We planned to synthesise and incorporate short-chain PEG lipids into liposomes to confer stealth liposome properties whilst enabling better exposure of the targeting moieties at the bilayer surface (*cf.* using PEG2000-conjugated lipids).

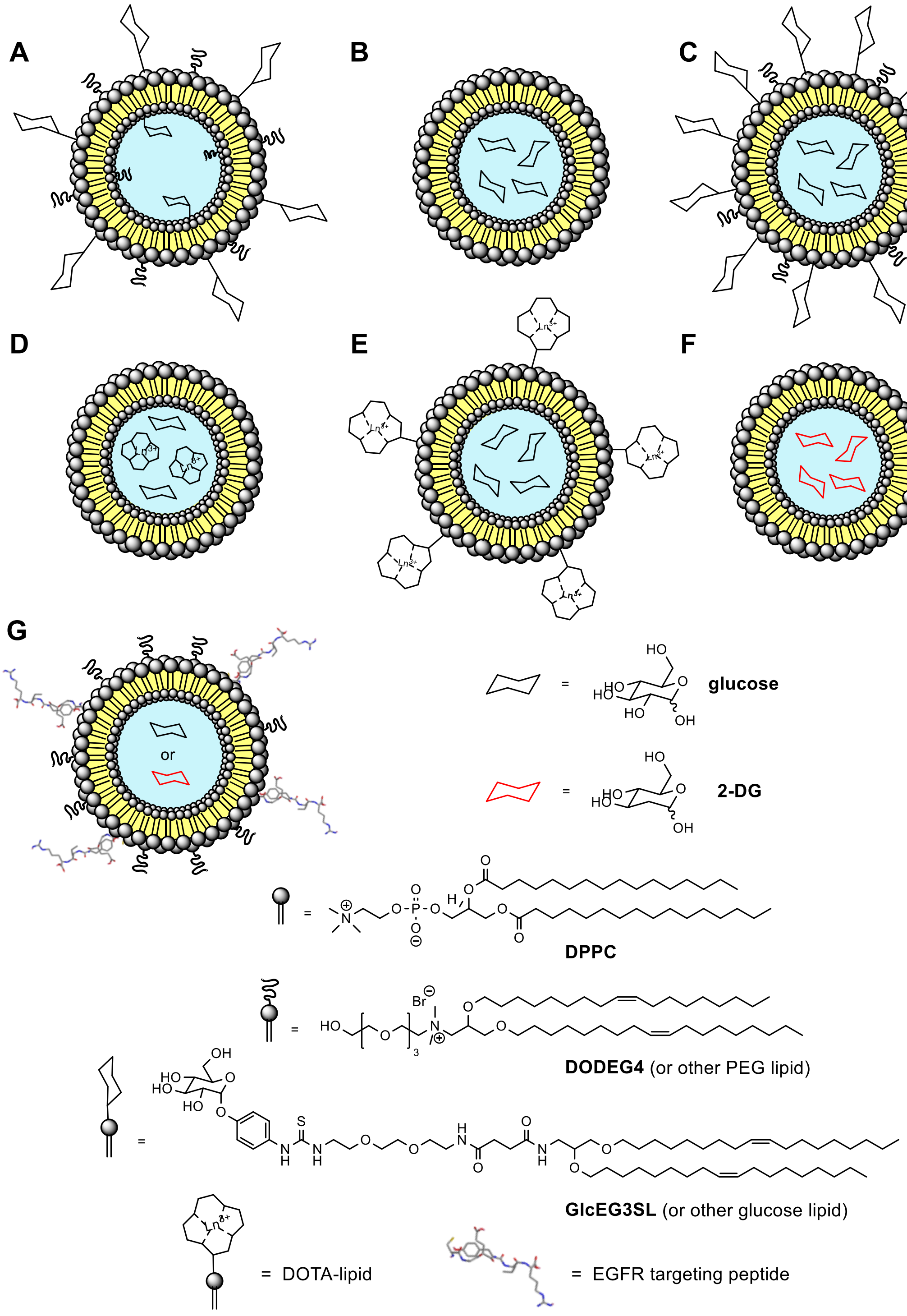

Figure 22. Liposome formulations with A) 7:2:1 molar ratio of DPPC:GlcEG3SL:DODEG4, formulated by Lim Win Gel,[196] B) glucose encapsulated in the aqueous interior, C) glucose encapsulated and increased glucose-lipid concentration in the bilayer, D) glucose and a lanthanide SR encapsulated, E) glucose encapsulated and an Ln-chelated DOTA-lipid in the bilayer, F) 2-DG encapsulated, G) PEGylation, EGFR-targeting and glucose or 2-DG encapsulated. Figure includes the chemical structure of DPPC, a short-chain PEG lipid reported by Hurley *et al.*, DODEG4,[154] and a glucose-lipid synthesised by Lim Win Gel, GlcEG3SL.[196]

2 Glucose loading of liposomes

2.1 Encapsulating glucose and incorporation of glucose-lipid in the bilayer

A novel glucose-lipid conjugate, GlcEG3SL (Figure 22), was previously synthesised by Lim Win Gel following an analogous synthetic route to that shown in Scheme 1.[196] As discussed in Section 1.4.1, DODEG4 is a cationic short-chain PEG lipid that has been previously reported by the Hailes/Tabor group which is based on the structure of DOTMA and bears 4 EG units at the polar terminus (Figure 22).[154,164] PEG coating of liposomes *via* incorporation of short-chain PEG lipids, such as DODEG4, has been shown to be highly advantageous for *in vivo* applications (Section 1.4.1). Lim Win Gel previously formulated liposomes with a 7:2:1 molar ratio of DPPC:GlcEG3SL:DODEG4 (Liposome **A**, Figure 22). A glucoCEST measurement of the sample was taken by Eleni Demetriou on a 9.4 T Agilent scanner. Unfortunately, no signal from the glucose hydroxyl protons could be detected in the Z or $\mathrm{MTR}_{\mathrm{asym}}$ spectra.[196] Lim Win Gel's liposomes were at a concentration of 5 mM and were comprised of 20 mol% GlcEG3SL, thus, the total glucose concentration was only 1 mM.

As a first attempt to observe a glucoCEST signal from a glucose liposome formulation both the lipid concentration and the GlcEG3SL content in the bilayer was increased, as well as attempting to encapsulate glucose in the aqueous interior (Liposomes **B** and **C**, Figure 22). Three liposome samples were prepared with an overall lipid concentration of 10 mM and varying lipid compositions: **L1**, **L2**, and **L3**. The lipid bilayer of **L1** was comprised solely of DPPC. **L2** was formulated with 20 mol% GlcEG3SL and 10 mol% DODEG4 whereas **L3** was formulated with 50 mol% GlcEG3SL and 10 mol% DODEG4. The remaining lipid content in **L2** and **L3** was made up by DPPC (Table 3). We hypothesised that GlcEG3SL could contribute to the overall number of hydroxyl protons participating in the glucoCEST mechanism and that the glucose moieties may aid in future targeting of the liposomes to tumors.

Liposomes were created *via* the thin-film hydration method with subsequent sonication.[150] The three lipid mixes were dissolved in $\mathrm{CHCl_3}$:MeOH (3:1) and then evaporated to dryness using a rotary evaporator to create a lipid thin film. The thin film was hydrated with the appropriate volume of 0.5 M glucose solution to give in an overall lipid concentration of 10 mM, twice the lipid concentration of the liposome sample reported by Lim Win Gel.[196] A 0.5 M glucose solution was chosen because this was the highest glucose concentration to be previously encapsulated by liposomes in the literature.[197] The solution was then sonicated above the T_m of the relevant lipids (DPPC has the highest T_m at 41 °C),[198] to give polydisperse liposomes encapsulating glucose. Extrusion was employed to create unilamellar vesicles with low polydispersity and a diameter between 100-200 nm. This was achieved by passing the liposomes first through a 400 nm pore polycarbonate filter and then through a 200 nm pore filter until the mean diameter (Z-Ave) fell below 200 nm, as measured by dynamic light scattering (DLS). See Section 7.2.1 for full details of general liposome formulation procedures.

We aimed to size liposomes within the range 100-200 nm because PEG-coated liposomes of this size are appropriate for effective accumulation in tumor tissue *via* the EPR effect.[199] Liposomes larger than 200 nm are less capable of passing through fenestrated vessels surrounding the tumor, whereas liposomes smaller than 100 nm are more likely to escape from capillaries and perfuse off-target tissues such as the lung heart or kidney, as well as not being able to carry as much glucose or other imaging cargo.[199]

With each additional pass of the liposomes through the polycarbonate filters in the extruder, the polydispersity index (PdI) and Z-Ave values simultaneously decreased (Figure 23). The PdI is a measure of the particle size distribution, for which a value of less than 0.2 is acceptable and less than 0.1 is very good. Following extrusion, the Z-Ave values for **L1**, **L2** and **L3** were 174 nm, 133 nm and 130 nm, respectively, and the PdI values were in the range 0.12-0.18 (Table 3). Despite higher PdI values, further extrusion was not carried out for **L2** and **L3** because the liposomes were approaching the lower limit of the desired size bracket. Following extrusion, the liposomes were dialysed against 0.25 M NaCl solution. The 0.5 M glucose and 0.25 M NaCl solutions have equal osmolarity which reduces swelling or shrinking of the liposomes as well as minimising glucose leakage from the liposome cavity.

Table 3. Table showing the parameters and measurements of liposome samples **L1**-**L3** with varying lipid content in the bilayer.

Liposome sample	Molar lipid composition (mol%)	[lipid] (mM)	Hydration solution [glucose]	Z-Ave (d.nm) (s)	PdI (s)	Exterior [glucose] (mM)	Overall [glucose] (mM)
L1	100% DPPC	10	0.5 M	174 (1.6)	0.12 (0.02)	0	4.2
L2	70% DPPC, 20% GlcEG3SL, 10% DODEG4	10	0.5 M	133 (1.0)	0.18 (0.01)	1.6	2.4
L3	40% DPPC, 50% GlcEG3SL, 10% DODEG4	10	0.5 M	130 (0.8)	0.16 (0.01)	0	0.1

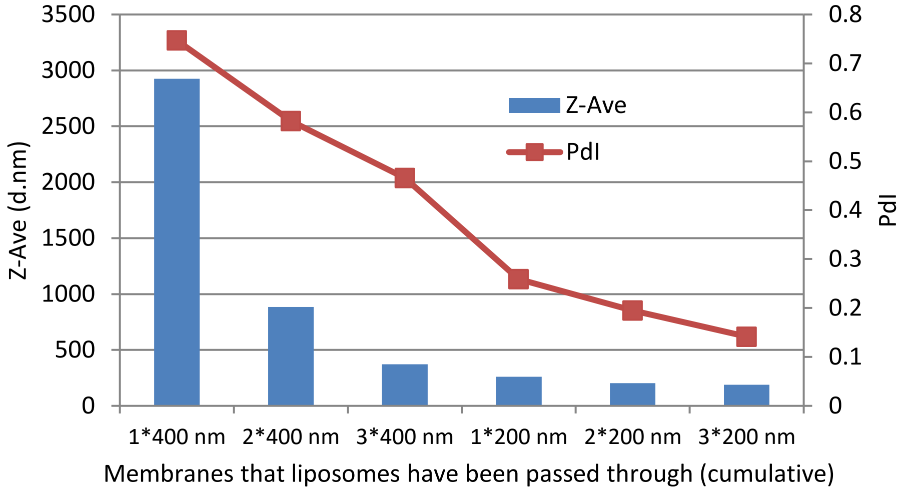

Figure 23. Graphical representation of the decrease in liposome Z-Ave (d.nm) and PdI with each pass through a 400 nm or 200 nm pore polycarbonate membrane during extrusion. This data was obtained using pure DPPC liposomes encapsulating 0.5 M glucose.

To assess the extent of glucose encapsulation, an enzymatic assay (Glucose HK Assay®, Sigma-Aldrich) was employed and adapted. The assay involves an enzymatic cascade that converts an equimolar amount of NAD to NADH as the number of moles of glucose present in the solution. NADH absorbs at 340 nm and the change in absorbance at this wavelength can therefore be used to calculate the glucose concentration. As the enzymes cannot penetrate the liposome bilayer, measurement of the intact liposome sample enables the glucose concentration exterior to the liposomes to be measured. Subsequently, the addition of Triton X-100 (Triton) solution to give an overall concentration of 0.03% Triton can disrupt and solubilise phosphatidylcholine bilayers,[200] causing the encapsulated glucose to be released, enabling the overall glucose concentration for the sample to be determined. A procedure for carrying out the assay is detailed in Section 7.2.2.1.

The assay gave rise to the UV-vis spectra shown in Figure 77, Section 7.2.2.1. For **L1**, a large increase in absorbance at 340 nm was observed after the addition of Triton, whereas no visible increase was observed before the lipid bilayer was disrupted. This suggests that the pure DPPC liposomes successfully encapsulated glucose in the aqueous interior with very little leakage into the exterior NaCl solution. Using the Glucose HK Assay®, the overall glucose concentration of **L1** was calculated as 4.2 mM with no detectable glucose exterior to the liposomes (Table 3).

For **L2** there was a less prominent increase in absorption at 340 nm and a small increase before the addition of Triton. This suggests that there was significant leakage of glucose out of the liposomes when the bilayer contained 20 mol% GlcEG3SL and 10 mol%

DODEG4. The measured overall and exterior concentrations for **L2** were 2.4 mM and 1.6 mM, respectively, indicating that bilayers containing 20 mol% GlcEG3SL and 10 mol% DODEG4 are able to retain glucose to some extent at RT but not throughout the full duration of dialysis (~ 2 days). If efficient glucose retention gives an overall concentration of 4.2 mM as for **L1**, the overall concentration of 2.4 mM for **L2** predicts that a significant amount of glucose is lost during the first two rounds of dialysis and more is lost during the third round to give an exterior glucose concentration of 1.6 mM.

For **L3,** with 50 mol% GlcEG3SL and 10 mol% DODEG4, there was no increase before or after addition of Triton, indicating that no glucose was present. Indeed, the calculations gave overall and exterior glucose concentrations equal to zero. The explanation for this is that glucose leaked of these liposomes so readily that it was entirely lost during dialysis. This is attribute to the fact that DPPC is in the more stable gel state at RT (T_m = 41°C), whereas GlcEG3SL and DODEG4 have similar fatty regions to DOPE which has a T_m of -16 °C. Bilayers comprised solely of GlcEG3SL and DODEG4 would be in the more disordered fluid state at RT, therefore, as DPPC lipid bilayers are diluted with GlcEG3SL and DODEG4, the less ordered and more permeable they become at RT.

This experiment has shown that low T_m lipids with unsaturated fatty chains, such as GlcEG3SL and DODEG4, do not form rigid enough liposome bilayers at room temperature to sustainably encapsulate high concentrations of glucose in the aqueous interior. Unfortunately, the pure DPPC liposomes **L1** which did encapsulate glucose with an overall sample concentration of 4.2 mM did not produce a detectable CEST signal when using low or high power saturation pulses (1.5 μT or 8.0 μT, respectively).

2.2 Investigating encapsulation limits

Table 4. Table showing the formulation parameters and measurements for DPPC liposomes encapsulating various concentrations of glucose, **L4**-**L6**.

Liposome sample	[DPPC] (mM)	Hydration solution [glucose]	Z-Ave (d.nm) (s)	PdI (s)	Exterior [glucose] (mM)	Overall [glucose] (mM)
L4	40	0.5 M	153 (2.6)	0.14 (0.01)	4.6	75
L5	40	1.0 M	159 (0.2)	0.12 (0.02)	38	114
L6	40	2.0 M	150 (4.6)	0.17 (0.01)	31	149

Since liposomal bilayers comprised solely of DPPC have been shown to efficiently encapsulate glucose in Section 2.1, various DPPC liposomes were formulated to investigate the necessary overall glucose concentration to produce an appreciable CEST signal. DPPC liposomes **L4**, **L5** and **L6** were formulated with a lipid concentration of 40 mM (4 times higher than in Section 2.1) and the thin films were hydrated with 0.5 M, 1 M and 2 M glucose solutions, respectively. **L4**, **L5** and **L6** were sized *via* extrusion to give average diameters ranging from 150 nm to 159 nm and PdI values between 0.12 and 0.17 (Table 4). **L4**, **L5** and **L6** were subsequently dialysed against 0.25 M, 0.5 M and 1 M NaCl solutions, respectively. Employing the Glucose HK Assay® as previously described, the exterior and overall glucose concentrations were determined. The overall glucose concentration for **L4** measured as 75 mM and the exterior concentration measured as 4.6 mM, which was deemed to be insignificant due to no signal being detected for **L1** which had an overall glucose concentration of 4.2 mM. No appreciable CEST signal was observed for a 5 mM solution of free glucose therefore we define a negligible exterior glucose concentration as being less than or equal to 5 mM. Significant exterior glucose concentrations were measured for **L5** and **L6** (38 mM and 31 mM, respectively) as well as high overall concentrations of 114 mM and 149 mM, respectively. These results show that glucose leaks out of liposome formulations **L5** and **L6** during dialysis and it was concluded that concentrations of 1 M glucose and above are too high to be successfully encapsulated inside DPPC bilayers. CEST measurement of liposomes **L4**, **L5** and **L6** was carried out and as expected, the signal intensity was greater for samples with higher overall glucose concentrations (Figure 24). The more pronounced signals obtained from **L5** and **L6** are attributed to both free and encapsulated glucose and the two components of the signal cannot be separated. However, **L4** had a negligible exterior glucose concentration and exhibited a satisfactory maximum water signal suppression *via* CEST of approximately 10%, demonstrating that an appreciable CEST signal can be generated by DPPC liposome encapsulated glucose.

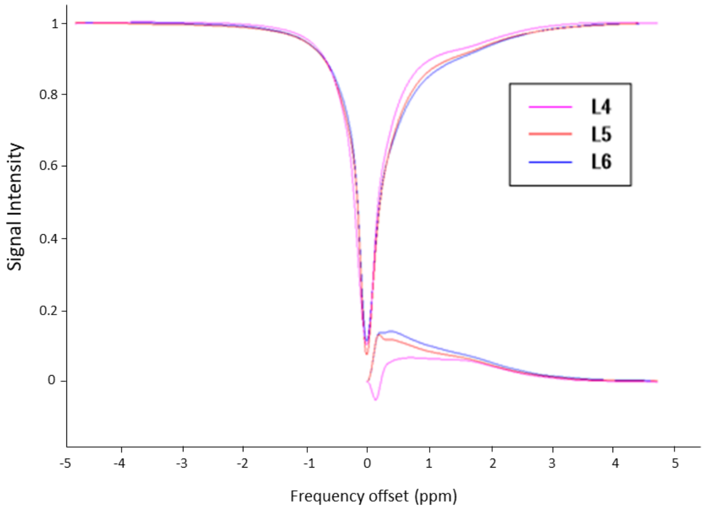

Figure 24. Z spectra (top) and $\mathrm{MTR}_{\mathrm{asym}}$ curves (bottom) for liposomal samples, **L4**, **L5** and **L6**, measured at RT with $B_0 = 9.4$ T and $B_1 = 1.2$ μT.

2.3 Relationship between overall glucose concentration and CEST detection of glucose loaded liposomes

Three new samples were formulated to further investigate the CEST detection of glucose encapsulated within DPPC liposomes. Instead of varying the encapsulated glucose concentration, the overall DPPC concentration was altered, effectively varying the liposome concentration if the diameter of the liposomes is kept constant. **L7**, **L8** and **L9** were formulated with DPPC concentrations of 20 mM, 30 mM and 35 mM, respectively, and hydrated with 0.5 M glucose solution as this appeared to be the highest concentration that can be successfully entrapped by DPPC bilayers (Section 2.2). Pleasingly, the measured diameters following extrusion were almost identical (168-170 nm) and the PdI values were exceptionally low and well grouped (0.094-0.12) (Table 5).

Table 5. Table showing the formulation parameters and measurements for DPPC liposomes encapsulating glucose with various lipid concentration, **L7**-**L9**.

Liposome sample	[DPPC] (mM)	Hydration solution [glucose]	Z-Ave (d.nm) (s)	PdI (s)	Exterior [glucose] (mM)	Overall [glucose] (mM)	pH
L7	20	0.5 M	170 (2.8)	0.12 (0.03)	2.0	22	5.6
L8	30	0.5 M	168 (2.4)	0.11 (0.01)	0.4	44	5.7
L9	35	0.5 M	168 (2.6)	0.09 (0.01)	4.0	55	5.8

Following dialysis, the exterior and overall glucose concentrations were measured for **L7**-**L9**. All three samples exhibited negligible amounts of glucose exterior to the liposomes (< 5 mM). The overall glucose concentrations were measured as 22 mM, 44 mM and 55 mM, which adequately span the concentration range of interest (between 5-75 mM overall glucose). As discussed in Section 1.2.2, the pH of a sample has a marked effect on the appearance of resultant Z spectra.[56] Therefore the pH of the three samples were measured and ensured to be roughly the same (within 0.2 pH units). Controls were made up for **L7**, **L8** and **L9** comprising free glucose in 10% PBS buffer with an identical pH and glucose concentration to the corresponding liposome sample. These controls were used to assess whether glucose that is concentrated inside the liposomes produces the same CEST effect as free glucose. **L7**-**L9**, pure PBS solution and the three controls were measured at both low (1.5 μT) and high (8.0 μT) power. The obtained Z spectra and MTR_{asym} curves are shown in Figure 25. To quantify the CEST effect for each measurement, an averaged signal intensity from the MTR_{asym} was taken between 0-4.5 ppm (where the majority of the signal is observed) and expressed as an average percentage inhibition of the bulk water peak across this range (Table 6). This was similar

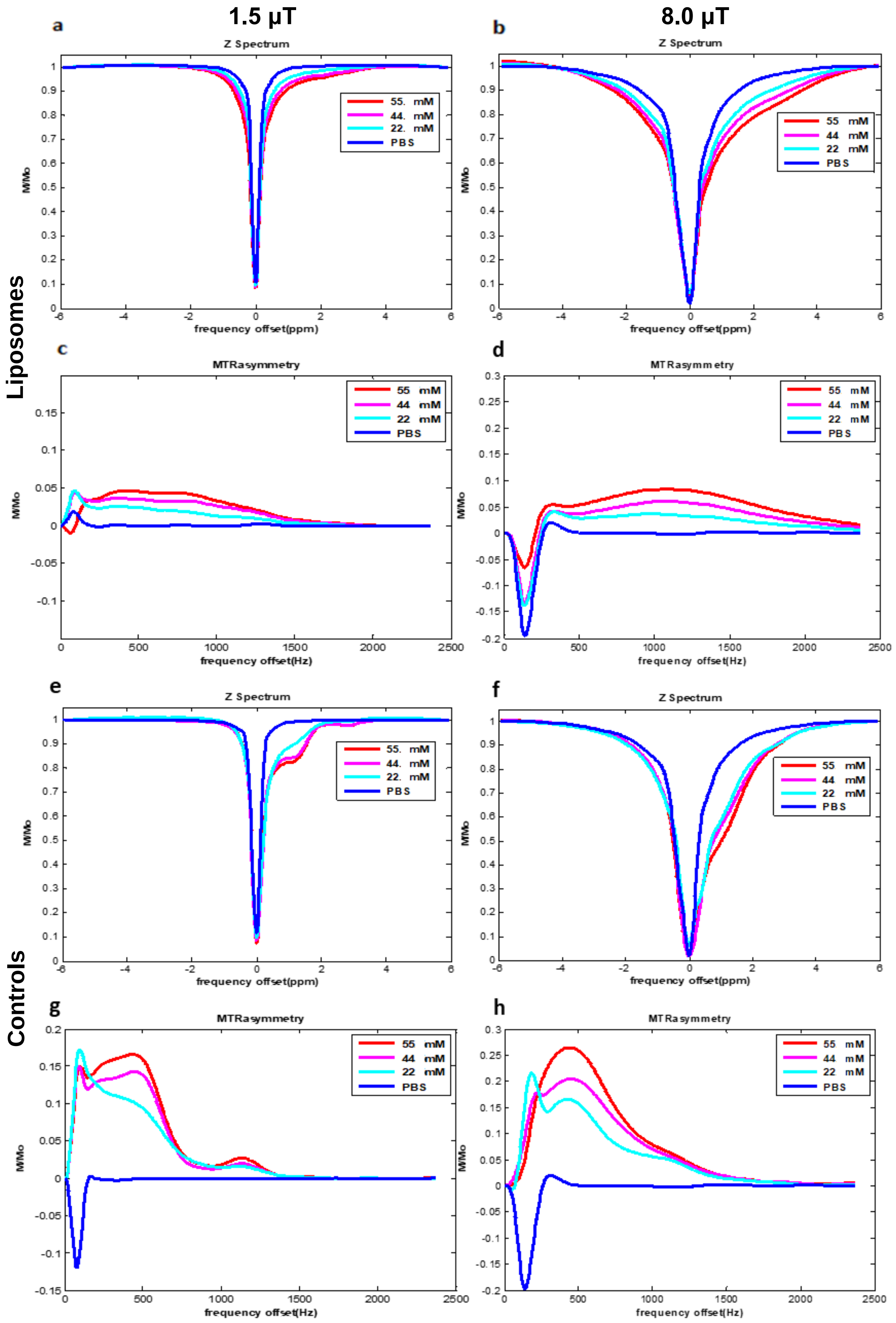

Figure 25. Z spectra (a,b,e,f) and MTR_{asym} curves (c,d,g,h) for liposome samples with overall glucose concentrations of 55 mM (**L9**), 44 mM (**L8**) and 22 mM (**L7**) (a,b,c,d) and their respective controls (e,f,g,h). Spectra were acquired with a saturation pulse frequency of 1.5 μT (a,c,e,g) or 8.0 μT (b,d,f,h) at 25 °C. The pH and glucose concentration of each liposomal sample is shown in Table 5. The controls were comprised of free glucose in 10% PBS with a pH and glucose concentration equal to that of the corresponding liposome sample.

to the method of quantification used in a glucoCEST study by Chan *et al*. (averaged MTR_{asym} over the range 0.8-2.2 ppm),[56] whereas Walker-Samuel *et al.* used the change in area under the MTR_{asym} curve in the range 0.75-4 ppm to obtain a GCE measurement (see Section 1.2.1.2).[84]

Across all the spectra, the higher RF saturation field of 8.0 μT produced a larger CEST mediated reduction of the water signal. This is in agreement with the fact that higher saturation fields allow a greater extent of saturation preceding chemical exchange during CEST measurements.[56] Across all types of sample tested, an average 56% increase in water suppression was induced by increasing B_1 from 1.5 μT to 8.0 μT. Notably, this increase was more pronounced for the liposomal samples in comparison to the free glucose controls (69% increase *vs*. 43% increase).

When assessing whether glucose that is encapsulated inside DPPC bilayers elicits a similar CEST effect to the same concentration of free glucose, the results from this study which was carried out at RT and in the pH range 5.6-5.8 are unambiguous. The free glucose controls exhibited a greater than two-fold average increase in water signal suppression (126% increase) compared to their corresponding liposomal samples with equivalent overall glucose concentration (Table 6). This is presumably a simple consequence of reduced exchange between the saturated glucose hydroxyl protons and bulk water protons due to the permeability barrier imposed by the lipid bilayer. This can be compared to the loss of relaxivity observed for Gd chelates such as Gd-DTPA when encapsulated inside liposomes due to reduced ability to transfer saturation to the bulk water.[37]

Table 6. CEST suppression of the water peak for 10% PBS, liposome samples **L7**-**L9** and the corresponding controls in 10% PBS measured at 25 °C with B_1 = 1.5 μT and 8.0 μT. CEST suppression is expressed as an average of the percentage reduction in water signal caused by presaturation across the range 0-4.5 ppm.

	1.5 μT power	8.0 μT power
10% PBS	-0.15 %	-0.03 %
L7	1.5 %	2.1 %
L8	2.3 %	4.0 %
L9	2.6 %	5.2 %
L7 control	4.3 %	5.4 %
L8 control	4.5 %	7.5 %
L9 control	6.8 %	9.2 %

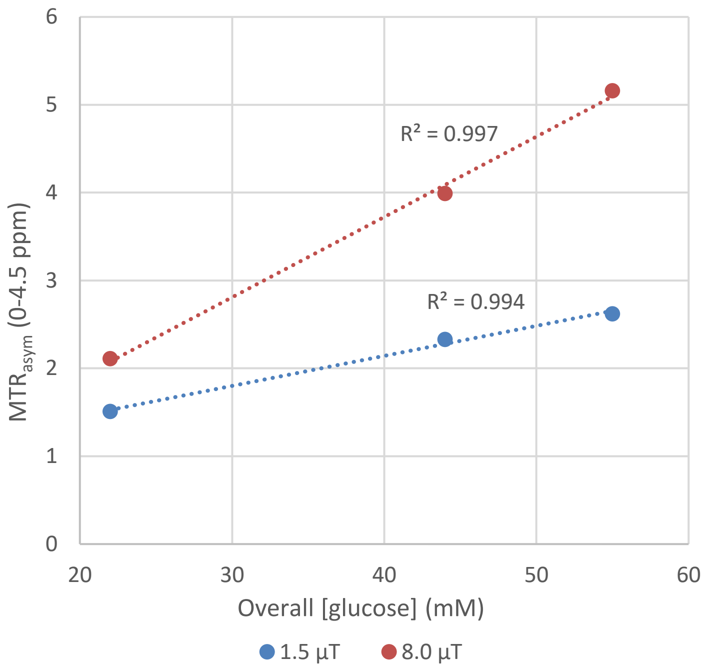

Figure 26. GlucoCEST signal magnitude (averaged MTR$_{asym}$ over 0-4.5 ppm) generated by **L7-L9** as a function of overall glucose concentration at B_1 = 1.5 µT and 8.0 µT.

Chan *et al.* have previously shown that glucoCEST signal is linear at low concentrations (up to approximately 50 mM), but becomes non-linear at higher concentrations, which is a well-known CEST phenomenon reflecting back-exchange of saturated protons.[56] The results from this experiment show that glucoCEST signal from glucose encapsulated inside DPPC bilayers is also linear up to concentrations of at least 55 mM (Figure 26).

2.4 pH and temperature dependence for CEST detection of glucose liposomes

The magnitude of CEST enhancement produced by a CEST agent is dependent on the solute proton concentration, the RF saturation power and duration and the exchange rate between solute protons and bulk water protons (k_{ex}).[58] As the exchange rate is dramatically altered by temperature and pH, the dependence of CEST signal magnitude generated by glucose liposomes on both pH and temperature was investigated. Liposomes **L10**, **L11**, **L12** and **L13** were formulated at pH 4, 5, 6 and 7, respectively. The liposome samples contained an overall DPPC concentration of 30 mM and the thin films were hydrated with 0.5 M glucose solution at the relevant pH. The liposomes were sized by extrusion and dialysed against 0.25 M NaCl solution at the relevant pH. The average diameter of the four formulations following dialysis ranged between 156-187 nm with low PdI values within the range 0.10-0.13 (Table 7). The samples were unbuffered and adjusted with 1 M NaOH or 1 M HCl to maintain the right pH.

Table 7. Table showing the formulation parameters and measurements for DPPC liposomes encapsulating glucose at various pH, **L10-L13**.

Liposome sample	[DPPC] (mM)	Hydration solution [glucose]	Z-Ave (d.nm) (s)	PdI (s)	Exterior [glucose] (mM) (s)	Overall [glucose] (mM) (s)	pH
L10	30	0.5 M	175 (2.5)	0.13 (0.01)	0.6 (0.4)	36 (3.9)	4.0
L11	30	0.5 M	156 (0.54)	0.11 (0.004)	3.1 (1.2)	37 (1.5)	5.0
L12	30	0.5 M	178 (1.9)	0.12 (0.02)	3.0 (1.1)	28 (0.4)	6.0
L13	30	0.5 M	187 (1.4)	0.10 (0.01)	1.6 (0.7)	30 (2.9)	7.0

The Glucose HK Assay® showed low exterior glucose concentrations between 0.6-3.1 mM for the four samples and overall glucose concentrations in the range 28-37 mM (Table 7). This variation in overall glucose concentration is unavoidable as the pH will affect the physicochemical properties of the liposome. For example, DPPC liposomes have been shown to be more rigid below their T_m with increasing acidity (based on differential scanning calorimetry and electron paramagnetic resonance studies).[201,202] It is thought that this is a result of phosphate group protonation in acidic environments and the formation of hydrogen bonds between this hydroxyl hydrogen atom and the oxygen atom of a vicinal DPPC phosphate group (Figure 27).[201] However, this effect will only be observed at realtively low pH as the pKa for DPPC is approximately 1.0.[203]

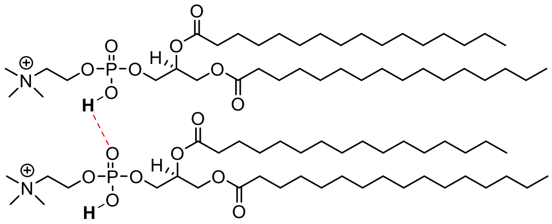

Figure 27. Proposed protonation and subsequent hydrogen bonding between DPPC phosphate groups at low pH.

The liposomes formulated at pH 4 and pH 5 exhibited the highest overall glucose concentrations despite having slightly smaller diameters, suggesting that this pH range favours plentiful encapsulation of glucose. This is in agreeance with Sulkowski *et al.* who reported that DPPC liposomes prepared at low pH (1.9 or 5.0) are more rigid below the T_m than those prepared at high pH (8.0 or 8.4).[201] Additionally, Roy *et al.* reported that DPPC liposomes exhibit enhanced entrapment efficiency of curcumin (an example drug) as the pH is decreased from pH 8 to pH 6.[202]

Due to the large pH differences between the samples, the relatively small fluctuations in glucose concentration were deemed acceptable. The samples were not buffered so the pH was kept as constant as possible throughout formulation *via* regular monitoring and addition of small volumes of 1 M HCl or NaOH and the pH was adjusted immediately before CEST measurement.

When glucose liposomes **L10**-**L13** were scanned at 25 °C, the largest CEST mediated water signal suppression was for **L12** at pH 6 closely followed by **L11** at pH 5 (2.3% *cf*. 2.0% average water suppression across the presaturation range 0-3.75 ppm) (Figure 28, Table 8). Whereas at 37 °C, the glucose liposomes at pH 6 produced a significantly larger signal than those at pH 5 (3.7% *cf*. 2.9%) (Figure 28, Table 8). The signals measured for the glucose liposomes at pH 4 and pH 7 were relatively low and unchanged by temperature, with a slightly larger signal from the liposomes at pH 7 at both 25 °C and 37 °C (Figure 28, Table 8). The Glucose HK Assay® showed that **L10** was the only liposome sample to release a significant portion of the encapsulated glucose, with an exterior glucose concentration of 12 mM after CEST measurement at 37 °C, whereas the other three samples remained intact (exterior concentrations ranging between 1-4 mM). This shows that the glucose liposomes are stable at 37 °C in the pH range 5-7 for short periods of time (a few hours). The CEST results indicate that at 25 °C, the optimum k_{ex} for CEST detection of the glucose liposomes is achieved between pH 5 and pH 6 but upon increasing the temperature to 37 °C, the optimum exchange rate at physiological temperature is closer to pH 6. These results are promising for the use of glucose liposomes to image tumors *in vivo* because the extracellular tumor microenvironment is more acidic than normal tissue and blood (pH 6-7 *cf*. pH 7.4, respectively).[92] Therefore, when the liposomes reach the tumor one would expect the glucoCEST signal to be enhanced. This intrinsic effect teamed with both passive and active targeting efforts is expected to increase the tumour contrast generated by glucose liposomes.

Table 8. CEST suppression of the water peak for glucose liposomes **L10-L13** measured at both 25 °C and 37 °C. The spectra were acquired with a saturation length of 80 pulses and B_1 = 1.5 μT. CEST suppression is expressed as an average of the percentage reduction in water signal caused by presaturation across the range 0-3.75 ppm.

	pH 4 (L10)	pH 5 (L11)	pH 6 (L12)	pH 7 (L13)
MTR_{asym} at 25 °C	0.095 %	2.0%	2.3%	1.2%
MTR_{asym} at 37 °C	0.27%	2.9%	3.7%	0.95%

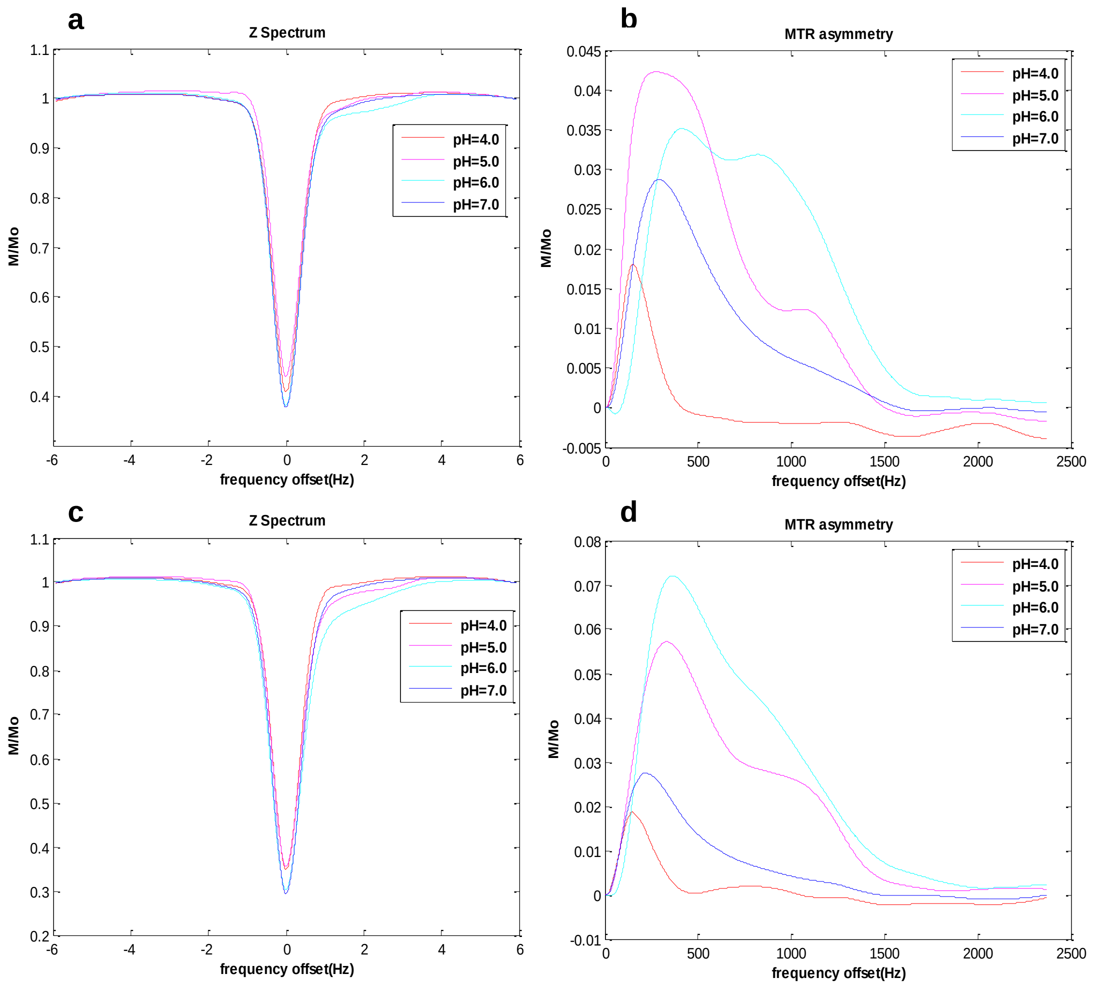

Figure 28. Z (a,c) and MTR$_{asym}$ (b,d) spectra showing the pH dependence of CEST signal magnitude produced by glucose loaded liposomes **L10-L13** at 25 °C (a,b) and 37 °C (c,d). The spectra were obtained with a saturation length of 80 pulses and B$_1$ = 1.5 μT.

2.5 Conjugating glucose to the lipid bilayer

2.5.1 Synthesis of a novel glucose-lipid

Studies on Gd-bearing liposomes have shown that MRI contrast is improved when Gd chelates are anchored to the surface of lipid nanoparticles as opposed to encapsulating them due to increased exposure to bulk water.[32,38] This principle can be applied to our liposomal CEST agents. By covalently attaching glucose molecules to the liposome surface, the number of water protons with which the hydroxyl protons can exchange is greatly increased and thus the potential for CEST detection is also increased.

Due to the finding that DPPC bilayers incorporating as little as 20 mol% GlcEG3SL were inadequate for encapsulating the high glucose concentrations necessary to produce a glucoCEST signal, a novel saturated glucose-lipid, GlcEG3SLc, was synthesised (Scheme 1). GlcEG3SLc is based on the structure of DPPC and should therefore have a similar T_m and produce more rigid liposomes than GlcEG3SL that are capable of encapsulating high concentrations of glucose. It was hypothesised that decorating the surface of liposomes with glucose moieties may help target them to glucose-avid tumor cells whilst increasing the number of glucose hydroxyl protons available per liposome to partake in CEST image generation.

The synthetic route was adapted from Lim Win Gel's synthesis of GlcEG3SL.[196] Lipid synthesis began with single Boc-protection of commercially available 3,6-dioxaoctane-1,8-diamine **1** using 0.2 equivalents of Boc anhydride to give **2** in 97% yield based on a theoretical yield calculated with respect to the amount of Boc anhydride used. Ring opening of succinic anhydride with amine **2** in the presence of base gave the key intermediate **3** as a triethylamine salt in 95% yield. The saturated chain cetyl alcohol **4** was activated with mesyl chloride to give a quantitative yield of the mesylate **5**.

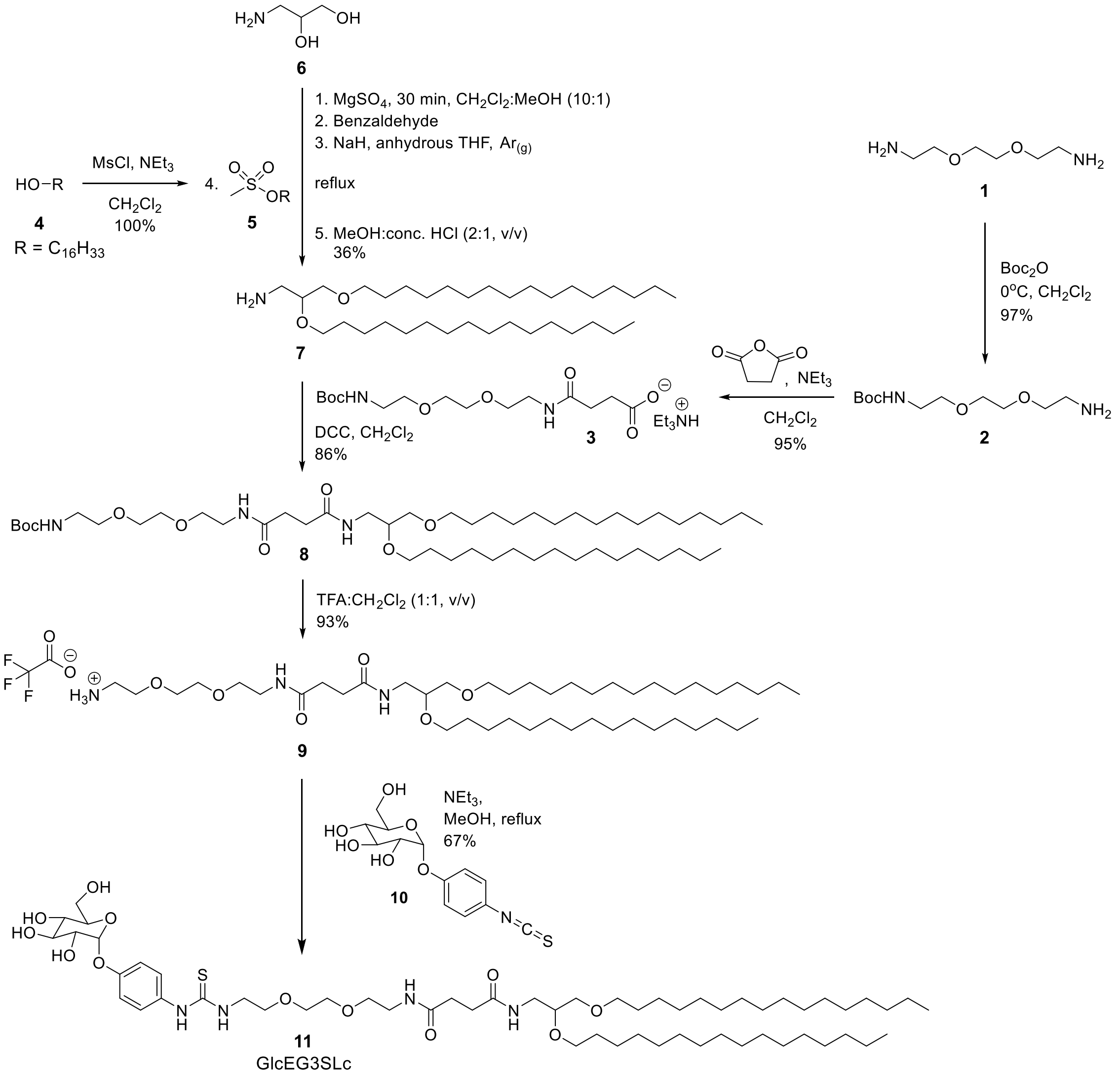

Scheme 1. Synthesis of novel glucose-lipid GlcEG3SLc **11**.

Commercially available 3-amino-1,2-propanediol **6** was *N*-protected by imine formation with benzaldehyde and the diol was subsequently deprotonated with sodium hydride and alkylated with mesylate **5**, then *N*-deprotected with a 2:1 (v/v) mixture of MeOH:concentrated HCl to give compound **7** with a yield of 36%. The relatively low yield was considered reasonable for a 5 step reaction and is in line with previous synthesis in the group.[154] An amide bond was formed between the previously synthesised acid **3** and amine **7** employing DCC as a coupling reagent to give **8** in 86% yield. The Boc group was removed with TFA to give the TFA salt **9** in 93% yield. TFA salt **9** was reacted with the glucose-linked isothiocyanate **10** under basic conditions to give the novel saturated chain glucose-lipid GlcEG3SLc **11** in 67% yield. Isothiocyanate **10** was previously synthesised by Lim Win Gel following literature procedures,[196] commencing with palladium catalysed hydration (Pd/C) of the nitro group of commercially available *p*-nitrophenyl-α-D-glucopyranoside to give *p*-aminophenyl-α-D-glucopyranoside,[204] followed by reaction with thiophosgene to give *p*-isothiocyanatophenyl-α-D-glucopyranoside **10**.[205]

2.5.2 Incorporation of GlcEG3SLc into liposomes

Incorporation of the saturated chain glucose-lipid, GlcEG3SLc **11**, into two liposomal formulations with varying GlcEG3SLc molar percentage in the bilayer and an overall lipid concentration of 35 mM was attempted. Thin lipid films were created containing DPPC and either 20 mol% GlcEG3SLc or 40 mol% GlcEG3SLc in preparation for liposome formulation. Unfortunately, upon hydration of the thin lipid films with 0.5 M glucose solution, the glucose-lipid precipitated out of solution. Freeze thawing was employed to facilitate the incorporation of GlcEG3SLc into the bilayer but it was apparent during extrusion that this was not successful. It was speculated that the head group of GlcEG3SLc was not soluble enough in water to incorporate into liposomes due to the glucose moiety not being polar enough. Possible solutions for this could include formulating liposomes with even less GlcEG3SLc in the bilayer (e.g. 10 mol%) or the synthesis of a different novel glucose-lipid with a charged moiety between the lipid tail and glucose head group to facilitate bilayer incorporation. Further research into the synthesis and liposomal incorporation of glucose-lipids was abandoned due to plans to execute a superior targeting strategy involving the covalent linking of short EGFR-targeting peptides to the bilayer surface (Section 5.1).

2.6 Summary – Section 2

In this section it was demonstrated that high concentrations of glucose can be encapsulated inside DPPC bilayers when thin films were hydrated with 0.5 M glucose solution. Saturated chain lipids were found to be integral for successful encapsulation

(Section 2.1). DPPC bilayers were able to encapsulate glucose with negligiable exterior glucose concentration after 3 rounds of dialysis when a 0.5 M glucose solution was used for the hydration of thin films, but not when concentrations of 1.0 M glucose or higher were used, which lead to high exterior glucose concentrations (Section 2.2). Glucose-ensapsulating DPPC liposomes were able to generate appreciate CEST signal at both low (1.5 µT) and high (8.0 µT) power, in a linearly concentration dependent manner for overall glucose concentrations in the range 22-55 mM (Section 2.3). Glucose-encapsulating DPPC liposomes produced the greatest CEST contrast at pH 6 at both 25 °C and 37 °C (Section 2.4). A novel saturated chain glucose-lipid, GlcEG3SLc **11**, was synthesised, however, insertion into DPPC-based bilayers at 20 mol% or 40 mol% was not achieved (Section 2.5).

3 Incorporation of a lanthanide shift reagent

Once liposome parameters and conditions that produce a robust glucoCEST signal were established, our next aim was to incorporate a lanthanide SR. The proposed role of the SR was to enlarge the chemical shift difference between the hydroxyl protons on glucose and the bulk water protons ($\Delta\omega$), to enable more selective and sensitive saturation during CEST detection. Additionally, a large $\Delta\omega$ allows much higher exchange rates to be employed whilst still adhering to the slow exchange condition on an MR time scale ($\Delta\omega \gg k_{ex}$).[58] This is a principle which has been demonstrated to be extremely effective when paramagnetic compounds bear exchangeable protons sites such as –OH, -NH or H_2O.[62]

3.1 ^{1}H NMR studies with glucose and Ln-DOTA chelates

Lanthanides are usually incorporated into structures *via* chelation to a DOTA-like moiety. Strong chelating ligands such as DOTA must be selected for *in vivo* applications due to the acute toxicity of lanthanide ions. A method of chelating Ln^{3+} ions to DOTA was established (Scheme 2). Dysprosium (Dy) and Thulium (Tm) DOTA-chelates **12** and **13** were obtained in 98% and 99% yield, respectively. The free Ln^{3+} content was quantitatively analysed using the Xylenol Orange assay.[206] It is important not to introduce free Ln^{3+} ions into our liposome formulations due to the interference of Ln^{3+} with Ca^{2+} voltage-gated channels and Ca^{2+}-mediated enzymes that could occur if they were tested *in vivo*.[30] Pleasingly, both the Dy-DOTA and Tm-DOTA chelates measured as having the same extremely low percentage of free Ln^{3+}, at 0.017%.

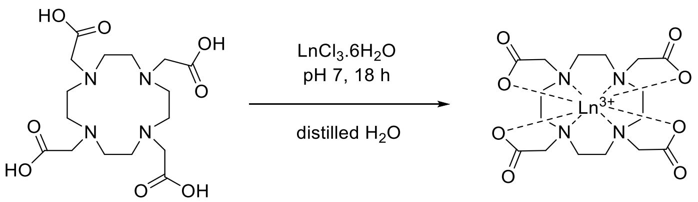

12 Ln = Dy, 98%
13 Ln = Tm, 99%

Scheme 2. Chelation of Ln^{3+} ions to DOTA.

^{1}H NMR studies were conducted in an attempt to observe the effect of Dy-DOTA **12** and Tm-DOTA **13** on the resonances of glucose signals, in particular those of the hydroxyl protons. Various concentrations of Dy-DOTA or Tm-DOTA were dissolved in either 125 mM or 0.5 M glucose in PBS and NMR data was acquired in the range –45 ppm to +55 ppm. Spectra are shown from +3 ppm to +25 ppm because all of the observed peaks were within this range. A D_2O insert was added to enable magnetic field (B_0) strength stabilisation, a process referred to as locking in NMR experiments.[207] The residual water peak at 4.8 ppm is visible in every spectrum and can be used as a reference peak, it is due to residual HOD in D_2O (the ^1H atoms exchange rapidly with the large pool of ^2H atoms in D_2O) as well as any water molecules that have been adsorbed into the sample from the atmosphere.[208]

The ^1H NMR spectrum of 125 mM glucose in water with PBS at pH 4 without water suppression is shown in Figure 29A. At 30 °C, D-glucose in water exists primarily as a mixture of α-pyranose (37.63%) and β-pyranose (61.96%), with tiny minorities existing in the α-furanose (0.108%), β-furanose (0.28), aldehyde (0.0040%) and hydrated form tautomers (0.0059%).[209] In agreement with the literature, the doublet at 4.6 ppm (J = 7.3 Hz, lit. 7.9 Hz in D_2O) is the anomeric C-H signal from the β anomer, whereas the doublet at 5.2 ppm (J = 3.6 Hz, lit. 3.7 Hz in D_2O) is the anomeric C-H signal from the α anomer.[210] The signals in the range 3.21-3.91 ppm represent all of the other C-H signals from both anomers.

The ^1H NMR spectrum of 125 mM Dy-DOTA in PBS buffer at pH 4 showed a broad peak at 18.9 ppm which has a Δω of 1.8 ppm downfield of the water peak (Figure 29B). When 125 mM or 500 mM glucose is present, this broad signal was no longer distinguished

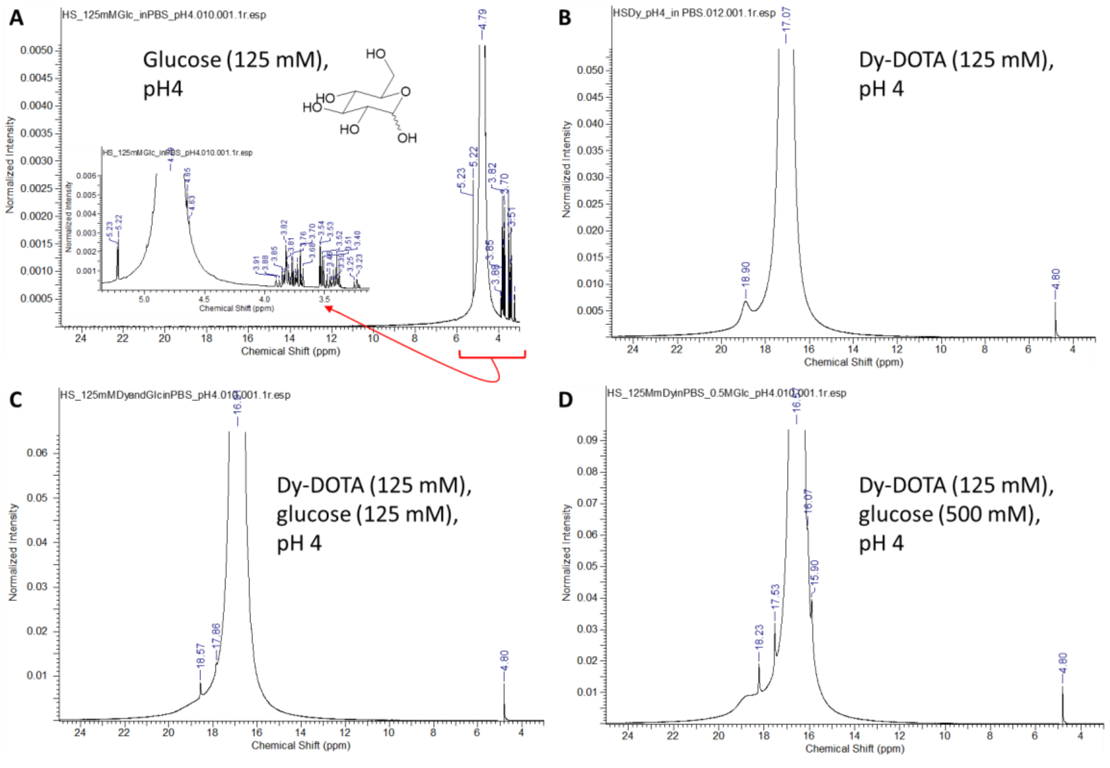

Figure 29. ^1H NMR (400 MHz) spectra in water with PBS at pH 4 and with a coaxial NMR insert tube containing D_2O for: 125 mM glucose (A), 125 mM Dy-DOTA (B), 125 mM Dy-DOTA and glucose (C) and 125 mM Dy-DOTA and 500 mM glucose (D).

E

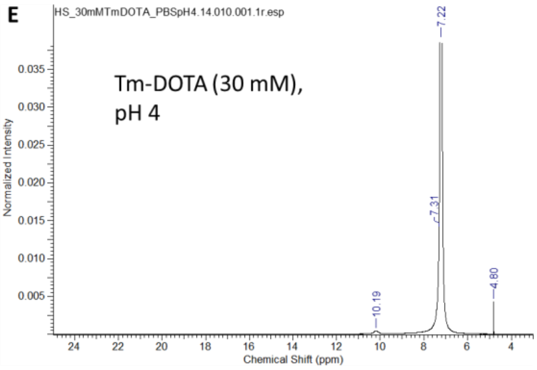
HS_30mMTmDOTA_PBSpH4.14.010.001.1r.esp
Tm-DOTA (30 mM),
pH 4
7.22
7.31
10.19
4.80
Normalized Intensity
Chemical Shift (ppm)

F

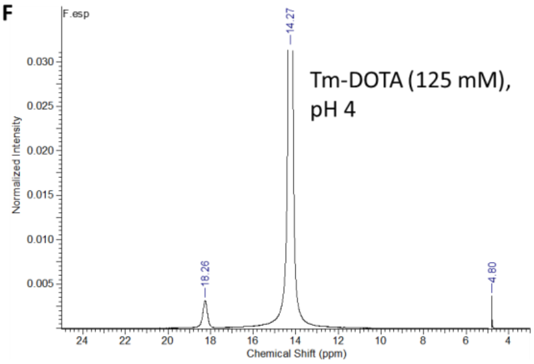
F.esp
Tm-DOTA (125 mM),
pH 4
14.27
18.26
4.80
Normalized Intensity
Chemical Shift (ppm)

G

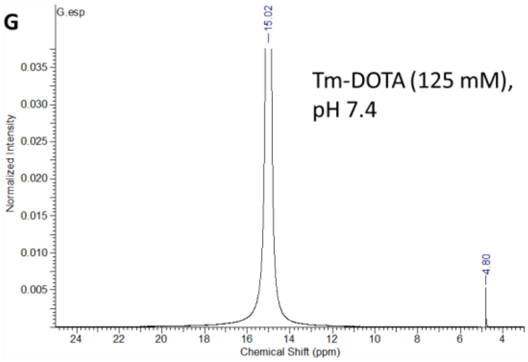
G.esp
Tm-DOTA (125 mM),
pH 7.4
15.02
4.80
Normalized Intensity
Chemical Shift (ppm)

H

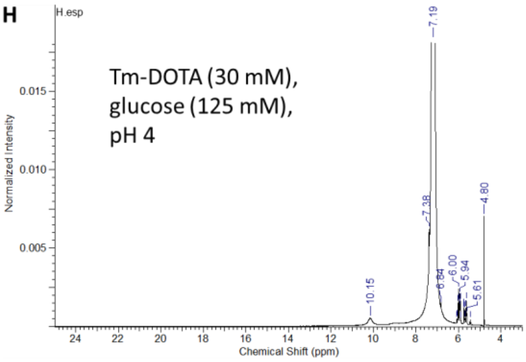
H.esp
Tm-DOTA (30 mM),
glucose (125 mM),
pH 4
7.19
7.38
10.15
6.84
6.00
5.94
5.61
4.80
Normalized Intensity
Chemical Shift (ppm)

I

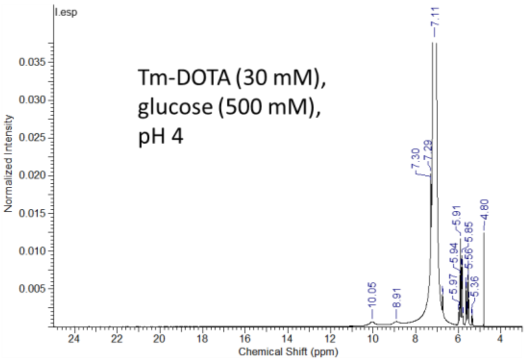
I.esp
Tm-DOTA (30 mM),
glucose (500 mM),
pH 4
7.11
7.30
7.29
10.05
8.91
5.97
5.94
5.91
5.56
5.85
5.36
4.80
Normalized Intensity
Chemical Shift (ppm)

J

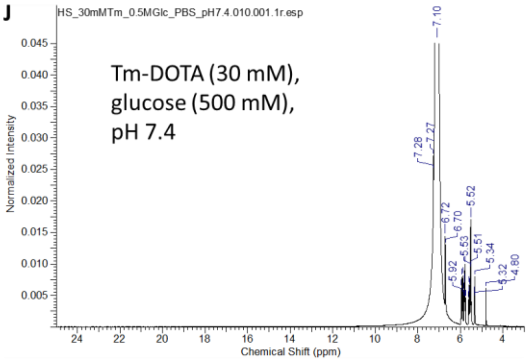
HS_30mMTm_0.5MGlc_PBS_pH7.4.010.001.1r.esp
Tm-DOTA (30 mM),
glucose (500 mM),
pH 7.4
7.10
7.28
7.27
6.72
6.70
5.92
5.53
5.52
5.51
5.34
5.32
4.80
Normalized Intensity
Chemical Shift (ppm)

K

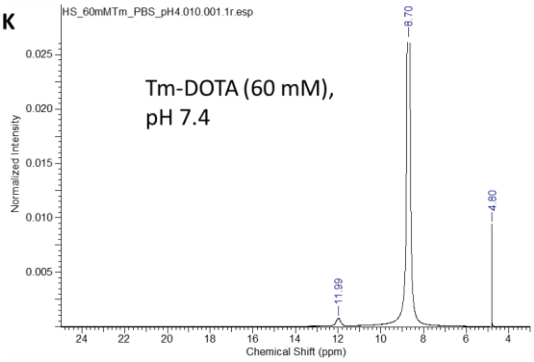
HS_60mMTm_PBS_pH4.010.001.1r.esp
Tm-DOTA (60 mM),
pH 7.4
8.70
11.99
4.80
Normalized Intensity
Chemical Shift (ppm)

L

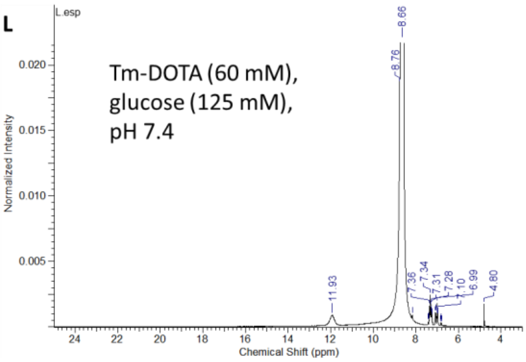
L.esp
Tm-DOTA (60 mM),
glucose (125 mM),
pH 7.4
8.66
8.76
11.93
7.36
7.34
7.31
7.28
7.10
6.99
4.80
Normalized Intensity
Chemical Shift (ppm)

M

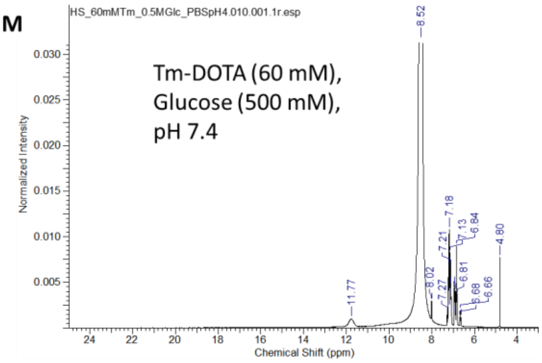
HS_60mMTm_0.5MGlc_PBSpH4.010.001.1r.esp
Tm-DOTA (60 mM),
Glucose (500 mM),
pH 7.4
8.52
11.77
8.02
7.27
7.21
7.18
7.13
6.84
6.81
6.68
6.66
4.80
Normalized Intensity
Chemical Shift (ppm)

Figure 30. ^{1}H NMR (400 MHz) spectra of solutions with various Tm-DOTA concentration with or without 125 mM or 500 mM glucose in water with PBS at pH 4 or pH 7.4, with a coaxial NMR insert tube containing D_2O.

and was replaced by broadening on the downfield side of the water peak, several weak and sharp signals appeared on top of the water peak but no significantly shifted peaks were visible (Figure 29C and D). The glucose C-H signals cannot be seen in the presence of 125 mM Dy-DOTA.

The ^{1}H NMR spectrum of 30 mM Tm-DOTA in PBS at pH 4 shows a peak at 10.2 ppm, which was 3 ppm downfield of the water signal at 7.2 ppm (Figure 30E). When the concentration of Tm-DOTA was increased to 125 mM the water signal was shifted to 14.3 ppm and the broad peak to 18.3 ppm to give a $\Delta\omega$ of 4ppm, thus, $\Delta\omega$ was only increased by 1 ppm when the SR concentration was increased more than 4-fold (Figure 30F). Upon addition of NaOH to achieve a pH of 7.4, the peak disappears entirely and only the water signal remains at 15 ppm (Figure 30G). The observed broad peak at ~ $\Delta\omega$ = 3 ppm could also be visualised for a 30 mM solution of Tm-DOTA when a CEST spectrum was obtained (Figure 32). Due to the disappearance of the peak in a ^{1}H NMR spectrum when the pH was altered and the presence in a CEST spectrum, the peak must be due to exchangeable protons and was hypothesised to be due to a protonated acid on the Tm-DOTA chelate or the protons of a chelated water molecule (Figure 31). Notably, no DOTA CH_2 signals were seen in the ^{1}H NMR spectra due to the presence of the lanthanide ion (Figure 30).

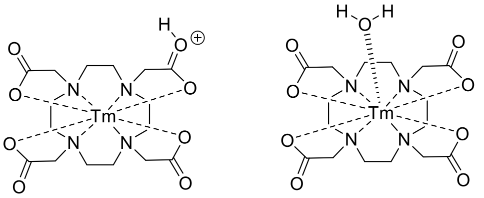

Figure 31. Tm-DOTA with protonation (left) or a chelated water molecule (right).

Upon addition of 125 mM glucose to 30 mM Tm-DOTA in PBS at pH 4, a very broad signal at 8.9 ppm appeared with $\Delta\omega$ ~ 2 ppm (Figure 30H), which increased in intensity when the glucose concentration was increased to 0.5 M (Figure 30I). All the C-H ^{1}H NMR signals were accounted for further upfield thus it was deduced that the broad peak at 8.9 ppm must represent the –OH protons belonging to glucose. Upon addition of NaOH to achieve a new pH of 7.4, both broad signals downfield of the water signal disappeared (Figure 30J), supporting the hypothesis that they both represent exchangeable protons.

It was speculated that increasing the concentration of Tm-DOTA in respect to glucose may shift the –OH signal further away from the water signal and into the paraCEST region. A solution of 60 mM Tm-DOTA in PBS at pH 4 gives rise to a water peak at 8.7 ppm and a broad signal at 12 ppm, i.e. Δω = 3.3 ppm (Figure 30K). Upon addition of 125 mM glucose, a broadening downfield of the water peak was observed (Figure 30L), which became slightly more prominent when the glucose concentration was increased to 0.5 M (Figure 30M). Comparing spectrum I with spectrum M in Figure 30 demonstrates that increasing the Tm-DOTA concentration from 30 mM to 60 mM in 0.5 M glucose solution generates an equivalent shift in both the water signal and the glucose –OH signal but there is additional broadening of the glucose –OH signal at higher Tm-DOTA concentration.

It was concluded that Tm-DOTA does significantly shift the glucose –OH signals but unfortunately this shift is parallel to the shift observed for the water signal, thus resulting in no notable increase in Δω. Therefore, it seems unlikely that co-encapsulation of Tm-DOTA and glucose inside liposomes could achieve a large chemical shift separation between the glucose hydroxyl protons and water protons in the resultant CEST spectrum, as was originally proposed.

3.1.1 CEST spectra for glucose and Tm-DOTA solutions

Similar to the ^{1}H NMR findings, the presence of the Tm-DOTA chelate **13** did not appear to shift the resonances of the CEST signals from glucose hydroxyl protons, but instead quenched some of the signal. Spectra were acquired in the range -100 ppm to +100 ppm but no signals were observed outside of the range -6 ppm to +6 ppm so that is the range shown. When 30 mM Tm-DOTA was added to 50 mM glucose at pH 7, the glucoCEST

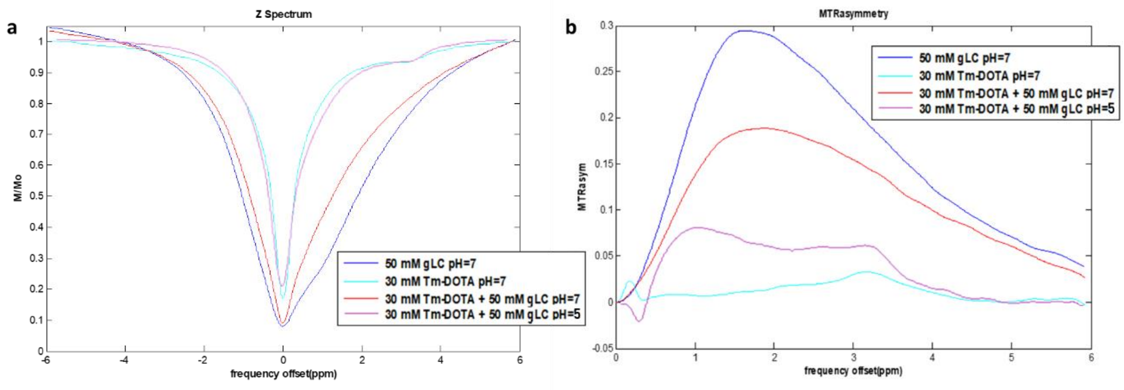

Figure 32. Z (a) and MTR$_{asym}$ (b) spectra acquired at 5.0 µT for solutions of: 50 mM glucose, 30 mM Tm-DOTA, 30 mM Tm-DOTA + 50 mM glucose at pH 7 and 30 mM Tm-DOTA + 50 mM glucose at pH 5.

signal line-shape remained similar but the magnitude was reduced (Figure 32). The spectrum for 30 mM Tm-DOTA at pH 7 shows a weak broad peak at ~ 3.1 ppm (Figure 32), which is analogous to the peak observed in the ^1H NMR spectrum of 30 mM Tm-DOTA at pH 4 ($\Delta\omega$ = 3 ppm, Figure 30E). This peak is visible in the spectrum of 30 mM Tm-DOTA and 50 mM glucose at pH 5 but not at pH 7, probably because the CEST signal from glucose at pH 7 was greater than at the more acidic pH 5 reducing the visibility of the Tm-DOTA peak (Figure 32).

More pronounced peaks at ~ 2.8 ppm could be observed when the concentration of Tm-DOTA was reduced to 10 mM (Figure 33). As before, the line shape of the CEST signal generated by glucose appeared unchanged by the presence of 10 mM Tm-DOTA and all signal was observed in the range 0-3.5 ppm. The peak attributed to Tm-DOTA was clearly visible in the spectrum where 50 mM glucose is also present (Figure 33).

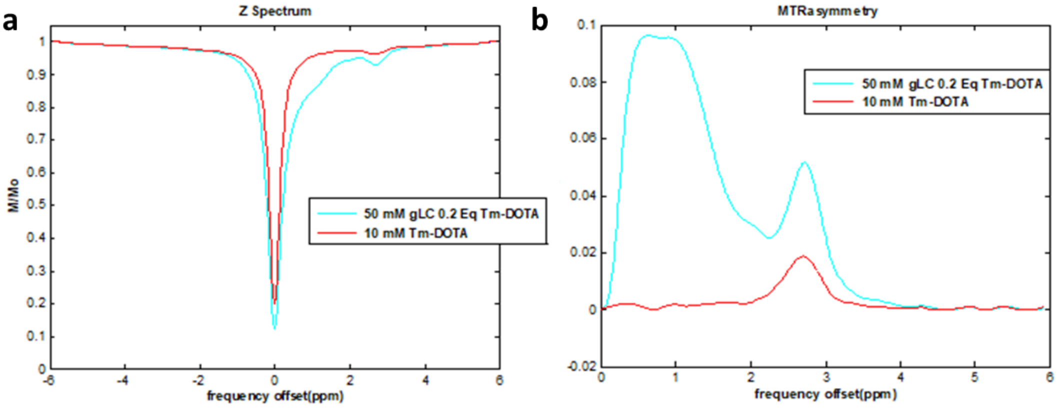

Figure 33. Z (a) and MTR_{asym} (b) spectra acquired at 1.5 µT for solutions of: 10 mM Tm-DOTA and 10 mM Tm-DOTA + 50 mM glucose at pH 7.

3.2 Co-encapsulation of glucose and a shift reagent in the aqueous interior of liposomes

Ln-DOTA chelates **12** and **13** can be incorporated into our liposomal CAs by co-encapsulation with glucose in the aqueous interior (Liposome **D**, Figure 22). Liposome samples **L14** and **L15** were formulated with 35 mM DPPC and thin films were hydrated with 0.5 M glucose and 0.25 molar equivalents (0.125 M) of Ln-chelates **12** and **13**, respectively. **L14** and **L15** were sized *via* extrusion to give vesicles with an average diameter of 172 nm and 166 nm and PdI values of 0.27 and 0.17, respectively (Table 9).

The liposomes were dialysed against 0.375 M NaCl to keep the osmolarity of the interior and exterior solutions equal and the pH of the samples were adjusted to pH 5.7 to enable comparison to liposome formulation **L9**. The Glucose HK Assay® showed successful

Table 9. Table showing the formulation parameters and measurements for Ln^{3+} DOTA complex and glucose encapsulating liposomes, **L14** and **L15**.

Liposome sample	[DPPC] (mM)	[glucose]/[Ln^{3+}) of hydration solution	Z-Ave (d.nm) (s)	PdI (s)	Exterior [glucose] (mM)	overall [glucose] (mM)	pH
L14	35	0.5 M Glc + 0.125 M **12**	172 (4.2)	0.27 (0.03)	1.1	27	5.7
L15	35	0.5 M Glc + 0.125 M **13**	166 (0.4)	0.17 (0.01)	4.5	31	5.7

encapsulation of glucose with exterior glucose concentrations for **L14** and **L15** of 1.1 mM and 4.5 mM and overall glucose concentrations of 27 mM and 31 mM, respectively (Table 9).

Unfortunately, CEST measurement of these samples gave rise to no determinable signals in the diaCEST or paraCEST region, the appearance of an extremely broad signal between approximately 0-50 ppm and severe broadening of the water peak (Figure 34).

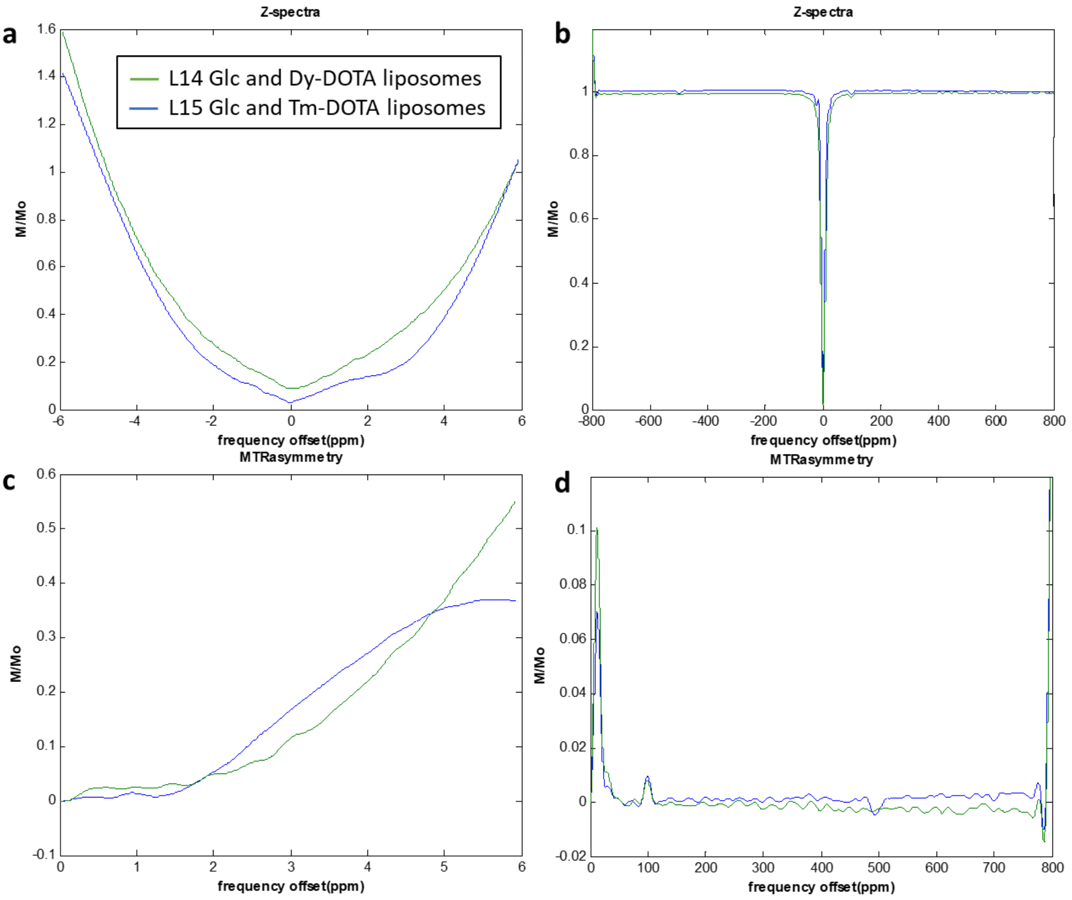

Figure 34. Z (a,b) and MTR_{asym} (c,d) spectra for **L14** and **L15** acquired with 7 µT and 40 pulses shown in the range -6 ppm to + 6ppm (a,c) and -800 ppm to +800 ppm (b,d).

A wealth of literature would suggest that the encapsulation of DOTA-chelates **12** and **13** inside liposomes **L14** and **L15**, respectively, should have given rise to lipoCEST signals. The encapsulated concentration of Tm-DOTA was equivalent to other Tm-chelates reported to produce lipoCEST signal,[105,109] furthermore a study by Zhao *et al.* reported lipoCEST signal from liposomes encapsulating 0.1-0.4 M Tm-DOTA inside PC:cholesterol (1:1) liposomes with 0.5 mol% of a rhodamine-B functionalised lipid and 3 mol% 1,2-dimyristoyl-*sn*-glycero-3-phosphoethanolamine-*N*-[methoxy(polyethylene glycol)-2000] (DMPE-PEG2000), all concentrations of which gave rise to appreciable lipoCEST signal ~ 1 ppm away from the water peak.[211] In agreement, Maruyama *et al.* reported that the ^{1}H NMR spectra of DPPC-based liposomes encapsulating Tm-DOTA and Dy-DOTA exhibited broad peaks at +1 ppm and -2 ppm away from the water peak, respectively.[110] When **L14** and **L15** were scanned by Eleni Demetriou on a 9.4 T Aligent scanner it is unclear why a lipoCEST signal was not generated, since lipoCEST signal has been generated by DPPC liposomes encapsulating similar concentrations of Ln-chelates in the literature,[105] a possible variable is the presence of high concentrations of glucose. However, in line with these findings, a recent study by Farashishiko *et al.* reported that encapsulation of paraCEST agents such as DyDOTAM^{3+} in reverse assembled nano-capsules (comprised of the chelate, polyacrylic acid, ethylene diamine, polyallylamine hydrochloride, and silica nanoparticles) gave rise to significantly quenched CEST signal.[212] The quenching effect of encapsulation was attributed to slowing molecular tumbling, which is inevitable when the chelate is incorporated into a nano-scale material. Slow molecular tumbling can increase the rate of transverse relaxation to such an extent that it outcompetes CEST by causing reductions in the intensity of observed CEST signal and extensive broadening. This effect is particularly expected to arise in the case of heavier lanthanide ions (such as Tm and Dy) due to their larger magnetic moments giving rise to more rapid transverse relaxation of proximate protons.[212]

3.3 Synthesis of a saturated chain DOTA-lipid

Another method to incorporate lanthanides into liposomes is by covalently anchoring Ln-chelates to the bilayer surface *via* inclusion of DOTA-lipids in the bilayer (Liposome **E**, Figure 22). An unsaturated DOTA-lipid based on DOPE, DEG3SL, has been previously synthesised and successfully employed in MRI studies of liposomes *via* chelation to Gd^{3+} and subsequent incorporation into the lipid bilayer.[164] In parallel with the ^{1}H NMR studies reported in Section 3.1**,** a novel saturated chain analogue of DEG3SL, DEG3SLc, was synthesised for proposed Ln-chelation and incorporation into liposomal CAs, to investigate whether this technique of lanthanide incorporation could shift the glucose hydroxyl resonances into the paraCEST region.

The tri-protected DOTA compound **17** was synthesised in 3 steps following a series of procedures reported by Wängler *et al*.[213] Commercially available cyclen **14** was reacted with 0.5 equivalents of benzyl bromoacetate to give the singly substituted cyclen **15** in 79% yield with respect to benzyl bromoacetate. The remaining amine moieties were alkylated with *tert*-butyl bromoacetate to give protected DOTA **16** in 47% yield. Benzyl protection of DOTA intermediate **16** was removed *via* palladium-catalysed hydrogenation to give the tri-protected DOTA intermediate **17** in 99% yield. Carboxylic acid **17** was coupled to the previously synthesised amine **9** (Scheme 1) using HBTU and DIPEA to give the Boc-protected DOTA-lipid **18** in 30% yield. Lipid **18** was Boc-deprotected with TFA to give the novel saturated DOTA-lipid DEG3SLc **19** in 65% yield (Scheme 3).

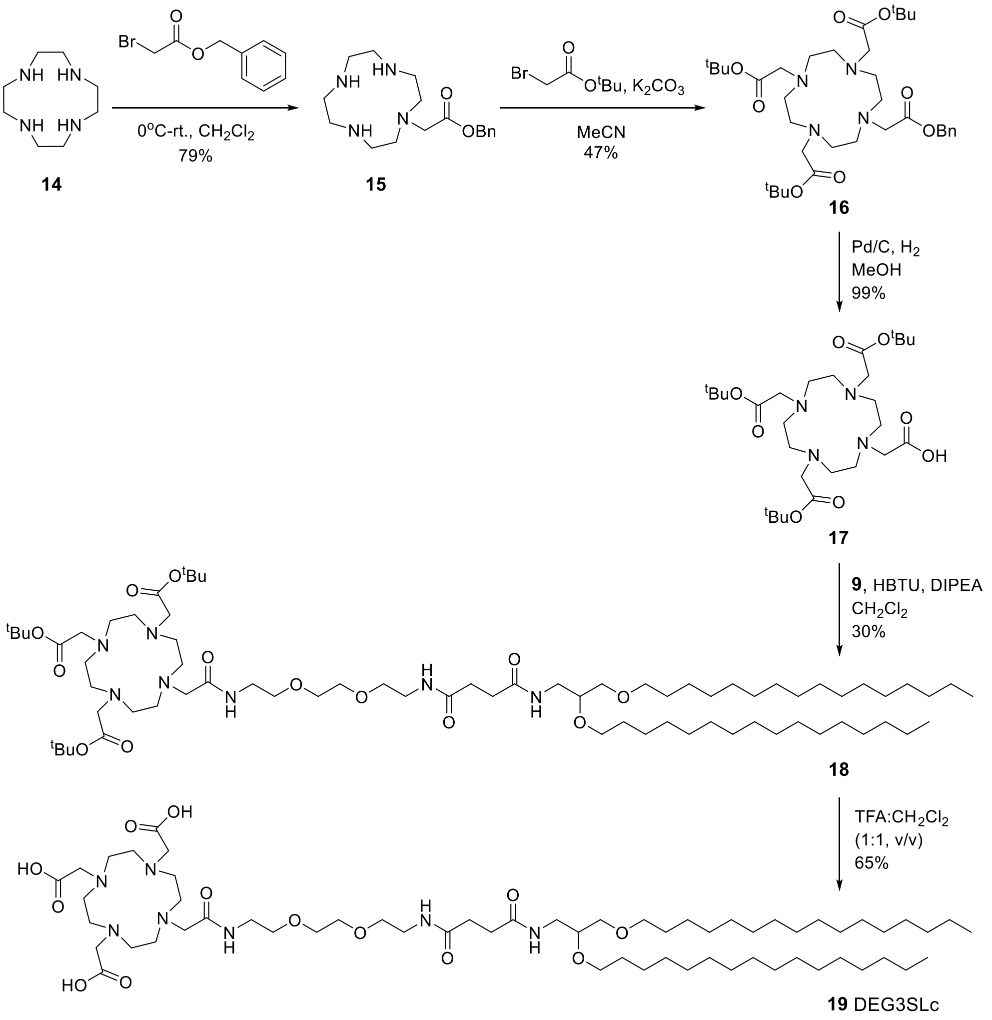

Scheme 3. Synthetic route to the novel saturated chain DOTA-lipid, DEG3SLc **19**.

The saturated chains of DEG3SLc are analogous to those of DPPC, therefore we expect DEG3SLc to facilitate durable glucose encapsulation. However, due to the results in Sections 3.1 and 3.2 indicating that the co-solvation of Ln-DOTA chelates and glucose does not produce an exaggerated chemical shift difference between the glucose hydroxyl protons and bulk water protons, the novel saturated chain DOTA-lipid DEG3SLc **19** was not employed in glucose liposome formulation in an attempt to produce paraCEST signal.

3.4 Synthesis of glucose-DOTA bioconjugates

It was hypothesised that the lanthanide SR was not in close enough proximity to the glucose hydroxyl groups to produce a large shift when simply co-encapsulated in the aqueous interior of the liposome and that this problem could be overcome by covalently linking the two moieties *via* a short linker to permanently hold them in close proximity. Thus, the aim of this section was to determine whether glucose paraCEST can be achieved *via* the synthesis of a glucose-DOTA bioconjugate with chelation to a lanthanide ion, circumventing the use of liposomes.

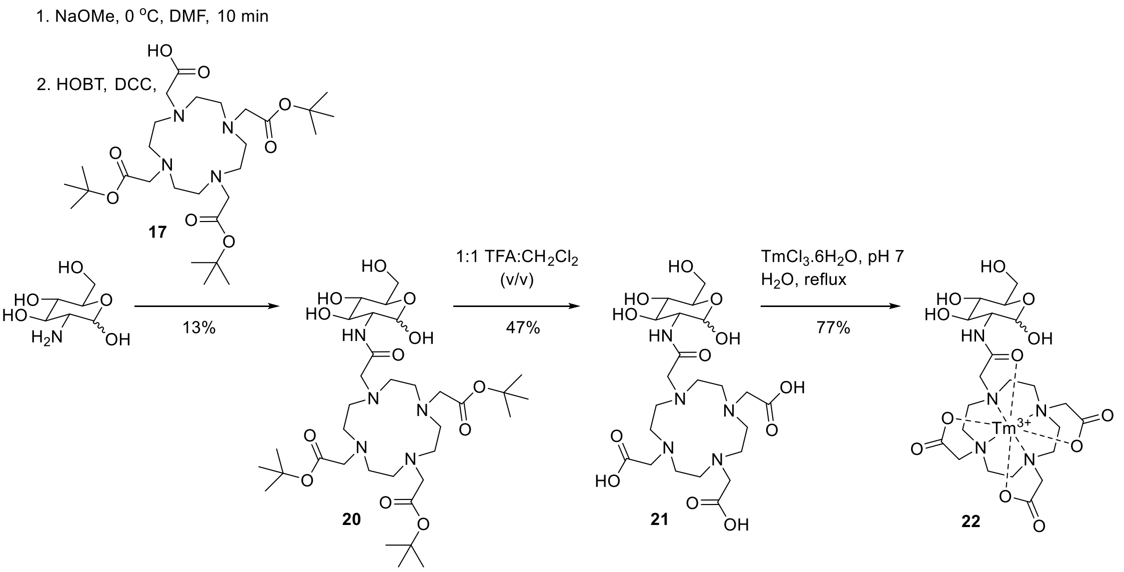

Scheme 4. Synthetic route to the thulium-containing glucose-DOTA bioconjugate **22**.

A glucose-DOTA bioconjugate can be synthesised from the previously obtained tri-protected DOTA intermediate **17** in just 3 steps (Scheme 4). D-(+)-Glucosamine hydrochloride was employed in an amide coupling reaction with acid **17**, using HOBt and DCC as the coupling reagents, to give the protected glucose-DOTA conjugate **20** in 13% yield after extensive purification. The *tert*-butyl groups on **20** were removed using a 1:1 (v/v) mixture of TFA:CH_2Cl_2 to give deprotected glucose-DOTA conjugate **21** in 47% yield. LC-MS analysis revealed that under the acidic deprotection conditions, the amide group of **21** cyclised onto the anomeric position of the glucose ring (50:50 cyclised:uncyclised product by LC-MS) (Figure 35).

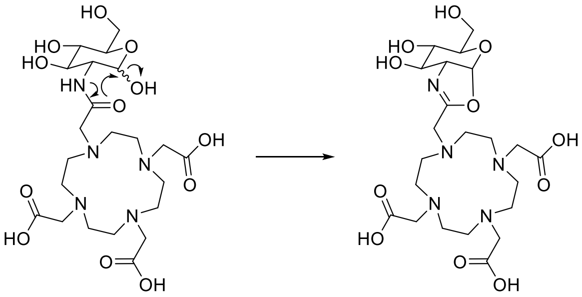

Figure 35. Cyclisation of glucose-DOTA bioconjugate **21**.

Refluxing was required to complex thulium to the DOTA moiety of **21** (mixture of cyclised and uncyclized product), whereas complexation of thulium to DOTA occurs readily at room temperature. This difficulty of complexation was speculated to be due to steric hindrance and a less strong co-ordinate bond being formed between the amide carbonyl/cyclised ether oxygen compared to the fourth acid group usually present on DOTA ring. Thulium (III) chloride hexahydrate and **21** were reacted to give the thulium-complexed bioconjugate **22** in 77% yield (5:4 cyclised:uncyclised product by LC-MS). The synthesis resulted in 25 mg (0.034 mmol) of a mixture of cyclised and uncyclised **22**, the cyclisatiion was considered unimportant at this point as CEST measurement of the mixture would still give us a good idea of whether Δω could be significantly increased by this method. Unfortunately, after characterisation there was too little of compound **22** for CEST measurement on the 9.4 T Agilent scanner because 2 mL of sample at a concentration of ~ 20 mM was required (0.04 mmol required). However, the Δω between the –OH protons of glucose and the water peak in a ^{1}H NMR spectrum is representative of the Δω observed in a CEST spectrum (conversion is dependent on the relative power of the two techniques). The ^{1}H NMR spectrum of **22** (5 mM) showed a broad singlet at 7.4 ppm (Figure 36a), which is analogous to the broad singlet at 7.3 ppm observed in the ^{1}H NMR spectrum of Tm-DOTA **13** (Figure 36b). Thus, it was concluded this peak was due to chelated water molecule protons or protonation of the DOTA portion of the molecule. When the concentration of **22** was increased from 5 mM to 12.5 mM in an attempt to visualise the glucose -OH protons, the intensity of the broad singlet was enhanced and shifted slightly downfield to 7.6 ppm, but no new signals appeared (Figure 36c). No C-H signals are visible in the ^{1}H NMR spectra of **22** presumably due to the presence of the lanthanide making them too broad to observe. Upon addition of 10% D_2O, the peak at ~ 7.5 ppm almost entirely disappeared, confirming that it is due to exchangeable protons. Since the glucose hydroxyl protons on compound **22** could not

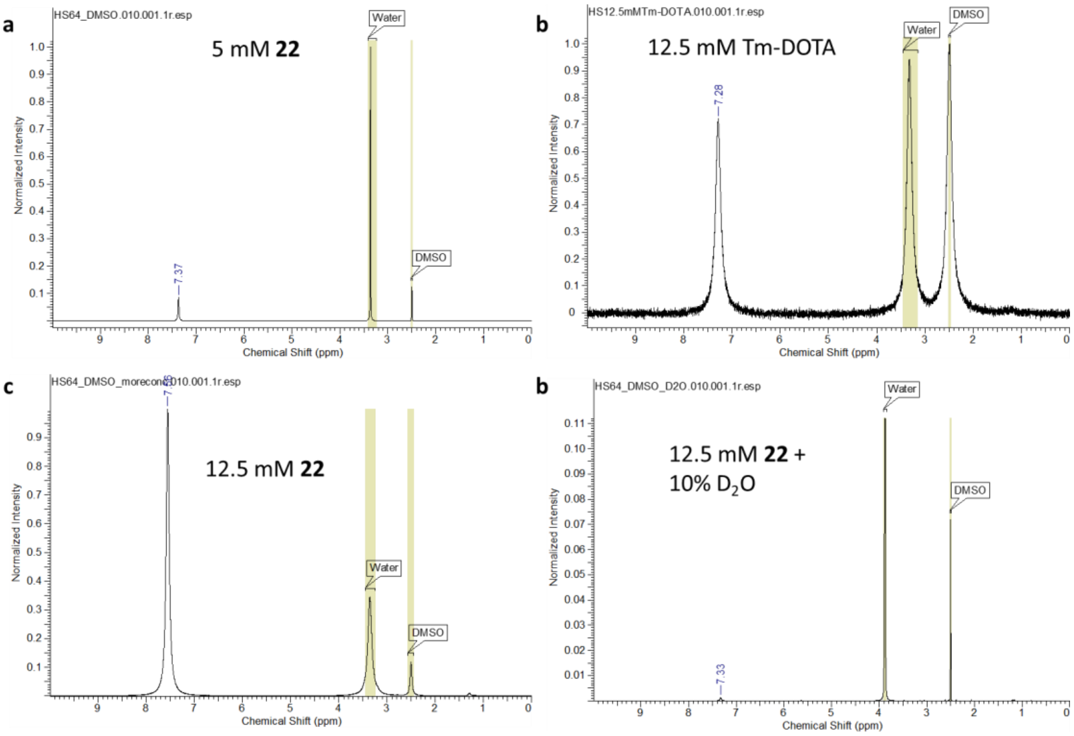

Figure 36. ^{1}H NMR spectra (600 MHz, DMSO) measured in the range -45 ppm to +55 ppm for a) 5 mM glucose-DOTA bioconjugate **22**, b) 12.5 mM Tm-DOTA **13**, c) 12.5 mM glucose-DOTA bioconjugate **22**, d) 12.5 mM glucose-DOTA bioconjugate **22** and 10% D$_2$O.

be observed by ^{1}H NMR, the synthesis of **22** was not scaled up and the synthesis of a new bioconjugate was planned.

It was speculated that the thulium atom in **22** would be very crowded and the co-ordination to a glucose hydroxyl proton would be sterically disfavoured. The synthetic route to an analogous bioconjugate was planned with a longer carbon linker to afford more flexibility, as well as excluding a carbonyl moiety in close proximity to the thulium atom to open up a potential co-ordination site for a glucose hydroxyl group.

First, a protected sugar with a free amine moiety was synthesised in a 3 step process with an overall yield of 27% (Scheme 5), following a series of procedures reported by Myszka *et al.*[214] D-(+)-Glucosamine hydrochloride was *N*-protected *via* a imine formation with *p*-anisaldehyde to give the protected amino-sugar **23** (> 90% β anomer) in 44% yield. The hydroxyl groups of **23** were acetylated with a 5:9 mixture of acetic anhydride and pyridine to give the β anomer of the fully protected glucosamine **24**. The imine was hydrolysed in 5 M HCl to give the β anomer of the O-protected glucosamine **25** in 93% yield.

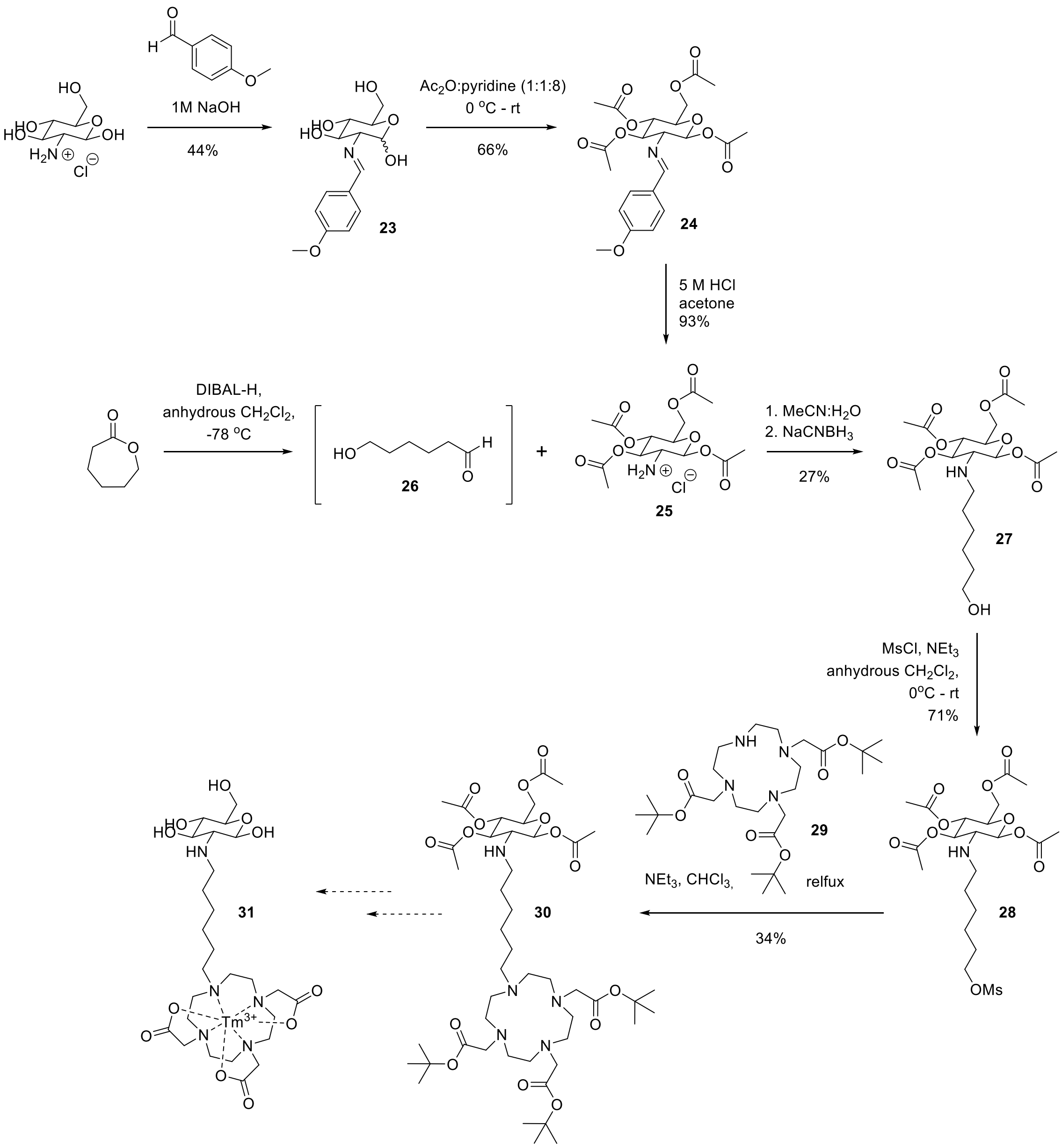

Scheme 5. Synthetic route to the glucose-DOTA bioconjugate **31** with a 6-carbon linker.

A 4-carbon linker was originally proposed between the sugar and DOTA moieties *via* the synthesis of 4-hydroxylbutanal and subsequent reductive amination with **25**, followed by activation and nucleophilic substitution of the alcohol with commercially available tri-*tert*-butyl 1,4,7,10-tetraazacyclododecane-1,4,7-triacetate (structure **29**, Scheme 5). γ-Butyrolactone was reduced using DIBAL-H in an attempt to form 4-hydroxybutanal, however only the cyclised hemi-acetal product was identified following FCC purification. The mildly acidic conditions of the column and favourable 5-membered ring formation were predicted to be the reasons for the cyclisation of any 4-hydroxylbutanal that may have been formed. This product formation was in agreement with the literature, which reports that tetrahydrofuran-2-ol is the main product of this reaction with yields as high as 92% (Scheme 6).[215]

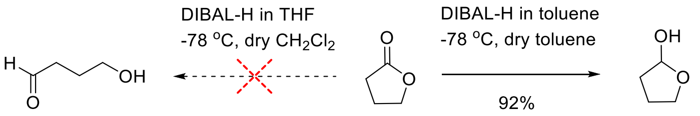

Scheme 6. Failed synthesis of 4-hydroxylbutanal (left), reported outcome of the reaction by Stephens *et al*. (right).[215]

To avoid lactone conversion to a hemiacetal, a 6-carbon linker between the sugar and DOTA moiety was proposed. ε-Caprolactone, with a ring size that is 2 carbons bigger, was employed in an analogous reaction following a procedure reported by Soubhye *et al*.[216] to form a small proportion of 6-hydroxyhexanal, however, the methyl ester was predominantly isolated. It was assumed that the methyl ester was formed during the quenching of DIBAL-H with methanol. Therefore, the reaction was repeated and adapted by quenching with 0.5 M HCl solution instead of methanol. ^{1}H NMR spectroscopy of impure **26** showed a prominent aldehyde peak at 9.76 ppm. To avoid cyclisation on silica gel, aldehyde **26** was used crude in a reductive amination reaction with protected amino-sugar **25**, employing an adapted procedure from Liberek *et al*.,[217] to give the novel substituted amino-sugar **27** in 27% yield (Scheme 5). Alcohol **27** was mesylated using mesyl chloride following an adapted procedure from Baranyai *et al*.,[218] to give **28** in 71% yield. Nucleophilic substitution of mesylate **28** with commercially available tri-*tert*-butyl 1,4,7,10-tetraazacyclododecane-1,4,7-triacetate **29**, also adapted from Baranyai *et al*.,[218] required additional heating to reflux to achieve significant conversion to the protected glucose-DOTA conjugate **30** (monitored by LC-MS). FCC purification resulted in 25 mg of the protected 6-carbon linked glucose-DOTA bioconjugate **30** with a yield of 34%. This was not enough material to complete the synthesis of **31** which required 3 further steps; two distinct deprotection reactions and the complexation of thulium to the DOTA moiety. This synthesis was not re-visited due to focus on other aspects of the project and due to difficulties in completely purifying the intermediates.

3.5 Summary – Section 3

In this Section, the incorporation of a lanthanide ion was investigated with the aim of shifting the resonances of the glucose hydroxyl protons further away from the water peak to enhance the selectivity and sensitivity of CEST detection. ^{1}H NMR studies were conducted that indicated co-solvation of glucose with Dy-DOTA or Tm-DOTA chelates can cause a shift in the resonance frequencies of glucose hydroxyl protons, however, there is significant broadening and, more importantly, the water peak is shifted in a similar manner, giving rise to small increases in Δω (Section 3.1). When DPPC bilayers were hydrated with 0.5 M glucose and 0.125 M Dy-DOTA or Tm-DOTA, the resultant liposomes produced no determinable CEST signals and there was severe broadening of the water signal (Section 3.2).

Due to these findings, attempts to synthesise a glucose-DOTA bioconjugate were not continued and the novel saturated chain DOTA-lipid, DEG3SLc **19**, was not utilised in liposome formulation by our group, however, it may find use in other liposome-labelling studies.

4 Formulation, characterisation and factors affecting CEST signal generated by glucose and 2-DG liposomes

Due to the metabolic, cytotoxic and reported radiomodifying properties of 2-DG (Section 1.3), it was proposed that it would be advantageous to encapsulate 2-DG instead of glucose in the aqueous interior of liposomes. Such 2-DG liposomes would have the potential to be developed into novel theragnostic agents for tumors; they would be able to generate CEST contrast for the diagnosis and staging of cancer with additional chemotherapeutic benefits in combination with radiation therapy.

4.1 CEST spectra of free glucose and 2-DG

The CEST signal generated by free glucose and free 2-DG solutions was investigated in the pH range 6-7.4, for comparison and to identify the optimal pH for CEST signal generation at RT and 37 °C for both monosaccharides. Monosaccharide solutions were made up at 35 mM in 20% PBS and the pH was adjusted with 1 M HCl or 1 M NaOH. The MTR_{asym} spectra for glucose and 2-DG exhibited very similar line-shapes (Figure 37 and Figure 38, respectively), with large peaks at ~ 0.7 and 1.3 ppm and smaller peaks at ~ 2.1 and 2.9 ppm. The CEST signal was quantified by averaging the percentage water signal suppression across the presaturation range 0-6 ppm (Table 10) and the results are presented in Figure 39 and Figure 40 for glucose and 2-DG, respectively.

Table 10. CEST suppression of the water peak for free glucose and 2-DG solutions at 35 mM in 20% PBS at various pH. The data was acquired at 25 °C and 37 °C with B_1 = 1.5 μT and 5.0 μT. CEST suppression is expressed as an average of the percentage reduction in water signal caused by presaturation across the range 0-6 ppm.

Monosaccharide	pH	1.5 μT		5.0 μT	
		MTR_{asym} 25 °C	MTR_{asym} 37 °C	MTR_{asym} 25 °C	MTR_{asym} 37 °C
glucose	6.0	5.6%	7.7%	9.5%	13.4%
glucose	6.25	5.7%	8.0%	10.8%	16.1%
glucose	6.5	6.5%	8.3%	12.5%	17.1%
glucose	6.75	7.1%	7.2%	15.7%	18.7%
glucose	7.0	7.6%	8.1%	16.6%	16.1%
glucose	7.4	5.4%	2.3%	15.4%	9.6%
2-DG	6.0	4.8%	6.3%	7.6%	10.9%
2-DG	6.25	4.9%	6.7%	7.8%	13.3%
2-DG	6.5	5.0%	6.7%	10.2%	14.3%
2-DG	6.75	6.4%	6.8%	12.1%	16.2%
2-DG	7.0	6.4%	5.8%	13.3%	15.7%
2-DG	7.4	4.7%	1.8%	13.2%	7.6%

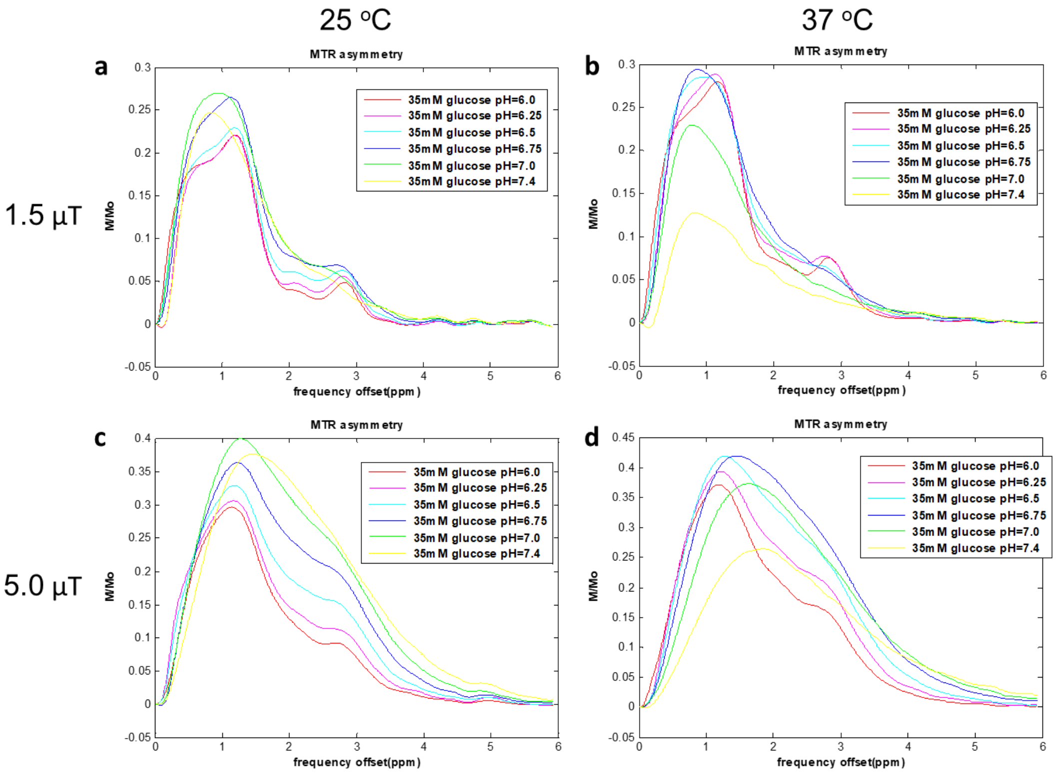

Figure 37. MTRasym spectra for free glucose solutions at 35 mM in 20% PBS at various pH. Spectra were obtained with B_1 = 1.5 μT (a,b) and B_1 = 5.0 μT (c,d), and at 25 °C (a,c) and 37 °C (b,d).

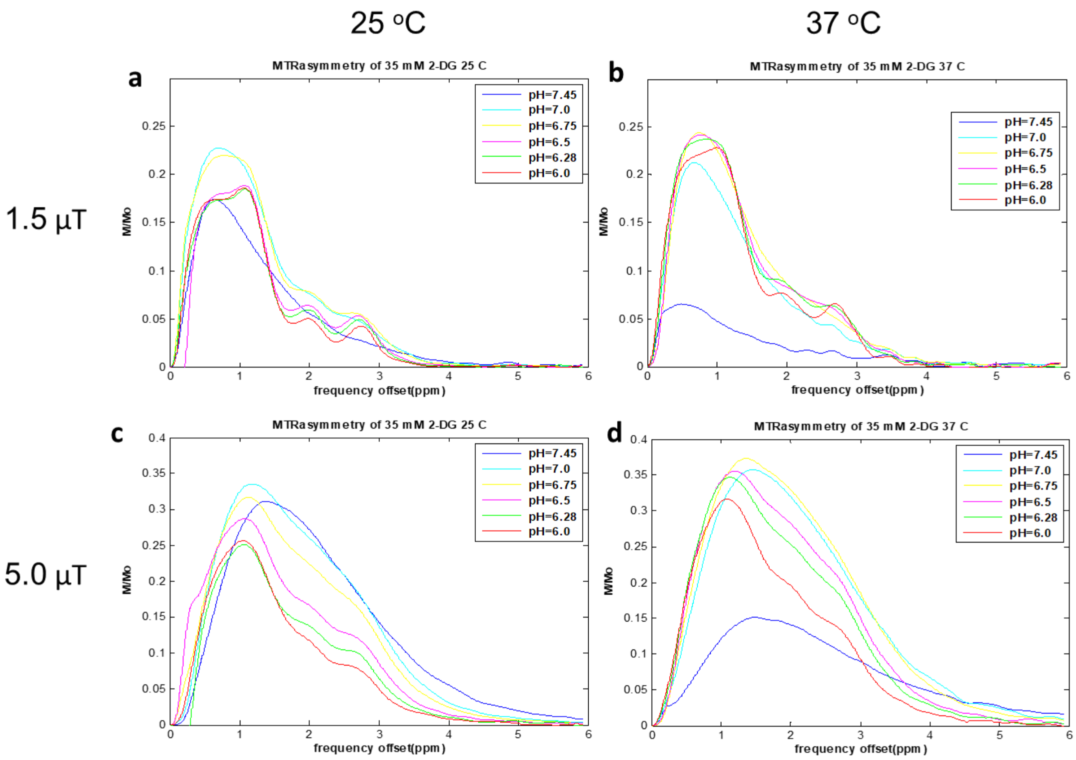

Figure 38. MTR_{asym} spectra for free 2-DG solutions at 35 mM in 20% PBS at various pH. Spectra were obtained with B_1 = 1.5 μT (a,b) and B_1 = 5.0 μT (c,d), and at 25 °C (a,c) and 37 °C (b,d).

When glucose was scanned at room temperature, the sample at pH 7.0 gave the best CEST signal at both powers. When glucose was scanned at physiological temperature, the results at 1.5 µT are not clear because the signals generated between pH 6 and 7 are similar. However, at 5.0 µT, pH 6.75 appears to be optimal, giving an average water signal suppression of 18.7% across the presaturation range 0-6 ppm (Table 10, Figure 39).

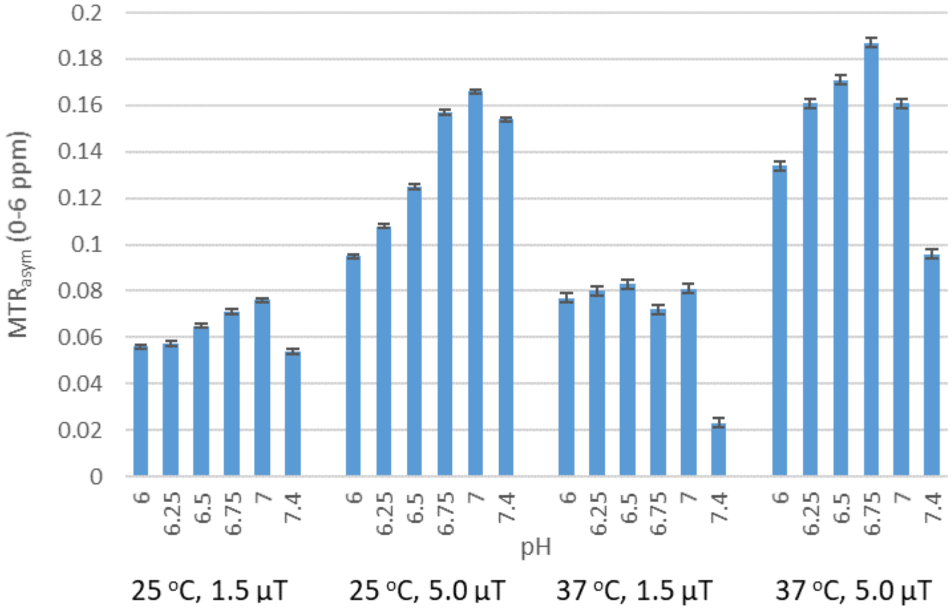

Figure 39. MTR$_{asym}$ (0-6 ppm) for free glucose solutions at 35 mM in 20% PBS at various pH, temperature (25 °C or 37 °C) and power (1.5 µT or 5.0 µT).

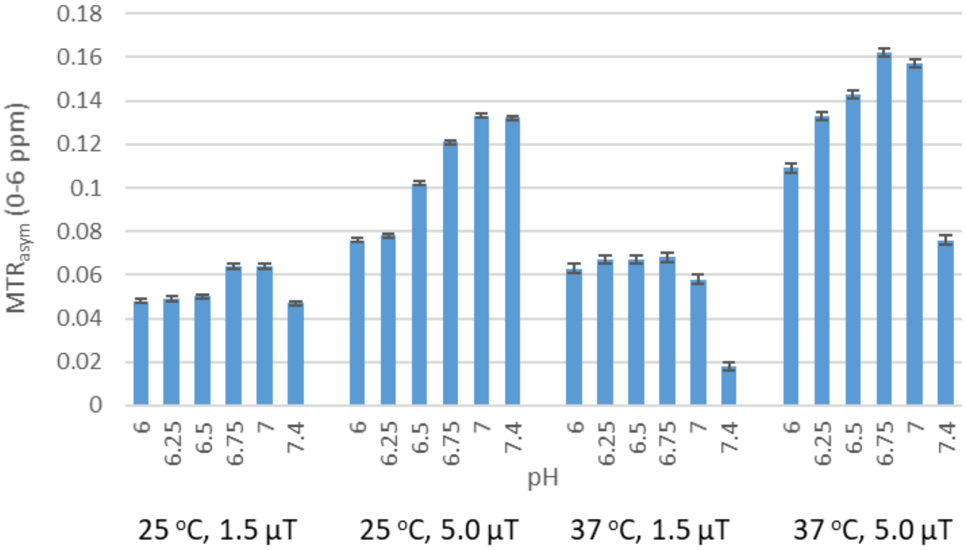

Figure 40. MTR$_{asym}$ (0-6 ppm) for free 2-DG solutions at 35 mM in 20% PBS at various pH, temperature (25 °C or 37 °C) and power (1.5 µT or 5.0 µT).

When 2-DG was scanned at room temperature, pH 7.0 was the optimal pH for CEST signal generation and when the temperature was increased to 37 °C, the optimum pH shifted only slightly to pH 6.75, achieving an average water signal suppression of 16.2% across the presaturation range 0-6 ppm when the higher saturation power of 5.0 µT was applied (Table 10, Figure 40).

Comparison of Figure 39 and Figure 40 shows that the pH dependency of CEST signal magnitude for glucose and 2-DG share a very similar profile. Figure 41 combines the glucose and 2-DG data, the solid lines represent glucose, the dashed lines represent 2-DG and colour pairs represent the same temperature and power conditions for the two monosaccharides. It is apparent that the CEST signal generated by 2-DG has a very similar pH dependency to glucose but with slightly less signal intensity. This was presumed to be due to 2-DG having one less exchangeable hydroxyl proton.

As expected, the higher power of 5.0 µT gave rise to greater CEST signal than the lower power of 1.5 µT, with an average 1.3-fold increase in signal magnitude across all temperature and pH conditions for both monosaccharides. For both glucose and 2-DG, increasing the temperature from 25 °C to 37 °C produced an enhanced signal for pH values between 6 and 6.75, at pH 7 the signal was very similar for the two temperatures, whereas at pH 7.4 the lower temperature of 25 °C generated better CEST signal.

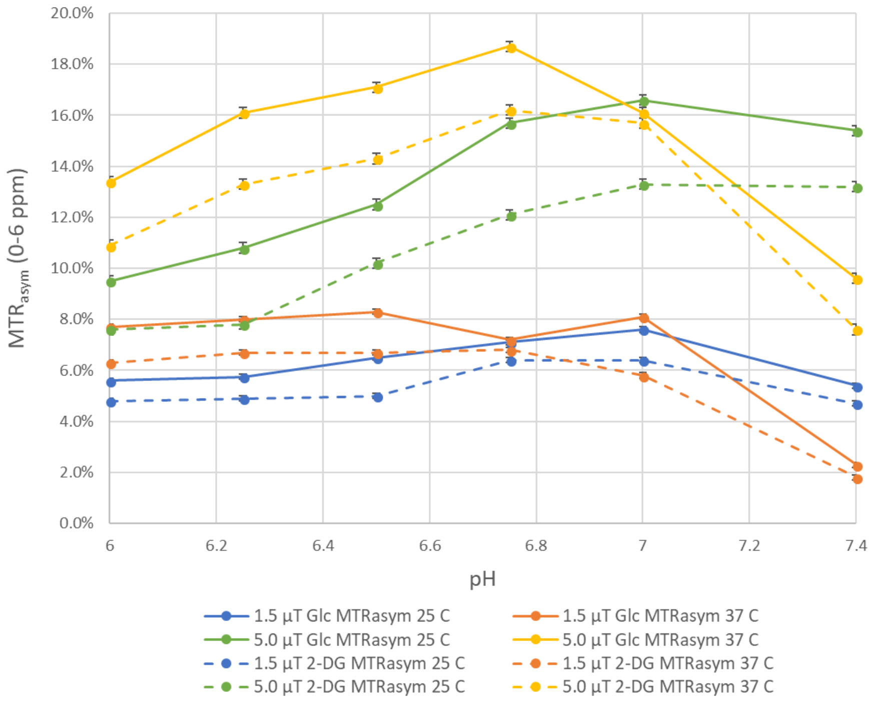

Figure 41. pH dependency of CEST signal generated by free glucose and 2-DG solutions (35 mM), expressed as an average of the percentage reduction in water signal caused by presaturation in the range 0-6 ppm.

4.1.1 Assigning glucose and 2-DG hydroxyl protons

It has been shown that the Z and MTR$_{asym}$ spectra are similar for glucose and 2-DG (Section 4.1). To better understand the line shapes observed, the hydroxyl protons in the MTR$_{asym}$ spectra for both monosaccharides were assigned using the hydroxyl signals observed in the ^{1}H NMR spectra of glucose and 2-DG in aqueous solution at 0.5 M and at various pH values. The -OH proton signals observed in the ^{1}H NMR spectra of glucose can be assigned using the downfield shifts relative to water from published NMR data:[219] 0.66ppm (O^{6}H), 1.28 ppm (O^{2,3,4}H) and the anomeric –OH protons at 2.08 ppm (O^{1}H$_{\alpha}$) and 2.88 ppm (O^{1}H$_{\beta}$) (Figure 42a). The spectra for 2-DG display almost identical resonances to glucose but with the presence of only two hydroxyl protons at 1.28 ppm (O^{3,4}H) (Figure 42b). The resonance frequencies of the hydroxyl protons of glucose and 2-DG with respect to water are analogous for ^{1}H NMR and MTR$_{asym}$ spectra (compare Figure 42 with Figure 37 and Figure 38).

The NMR spectra in Figure 42 demonstrate that pH does not alter the resonance frequencies of the hydroxyl protons with respect to water. As neutral pH is approached, the ability to see the -OH protons is reduced, as has been previously reported.[219] Similar

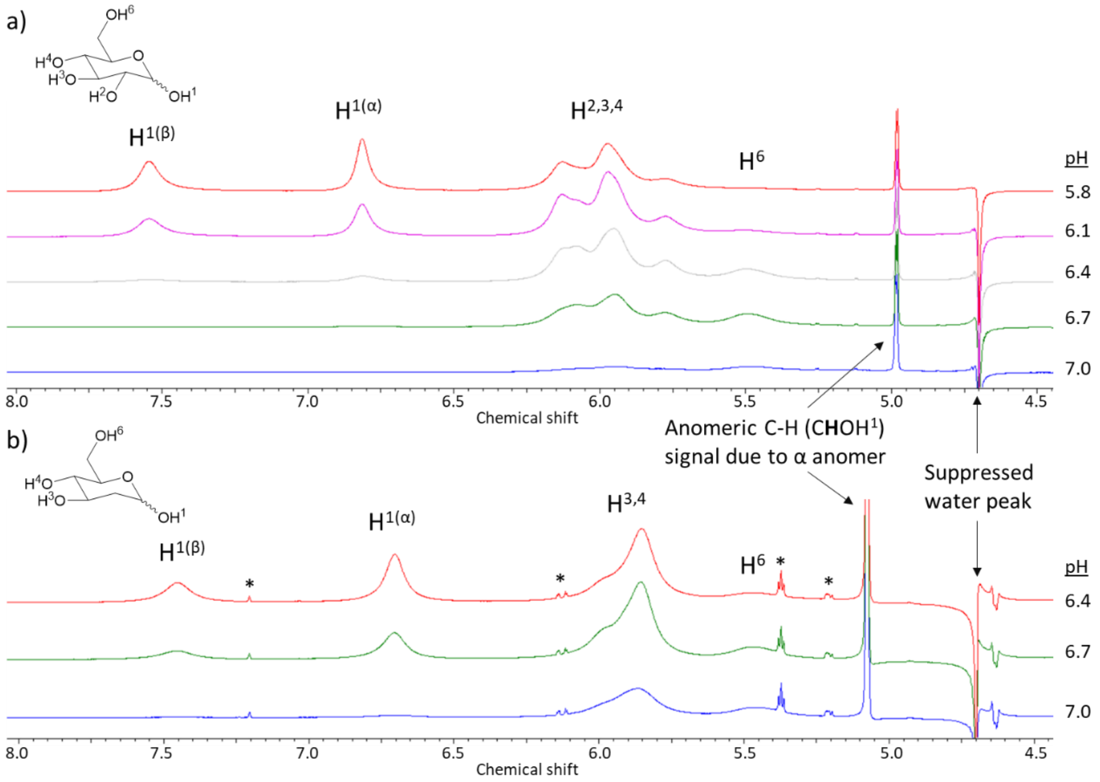

Anomeric C-H (C**H**OH^{1}) signal due to α anomer

Suppressed water peak

Figure 42. ^{1}H NMR spectra (600 MHz) of 0.5 M monosaccharides in DI water with 20% PBS at various pH a) 0.5 M glucose at pH 7.0, 6.7, 6.4, 6.1 and 5.8 and b) 0.5 M 2-DG at pH 7.0, 6.7 and 6.4. The suppressed water signal and anomeric C-H signal are labelled and the asterisks mark impurities in the commercially available 2-DG.

NMR experiments were carried out with solutions of glucose and 2-DG at varying concentrations, resulting in the same finding (Figure 43); that monosaccharide concentration does not alter the resonance frequencies of the hydroxyl protons. The consistency of glucose hydroxyl resonances with respect to water at varying temperatures has been previously reported by Bociek *et al.* (± 0.1 ppm over a range of 60 °C).[219] Thus, we expect the hydroxyl peak assignments for glucose and 2-DG in CEST spectra to remain constant across all experiments, irrespective of varying pH, concentration and temperature.

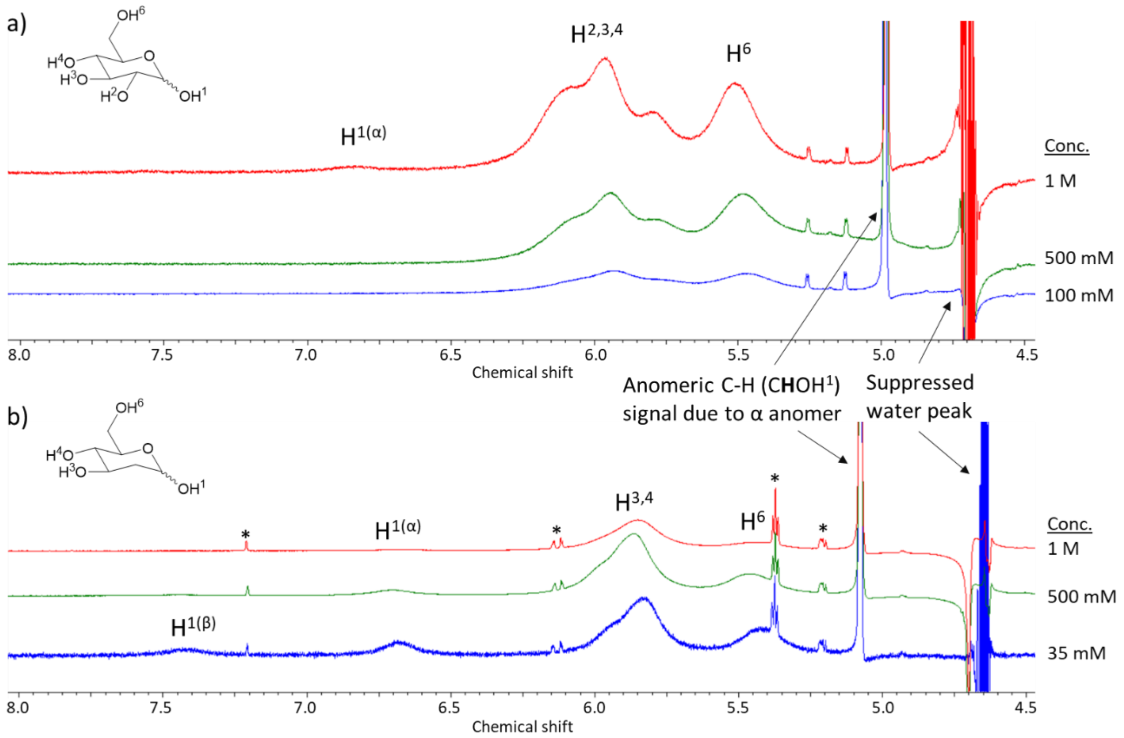

Figure 43. ^1H NMR (600 MHz) spectra of monosaccharides in DI water with 20% PBS at pH 7, a) glucose at concentrations of 1 M, 500 mM and 100 mM, and b) 2-DG at concentrations of 1 M, 500 mM and 35 mM. The suppressed water and anomeric C-H signals are labelled and asterisks mark impurities present in the commercially available 2-DG. N.B. The signal intensity was increased for lower concentrations of 2-DG to enable observation of the hydroxyl peaks.

4.2 Formulation of pH-sensitive 2-DG encapsulating liposomes

Given that the CEST signals obtained from the glucose liposomes in Section 2.3 were significantly smaller than the CEST signals observed for the free glucose controls, it was speculated that the development of pH-sensitive 2-DG liposomes could enhance tumor contrast as well as reduce the toxicity of 2-DG. The reasoning behind this was that whilst the liposomes are in the circulation (pH 7.4) they will remain intact, thereby reducing off-target toxicity and effectively “shielding” the CEST signal produced by 2-DG. Subsequent exposure to the more acidic tumor microenvironment would cause destabilisation of the liposomes and release of encapsulated 2-DG, resulting in an increase in observed CEST signal and specific exposure of tumor cells to cytotoxic 2-DG, which is taken up into cells by the same molecular transporters as glucose.[144] Additionally, liposomes of a specific size are passively targeted to tumors *via* the EPR effect (Section 1.4.1.1).[155] However, the lipid bilayer composition significantly affects the extent of glucose encapsulation (Section 2.1) and is therefore likely to dramatically affect 2-DG encapsulation as well.

Three pH-sensitive lipid mixtures that have been reported to form liposomes which destabilise in the pH range 5.5-6.5 and release encapsulated contents within a short time frame (minutes) were selected from the literature and a fourth novel lipid mixture was trialled for pH sensitivity. The lipid compositions of liposomes **L16**,[177] **L17**,[178,220] **L18**,[221] and the non-literature mixture **L19** are shown in Table 11. **L16** had the most desirable reported pH sensitivity profile with no calcein leakage at pH 6.6 or above, complete leakage over the course of 4-7 minutes at pH 6.1-6.3 and almost immediate release of encapsulated contents below pH 5.8.[177] Calcein is a fluorescent probe often used in liposome encapsulation studies.

All lipid mixtures contained DOPE and a stabilising acid, such as OA or the cholesterol derivative CHEMS, that is negatively charged at neutral pH but becomes protonated at lower pH, causing the liposome to disassemble when exposed to a more acidic environment.[175] Two of the liposome formulations exhibit PEG coating *via* incorporation of PEG-linked lipids such as the commercially available long chain PEG lipid, DSPE-PEG2000, or the short-chain PEG lipid DODEG4 initially reported by the Hailes/Tabor group. DODEG4 can be incorporated in much higher molar percentages to achieve a more uniform coating of the liposome surface than DSPE-PEG2000.[154]

The lipid mixtures were dissolved in $CHCl_3$ and the solvent was removed under reduced pressure to form lipid thin films. The thin films were hydrated with 0.5 M 2-DG at pH 8.5

Table 11. Formulation parameters and measurements for pH-sensitive 2-DG liposomes **L16**-**L19**.

Liposome sample	[lipid] (mM)	Lipid composition (molar ratio)	Hydration solution	Z-Ave (d.nm) (s)	PdI (s)	Overall [2-DG] (mM)	pH
L16	30	DOPE: OA (7:3)	0.5 M 2-DG in 20% PBS	133 (0.3)	0.19 (0.02)	0	8.1
L17	30	DOPE:CHEMS (6:4)	0.5 M 2-DG in 20% PBS	124 (0.3)	0.10 (0.01)	0	8.0
L18	30	DOPE:CHEMS: DSPE-PEG2000 (0.58:0.39:0.03)	0.5 M 2-DG	110 (17)	0.24 (0.04)	0	8.6
L19	30	DOPE:CHEMS: DODEG4 (2:4:4)	0.5 M 2-DG	315 (37)	0.35 (0.09)	0	8.8

and dialysed against 0.25 M NaCl at pH 8.5. The pH-sensitive liposomes must be formulated under neutral or mildly basic conditions. When required, NaOH was added to maintain a pH above 8. The liposome formulations that contained PEG lipids, **L18** and **L19**, formed most readily and required less heating, sonication and freeze thawing. Liposomes **L16**-**L19** were sized *via* probe sonication giving rise to less uniform size distributions compared to extrusion. However, given that the aim was to evaluate the 2-DG encapsulating capabilities of the liposomes, the diameter and poor polydispersity was not considered important. **L16** and **L17** were difficult to form, potentially due to unstable pH during formulation, so these mixtures were re-formulated in 20% PBS at pH 8.8, which facilitated liposome assembly. When **L16** and **L17** in 20% PBS were sized *via* probe sonication, more uniform liposomes with better PdI values were formed than for **L18** and **L19** (Table 11). The liposomes were acidified using 1 M HCl solution to produce observable disruption of the lipid bilayers as some components formed a precipitate. ^{1}H NMR was employed to show that no 2-DG was successfully encapsulated by any of the pH-sensitive lipid mixtures **L16**, **L17**, **L18** or **L19** (method described in Section 7.2.2.2). It was concluded that none of the pH-sensitive bilayer compositions tested were rigid enough to encapsulate 2-DG and that lipid mixtures with entirely saturated chains may be required. An alternative approach would be to synthesise a lipid with saturated chains (based on DPPC or DSPC) and an acid-cleavable moiety to incorporate into liposomes that would be capable of encapsulating high concentrations of 2-DG at pH 7.4 but that is cleaved to destabilise liposomes when exposed to the acidic tumour microenvironment.

4.3 Comparison of 2-DG liposomes with glucose liposomes

The pH-sensitive lipid mixtures described in Section 4.2 were sized using probe sonication which formed liposomes with smaller diameters and deposits a large amount of energy into the lipid dispersion,[151] thus this different method of sizing liposomes in comparison to extrusion may affect the distribution of 2-DG between the aqueous and lipid phase and thereby affect the encapsulation efficiency. Liposomes were sized *via* extrusion in this Section to investigate whether 2-DG can be encapsulated by DPPC bilayers in similar quantities as glucose was in Section 2, and to give better control over the diameter of liposomes. 2-DG is more lipophilic than glucose therefore the efficiency of encapsulation during the liposome formulation process may vary.

Liposomes were formulated with a lipid concentration of 30 mM and hydrated with 0.5 M glucose (**L20**) or 0.5 M 2-DG (**L21**) in 20% PBS at pH 8, mimicking the conditions under which pH-sensitive liposomes were formed. Following extrusion, **L20** and **L21** measured

Table 12. Formulation parameters and measurements for liposomes **L20-L23**.

Liposome sample	[DPPC] (mM)	Hydration solution	Z-Ave (d.nm) (s)	PdI (s)	Exterior [sugar] (mM)	Overall [sugar] (mM)	pH
L20	30	0.5 M Glc	163 (1.3)	0.12 (0.01)	3.6[a]	31[a], 30[b]	8.0
L21	30	0.5 M 2-DG	174 (2.3)	0.11 (0.01)	unknown	34[b]	8.0
L22	30	0.5 M Glc	204 (2.8)	0.17 (0.02)	2.7[a]	34[a]	5.8
L23	30	0.5 M 2-DG	214 (0.6)	0.25 (0.02)	0.28[c]	23[b], 23[c]	5.8

[a]Measured using the Glucose HK Assay®, [b]Measured using NMR methods, [c]Measured using the Glucose GO Assay®.

as having similar Z-Ave values, 163 nm and 174 nm, respectively, with low PdI values (Table 12). The pH was stable during dialysis against 0.25 M NaCl in 20% PBS buffer at pH 8. The Glucose HK Assay® revealed successful glucose encapsulation for **L20** with an exterior concentration of 3.6 mM and overall concentration of 31 mM (Table 12).

It is known that 2-DG is phosphorylated by hexokinase to form 2-DG6P but only minimally further metabolised by G6PDH,[144] thus the Glucose HK Assay® cannot be used to measure 2-DG concentration. Therefore, the quantity of 2-DG encapsulated by **L21** was measured using a ^{1}H NMR method utilising a known concentration of 4,4-dimethyl-4-silapentane-1-sulfonic acid (DSS) inside a coaxial NMR insert tube and calibrating the technique with known concentrations of 2-DG in 20% PBS (Section 7.2.2.2). The ^{1}H NMR spectrum of the intact 2-DG liposomes **L21** was broad suggesting that the majority of 2-DG was inside the liposomes following dialysis (Figure 79, Section 7.2.2.2), however the exterior 2-DG concentration could not be quantified. Upon addition of 40 µL Triton, the NMR signals became sharp (Figure 80), suggesting that 2-DG was released from the liposomes. The overall concentrations of glucose and 2-DG for **L20** and **L21** were measured as 30 mM and 34 mM, respectively, using the described ^{1}H NMR method (Section 7.2.2.2). This glucose concentration for **L20** was in agreement with the 31 mM concentration measured using the Glucose HK Assay®, supporting the accuracy of the ^{1}H NMR technique. In 20% PBS buffer and at pH 8, DPPC bilayers encapsulated slightly higher quantities of 2-DG than glucose (34 mM *vs.* 30 mM). The pH experiment described in Section 2.4 showed that the CEST signal generated by glucose liposomes at pH 7 is suboptimal, and no signal is to be expected from the liposomes at pH 8. Thus, in order to obtain CEST signals, glucose (**L22**) and 2-DG (**L23**) liposomes were formulated in the same way as **L20** and **L21**, except the pH was kept constant at pH 5.8 to enable facile CEST detection. **L22** and **L23** were sized to give similar average diameters with sufficient PdI values (Table 12). The liposomes were dialysed against

0.25 M NaCl in 20% PBS at pH 5.8. The Glucose HK Assay® measured exterior and overall glucose concentrations of 2.7 mM and 34 mM for **L22**, respectively (Table 12).

Although the Glucose HK Assay® cannot be used to measure 2-DG, another commercially available and affordable assay, the Glucose GO Assay® (Sigma-Aldrich), employs glucose oxidase which has been reported to catalyse the oxidation of 2-DG at a rate which is approximately 12% of that for glucose.[222] The enzymatic cascade is initiated by the oxidation of glucose by glucose oxidase and finishes with the formation of oxidised o-Dianisidine which absorbs strongly at 540 nm in the presence of H_2SO_4 and can be observed as a pink colour (Figure 44). The assay was calibrated for 2-DG using an appropriate range of known 2-DG concentrations and a linear equation describing the relationship between 2-DG concentration and absorbance at 540 nm was obtained (Figure 82, method detailed in Section 7.2.2.3).

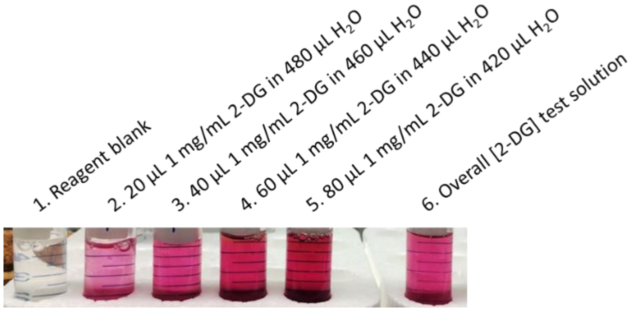

Figure 44. Glucose GO Assay® calibration with 2-DG solutions (Tubes 1-5) and overall 2-DG concentration measurement for **L23** (Tube 6).

Employing the Glucose GO Assay®, the overall 2-DG concentration of **L23** was measured as 23 mM but the exterior concentration measured was high (7 mM, approximately a third of the total 2-DG and > 5 mM). It was hypothesised that addition of the Glucose GO Assay® reagent to the liposomes caused significant leakage of 2-DG from liposomes. To test this hypothesis, the liposomes were stored at 4 °C in the fridge for 3 days, during which time the liposomes sank to the bottom and a small volume of supernatant (exterior solution) could be carefully pipetted off without disturbing the liposomes. Measurement of the 2-DG concentration of the supernatant using the Glucose GO Assay® gave a much lower exterior 2-DG concentration for **L23** (0.28 mM), supporting the hypothesis. By this method, the Glucose GO Assay® provides an accurate measurement of 2-DG concentration exterior to the liposomes. Quantifying the 2-DG concentration of the supernatant by ^{1}H NMR methods may be less accurate due to the low accuracy of signal integration at low concentrations and high signal-to-noise ratio. To check the accuracy of the Glucose GO Assay®, the overall 2-DG concentration of **L23** was also measured by the previously described ^{1}H NMR method to yield a measurement of 23 mM, which was in excellent agreement with the assay, further supporting the validity of both methods.

As the glucose liposomes **L22** had a higher overall monosaccharide concentration than the 2-DG liposomes **L23**, **L22** was diluted with 0.25 M NaCl in 20% PBS at pH 5.8 to reduce the overall glucose concentration to 23 mM to match that of the 2-DG liposomes. The glucose concentration of the diluted **L22** sample was confirmed as 23 mM using the Glucose HK Assay®. Free glucose and 2-DG controls were made up in 20% PBS at pH 5.8 with a monosaccharide concentration of 23 mM. Z and MTR_{asym} spectra were obtained for **L22**, **L23** and the controls at 20 °C and 37 °C (Figure 45). Following CEST measurement, the pH was unchanged and the exterior monosaccharide leakage from liposomes was not extensive after heating to 37 °C during scanning, 1.5 mM for **L22** and 6.2 mM for **L23** (Glucose HK and GO Assay®, respectively).

Surprisingly, the 2-DG liposomes **L23** produced a greater CEST signal than the glucose liposomes **L22** at both 20 °C and 37 °C, as did the free 2-DG control compared to the free glucose control (Table 13). This was unexpected due to 2-DG having one less hydroxyl group to participate in the CEST mechanism (-OH^2, $\Delta\omega$ ~ 1.3 ppm, Section

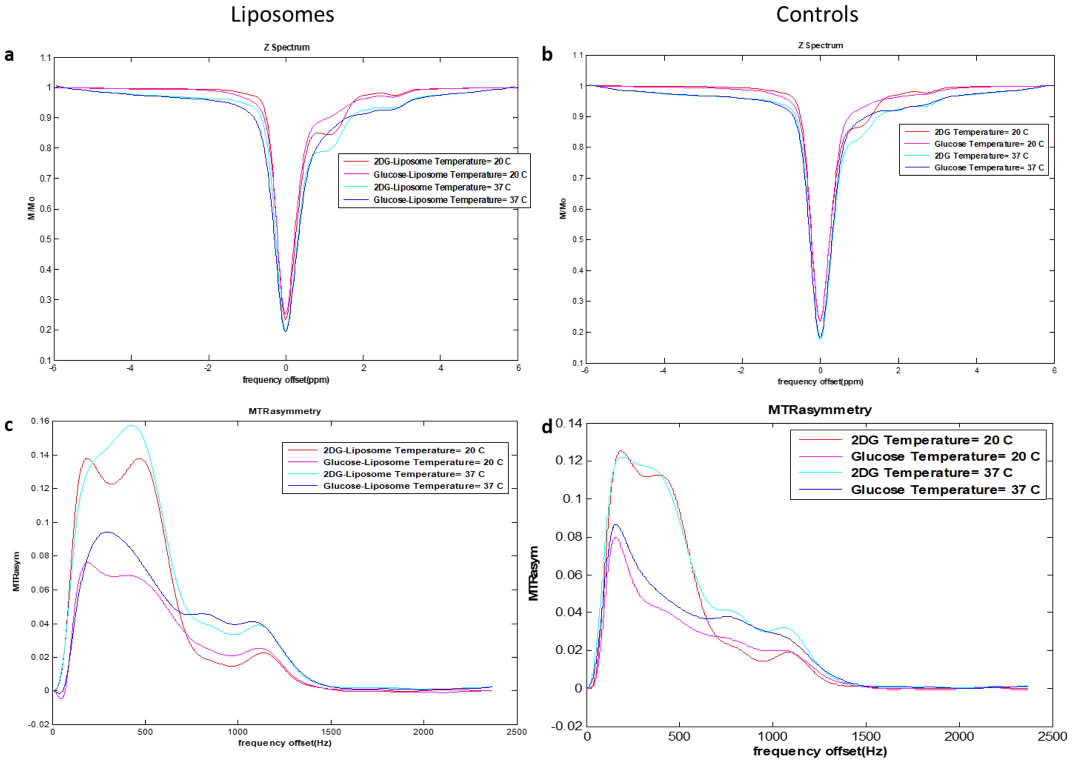

Figure 45. Z (a,b) and MTR_{asym} (c,d) spectra for 2-DG liposomes **L22** and glucose liposomes **L23** (a,c) and free glucose and 2-DG controls (b,d), pH 5.8 in 20% PBS measured at 20 °C and 37 °C, B_1 = 1.5 μT.

4.1.1). The CEST signals generated by free glucose, free 2-DG and the liposomal samples **L22** and **L23** were enhanced when the temperature was increased from 20 °C to 37 °C, due to changes in hydroxyl proton exchange rate and bilayer permeability for the liposomes.

The greatest CEST contrast was achieved by 2-DG liposomes **L23** at physiological temperature (Table 13). These early results bode well for the replacement of glucose with 2-DG in the aqueous interior of our liposomal CEST CAs for imaging of tumors *in vivo*. The enhanced CEST detectability of free 2-DG compared to free glucose in this experiment could be due to a difference in the k_{ex} of the hydroxyl protons on 2-DG versus glucose at pH 5.8. However, when considering the enhanced CEST signal from 2-DG liposomes compared to glucose liposomes observed in this experiment, it is important to note that the glucose liposomes were diluted to give equal overall monosaccharide concentrations for **L22** and **L23**. Thus, the glucose liposomes **L22** had a higher encapsulated monosaccharide concentration and a lower liposome concentration. The enhanced CEST detectability of the 2-DG liposomes was therefore much more likely to be due to the increased liposome surface area for **L23** over which water can exchange and transfer saturation to the bulk water pool during CEST measurement.

The finding that the 2-DG liposomes produce greater contrast than free 2-DG under the tested temperature and pH conditions could be explained by the permeability barrier presented by the lipid bilayer, reducing the apparent k_{ex} values of hydroxyl protons to achieve the slow-intermediate exchange regime that is favourable for CEST detection (Section 1.2). Importantly, 2-DG was readily encapsulated by DPPC liposomes at pH 5.8 and gave rise to appreciable CEST signal in the range 0-3.75 ppm (6.7% average water signal reduction at 37 °C and 1.5 μT).

Table 13. CEST suppression of the water peak for glucose and 2-DG liposomes, **L22** and **L23**, at pH 5.8 in 20% PBS measured at 20 °C and 37 °C, B_1 = 1.5 μT. CEST suppression is expressed as an average of the percentage reduction in water signal caused by presaturation across the range 0-3.75 ppm.

	Glucose control	**Glucose liposomes (L22)**	**2-DG control**	**2-DG liposomes (L23)**
MTR_{asym} at 20 °C	2.7%	3.5%	4.5%	5.6%
MTR_{asym} at 37 °C	3.5%	4.6%	5.2%	6.7%

4.4 Factors affecting CEST signal from 2-DG liposomes

4.4.1 PBS concentration

It is necessary to use a buffer system to ensure that the pH of samples remain stable during CEST scanning. PBS was used because it buffers the relevant pH range (pH 5.8-8). It is possible that the exchangeable groups in PBS could quench some of the CEST signal from samples that are evaluated in this buffer system because saturated hydroxyl protons can exchange with a water hydrogen or a phosphate group hydrogen, creating a 3-site exchange rather than a 2-site exchange regime. To investigate the effect that PBS has on the CEST signal generated by 2-DG liposomes, a variety of liposomes were formulated at pH 6 and pH 7 with 0-20% PBS (0-20% of 1× PBS, which is defined as 10 mM PO_4^{3-}), to give **L24**-**L31** (Table 14). Liposomes were formulated with 30 mM DPPC and the thin films were hydrated with 0.5 M 2-DG solution with the relevant PBS concentration and pH. Extrusion was carried out to give liposome samples with diameters in the range 170-192 nm and PdI values in the range 0.09-0.15. The liposomes were dialysed into 0.25 M NaCl solution with the relevant PBS concentration and pH. The overall 2-DG concentrations of the liposome samples were in the range 39-47 mM (Glucose GO Assay®, measured in triplicate), with negligible exterior 2-DG concentrations (maximum 1.5 mM, exterior concentrations were determined in a single measurement). Controls were made up with the correct PBS concentration and the same 2-DG concentration as the corresponding liposome sample, as measured by the Glucose GO Assay®.

Table 14. Formulation parameters for DPPC (30 mM) liposomes encapsulating 0.5 M 2-DG with varying PBS concentration **L24-L31**.

Liposome sample	PBS	Z-Ave (d.nm) (s)	PdI (s)	Exterior [2-DG] (mM)	Overall [2-DG] (mM) (s)	pH
L24	0%	185 (0.4)	0.09 (0.01)	1.0	44 (3.8)	6
L25	5%	189 (3.6)	0.12 (0.02)	0.9	41 (1.3)	6
L26	10%	192 (4.7)	0.11 (0.01)	0.6	39 (3.7)	6
L27	20%	189 (3.3)	0.11 (0.03)	1.5	43 (2.4)	6
L28	0%	179 (2.6)	0.09 (0.02)	1.3	47 (3.8)	7
L29	5%	187 (1.9)	0.12 (0.02)	0.7	43 (0.4)	7
L30	10%	187 (4.2)	0.15 (0.01)	0.4	42 (0.5)	7
L31	20%	170 (2.3)	0.11 (0.02)	1.2	39 (3.1)	7

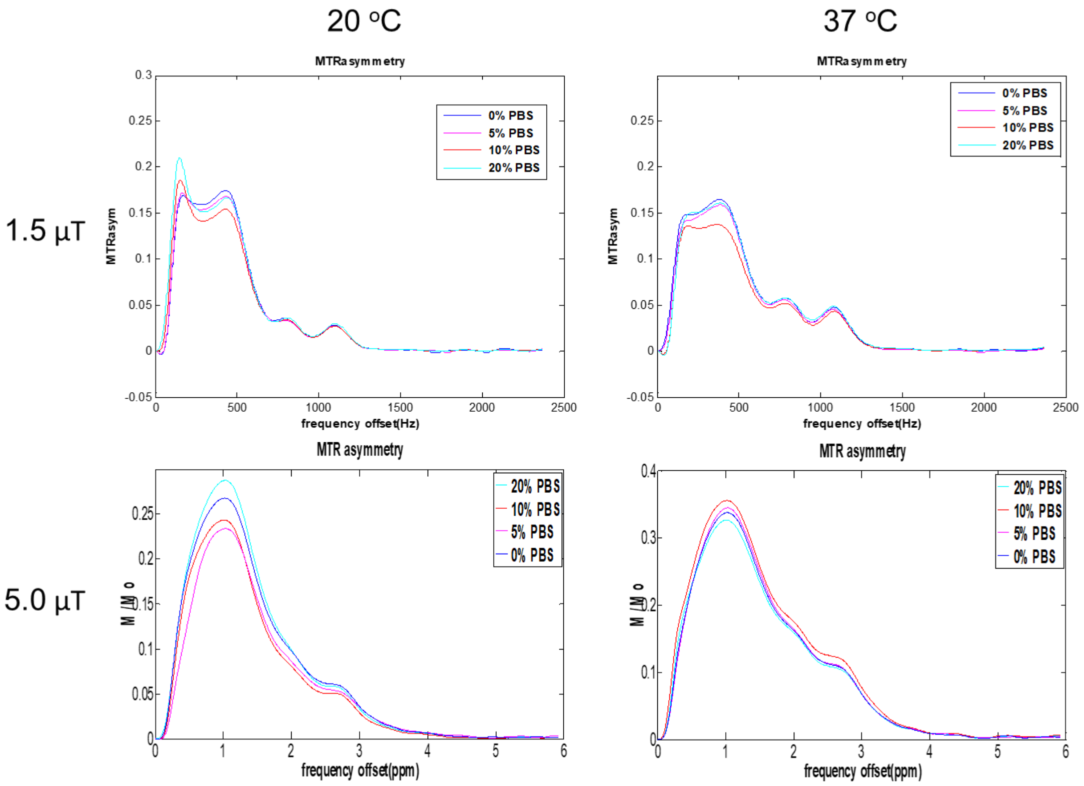

Figure 46. MTR$_{asym}$ spectra for 2-DG liposomes **L24-L27** at pH 6 with varying PBS concentration. Spectra were obtained with B$_1$ = 1.5 µT (a,b) and B$_1$ = 5.0 µT (c,d), at 20 °C (a,c) and 37 °C (b,d).

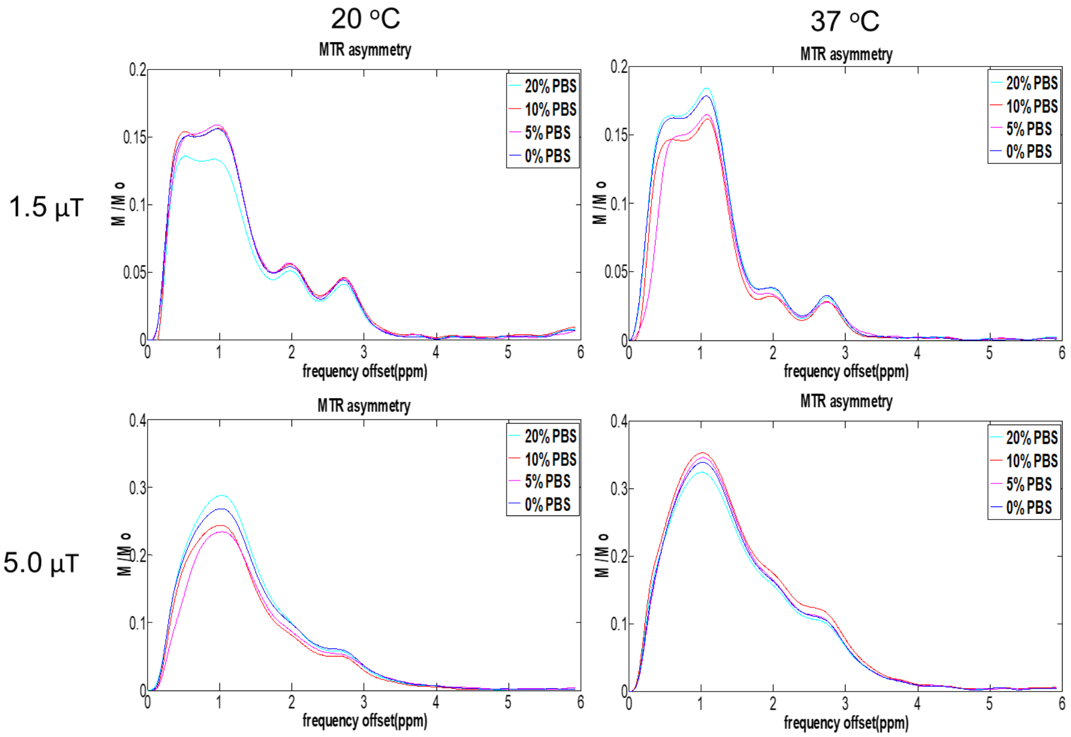

Figure 47. MTR$_{asym}$ spectra for 2-DG controls to match the liposomes **L24-L27** at pH 6 with varying PBS concentration. Spectra were obtained with B$_1$ = 1.5 µT (a,b) and B$_1$ = 5.0 µT (c,d), at 20 °C (a,c) and 37 °C (b,d).

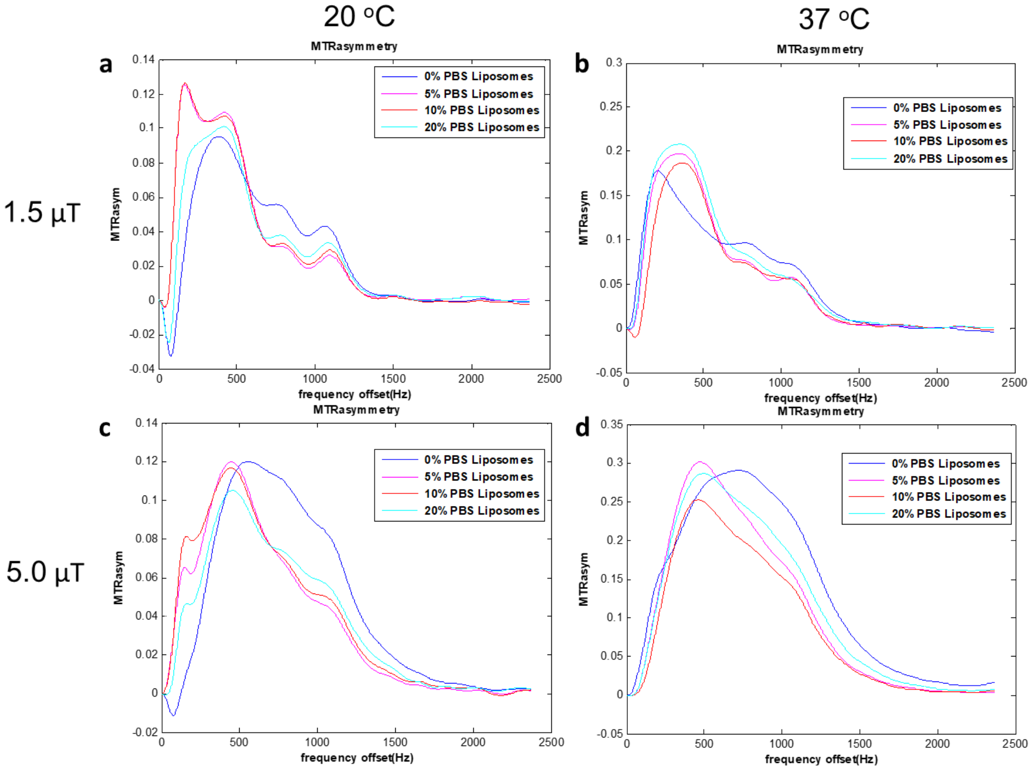

Figure 48. MTR$_{asym}$ spectra for 2-DG liposomes **L28-L31** at pH 7 with varying PBS concentration. Spectra were obtained with B_1 = 1.5 µT (a,b) and B_1 = 5.0 µT (c,d), at 20 °C (a,c) and 37 °C (b,d).

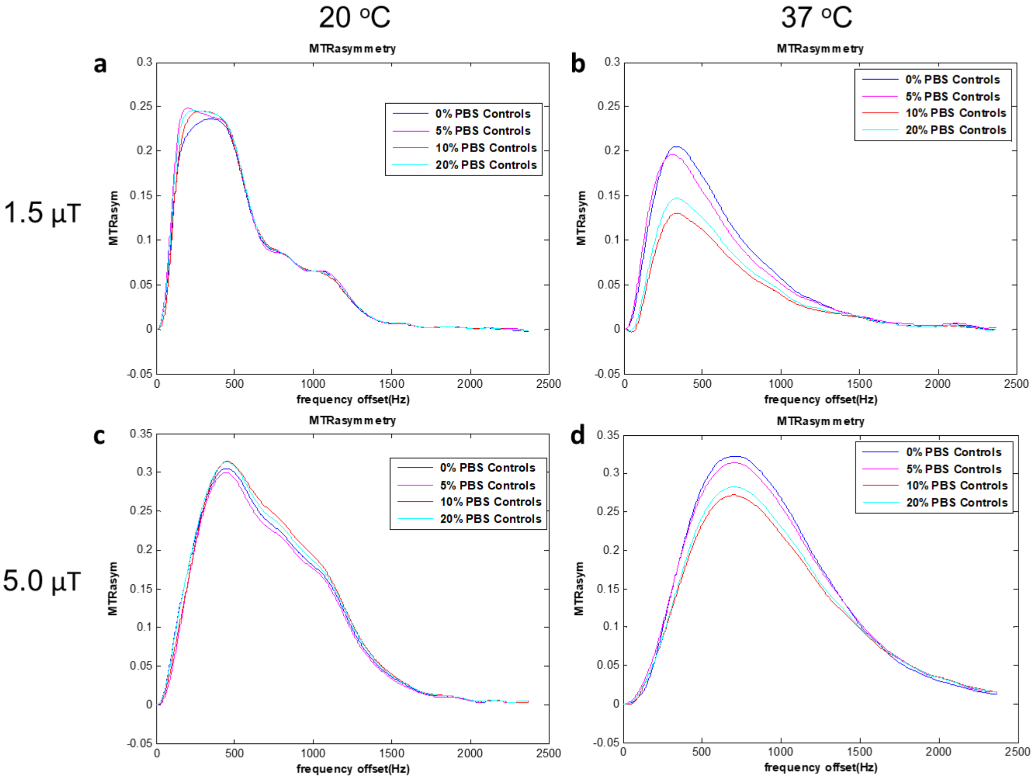

Figure 49. MTR$_{asym}$ spectra for 2-DG controls to match the liposomes **L28-L31** at pH 7 with varying PBS concentration. Spectra were obtained with B_1 = 1.5 µT (a,b) and B_1 = 5.0 µT (c,d), at 20 °C (a,c) and 37 °C (b,d).

Table 15. CEST suppression of the water peak for 2-DG liposomes **L24**-**L31** and controls at pH 6 and pH 7 with varying PBS concentration. The data was acquired at 20 °C and 37 °C, B_1 = 1.5 μT and 5.0 μT. CEST suppression is expressed as an average of the percentage reduction in water signal caused by presaturation across the range 0.2-3.5 ppm.

Liposomes (PBS conc)	**[2-DG] (mM)**	**Power (μT)**	**pH**	**MTR_{asym} 20 °C**	**MTR_{asym} 37 °C**	**Controls, PBS conc**	**MTR_{asym} 20 °C**	**MTR_{asym} 37 °C**
L24 (0%)	48	1.5	6	6.7%	6.8%	0%	7.1%	9.7%
L25 (5%)	43	1.5	6	6.5%	6.6%	5%	7.4%	9.8%
L26 (10%)	42	1.5	6	6.3%	6.0%	10%	8.0%	10.9%
L27 (20%)	46	1.5	6	6.7%	6.8%	20%	7.7%	11.2%
L28 (0%)	47	1.5	7	4.4%	8.9%	0%	11.9%	10.3%
L29 (5%)	43	1.5	7	4.9%	8.8%	5%	12.4%	9.8%
L30 (10%)	42	1.5	7	5.0%	8.0%	10%	12.2%	6.5%
L31 (20%)	39	1.5	7	4.4%	9.7%	20%	12.4%	7.4%
L24 (0%)	48	5	6	10.7%	14.7%	0%	12.2%	20.1%
L25 (5%)	43	5	6	10.5%	14.5%	5%	13.6%	22.3%
L26 (10%)	42	5	6	9.6%	13.9%	10%	13.3%	21.7%
L27 (20%)	46	5	6	9.7%	15.0%	20%	11.7%	20.3%
L28 (0%)	47	5	7	7.3%	20.5%	0%	19.5%	21.8%
L29 (5%)	43	5	7	6.1%	17.3%	5%	18.7%	21.4%
L30 (10%)	42	5	7	6.4%	14.7%	10%	20.1%	18.4%
L31 (20%)	39	5	7	6.0%	18.1%	20%	20.1%	19.1%

The liposomes and controls were scanned at low (1.5 μT) and high (5.0 μT) power, at low (20 °C) and high (37 °C) temperature and at pH 6 or 7 (MTR_{asym} spectra are shown in Figure 46-Figure 49). To quantify the CEST signal, the average water signal suppression caused by presaturation in the range 0.2-3.5 ppm was determined (Table 15).

The MTR_{asym} for all liposomal samples **L24**-**L31** with various PBS concentration and at varying pH, temperature and power are displayed in Figure 50. There were small fluctuations in CEST signal magnitude for analogous liposomes with varying PBS content, however, these small differences can be largely attributed to the small variations in overall 2-DG concentration achieved during formulation. For most temperature and power combinations, the liposomes formulated with 20% PBS do not exhibit the lowest CEST signal, even though the formulation in 20% PBS at pH 7 (**L31**) had the lowest measured overall 2-DG concentration at 39 mM. This suggests that PBS concentration in the range 0-20% as has no quenching effect on CEST signal.

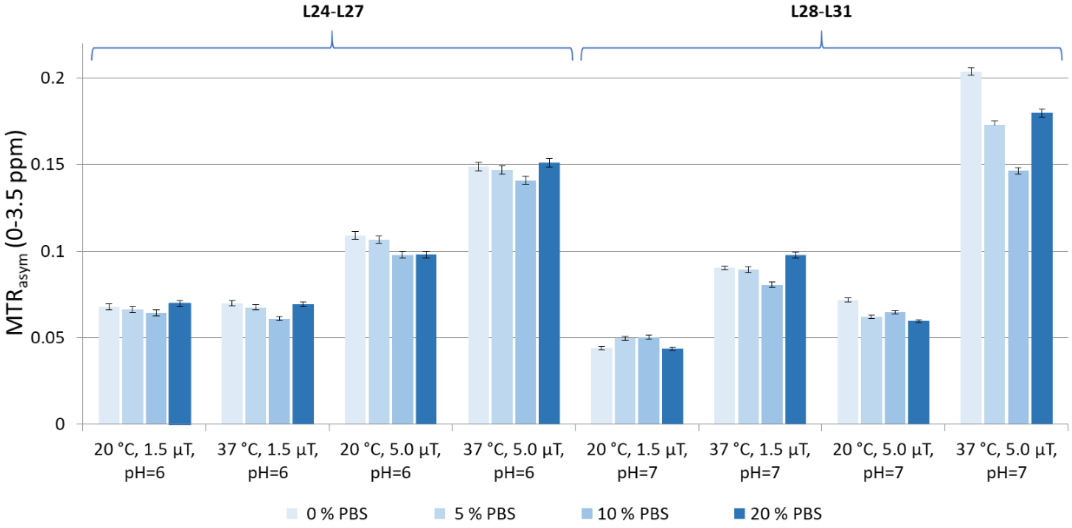

Figure 50. MTR$_{asym}$ (0.2-3.5 ppm) for 2-DG liposomes **L24-L31** at 20 °C and 37 °C**,** B$_1$ = 1.5 µT and 5.0 µT, pH 6 and pH 7.

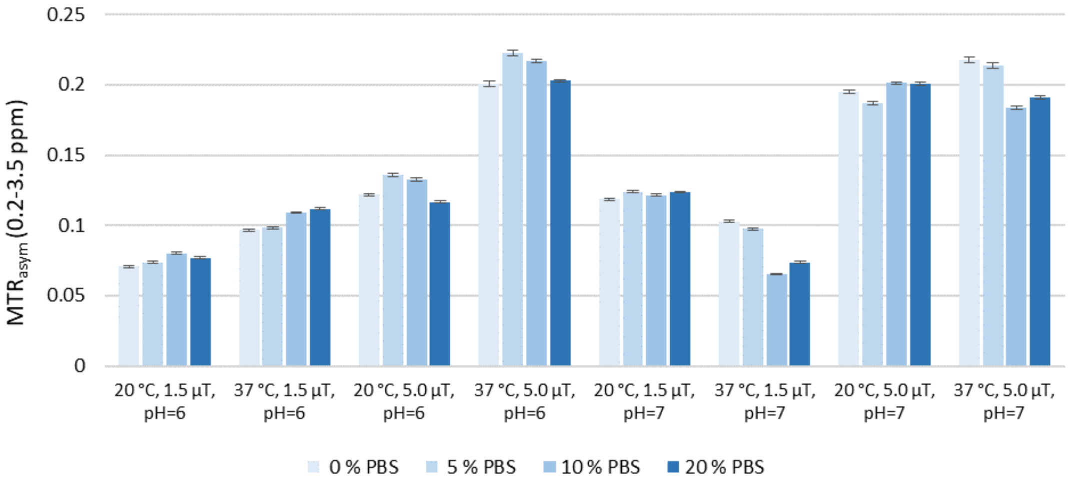

Figure 51. MTR$_{asym}$ (0.2-3.5 ppm) for 2-DG liposome (**L24-L31**) controls at 20 °C and 37 °C**,** B$_1$ = 1.5 µT and 5.0 µT, pH 6 and pH 7.

As expected, increasing the power from 1.5 µT to 5.0 µT created greater CEST signal for all liposome samples, and increasing the temperature from 20 °C to 37 °C also produced an increase in CEST signal for all liposome samples apart from those formulated at pH 6 and scanned at with a power of 1.5 µT, for which the signal intensity was approximately equal (Figure 50). At 20 °C the CEST signal was greater from 2-DG liposomes at pH 6 **L24-27** as opposed to pH 7 **L28-L31**, whereas at 37 °C the signal magnitude is greater for the liposomes at pH 7. The largest CEST contrast was seen for liposomes formulated at pH 7 and scanned at 5.0 µT and 37 °C. This is ideal for *in vivo* use as the temperature and pH will be most similar to these conditions. The largest signal generated by the pH 7 liposomes **L28**-**L31** at 5.0 µT and 37 °C was for **L28**, the liposomes formulated at 0% PBS. This is presumed to be due to the fact that this liposome sample had the highest overall 2-DG concentration of the liposomes formulated at pH 7, measuring as 47 mM, not due to the lack of PBS.

Figure 51 shows the control data for free 2-DG solutions with various PBS content and the same 2-DG concentration as that measured for the corresponding liposome sample (**L24**-**L31**). The controls show no dependency on PBS concentration. It may appear that CEST signal quenching due to increasing PBS concentration is occurring at pH 7 and 37 °C, but it was assumed that this effect was due to the declining 2-DG concentrations across the PBS controls since it is not observed under other pH and temperature conditions (0% = 47 mM, 5% = 43 mM, 10% = 42 mM and 20% = 39 mM). The CEST signal magnitude dependency on temperature and power combinations is very similar to that of the liposomal samples. As seen for the liposomes, increasing the power or temperature gave rise to enhanced CEST signal magnitude, with the exception of increasing the temperature for samples at pH 7. When the free 2-DG solutions were scanned at pH 7 and 1.5 µT the CEST signal was significantly reduced when the temperature was increased from 20 °C to 37 °C (on average 30% less CEST signal) due to a temperature-induced increase in the hydroxyl proton exchange rates. The increase in CEST signal when the temperature of free 2-DG solutions at pH 6 is increased from 20 °C to 37 °C, and the contrasting decrease in CEST signal for free 2-DG solutions at pH 7, were previously seen in Section 4.1, Figure 40.

The main finding of this subsection was that 0-20% PBS did not affect the generated CEST signal from 2-DG or 2-DG liposomes, thus, all future liposomes samples and controls will contain 20% PBS to ensure a constant pH throughout formulation and CEST experiments.

4.4.2 Temperature

Lipid bilayer permeability is closely linked to temperature, therefore, one would expect the CEST signal from monosaccharide encapsulating liposomes to be altered by temperature-induced changes in bilayer water permeability as well as temperature effects on hydroxyl proton exchange rates. To investigate this effect, large batches (> 6 mL) of glucose (**L32**) and 2-DG (**L33**) liposomes were formulated. The bilayers consisted of pure DPPC at a lipid concentration of 30 mM and the thin films were hydrated with 0.5 M monosaccharide solution in 20% PBS. The liposomes were sized by extrusion to give liposomes with diameters of approximately 180 nm and low PdI values, which were then

Table 16. Formulation parameters and measurements for DPPC liposomes encapsulating 0.5 M glucose or 0.5 M 2-DG for temperature experiments.

Liposome sample	[DPPC] (mM)	Hydration solution	Z-Ave (d.nm) (s)	PdI (s)	Exterior [sugar] (mM)	Overall [sugar] (mM) (s)	pH
L32	30	0.5 M Glc	180 (0.7)	0.10 (0.003)	0.3	24 (1.6)	7
L33	30	0.5 M 2-DG	178 (1.7)	0.14 (0.01)	0.3	38 (3.3)	7

dialysed into 0.25 M NaCl solution with 20% PBS. The Glucose GO Assay® was used to measure the overall monosaccharide concentrations as 24 mM glucose for **L32** and 38 mM 2-DG for **L33** and as expected, exterior monosaccharide concentrations were low (0.3 mM) (Table 16). At elevated temperatures, glucose and 2-DG will continuously leak out of the liposomes, so in order to limit the exterior concentration of monosaccharides during CEST measurement, the liposomes were split into 5 equal batches, each of which were scanned at an individual temperature. Control samples for **L32** (24 mM glucose in 20% PBS) and **L33** (38 mM 2-DG in 20% PBS) were also evaluated. The MTR_{asym} spectra for **L32** and **L33** are shown in Figure 52 and Figure 53, respectively, including the control spectra. The average CEST suppression in the presaturation range 0-3.5 ppm for all samples are reported in Table 17.

For both the glucose and 2-DG liposomes, **L32** and **L33**, the CEST signal was gradually enhanced by increasing the temperature in the range 25 °C to 37 °C (Figure 54 and Figure 55). For the glucose liposomes, the percentage increase in CEST signal caused by increasing the temperature from 25 °C to 37 °C was 41% and 91% at 1.5 μT and 5.0 μT, respectively. For the 2-DG liposomes, it was 61% and 99% at 1.5 μT and 5.0 μT, respectively. The same positive trend was much less pronounced for the free 2-DG control experiment and CEST signal from the free glucose control appeared to have the opposite dependency on temperature to the liposomes; the signal was slightly reduced as the temperature was increased between 25 °C and 37 °C. This suggests that the large positive correlation between temperature and CEST signal for the liposomes was due to temperature-induced changes in the lipid bilayer.

Below their T_m lipids exist in an ordered gel phase, as they approach their T_m they assume an intermediate pre-transition state (also termed the ripple phase) and finally at temperatures above the T_m they enter a disordered fluid state associated with trans-gauche isomerisations.[198] When a bilayer passes through its T_m into the fluid state, it becomes much more permeable to water with measured increments in the range of 30-100-fold.[223–225] A study by Lawaczeck *et al.* reported the permeability constants for water

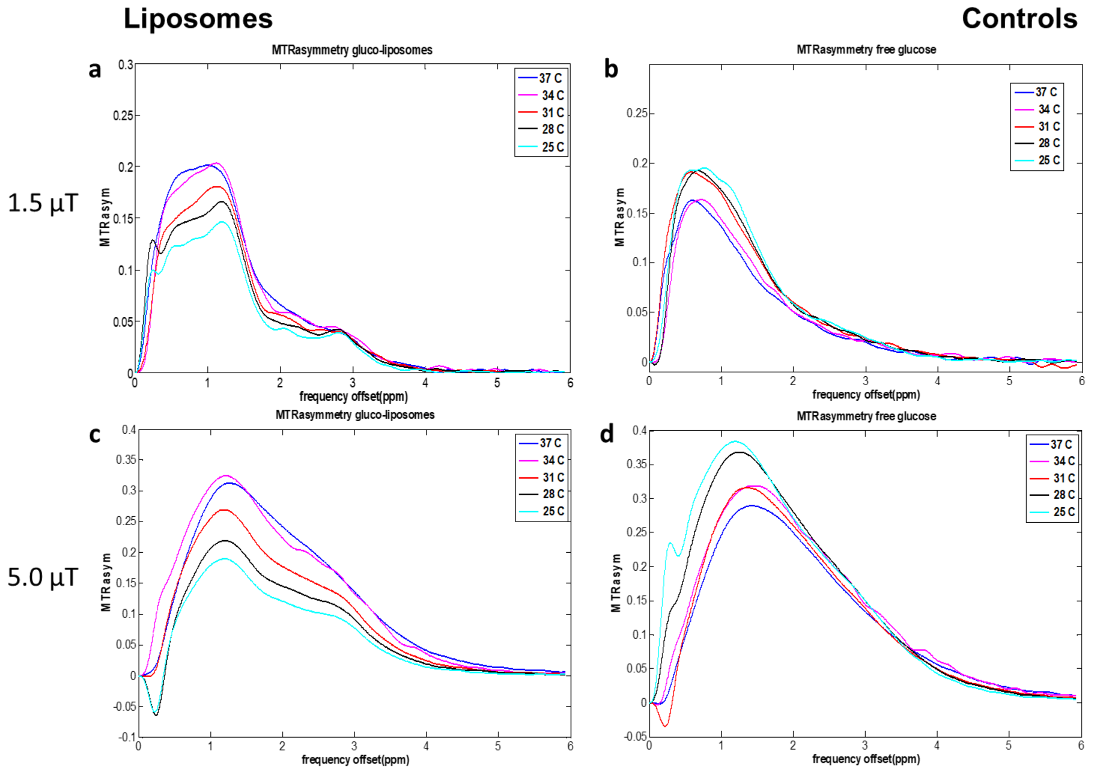

Figure 52. MTR$_{asym}$ spectra for glucose liposomes **L32** (a,c) and free glucose controls (b,d) scanned at various temperatures. Spectra were obtained with B_1 = 1.5 µT (a,b) and B_1 = 5.0 µT (c,d).

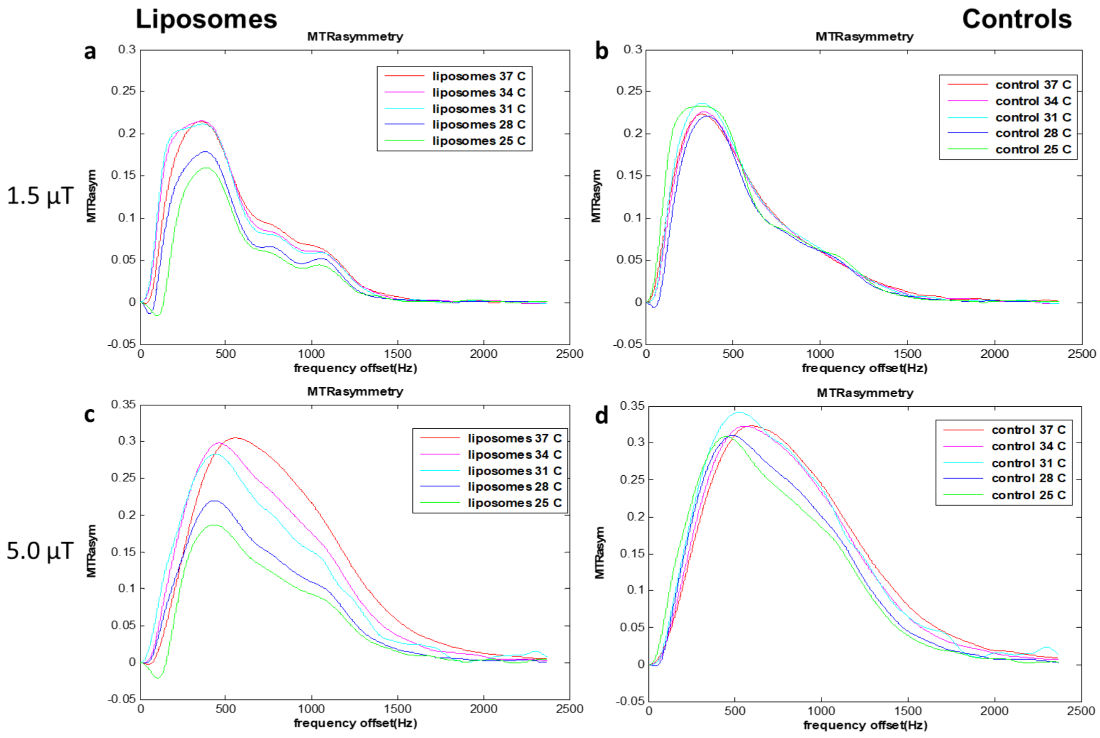

Figure 53. MTR$_{asym}$ spectra for 2-DG liposomes **L33** (a,c) and free 2-DG controls (b,d) scanned at various temperatures. Spectra were obtained with B_1 = 1.5 µT (a,b) and B_1 = 5.0 µT (c,d).

Table 17. CEST suppression of the water peak for glucose (**L32**) and 2-DG (**L33**) liposomes and controls scanned at B_1 = 1.5 μT and 5.0 μT at various temperature. CEST suppression is expressed as an average of the percentage reduction in water signal caused by presaturation across the range 0-3.5 ppm.

Sample	[sugar] (mM)	Power (μT)	25 °C	28 °C	31 °C	34 °C	37 °C
glucose liposomes **L32**	24	1.5	4.1%	4.7%	5.0%	5.8%	5.8%
glucose liposomes **L32**	24	5	6.6%	7.8%	10.0%	12.9%	12.6%
glucose control	24	1.5	5.4%	5.2%	5.1%	4.4%	4.2%
glucose control	24	5	14.7%	14.5%	13.2%	13.7%	12.5%
2-DG liposomes **L33**	38	1.5	6.1%	7.4%	10.0%	10.1%	9.8%
2-DG liposomes **L33**	38	5	9.6%	12.0%	16.5%	17.8%	19.1%
2-DG control	38	1.5	11.2%	9.6%	10.9%	10.4%	10.6%
2-DG control	38	5	19.0%	19.2%	21.8%	20.8%	21.0%

across DPPC vesicular bilayers as 4.2 x 10^{-6} cms^{-1} at 26.5 °C, which increased more than 8-fold to 3.5 x 10^{-5} cms^{-1} when the temperature was increased to 37 °C, which then increased more than 68-fold to 2.4 x 10^{-3} cms^{-1} when the temperature was increased above the T_m of DPPC to 46 °C.[223] Differential scanning calorimetry, electron spin resonance and Laurdan fluorescence experiments have demonstrated that the pre-transition phase can be characterised by up to 20% of the lipid population existing in the fluid state, and that DPPC bilayers can enter this state at temperatures as low as 32 °C.[198,226] This can explain why water permeability is enhanced at temperatures below but approaching the T_m of a bilayer.

Thus, it would be reasonable to conclude that the increased CEST signal observed at higher temperatures for the liposomal samples **L32** and **L33** can be partly attributed to increased bilayer fluidity and therefore water permeability of the liposome membranes. Increased membrane permeability allows a greater extent of saturation to be transferred to the extra-liposomal water population, which accounts for a large majority of the water in the sample, resulting in greater CEST water signal reduction. At lower temperatures, due to reduced water mobility across the membrane, the transfer of saturation will be more limited to the intraliposomal water portion, which only makes up a small percentage of the total water volume in the sample (12-13% for **L32** and **L33**, see Section 7.2.3). It was concluded that the enhanced CEST signal was a consequence of the lipid bilayers of **L32** and **L33** becoming more water permeable at temperatures approaching the T_m, due to increasing proportions of the lipid population adopting the fluid state.

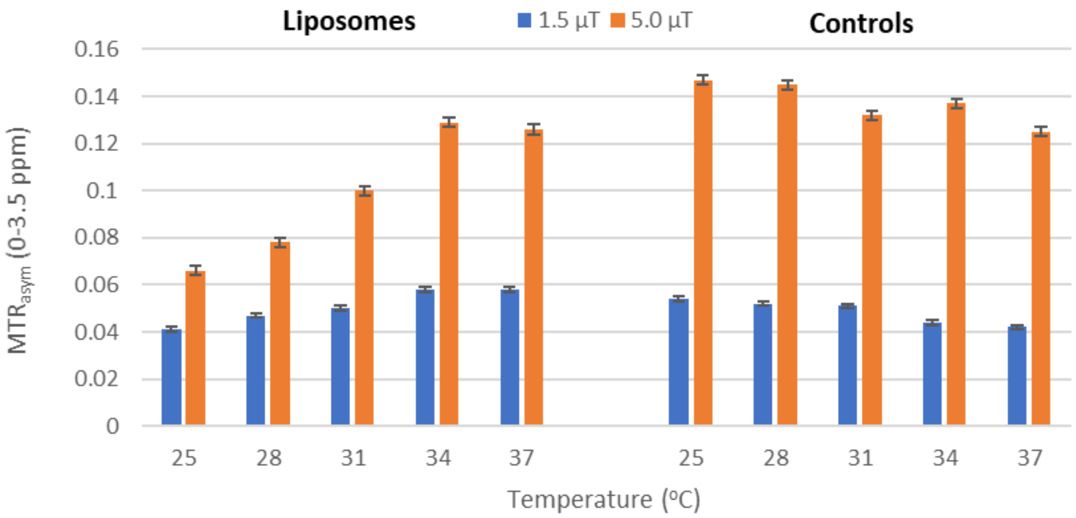

Figure 54. MTR$_{asym}$ (0-3.5 ppm) for glucose liposomes **L32** and a free glucose control scanned at various temperatures and powers.

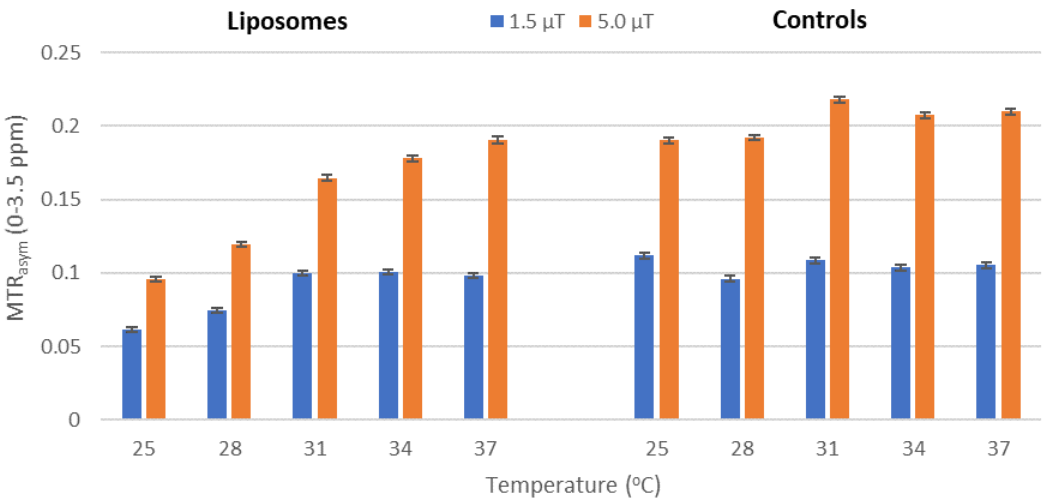

Figure 55. MTR$_{asym}$ (0-3.5 ppm) for 2-DG liposomes **L33** and a free 2-DG control scanned at various temperatures and powers.

However, changing the temperature also alters the exchange rate between hydroxyl protons and intraliposomal water, so the temperature-induced increase in bilayer fluidity is not the only factor to modify CEST signal magnitude in this experiment. Additionally, changes in temperature can also affect the longitudinal and transverse relaxation times of water, which can further enhance CEST contrast. In particular, a change from 25 °C to 37 °C produces an increase in T_1 from 3 s to 4.2 s for a 9.4 T MRI scanner, resulting in more pronounced MTR$_{asym}$ spectra.[227] However, this effect was not obvious for the control samples, thus it is reasonable to assume that it does not significantly contribute to the liposome results.

4.4.3 Bilayer Composition

To further investigate the effect of bilayer rigidity and permeability on generated CEST contrast from monosaccharide encapsulating liposomes, glucose and 2-DG encapsulating DPPC and DSPC liposomes were formulated. DSPC has two C18 saturated acyl chains compared to the two C16 saturated acyl chains of DPPC, which causes a drastic change in the T_m from 41°C for DPPC, to 55 °C for DSPC.[184] It was hypothesized that the more rigid bilayer formed by DSPC could reduce the transfer of saturation to the bulk exterior water pool due to more hindered movement of water across the bilayer, further reducing the apparent exchange rate between hydroxyl protons and bulk water protons. Whether this alteration to the overall exchange regime would be beneficial for CEST signal generation or not was investigated.

Glucose liposomes **L34**-**L37** and 2-DG liposomes **L38**-**L41** were formulated with bilayers comprised of pure DPPC or DSPC at pH 6 or 7. Due to the higher T_m, DSPC liposomes were sonicated and extruded at higher temperatures (> 55 °C). The Z-Ave values after sizing by extrusion were in the range 146-190 nm with overall monosaccharide concentrations in the range 29-37 mM and negligible exterior monosaccharide concentrations (Table 18). Both glucose and 2-DG concentrations were determined using the Glucose GO Assay®. CEST spectra were obtained at 25 °C or 37 °C and 1.5 µT or 5.0 µT (Figure 56), and CEST signal magnitude is expressed as an average water signal suppression across the presaturation range 0.2-3.5 ppm (Table 19).

Table 18. Formulation parameters and measurements for DPPC and DSPC liposomes encapsulating glucose and 2-DG at pH 6 and 7, **L34-L41**.

Liposome sample	Lipid (30 mM)	Hydration solution	Z-Ave (d.nm) (s)	PdI (s)	Exterior [sugar] (mM) (s)	Overall [sugar] (mM) (s)	pH
L34	DPPC	0.5 M glucose	168 (3.2)	0.23 (0.01)	1.7 (0)	33 (0.5)	6
L35	DPPC	0.5 M glucose	155 (1.8)	0.15 (0.01)	2.3 (0.3)	32 (0.6)	7
L36	DSPC	0.5 M glucose	147 (2.4)	0.11 (0.01)	2.0 (0.1)	30 (0.4)	6
L37	DSPC	0.5 M glucose	146 (1.5)	0.10 (0.01)	1.0 (0.4)	29 (1.1)	7
L38	DPPC	0.5 M 2-DG	188 (1.7)	0.10 (0.02)	0.6 (0)	30 (1.5)	6
L39	DPPC	0.5 M 2-DG	184 (1.0)	0.11 (0.05)	1.3 (0.3)	34 (1.0)	7
L40	DSPC	0.5 M 2-DG	190 (1.5)	0.24 (0.02)	2.4 (0)	37 (1.2)	6
L41	DSPC	0.5 M 2-DG	187 (1.2)	0.13 (0.01)	1.1 (0.1)	33 (1.7)	7

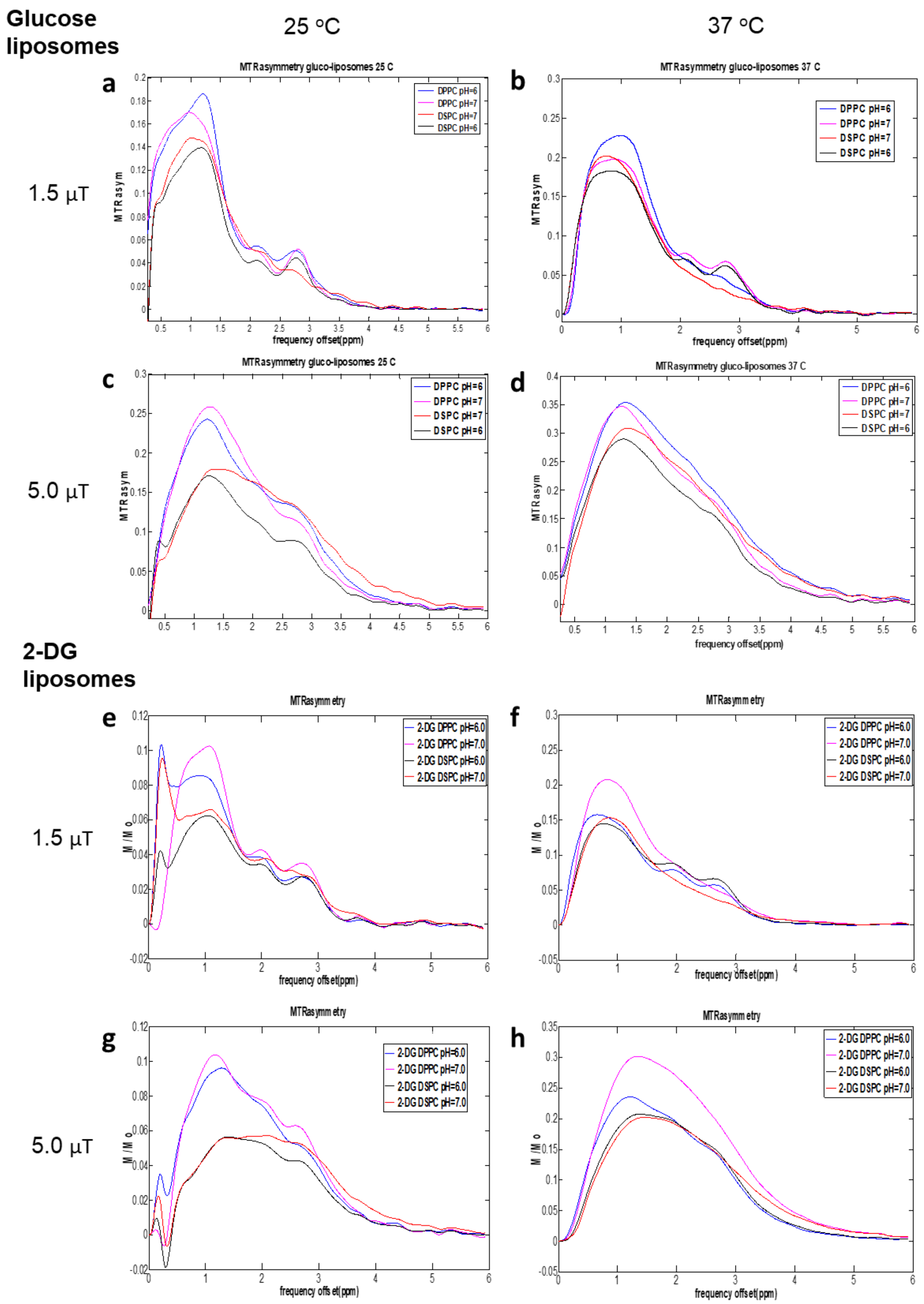

Figure 56. MTR_{asym} spectra for DPPC and DSPC liposomes encapsulating glucose **L34-L37** (a,b,c,d) and 2-DG **L38-L41** (e,f,g,h). The data was acquired at 25 °C (a,c,e,g) and 37 °C (b,d,f,h), B_1 = 1.5 µT (a,b,e,f) and B_1 = 5.0 µT (c,d,g,h).

Table 19. CEST suppression of the water peak for DPPC and DSPC liposomes encapsulating glucose **L34-L37** and 2-DG **L38-L41**. The data was acquired at 25 °C and 37 °C, B_1 = 1.5 μT and 5.0 μT. CEST suppression is expressed as an average of the percentage reduction in water signal caused by presaturation across the range 0.2-3.5 ppm.

Liposome sample	**Lipid and pH**	**Overall [monosaccharide] (mM)**	**1.5 μT**		**5.0 μT**	
			25 °C	**37 °C**	**25 °C**	**37 °C**
L34	DPPC, pH 6	33	5.0%	6.4%	9.2%	14.7%
L35	DPPC, pH 7	32	4.8%	6.1%	9.2%	13.3%
L36	DSPC, pH 6	30	3.7%	5.6%	6.3%	11.2%
L37	DSPC, pH 7	29	4.2%	5.5%	8.4%	13.0%
L38	DPPC, pH 6	30	4.7%	6.1%	8.4%	15.7%
L39	DPPC, pH 7	34	4.8%	6.3%	10.2%	20.6%
L40	DSPC, pH 6	37	3.5%	3.8%	8.3%	14.5%
L41	DSPC, pH 7	33	4.3%	4.3%	7.6%	14.2%

For the liposomes encapsulating glucose **L34-L37**, DPPC liposomes produced greater CEST contrast than the corresponding DSPC liposomes scanned at the same pH, temperature and power (Figure 57). The signal enhancement produced by DPPC versus DSPC was slightly more pronounced at pH 7 than at pH 6, with average increases in CEST signal of 26% ± 14% at pH 7 versus 15% ± 4% at pH 6.

In line with previous results, higher temperatures gave rise to enhanced MTR_{asym} for both DPPC and DSPC glucose encapsulating liposomes, presumably due to the increased water permeability of the lipid bilayers at higher temperature, enabling more facile saturation transfer to the bulk water pool. However unexpectedly, the CEST signal enhancement produced by this temperature increase was similar for DPPC and DSPC liposomes, with an average signal increase of 40% ± 13% versus 54% ± 17%, respectively. One may have expected the increase to be larger for DPPC as 37 °C is close to DPPC's T_m of 41 °C, whereas it is not close to DSPC's T_m of 55 °C. The overall glucose concentrations for liposome batches **L34-L37** were very well grouped (29-33 mM), thus it can be concluded that the optimal CEST signal was produced by DPPC liposomes encapsulating glucose at pH 6, 37 °C and at the higher power of 5.0 μT.

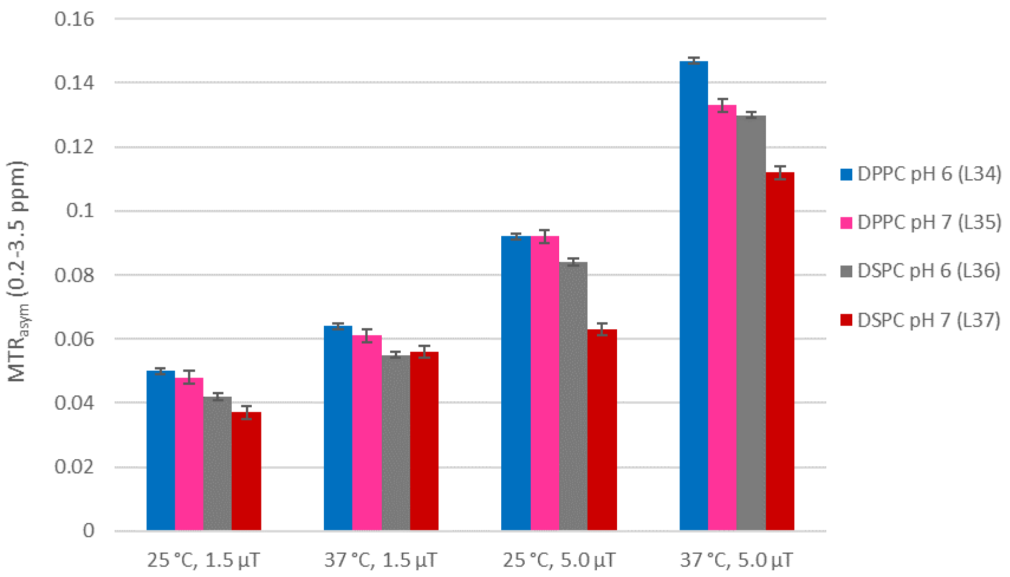

Figure 57. MTR_{asym} (0.2-3.5 ppm) for DPPC and DSPC glucose liposomes **L34**-**L37** scanned at 25 °C and 37 °C and B_1 = 1.5 µT and 5.0 µT.

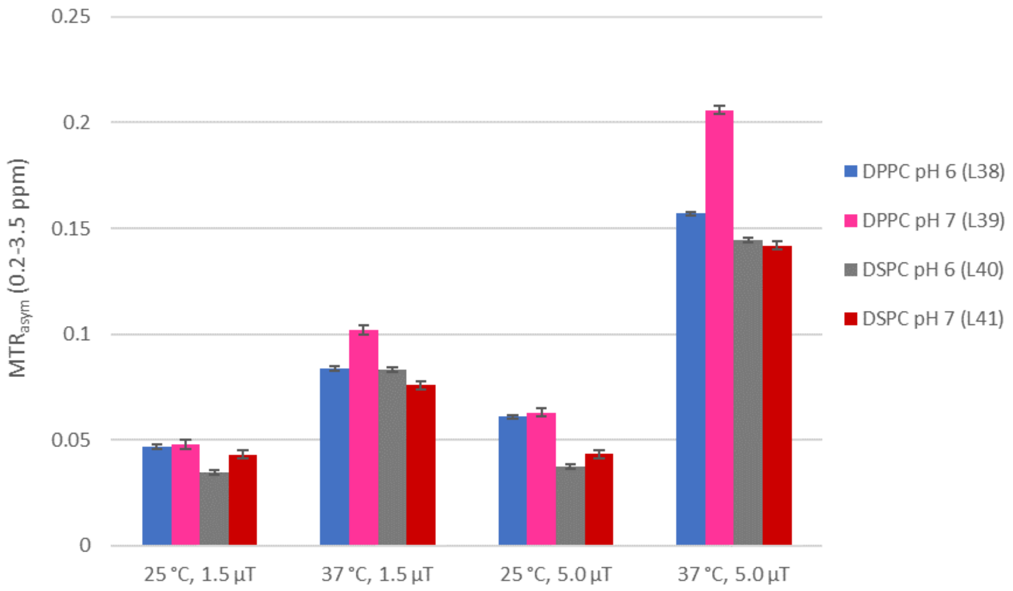

Figure 58. MTR_{asym} (0.2-3.5 ppm) for DPPC and DSPC 2-DG liposomes **L38**-**L41** scanned at 25 °C and 37 °C and B_1 = 1.5 µT and 5.0 µT.

For the 2-DG encapsulating liposomes **L38**-**L41**, DPPC also produced greater CEST contrast than the corresponding DSPC liposomes across all temperature and power combinations when the liposomes were formulated at pH 6 and pH 7 (average signal increase of 30% for DPPC versus DSPC). This is thought to be due to the increased water permeability of DPPC bilayers and therefore enhanced ability to transfer saturation to the bulk water population.

Increasing the temperature from 25 °C to 37 °C gave greater CEST signal across all results for 2-DG liposomes **L38**-**L41** (Figure 58). As was observed for glucoses liposomes **L34**-**L37**, the temperature-induced increase in CEST signal from 2-DG liposomes **L38**-**L41** was the similar for DPPC versus DSPC liposomes (144% *vs.* 182%). However, the magnitude of this temperature effect was much more pronounced for 2-DG liposomes **L38**-**L41** (102% ± 26% increase at 1.5 µT and 224% ± 45% increase at 5.0 µT) than it was for the glucose liposomes **L34**-**L37** (average increase of 34% ± 10% at 1.5 µT and 59% ± 12% increase at 5.0 µT). This may be in part due to higher levels of 2-DG leakage from liposomes during CEST scanning at 37 °C compared to glucose leakage (see Section 5.3).

The differences in water permeability between DPPC and DSPC bilayers at temperatures markedly below their T_m have been shown to have little dependence on chain length.[225] At 25 °C, all DSPC liposomes produced less CEST signal than the corresponding DPPC sample under the same conditions, thus it was assumed that 25 °C was not a low enough temperature for chain length to approach irrelevance regarding bilayer water permeability. In the fluid state, the permeabilities of DPPC and DSPC are also similar, both being more than 2 orders of magnitude greater than when in the crystalline state.[224,225] No experiments were done past the T_m of the lipids because this would lead to release of encapsulated contents. At physiological temperature, DSPC is still far from its T_m but DPPC is approaching its T_m of 41 °C and is most likely exhibiting pre-transition ripple phase charactersitics.[198,226] Which can explain the finding that CEST contrast was larger for DPPC liposomes than for DSPC liposomes at 37 °C. This is due to the difference in ability of monosaccharide encapsulating DPPC liposomes versus more rigid DSPC liposomes to transfer saturation to the bulk water during a CEST experiment at 37 °C.

The results from liposomes **L34**-**L37** suggest that the optimal conditions for CEST signal generation by glucose liposomes at physiological temperature are from DPPC liposomes at pH 6 (**L34**), whereas results generated by liposomes **L38**-**L41** suggest that the optimal conditions for CEST signal generation by 2-DG liposomes at physiological temperature are from DPPC liposomes at pH 7 (**L39**). However, the small fluctuations in overall monosaccharide concentration between samples must be taken into consideration, the glucose concentration was slightly higher for the glucose encapsulating DPPC liposomes at pH 6 (33 mM for **L34** at pH 6 *vs.* 32 mM for **L35** at pH 7), and the 2-DG concentration was higher for the 2-DG encapsulating DPPC liposomes at pH 7 (34 mM for **L39** at pH 7 *vs.* 30 mM for **L38** at pH 6). It was apparent that slower movement of water across more rigid DSPC bilayers reduces the transfer of saturation from monosaccharide hydroxyl protons to the bulk water pool, producing smaller CEST signal magnitudes. In the interest of maximising CEST contrast, we continued to formulate liposome bilayers with DPPC or lipids with analogous palmitoyl or cetyl chains.

4.4.4 Liposome diameter

To investigate the effect of changing the liposome diameter on generated CEST signal, three liposome samples were formulated encapsulating 2-DG and sized *via* extrusion to give liposomes **L42**-**L44** with measured Z-ave values of 201 nm, 153 nm and 121 nm, respectively (Table 20). All liposomes were formulated with 20% PBS at pH 7. We aimed to form liposomes with diameters that remain inside the size range that is known to be optimal for EPR accumulation of nanoparticle carriers in tumor tissue (10-200 nm).[166] To size the liposomes to ~ 200 nm, they were passed through a 400 nm pore polycarbonate filter 4 times and then through a 200 nm pore filter 3 times. To size the liposomes to ~ 150 nm, the liposomes were additionally passed through a 100 nm pore filter 24 times. To achieve a diameter of ~ 120 nm the liposomes were passed through a 100 nm pore filter 7 times and then through two 100 nm pore filters placed on top of each other 13 times. As the diameter deceased so did the PdI, which is typical of the extrusion process. As the diameter decreased from 200 nm to 150 nm to 120 nm, so did the overall 2-DG concentration (from 42 mM to 40 mM to 36 mM), presumably due to the small reductions in intraliposomal volume and therefore encapsulation efficiency (15% for **L42**, 10% for **L43** and 8% for **L44**, see Section 7.2.3). Additionally, as the diameter was reduced, the exterior 2-DG concentration marginally increased, whilst still remaining low (< 5 mM). This could be a result of the increased curvature of the smaller liposomes, giving rise to a less densely packed bilayer and allowing a small amount of 2-DG to leak out.

Table 20. Formulation parameters and measurements for DPPC liposomes encapsulating 0.5 M 2-DG and sized by extrusion **L42**-**L44**, and **L45** sized by probe sonication at various time points during formulation.

Liposome sample	[DPPC] (mM)	Z-Ave (d.nm) (s)	PdI (s)	Exterior [2-DG] (mM)	Overall [2-DG] (mM)	pH
L42	30	201 (1.0)	0.17 (0.02)	0.5	42	7
L43	30	153 (3.4)	0.11 (0.004)	2.4	40	7
L44	30	121 (4.2)	0.05 (0.003)	4.9	36	7
L45 0 h after probe sonication	30	76 (4.1)	0.26 (0.01)	-	-	7
L45 0 h after dialysis	30	116 (1.3)	0.16 (0.01)	-	-	7
L45 24 h after dialysis	30	115 (1.7)	0.18 (0.01)	1.4	14	7

Forming DPPC liposomes with a diameter smaller than 120 nm proved to be difficult *via* extrusion, therefore a fourth liposome batch was sized using probe sonication. The liposomes were subjected to 10 cycles of probe sonication at 8 W. Each cycle consisted of 20 seconds on and 20 seconds off, to avoid excessive sample heating. This produced liposomes with a measured Z-ave value of 76 nm and a PdI of 0.26. The liposomes were dialysed into 0.25 M NaCl solution during which the hydrodynamic diameter of the liposomes was unstable, measuring as 116 nm after dialysis was complete and remaining stable from therein (the diameter measured as 115 nm 24 h later, Table 20). The Glucose GO Assay® was used to measure the overall and exterior 2-DG concentrations for **L42**-**L45**.

The CEST signals generated by **L42**, **L43** and **L44** were measured and the MTR$_{asym}$ spectra are shown in Figure 59. Across both temperatures and powers used, the liposomes with the largest diameter gave the greatest CEST signal and the liposomes with the smallest diameter produced the least signal (Table 21, Figure 60). However, it is likely these results simply reflect the differences in encapsulation efficiency for liposomes of a given diameter and the resultant small measured differences in overall 2-DG concentration. As seen previously with DPPC liposomes encapsulating 2-DG, higher temperature (37 °C) and higher power (5.0 µT) gave greater CEST signal.

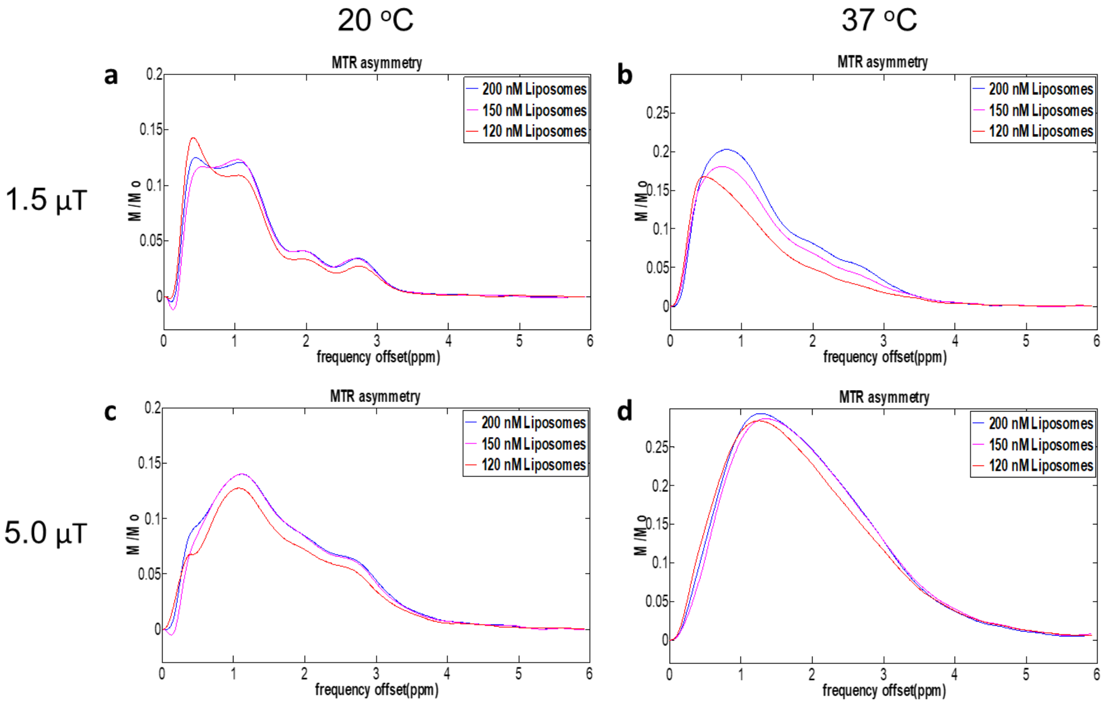

Figure 59. MTR$_{asym}$ spectra for 2-DG encapsulating DPPC liposomes **L42**-**L44** with varying diameter. Spectra were obtained with B_1 = 1.5 µT (a,b) and B_1 = 5.0 µT (c,d), and at 20 °C (a,c) and 37 °C (b,d).

Table 21. CEST suppression of the water peak for 2-DG encapsulating DPPC liposomes **L42**-**L44** with varying diameter. The data was acquired at 20 °C and 37 °C, B_1 = 1.5 μT and 5.0 μT. CEST suppression is expressed as an average of the percentage reduction in water signal caused by presaturation across the range 0-3.5 ppm.

Liposome sample	Overall [2-DG] (mM)	1.5 μT		5.0 μT	
		MTR$_{asym}$ 20 °C	MTR$_{asym}$ 37 °C	MTR$_{asym}$ 20 °C	MTR$_{asym}$ 37 °C
L42	42	5.6%	9.5%	7.9%	18.4%
L43	40	5.4%	8.4%	7.6%	18.0%
L44	36	5.3%	6.9%	6.8%	17.8%
L42 diluted	14	3.2%	3.3%	3.2%	7.9%
L43 diluted	14	3.5%	3.9%	3.1%	10.3%
L44 diluted	14	3.0%	4.1%	3.2%	10.3%

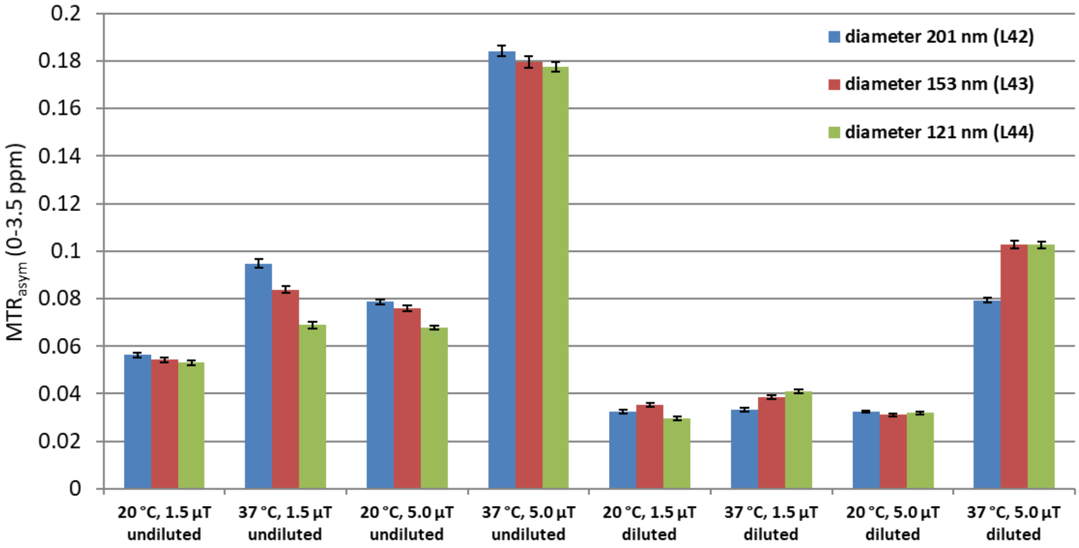

Figure 60. MTR$_{asym}$ (0-3.5 ppm) for 2-DG encapsulating DPPC liposomes **L42**-**L44** at pH 7. Samples were scanned before and after dilution, at 20 °C and 37 °C and B_1 = 1.5 μT and 5.0 μT.

To investigate the effect of liposome diameter on generated CEST signal more accurately, **L42**-**L44** were diluted with the appropriate volume of 0.25 M NaCl solution in 20% PBS to give an overall 2-DG concentration comparable to the liposomes sized by probe sonication, **L45** (~ 14 mM). Dilution volumes were calculated using the overall 2-DG concentration measurements obtained using the Glucose GO Assay®. The resulting overall 2-DG concentrations for the diluted liposomes were confirmed to be 14 mM by the Glucose GO Assay®, with negligible exterior 2-DG concentrations (in the range 0.4-1.4 mM). The MTR$_{asym}$ spectra for the diluted liposomes **L42**-**L44** and **L45** were obtained (Figure 61). The probe sonicated liposomes **L45** showed a marked decrease in MTR$_{asym}$

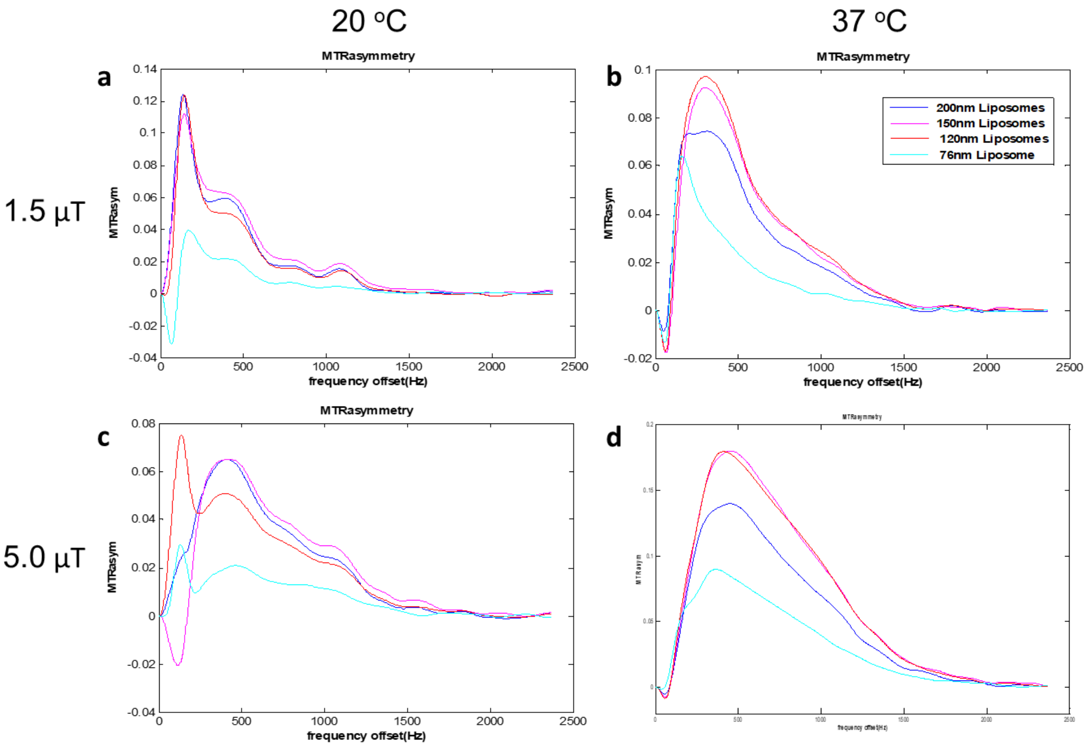

Figure 61. $\mathrm{MTR_{asym}}$ spectra for **L42**-**L45** after **L42**-**L44** had been diluted to give the same overall 2-DG concentration as **L45**. Spectra were obtained with B_1 = 1.5 µT (a,b) and B_1 = 5.0 µT (c,d), and at 20 °C (a,c) and 37 °C (b,d).

signal compared to the extruded and diluted liposomes, despite measuring as having the same overall 2-DG concentration (Figure 61). An explanation for this could be that the increased power deposition experienced by **L45** during probe sonication could force a portion of 2-DG into the bilayer, hindering the facile exchange between the 2-DG hydroxyl protons and water molecules. Sonication is a well-documented method for solubilising small molecule drugs in the lipid bilayer of liposomes, although usually for more hydrophobic small molecules than 2-DG, such as ibuprofen and diazepam.[228]

The average percentage water suppression observed by $\mathrm{MTR_{asym}}$ analysis in the presaturation range 0-3.5 ppm for liposomes **L42**-**L44** following dilution were determined (Table 21) and shown alongside the non-diluted liposome results (Figure 60). After dilution of **L42**-**L44** to an overall 2-DG concentration of 14 mM, the generated CEST signal at room temperature was the same for all three sizes of liposome. However, at 37 °C the lower diameter liposomes appear to have slightly higher CEST contrast. This is in line with findings reported by Zhao *et al.* who observed greater CEST contrast from lipoCEST agents with smaller diameter.[211] The slight increases in CEST contrast produced by smaller liposomes could be partly attributed to a larger surface-area-to-volume ratio allowing more efficient exchange of water across the membrane, which gives rise to enhanced saturation-labelling of bulk water. Secondly, larger liposomes have a shallower curvature and more closely packed lipid architecture and are therefore expected to have a reduced membrane permeability to water. It has been previously shown that liposomes of varying size exhibit different water permeability due to disrupted packing integrity in smaller vesicles.[229] The results from the study by Zhou *et al.* are much more exaggerated than the findings reported here because they investigated a larger range of diameters (99-536 nm *cf.* 121-201 nm),[211] thus the differences in surface-area-to-volume ratio and lipid packing between our liposome samples **L42**-**L44** will be more modest. In addition, the concentration of exchangeable water protons inside a lipoCEST agents is approximately 110 M, all of which can be saturated during lipoCEST. Even if the concentration of 2-DG inside the liposomes was as high as the 0.5 M solution used for thin film hydration during formulation, this still only equates to a 2 M concentration of hydroxyl protons inside the liposomes that can be saturated during CEST measurement. Thus, the higher concentration of exchangeable protons taking part in the CEST mechanism for the lipoCEST experiment may also help to observe trends across vesicles of varying diameter.

Nonetheless, the small increase in signal obtained from 2-DG liposomes of smaller size when overall 2-DG concentrations are normalised *via* dilution is offset by the higher loading capacity of larger liposomes, giving rise to an overall larger signal, as was seen for undiluted liposomes **L42**-**L44**. Therefore, liposomes will continue to be sized in the 150-200 nm range to obtain optimal CEST signal.

4.5 Rhodamine labelling of 2-DG liposomes

Fluorescently labelled 2-DG encapsulating liposomes could be used to determine the biodistribution and tumor accumulation of liposomes *in vivo via* postmortem analysis by fluorescence microscopy.[170] However, the effect of the presence of the fluorescently labelled lipid on 2-DG encapsulation and generated CEST signal would first need to be assessed. Fluorescently labelled liposomes **L46** were formulated with 99.5 mol% DPPC and 0.5 mol% 1,2-dipalmitoyl-*sn*-glycero-3-phosphoethanolamine-*N*-(lissamine rhodamine B sulfonyl) (triethylammonium salt) (DPPE-Rh, supplied by Biotium) and a control liposome sample **L47** was formulated with 100% DPPC. Liposomes **L46** and **L47** were hydrated with 0.5 M 2-DG in 20% PBS at pH 7, extruded and dialysed to yield liposomes with similar diameters, low PdI values, negligible exterior 2-DG concentrations and overall 2-DG concentrations of 31 mM and 37 mM, respectively, as measured by the Glucose GO Assay® (Table 22). In order to account for the fact that the rhodamine B

Table 22. Formulation parameters and measurements for Rhodamine labelled liposomes **L46** and control DPPC liposomes **L47** encapsulating 0.5 M 2-DG in 20% PBS.

Liposome sample	Lipid (mM)	Bilayer composition (mol%)	Z-Ave (d.nm) (s)	PdI (s)	Exterior [2-DG] (mM) (s)	Overall [2-DG] (mM) (s)	pH
L46	30	0.5% DPPE-Rh, 99.5% DPPC	187 (2.2)	0.07 (0.04)	1.0 (0.7)	31 (2.4)	7
L47	30	100% DPPC	177 (0.7)	0.08 (0.02)	1.3 (0.3)	37 (1.3)	7

fluorophore of DPPE-Rh absorbs strongly at 560 nm, which is close to the absorbance wavelength of 540 nm which is measured in the Glucose GO Assay®, liposome blank measurements were obtained and subtracted from the overall and exterior concentration measurements (the liposome blanks consisted of the same volume of **L46** liposomes as the test solutions, diluted in the same volume of DI water instead of assay reagent, with or without the addition of 5 μL Triton depending on whether the blank was for an exterior or overall 2-DG concentration). A control comprising free 2-DG in 20% PBS with an intermediate 2-DG concentration of 34 mM was also evaluated.

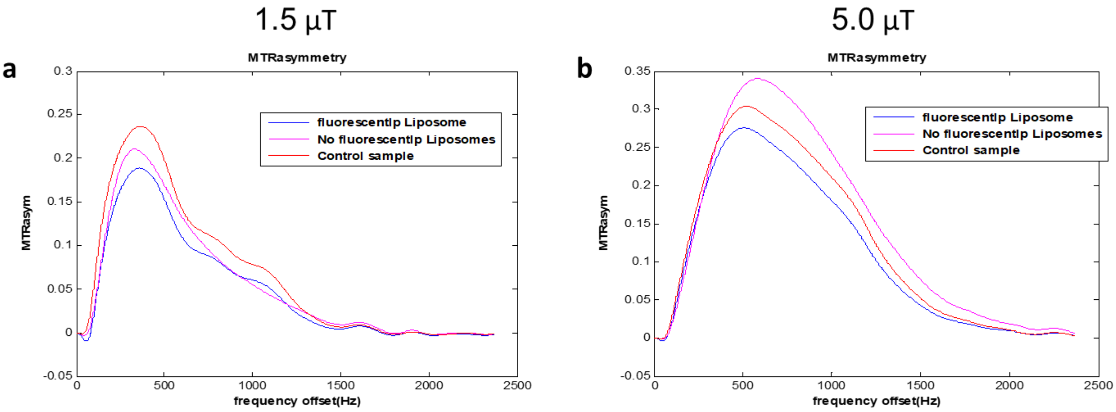

Figure 62. MTR$_{asym}$ spectra for **L46**, **L47** and a free 2-DG control (34 mM). Spectra were obtained at 37 °C with B_1 = 1.5 μT (a) and B_1 = 5.0 μT (b).

Table 23. CEST suppression of the water peak for 2-DG encapsulating liposomes **L46**, **L47** and free 2-DG control (34 mM). The data was acquired at 37 °C, B_1 = 1.5 μT and 5.0 μT. CEST suppression is expressed as an average of the percentage reduction in water signal caused by presaturation across the range 0-3.5 ppm.

	MTR$_{asym}$ 1.5 μT	**MTR$_{asym}$ 5.0 μT**
L46	8.5%	17.1%
L47	9.3%	21.5%
Control	11.2%	19.4%

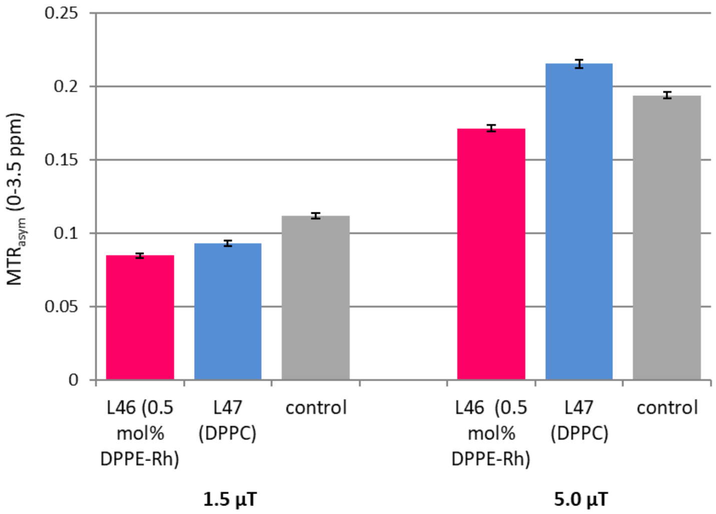

Figure 63. MTR$_{asym}$ (0-3.5 ppm) for 2-DG encapsulating rhodamine-labelled liposomes **L46**, DPPC liposomes **L47** and a free 2-DG control. Samples were scanned at 37 °C and B_1 = 1.5 µT and 5.0 µT.

Since the rhodamine-labelled liposomes **L46** are for future *in vivo* use, they were scanned at a physiologically relevant temperature, 37 °C (Figure 62), and the resultant water signal reduction was averaged across the presaturation range 0-3.5 ppm (Table 23). Across both powers, 1.5 µT and 5.0 µT, the pure DPPC liposomes encapsulating 2-DG exhibited greater CEST signal than the rhodamine-labelled liposomes (Figure 63). However, this probably reflects the higher overall 2-DG concentration encapsulated by DPPC liposomes during formulation (37 mM *vs*. 31 mM). At the higher power of 5.0 µT, the 2-DG concentration of the sample determined the CEST signal magnitude, irrespective of the presence of a lipid bilayer, with the intermediate concentration of the free 2-DG control producing intermediate CEST signal magnitude (Figure 63). It was concluded that incorporation of 0.5 mol% DPPE-Rh to 2-DG encapsulating DPPC liposomes did not drastically reduce 2-DG encapsulation or CEST signal generation and that these liposome formulation parameters are fit for use in future biodistribution studies.

4.4 Summary – Section 4

This Section explored the factors affecting CEST signal generated by glucose and 2-DG encapsulating liposomes. It was found that optimal CEST signals from both free glucose and free 2-DG solutions at physiological temperature were obtained at approximately pH 6.75 (Section 4.1). The exchangeable hydroxyl protons on glucose and 2-DG were visualised by ^{1}H NMR and assigned using literature values (Section 4.1.1). The hydroxyl signal resonance frequencies remained constant when the pH and monosaccharide concentrations were varied. Thus, we expect the Δω of individual glucose and 2-DG hydroxyl protons to remain constant in the obtained CEST spectra irrespective of concentration or pH.

DPPC bilayers were able to encapsulate 2-DG in similar quantities to glucose, however, pH-sensitive lipid mixtures from the literature were not rigid enough to encapsulate 2-DG (Section 4.2). The Glucose GO Assay® was employed to measure overall and exterior 2-DG concentrations for liposome samples and was found to strongly agree with the Glucose HK Assay® and NMR methods, supporting the reliability of the three techniques (Section 4.3).

It is possible that the exchangeable groups in PBS could quench some of the CEST signal from glucose or 2-DG samples evaluated in this buffer system. However, concentrations between 0-20% PBS were found to have no significant effect on CEST signal magnitude generated by free or liposomal 2-DG at 25 °C or 37 °C, pH 6 or pH 7 and low (1.5 µT) or high (5.0 µT) power (Section 4.4.1).

Increasing the temperature in the range 25-37 °C produced progressively larger CEST signals from glucose and 2-DG encapsulating DPPC liposomes, which was thought to be due to the increasing water permeability of the bilayer, enabling enhanced saturation transfer to the bulk water pool. Conversely, increasing the temperature in the same range had little effect on the CEST signal generated by an equal concentration of free 2-DG solution and caused a slight reduction in signal from an equal concentration of free glucose solution (Section 4.4.2).

Formulation of DSPC liposomes encapsulating glucose or 2-DG produced similar overall monosaccharide concentrations as DPPC liposomes encapsulating glucose or 2-DG. DPPC liposomes produced greater CEST contrast than the corresponding DSPC liposomes for both monosaccharides and when scanned at all pH, temperature and power combinations (Section 4.4.3). On average, glucose encapsulating DPPC liposomes **L34** and **L35** gave 21% greater CEST signal than glucose encapsulating DSPC liposomes **L36** and **L37** and 2-DG encapsulating DPPC liposomes **L38** and **L39** gave 30% greater CEST signal than 2-DG encapsulating DSPC liposomes **L40** and **L41**. This was thought to be due to the relatively higher water permeability of DPPC liposomes and therefore enhanced ability to transfer saturation to the bulk water pool. Interestingly, the increase in CEST signal caused by increasing the temperature from 25 °C to 37 °C was similar for both DPPC and DSPC monosaccharide encapsulating liposomes, however, the increase was significantly more exaggerated for 2-DG encapsulating liposomes (163% for 2-DG liposomes **L38**-**L41** *vs.* 47% for glucose liposomes **L34**-**L37**). This was hypothesised to be in part due to higher 2-DG leakage from liposomes.

When 2-DG encapsulating DPPC liposomes were sized to 200 nm (**L42**), 150 nm (**L43**) and 120 nm (**L44**), the larger liposomes produced greater CEST signal (Section 4.4.4). However, this was thought to be due to the fact that liposome samples with larger average diameters having greater internal volumes and therefore greater overall 2-DG concentrations. When the liposomes were differentially diluted to give the same overall 2-DG concentration, a small trend in the opposite direction was observed; the smaller liposomes generated slightly larger CEST signals (Figure 60, Section 4.4.4). This was attributed to smaller liposomes having a greater surface-area-to-volume ratio and greater curvature leading to a less closely packed lipid bilayer. Both of these factors can give rise to greater water exchange across the bilayer to enable transfer of saturation to the bulk exterior water population, as has been previously reported.[211] Notably, this trend was extremely modest our data, partly due to a tight range of liposome diameters.

Finally, DPPC-based 2-DG encapsulating liposomes were fluorescently labelled *via* incorporation of 0.5% DPPE-Rh to confirm that this alteration to the bilayer did not significantly affect encapsulation or the CEST signal generated by encapsulated 2-DG (Section 4.5). Thus, these liposomes could be used in future *in vivo* biodistribution experiments.

5 Functionalisation of liposomes

5.1 EGFR-targeted liposome strategy

The decoration of nanoparticles with ligands specific for biomarkers exhibited by cancer cells has been widely used in the literature to achieve selective targeting of tumors.[160] We aimed to covalently attach EGFR-targeting ligands to the surface of liposomal CAs encapsulating glucose or 2-DG to increase tumor retention and cellular internalisation. Tumor retention was expected to enhance the generated CEST signal from encapsulated or released glucose or 2-DG, whereas, cellular internalisation of liposomes would aid the uptake of 2-DG by tumor cells, allowing the chemotherapeutic or radiomodifying effects to be realised.

Active targeting moieties can become masked on the surface of the liposomes when long PEG chains, such as PEG2000, are also grafted.[230] It was proposed that short-chain PEG lipids could allow targeting peptides to extend beyond the PEG layer and promote binding to cellular receptors, as has been previously reported in the literature.[154,231]

Liposomes were planned to be formulated with 10 mol% maleimide-functionalised lipids to enable surface decoration with EGFR-targeting peptides, as has been previously described in the literature.[232,233] Cysteine-modified EGFR-targeting peptides can be covalently linked to preformed liposomes *via* reaction with maleimide-lipids at the surface to form a thioether bond (Figure 64).[233]

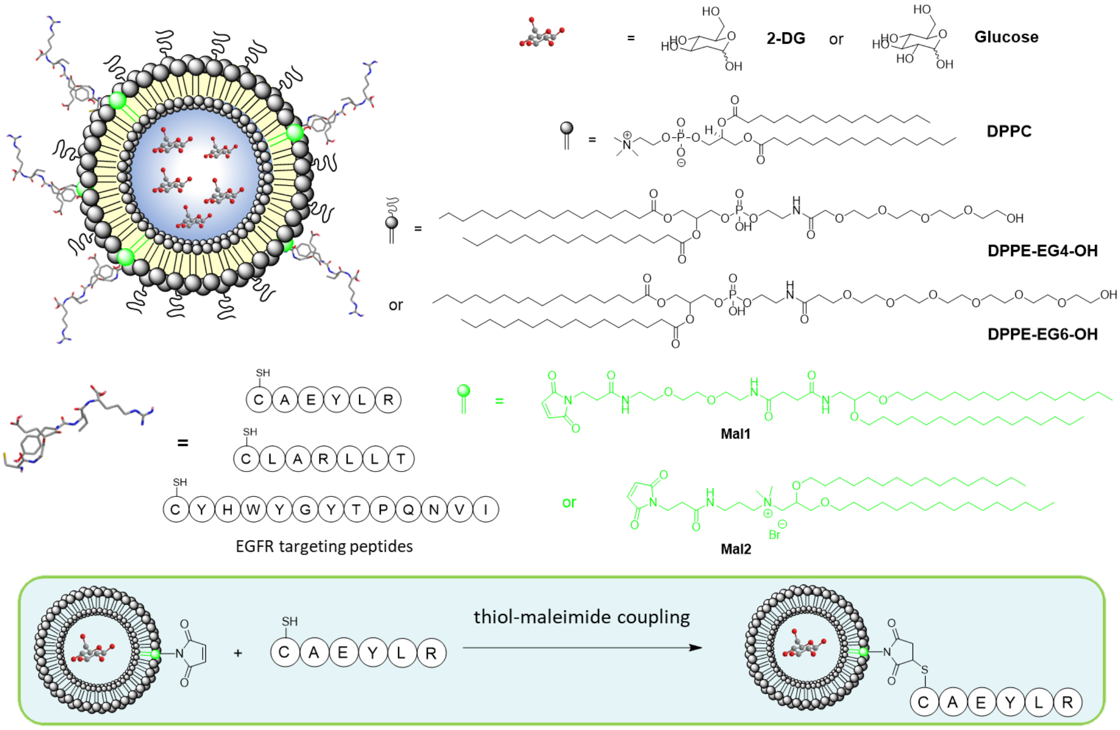

Figure 64. Strategy for EGFR-targeted monosaccharide encapsulating liposomes.

5.1.1 Synthesis of short-chain PEG lipids

PEGylation of liposomes is a well-documented strategy to improve systemic circulation time and decrease immunogenicity (Section 1.4.1).[155] However, long chain PEG lipids such as DSPE-PEG2000 have a maximum loading of approximately 10 mol%, resulting in incomplete surface coverage.[164] Liposomes coated with high percentages of long chain PEGs (in ratios required for *in vivo* stealth properties) have been shown to have limited uptake to cells *in vitro*.[230,234] Additionally, PEG-coated liposomes are often too stable to disassemble once internalized in the endosome.[234] The decreased cellular uptake and content release due to PEGylation of nanoparticles has been referred to as the "PEG dilemma".[230,234,235]

Several studies on the stabilisation of lipid structures with shorter PEG chains have been reported in the literature, for example, Tirrell *et al.* investigated PEG-lipids with different lengths of EG units in a membrane containing a peptide-lipid conjugate (1:1 PEG-lipid:peptide-lipid) and determined that shorter EG chains (nEG = 120 and 750) ensured accessibility of the peptide ligand to cell surface receptors, whereas longer EG chains (nEG = 2000 and 5000) masked the targeting capabilities of the peptide.[231] Hurley *et al.* synthesised a series of DOTMA analogues bearing short EG chains (nEG = 2-6) and reported that the tetraethylene glycol-bearing lipid DODEG4 formulated lipopolyplexes with enhanced serum stability and increased cellular uptake (transfection efficiency) compared to lipopolyplexes formulated with DOTMA, and better exposure of targeting moieties displayed on the liposome surface compared to the nEG = 6 analogue.[154] DODEG4 could be incorporated in large quantities, up to 50 mol%, and at this high percentage it is thought to create a uniform surface coverage to confer stealth properties.[154] Mustapa *et al.* also found that the transfection efficiency was most improved by the triethylene glycol analogue of their series of cleavable short-chain PEG lipids based on the structure of DOTMA.[236] Finally, Mitchell *et al.* reported that formulation of liposomes with high quantities of DODEG4 produced liposomes with improved cellular internalisation in a range of tumour cell lines, in comparison to liposomes formulated with 7 mol% DSPE-PEG2000, whilst maintaining similar distributions and blood half-lives to DSPE-PEG2000-stabilised liposomes.[164] Various studies of vesicles with grafted PEG have shown that the PEG molecular weight and loading, as well as whether the PEG is capped or uncapped, all have a significant influence on vesicle aggregation and the length of *in vivo* circulation.[236]

In light of these studies, we set out to synthesise novel short-chain PEG phospholipids (nEG = 4) with various terminal moieties (-OH, -OMe and -NH_2). The lipids were based on DPPC, with two saturated C16 acyl chains, as these saturated chains have been shown to be essential for high loading of liposomes with glucose or 2-DG (Section 2.1).

The synthesis of the methoxy analogue, DPPE-EG4-OMe **35**, began with an alkylation reaction between the commercially available desymmetrised tetraethylene glycol **31** and ethyl bromoacetate to give ester **32** in 33% yield (Scheme 7). The relatively low yield was consistent with literature yields for analogous alkylation reactions employing ethyl bromoacetate (21-59%).[237,238] Ester **32** was hydrolysed under basic conditions to give acid **33** in 86% yield. Acid **33** was converted into the NHS ester **34** using NHS and EDC to give activated ester **34** in 60% yield. Activated ester **34** was coupled to the commercially available lipid DPPE in the presence of triethylamine to give DPPE-EG4-OMe **35** in 96% yield.

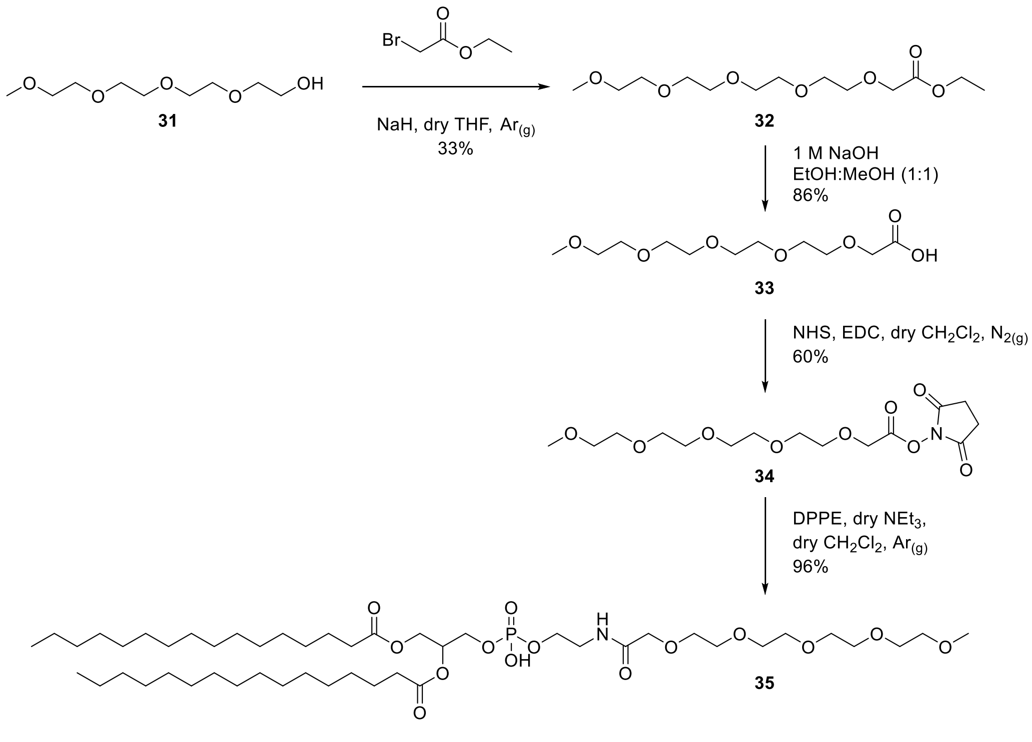

Scheme 7. Synthetic route to novel short-chain PEG lipid, DPPE-EG4-OMe **35**.

Novel short-chain PEG lipids (nEG = 4 and 6) with terminal hydroxyl groups, DPPE-EG4-OH **48** and DPPE-EG6-OH **49**, were prepared *via* an analogous route to DPPE-EG4-OMe **35** (Scheme 8). The hexaethylene glycol analogue DPPE-EG6-OH **49** was synthesised at a later date in light of the results reported in Section 5.1.2.

Synthesis began with mono-TIPS-protection of short-chain PEGs tetraethylene glycol **36** and hexaethylene glycol **37** to give **38** and **39** in 61% and 51% yield w.r.t. TIPSCl, respectively. Mono-protected PEG **38** underwent an alkylation reaction with ethyl bromoacetate to give ester **40** in 51% yield. Ester **40** was hydrolysed under basic

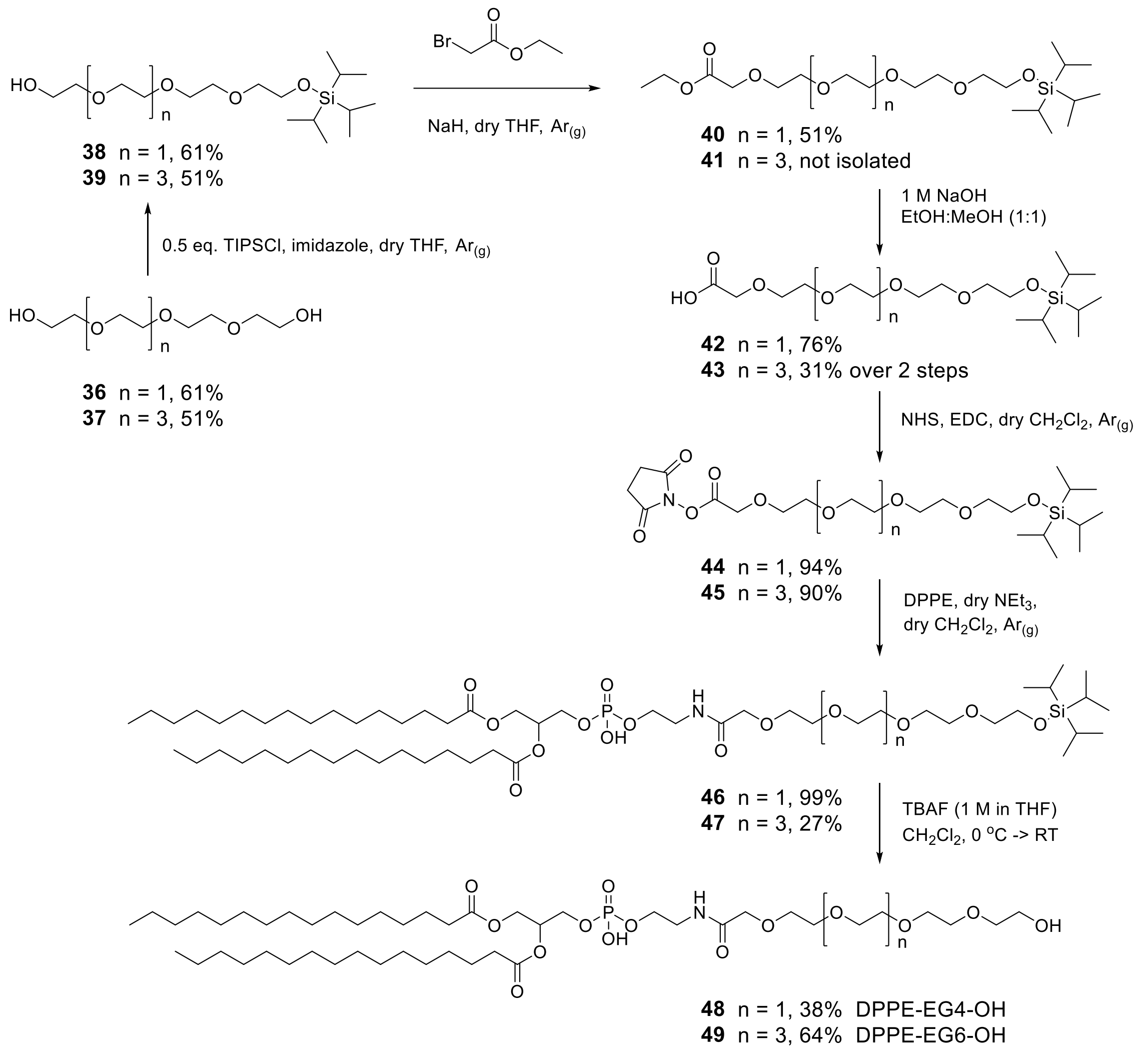

Scheme 8. Synthetic route to novel short-chain PEG lipids, DPPE-EG4-OH **48** and DPPE-EG6-OH **49**.

conditions to give acid **42** in 76% yield. Mono-protected PEG **39** was also alkylated with ethyl bromoacetate to give ester **41** which was not isolated and was immediately hydrolysed under basic conditions to give acid **43** in 31% yield over 2 steps. The reasoning for this was that the alkylation reaction with ethyl bromoacetate was difficult to push to completion and it was easier to separate acid **43** from unreacted alcohol **39** *via* flash silica chromatography than it was to separate ester **41** from alcohol **39**. Acids **42** and **43** were converted to the NHS esters **44** and **45** in excellent yields, 94% and 90%, respectively. Activated esters **44** and **45** were coupled to DPPE in the presence of triethylamine to give the protected short-chain PEG lipids, **46** and **47** in 97% and 27% yield, respectively. The need to purify **47** by flash silica chromatography, whereas **46** was clean enough to proceed to the next step after a work-up, accounts for the difference in yields for the analogous coupling reactions due to partial retention of lipid molecules such as **46** and **47** on the column. Protected PEG lipids **46** and **47** were TIPS-deprotected using TBAF to give DPPE-EG4-OH **48** and DPPE-EG6-OH **49** in 38% and 64% yield, respectively. Extensive flash silica chromatography efforts could not separate the final lipids **48** and **49** from the tetrabutylammonium ion arising from the use of TBAF, which may have formed a counter ion to the phosphate group. A cation exchange resin (Dowex® 50WX8 hydrogen form) was found to be highly effective for removal of this contaminating ion.

The synthesis of a short-chain PEG lipid (nEG = 4) with an amine moiety at the polar terminus commenced with the reaction of commercially available unnatural PEG4 Fmoc-protected amino acid **50** with NHS in the presence of EDC to form the NHS ester **51** in 75% yield (Scheme 9). Activated ester **51** was coupled to DPPE in the presence of triethylamine to give Fmoc-protected short-chain PEG lipid **52** in quantitative yield. Fmoc-deprotection of lipid **52** with 20% piperidine gave DPPE-EG4-NH$_2$ **53** in 33% yield, the yield was low due to partial retention of **53** on the column during purification by FCC.

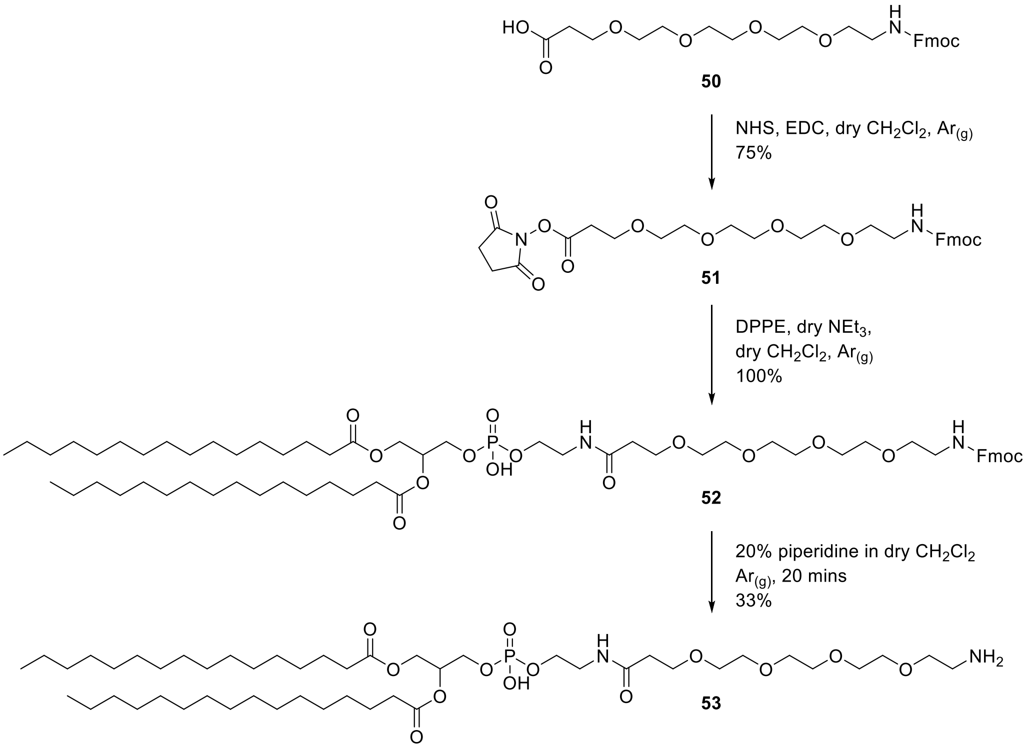

Scheme 9. Synthetic route to novel short-chain PEG lipid, DPPE-EG4-NH$_2$ **53**.

5.1.2 Formulation of PEGylated liposomes and resultant CEST contrast

In order to assess the ability of our novel short-chain PEG lipids to form bilayers that can successfully encapsulate monosaccharides, 2-DG encapsulating liposomes **L48**, **L49** and **L50** were formulated with 70 mol% DPPC and 30 mol% DPPE-EG4-OMe **35**, DPPE-

Table 24. Formulation parameters and measurements for liposomes **L48**-**L52** hydrated with 0.5 M 2-DG with various PEGylation.

Liposome sample	[lipid] (mM)	Bilayer composition (mol%)	Z-Ave post dialysis (d.nm) (s)	PdI (s)	Exterior [2-DG] (mM)	Overall [2-DG] (mM) (s)	pH
L48	30	70% DPPC, 30% DPPE-EG4-OMe	-	-	-	-	7
L49	30	70% DPPC, 30% DPPE-EG4-OH	172 (0.8)	0.16 (0.02)	0.7	41 (0.6)	7
L50	30	70% DPPC, 30% DPPE-EG4-NH_2	221 (1.8)	0.20 (0.01)	0.6	14 (2.0)	7
L51	30	97% DPPC, 3% DPPE-PEG2000	163 (2.8)	0.14 (0.04)	0.3	35 (1.1)	7
L52	30	100% DPPC	184 (2.7)	0.11 (0.03)	0.3	34 (2.3)	7

EG4-OH **48** or DPPE-EG4-NH_2 **53**, respectively. For comparison, 2-DG liposomes with a bilayer comprising 3 mol% DPPE-PEG2000 and 97% DPPC **L51**, and pure DPPC **L52**, were also formulated. Thin films were hydrated with 0.5 M 2-DG solution with 20% PBS at pH 7. Following extrusion, the diameters of **L48**-**L52** ranged between 123-192 nm and after dialysis they ranged between 163-221 nm (Table 30, Section 7.2.1). The liposomes with 30 mol% DPPE-EG-OMe **35** in the bilayer sized quickly and easily by extrusion, reaching a small size of 123 nm with few passes through polycarbonate filters. However, during dialysis into 0.25 M NaCl solution with 20% PBS at pH 7, the liposomes formed a viscous hydrogel (Figure 65). To check the reproducibility of this result, liposomes analogous to **L48** were re-formulated. However, the same viscous gel was observed. Therefore, DPPE-EG4-OMe **35** cannot be used to formulate liposomes under these conditions, the reasons for which are not clear. Similarly, Mustapa *et al*. found that their short-chain (nEG = 3) cleavable PEG lipid based on DOTMA and “capped” with an -OMe group performed significantly less well than the “uncapped” hydroxyl analogue when assessing transfection efficiency of the formulated lipopolyplexes.[236]

The overall 2-DG concentrations for **L49**, **L51** and **L52** were well grouped in the range 34-41 mM, whereas the overall 2-DG concentration measured for DPPE-EG4-NH_2 **53** containing liposomes **L50** was considerably lower at 14 mM (Table 24). The exterior 2-DG concentrations measured for **L49**-**L52** were negligible.

Figure 65. Liposomes **L48** (30 mol% DPPE-EG4-OMe **35**) formed a viscous gel during dialysis.

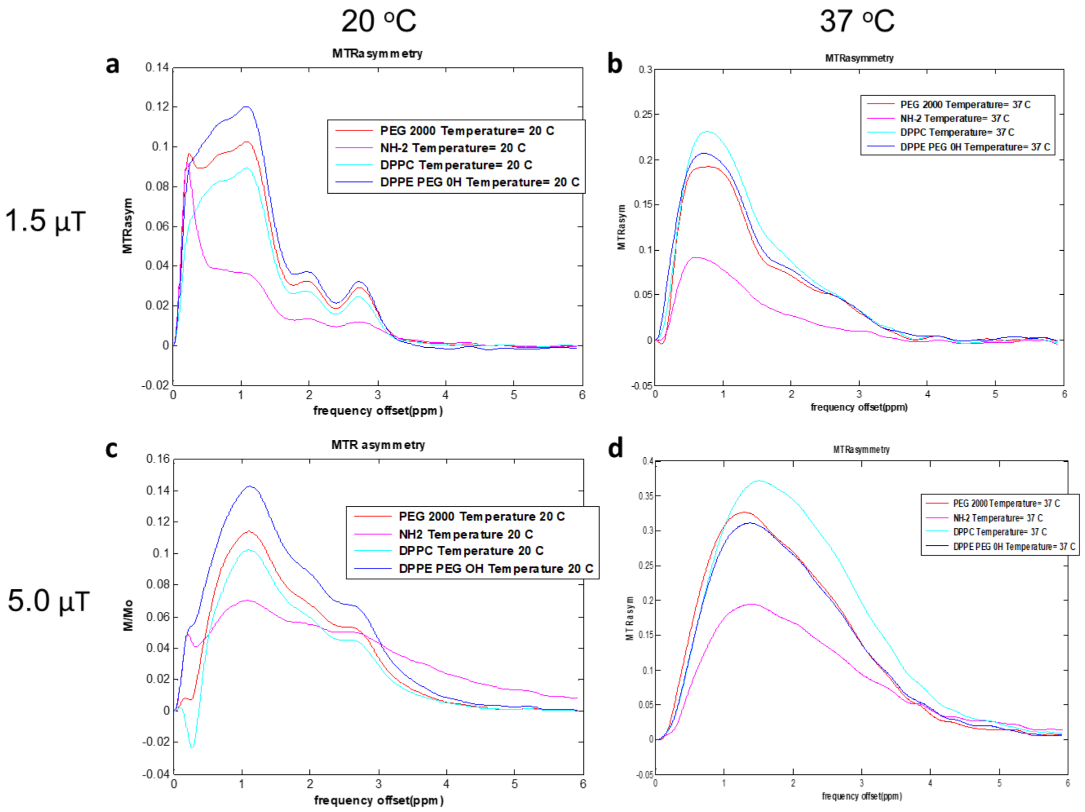

Figure 66. MTR_{asym} spectra for 2-DG liposomes **L49-L52** with various PEGylation, spectra were obtained with B_1 = 1.5 μT (a,b) and B_1 = 5.0 μT (c,d), and at 20 °C (a,c) and 37 °C (b,d).

Table 25. CEST suppression of the water peak for 2-DG encapsulating liposomes **L49-L52** with varying PEGylation. The data was acquired at 20 °C and 37 °C, B_1 = 1.5 μT and 5.0 μT. CEST suppression is expressed as an average of the percentage reduction in water signal caused by presaturation across the range 0-6 ppm.

Liposome sample	[2-DG] (mM)	1.5 μT		5.0 μT	
		20 °C	**37 °C**	**20 °C**	**37 °C**
L49 (30 mol% DPPE-EG4-OH)	41	3.0%	7.6%	3.4%	13.2%
L50 (30 mol% DPPE-EG4-NH_2)	14	3.6%	6.4%	3.6%	11.6%
L51 (3 mol% DPPE-PEG2000)	35	4.2%	6.8%	4.7%	11.0%
L52 (100% DPPC)	34	1.9%	3.0%	3.6%	6.4%

Liposome samples **L49-L52** were scanned, the resultant MTR_{asym} spectra are shown in Figure 66 and the averaged water signal suppression across the range 0-6 ppm are reported in Table 25 and plotted in Figure 67. Although the CEST signal measured was greatest for DPPE-EG4-OH **48** containing liposomes **L49** at 20 °C (which had the highest overall 2-DG concentration) and greatest for the unPEGylated liposomes **L52** at 37 °C, all CEST signal magnitudes for the liposomes **L49**, **L51** and **L52** were within experimental error (Figure 67).

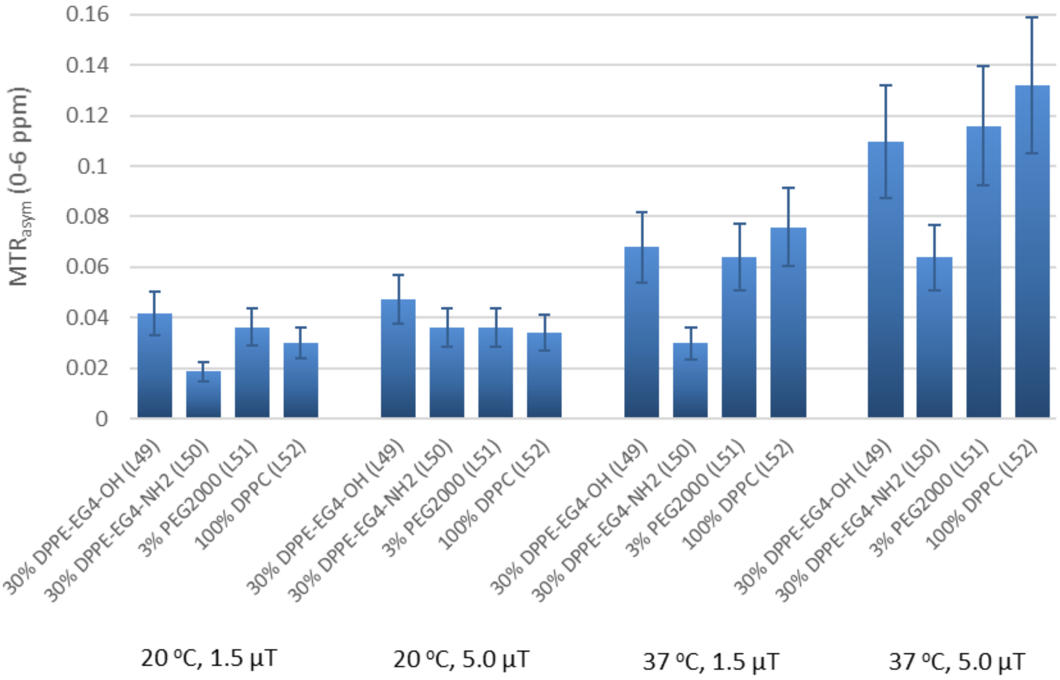

Figure 67. MTR$_{asym}$ (0-6 ppm) for 2-DG liposomes **L49**-**L52** at 20 °C and 37 °C, B_1 = 1.5 µT and 5.0 µT.

DPPE-EG4-NH$_2$ **53** containing liposomes **L50** exhibited significantly lower CEST signal, which was to be expected due to the lower levels of 2-DG encapsulation during formulation, i.e. lower overall 2-DG concentration (14 mM *vs.* 34-41 mM).

The PEGylation of liposomes by incorporation of 3 mol% DPPE-PEG2000 versus 30 mol% DPPE-EG4-OH **48** did not appear to have a significant effect on the CEST signal generated by entrapped 2-DG. Furthermore, the novel short-chain PEG lipid DPPE-EG4-OH **48** performed as well as commercial lipids, DPPC and DPPE-PEG2000, when encapsulating high concentrations of 2-DG and enabling CEST signal generation from encapsulated 2-DG. Thus, DPPE-EG4-OH **48** was our lead novel short-chain lipid for formation of PEGylated liposomes with potential for enhanced cellular uptake and exposure of targeting ligands.

5.1.2.1 The effect of pH on 2-DG encapsulation by DPPE-EG4-NH$_2$ containing liposomes

Since the charge of the amine moiety at the polar terminus of DPPE-EG4-NH$_2$ **53** can vary with pH, which may affect the properties of resultant liposomes, the ability of DPPE-EG4-NH$_2$ **53** to entrap high concentrations of 2-DG at pH 6 and 8 was examined, in comparison to pH 7 (Section 5.1.2). As before, the Z-Ave and PdI values increased during dialysis (Table 26).

Table 26. Formulation parameters and measurements for liposomes **L53**-**L54** (30 mM lipid) with 30 mol% DPPE-EG4-NH_2 **53** hydrated with 0.5 M 2-DG at pH 6 and 8.

Liposome sample	Bilayer composition (mol%)	Z-Ave post extrusion (d.nm) (s)	PdI (s)	Z-Ave post dialysis (d.nm) (s)	PdI (s)	Exterior [2-DG] (mM)	Overall [2-DG] (mM) (s)	pH
L53	70% DPPC, 30% DPPE-EG4-NH_2	173 (7.2)	0.18 (0.05)	219 (7.0)	0.27 (0.04)	0.2	20	6
L54	70% DPPC, 30% DPPE-EG4-NH_2	180 (5.0)	0.14 (0.01)	207 (1.9)	0.20 (0.01)	0.5	18	8

The exterior 2-DG concentrations measured for **L53** and **L54** were negligible and the overall 2-DG concentrations were only slightly improved *cf.* **L50** at pH 7 (14 mM), measuring as 20 mM and 18 mM, respectively. Batches of liposomes that were dialysed at separate times cannot be accurately compared due to dialysis being carried out at room temperature, thus, encapsulation efficiency is partly dependent on the temperature of the lab at that time. However, the overall 2-DG concentrations measured for liposomes with 30 mol% DPPE-EG4-NH_2 **53** (**L50**, **L53** and **L54**) were approximately half of those achieved with lipid mixtures including DPPC, DPPE-PEG2000 and DPPE-EG4-OH **48**, a large discrepancy which was not expected to be caused by small fluctuations in room temperature. Therefore, DPPE-EG4-OH **48** and the PEG6 analogue, DPPE-EG6-OH **49**, were the lead short-chain PEG lipids going forward and DPPE-EG4-NH_2 **53** will not be used.

5.1.3 Synthesis of maleimide-lipids

The strategy for covalent anchoring of targeting peptides to the liposome surface consisted of the design and synthesis of novel maleimide-lipids, inclusion in the lipid bilayer and subsequent reaction with N-terminal cysteine-modified targeting peptides to form a thioether bond (Figure 64). The use of maleimide functionalised lipids to attach peptides to lipid bilayers has been previously reported.[239–241] The maleimide moiety is routinely used as a thiol acceptor because it exhibits high selectivity and reactivity under neutral aqueous conditions.[239] A study by Fleiner *et al.* showed that maleimide-lipids with hydrophilic spacers, such as PEG, between the lipid anchor and maleimide group had better coupling efficiencies to thiolated peptides than lipids with hydrophobic linkers such as dodecyl.[240] It is thought that nonpolar spacers interact with the hydrophobic part of the liposome membrane, thereby reducing the availability of the maleimide group to react. A maleimide-lipid was synthesised with an EG spacer between a maleimide head group and two saturated cetyl lipid chains, Mal1 **54** (Scheme 10). The previously

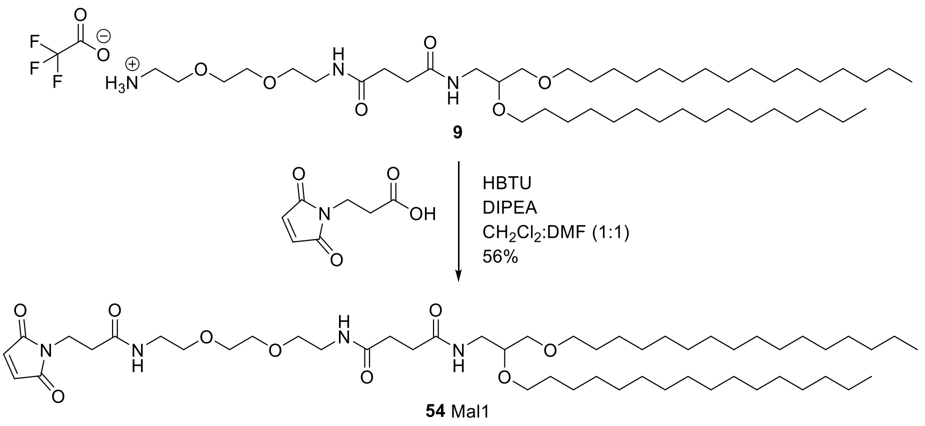

Scheme 10. Synthesis of maleimide-lipid Mal1 **54** from previously synthesised intermediate **9**.

synthesised amine **9** (Scheme 1, Section 2.5.1) was coupled to commercially available 3-maleimidopropionic acid, using HBTU and DIPEA, to give the novel maleimide-lipid Mal1 **54** in 56% yield.

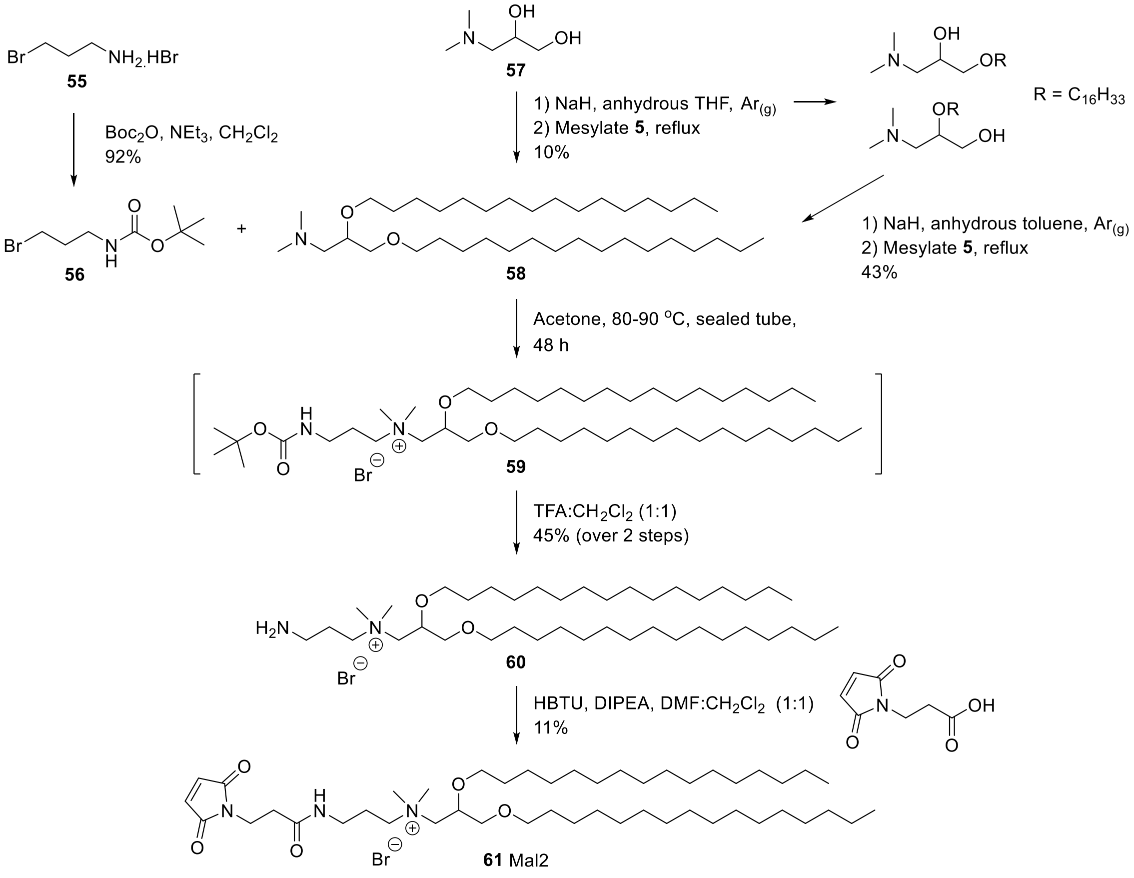

Scheme 11. Synthesis of charged maleimide-lipid, Mal2 **61**.

Considering the problems faced when incorporating the novel glucose-lipid GlcEG3SLc into liposomes (Section 2.5.2), probably due to lack of polarity in the head region of the lipid, a second maleimide-lipid with a quaternary amine group, Mal2 **61**, was synthesised (Scheme 11). 3-Bromopropylamine hydrobromide **55** was reacted with Boc anhydride to give the protected amine **56** in 92% yield. 3-(Dimethylamino)-1,2-propanediol **57** was alkylated with cetyl mesylate **5** (previously synthesised in Scheme 1, Section 2.5.1) using sodium hydride to give doubly alkylated **58** in 10% yield. The singly alkylated products were also isolated and reacted with mesylate **5** again to give doubly alkylated product **58** in 43% yield. This increased the overall yield of **58** based on the number of moles of diol **57** used from 10% to 22%. Alkyl bromide **56** was reacted with tertiary amine **58** in acetone at 80-90 °C in a sealed pressure tube, *via* an adapted procedure from Hurley *et al.*,[154] to give the un-isolated intermediate **59**, which was deprotected with TFA to give amine **60** in 45% yield over two steps. Amine **60** was coupled to 3-maleimidopropionic acid using HBTU and DIPEA to give the novel cationic maleimide-lipid Mal2 **61** in 11% yield.

5.1.4 Selection and synthesis of EGFR-targeting peptides

5.1.4.1 Selection

Epidermal growth factor receptor (EGFR) is a growth-factor-receptor tyrosine kinase and an important target in anticancer therapy. Elevated levels of EGFR and/or its cognate ligands have been identified as a common characteristic of many different types of cancer and appear to promote solid tumour proliferation.[242] As a target antigen, EGFR is a readily accessible cell surface receptor, and when overexpressed, provides a basis for selective targeting of tumor cells.[243] A variety of EGFR-targeted nanoparticles have shown promising results *in vitro* and in pre-clinical models *in vivo*.[244]

Antibodies present attractive targeting moieties due to their high affinity and specificity, however, their large size precludes multivalent decoration of nanoparticles. In addition to the size obstacle, antibodies can pose immunogenicity issues and require very costly processes of protein sequence modification to yield chimeric or humanised antibodies in order to minimize immunogenicity risks. Antibody fragments can overcome size-related limitations but may exhibit much lower receptor affinities and due to similar development processes to full antibodies, may still produce problems with immunogenicity and cost. Employing the endogenous ligand of EGFR, specifically epidermal growth factor (EGF), has demonstrated successful targeting due to its high binding affinity and relatively small size (53 amino acids) allowing multivalent decoration of the nanoparticle surface.[244] However, isolating and purifying EGF from murine or human sources can also raise concerns over antigenicity and raise expenses. Additionally, EGF binding to EGFR produces downstream signalling cascades to promote cell proliferation and survival, which could offset the therapeutic efforts of the nanocarrier system. Three short EGFR-specific peptides were chosen from the literature as targeting ligands due to their relatively small size, low immunogenicity, ease of synthesis and low cost. These peptides have been reported to specifically bind to EGFR and thereby enhance nanocarrier accumulation in EGFR-overexpressing tumors.[232,245–247]

The EGFR-targeting peptide, YHWYGYTPQNVI (GE11), was identified by Li *et al*. in 2005 using phage display library screening,[248] and has been conjugated to the surface of liposomes to produce enhanced liposomal binding to EGFR high-expressing cancer cells *in vitro*.[245] In a H1299 xenograft mouse model for non-small cell lung carcinoma, GE11-bearing liposomes extravasated and accumulated in the tumor tissue preferentially and demonstrated enhanced drug delivery capacities.[245]

The peptide LARLLT was identified as an EGFR ligand by Song *et al.* in 2009 using a computer-assisted design approach.[246] LARLLT-conjugated liposomes were found to specifically and efficiently bind to and enter cells by endocytosis *in vitro* in a process that appeared to be mediated by EGFR-overexpressing cancer cells (H1299). *In vivo*, the peptide-conjugated liposomes were found to accumulate in EGFR-overexpressing xenograft tumor tissues for up to 80 h after intravenous delivery, in marked contrast to controls.[246]

LARLLT and GE11 peptides have been used extensively for the development of EGFR-targeted nanoparticles for cancer-specific drug delivery and as positive controls for the development of new EGFR-targeting sequences.[244,249,250] A third peptide, AEYLR, was reported in 2013 by Han *et al.* as the best performing out of three evaluated EGFR-targeting sequences that were derived from the major autophosphorylation sites of the EGFR C-terminus domain.[249] Small peptides derived from the C-terminal of EGFR show inhibition effects of autophosphorylation, thus employing these peptides as targeting ligands could produce synergistic effects with therapeutic cargo.[249] When AEYLR was conjugated to lipid nanocarriers, they showed enhanced specific binding and *in vitro* uptake into high-EGFR-expressing cells.[232,249] The AEYLR peptide alone did not significantly stimulate or inhibit the growth activity of cells so it is safe to use as a targeting ligand.[249] AEYLR-conjugated nanostructured lipid carriers have demonstrated effective tumour targeting in mouse xenograft models.[232,247]

5.1.4.2 Synthesis

In previous tumor targeting studies using the EGFR peptide ligands, YHWYGYTPQNVI, LARLLT and AEYLR, the peptide was conjugated to the nanoparticle at the N-terminal end *via* various chemical coupling strategies.[232,246,247] Therefore, the peptides were modified with the addition of an N-terminal cysteine residue (Figure 68), that can be employed in a coupling reaction with the maleimide moiety at the polar end of maleimide-lipids, Mal1 **54** and Mal2 **61**, on the surface of preformed liposomes.

Peptides were synthesised *via* an Fmoc solid phase synthesis approach.[251] CYHWYGYTPQNVI and CLARLLT were synthesised using a MultiSynTech Syro Automated Peptide Synthesiser whereas CAEYLR was synthesised manually (Section 7.3.5). Yields were in the range 2-46%. The lowest yield of 2% was obtained for the longest peptide CYHWYGYTPQNVI, an intermediate yield of 11% was obtained for CLARLLT and the highest yield of 46% was obtained for the shortest peptide CAEYLR when synthesised by hand.

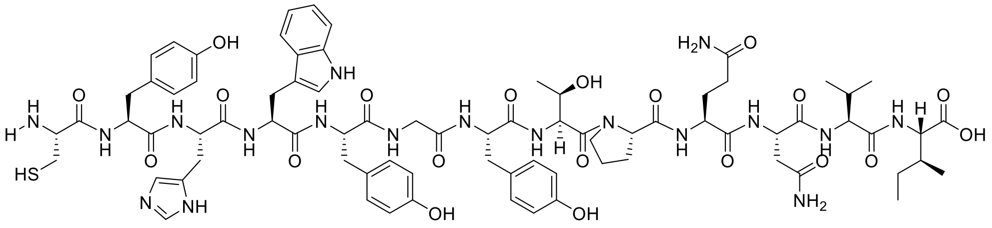

CYHWYGYTPQNVI

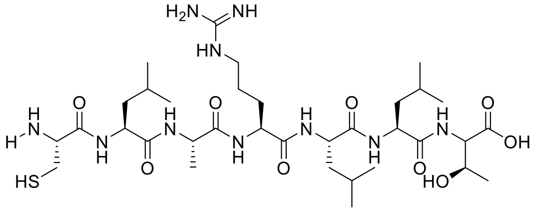

CLARLLT

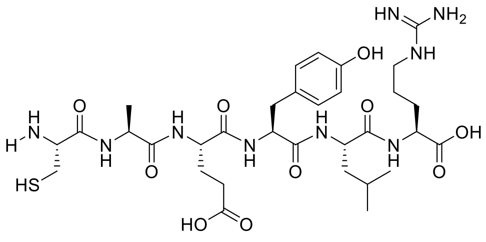

CAEYLR

Figure 68. Structures of CYHWYGYTPQNVI, CLARLLT and CAEYLR.

5.1.5 Targeted liposome summary

A lead novel short-chain PEG lipid, DPPE-EG4-OH **48** (nEG = 4), has been synthesised and incorporated into liposomes at 30 mol%, to produce liposomes that are capable of encapsulating high concentrations of 2-DG and which generate appreciable CEST signal. An analogue of this lipid with nEG = 6, DPPE-EG6-OH **49**, was also synthesised for future evaluation. Studies are required to optimise the *in vivo* biodistribution of liposomes formulated with different mol% of these short-chain PEG lipids, with the aim of achieving maximal accumulation in tumors. Two novel maleimide-functionalised lipids, Mal1 **54** and Mal2 **61**, have been synthesised and three cysteine-modified EGFR-targeting peptides were obtained *via* an Fmoc solid phase synthesis approach. Unfortunately, time did not permit the formulation of EGFR-targeted liposomes.

5.2 Effect of 2-DG liposomes on colorectal cancer cell lines

The effect of 2-DG liposomes **L55-L61** and empty liposomes **L62-L66** (Table 27) on the survival of various colorectal cancer (CRC) cell lines (Table 28) were tested in resazurin cell viability assays (procedure details can be found in Section 7.4.1). The maximum extruder volume was 10 mL so multiple batches of analogous liposomes were prepared when needed.

Table 27. Formulation parameters and measurements for 2-DG liposomes **L55-L61** and empty liposomes **L62-L66**, for use in clonogenic assays. All bilayers were comprised of 97 mol% DPPC and 3 mol% DPPE-PEG2000 and 2-DG liposome thin films were hydrated with 0.5 M 2-DG.

Liposome sample	[lipid] (mM)	Z-Ave post dialysis (d.nm) (s)	PdI (s)	Exterior [2-DG] (mM)	Overall [2-DG] (mM) (s)	mL
2-DG inside, NaCl exterior						
L55	35	142 (0.76)	0.13 (0.01)	0.9	36 (1.9)	6
L56	35	161 (4.5)	0.14 (0.01)	0.4	40 (2.1)	10
L57	35	163 (7.0)	0.14 (0.05)	1.6	39 (0.3)	10
2-DG inside, 1.6 × PBS outside						
L58	35	168 (1.2)	0.6 (0.01)	0.5	48 (2.1)	10
L59	35	165 (1.5)	0.13 (0.03)	0.3	42 (2.0)	8
L60	35	167 (2.2)	0.14 (0.01)	2.3	59 (3.4)	5
L61	35	150 (2.6)	0.13 (0.003)	0.6	54 (3.1)	10
Empty liposomes in 1 × PBS						
L62	35	174 (0.5)	0.11 (0.02)	none	none	5
L63	35	153 (1.2)	0.17 (0.01)	none	none	10
L64	35	153 (1.6)	0.17 (0.01)	none	none	5
Empty liposomes in cell culture media						
L65	35	172 (1.6)	0.12 (0.003)	none	none	10
L66	35	163 (0.1)	0.13 (0.02)	none	none	4.4

Table 28. CRC cancer cell lines used in cell viability or clonogenic assays.

Cell line	Derivation	p53	GLUT1 expression*	EGFR expression*
DLD1	Colon	mut	High	High
HT29	Colon	mut	High	Average
SW1222	Colon	mut	Low	Not known
SW1417	Colon	mut	Low**	Average
HCT116	Colon	wt	Low - average	Average
CW2	Colon	wt	Not known	Not known
RKO	Colon	wt	Low**	Average
C99	Colon/Rectal	wt	Not known	Not known
SW1463	Rectal	mut	Average	Not known
DiFi	Rectal	mut	Not known	High

*From mRNA expression data available online and **Zhang *et al*.[252]

2-DG liposomes with 0.25 M NaCl exterior to the liposomes have been predominantly used throughout this thesis study, but were found to cause high levels of cell death, so 2-DG liposomes were dialysed into 1.6 × PBS instead (**L58**-**L61**) to investigate whether this altered cell viability. Empty liposomes in 1 × PBS (**L62**-**L64**) were used as a control and the appropriate volume of concentrated (10 ×) PBS was added to create the same overall PBS concentration in the wells as when 2-DG liposomes in 1.6 × PBS were added. Empty liposomes in PBS still caused significant cell death in most cell lines, in comparison to untreated control cells. To assess the effects of PBS and empty liposomes separately, 1.6 × PBS without any lipid content was trialled and empty liposomes were formulated in cell media (**L65** and **L66**) to eradicate the PBS variable and determine whether solely the presence of empty liposomes affect cell viability.

Addition of 10 × PBS to cells to create a total concentration of 1.6 × PBS did not affect cell viability compared to the untreated controls, confirming that PBS alone does not kill the screened CRC cell lines (Figure 69). Empty liposomes in cell media did not have a large effect on cell viability except in the case of RKO, which consistently showed high levels of cell death upon treatment with any liposomal sample, whether 2-DG was encapsulated or not (Figure 69). For RKO, cell death was more prominent in response to empty liposome treatment than treatment with free 2-DG (5 mM), suggesting intolerance of this cell line to liposomes (97:3 mol% DPPC:DPPE-PEG2000) and potential membrane instability. In every other CRC cell line except RKO, there was a significant difference in cell survival between treatment with empty liposomes in cell media and treatment with 2-DG liposomes in 1.6 × PBS, suggesting cytotoxicity of liposomal 2-DG once 2-DG is either delivered intracellularly by liposomes or released from liposomes and taken up *via* GLUT transporters. SW1417 was the only cell line to demonstrate significantly worse cell survival for liposomal 2-DG than free 2-DG, suggesting good liposomal uptake and/or poor free 2-DG uptake *via* GLUT transporters (RT-qPCR has shown that GLUT1 expression is low in SW1417 cells).[252] The reported levels of GLUT1 transporters for cell lines did appear to correlate with the cytotoxicity of free 2-DG *vs*. controls or liposomal 2-DG, a result one might have expected to see due to increased ability of cells to take up free 2-DG *via* GLUT1. It has been previously

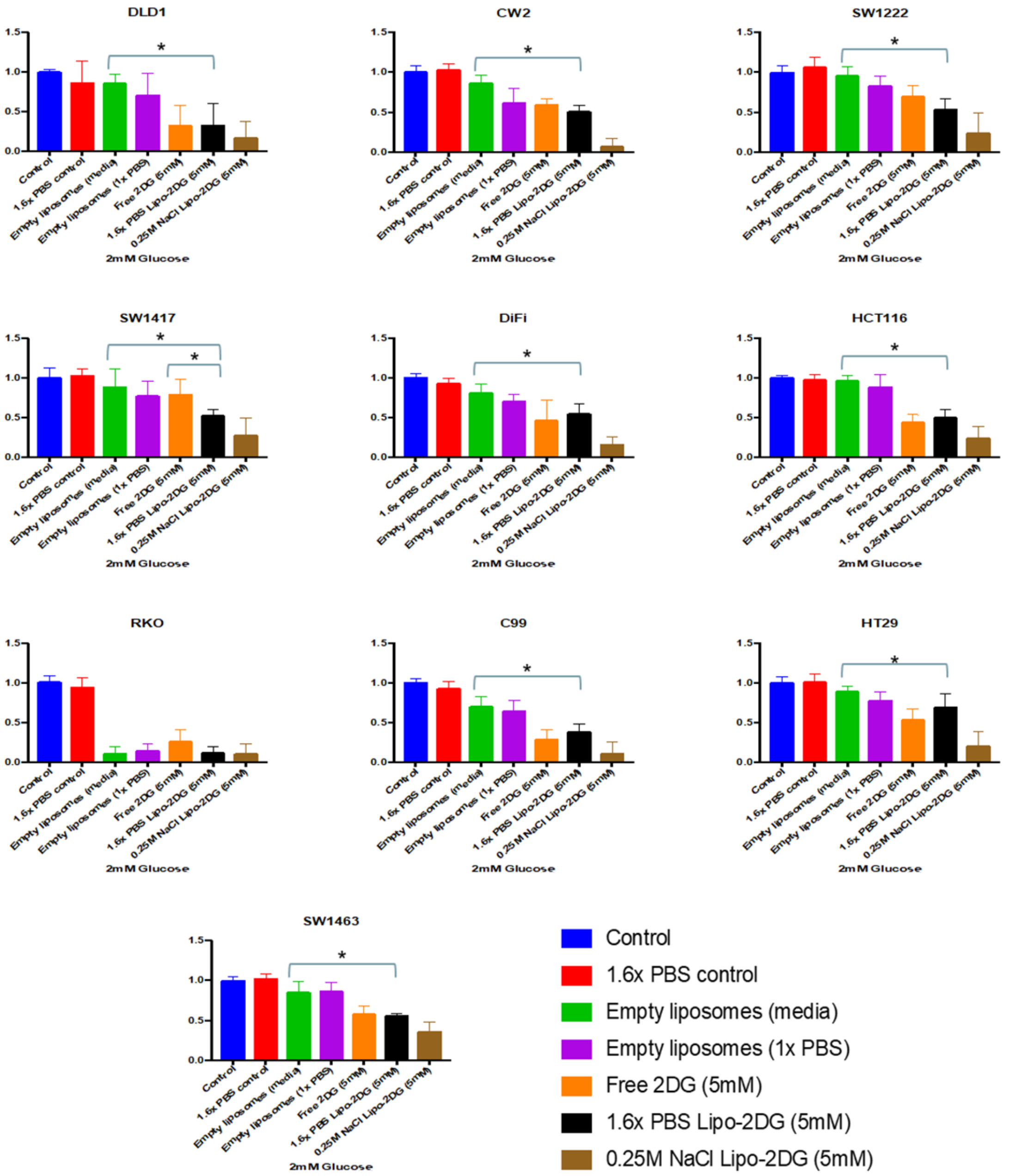

Figure 69. Resazurin cell viability assays for various colon and/or rectal cancer cell lines employing 2-DG liposomes in 0.25 M NaCl (**L55**-**L57**), 2-DG liposomes in 1.6 × PBS (**L58**-**L61**), empty liposomes in 1 × PBS (**L62**-**L64**) and empty liposomes in cell media (**L65** and **L66**).

In vitro assays in this subsection were carried out by Adam Westhorpe, UCL Cancer Institute.

reported in the literature that the cytotoxicity of 2-DG to cancer cells is p53-dependent, with p53 deficient (-/-) cancers (which account for more than 50% of all types of cancer) being more susceptible to 2-DG-induced cell death.[253] This finding was not reflected in our cell viability assay results, with CRC cell lines expressing wild type p53 often exhibiting more cell death in response to free or liposomal 2-DG than p53-deficient cell lines (Figure 69, Table 28).

Preliminary cell viability assays were carried out to investigate the radiosensitisation effect on various CRC cell lines from free 2-DG and liposomal 2-DG with 1.6 × PBS exterior to the liposomes **L58**-**L61**, with an applied radiation dose of 4 Gy (Section 7.4.1). The most promising cell line was HCT116, demonstrating radiation enhanced cell killing for both free and liposomal 2-DG (Figure 70). All other tested cell lines demonstrated no sign of radiosensitisation, with similar or more cell death without the application of a 4 Gy radiation dose. Cell viability assays are used as less accurate predictors of which cells to take through to clonogenic assays. Clonogenic assays are more reliable because the cell numbers are adjusted per plate to allow for radiation-induced death and larger well surfaces are provided so as not to inhibit cell growth due to proximity to other cells.

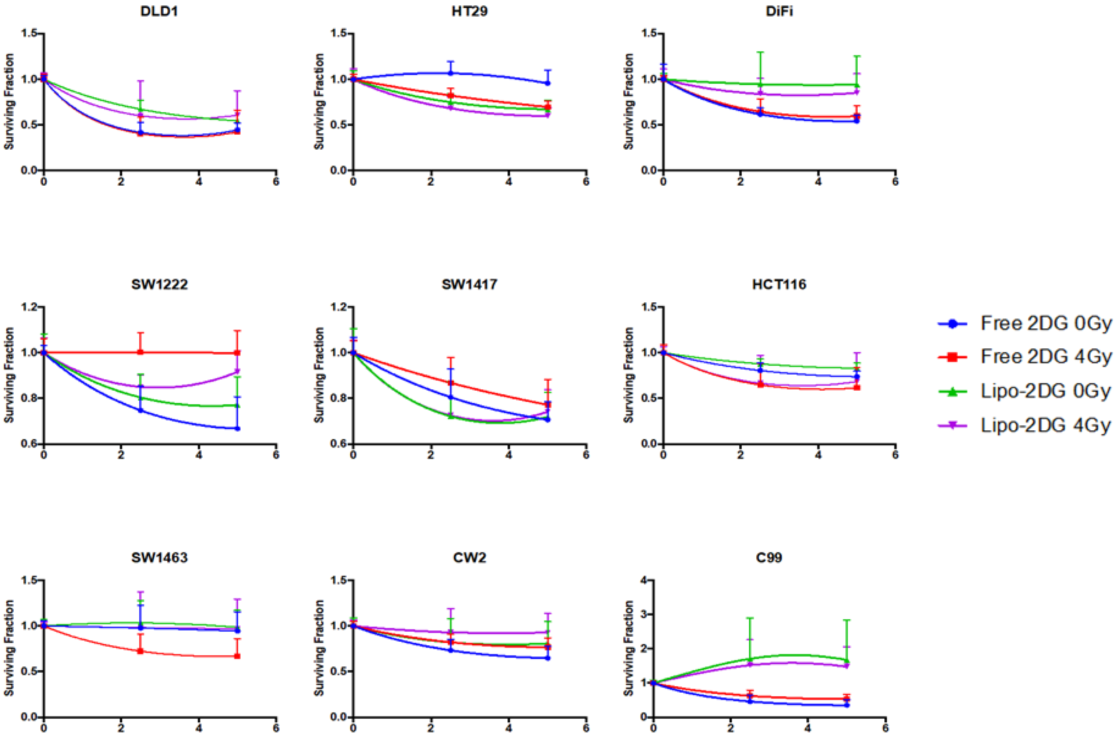

Figure 70. Resazurin cell viability assays investigating effect of 4 Gy on cell lines treated with 2.5 mM and 5 mM liposomal (**L58**-**L61**) or free 2-DG.

The radiosensitisation properties of free 2-DG were tested more thoroughly in HCT116 cells using a classical clonogenic assay procedure (Section 7.4.2), in an attempt to observe similar radiosensitisation results to those reported in the literature for other cell lines.[121,137] Sinthupibulyakit *et al.* reported that the radiosensitisation effects of 2-DG were p53 dependent,[253] thus, both wild type (+/+) and p53-deficient (-/-) HCT116 cells were tested. Unfortunately, no appreciable radiosensitisation was observed for either p53 variant, with calculated radiation enhancement ratios of 1.12-1.16, where values below 1.2 are considered as poor radiosensitisers (Figure 71).

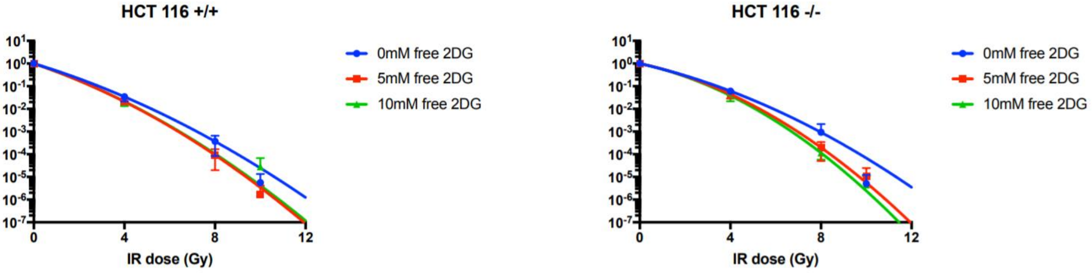

Radiation enhancement ratio (RER):
5 mM = 1.12
10 mM = 1.12

RER:
5 mM = 1.12
10 mM = 1.16

Figure 71. Classical clonogenic assays with free 2-DG in HCT116 CRC cells, +/+ and -/- for p53 to test for radiosensitisation with radiation doses from 0-10 Gy.

Clonogenic assays following the reported procedure by Sinthupibulyakit *et al.* (Section 7.4.3) and employing the same cell line (A549 lung cancer cells) were carried out in an attempt to replicate the findings.[137] They reported that cell numbers were in the range of 100-500 cells per well, thus, we used a low (200) and high (500) number of cells within this range, to determine whether cell number affected the results. As before with HCT116 cells, doses of 2-DG up to 20 mM did not appear to cause radiosensitisation in A549 lung cancer cells at either cell number (Figure 72a-c), in contrast to the radiosensitisation reported by Sinthupibulyakit *et al.* (Figure 72d). In this paper, the cell number alterations due to exposure to increasing radiation doses were not specified (all that was stated was that “between 100-500 cells were plated”), thus, it is unclear if pure radiation-induced cell death was corrected for by altering cell number. For comparison, in our experiments the cell numbers were increased 10-fold per 4 Gy increase. In addition, the scale of the y-axis was short (0.01-1), emphasising the observed effect, which was only 0.5log. On this topic, an interesting news paper was published in Nature that reported more than 70% of researchers have tried and failed to reproduce another scientist’s experiments, highlighting the problem and importance of replicability in biomedical science.[254]

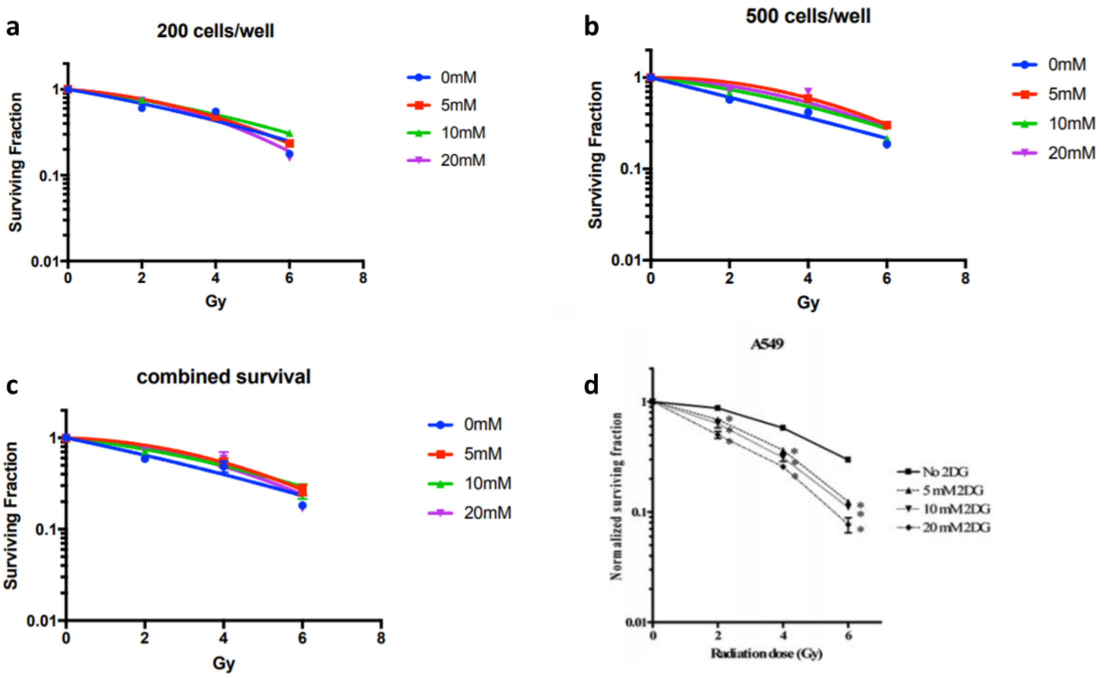

Figure 72. Clonogenics assays repeating the procedure by Sinthupibulyakit *et al.* in the same cell line (A549) using 0-20 mM 2-DG and irradiating at 0-6 Gy a) with 200 cells/well, b) with 500 cells/well, c) combining the data from both 200 and 500 cells/well, d) results reported by Sinthupibulyakit *et al*.[137]

It was concluded that despite previous reports in the literature, 2-DG does not appear to be an effective radiosensitiser in the CRC cell lines tested here or in A549 lung cancer cells, thus, the liposomal CAs encapsulating 2-DG will not be employed in further radiosensitisation experiments. However, cytotoxicity was observed excluding a radiation dose (Figure 69), so the therapeutic benefits of liposomal 2-DG as a glycolytic inhibitor in cancer cell lines *in vivo* will be investigated in future work.

5.3 Release over time studies

An important question to investigate prior to the use the liposomal CAs *in vivo* is how quickly will the monosaccharide contents be released under physiological conditions at 37 °C? To investigate this, glucose and 2-DG liposomes **L67**-**L69** were formulated in 20% PBS at pH 7 (Table 29) and incubated at 37 °C, monitoring the release of monosaccharide over time using the Glucose GO Assay® (method detailed in Section 7.2.4). Liposome bilayers were comprised of 3 mol% DPPE-PEG2000 and 97 mol% DPPC, the bilayer composition used in clonogenic assays, or 100% DPPC, the bilayer composition employed in most CEST imaging studies reported in this thesis.

Table 29. Formulation parameters and measurements for liposomes encapsulating glucose or 2-DG **L67**-**L69** for use in release at 37 °C studies.

Liposome sample	Lipid composition	Overall [lipid]	Hydration solution	Z-Ave (d.nm) (s)	PdI (s)	Exterior [sugar] (mM)	Overall [sugar] (mM) (s)	pH
L67	3% DPPE-PEG2000, 97% DPPC	> 35 mM*	0.5 M glucose	156 (4.0)	0.18 (0.01)	0.3	59 (0.3)	7
L68	3% DPPE-PEG2000, 97% DPPC	30 mM	0.5 M 2-DG	166 (1.6)	0.10 (0.02)	0.7	38	7
L69	100% DPPC	30 mM	0.5 M 2-DG	197 (3.9)	0.16 (0.01)	0.5	30	7

*this liposome sample had been centrifuged and some exterior solution pipetted off to increase lipid and monosaccharide concentration. This was carried out to aid detection of small quantities of leakage in the early stages of the experiment.

Glucose was released in an almost linear fashion from DPPC liposomes with a PEG coating comprised of 3 mol% DPPE-PEG2000 **L67** (Figure 73). During CEST experiments at 37 °C, the liposomes were held at 37 °C for 2 h, thus, using the equation of the linear trendline we can equate this to 1.7% glucose leakage, which given the overall glucose concentration of **L67** was 59 mM, is equal to 1 mM glucose exterior to the liposomes at the end of a CEST experiment at 37 °C.

When comparing 2-DG leakage from **L68** and **L69**, 2-DG release was slightly slower from the PEGylated liposomes **L68** (Figure 73). Using the measurements acquired at the 2 h time point, 2-DG release after 2 h at 37 °C was calculated as 10% for PEGylated **L68** and 15% for unPEGylated **L69**, equating to 3.8 mM and 4.5 mM 2-DG concentrations exterior to the liposomes at the end of a 37 °C CEST experiment. Therefore, it is assumed that the glucose and 2-DG concentrations exterior to liposomes during 2 h CEST experiments at 37 °C remained below 5 mM, the monosaccharide concentration that we have defined as negligible in terms of CEST signal generation.

2-DG was released from DPPC and 3 mol% DPPE-PEG2000 liposomes (**L68** and **L69**) more quickly than glucose was released from PEGylated liposomes **L67** (Figure 73). This is presumably due to the higher lipophilicity of 2-DG (logP = -2.19),[255] compared to glucose (logP = -2.82).[256] The lower the logP value, the more hydrophilic a molecule is, therefore, whilst glucose and 2-DG both have a strong preference for the aqueous phase, glucose is more polar than 2-DG owing to an extra hydroxyl moiety, making it less likely to permeate lipid bilayers.

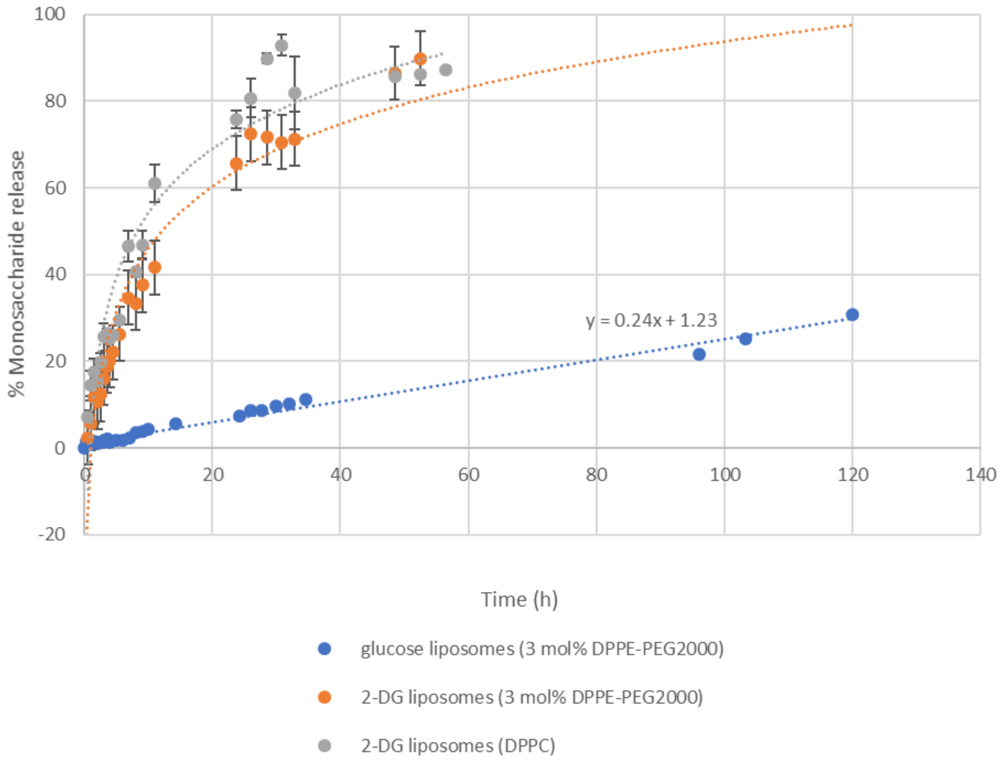

Figure 73. Release of glucose from **L67** and 2-DG from **L68** and **L69** when incubated at 37 °C.

In an attempt to better emulate physiological conditions *in vitro*, the liposomes were diluted with human plasma (Sigma-Aldrich) by a factor of 2, as Shibata *et al.* did to investigate the leakage of DOX from Doxil®.[257] Unfortunately, the high glucose and other sugar content of human plasma produced a large background signal and made results obtained using the Glucose GO Assay® difficult to interpret (Section 7.2.4.2). The release profiles of glucose and 2-DG from DPPC-based liposomes reported in Figure 73 may differ *in vivo* because factors such as the pH, salt concentration, dilution factor and contact with plasma components can all affect drug release from liposomes.[257,258] The tumor microenvironment is often associated with lower pH values, higher temperatures and overexpression of several proteolytic enzymes which can alter the rate of content leakage from liposomes comparative to the bloodstream or other healthy tissues.[259]

5.4 Preliminary *in vivo* experiments

One of the negative effects related to large glucose bolus injection that we hoped to circumvent with the use of liposomes was the rapid stimulation of the insulin response and therefore rapid metabolism of glucose and danger of hyperglycaemia in diabetic individuals. It was hypothesised that if rodents were to be injected with the same overall concentration of free or liposome encapsulated glucose, the blood glucose concentration would rise quickly for the free glucose solution and would rise more slowly for the liposome encapsulated glucose, potentially reaching a lower peak blood glucose value. A steadier incline in blood glucose was assumed due to the slow release of glucose from liposomes *in vivo*. For future applications, this would be beneficial because susceptible patients could be protected from hyperglycaemia and the glucoCEST signal generated by glucose liposomes could be prolonged *in vivo*. To test this hypothesis, old, fat rats (~ 500 g each) were used as a mammalian model for older, obese patients who are at risk of developing type II diabetes or who have already developed type II diabetes.

Four fat rats were administered with concentrated glucose liposomes **L67** (3:97 mol% DPPE-PEG2000:DPPC, Table 29) or a free glucose solution with an equal glucose concentration to the liposome sample (as determined by the Glucose GO Assay®), to assess the ability of liposomes to prevent rapid increases in blood glucose and thereby avoid triggering a pronounced insulin response. Prior to the injection of glucose or liposomal glucose, baseline blood glucose levels were measured. Glucose or liposomal glucose **L67** (1 mL) was administered *via* tail vein injection and blood glucose measurements were taken up to 1 hour after injection. Animals were fasted for 20 hours prior the experiment and were kept under the effect of 2% isoflurane in air throughout the experiment. The readings were taken using the Accu-Chek Aviva Starterskit blood glucose meter. A sample of readings were compared to readings taken with an i-STAT Handheld Blood Analyzer (Abbott Point of Care Inc.), a device that is used for patients in hospitals which is more accurate but more expensive. The readings were in agreement, supporting the reliability of the results (both devices were used according to the manufacturer’s instructions).

The glucose meter measured 0 mM for the liposomal glucose sample **L67**, whereas 59 mM was measured for the free glucose solution, indicating that there was negligible glucose concentration exterior to the liposomes and that glucose cannot be detected by the glucose meter whilst it is still encapsulated inside liposomes.

For all rats, the peak blood glucose levels occurred approximately 30 min after injection of free glucose (Figure 74), suggesting they were mildly diabetic. The average peak blood glucose level after liposomal glucose injection also measured around 30 min after injection. The blood glucose levels dropped to baseline 1 hour following injection of liposomal glucose, suggesting that the rats were not severely diabetic. Generally, injection of liposomal glucose **L67** led to lower blood glucose levels than injection of the same concentration of free glucose, indicating some shielding effects. As the blood glucose levels still rose to a maximum around 30 min, it was concluded that the experiment should be repeated in the future with more rigid liposomes (addition of DSPC

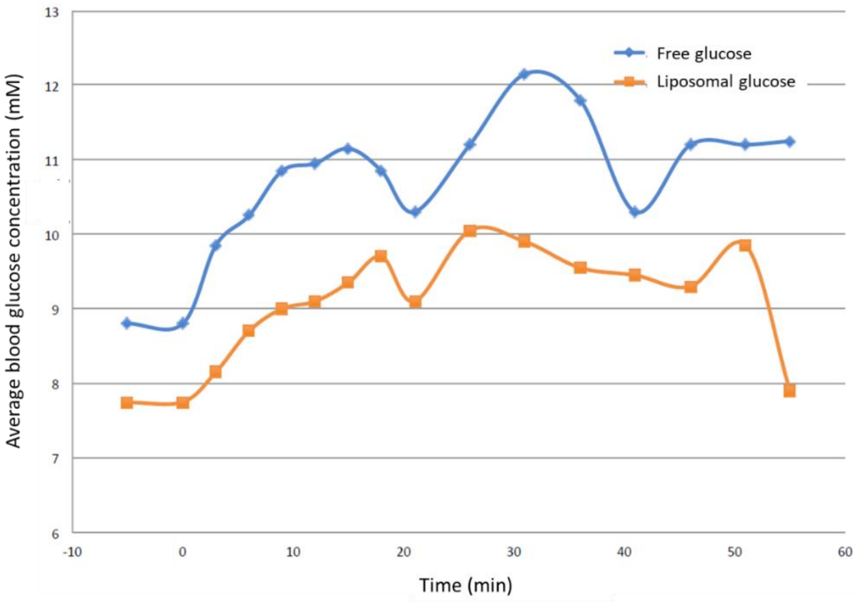

Figure 74. Average blood glucose levels for four fat rats (500 g) following injection of 1 mL of free or liposomal glucose **L67** (59 mM).

or cholesterol) to slow down leakage upon exposure to the physiological environment, such as temperatures of approximately 37 °C and changes in osmotic pressure.

Experiments were conducted with younger rats (300 g each) and a dose of 0.1 g/kg glucose (rat1 & rat2) or 0.2 g/kg glucose (rat 3 & rat4). The rats were awake to minimise the effect of isoflurane on physiological variables. Rat1 and rat2 showed very similar

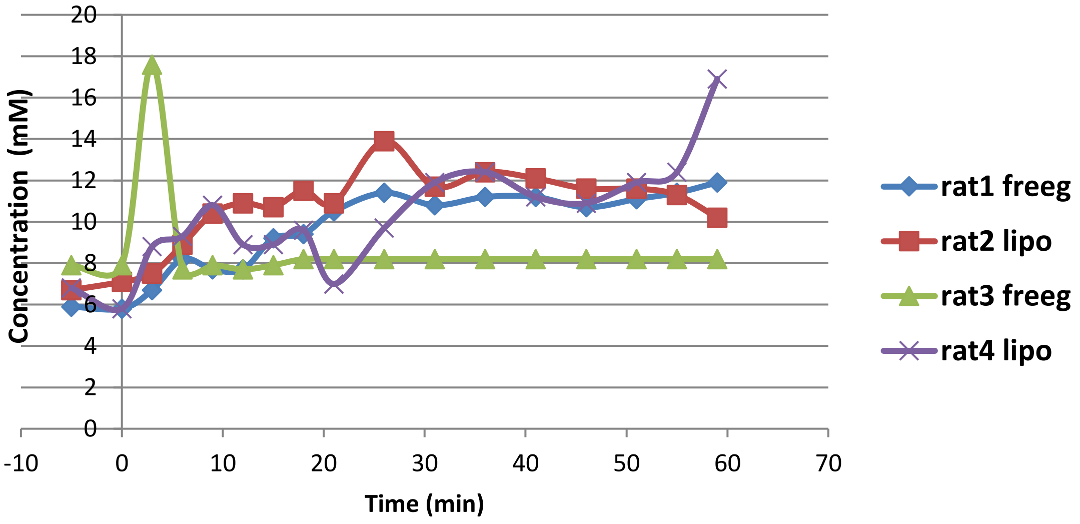

Figure 75. Blood glucose levels for healthy rats (300 g) following administrating of free (rat1&3) or liposomal glucose **L67** (rat2&4) at a dose of 0.1 g/kg (rat1&2) or 0.2 g/kg (rat3&4).

responses in blood glucose levels to injection of free and liposome encapsulated glucose, respectively, at a dose of 0.1 g/kg (Figure 75). The blood glucose profile observed for rat3 following injection of 0.2 g/kg free glucose was exactly what would be expected for a healthy non-diabetic rat, showing a large surge in blood glucose levels approximately 5 min after injection followed by almost immediate return to baseline (Figure 75).[144] The blood glucose levels measured for rat4 after administration of a 0.2 g/kg dose of liposome encapsulated glucose **L67** increased slowly over a 60 min period, reaching a maximum at 60 min that was lower than the peak blood glucose level for rat3 (which received a free glucose bolus injection). These results suggest that peak blood glucose levels can be delayed and reduced *via* liposomal encapsulation.

In conclusion, experiments were carried out *in vivo* to verify that encapsulation of glucose inside liposomes shields the glucose to some extent and could avoid triggering a pronounced insulin response. Old, fat rats were employed as a mammalian model of older, obese patients who are at risk of developing type II diabetes (or have already developed this). Generally, injection of liposomal glucose **L67** led to overall lower blood glucose levels than the same concentration of free glucose. This is significant as it has the potential to make glucoCEST accessible to older/obese patients with type II diabetes. Additionally, liposomal encapsulation could aid in making glucoCEST imaging results more robust and reproducible, as fluctuations in the strength of insulin response between different patients will only be a contributing factor once glucose is released from liposomes.

5.5 Summary – Section 5

This Section described the synthesis of novel saturated short-chain PEG lipids (nEG = 4 or 6) with varying polar termial moieties; -OMe, -OH and -NH_2 (Section 5.1.1). Novel lipids DPPE-EG4-OMe **35**, DPPE-EG4-OH **48** and DPPE-EG4-NH_2 **53** were incorporated into 2-DG encapsulating DPPC-based liposomes at 30 mol% and compared to unPEGylated DPPC liposomes and liposomes PEGylated with 3 mol% DPPE-PEG2000. DPPE-EG4-OMe **35** was unable to be incorporated into DPPC-based liposomes at 30 mol% and formed a viscous gel instead. The encapsulation efficiently of liposomes comprising 30 mol% DPPE-EG4-NH_2 **53** (**L50**) had approximately half the 2-DG loading capacity of liposomes comprising mixtures of DPPC, DPPE-PEG2000 and DPPE-EG4-OH **48**, and therefore produced less CEST signal intensity. Liposomes formulated with 30 mol% DPPE-EG4-OH **48** (**L49**) encapsulated 2-DG well and generated comparable signal to liposomes comprised of commercially available lipids, DPPC and DPPE-PEG2000

(Figure 67, Section 5.1.2). An analogue of this lipid with nEG = 6, DPPE-EG6-OH **49**, was synthesised for future evaluation and comparison to DPPE-EG4-OH **48**.

Two novel saturated chain maleimide-functionalised lipids, Mal1 **54** and Mal2 **61**, were synthesised with a short PEG chain and a quaternary amine moiety as a linker between the lipid tails and the maleimide group, respectively (Section 5.1.3). Three EGFR-targeting peptides were identified in the literature and synthesised *via* an Fmoc solid phase synthesis approach with cysteine-modification at the N-termini, to give CYHWYGYTPQNVI, CLARLLT and CAEYLR (Section 5.1.4). Unfortunately, time did not permit the formulation of EGFR-targeted liposomes.

Cell-based assays were employed to assess the cytotoxic and radiosensitising effects of 2-DG liposomes on a variety of CRC cell lines with a range of different GLUT1 and EGFR expression levels (Section 5.2). The treatment of cells with analogous concentrations of empty liposomes and free PBS solutions were used as control conditions. In every cell line except RKO, there was significantly worse cell survival after treatment with 2-DG encapsulating liposomes in comparison to empty liposomes (Figure 69, Section 5.2), suggesting cytotoxicity of 2-DG to cancer cells once it is either delivered intracellularly by the liposomes, or released from liposomes exterior to the cells and taken up *via* GLUT transporters. SW1417 was the only cell line to demonstrate significantly worse cell survival for liposomal 2-DG versus free 2-DG, suggesting good liposomal uptake and/or poor free 2-DG uptake *via* GLUT transporters (Figure 69). Previous literature has reported low GLUT1 expression for SW1417 cells.[252] Preliminary cell viability assays to test CRC cell lines for 2-DG-induced radiosensitisation from free 2-DG and liposomal 2-DG identified HCT116 as the most promising cell line (Figure 70). However, classic clonogenic assays revealed no appreciable 2-DG-induced radiosensitisation, with poor radiation enhancement ratios of 1.12-1.16 (Figure 71). A literature procedure from Sinthupibulyakit *et al.*[137] was carried out using the same reported cell line (A549 lung cancer cells) and the reported findings coud not be replicated (Figure 72). A potential error in their methods was identified that may have led to false positive results; there was no reported aspect of their procedure to correct for radiation-induced cell death. These results suggest that 2-DG may not be a good radiosensitiser of cancer cells.

Release over-time studies were conducted to determine the nature of glucose and 2-DG leakage from DPPC-based liposomes at 37 °C. It was found that leakage of glucose from liposomes containing 3 mol% DPPE-PEG2000 was slower than for 2-DG, with 1.7% and 10% of encapsulated monosaccharide being released to the exterior solution after 2 hours at 37 °C, respectively (Figure 73, Section 5.3).

Finally, preliminary *in vivo* experiments were conducted in rats to suggest that the shielding of glucose inside liposomes can protect from the immediate and prominent increase in blood glucose following i.v. injection of a glucose bolus, which is a potentially lethal consequence in diabetic patients (Section 5.4). Further experments must be conducted to confirm these results.

6 Conclusion

In Section 2 it was demonstrated that high concentrations of glucose can be encapsulated inside DPPC bilayers when thin films were hydrated with 0.5 M glucose solution. Saturated chain lipids were found to be integral for successful encapsulation (Section 2.1). Using a liposome encapsulation efficiency model developed by Xu *et al.*,[260] it was estimated that the glucose concentration inside liposomes after completing three dialysis cycles was approximately 0.25 M (Section 7.2.3). DPPC liposomes encapsulating glucose were able to generate appreciate CEST signal at both low (1.5 µT) and high (8.0 µT) power, in a linearly concentration-dependent manner for overall glucose concentrations in the range 22-55 mM (Section 2.3). A novel saturated chain glucose-lipid, GlcEG3SLc **11**, was synthesised, however, insertion into DPPC-based bilayers at 20 mol% or 40 mol% was not achieved (Section 2.5).

In Section 3, the incorporation of a lanthanide ion was investigated with the aim of shifting the resonances of the glucose hydroxyl protons further away from the water peak to enhance the selectivity and sensitivity of CEST detection. ^{1}H NMR studies were conducted that indicated that co-encapsulation of glucose with Dy-DOTA or Tm-DOTA chelates can cause a shift in the resonance frequencies of glucose hydroxyl protons, however, there is significant broadening and, more importantly, the water peak is shifted in a similar way, giving rise to small increases in $\Delta\omega$ (Section 3.1). Due to these findings, attempts to synthesise a glucose-DOTA bioconjugate were abandoned and the novel saturated chain DOTA-lipid, DEG3SLc **19**, was not utilised in liposome formulation by our group.

Section 4 explored the factors affecting CEST signal generated by glucose and 2-DG encapsulating liposomes. It was found that optimal CEST signals from both free glucose and free 2-DG solutions at physiological temperature were obtained at approximately pH 6.75 (Section 4.1). The exchangeable hydroxyl protons on glucose and 2-DG were visualised by ^{1}H NMR and assigned using literature values (Section 4.1.1). The hydroxyl signal resonance frequencies remained constant when the pH and monosaccharide concentrations were varied. Thus, we expect the $\Delta\omega$ of individual glucose and 2-DG hydroxyl protons to remain constant in the obtained CEST spectra irrespective of concentration or pH.

DPPC bilayers were able to encapsulate 2-DG in similar quantities to glucose, however, pH-sensitive lipid mixtures from the literature were not rigid enough to encapsulate 2-DG (Section 4.2). The Glucose GO Assay® was employed to measure overall and exterior

2-DG concentrations for liposome samples and was found to have a good agreement with the Glucose HK Assay® and NMR methods, supporting the reliability of the three techniques (Section 4.3).

It is possible that the exchangeable groups in PBS could quench some of the CEST signal from glucose or 2-DG samples evaluated in this buffer system. However, concentrations between 0-20% PBS were found to have no significant effect on CEST signal magnitude generated by free or liposomal 2-DG at 25 °C or 37 °C, pH 6 or pH 7 and low (1.5 µT) or high (5.0 µT) power (Section 4.4.1).

Increasing the temperature in the range 25-37 °C produced progressively larger CEST signals from glucose and 2-DG encapsulating DPPC liposomes, which was thought to be due to the increasing water permeability of the bilayer, enabling enhanced saturation transfer to the bulk water pool. Conversely, increasing the temperature in the same range had little effect on the CEST signal generated by an equal concentration of free 2-DG solution and caused a slight reduction in signal from an equal concentration of free glucose solution (Section 4.4.2).

Formulation of glucose or 2-DG encapsulating DSPC liposomes produced similar overall monosaccharide concentrations as for DPPC liposomes. Monosaccharide encapsulating DPPC liposomes produced greater CEST contrast than the corresponding DSPC liposomes when scanned at all pH, temperature and power combinations (Section 4.4.3). On average, glucose encapsulating DPPC liposomes **L34** and **L35** gave 21% greater CEST signal than glucose encapsulating DSPC liposomes **L36** and **L37** and 2-DG encapsulating DPPC liposomes **L38** and **L39** gave 30% greater CEST signal than 2-DG encapsulating DSPC liposomes **L40** and **L41**. This was assumed to be a product of increased water permeability of the DPPC liposomes and therefore an enhanced ability to transfer saturation to the bulk water population. Interestingly, the increase in CEST signal caused by increasing the temperature from 25 °C to 37 °C was similar for both DPPC and DSPC monosaccharide encapsulating liposomes, however, the increase was significantly more exaggerated for 2-DG encapsulating liposomes (163% for 2-DG liposomes **L38**-**L41** *vs.* 47% for glucose liposomes **L34**-**L37**). This was hypothesised to be in part due to 2-DG leakage from liposomes.

When 2-DG encapsulating DPPC liposomes were sized to 200 nm (**L42**), 150 nm (**L43**) and 120 nm (**L44**), the larger liposomes produced greater CEST signal (Section 4.4.4). However, this was thought to be due to the fact that liposome samples with larger average diameters having greater internal volumes and therefore greater overall 2-DG concentrations. When the liposomes were differentially diluted to give the same overall

2-DG concentration, a small trend in the opposite direction was observed; the smaller liposomes generated slightly larger CEST signals (Figure 60, Section 4.4.4). This was attributed to smaller liposomes having a greater surface-area-to-volume ratio and greater curvature leading to a less closely packed lipid bilayer. Both of these factors can give rise to greater water exchange across the bilayer to enable transfer of saturation to the bulk exterior water population.[211]

Finally in Section 4, DPPC-based 2-DG encapsulating liposomes were fluorescently labelled *via* incorporation of 0.5% DPPE-Rh to confirm that this alteration to the bilayer did not significantly affect encapsulation or CEST signal generation from encapsulated 2-DG (Section 4.5). Therefore, these liposomes could be used in future *in vivo* biodistribution experiments.

Section 5 described the synthesis of novel saturated short-chain PEG lipids (nEG = 4 or 6) with varying polar termial moieties; -OMe, -OH and -NH_2 (Section 5.1.1). These lipids, DPPE-EG4-OMe **35**, DPPE-EG4-OH **48** and DPPE-EG4-NH_2 **53** were incorporated into 2-DG encapsulating DPPC-based liposomes at 30 mol% and compared to unPEGylated DPPC liposomes and liposomes PEGylated with 3 mol% DPPE-PEG2000. DPPE-EG4-OMe **35** was unable to be incorporated into DPPC-based liposomes at 30 mol% and formed a viscous gel instead. The encapsulation efficiently of liposomes comprising 30 mol% DPPE-EG4-NH_2 **53** (**L50**) had approximately half the 2-DG loading capacity of liposomes comprising mixtures of DPPC, DPPE-PEG2000 and DPPE-EG4-OH **48**, and therefore produced less CEST signal intensity. Whereas, liposomes formulated with 30 mol% DPPE-EG4-OH **48** (**L49**) encapsulated 2-DG well and generated comparable signal to liposomes comprised of commercially available lipids, DPPC and DPPE-PEG2000 (Figure 67, Section 5.1.2). An analogue of this lipid with nEG = 6, DPPE-EG6-OH **49**, was synthesised for future evaluation and comparison to DPPE-EG4-OH **48**.

Two novel saturated chain maleimide-functionalised lipids, Mal1 **54** and Mal2 **61**, were synthesised with a short PEG chain and a quaternary amine moiety as a linker between the lipid tails and the maleimide group, respectively (Section 5.1.3). Three EGFR-targeting peptides were identified in the literature and synthesised *via* an Fmoc solid phase synthesis approach with cysteine-modification at the N-termini, to give CYHWYGYTPQNVI, CLARLLT and CAEYLR (Section 5.1.4). Unfortunately, time did not permit the formulation of EGFR-targeted liposomes.

Cell-based assays were employed to assess the cytotoxic and radiosensitising effects of 2-DG liposomes on a variety of CRC cell lines with a range of different GLUT1 and EGFR expression levels (Section 5.2). Treatment of cells with analogous concentrations of empty liposomes and free PBS solutions were used as control conditions. In every cell line except RKO, there was significantly worse cell survival after treatment with 2-DG encapsulating liposomes in comparison to empty liposomes (Figure 69, Section 5.2), suggesting cytotoxicity of 2-DG to cancer cells once it is either delivered intracellularly by the liposomes or released from liposomes exterior to the cells and taken up *via* GLUT transporters. SW1417 was the only cell line to demonstrate significantly worse cell survival for liposomal 2-DG versus free 2-DG, suggesting good liposomal uptake and/or poor free 2-DG uptake *via* GLUT transporters (Figure 69). Previous literature has reported low GLUT1 expression for SW1417 cells.[252] Preliminary cell viability assays to test colorectal cancer cell lines for 2-DG-induced radiosensitisation from free 2-DG and liposomal 2-DG identified HCT116 as the most promising cell line (Figure 70). However, classic clonogenic assays revealed no appreciable 2-DG-induced radiosensitisation, with poor radiation enhancement ratios of 1.12-1.16 (Figure 71). A literature procedure from Sinthupibulyakit *et al.*[137] was carried out using the same reported cell line (A549 lung cancer cells), the reported findings were not replicated (Figure 72). A potential error in their methods was identified that may have led to false positive results; there was no reported aspect of their procedure to correct for radiation-induced cell death. These results suggest that 2-DG may not be a good radiosensitiser of cancer cells.

Release over-time studies were conducted to determine the nature of glucose and 2-DG leakage from DPPC-based liposomes at 37 °C. It was found that leakage of glucose from liposomes containing 3 mol% DPPE-PEG2000 was slower than for 2-DG, with 1.7% and 10% of encapsulated monosaccharide being released to the exterior solution after 2 hours at 37 °C, respectively (Figure 73, Section 5.3).

Finally, preliminary *in vivo* experiments were conducted in rats to suggest that the shielding of glucose inside liposomes can protect from the immediate and prominent increase in blood glucose following i.v. injection of a glucose bolus, which is a potentially lethal consequence in diabetic patients (Section 5.4).

6.1 Future work

6.1.1 Tuning the rigidity of the bilayer

DPPC-based lipid compositions have been identified as suitable for encapsulating high concentrations of glucose or 2-DG (~ 0.25 M encapsulated concentration) at room temperature and the leakage of monosaccharides at 37 °C has been characterised. However, the leakage profiles of glucose and 2-DG from various liposomes must be determined *in vivo*. Preliminary experiments reported in Section 5.4 suggest that blood glucose levels rise at a slightly slower rate and reach slightly smaller maximum values when liposomal glucose is administered versus free glucose. However, more rigid liposomes such as those based on DSPC instead of DPPC, or incorporating cholesterol, should be investigated to achieve a slower release profile and further reduce maximum blood glucose levels. This would prolong the length of generated CEST signal *in vivo*, correct for large inter-person differences in the strength of insulin response and make the use of glucose liposomes safer in diabetic patients. However, the CEST signal generated by more rigid liposomes encapsulating monosaccharides may be smaller than for DPPC liposomes, as was found for DSPC liposomes in Section 4.4.3. The effect of including cholesterol in the liposome bilayer on monosaccharide retention under physiological conditions and the generated CEST signal could be investigated in future work.

6.1.2 Optimising PEGylation

The stealth liposome properties conferred by incorporation of DPPE-EG4-OH **48** and the hexaethylene glycol analogue, DPPE-EG6-OH **49**, must be investigated in future work. Studies are required to optimise the *in vivo* biodistribution of liposomes formulated with these novel short-chain PEG lipids. The biodistribution of liposomes formulated with 30 mol%, 40 mol% and 50 mol% of DPPE-EG4-OH **48** or DPPE-EG6-OH **49** should be characterised and compared to optimise the PEG coating and achieve maximum accumulation in tumors. The extent of tumor accumulation could be assessed by both CEST imaging and fluorescent techniques made possible *via* the incorporation of a small molar percentages of DPPE-Rh (0.5-2 mol%).

Additionally, resazurin cell viability assays could be used to assess whether the shallower, more uniform PEG coating conferred by DPPE-EG4-OH **48** or DPPE-EG6-OH **49** could enhance 2-DG encapsulating liposome uptake by cancer cell lines *in vitro*.

6.1.3 Formulation of EGFR-targeted liposomes

With the aim of producing EGFR-targeted liposomes, liposomes should be formulated with 10 mol% of a novel saturated maleimide-lipid, Mal1 **54** or Mal2 **61**. These liposomes must first be tested for their ability to stably encapsulate high concentrations of glucose and 2-DG. Following formulation, the synthesised cysteine-modified EGFR-targeting peptides, CYHWYGYTPQNVI, CLARLLT and CAEYLR, should be coupled to the surface of liposomes *via* a thiol-maleimide coupling reaction that can be carried out in water at neutral pH (Figure 64, Section 5.1).[239,261] Unconjugated peptide can be removed *via* dialysis and the efficiency of peptide conjugation to liposomes should be evaluated. A literature example of how this could be done is by indirectly quantifying the number of un-conjugated maleimide groups on the surface of liposomes by adding a known amount of cysteine, assuming all external maleimide moieties are blocked stoichiometrically by cysteine addition, and determining the amount of unreacted cysteine using an Ellman's reaction.[261] In Ellman's reaction, a known amount of 5,5'-dithiobis-(2-nitrobenzoic acid) (DTNB) is added to react with the unreacted cysteine, leading to the formation of a cysteine-TNB (5-thio-2-nitrobenzoic acid) adduct and causing the concomitant release of an equivalent of free TNB. The amount of liberated TNB can be analysed by HPLC to estimate the amount of cysteine used for adduct formation and therefore the amount of cysteine that reacted to block free maleimide groups on the liposome surface. An initial Ellman reaction is required to quantify the percentage of maleimide lipid that is outward facing (Kang *et al.* found this to be 51 ± 2.3% for liposomes with an average diameter of 165 nm, irrespective of the amount of DSPE-PEG2000-mal in the range 0.2-4 mol%).[261]

It has been reported that cysteine functionalised peptides that have been conjugated to nanoparticles or other functional molecules *via* reaction with maleimide moieties can undergo an irreversible cyclization reaction (Figure 76).[262,263] The intramolecular rearrangement could prevent a possible retro-Michael reaction of the maleimide moiety with thiol-containing peptides and therefore increase the stability of peptide-conjugated liposomes in biological environments such as blood serum. Determining whether this process occurs in our liposomal system could be investigated in future work.

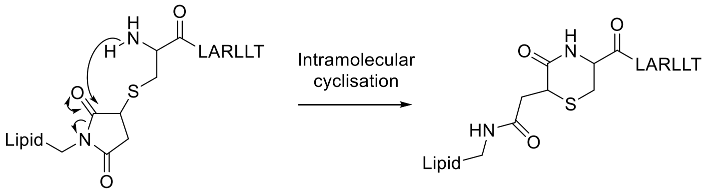

Figure 76. Reported intramolecular cyclisation for maleimide-cysteine coupled conjugates.

6.1.4 Assessing the efficacy of the EGFR-targeting strategy

Liposomes exhibiting targeting moieties have been shown to achieve enhanced cellular uptake by target cells.[171] The ability of the EGFR-targeting peptides to achieve cellular internalisation of 2-DG encapsulating liposomes could be assessed using resazurin cell viability assays due to the cytotoxicity caused by 2-DG. A more accurate method would be to include a fluorescent lipid in the bilayer of liposomes to enable quantitative analysis of cellular uptake *via* fluorescence-activated cell sorting (FACS). EGFR-targeted liposomes should be compared to un-targeted control liposomes. The targeting efficiencies of the three peptides CYHWYGYTPQNVI, CLARLLT and CAEYLR should be comparatively evaluated. Other peptide sequences from the literature could also be trialled, or C-terminal cysteine modification could be carried out for YHWYGYTPQNVI, LARLLT and AEYLR to assess whether conjugation to the liposomes *via* the C-terminus instead of the N-terminus can affect targeting efficiency.

Once the optimal targeting peptide has been indentified *in vitro*, *in vivo* experiments should be carried out in murine xenograft models to assess the differences in tumor accumulaton over time of EGFR-targeted liposomes versus untargeted liposomes. Literature *in vivo* studies on targeted liposomes have shown that liposome accumulation at the tumor site can be enhanced and prolonged in comparison to control liposomes.[107,245,246]

6.1.5 Evaluate glucose and 2-DG liposomes as viable CEST imaging agents *in vivo*

The monosaccharide encapsulating liposomal CEST CAs with optimised PEGylation and EGFR-targeting moieties should be employed in imaging studies carried out in murine xenograft models. The magnitude and length of tumor CEST contrast should be assessed for: both free glucose and free 2-DG; liposome encapsulated glucose and 2-DG with optimised PEGylation; and EGFR-targeted versus untargeted monosaccharide encapsulating liposomes.

To evaluate the reliability of CEST results, images could be compared to standard FDG-PET imaging techniques. It would be interesting to compare the CEST imaging results to findings from fluorescent imaging techniques, for example using small amounts of DPPE-Rh (0.5-2 mol%). The culling of mice followed by fluorescence microscopy would need to be carried out directly after CEST image acquitiion to investigate whether the greatest signal intensity correlates with the location of the liposomes or whether the glucose or 2-DG has leaked from liposomes and accumulated separately. Alternatively, near-infrared fluorescence studies can be used to monitor the biodistribution pattern of liposomes over time in the same live animals by labelling liposomes with dyes such as Cy7.[247]

6.1.6 Evaluating the cytotoxicity of 2-DG to cancer cells

2-DG was not found to be an effective radiosensitiser in the tested CRC cell lines, or in a cell line for which 2-DG-induced radiosensitivity was reported in the literature (A549) when repeating the same experimental conditions. Thus, further radiosensitisation experiments employing liposomal 2-DG are not warranted due to uncertainty over whether 2-DG is a good radiosensitiser in cancer cells. Nonetheless, cytotoxicity was observed in various CRC cell lines excluding a radiation dose, so the therapeutic benefits of liposomal 2-DG as a glycolytic inhibitor in cancer cell lines should be investigated *in vivo* in future work.

Firstly, the cytotoxic effect of liposomal 2-DG should be investigated in selected cell lines *in vitro* employing resazurin assays once PEGylation and targeting parameters have been optimised. Secondly, the cytotoxic properties can be studied *in vivo* by observing the effect of 2-DG liposome administration on tumor size over time. This experiment could be done on the same mice used in the imaging studies discussed in Section 6.1.5. Tumor size can be evaluated by imaging techniques (CEST or FDG-PET) or by culling the animals and manually measuring tumor size for two experimental groups, e.g. one group which was administered with liposomal glucose over a certain time period and one group which was administered with liposomal 2-DG.

References

1 F. Torre, R. L. Siegel, J. Ferlay, J. Lortet-Tieulent, A. Jemal and L. A. Bray, Global cancer statistics, 2012, *CA Cancer J. Clin.*, 2015, **65**, 87–108.

2 J. Ferlay, I. Soerjomataram and R. Dikshit, Cancer incidence and mortality worldwide: sources, methods and major patterns in GLOBOCAN 2012, *Int. J. Cancer*, 2015, **136**, E359-86.

3 American Cancer Society, *Global Cancer Facts & Figures 3rd Edition*, Atlanta, 2015.

4 D. Hanahan and R. A. Weinberg, The hallmarks of cancer, *Cell*, 2000, **100**, 57–70.

5 D. Hanahan and R. A. Weinberg, Hallmarks of cancer: The next generation, *Cell*, 2011, **144**, 646–674.

6 M. Potter, E. Newport and K. J. Morten, The Warburg effect: 80 years on, *Biochem. Soc. Trans.*, 2016, **44**, 1499–1505.

7 C. C. Barron, P. J. Bilan, T. Tsakiridis and E. Tsiani, Facilitative glucose transporters: Implications for cancer detection, prognosis and treatment, *Metabolism.*, 2016, **65**, 124–139.

8 T. A. D. Smith, Mammalian hexokinases and their abnormal expression in cancer, *Br. J. Biomed. Sci.*, 2000, **57**, 170–178.

9 R. A. Gatenby and R. J. Gillies, Why do cancers have high aerobic glycolysis?, *Nat. Rev. Cancer*, 2004, **4**, 891–899.

10 M. Vander Heiden, L. Cantley and C. Thompson, Understanding the Warburg effect: The metabolic Requirements of cell proliferation, *Science (80-.).*, 2009, **324**, 1029–1033.

11 R. L. Krisher and R. S. Prather, A Role for the Warburg Effect in Preimplantation Embryo Development: Metabolic Modification to Support Rapid Cell Proliferation, *Mol. Reprod. Dev.*, 2012, **79**, 311–320.

12 J. Condeelis and R. Weissleder, In vivo imaging in cancer, *Cold Spring Harb. Perspect. Biol.*, 2010, **2**, 1–22.

13 P. W. Miller, N. J. Long, R. Vilar and A. D. Gee, Synthesis of 11C, 18F, 15O, and 13N radiolabels for positron emission tomography, *Angew. Chemie - Int. Ed.*, 2008, **47**, 8998–9033.

14 E. Arstad and E. Robins, PET Radiotracers, *Clin. PET PET/CT*, 2008, **167**, 45–68.

15 L. Fass, Imaging and cancer: A review, *Mol. Oncol.*, 2008, **2**, 115–152.

16 J. V. Frangioni, New technologies for human cancer imaging, *J. Clin. Oncol.*, 2008, **26**, 4012–4021.

17 L. K. Griffeth, Use of PET/CT scanning in cancer patients: technical and practical considerations, *Proc. (Bayl. Univ. Med. Cent).*, 2005, **18**, 321–30.

18 W. W. Moses, Fundamental Limits of Spatial Resolution in PET, *Nucl. Instrum. Methods Phys. Res. A.*, 2011, **684**, S236–S240.

19 A. Almuhaideb, N. Papthanasiou and J. Bomanji, 18F-FDG PET/CT Imaging In Oncology, *Ann. Saudi Med.*, 2011, **31**, 3–13.

20 U. G. Mueller-Lisse and U. L. Mueller-Lisse, Imaging of advanced renal cell carcinoma, *World J. Urol.*, 2010, **28**, 253–261.

21 S. Pavlides, D. Whitaker-Menezes, R. Castello-Cros, N. Flomenberg, A. K. Witkiewicz, P. G. Frank, M. C. Casimiro, C. Wang, P. Fortina, S. Addya, R. G. Pestell, U. E. Martinez-Outschoorn, F. Sotgia and M. P. Lisanti, The reverse Warburg effect: Aerobic glycolysis in cancer associated fibroblasts and the tumor stroma, *Cell Cycle*, 2009, **8**, 3984–4001.

22 D. J. Brenner, C. D. Elliston, E. J. Hall and W. E. Berdon, Estimated Risks of Radiation - Induced Fatal Cancer from Pediatric CT, *Am. J. Roentgenol.*, 2001, **176**, 289–296.

23 C. Tu, E. A. Osborne and A. Y. Louie, Activatable T1 and T2 magnetic resonance imaging contrast agents, *Ann. Biomed. Eng.*, 2011, **39**, 1335–1348.

24 M. Van Der Graaf, In vivo magnetic resonance spectroscopy: Basic methodology and clinical applications, *Eur. Biophys. J.*, 2010, **39**, 527–540.

25 R. Damadian, Tumor Detection by Nuclear Magnetic Resonance, *Science (80-.).*, 1971, **171**, 1151–1153.

26 G. J. Strijkers, W. J. M. Mulder, G. A. F. van Tilborg and K. Nicolay, MRI Contrast Agents: Current Status and Future Perspectives, *Anticancer. Agents Med. Chem.*, 2007, **7**, 291–305.

27 Z. Zhou and Z.-R. Lu, Gadolinium-Based Contrast Agents for MR Cancer Imaging, *Wiley Interdiscp. Rev. Nanomed. Nanobiotechnol.*, 2013, **5**, 1–18.

28 J. R. Morrow and É. Tóth, Next-Generation Magnetic Resonance Imaging Contrast Agents, *Inorg. Chem.*, 2017, **56**, 6029–6034.

29 J. Garcia, S. Z. Liu and A. Y. Louie, Biological effects of MRI contrast agents: gadolinium retention, potential mechanisms and a role for phosphorus, *Philos. Trans. A Math. Phys. Eng. Sci.*, 2017, **375**, 1–28.

30 J. B. Lansman, Blockade of current through single calcium channels by trivalent lanthanide cations. Effect of ionic radius on the rates of ion entry and exit, *J. Gen. Physiol.*, 1990, **95**, 679–696.

31 https://www.gov.uk/drug-safety-update/gadolinium-containing-contrast-agents-removal-of-omniscan-and-iv-magnevist-restrictions-to-the-use-of-other-linear-agents, accessed 11/08/18.

32 C.-H. Huang and A. Tsourkas, Gd-based macromolecules and nanoparticles as magnetic resonance contrast agents for molecular imaging, *Curr. Top. Med. Chem.*, 2013, **13**, 411–421.

33 S. L. Fossheim, A. K. Fahlvik, J. Klaveness and R. N. Muller, Paramagnetic liposomes as MRI contrast agents: Influence of liposomal physicochemical properties on the in vitro relaxivity, *Magn. Reson. Imaging*, 1999, **17**, 83–89.

34 M. Botta and L. Tei, Relaxivity enhancement in macromolecular and nanosized Gd III-based MRI contrast agents, *Eur. J. Inorg. Chem.*, 2012, **2012**, 1945–1960.

35 H. Daldrup, D. M. Shames, M. Wendland, Y. Okuhata, T. M. Link, W. Rosenau, L. Ying and R. C. Brasch, Correlation of Dynamic Contrast Enhanced MR Imaging with Histologic Tumor Grade: Comparison of Macromolecular and Small-Molecular Contrast Media, *Pediatr. Radiol.*, 1998, **28**, 67–78.

36 E. C. Unger, T. Winokur, P. Macdougall, J. Rosenblum, M. Clair, R. Gatenby and C. Tilcock, Hepatic metastases: liposomal Gd-DTPA-enhanced MR imaging, *Radiology*, 1989, **171**, 81–85.

37 C. Tilcock, E. Unger, P. Cullis and P. Macdougall, Liposomal Gd-DTPA: Preparation and Characterization of Relaxivity, *Radiology*, 1989, **171**, 77–80.

38 K. B. Ghaghanda, M. Ravoori, D. Sabapathy, J. Bankson, V. Kundra and A.

Annapraganda, New dual mode gadolinium nanoparticle contrast agent for magnetic resonance imaging, *PLoS One*, 2009, **4**, 1–7.

39 M. Bottrill, L. Kwok and N. J. Long, Lanthanides in magnetic resonance imaging, *Chem. Soc. Rev.*, 2006, **35**, 557.

40 M. Haris, S. K. Yadav, A. Rizwan, A. Singh, E. Wang, H. Hariharan, R. Reddy and F. M. Marincola, Molecular magnetic resonance imaging in cancer, *J. Transl. Med.*, 2015, **13**, 313.

41 K. Glunde and Z. M. Bhujwalla, Metabolic Tumor Imaging Using Magnetic Resonance Spectroscopy, *Semin Oncol.*, 2012, **38**, 26–41.

42 B. Wu, G. Warnock, M. Zaiss, C. Lin, M. Chen, Z. Zhou, L. Mu, D. Nanz, R. Tuura and G. Delso, An overview of CEST MRI for non-MR physicists, *EJNMMI Phys.*, 2016, **3**, 19.

43 R. J. Gillies and D. L. Morse, In Vivo Magnetic Resonance Spectroscopy in Cancer, *Annu. Rev. Biomed. Eng.*, 2005, **7**, 287–326.

44 H. Shimizu, T. Kumabe, R. Shirane and T. Yoshimoto, Correlation between choline level measured by proton MR spectroscopy and Ki-67 labeling index in gliomas, *Am. J. Neuroradiol.*, 2000, **21**, 659–665.

45 P. J. Bolan, S. Meisamy, E. H. Baker, J. Lin, T. Emory, M. Nelson, L. I. Everson, D. Yee and M. Garwood, In Vivo Quantification of Choline Compounds in the Breast with 1H MR Spectroscopy, *Magn. Reson. Med.*, 2003, **50**, 1134–1143.

46 L. Porto, M. Kieslich, K. Franz, T. Lehrnbecher, F. Zanella, U. Pilatus and E. Hattingen, MR spectroscopy differentiation between high and low grade astrocytomas: A comparison between paediatric and adult tumours, *Eur. J. Paediatr. Neurol.*, 2011, **15**, 214–221.

47 R. G. Steen, Review Response of Solid Tumors to Chemotherapy Monitored by in Vivo 31P Nuclear Magnetic Resonance Spectroscopy : A Review, *Cancer Res.*, 1989, **49**, 4075–4085.

48 S. M. Ronen and M. O. Leach, Imaging biochemistry: applications to breast cancer, *Breast Cancer Res.*, 2001, **3**, 36–40.

49 M. J. Albers, R. Bok, A. P. Chen, C. H. Cunningham, M. L. Zierhut, V. Y. Zhang, S. J. Kohler, J. Tropp, R. E. Hurd, Y. Yen, S. J. Nelson, D. B. Vigneron and J. Kurhanewicz, Hyperpolarized 13C Lactate, Pyruvate, and Alanine: Noninvasive Biomarkers for Prostate Cancer Detection and Grading, *Cancer Res.*, 2008, **68**, 8607–8616.

50 J. Kurhanewicz, D. B. Vigneron, K. Brindle, E. Y. Chekmenev, R. J. Deberardinis, G. G. Green, R. R. Rizi, B. D. Ross, W. S. Warren and C. R. Malloy, Analysis of Cancer Metabolism by Imaging Hyperpolarized Nuclei: Prospects for Translation to Clinical Research, *Neoplasia*, 2011, **13**, 81–97.

51 C. Najac and S. M. Ronen, MR molecular imaging of brain cancer metabolism using hyperpolarized 13C magnetic resonance spectroscopy, *Top. Magn. Reson. Imaging*, 2016, **25**, 187–196.

52 S. J. Nelson, J. Kurhanewicz, D. B. Vigneron, P. E. Z. Larson, A. L. Harzstark, M. Ferrone, M. Van Criekinge, J. W. Chang, I. Park, G. Reed, L. Carvajal, E. J. Small, P. Munster, K. Weinberg, J. H. Ardenkjaer-larsen, A. P. Chen, R. E. Hurd, F. J. Robb, J. Tropp and J. A. Murray, Metabolic Imaging of Patients with Prostate Cancer Using Hyperpolarized [1-13C]Pyruvate, *Sci. Transl. Med.*, 2013, **5**, 1–22.

53 W. K. J. Renema, H. E. Kan, B. Wieringa and A. Heerschap, In vivo magnetic resonance spectroscopy of transgenic mouse models with altered high-energy

phosphoryl transfer metabolism, *NMR Biomed.*, 2007, **20**, 448–467.

54 C. Li, M. F. Penet, P. Winnard, D. Artemov and Z. M. Bhujwalla, Image-guided enzyme/prodrug cancer therapy, *Clin. Cancer Res.*, 2008, **14**, 515–522.

55 S. Blüml and A. Panigrahy, in *MR Spectroscopy of Pediatric Brain Disorders*, Springer-Verlag New York Inc., 2013, pp. 11–23.

56 K. W. Y. Chan, M. T. McMahon, Y. Kato, G. Liu, J. W. M. Bulte, Z. M. Bhujwalla, D. Artemov and P. C. M. van Zijl, Natural D-glucose as a biodegradable MRI contrast agent for detecting cancer, *Magn. Reson. Med.*, 2012, **68**, 1764–1773.

57 K. W. Y. Chan, J. W. M. Bulte and M. T. McMahon, Diamagnetic chemical exchange saturation transfer (diaCEST) liposomes: Physicochemical properties and imaging applications, *Wiley Interdiscip. Rev. Nanomedicine Nanobiotechnology*, 2014, **6**, 111–124.

58 P. C. M. van Zijl and N. N. Yadav, Chemical exchange saturation transfer (CEST): what is in a name and what isn't?, *Magn. Reson. Med.*, 2011, **65**, 927–948.

59 P. C. M. van Zijl, W. W. Lam, J. Xu, L. Knutsson and G. J. Stanisz, Magnetization Transfer Contrast and Chemical Exchange Saturation Transfer MRI. Features and analysis of the field-dependent saturation spectrum, *Neuroimage*, 2018, **168**, 222–241.

60 O. M. Evbuomwan, E. Terreno, S. Aime and A. D. Sherry, in *The Chemistry of Molecular Imaging*, Wiley Blackwell, 1 edition., 2015, pp. 225–243.

61 K. M. Ward, A. H. Aletras and R. S. Balaban, A New Class of Contrast Agents for MRI Based on Proton Chemical Exchange Dependent Saturation Transfer (CEST), *J. Magn. Reson.*, 2000, **143**, 79–87.

62 M. Woods, D. E. Woessner and A. D. Sherry, Paramagnetic lanthanide complexes as PARACEST agents for medical imaging, *Chem. Soc. Rev.*, 2006, **35**, 500–511.

63 K. Cai, M. Haris, A. Singh, F. Kogan, J. Greenberg, H. Hariharan, J. A. Detre and R. Reddy, Magnetic Resonance Imaging of Glutamate, *Nat. Med.*, 2012, **18**, 302–306.

64 E. Vinogradov, A. D. Sherry and R. E. Lenkinski, CEST: From basic principles to applications, challenges and opportunities, *J. Magn. Reson.*, 2013, **229**, 155–172.

65 A. D. Sherry and M. Woods, Chemical Exchange Saturation Transfer Contrast Agents for Magnetic Resonance Imaging, *Annu. Rev. Biomed. Eng.*, 2008, **10**, 391–411.

66 J. Zhou, B. Lal, D. A. Wilson, J. Laterra and P. C. M. van Zijl, Amide Proton Transfer (APT) Contrast for Imaging of Brain Tumors, *Magn. Reson. Med.*, 2003, **50**, 1120–1126.

67 W. Ling, R. R. Regatte, G. Navon and A. Jerschow, Assessment of glycosaminoglycan concentration in vivo by chemical exchange-dependent saturation transfer (gagCEST), *Proc. Natl. Acad. Sci.*, 2008, **105**, 2266–2270.

68 P. C. van Zijl, C. K. Jones, J. Ren, C. R. Malloy and A. D. Sherry, MRI detection of glycogen in vivo by using chemical exchange saturation transfer imaging (glycoCEST), *Proc. Natl. Acad. Sci.*, 2007, **104**, 4359–4364.

69 J. Zhou, J. F. Payen, D. A. Wilson, R. J. Traystman and P. C. M. van Zijl, Using the amide proton signals of intracellular proteins and peptides to detect pH effects in MRI, *Nat. Med.*, 2003, **9**, 1085–1090.

70 J. Zhou, E. Tryggestad, Z. Wen, B. Lal, T. Zhou, R. Grossman, S. Wang, K. Yan, D. X. Fu, E. Ford, B. Tyler, J. Blakeley, J. Laterra and P. C. M. van Zijl, Differentiation between glioma and radiation necrosis using molecular magnetic resonance imaging of endogenous proteins and peptides, *Nat. Med.*, 2011, **17**, 130–134.

71 X. Zhao, Z. Wen, G. Zhang, F. Huang, S. Lu, X. Wang, S. Hu, M. Chen and J. Zhou, Three-Dimensional Turbo-Spin-Echo Amide Proton Transfer MR Imaging at 3 Tesla and Its Application to High-Grade Human Brain Tumors, *Mol. Imaging Biol.*, 2013, **15**, 114–122.

72 O. Togao, T. Yoshiura, J. Keupp, A. Hiwatashi, K. Yamashita, K. Kikuchi, Y. Suzuki, S. O. Suzuki, T. Iwaki, N. Hata, M. Mizoguchi, K. Yoshimoto, K. Sagiyama, M. Takahashi and H. Honda, Amide proton transfer imaging of adult diffuse gliomas: Correlation with histopathological grades, *Neuro. Oncol.*, 2014, **16**, 441–448.

73 C. K. Jones, M. J. Schlosser, P. C. M. van Zijl, M. G. Pomper, X. Golay and J. Zhou, Amide proton transfer imaging of human brain tumors at 3T, *Magn. Reson. Med.*, 2006, **56**, 585–592.

74 Y. Ohno, M. Yui, H. Koyama, T. Yoshikawa, S. Seki, Y. Ueno, M. Miyazaki, C. Ouyang and K. Sugimura, Chemical Exchange Saturation Transfer MR Imaging : Preliminary Results for Differentiation of Malignant and Benign Thoracic Lesions, *Radiology*, 2016, **279**, 578–589.

75 A. N. Dula, L. R. Arlinghaus, R. D. Dortch, B. E. Dewey, J. G. Whisenant, G. D. Ayers, T. E. Yankeelov and S. A. Smith, Amide Proton Transfer Imaging of the Breast at 3 T: Establishing Reproducibility and Possible Feasibility Assessing Chemotherapy Response, *Magn. Reson. Med.*, 2013, **70**, 216–224.

76 O. Togao, C. W. Kessinger, G. Huang, T. C. Soesbe, K. Sagiyama, I. Dimitrov, A. D. Sherry, J. Gao and M. Takahashi, Characterization of Lung Cancer by Amide Proton Transfer (APT) Imaging: An In-Vivo Study in an Orthotopic Mouse Model, *PLoS One*, 2013, **8**, 1–6.

77 X. Song, R. D. Airan, D. R. Arifin, A. Bar-Shir, D. K. Kadayakkara, G. Liu, A. A. Gilad, P. C. M. van Zijl, M. T. McMahon and J. W. M. Bulte, Label-free in vivo molecular imaging of underglycosylated mucin-1 expression in tumour cells, *Nat. Commun.*, 2015, **6**, 1–7.

78 D. W. Kufe, Mucins in cancer: function, prognosis and therapy, *Nat. Rev. Cancer*, 2009, **9**, 874–885.

79 M. Haris, A. Singh, I. Mohammed, R. Ittyerah, K. Nath, R. P. R. Nanga, C. Debrosse, F. Kogan, K. Cai, H. Poptani, D. Reddy, H. Hariharan and R. Reddy, In vivo magnetic resonance imaging of tumor protease activity, *Sci. Rep.*, 2014, **4**, 1–5.

80 C. Li, Poly(L-glutamic acid)-anticancer drug conjugates, *Adv. Drug Deliv. Rev.*, 2002, **54**, 695–713.

81 H. Liu, A. Jablonska, Y. Li, S. Cao, D. Liu, H. Chen, P. C. M. van Zijl, J. W. M. Bulte, M. Janowski, P. Walczak and G. Liu, Label-free CEST MRI detection of citicoline-liposome drug delivery in ischemic stroke, *Theranostics*, 2016, **6**, 1588–1600.

82 M. M. Pagel, The pursuit of theranostics with CEST MRI, *Theranostics*, 2016, **6**, 1601–1602.

83 Y. Li, H. Chen, J. Xu, N. N. Yadav, K. W. Y. Chan, L. Luo, M. T. McMahon, B. Vogelstein, P. C. M. van Zijl, S. Zhou and G. Liu, CEST theranostics: label-free MR imaging of anticancer drugs., *Oncotarget*, 2016, **7**, 6369–78.

84 S. Walker-Samuel, R. Ramasawmy, F. Torrealdea, M. Rega, V. Rajkumar, S. P. Johnson, S. Richardson, M. Gonçalves, H. G. Parkes, E. Årstad, D. L. Thomas, R. B. Pedley, M. F. Lythgoe and X. Golay, In vivo imaging of glucose uptake and metabolism in tumors, *Nat. Med.*, 2013, **19**, 1067–1072.

85 J. Wang, J. Weygand, K.-P. Hwang, A. S. R. Mohamed, Y. Ding, C. D. Fuller, S. Y. Lai, S. J. Frank and J. Zhou, Magnetic Resonance Imaging of Glucose Uptake and Metabolism in Patients with Head and Neck Cancer, *Sci. Rep.*, 2016, **6**, 1–7.

86 M. Rivlin, J. Horev, I. Tsarfaty and G. Navon, Molecular imaging of tumors and metastases using chemical exchange saturation transfer (CEST) MRI, *Sci. Rep.*, 2013, **3**, 1–7.

87 T. Jin, H. Mehrens, K. S. Hendrich and S.-G. Kim, Mapping Brain Glucose Uptake with Chemical Exchange-Sensitive Spin-Lock Magnetic Resonance Imaging, *J. Cereb. Blood Flow Metab.*, 2014, **34**, 1402–1410.

88 X. Xu, N. N. Yadav, L. Knutsson, J. Hua, R. Kalyani, E. Hall, J. Laterra, J. Blakeley, R. Strowd, M. Pomper, P. Barker, G. Liu, M. T. Mcmahon, R. D. Stevens and C. M. van Zijl, Peter, Dynamic glucose-enhanced (DGE) MRI: translation to human scanning and first results in glioma patients, *Tomography*, 2015, **1**, 105–114.

89 X. Xu, K. W. Chan, L. Knutsson, D. Artemov, J. Xu, G. Liu, Y. Kato, B. Lal, J. Laterra, M. T. McMahon and P. C. M. van Zjil, Dynamic Glucose Enhanced (DGE) MRI for Combined Imaging of Blood Brain Barrier Break Down and Increased Blood Volume in Brain Cancer, *Magn. Reson. Imaging*, 2015, **74**, 1556–1563.

90 D. Kentrup, P. Bovenkamp, A. Busch, K. Schuette-Nuetgen, H. Pawelski, H. Pavenstädt, E. Schlatter, K. H. Herrmann, J. R. Reichenbach, B. Löffler, B. Heitplatz, V. Van Marck, N. N. Yadav, G. Liu, P. C. M. van Zijl, S. Reuter and V. Hoerr, GlucoCEST magnetic resonance imaging in vivo may be diagnostic of acute renal allograft rejection, *Kidney Int.*, 2017, **92**, 757–764.

91 D. Artemov, Z. M. Bhujwalla, U. Pilatus and J. D. Glickson, Two-compartment model for determination of glycolytic rates of solid tumors by in vivo 13C NMR spectroscopy, *NMR Biomed.*, 1998, **11**, 395–404.

92 F. Danhier, O. Feron and V. Préat, To exploit the tumor microenvironment: Passive and active tumor targeting of nanocarriers for anti-cancer drug delivery, *J. Control. Release*, 2010, **148**, 135–146.

93 X. Golay, *Unpublished Results*, 2016.

94 D. W. Vere, C. H. Sykes and P. Armitage, Venous thrombosis during dextrose infusion, *Lancet*, 1960, **276**, 627–630.

95 Peterson Jr M. R. and J. G. H. Wahl, Lanthanide NMR shift reagents. A powerful new stereochemical tool, *J. Chem. Educ.*, 1972, **49**, 790–793.

96 F. I. Carroll and J. T. Blackwell, Structure and conformation of cis and trans-3,5-dimethylvalerolactones, *Tetrahedron Lett.*, 1970, **11**, 4173–4176.

97 D. R. Crump, J. K. M. Sanders and D. H. Williams, Evaluation of some Tris(Dipivalomethanato) Lanthanide Complexes, *Tetrahedron Lett.*, 1970, **11**, 4419–4422.

98 M. M. Ali, G. Liu, T. Shah, C. A. Flask and M. D. Pagel, Using Two Chemical Exchange Saturation Transfer Magnetic Resonance Imaging Contrast Agents for Molecular Imaging Studies, *Acc. Chem. Res.*, 2009, **42**, 915–924.

99 S. Aime, A. Barge, J. I. Bruce, M. Botta, J. A. K. Howard, J. M. Moloney, D.

Parker, A. S. De Sousa and M. Woods, NMR, relaxometric, and structural studies of the hydration and exchange dynamics of cationic lanthanide complexes of macrocyclic tetraamide ligands, *J. Am. Chem. Soc.*, 1999, **121**, 5762–5771.

100 S. Zhang, P. Winter, K. Wu and A. D. Sherry, A Novel Europium(III)-Based MRI Contrast Agent, *J. Am. Chem. Soc.*, 2001, **123**, 1517–1518.

101 W. S. Fernando, A. F. Martins, P. Zhao, Y. Wu, G. E. Kiefer, C. Platas-Iglesias and A. D. Sherry, Breaking the Barrier to Slow Water Exchange Rates for Optimal Magnetic Resonance Detection of paraCEST Agents, *Inorg. Chem.*, 2016, **55**, 3007–3014.

102 M. Suchý, M. Milne, A. A. H. Elmehriki, N. McVicar, A. X. Li, R. Bartha and R. H. E. Hudson, Introduction of Peripheral Carboxylates to Decrease the Charge on Tm^{3+} DOTAM-Alkyl Complexes: Implications for Detection Sensitivity and in Vivo Toxicity of PARACEST MRI Contrast Agents, *J. Med. Chem.*, 2015, **58**, 6516–6532.

103 M. Woods, P. Caravan, C. F. G. C. Geraldes, T. Matthew, G. E. Kiefer, M. Lin, K. Mcmillan, M. M. Isabel, A. C. Santos, X. Sun, J. Wang and S. Zhang, The Effect of the Amide Substituent on the Biodistribution and Tolerance of Lanthanide(III) DOTA-Tetraamide Derivatives, *Invest. Radiol.*, 2008, **43**, 861–870.

104 D. D. Castelli, E. Terreno, D. Longo and S. Aime, Nanoparticle-based chemical exchange saturation transfer (CEST) agents, *NMR Biomed.*, 2013, **26**, 839–849.

105 E. Terreno, D. D. Castelli, E. Violante, H. M. H. F. Sanders, N. A. J. M. Sommerdijk and S. Aime, Osmotically shrunken LIPOCEST Agents: An innovative class of magnetic resonance imaging contrast media based on chemical exchange saturation transfer, *Chem. Eur. J.*, 2009, **15**, 1440–1448.

106 E. Terreno, C. Cabella, C. Carrera, D. Delli Castelli, R. Mazzon, S. Rollet, J. Stancanello, M. Visigalli and S. Aime, From spherical to osmotically shrunken paramagnetic liposomes: An Improved generation of LIPOCEST MRI agents with highly shifted water protons, *Angew. Chemie - Int. Ed.*, 2007, **46**, 966–968.

107 J. Flament, F. Geffroy, C. Medina, C. Robic, J. F. Mayer, S. Mériaux, J. Valette, P. Robert, M. Port, D. Le Bihan, F. Lethimonnier and F. Boumezbeur, In vivo CEST MR imaging of U87 mice brain tumor angiogenesis using targeted LipoCEST contrast agent at 7 T, *Magn. Reson. Med.*, 2013, **69**, 179–187.

108 A. C. L. Opina, K. B. Ghaghada, P. Zhao, G. Kiefer, A. Annapragada and A. D. Sherry, TmDOTA-tetraglycinate encapsulated liposomes as pH-sensitive lipoCEST agents, *PLoS One*, 2011, **6**, 1–10.

109 S. Aime, D. Delli Castelli and E. Terreno, Highly sensitive MRI chemical exchange saturation transfer agents using liposomes, *Angew. Chemie - Int. Ed.*, 2005, **44**, 5513–5515.

110 S. Maruyama, J. Ueda, A. Kimura and K. Murase, Development and Characterization of Novel LipoCEST Agents Based on Thermosensitive Liposomes, *Magn. Reson. Med. Sci.*, 2016, **15**, 324–334.

111 E. Terreno, D. D. Castelli, L. Milone, S. Rollet, J. Stancanello, E. Violante and S. Aime, First ex-vivo MRI co-localization of two LIPOCEST agents, *Contrast Media Mol. Imaging*, 2008, **3**, 38–43.

112 S. Langereis, J. Keupp, J. L. J. van Velthoven, I. H. C. de Roos, D. Burdinski, J. A. Pikkemaat and H. Grull, A Temperature-Sensitive Liposomal 1H CEST and 19F Contrast Agent for MR Image-Guided Drug Delivery, *J. Am. Chem. Soc.*, 2009, **131**, 1380–1381.

113 M. W. Dewhirst, C. D. Landon, C. L. Hofmann and P. R. Stauffer, Novel Approaches to Treatment of Hepatocellular Carcinoma and Hepatic Metastases Using Thermal Ablation and Thermosensitive Liposomes, *Surg. Oncol. Clin. N. Am.*, 2013, **22**, 545–561.

114 P. P. Deshpande, S. Biswas and V. P. Torchilin, Current trends in the use of liposomes for tumor targeting, *Nanomedicine*, 2013, **8**, 1509–1528.

115 S. Massari, E. Folena, V. Ambrosin, G. Schiavo and R. Colonna, pH-dependent lipid packing, membrane permeability and fusion in phosphatidylcholine vesicles, *BBA - Biomembr.*, 1991, **1067**, 131–138.

116 G. Liu, M. Moake, Y. El Har-El, C. M. Long, K. W. Y. Chan, A. Cardona, M. Jamil, P. Walczak, A. A. Gilad, G. Sgouros, P. C. M. van Zijl, J. W. M. Bulte and M. T. McMahon, In vivo multicolor molecular MR imaging using diamagnetic chemical exchange saturation transfer liposomes, *Magn. Reson. Med.*, 2012, **67**, 1106–1113.

117 K. W. Y. Chan, T. Yu, Y. Qiao, Q. Liu, M. Yang, H. Patel, G. Liu, K. W. Kinzler, B. Vogelstein, J. W. M. Bulte, P. C. M. van Zijl, J. Hanes, S. Zhou and M. T. McMahon, A diaCEST MRI approach for monitoring liposomal accumulation in tumors, *J. Control. Release*, 2014, **180**, 51–59.

118 T. Yu, K. W. Y. Chan, A. Anonuevo, X. Song, B. S. Schuster, S. Chattopadhyay, Q. Xu, N. Oskolkov, H. Patel, L. M. Ensign, P. C. M. van Zjil, M. T. McMahon and J. Hanes, Liposome-based mucus-penetrating particles (MPP) for mucosal theranostics: Demonstration of diamagnetic chemical exchange saturation transfer (diaCEST) magnetic resonance imaging (MRI), *Nanomedicine NBM*, 2015, **11**, 401–405.

119 A. N. Wick, D. R. Drury, H. I. Nakada and J. B. Wolfe, Localization of The Primary Metabolic Block Produced by 2-Deoxyglucose, *J. Biol. Chem.*, 1957, **224**, 963–969.

120 G. E. Woodward and M. T. Hudson, The Effect of 2-Desoxy-D-glucose on Glycolysis and Respiration of Tumor and Normal Tissues, *Cancer Res.*, 1954, **14**, 599–605.

121 X. Lin, F. Zhang, C. M. Bradbury, A. Kaushal, L. Li, D. R. Spitz, R. L. Aft and D. Gius, 2-Deoxy-D-Glucose-induced Cytotoxicity and Radiosensitization in Tumor Cells Is Mediated via Disruptions in Thiol Metabolism, *Cancer Res.*, 2003, **63**, 3413–3417.

122 B. S. Dwarakanath, F. Zolzer, S. Chandana, T. Bauch, J. S. Adhikari, W. U. Muller, C. Streffer and V. Jain, Heterogeneity in 2-deoxy-D-glucose-induced modifications in energetics and radiation responses of human tumor cell lines, *Int. J. Radiat. Oncol. Biol. Phys.*, 2001, **50**, 1051–1061.

123 I. M. Ahmad, E. H. Mustafa, N. H. Mustafa, L. H. Tahtamouni and M. Y. Abdalla, 2DG enhances the susceptibility of breast cancer cells to doxorubicin, *Cent. Eur. J. Biol.*, 2010, **5**, 739–748.

124 K. A. Kern and J. A. Norton, Inhibition of established rat fibrosarcoma growth by the glucose antagonist 2-deoxy-D-glucose, *Surgery*, 1987, **102**, 380–385.

125 Y. Zhao, H. Liu, Z. Liu, Y. Ding, S. P. Ledoux, G. L. Wilson, R. Voellmy, Y. Lin, W. Lin, R. Nahta, B. Liu, O. Fodstad, J. Chen, Y. Wu, J. E. Price and M. Tan, Overcoming trastuzumab resistance in breast cancer by targeting dysregulated glucose metabolism, *Cancer Res.*, 2011, **71**, 4585–4597.

126 G. Maschek, N. Savaraj, W. Priebe, P. Braunschweiger, K. Hamilton, G. F. Tidmarsh, L. R. De Young and T. J. Lampidis, 2-Deoxy-D-glucose Increases the Efficacy of Adriamycin and Paclitaxel in Human Osteosarcoma and Non-Small

Cell Lung Cancers in Vivo, *Cancer Res.*, 2004, **64**, 31–34.

127 B. S. Dwarakanath, D. Singh, A. K. Banerji, R. Sarin, N. K. Venkataramana, R. Jalali, P. N. Vishwanath, B. K. Mohanti, R. P. Tripathi, V. K. Kalia and V. Jain, Clinical studies for improving radiotherapy with 2-deoxy-D-glucose, *J. Caner Res. Ther.*, 2009, **5**, 21–26.

128 Y. Zhao, E. B. Butler and M. Tan, Targeting cellular metabolism to improve cancer therapeutics, *Cell Death Dis.*, 2013, **4**, 1–10.

129 L. E. Raez, K. Papadopoulos, A. D. Ricart, E. G. Chiorean, R. S. Dipaola, M. N. Stein, C. M. Rocha Lima, J. J. Schlesselman, K. Tolba, V. K. Langmuir, S. Kroll, D. T. Jung, M. Kurtoglu, J. Rosenblatt and T. J. Lampidis, A phase I dose-escalation trial of 2-deoxy-D-glucose alone or combined with docetaxel in patients with advanced solid tumors, *Cancer Chemother. Pharmacol.*, 2013, **71**, 523–530.

130 M. Stein, H. Lin, C. Jeyamohan, D. Dvorzhinski, K. Bray, S. Eddy, S. Goodin, E. White and S. Robert, Targeting Tumor Metabolism With 2-Deoxyglucose in Patients With Castrate-Resistant Prostate Cancer and Advanced Malignancies, *Prostate*, 2010, **70**, 1388–1394.

131 B. K. Mohanti, G. K. Rath, N. Anantha, V. Kannan, B. S. Das, B. A. R. Chandramouli, A. K. Banerjee, S. Das, A. Jena, R. Ravichandran, U. P. Sahi, R. Kumar, N. Kapoor, V. K. Kalia, B. S. Dwarakanath and V. Jain, Improving cancer radiotherapy with 2-deoxy-D-glucose: phase I/II clinical trials on human cerebral gliomas, *Int. J. Radiat. Oncol.*, 1996, **35**, 103–111.

132 R. Baskar, K. A. Lee, R. Yeo and K.-W. Yeoh, Cancer and Radiation Therapy: Current Advances and Future Directions, *Int. J. Med. Sci.*, 2012, **9**, 193–199.

133 D. Singh, A. K. Banerji, B. S. Dwarakanath, R. P. Tripathi, J. P. Gupta, T. L. Mathew, T. Ravindranath and V. Jain, Optimizing cancer radiotherapy with 2-deoxy-D-glucose: Dose escalation studies in patients with glioblastoma multiforme, *Strahlentherapie und Onkol.*, 2005, **181**, 507–514.

134 V. Jain, W. Pohlit and S. C. Purohit, Influence of energy metabolism on the repair of X-ray damage in living cells. III. Effects of 2-deoxy-D-glucose on liquid holding reactivation in yeast, *Biophysics (Oxf).*, 1973, **320**, 137–142.

135 B. S. Dwarakanath and V. K. Jain, Modification of the radiation induced damage by 2-deoxy-D-glucose in organ cultures of human cerebral gliomas, *Int. J. Radiat. Oncol. Biol. Phys.*, 1987, **13**, 741–746.

136 V. K. Jain, V. K. Kalia, R. Sharma, V. Maharajan and M. Menon, Effects of 2-deoxy-D-glucose on glycolysis, proliferation kinetics and radiation response of human cancer cells, *Int. J. Radiat. Oncol. Biol. Phys.*, 1985, **11**, 943–950.

137 C. Sinthupibulyakit, K. R. Grimes, F. E. Domann, Y. Xu, F. Fang, W. Ittarat, D. K. S. Clair and W. S. Clair, p53 is an important factor for the radiosensitization effect of 2-deoxy-D-glucose, *Int J Oncol.*, 2009, **35**, 609–615.

138 V. Perumal, P. F. D. Solomon and V. R. Jayanth, Modification of 2-deoxy-D-glucose on radiation-and chemotherapeutic drug-induced chromosomal aberrations, *J. Cancer Res. Ther.*, 2009, **5**, S48–S52.

139 B. S. Dwarakanath, S. Singh and V. Jain, Optimization of tumour radiotherapy: Part V - Radiosensitization by 2- deoxy-D-glucose and DNA ligand Hoechst-33342 in a murine tumour, *Indian J. Exp. Biol.*, 1999, **37**, 865–870.

140 S. C. Purohit and W. Pohlit, Experimental evaluation of the glucose antimetabolite, 2-deoxy-D-glucose (2-DG), as a possible adjuvant to radiotherapy of tumours: I. Kinetics of growth and survival of Ehrlich ascites

tumour cells (EATC) in vitro and growth of solid tumours after 2-DG a, *Int. J. Radiat. Oncol. Biol. Phys.*, 1982, **8**, 495–499.

141 S. P. Singh, S. Singh and V. Jain, Effects of 5-bromo-2-deoxyuridine and 2-deoxy-D-glucose on radiation-induced micronuclei in mouse bone marrow, *Int. J. Radiat. Biol.*, 1990, **58**, 791–797.

142 R. K. Swamy, J. Manickam, J. S. Adhikari and B. S. Dwarakanath, The glycolytic inhibitor 2-deoxy-D-glucose does not enhance radiation-induced apoptosis in mouse thymocytes and splenocytes in vitro, *Indian J. Exp. Biol.*, 2005, **43**, 686–692.

143 L. Sokoloff, M. Reivich, C. Kennedy, M. H. Des Rosiers, C. S. Patlak, K. D. Pettigrew, O. Sakurada, M. Shinohara, M. H. Des Rosiers, C. S. Patlak, K. D. Pettigrew, O. Sakurada and M. Shinohara, The [14C]Deoxyglucose Method for the Measurement of Local Cerebral Glucose Utilization: Theory, Procedure, and Normal Values in the Conscious and Anesthetized Albino Rat, *J. Neurochem.*, 1977, **28**, 897–916.

144 F. A. Nasrallah, G. Pagès, P. W. Kuchel, X. Golay and K.-H. Chuang, Imaging Brain Deoxyglucose Uptake and Metabolism by Glucocest MRI, *J. Cereb. Blood Flow Metab.*, 2013, **33**, 1270–1278.

145 J. J. Kotyk, R. S. Rust, J. J. Ackerman and R. K. Deuel, Simultaneous in vivo monitoring of cerebral deoxyglucose and deoxyglucose-6-phosphate by 13C[1H] nuclear magnetic resonances spectroscopy, *J. Neurochem.*, 1989, **53**, 1620–8.

146 K. M. Jones, A. C. Pollard and M. D. Pagel, Clinical applications of chemical exchange saturation transfer (CEST) MRI, *J. Magn. Reson. Imaging*, 2018, **47**, 11–27.

147 G. Navon, R. C. Lyon, O. Kaplan and J. S. Cohen, Monitoring the transport and phosphorylation of 2-deoxy-D-glucose in tumor cells in vivo and in vitro by 13C nuclear magnetic resonance spectroscopy, *FEBS Lett.*, 1989, **247**, 86–90.

148 T. Jin, H. Mehrens, P. Wang and S. G. Kim, Glucose metabolism-weighted imaging with chemical exchange-sensitive MRI of 2-deoxyglucose (2DG) in brain: Sensitivity and biological sources, *Neuroimage*, 2016, **143**, 82–90.

149 Z. Zu, J. Spear, H. Li, J. Xu and J. C. Gore, Measurement of regional cerebral glucose uptake by magnetic resonance spin-lock imaging, *Magn. Reson. Imaging*, 2014, **32**, 1078–1084.

150 H. Zhang, Thin-Film Hydration Followed by Extrusion Method for Liposome Preparation., *Methods Mol. Biol.*, 2017, **1522**, 17–22.

151 A. Akbarzadeh, R. Rezaei-Sadabady, S. Davaran, S. W. Joo, N. Zarghami, Y. Hanifehpour, M. Samiei, M. Kouhi and K. Nejati-Koshki, Liposome: classification, preparation, and applications, *Nanoscale Res. Lett.*, 2013, **8**, 102.

152 V. P. Torchilin, Recent advances with liposomes as pharmaceutical carriers, *Nat. Rev. Drug Discov.*, 2005, **4**, 145–160.

153 M. L. Immordino, F. Dosio and L. Cattel, Stealth liposomes: Review of the basic science, rationale, and clinical applications, existing and potential, *Int. J. Nanomedicine*, 2006, **1**, 297–315.

154 C. A. Hurley, J. B. Wong, J. Ho, M. Writer, S. A. Irvine, M. J. Lawrence, S. L. Hart, A. B. Tabor and H. C. Hailes, Mono- and dicationic short PEG and methylene dioxyalkylglycerols for use in synthetic gene delivery systems, *Org. Biomol. Chem.*, 2008, **6**, 2554–2559.

155 J. S. Suk, Q. Xu, N. Kim, J. Hanes and L. M. Ensign, PEGylation as a strategy for improving nanoparticle-based drug and gene delivery, *Adv .Drug Deliv. Rev.*,

2016, **99**, 28–51.

156 D. Needham, T. J. McIntosh and D. D. Lasic, Repulsive interactions and mechanical stability of polymer-grafted lipid membranes, *BBA - Biomembr.*, 1992, **1108**, 40–48.

157 Q. Yang and S. K. Lai, Anti-PEG immunity: emergence, characteristics, and unaddressed questions, *Wiley Interdiscip. Rev. Nanomedicine Nanobiotechnology*, 2015, **7**, 655–677.

158 A. L. Klibanov, K. Maruyama, V. P. Torchilin and L. Huang, Amphipathic polyethyleneglycols effectively prolong the circulation time of liposomes, *FEBS Lett.*, 1990, **268**, 235–237.

159 D. Papahadjopoulos, T. M. Allen, A. Gabizon, E. Mayhew, K. Matthay, S. K. Huang, K. D. Lee, M. C. Woodle, D. D. Lasic and C. Redemann, Sterically stabilized liposomes: improvements in pharmacokinetics and antitumor therapeutic efficacy, *Proc. Natl. Acad. Sci. U. S. A.*, 1991, **88**, 11460–4.

160 Y. Malam, M. Loizidou and A. M. Seifalian, Liposomes and nanoparticles: nanosized vehicles for drug delivery in cancer, *Trends Pharmacol. Sci.*, 2009, **30**, 592–599.

161 Y. Barenholz, Doxil® - The first FDA-approved nano-drug: Lessons learned, *J. Control. Release*, 2012, **160**, 117–134.

162 T. M. Allen, C. Hansen, F. Martin, C. Redemann and A. Yau-Young, Liposomes containing synthetic lipid derivatives of poly(ethylene glycol) show prolonged circulation half-lives in vivo, *BBA - Biomembr.*, 1991, **1066**, 29–36.

163 J. J. F. Verhoef and T. J. Anchordoquy, Questioning the use of PEGylation for drug delivery, *Drug Deliv. Transl. Res.*, 2013, **3**, 499–503.

164 N. Mitchell, T. L. Kalber, M. S. Cooper, K. Sunassee, S. L. Chalker, K. P. Shaw, K. L. Ordidge, A. Badar, S. M. Janes, P. J. Blower, M. F. Lythgoe, H. C. Hailes and A. B. Tabor, Incorporation of paramagnetic, fluorescent and PET/SPECT contrast agents into liposomes for multimodal imaging, *Biomaterials*, 2013, **34**, 1179–1192.

165 J. M. Chan, P. M. Valencia, L. Zhang, R. Langer and O. C. Farokhzad, Polymeric Nanoparticles for Drug Delivery, *Methods Mol. Biol.*, 2010, **624**, 163–175.

166 H. Kobayashi, R. Watanabe and P. L. Choyke, Improving conventional enhanced permeability and retention (EPR) effects; What is the appropriate target?, *Theranostics*, 2014, **4**, 81–89.

167 J. W. Nichols and Y. Han, EPR : Evidence and fallacy, *J. Control. Release*, 2014, **190**, 451–464.

168 F. Danhier, To exploit the tumor microenvironment : Since the EPR effect fails in the clinic , what is the future of nanomedicine ?, *J. Control. Release*, 2016, **244**, 108–121.

169 A. L. Petersen, A. E. Hansen, A. Gabizon and T. L. Andresen, Liposome imaging agents in personalized medicine, *Adv. Drug Deliv. Rev.*, 2012, **64**, 1417–1435.

170 N. Kamaly, T. Kalber, M. Thanou, J. D. Bell and A. D. Miller, Folate Receptor Targeted Bimodal Liposomes for Tumor Magnetic Resonance Imaging, *Bioconjug. Chem.*, 2009, **20**, 648–655.

171 R. van der Meel, L. J. C. Vehmeijer, R. J. Kok, G. Storm and E. V. B. van Gaal, Ligand-targeted particulate nanomedicines undergoing clinical evaluation: Current status, *Adv. Drug Deliv. Rev.*, 2013, **65**, 1284–1298.

172 C. Mamot, D. C. Drummond, C. O. Noble, V. Kallab, Z. Guo, K. Hong, D. B. Kirpotin and J. W. Park, Epidermal growth factor receptor-targeted immunoliposomes significantly enhance the efficacy of multiple anticancer drugs in vivo, *Cancer Res.*, 2005, **65**, 11631–11638.

173 Anti-EGFR-immunoliposomes Loaded With Doxorubicin in Patients With Advanced Triple Negative EGFR Positive Breast Cancer, https://clinicaltrials.gov/ct2/show/NCT02833766, accessed 18/08/18.

174 D. S. Ferreira, S. C. A. Lopes, M. S. Franco and M. C. Oliveira, pH-sensitive liposomes for drug delivery in cancer treatment, *Ther. Deliv.*, 2013, **4**, 1–24.

175 H. Karanth and R. S. R. Murthy, pH-Sensitive liposomes - principle and application in cancer therapy, *J. Pharm. Pharmacol.*, 2007, **59**, 469–483.

176 P. R. Cullis, M. J. Hope and C. P. S. Tilcock, Lipid polymorphism and the roles of lipids in membranes, *Chem. Phys. Lipids*, 1986, **40**, 127–144.

177 N. Düzgüneş, R. M. Straubinger, P. A. Baldwin, D. S. Friend and D. Papahadjopoulos, Proton-Induced Fusion of Oleic Acid-Phosphatidylethanolamine Liposomes, *Biochemistry*, 1985, **24**, 3091–3098.

178 J. J. Sudimack, W. Guo, W. Tjarks and R. J. Lee, A Novel pH-Sensitive Liposome Formulation Containing Oleyl Alcohol, *BBA - Biomembr.*, 2002, **1564**, 31–37.

179 C. J. Chu, J. Dijkstra, M. Z. Lai, K. Hong and F. C. Szoka, Efficiency of Cytoplasmic Delivery by pH-Sensitive Liposomes to Cells in Culture, *Pharm. Res.*, 1990, **7**, 824–834.

180 Z. Huang, X. Guo, W. Li, J. A. MacKay and F. C. Szoka, Acid-triggered transformation of diortho ester phosphocholine liposome, *J. Am. Chem. Soc.*, 2006, **128**, 60–61.

181 D. C. Drummond and D. L. Daleke, Synthesis and characterization of N-acylated, pH-sensitive ‘caged’ aminophospholipids, *Chem. Phys. Lipids*, 1995, **75**, 27–41.

182 J. B. Wong, S. Grosse, A. B. Tabor, S. L. Hart and H. C. Hailes, Acid cleavable PEG-lipids for applications in a ternary gene delivery vector, *Mol. Biosyst.*, 2008, **4**, 532–541.

183 U. Bulbake, S. Doppalapudi, N. Kommineni and W. Khan, Liposomal formulations in clinical use: An updated review, *Pharmaceutics*, 2017, **9**, 1–33.

184 R. Biltonen and D. Lichtenberg, The use of differential scanning calorimetry as a tool to characterize liposome preparation, *Chem. Phys. Lipids*, 1993, **64**, 129–142.

185 H. Mok and M. Zhang, Superparamagnetic iron oxide nanoparticle-based delivery systems for biotherapeutics, *Expert Opin. Drug Deliv.*, 2013, **10**, 73–87.

186 G. Batist, Cardiac safety of liposomal anthracyclines, *Cardiovasc. Toxicol.*, 2007, **7**, 72–74.

187 P. S. Gill, B. M. Espina, F. Muggia, S. Cabriales, A. Tulpule, J. A. Esplin, H. A. Liebman, E. Forssen, M. E. Ross and A. M. Levine, Phase I/II clinical and pharmacokinetic evaluation of liposomal daunorubicin, *J. Clin. Oncol.*, 1995, **13**, 996–1003.

188 M. S. Angst and D. R. Drover, Pharmacology of drugs formulated with DepoFoam^{TM}: A sustained release drug delivery system for parenteral administration using multivesicular liposome technology, *Clin. Pharmacokinet.*, 2006, **45**, 1153–1176.

189 D. J. Murry and S. M. Blaney, Clinical pharmacology of encapsulated sustained-release cytarabine, *Ann. Pharmacother.*, 2000, **34**, 1173–1178.

190 R. C. F. Leonard, S. Williams, A. Tulpule, A. M. Levine and S. Oliveros, Improving the therapeutic index of anthracycline chemotherapy: Focus on liposomal doxorubicin (Myocet^{TM}), *Breast*, 2009, **18**, 218–224.

191 D. C. Drummond, C. O. Noble, Z. Guo, K. Hong, J. W. Park and D. B. Kirpotin, Development of a highly active nanoliposomal irinotecan using a novel intraliposomal stabilization strategy, *Cancer Res.*, 2006, **66**, 3271–3277.

192 R. Glück and I. C. Metcalfe, New technology platforms in the development of vaccines for the future, *Vaccine*, 2002, **20**, 10–16.

193 B. M. Richard, D. E. Rickert, P. E. Newton, L. R. Ott, D. Haan, A. N. Brubaker, P. I. Cole, P. E. Ross, M. C. Rebelatto and K. G. Nelson, Safety Evaluation of EXPAREL (DepoFoam Bupivacaine) Administered by Repeated Subcutaneous Injection in Rabbits and Dogs: Species Comparison, *J. Drug Deliv.*, 2011, **2011**, 1–14.

194 R. K. Chowdhary, I. Shariff and D. Dolphin, Drug release characteristics of lipid based benzoporphyrin derivative, *J. Pharm. Pharm. Sci.*, 2003, **6**, 13–19.

195 T. Boulikas, G. P. Stathopoulos, N. Volakakis and M. Vougiouka, Systemic lipoplatin infusion results in preferential tumor uptake in human studies, *Anticancer Res.*, 2005, **25**, 3031–3040.

196 L. Win Gel, Liposomal glucoCEST MRI: Synthesis and characterisation of an α-glucolipid for liposomes, *2014, MRes Thesis, UCL*.

197 W. Stillwell, K. Doram and S. Karimi, Increase in proton and glucose diffusion in liposomes as a function of trans-retinal concentration, *J. Memb. Sci.*, 1981, **8**, 3–9.

198 K. A. Riske, R. P. Barroso, C. C. Vequi-Suplicy, R. Germano, V. B. Henriques and M. T. Lamy, Lipid bilayer pre-transition as the beginning of the melting process, *BBA - Biomembr.*, 2009, **1788**, 954–963.

199 J. C. Kraft, J. P. Freeling, Z. Wang and R. J. Y. Ho, Emerging Research and Clinical Development Trends of Liposome and Lipid Nanoparticle Drug Delivery Systems, *J. Pharm. Sci.*, 2014, **103**, 29–52.

200 F. M. Goñi, M. Urbaneja, J. L. R. Arrondo, A. Alonso, A. A. Durrani and D. Chapman, The interaction of phosphatidylcholine bilayers with Triton X-100, *Eur. J. Biochem.*, 1986, **160**, 659–665.

201 W. W. Sułkowski, D. Pentak, K. Nowak and A. Sułkowska, The influence of temperature, cholesterol content and pH on liposome stability, *J. Mol. Struct.*, 2005, **744**, 737–747.

202 B. Roy, P. Guha, R. Bhattarai, P. Nahak, G. Karmakar, P. Chettri and A. K. Panda, Influence of Lipid Composition, pH, and Temperature on Physicochemical Properties of Liposomes with Curcumin as Model Drug, *J. Oleo Sci.*, 2016, **65**, 399–411.

203 https://avantilipids.com/tech-support/physical-properties/ionization-constants - accessed 14/01/19.

204 J. H. Jung, Y. Do, Y. A. Lee and T. Shimizu, Self-assembling structures of long-chain sugar-based amphiphiles influenced by the introduction of double bonds, *Chem. Eur. J.*, 2005, **11**, 5538–5544.

205 P. Studer, D. Limal, P. Breton and G. Riess, Synthesis and characterization of poly(ethylene oxide)-block- poly(methylidene malonate 2.1.2) block copolymers

bearing a mannose group at the PEO chain end, *Bioconjug. Chem.*, 2005, **16**, 223–229.

206 A. Barge, G. Cravotto, E. Gianolio and F. Fedeli, How to determine free Gd and free ligand in solution of Gd chelates. A technical note, *Contrast Media Mol. Imaging*, 2006, **1**, 184–188.

207 L. H. Perruchoud, M. D. Jones, A. Sutrisno, D. B. Zamble, A. J. Simpson and X. -a. Zhang, A ratiometric NMR pH sensing strategy based on a slow-proton-exchange (SPE) mechanism, *Chem. Sci.*, 2015, **6**, 6305–6311.

208 G. R. Fulmer, A. J. M. Miller, N. H. Sherden, H. E. Gottlieb, A. Nudelman, B. M. Stoltz, J. E. Bercaw and K. I. Goldberg, NMR chemical shifts of trace impurities: Common laboratory solvents, organics, and gases in deuterated solvents relevant to the organometallic chemist, *Organometallics*, 2010, **29**, 2176–2179.

209 S. Feng, C. Bagia and G. Mpourmpakis, Determination of proton affinities and acidity constants of sugars, *J. Phys. Chem. A*, 2013, **117**, 5211–5219.

210 J. E. Gurst, NMR and the structure of D-glucose, *J. Chem. Educ.*, 1991, **68**, 1003.

211 J. M. Zhao, M. T. Mcmahon, J. Zhou, D. Sherry, G. Sgouros, J. W. M. Bulte, P. C. M. Van Zijl and A. D. Sherry, Size-Induced Enhancement of Chemical Exchange Saturation Transfer (CEST) Contrast in Liposomes, *J. Am. Chem. Soc.*, 2008, **130**, 5178–5184.

212 A. Farashishiko, J. R. Slack, M. Botta and M. Woods, ParaCEST Agents Encapsulated in Reverse Nano-Assembled Capsules (RACs): How Slow Molecular Tumbling Can Quench CEST Contrast, *Front. Chem.*, 2018, **6**, 1–7.

213 C. Wängler, B. Wängler, M. Eisenhut, U. Haberkorn and W. Mier, Improved syntheses and applicability of different DOTA building blocks for multiply derivatized scaffolds, *Bioorganic Med. Chem.*, 2008, **16**, 2606–2616.

214 H. Myszka, D. Bednarczyk, M. Najder and W. S. Kaca, Synthesis and induction of apoptosis in B cell chronic leukemia by diosgenyl 2-amino-2-deoxy-β-D-glucopyranoside hydrochloride and its derivatives, *Carbohydr. Res.*, 2003, **338**, 133–141.

215 B. E. Stephens and F. Liu, A regio- and diastereoselective intramolecular nitrone cycloaddition for practical 3- and 2,3-disubstituted piperidine synthesis from γ-butyrolactone, *J. Org. Chem.*, 2009, **74**, 254–263.

216 J. Soubhye, I. Aldib, B. Elfving, M. Gelbcke, P. G. Furtmüller, M. Podrecca, R. Conotte, J. M. Colet, A. Rousseau, F. Reye, A. Sarakbi, M. Vanhaeverbeek, J. M. Kauffmann, C. Obinger, J. Nève, M. Prévost, K. Zouaoui Boudjeltia, F. Dufrasne and P. Van Antwerpen, Design, synthesis, and structure-Activity relationship studies of novel 3-alkylindole derivatives as selective and highly potent myeloperoxidase inhibitors, *J. Med. Chem.*, 2013, **56**, 3943–3958.

217 B. Liberek, A. Melcer, A. Osuch, R. Wakieć, S. Milewski and A. Wiśniewski, N-Alkyl derivatives of 2-amino-2-deoxy-D-glucose, *Carbohydr. Res.*, 2005, **340**, 1876–1884.

218 Z. Baranyai, G. A. Rolla, R. Negri, A. Forgács, G. B. Giovenzana and L. Tei, Comprehensive evaluation of the physicochemical properties of Ln III complexes of aminoethyl-DO3A as pH-responsive T1-MRI contrast agents, *Chem. Eur. J.*, 2014, **20**, 2933–2944.

219 S. Bociek and F. Franks, Proton exchange in aqueous solutions of glucose – hydration of carbohydrates, *J. Chem. Soc., Faraday Trans. 1*, 1979, **75**, 262–270.

220 V. A. Slepushkin, S. Simoes, P. Dazin, M. S. Newman, L. S. Guo, M. C. Pedroso de Lima and N. Duzgunes, Sterically Stabilized pH-sensitive Liposomes, *J. Biol. Chem.*, 1997, **272**, 2382–2388.

221 A. D. Carvalho, F. P. Vieira, V. J. De Melo, M. T. P. Lopes, J. N. Silveira, G. A. Ramaldes, A. Garnier-Suillerot, E. C. Pereira-Maia and M. C. De Oliveira, Preparation and cytotoxicity of cisplatin-containing liposomes, *Brazilian J. Med. Biol. Res.*, 2007, **40**, 1149–1157.

222 R. B. McComb, W. D. Yushok and W. G. Batt, 2-Deoxy-D-glucose, a new substrate for glucose oxidase (glucose aerodehydrogenase), *J. Franklin Inst.*, 1957, **263**, 161–165.

223 R. Lawaczeck, On the permeability of water molecules across vesicular lipid bilayers, *J. Membr. Biol.*, 1979, **51**, 229–261.

224 D. W. Deamer and J. Bramhall, Permeability of lipid bilayers to water and ionic solutes, *Chem. Phys. Lipids*, 1986, **40**, 167–188.

225 A. Carruthers and D. L. Melchior, Studies of the Relationship between Bilayer Water Permeability and Bilayer Physical State, *Biochemistry*, 1983, **22**, 5797–5807.

226 P. C. Mason, B. D. Gaulin, R. M. Epand, G. D. Wignall and J. S. Lin, Small angle neutron scattering and calorimetric studies of large unilamellar vesicles of the phospholipid dipalmitoylphosphatidylcholine, *Phys. Rev. E*, 1999, **59**, 3361–3367.

227 P. C. M. van Zjil and A. A. Sehgal, Proton Chemical Exchange Saturation Transfer (CEST) MRS and MRI, *eMagRes.*, 2016, **5**, 1307–1332.

228 S. Khadke, P. Stone, A. Rozhin, J. Kroonen and Y. Perrie, Point of use production of liposomal solubilised products, *Int. J. Pharm.*, 2018, **537**, 1–8.

229 S. I. Chan, M. P. Sheetz, C. H. Seiter, G. W. Feigenson, M. C. Hsu, A. Lau and A. Yau, Nuclear magnetic resonance studies of the structure of model membrane systems: the effect of surface curvature, *Ann. N. Y. Acad. Sci.*, 1973, **222**, 499–522.

230 J. Estelrich, M. A. Busquets and M. Del Carmen Morán, Effect of PEGylation on ligand-targeted magnetoliposomes: A missed goal, *ACS Omega*, 2017, **2**, 6544–6555.

231 Y. Dori, H. Bianco-Peled, S. K. Satija, G. B. Fields, J. B. McCarthy and M. Tirrell, Ligand accessibility as means to control cell response to bilayer membranes, *J. Biomed. Mater. Res.*, 2000, **50**, 75–81.

232 M. Sun, Z. Zhu, H. Wang, S. Jin, X. Yang, C. Han and W. Pan, Polyarginine and PEG-AEYLR comodified nanostructured lipid carrier: 10mol% uncleavable PEG-AEYLR showed no shielding effect to polyarginine in vitro while maintaining good tumor targeting in vivo, *Artif. Cells, Nanomedicine Biotechnol.*, 2018, **46**, 284–292.

233 P. Marqués-Gallego and A. I. P. M. De Kroon, Ligation strategies for targeting liposomal nanocarriers, *Biomed Res. Int.*, 2014, **2014**, 1–12.

234 H. Hatakeyama, H. Akita and H. Harashima, A multifunctional envelope type nano device (MEND) for gene delivery to tumours based on the EPR effect: A strategy for overcoming the PEG dilemma, *Adv. Drug Deliv. Rev.*, 2011, **63**, 152–160.

235 D. Pozzi, V. Colapicchioni, G. Caracciolo, S. Piovesana, A. L. Capriotti, S. Palchetti, S. De Grossi, A. Riccioli, H. Amenitsch and A. Laganà, Effect of polyethyleneglycol (PEG) chain length on the bio–nano-interactions between

PEGylated lipid nanoparticles and biological fluids: from nanostructure to uptake in cancer cells, *Nanoscale*, 2014, **6**, 2782.

236 M. F. M. Mustapa, S. M. Grosse, L. Kudsiova, M. Elbs, E. A. Raiber, J. B. Wong, A. P. R. Brain, H. E. J. Armer, A. Warley, M. Keppler, T. Ng, M. J. Lawrence, S. L. Hart, H. C. Hailes and A. B. Tabor, Stabilized integrin-targeting ternary LPD (lipopolyplex) vectors for gene delivery designed to disassemble within the target cell, *Bioconjug. Chem.*, 2009, **20**, 518–532.

237 P. Ranjitkar, A. M. Brock and D. J. Maly, Affinity Reagents that Target a Specific Inactive Form of Protein Kinases, *Chem. Biol.*, 2010, **17**, 195–206.

238 L. Zhang, C. R. Robertson, B. R. Green, T. H. Pruess, H. S. White and G. Bulaj, Structural requirements for a lipoamino acid in modulating the anticonvulsant activities of systemically active galanin analogues, *J. Med. Chem.*, 2009, **52**, 1310–1316.

239 J. T. Elliott and G. D. Prestwich, Maleimide-functionalized lipids that anchor polypeptides to lipid bilayers and membranes, *Bioconjug. Chem.*, 2000, **11**, 832–841.

240 M. Fleiner, P. Benzinger, T. Fichert and U. Massing, Studies on protein-liposome coupling using novel thiol-reactive coupling lipids: Influence of spacer length and polarity, *Bioconjug. Chem.*, 2001, **12**, 470–475.

241 C.-W. Chen, Lu, Yeh, Shiau and Chiang, Novel RGD-lipid conjugate-modified liposomes for enhancing siRNA delivery in human retinal pigment epithelial cells, *Int. J. Nanomedicine*, 2011, 2567.

242 R. I. Nicholson, J. M. W. Gee and M. E. Harper, EGFR and cancer prognosis, *Eur. J. Cancer*, 2001, **37**, 9–15.

243 C. Mamot, D. C. Drummond, U. Greiser, K. Hong, D. B. Kirpotin, J. D. Marks and J. W. Park, Epidermal Growth Factor Receptor (EGFR)-targeted Immunoliposomes Mediate Specific and Efficient Drug Delivery to EGFR- and EGFRvIII-overexpressing Tumor Cells, *Cancer Res.*, 2003, **63**, 3154–3161.

244 A. M. Master and A. Sen Gupta, EGF receptor-targeted nanocarriers for enhanced cancer treatment, *Nanomedicine*, 2012, **7**, 1895–1906.

245 S. Song, D. Liu, J. Peng, Y. Sun, Z. Li, J. R. Gu and Y. Xu, Peptide ligand-mediated liposome distribution and targeting to EGFR expressing tumor in vivo, *Int. J. Pharm.*, 2008, **363**, 155–161.

246 S. Song, D. Liu, J. Peng, H. Deng, Y. Guo, X. L. X., A. D. Miller and Y. Xu, Novel peptide ligand directs liposomes toward EGF-R high-expressing cancer cells in vitro and in vivo, *FASEB J.*, 2009, **23**, 1396–1404.

247 C. Han, Y. Li, M. Sun, C. Liu, X. Ma, X. Yang, Y. Yuan and W. Pan, Small peptide-modified nanostructured lipid carriers distribution and targeting to EGFR-overexpressing tumor in vivo, *Artif. Cells, Nanomedicine Biotechnol.*, 2014, **42**, 161–166.

248 Z. Li, R. Zhao, X. Wu, Y. Sun, M. Yao, J. Li, Y. Xu and J. Gu, Identification and characterization of a novel peptide ligand of epidermal growth factor receptor for targeted delivery of therapeutics, *FASEB J.*, 2005, **19**, 1978–1985.

249 C. Y. Han, L. L. Yue, L. Y. Tai, L. Zhou, X. Y. Li, G. H. Xing, X. G. Yang, M. S. Sun and W. S. Pan, A novel small peptide as an epidermal growth factor receptor targeting ligand for nanodelivery in vitro, *Int. J. Nanomedicine*, 2013, **8**, 1541–1549.

250 G. Weitsman, N. J. Mitchell, R. Evans, A. Cheung, T. L. Kalber, R. Bofinger, G. O. Fruhwirth, M. Keppler, Z. V. F. Wright, P. R. Barber, P. Gordon, T. De Koning,

W. Wulaningsih, K. Sander, B. Vojnovic, S. Ameer-Beg, M. Lythgoe, J. N. Arnold, E. Arstad, F. Festy, H. C. Hailes, A. B. Tabor and T. Ng, Detecting intratumoral heterogeneity of EGFR activity by liposome-based in vivo transfection of a fluorescent biosensor, *Oncogene*, 2017, **36**, 3618–3628.

251 M. Stawikowski and G. B. Fields, Introduction to Peptide Synthesis, *Curr. Protoc. Protein Sci.*, 2012, **18**, 1–17.

252 R. Zhang, J. Li, X. Yan, K. Jin, W. Li, J. Xu, J. Zhao, J. Bai and X. Su, SODD promotes glucose uptake of colorectal cancer cells via AKT pathway, *Cell Biol. Int.*, 2017, 1–27.

253 C. Sinthupibulyakit, W. Ittarat, W. H. St. Clair and D. K. St. Clair, P53 Protects Lung Cancer Cells Against Metabolic Stress, *Int. J. Oncol.*, 2010, **37**, 1575–1581.

254 M. Baker, 1,500 scientists lift the lid on reproducibility, *Nature*, 2016, **533**, 452–454.

255 S. A. Wildman and G. M. Crippen, Prediction of physicochemical parameters by atomic contributions, *J. Chem. Inf. Comput. Sci.*, 1999, **39**, 868–873.

256 M. F. Mazzobre, M. V. Román, A. F. Mourelle and H. R. Corti, Octanol-water partition coefficient of glucose, sucrose, and trehalose, *Carbohydr. Res.*, 2005, **340**, 1207–1211.

257 H. Shibata, K.-I. Izutsu, C. Yomota, H. Okuda and Y. Goda, Investigation of factors affecting in vitro doxorubicin release from PEGylated liposomal doxorubicin for the development of in vitro release testing conditions, *Drug Dev. Ind. Pharm.*, 2015, **41**, 1376–1386.

258 W. Jiang, R. Lionberger and L. X. Yu, In vitro and in vivo characterizations of PEGylated liposomal doxorubicin, *Bioanalysis*, 2011, **3**, 333–44.

259 V. P. Torchilin, Targeted pharmaceutical nanocarriers for cancer therapy and imaging, *AAPS J.*, 2007, **9**, E128–E147.

260 X. Xu, M. A. Khan and D. J. Burgess, Predicting hydrophilic drug encapsulation inside unilamellar liposomes, *Int. J. Pharm.*, 2012, **423**, 410–418.

261 M. H. Kang, M. J. Park, H. J. Yoo, K. Y. Hyuk, S. G. Lee, S. R. Kim, D. W. Yeom, M. J. Kang and Y. W. Choi, RIPL peptide (IPLVVPLRRRRRRRRC)-conjugated liposomes for enhanced intracellular drug delivery to hepsin-expressing cancer cells, *Eur. J. Pharm. Biopharm.*, 2014, **87**, 489–499.

262 J. Mayr, S. Hager, B. Koblmüller, M. H. M. Klose, K. Holste, B. Fischer, K. Pelivan, W. Berger, P. Heffeter, C. R. Kowol and B. K. Keppler, EGFR-targeting peptide-coupled platinum(IV) complexes, *J. Biol. Inorg. Chem.*, 2017, **22**, 591–603.

263 X. Li, Y. Zheng, H. Tong, R. Qian, L. Zhou, G. Liu, Y. Tang, H. Li, K. Lou and W. Wang, Rational Design of an Ultrasensitive and Highly Selective Chemodosimeter by a Dual Quenching Mechanism for Cysteine Based on a Facile Michael-Transcyclization Cascade Reaction, *Chem. - A Eur. J.*, 2016, **22**, 9247–9256.

264 A. P. Ramos, in *Nanocharacterization Techniques*, William Andrew Publishing, Norwich, United States, 1st edn., 2017, pp. 99–110.

265 J. Marra and J. Israelachvili, Direct Measurements of Forces between Phosphatidylcholine and Phosphatidylethanolamine Bilayers in Aqueous Electrolyte Solutions, *Biochemistry*, 1985, **24**, 4608–4618.

266 W. J. Sun, S. Tristram-Nagle, R. M. Suter and J. F. Nagle, Structure of gel phase

saturated lecithin bilayers: temperature and chain length dependence, *Biophys. J.*, 1996, **71**, 885–891.

267 R. Zhang, R.M. Suter, C.R. Worthington, W. Sun and J.F. Nagle, Measurement of chain tilt order angle in fully hydrated bilyers of gel phase lecithins, *Biophys. J.*, 1994, **64**, 1097–1109.

268 P. D. Beer, J. Cadman, J. M. Lloris, R. Martínez-Máñez, J. Soto, T. Pardo and M. D. Marcos, Anion interaction with ferrocene-functionalised cyclic and open-chain polyaza and aza-oxa cycloalkanes, *J. Chem. Soc. Dalt. Trans.*, 2000, **11**, 1805–1812.

269 M. Collet, J. Lenger, K. Jenssen, H. P. Plattner and N. Sewald, Molecular tools for metalloprotease sub-proteome generation, *J. Biotechnol.*, 2007, **129**, 316–328.

270 E. S. Coimbra, M. V. De Almeida, C. O. R. Júnior, A. F. Taveira, C. F. Da Costa, A. C. De Almeida, E. F. C. Reis and A. D. Da Silva, Synthesis and antileishmanial activity of lipidic amino alcohols, *Chem. Biol. Drug Des.*, 2010, **75**, 233–235.

271 J. A. Heyes, D. Niculescu-Duvaz, R. G. Cooper and C. J. Springer, Synthesis of novel cationic lipids: Effect of structural modification on the efficiency of gene transfer, *J. Med. Chem.*, 2002, **45**, 99–114.

272 F. Benetollo, G. Bombieri, L. Calabi, S. Aime and M. Botta, Structural variations across the lanthanide series of macrocyclic DOTA complexes: Insights into the design of contrast agents for magnetic resonance imaging, *Inorg. Chem.*, 2003, **42**, 148–157.

273 R. Li, T. Muraoka and K. Kinbara, Contrasting topological effect of PEG-containing amphiphiles to natural lipids on stability of vesicles, *Langmuir*, 2016, **32**, 4546–4553.

274 F. R. C. Backwell and C. H. Williams, A tritiated photolabel specific for the active site of monoamine oxidase, *J. Label. Comp. Radiopharm.*, 1990, **28**, 421–426.

275 A. Bajaj, B. Paul, P. Kondaiah and S. Bhattacharya, Structure-activity investigation on the gene transfection properties of cardiolipin mimicking gemini lipid analogues, *Bioconjug. Chem.*, 2008, **19**, 1283–1300.

7 Experimental

7.1 General experimental

CEST techniques

CEST results were obtained on a 9.4 T Agilent scanner with 150 pulses (unless otherwise stated) using a transmit/receive RF coil with 33 mm inner diameter (Rapid Biomedical) and were acquired by Eleni Demetriou, UCL Institute of Neurology. CEST measurements were acquired using a single-shot spin-echo (SE) echo planar imaging (EPI), (TR = 65.3 ms, TE = 4.07 ms, FOV = 20 x 20 mm^2, slice thickness = 5 mm, matrix size = 64 x 64) with a saturation train prior to the readout consisting of 80 Gaussian pulses at three different power levels, 1.5 μT (pulse length = 50 ms, FA = 982°, 99% duty cycle), 5.0 uT (pulse length = 50 ms, FA = 3000°, 99% duty cycle) and 8.0 μT (pulse length = 50 ms, FA = 5000°, 99% duty cycle).

Samples for CEST measurement were prepared using 20% PBS and were scanned the same day as preparation. The pH was measured using a micro pH probe (Hanna, HI1330B) and adjusted where necessary *via* addition of small volumes of 1 M NaOH or 1 M HCl solution. Syringes of 1 mL volume capacity were used as phantom containers for CEST measurement, sealed with silicon glue. The temperature was kept constant at the specified temperature throughout the experiment. Errors were calculated using a MATLAB function that returns 95% confidence bounds.

Chromatography

Flash column chromatography was carried out on Merck SiO_2 (silica gel 60, SDS, 0.04–0.06 mm). Reverse-phase column chromatography was carried out on C_{18}-reverse-phase silica gel (Sigma-Aldrich). The solvent system employed for purification of each individual compound is reported in Section 7.3.

Analytical thin layer chromatography was carried out using Merck Keiselgel aluminium-backed plates coated with silica gel (silica gel 60, RP-2 F254, Merck) or silica gel C_{18} on TLC plates (Sigma-Aldrich). Components were visualised using a mixture of ultra-violet, potassium permanganate, ninhydrin, phosphomolybdic acid and ceric ammonium molybdate.

Starting materials and solvents

The starting materials and solvents used were obtained from commercial suppliers (Fisher Scientific, Sigma Aldrich, Alfa Aesar, CheMatech and VWR International) and were used as supplied, including anhydrous solvents. The Fmoc-protected amino acid **50** was supplied by Iris Biotech GmbH. DPPE-PEG2000, DPSC and DPPE-Rh were supplied by Avanti Polar Lipids Inc. and DPPC was supplied by Generon.

Spectroscopy

Proton nuclear magnetic resonance spectra (^{1}H NMR) were recorded at 300 MHz, 400 MHz, 500 MHz or 600 MHz on a Bruker Avance spectrometer using $CDCl_3$, CD_3OD or d_6-DMSO, water or D_2O as a solvent. Chemical shifts (δ_H) are stated in ppm downfield of tetramethylsilane relative to the residual protiosolvent. Coupling constants (*J*) are listed in Hertz (Hz). All ^{1}H NMR data are reported as follows: δ_H/ppm [number of protons, multiplicity (s = singlet, d = doublet, t = triplet, q = quartet, quint = quintet, m = multiplet, br = broad), coupling constants *J*/Hz (where relevant) and assignment. DEPT135, 2D spectra (COSY, HSQC, HMBC) and NOE/NOSEY NMR spectroscopy was employed where appropriate to aid in the assignment of signals in ^{1}H and ^{13}C NMR spectra. Carbon magnetic resonance spectra (^{13}C NMR) were recorded at 75 MHz, 100 MHz or 150 MHz on a Bruker Avance spectrometer using $CDCl_3$, CD_3OD or D_2O as a solvent.

Infrared (IR) spectra were recorded on a Perkin-Elmer 1605 Fourier transform spectrometer or a Perkin-Elmer spectrum 100 FT-IR spectrometer. Only key IR absorptions are listed.

Ultra-Performance Liquid Chromatography Mass Spectrometry (LC-MS) analyses were carried out on an Acquity UPLC-MS system consisting of a 515 pump, 2525 mixer and 1998 UV detector set at 254 nM (Waters, UK). The UPLC system was connected to a Micromass ZQ mass spectrometer, which scanned the *m/z* range from 100 to 700. Ten µL of the sample was injected on a C18 column, 1.9 µM pore size, 2.1 mm x 150 mm (Thermo Scientific, UK). The flow rate was 0.6 mL/min. Mobile phases were (A) 0.1% formic acid in water and (B) 0.1% formic acid in acetonitrile. The gradient was employed as follows: 5% (B) for 0.5 min followed by a gradual increase to 95% (B) over 4.5 min and return to 5% (B) in 30 sec and held for 1 min at 5% (B).

HRMS was performed at the UCL Chemistry Mass Spectrometry Facility on a Waters LCT Premier XE instrument, in W mode, referenced against sulfadimethoxine. Ionisation was *via* electron ionisation (EI) or electrospray ionisation (ESI+).

UV-vis spectroscopy was carried out on an Agilent Cary 100 spectrophotometer, a SpectraMax Plus 384 Microplate Reader or an Infinite M200 PRO Multimode Microplate Reader from Tecan.

Melting points (MP) were measured using a Gallenkamp apparatus and are uncorrected.

7.2 Liposome experimental

7.2.1 Liposome formulation

The appropriate molar ratios of lipids were dissolved in a mixture of pure $CHCl_3$ or $CHCl_3$:MeOH (3:1, v/v). The solvent was removed under reduced pressure to form a thin lipid film on the inside of a round bottom flask. The thin lipid film was thoroughly dried under reduced pressure to remove any residual organic solvent. Hydration of the lipid film was accomplished by addition of the appropriate volume of a given concentration of monosaccharide solution to yield the desired lipid concentration. Sonication at a temperature above the T_m of the relevant lipids caused the assembly of polydisperse liposomes. Sonication was by bath sonication (VWR ultrasonic bath from the USC THD range, power level 9 which corresponds to a frequency of 45 kHz and effective power of 80 W) unless specified that it was by probe sonication (Branson Sonifier® SFX150, 10 cycles of 20 seconds on and 20 seconds off, with an output power of 8 W).

Liposomes were sized using a LIPEX™ 10 mL extruder with a thermobarrel (Northern Lipids Inc.). During extrusion, liposome samples were passed through 400 nm, 200 nm or 100 nm pore polycarbonate membranes (Whatman Nuclepore Track-Etched, Hydrophilic) at a temperature higher than the T_m of the included lipids until the desired diameter was achieved and the PdI value approached 0.1. The liposomes were dialysed into the appropriate concentration of NaCl solution and/or PBS solution at RT and the relevant pH (Biodesign™ Cellulose Dialysis Tubing by Fischer Scientific, 14000 Da MW cut off). Dialysis solutions were changed twice over the course of 2 days.

The hydrodynamic size distribution of each liposome sample was measured *via* DLS with a 633 nm He-Ne laser light source (Malvern Ltd. Zetasizer Nano Series ZS, Worcester, UK) according to the manufacturers recommendations. DLS was used to monitor liposome diameter during extrusion cycles. Samples were prepared by diluting 4.5-5 µL aliquots of liposome sample in ~ 1 mL of DI water that was previously passed through a 0.45 µM PVDF syringe filter. DLS measurements were taken in triplicate at 25 °C using clear 1 mL zeta potential cuvettes. The mean diameter (Z-Ave) and polydispersity index (PdI) are reported for each liposomal sample after completion of dialysis, as well as the standard deviation (s) for both of these measurements.

Examples for the number of times liposomes **L48-L52** were passed through various polycarbonate filters during extrusion and how the Z-Ave and PdI values can vary before and after dialysis are shown in Table 30.

Table 30. The number of passes through 400 nm and 200 nm pore polycarbonate filters during extrusion to size **L48-L52** and their resultant diameter and PdI values after extrusion or dialysis.

Liposome sample	Bilayer composition (mol%)	Passes through filters	Z-Ave post extrusion (s)	PdI post extrusion (s)	Z-Ave post dialysis (s)	PdI post dialysis (s)
L48	70% DPPC, 30% DPPE-EG4-OMe	2 × 400 nm, 3 × 200 nm	123 (1.7)	0.14 (0.01)	Emulsion/gel	
L49	70% DPPC, 30% DPPE-EG4-OH	3 × 400 nm, 4 × 200 nm	157 (3.6)	0.12 (0.02)	172 (0.8)	0.16 (0.02)
L50	70% DPPC, 30% DPPE-EG4-NH_2	3 × 400 nm, 9 × 200 nm	192 (6.2)	0.12 (0.01)	221 (1.8)	0.20 (0.01)
L51	97% DPPC, 3% DPPE-PEG2000	3 × 400 nm, 3 × 200 nm	155 (2.2)	0.15 (0.01)	163 (2.8)	0.14 (0.04)
L52	100% DPPC	3 × 400 nm, 5 × 200 nm	179 (7.2)	0.11 (0.02)	184 (2.7)	0.11 (0.03)

7.2.2 Determination of exterior and overall monosaccharide concentrations of liposomal samples

7.2.2.1 Glucose HK Assay®

Exterior and overall glucose concentrations for glucose liposome formulations were obtained using the Glucose HK Assay® (Sigma-Aldrich) or the Glucose GO Assay® (see Section 7.2.2.3). Prior to use of the assay an accuracy test was carried out using the supplied 1.0 mg/mL D-glucose standard solution, according to the supplier's instructions. Five measurements of absorption at 340 nm (A_{340}) were taken during each liposomal characterisation; a sample blank with intact liposomes in distilled water (SB1), a sample blank after disruption of the liposomes with Triton (SB2), a reagent blank (RB) and two measurements of the glucose liposome sample, one for the exterior concentration with the liposomes intact (T1) and one for the overall concentration following bilayer disruption with Triton (T2). The volume of the various substituents required for these five measurements are given for a typical glucose liposome sample (30 mM DPPC encapsulating 0.5 M glucose) in Table 31. Liposome sample volumes were slightly decreased for more concentrated formulations to keep resultant diluted concentrations within the ideal range for measurement using the assay. For SB1, SB2 and RB measurement of A_{340} could be carried out immediately after addition of assay reagent to the detailed components in a measuring cuvette because no reaction is expected to occur due to either lack of assay reagent or glucose. However, for T1 and T2, 15 min was allowed after assay reagent addition to ensure completion of the enzymatic cascade, as recommended by the supplier. After this time, the A_{340} values were measured and the glucose quantities present were calculated using Equation 1 (for mg/mL) or Equation 2 (for concentration in mM).

Table 31. Table showing the volume of glucose assay reagent, liposome sample, deionised water and 3% Triton solution used for each measurement of A_{340} taken during the Glucose HK Assay®. Volumes stated were used for 30 mM liposome samples encapsulating 0.5 M glucose.

Sample	Glucose assay reagent (μL)	Liposome sample volume (μL)	Volume of deionised water (μL)	Volume of Triton (μL)
SB1	-	7	1000	-
SB2	-	7	1000	10
RB	1000	-	-	-
T1	1000	7	-	-
T2	1000	7	-	10

For T1, $A_{totalblank} = A_{SB1} + A_{RB}$, For T2 $A_{totalblank} = A_{SB2} + A_{RB}$

$$\Delta A = A_{T1/T2} - A_{totalblank}$$

$$\text{glucose (mg/mL)} = \frac{(0.029)(\Delta A)(\text{total volume, mL})}{\text{sample volume (mL)}} \qquad \text{(Eq. 1)}$$

$$[\text{glucose}](\text{mM}) = \frac{(0.161)(\Delta A)(\text{total volume, mL})}{\text{sample volume (mL)}} \qquad \text{(Eq. 2)}$$

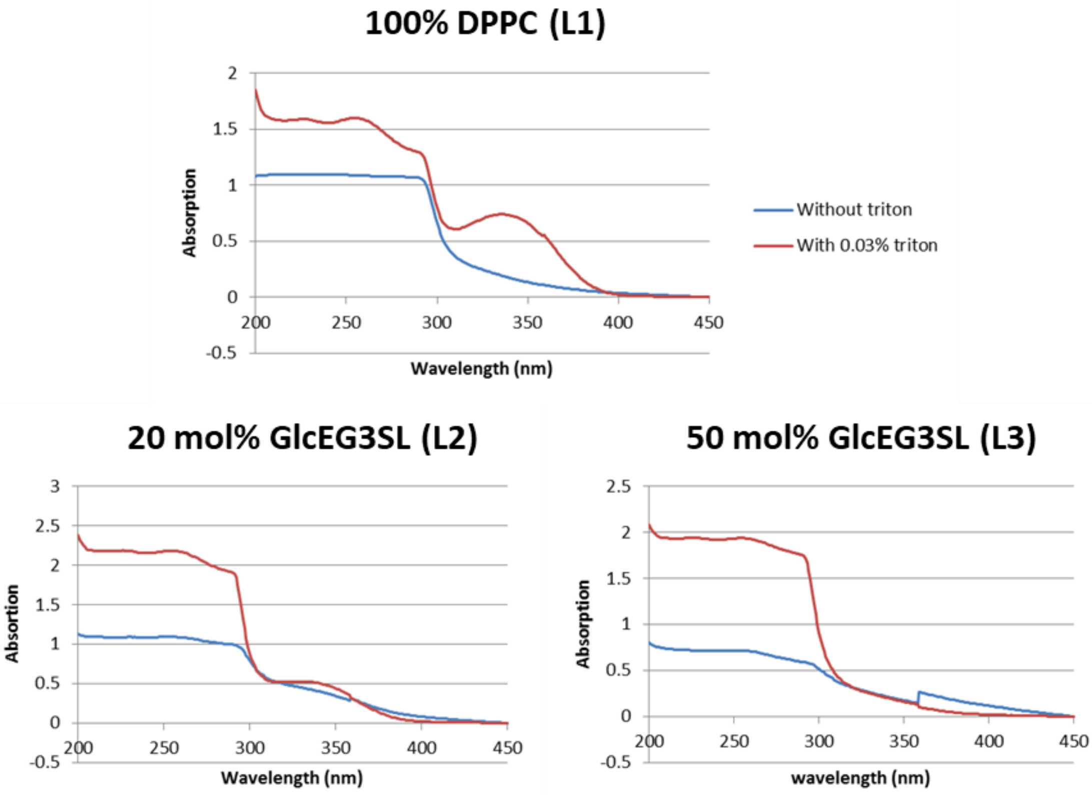

Figure 77. Glucose HK Assay® UV-vis traces for liposomal samples **L1**, **L2** and **L3** with varying concentrations of glucose-lipid **GlcEG3SL** in the bilayer, with and without the addition of 0.03% Triton.

7.2.2.2 Determination of 2-DG concentration by NMR

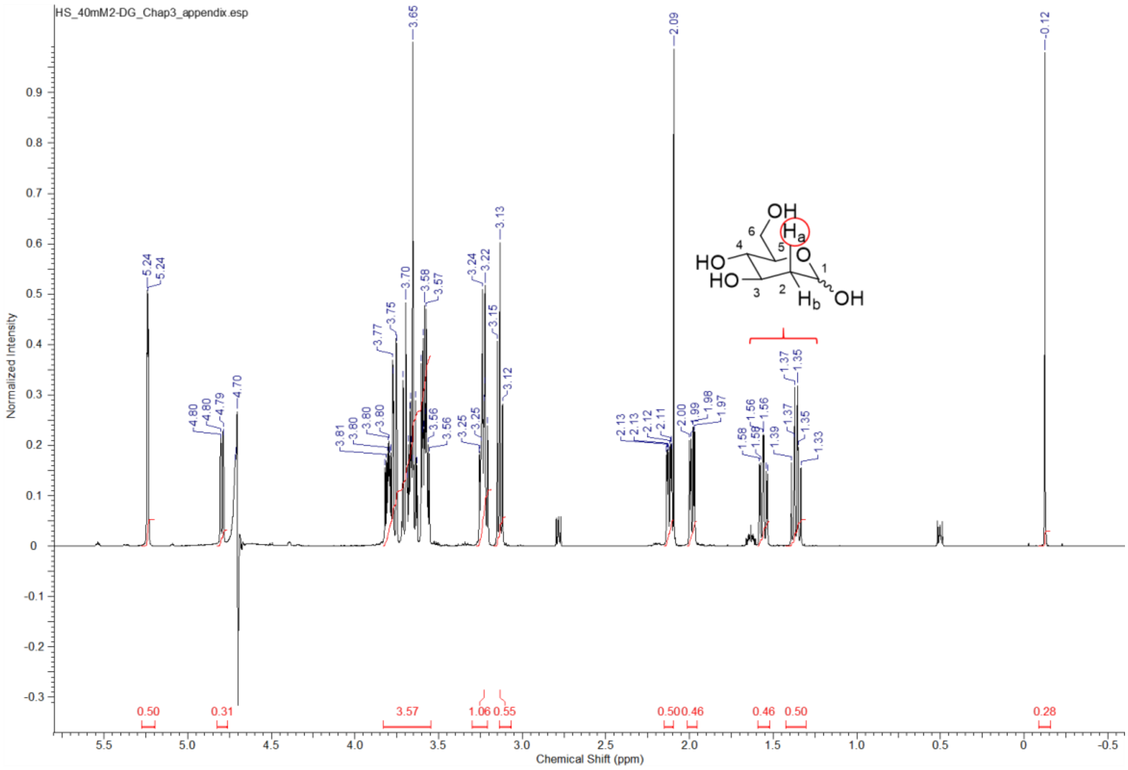

Figure 78. ^{1}H NMR spectrum (600 MHz) of 40 mM 2-DG in water with a coaxial NMR insert tube containing 10 mM DSS in D_2O with water suppression.

The ^{1}H NMR of 2-DG was acquired in distilled water with a coaxial NMR insert tube containing a 10 mM solution of DSS in D_2O (Figure 78), which was assigned as follows:

^{1}H NMR (600 MHz; H_2O+D_2O) δ_H 1.36 (~ 0.5H, ddd, J = 12.2, 12.0, 9.9, β-C^2H_a), 1.56 (~ 0.5H, ddd, J = 12.6, 12.6, 3.4, α-C^2H_a), 1.98 (~ 0.5H, dd, J = 13.3, 5.0, α-C^2H_b), 2.12 (~ 0.5H, ddd, J = 12.2, 5.0, 1.8, β-C^2H_b), 3.10-3.13 (0.5H, m), 3.19-3.24 (1H, m), 3.48-3.80 (3.5 H, m), 4.79 (0.5H, dd, J = 9.9, 1.8, βC^1H), 5.24 (0.5H, d, J = 3.4, αC^1H).

Note that the two signals at 1.36 ppm and 1.56 ppm integrate to a sum of 1H because they account for a C^2-H proton H_a in the β and α anomers, respectively (the α:β ratio is close to 50:50). The intensity of the signal at ~ 4.8 ppm (β-anomeric C-H) is reduced because it is close to the frequency of the suppressed water peak. The volume of the insert contributing to the NMR signal was approximately 0.1 mL, with 0.4 mL of liposome sample. Since the signal at 0.12 ppm for DSS accounts for 9H, the overall concentration of hydrogens contributed by DSS to that peak was assumed to be 18 mM ((0.1 mL/0.5mL)* 10 mM)*9H = 18 mM). Therefore, if an 18H integration is applied to the peak at 0.12 ppm, the sum of the integrals at 1.35 and 1.54 ppm (which correspond to 1H of

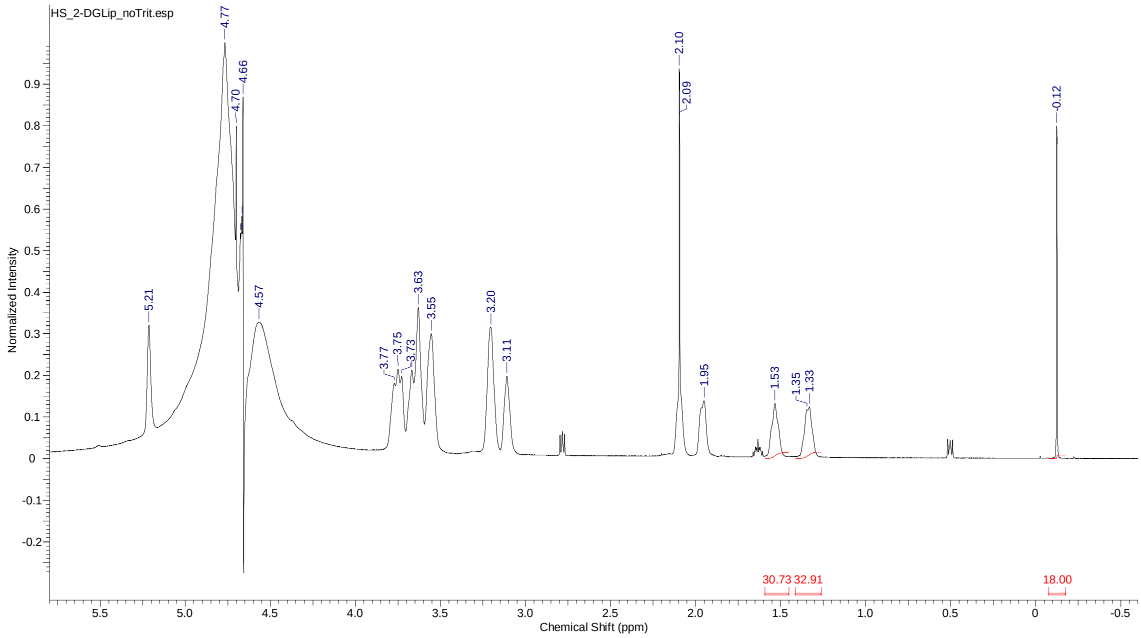

Figure 79. ^1H NMR spectrum (600 MHz) of **L21** with a 10 mM DSS in D_2O insert. The broad signals at 1.34 ppm and 1.53 ppm correspond to the signals at 1.36 ppm and 1.58 ppm in the spectrum above. All 2-DG signals are broad because a large majority of the sugar is encapsulated inside the liposome bilayer.

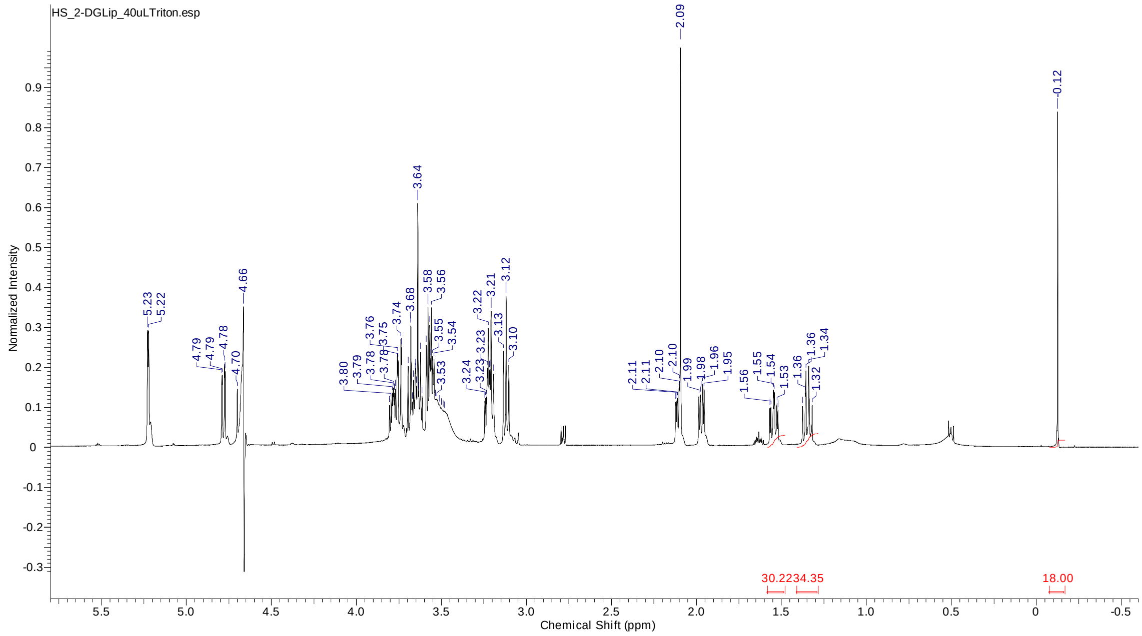

Figure 80. ^1H NMR spectrum (600 MHz) of **L21** with addition of 40 μL Triton and a 10 mM DSS in D_2O coaxial NMR insert tube. All 2-DG signals become sharp due to disruption of the lipid bilayer with Triton and resultant release. The signals at 1.35 ppm and 1.54 ppm were used to determine concentration.

2-DG, namely the C^2H of the β and α anomer, respectively) should equal 4/5th of the 2-DG concentration (0.4 mL/0.5 mL volume in the NMR tube is contributed by the sample).

^{1}H NMR spectra were acquired with the same coaxial NMR insert tube containing 10 mM DSS in D_2O for liposome sample **L21** without Triton (Figure 79) and with Triton (Figure 80). The 2-DG signals were broad when no Triton was present, indicating that most 2-DG was encapsulated inside liposomes (Figure 79). When Triton was added, the signals became sharp as 2-DG was released from liposomes (Figure 80). The sum of the integrals for the two signals at 1.35 ppm and 1.54 ppm in Figure 80 was 64.5 H (*4/5 = 51.6 mM). The technique was calibrated using known concentrations of 2-DG in H_2O with the same DSS in D_2O coaxial NMR insert tube to give a linear calibration curve (Figure 81). Using the calibration curve, the measured 2-DG concentration of 51.6 mM corresponded to an actual concentration of 33.5 mM. This technique could be carried out for glucose in the same way.

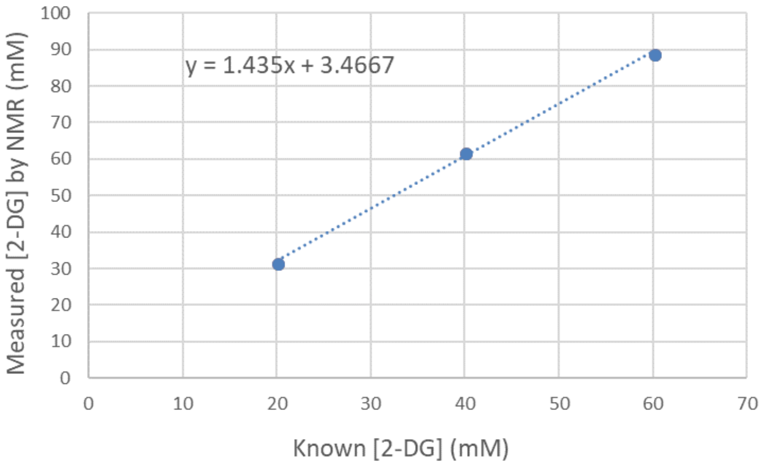

Figure 81. Calibration curve for the measurement of 2-DG concentration *via* an NMR method.

7.2.2.3 Glucose GO Assay®

Overall and exterior concentrations for 2-DG liposome formulations and some glucose liposome formulations were obtained using the Glucose GO Assay Kit® (Sigma-Aldrich). The kit is an enzymatic, colorimetric assay intended to measure glucose concentration however the employed enzyme, glucose oxidase, is reported to catalyse the oxidation of 2-DG as well.[222] The assay reagent contains glucose oxidase (500 units), peroxidase (horseradish, 100 purpurogallin units), o-dianisidine dihydrochloride (4 mg), buffer salts and 40 mL DI water. When the assay reagent is added to glucose/2-DG solutions, the glucose/2-DG is oxidised by glucose oxidase producing hydrogen peroxide as a side product. Hydrogen peroxidase reacts with o-dianisidine in the presence of peroxidase to form a coloured product. To terminate the assay, sulfuric acid is added to react with oxidised o-dianisidine and form a more stable coloured product. The intensity of this pink colour measured at 540 nm (A_{540}) is proportional to the glucose/2-DG concentration.

Test and calibration solutions were made up to a total volume of 0.5 mL, the contents of which are listed in Table 32. Calibration solutions were made up using 0-40 µL of a 1 mg/mL solution of monosaccharide in DI water, giving rise to linear calibration curves (Figure 82). A new calibration curve was constructed alongside every run of the assay to correct for slight differences in temperature, assay run length and time passed since assay reagent was prepared (assay reagent is viable for up to 1 month according to manufacturer's instructions).

Table 32. Typical volumes of DI water, 1 mg/mL 2-DG standard solution, liposome sample and Triton used in the measurement of overall and exterior 2-DG concentrations.

Tube	Deionised water (µL)	1 mg/mL 2-DG standard solution (µL)	Liposome sample volume (µL)	Volume of 3% Triton (µL)
Cal #1	500	-	-	-
Cal #2	495	5	-	-
Cal #3	490	10	-	-
Cal #4	480	20	-	-
Cal #5	470	30	-	-
Cal #6	460	40	-	-
Exterior	495	-	5 (centrifuged)	-
Overall	490	-	5	5

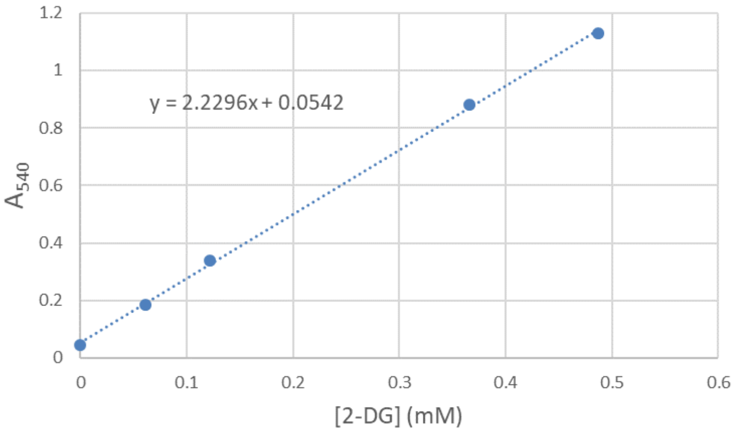

Figure 82. Example of a linear calibration curve used for calculating 2-DG concentrations *via* the Glucose GO Assay®.

Overall monosaccharide concentrations for liposome samples were measured after addition of Triton X-100, which was used to disrupt the liposome bilayer and cause uniform dispersion of the encapsulated contents throughout the total sample volume. Overall concentration test solutions consisted of DI water (490 µL), 3% Triton X-100 (5 µL) and liposomal sample (5 µL).

The assay reagent conditions were found to cause monosaccharide leakage from liposomes. Thus, in order to measure exterior concentrations, liposome samples were subjected to several conditions to cause the liposomes to sink to the bottom of the sample. For unPEGylated formulations, liposomes settled to the bottom of the sample after 3 days in the fridge, or centrifugation for 3.5 min at 4000 rpm was sufficient. For PEGylated formulations, centrifugation for at least 1 h at 10,400 rpm was required. This allowed 5 µL of the supernatant (or exterior liposome solution) to be pipetted off without disturbing the liposomes. Exterior solution (5 µL) was added to DI water (495 µL) to create the test solution for exterior monosaccharide concentration.

Once all calibration and test tubes were prepared, assay reagent (1.0 mL) was added and tubes were agitated for exactly 30 min at room temperature *via* shaking on an IKA KS130 basic platform shaker at 320 rpm. After this time, 6 M H_2SO_4 (1.0 mL) was added to terminate the reaction. The absorbance at 540 nm was measured in triplicate for test and calibration solutions using an Agilent Cary 100 spectrophotometer or a Tecan Infinite M200 Pro. The unknown overall and exterior concentration values were derived using the constructed calibration curves.

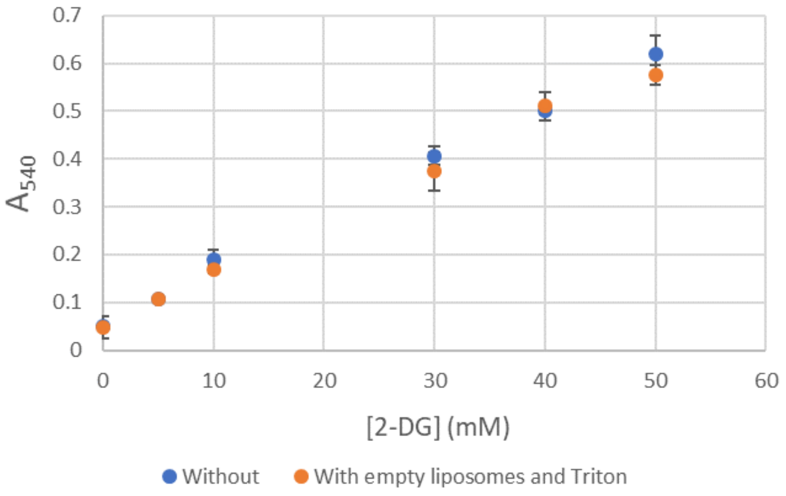

Figure 83. Calibration curves for various 2-DG concentrations with and without the lipid and triton content that is present in the test solutions used to measure overall 2-DG concentration.

The reported overall monosaccharide concentrations are average values for three separate assay measurements, whereas, exterior monosaccharide concentrations were obtained from a single assay measurement and were deemed negligible below 5 mM.

A calibration curve was constructed using empty liposomes from Section 5.2 comprising 97 mol% DPPC and 3 mol% DPPE-PEG2000 (5 µL) and Triton (5 µL) and compared to a calibration curve without these components. It was found that the small amount of lipid (5 µL of 30 mM lipid) and Triton present in the overall 2-DG measurement solution does not affect A_{540} (Figure 83). Thus, for simplicity and to avoid unnecessary use of lipid, calibration curves were constructed without the use of empty liposomes or Triton.

7.2.3 Calculation of liposome internal volumes

A mathematical model developed by Xu *et al.*[260] can be used to calculate the total interior volume for liposome samples. The model requires the following parameters; average hydrodynamic diameter, size distribution standard deviation, bilayer thickness, average surface area per lipid on the bilayer-aqueous phase interface and the lipid concentration. PdI values measured by DLS must be converted into standard deviation (σ) values. When the particle size distribution can be fitted to a Gaussian distribution, the relationship between PdI and σ and the average hydrodynamic radius (r) can be described by the following equation:[264]

$$\mathrm{PdI} = \sigma^2/\mathrm{r}^2 \text{ (Eq. 3)}$$

Table 33. The interior volume percentage for liposome samples **L32-L44** and the parameters used to calculate the interior volume employing a model reported by Xu *et al*.[260]

Liposome sample	Z-Ave (r.nm)	Standard deviation (σ)	Bilayer thickness (nm)	Average area per lipid (*A*.Å^2)	Lipid concentration (mM)	Internal volume
L32	90	28.5	4.6	47.3	30	12%
L33	89	33.3	4.6	47.3	30	13%
L34	84	40.3	4.6	47.3	30	13%
L35	77.5	30.0	4.6	47.3	30	11%
L36	73.5	24.4	5.1	47.3	30	10%
L37	73	25.9	5.1	47.3	30	10%
L38	94	29.7	4.6	47.3	30	13%
L39	92	30.5	4.6	47.3	30	13%
L40	95	46.5	5.1	47.3	30	14%
L41	93.5	37.0	5.1	47.3	30	13%
L42	100.5	41.4	4.6	47.3	30	15%
L43	76.5	25.4	4.6	47.3	30	10%
L44	60.5	13.5	4.6	47.3	30	8%

The literature values used for bilayer thickness were measured by refractive index at 21 °C and were 4.6 nm for DPPC and 5.1 nm for DSPC.[265] The average area per lipid (*A*) for both DPPC and DSPC bilayers was found to be 47.3 Å^2 when measured at 25 °C in the gel state, which is approximately equal to the headgroup steric limit of about 48 Å^2.[266,267] X-ray diffraction studies have shown that increases in chain length of disaturated phosphatidylcholines (chain lengths 16-24) have a negligible effect on *A* which is in agreement with the headgroups already being pushed to the steric repulsive limit, thus the extra Van der Waals attractions contributed by additional methylene groups fail to compress the head groups any closer together.[266,267] As examples, inputting these parameters for liposome samples **L32**-**L44** gives calculated internal volumes in the range 8-15% (Table 33), the remaining 85-92% is made up by the extra-liposomal water.

Having calculated the internal volume and assuming that the encapsulated concentration of monosaccharide remains as high as 0.5 M, one can predict the overall monosaccharide concentration. The measured overall monosaccharide concentrations for **L32**-**L42** (Glucose GO Assay®) were on average only 53% of these predicted concentrations, suggesting that the monosaccharide concentration inside liposomes following dialysis is approximately 0.25 M, due to liposome leakage and subsequent removal of monosaccharide during the dialysis procedure.

7.2.4 Release over time experiments

7.2.4.1 Release of over procedure

Glucose (**L67**) and 2-DG (**L68** and **L69**) liposomes were incubated at 37 °C using a BIOER mixing block with slow agitation at 350 rpm. Before the start of an experiment the initial exterior monosaccharide concentration was confirmed to be negligible (< 1 mM) using the Glucose GO Assay® and an aliquot of exterior solution was kept aside to obtain a 0 min data point in the assay conducted at the end of the experiment. Overall monosaccharide test solutions were obtained as usual (5 µL liposomes, 5 µL 3% Triton).

Once heating at 37 °C was commenced, aliquots (40 µL) were taken from the incubated liposome sample at regular time points, decanted into a 0.35 mL Eppendorf, dipped in an ice bath to immediately stop leakage and then stored in the fridge until the end of the experiment. Once aliquots for all time points had been collected, the aliquots were centrifuged at 10,400 rpm and 4 °C for 1 h, and 5 µL of supernatant was pipetted off to be used in the Glucose GO Assay® to determine exterior monosaccharide concentration. Determining exterior concentrations for all time points in a single assay was found to be more accurate than conducting several assays throughout the experiment. Following completion of the assay, the A_{540} of test solutions were measured in triplicate and readings obtained for the original exterior monosaccharide and overall monosaccharide concentrations (measured in the same assay) were used to convert each time point A_{540} reading into a percentage leakage value (Figure 73).

7.2.4.2 Human plasma experiment

Human plasma was purchased from Sigma-Aldrich. The liposomes were diluted by a factor of 2 with reconstituted human plasma and the same procedure as above was used. A single set of data is shown in Figure 84, showing almost complete 2-DG leakage around the 25 h timepoint, which was slightly faster than for PEGylated 2-DG liposomes in the absence of plasma (Figure 73).

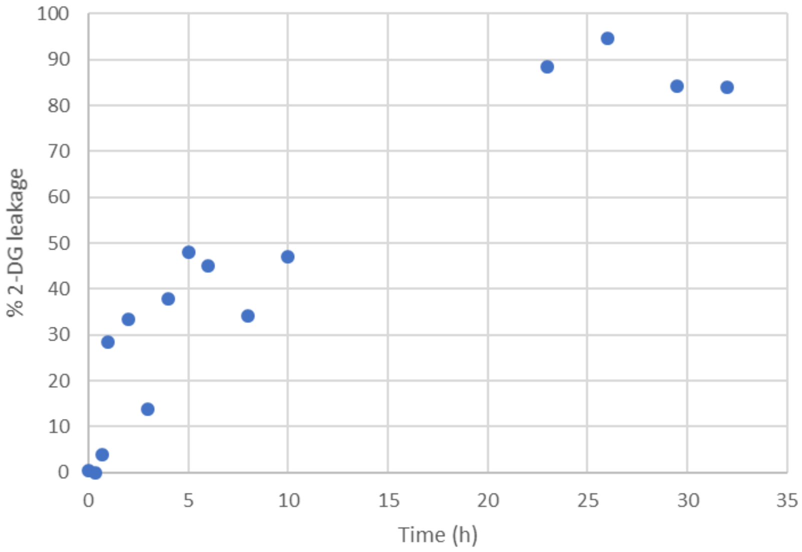

Figure 84. Release of 2-DG over time when 97:3 mol% DPPC:DPPE-PEG2000 liposomes **L68** were incubated at 37 °C in 50% human plasma.

7.2.5 CEST spectra of empty liposomes

To show that no CEST signal was generated by the liposomes themselves in 2-DG or glucose encapsulating liposome experiments, data from an empty liposome sample **L70** was acquired (Figure 85) showing no asymmetry about the water peak. The liposome sample had 35 mM lipid concentration, the bilayer was comprised of 97 mol% DPPC and 3 mol% DPPE-PEG2000 and the hydration solution was DI water (Table 34).

Table 34. Formulation parameters and measurements for empty liposomes in water, **L70**.

Liposome sample	[lipid] (mM)	Bilayer Composition (mol%)	Hydration Solution	Z-Ave (d.nm) (s)	PdI (s)	mL
L70	35	97% DPPC, 3% DPPE-PEG2000	Water	163 (0.35)	0.15 (0.02)	2

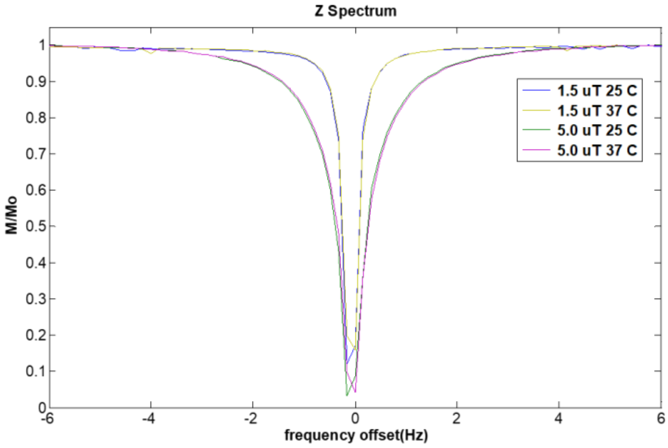

Figure 85. Z-spectra for **L70** acquired at 25 °C and 37 °C, B_1 = 1.5 μT and 5.0 μT.

7.3 Chemical synthesis

7.3.1 Glucose-lipid synthesis

***tert*-Butyl 8-amino-3,6-dioxaoctylcarbamate (2)**[268]

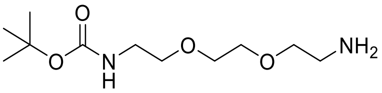

To an ice-cooled solution of 3,6-dioxaoctane-1,8-diamine (6.79 g, 6.69 mL, 45.8 mmol) in CH_2Cl_2 (50 mL) was added di-*tert*-butyl dicarbonate (2.06 g, 9.45 mmol) in CH_2Cl_2 (15 mL) dropwise over 75 min. The reaction was allowed to warm to RT and was left to stir overnight. After this time, the reaction mixture was washed with brine (3 × 40 mL) and distilled water (3 × 40 mL). The aqueous layers were extracted with CH_2Cl_2 (3 × 50 mL) and the organic layers were combined, dried ($MgSO_4$) and concentrated under reduced pressure. The resulting oil was dried under high vacuum to give *tert*-butyl 8-amino-3,6-dioxaoctylcarbamate **2** (2.28 g, 97%) as a cloudy oil.

^{1}H NMR (300 MHz; $CDCl_3$) δ_H 1.41 (9H, s, 3 × C**H₃**), 1.55 (2H, br s, N**H₂**), 2.86 (2H, t, *J* = 5.2, C**H₂**NH₂), 3.27-3.32 (2H, m, C(O)NHC**H₂**), 3.48-3.54 (4H, m, 2 × C**H₂**O), 3.58-3.63 (4H, m, OC**H₂**C**H₂**O), 5.15 (1H, br s, N**H**); **^{13}C NMR** (150 MHz; $CDCl_3$) δ_C 28.5 (C(**C**H₃)₃), 40.4 (**C**H₂), 41.8 (**C**H₂), 70.3 (**C**H₂, signals superimposed), 70.3 (**C**H₂), 73.4 (**C**H₂), 79.3 (**C**(CH₃)₃), 156.2 (**C**=O); **IR** ν_{max}/cm^{-1} 3345 (N-H), 2970 (C-H), 2863 (C-H), 1694 (C=O); **LRMS** (LC-MS ES+) *m/z* 249.3 (100%, $[M+H]^+$); **R$_f$** 0.32 (5% MeOH in CH_2Cl_2). Data corresponds with the literature.[268]

2,2-Dimethyl-4,15-dioxo-3,8,11-trioxa-5,14-diazaoctadecan-18-oic acid, triethylamine salt (3)[269]

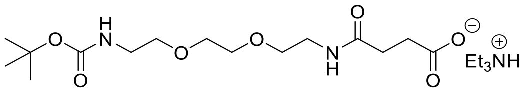

tert-Butyl 8-amino-3,6-dioxaoctylcarbamate **2** (2.25 g, 9.07 mmol) was dissolved in CH_2Cl_2 (60 mL). Triethylamine (1.84 g, 2.53 mL, 18.2 mmol) and succinic anhydride (1.00 g, 9.99 mmol) were added to the solution and the reaction was stirred at RT. for 2 h. After this time, succinic anhydride (0.2 eq.) was added and the reaction was stirred at RT. After another hour, succinic anhydride (0.2 eq.) was added and the reaction was stirred at RT overnight. After this period the solvent was removed under reduced pressure to give a crude purple oil which was purified by FCC (on silica gel eluting 2-10% MeOH and 1% NEt_3 in CH_2Cl_2) to afford 2,2-dimethyl-4,15-dioxo-3,8,11-trioxa-5,14-diazaoctadecan-18-oic acid **3** (3.87 g, 95%) as a pale yellow oil.

^{1}H NMR (300 MHz; $CDCl_3$) δ_H 1.17 (9H, t, *J* = 7.3, $^+NHEt_3$; 3 × $\mathbf{C}H_3$), 1.39 (9H, s, $C(C\mathbf{H_3})_3$), 2.42-2.50 (4H, m, $C(O)C\mathbf{H_2}C\mathbf{H_2}C(O)$), 2.88 (6H, q, *J* = 7.3, $^+NHEt_3$; 3 × $C\mathbf{H_2}$), 3.25-3.28 (2H, m, $BocNHC\mathbf{H_2}$), 3.34-3.39 (2H, m, $C\mathbf{H_2}NHC(O)$), 3.49 (4H, t, 2 × $NHCH_2C\mathbf{H_2}O$), 3.55 (4H, s, $OC\mathbf{H_2}C\mathbf{H_2}O$), 5.21 (1H, br s, N**H**), 7.07 (1H, br s, N**H**), 12.19 (1H, br s, $^+NHEt_3$; $^+N\mathbf{H}$); **^{13}C NMR** (150 MHz; $CDCl_3$) δ_C 9.1 ($^+NHEt_3$; 3 × $\mathbf{C}H_3$), 28.5 ($C(\mathbf{C}H_3)_3$), 33.0 ($C(O)\mathbf{C}H_2$), 33.2 ($C(O)\mathbf{C}H_2$), 39.1 ($OCH_2\mathbf{C}H_2NH$), 40.4 ($NH\mathbf{C}H_2CH_2O$), 45.0 ($^+NHEt_3$; 3 × $\mathbf{C}H_2$), 70.1 ($O\mathbf{C}H_2CH_2$), 70.2 (2 × $O\mathbf{C}H_2CH_2$, signals superimposed), 70.3 ($O\mathbf{C}H_2CH_2$), 79.2 ($\mathbf{C}(CH_3)_3$), 156.2 ($O\mathbf{C}(O)NH$), 173.8 ($NH\mathbf{C}(O)CH_2$), 178.8 ($CH_2\mathbf{C}(O)O^-$); **IR** ν_{max}/cm^{-1} 3324 (N-H), 2973 (C-H), 2927 (C-H), 2876 (C-H), 1699 (C=O), 1652 (C=O); **LRMS** (LC-MS ES+) *m/z* 249.2 (100%, $[M+H-Boc]^+$), 349.2 (40%, $[M+H]^+$), 371.4 (75%, $[M+Na]^+$); **R$_f$** 0.47 (5% MeOH in CH_2Cl_2). Data corresponds with the literature.[269]

Hexadecyl methanesulfonate (5)[270]

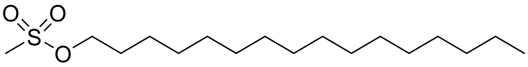

Triethylamine (12.2 mL, 8.85 g, 87.5 mmol) was added to a solution of cetyl alcohol (10.0 g, 41.3 mmol) in CH_2Cl_2 (175 mL). The reaction solution was cooled to 0 °C and mesyl chloride (5 mL, 7.40 g, 64.6 mmol) in CH_2Cl_2 (10 mL) was added dropwise over a period of 3 h. After the addition was complete the reaction mixture was stirred at RT for 20 h. After this time, the reaction solution was washed with 1 M HCl (3 × 75 mL), saturated $NaHCO_3$ solution (3 × 75 mL) and brine (2 × 100 mL). The organic layer was separated, dried ($MgSO_4$), concentrated under reduced pressure and dried under high vacuum to give hexadecyl methanesulfonate **5** (13.3 g, 100%) as a peach foam.

^{1}H NMR (600 MHz; $CDCl_3$) δ_H 0.88 (3H, t, *J* = 7.1, C**H₃**), 1.26-1.30 (24H, m, cetyl chain), 1.37-1.44 (2H, m, $OCH_2CH_2C\mathbf{H_2}$), 1.75 (2H, apparent quint, *J* = 6.8, $OCH_2C\mathbf{H_2}$), 3.01 (3H, s, sulfonyl C**H₃**), 4.23 (2H, t, *J* = 6.8, $OC\mathbf{H_2}$); **^{13}C NMR** (75 MHz; $CDCl_3$) δ_C 14.3 (**C**H_3), 22.8 (**C**H_2), 25.5 (**C**H_2), 29.2 (**C**H_2), 29.2 (**C**H_2), 29.5 (**C**H_2), 29.6 (**C**H_2), 29.6 (**C**H_2), 29.7 (**C**H_2), 29.8 (**C**H_2, signals superimposed), 29.8 (**C**H_2, signals superimposed), 32.1 (**C**H_2), 37.5 (S**C**H_3), 70.4 (O**C**H_2); **IR** ν_{max}/cm^{-1} 2911 (C-H), 2846 (C-H), 1339 (S=O), 1165 (S=O), 980 (S-O); **LRMS** (TOF MS ES-) *m/z* 320.4 (100%, M^-); **R$_f$** 0.40 (5% MeOH, 1% NEt_3 in CH_2Cl_2). Data corresponds with the literature.[270]

2,3-Bis(hexadecyloxy)propan-1-amine (7)[271]

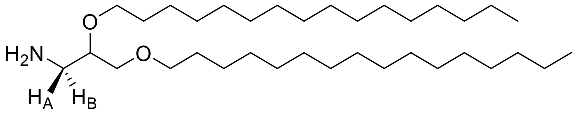

3-Amino-1,2-propanediol (0.960 g, 10.5 mmol) and anhydrous $MgSO_4$ (6.26 g, 52.0 mmol) were stirred in CH_2Cl_2:MeOH (10:1, 110 mL) at RT for 30 min. Benzaldehyde (1.08 mL, 1.12 g, 10.6 mmol) was added and the reaction mixture was stirred for 17.5 h. After this period the slurry was filtered and the filtrate was concentrated under reduced pressure and dried under high vacuum to give 1.65 g of crude imine as a yellow crystalline solid. NaH (0.813 g, 33.9 mmol; dry, 95%) was placed in an oven dried RBF and purged with vacuum/$Ar_{(g)}$. Anhydrous THF (30 mL) was added followed by the dropwise addition of the imine (1.65 g, 9.19 mmol) in anhydrous THF (20 mL) over a period of 30 min. The reaction vessel was purged again using vacuum/$Ar_{(g)}$ and the reaction mixture was stirred at RT for 3 h. Hexadecyl methanesulfonate **5** (8.84 g, 27.6 mmol) in anhydrous THF (35 mL) was added dropwise over a 15 min period and the reaction was heated at reflux for 21 h under $Ar_{(g)}$. After this period 100 mL of distilled water was added and the product was extracted into EtOAc (4 × 100 mL), washed with brine (3 × 50 mL), separated and dried ($MgSO_4$). The solvent was removed under reduced pressure to give a crude yellow oil (8.55 g) which was stirred in 100 mL MeOH and 50 mL conc. HCl (37%) overnight. After this time, the product was extracted into $CHCl_3$ (4 × 100 mL), washed with deionised water (2 × 100 mL) and saturated $NaHCO_3$ solution (3 × 100 mL) and dried ($MgSO_4$). The solvent was removed under reduced pressure to give a crude yellow/brown oil which was purified by FCC (on silica gel eluting 0-5% MeOH in CH_2Cl_2). The desired fractions were combined and concentrated to give 2,3-bis(hexadecyloxy)propan-1-amine **7** (2.07 g, 36%) as a light brown oil.

^{1}H NMR (600 MHz; $CDCl_3$) δ_H 0.88 (6H, apparent t, *J* = 6.6, $2 \times C\mathbf{H_3}$), 1.25 (52H, br s, cetyl chain), 1.53-1.57 (4H, m, $2 \times OCH_2C\mathbf{H_2}$), 1.87 (2H, br s, $N\mathbf{H_2}$), 2.82 (ABX, 2H, $NC\mathbf{H_2}_{\text{(A and B)}}$, J_{AB} = 13.1, J_{AX} = 3.7, J_{BX} = 6.1), 3.37-3.51 (6H, m, $3 \times OC\mathbf{H_2}$), 3.57-3.64 (1H, m, C**H**); **^{13}C NMR** (150 MHz; $CDCl_3$) δ_C 14.3 (**C**H_3, signals superimposed), 22.8 (**C**H_2, signals superimposed), 26.3 (**C**H_2), 26.3 (**C**H_2), 29.5 (**C**H_2), 29.6 (**C**H_2), 29.6 (**C**H_2), 29.8 (**C**H_2, signals superimposed), 29.8 (**C**H_2, signals superimposed), 29.8 (**C**H_2, signals superimposed), 30.3 (**C**H_2), 32.1 (**C**H_2), 43.7 (**C**H_2), 70.52 (**C**H_2), 71.4 (**C**H_2), 71.8 (**C**H_2), 80.0 (**C**H); **IR** ν_{max}/cm^{-1} 2952 (C-H), 2913 (C-H), 2846 (C-H), 1115 (C-N); **LRMS** (LC-MS ES+) *m/z* 540.8 (100%, $[M+H]^+$); **R$_f$** 0.32 (5% MeOH in CH_2Cl_2). Data corresponds with the literature.[271]

tert-Butyl (16-(hexadecyloxy)-10,13-dioxo-3,6,18-trioxa-9,14-diazatetratriacontyl)carbamate **(8)**

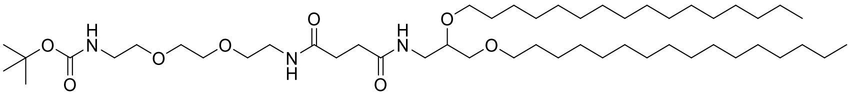

The starting acid **3** (0.750 g, 1.67 mmol) was dissolved in the minimum volume of CH_2Cl_2 (10 mL). 2,3-Bis(hexadecyloxy)propan-1-amine **7** (0.813 g, 1.51 mmol) and DCC (0.346 g, 1.66 mmol) were added to the solution and the reaction was stirred overnight at RT under $Ar_{(g)}$. After this period 0.25 eq. of both the starting acid and DCC were added and the reaction was stirred for a further 4 h under $Ar_{(g)}$. The urea by-product was filtered off and the remaining solvent was removed under reduced pressure. The crude was dry loaded onto a column and purified *via* FCC (on silica eluting 1-3% MeOH and 1% NEt_3 in CH_2Cl_2) to give *tert-butyl (16-(hexadecyloxy)-10,13-dioxo-3,6,18-trioxa-9,14-diazatetratriacontyl)carbamate* **8** (1.13 g, 86 %) as an off-white crystalline solid.

^{1}H NMR (600 MHz; $CDCl_3$) δ_H 0.88 (6H, apparent t, *J* = 7.0, $2 \times C\mathbf{H_3}$), 1.25-1.31 (52H, m, cetyl chain), 1.45 (9H, s, $C(C\mathbf{H_3})_3$), 1.53-1.55 (4H, m, $2 \times OCH_2C\mathbf{H_2}$), 2.53 (4H, s, $C(O)C\mathbf{H_2}C\mathbf{H_2}C(O)$), 3.28-3.61 (21H, m, $7 \times OC\mathbf{H_2}$, C**H**, $3 \times NHC\mathbf{H_2}$), 5.15 (1H, br s, N**H**), 6.23 (1H, br s, N**H**), 6.41 (1H, br s, N**H**); **^{13}C NMR** (150 MHz; $CDCl_3$) δ_C 14.3 (**C**H_3, signals superimposed), 22.8 (**C**H_2), 24.9 (**C**H_2), 25.5 (**C**H_2), 25.6 (**C**H_2), 26.2 (**C**H_2, signals superimposed), 28.5 ($C(\mathbf{C}H_3)_3$), 29.5 (**C**H_2), 29.6 (**C**H_2), 29.8 (**C**H_2), 29.8 (**C**H_2, signals superimposed), 29.8 (**C**H_2, signals superimposed), 30.2 (**C**H_2), 30.7 (**C**H_2), 31.7 (**C**H_2), 31.8 (**C**H_2), 32.1 (**C**H_2, signals superimposed), 32.5 (**C**H_2), 39.4 (**C**H_2), 40.5 (**C**H_2), 41.0 (**C**H_2), 69.9 (**C**H_2), 69.9 (**C**H_2), 70.3 (**C**H_2), 70.4 (**C**H_2), 71.6 (**C**H_2), 72.0 (**C**H_2), 76.4 (**C**H), 156.2 (**C**(O)), 172.2 (**C**(O)), 172.2 (**C**(O)); **MP** 65-67 **°**C; **IR** ν_{max}/cm^{-1} 3290 (N-H), 2912 (C-H), 2846 (C-H), 1683 (C=O), 1636 (C=O); **LRMS** (LC-MS ES+) *m/z* 870.9 (100%,

$[M+H]^+$), 892.9 (30%, $[M+Na]^+$); **HRMS** (TOF ES+) calculated mass 870.7510 g.mol^{-1} ($[C_{50}H_{100}N_3O_8]^+$), observed *m/z* 870.7509 ($[M+H]^+$); **R$_f$** 0.47 (4% MeOH and 1% NEt_3 in CH_2Cl_2).

16-(Hexadecyloxy)-10,13-dioxo-3,6,18-trioxa-9,14-diazatetratriacontan-1-aminium 2,2,2-trifluoroacetate **(9)**

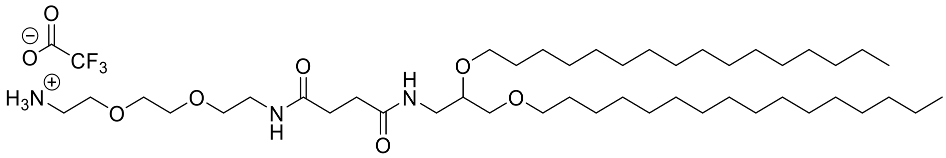

tert-Butyl (16-(hexadecyloxy)-10,13-dioxo-3,6,18-trioxa-9,14-diazatetratriacontyl)-carbamate **8** (1.12 g, 1.29 mmol) was dissolved in a 1:1 (v/v) solution of CH_2Cl_2 and TFA (10 mL/10 mL) and stirred at RT for 3 h. After this time, the reaction mixture was concentrated under reduced pressure to give a crude yellow oil which was solid loaded onto a column and purified by FCC (on silica gel eluting 5-10% MeOH in CH_2Cl_2) to give *16-(hexadecyloxy)-10,13-dioxo-3,6,18-trioxa-9,14-diazatetratriacontan-1-aminium 2,2,2-trifluoroacetate* **9** (1.05 g, 93%) as a white solid.

^{1}H NMR (600 MHz; $CDCl_3$) δ_H 0.88 (6H, apparent t, J = 7.0, 2 × C**H$_3$**), 1.25-1.33 (52H, m, cetyl chain), 1.52-1.56 (4H, apparent quint, J = 6.9, 2 × $OCH_2C\mathbf{H_2}$), 2.49-2.56 (4H, m, $C(O)C\mathbf{H_2}C\mathbf{H_2}C(O)$), 3.16 (2H, br s, $H_3N^+C\mathbf{H_2}$), 3.22-3.26 (1H, m, NHC**H**HCH), 3.39-3.47 (9H, m, NHCH**H**CH, CHC**H**HO, $OCH_2C\mathbf{H_2}NH$, C**H**, 2 × $OC\mathbf{H_2}CH_2CH_2$), 3.52-3.55 (1H, m, CHCH**H**O), 3.60-3.61 (4H, m, $OCH_2C\mathbf{H_2}O$, $OC\mathbf{H_2}CH_2NH$), 3.68-3.70 (2H, m, $OC\mathbf{H_2}CH_2O$), 3.78 (2H, t, J = 5.0, $H_3N^+CH_2C\mathbf{H_2}$), 6.49 (1H, br s, N**H**), 7.84 (1H, br s, N**H**), 8.34 (3H, br s, $^+N\mathbf{H_3}$); **^{13}C NMR** (150 MHz; $CDCl_3$) δ_C 14.2 (**C**H_3, signals superimposed), 22.8 (**C**H_2, signals superimposed), 26.2 (**C**H_2), 29.5 (**C**H_2, signals superimposed), 29.6 (**C**H_2), 29.7 (**C**H_2), 29.8 (**C**H_2, signals superimposed), 29.8 (**C**H_2, signals superimposed), 30.1 (**C**H_2), 30.5 ($C(O)\mathbf{C}H_2$), 30.8 ($C(O)\mathbf{C}H_2$), 32.0 (**C**H_2, signals superimposed), 39.6 (**C**H_2), 39.8 ($^+NH_3\mathbf{C}H_2$), 41.2 ($NH\mathbf{C}H_2CH$), 66.8 (**C**H_2O), 69.8 (**C**H_2O), 69.9 (**C**H_2O), 70.4 (**C**H_2), 71.3 ($CH\mathbf{C}H_2O$), 71.9 (**C**H_2), 76.5 (**C**H), 116.6 (q, $^1J_{C,F}$ = 293.3, **C**F_3) 162.5 (q, $^2J_{C,F}$ = 36.2, **C**$(O)CF_3$), 173.3 (**C**(O)), 173.5 (**C**(O)); **MP** 75-86 °C; **IR** ν_{max}/cm^{-1} 3286 (N-H), 2913 (C-H), 2846 (C-H), 1671 (C=O), 1642 (C=O); **LRMS** (LC-MS ES+) *m/z* 770.9 (100%, $[M+H]^+$), 792.9 (10%, $[M+Na]^+$); **HRMS** (TOF MS ES+) calculated mass 770.6981 g.mol^{-1} ($[C_{45}H_{92}N_3O_6]^+$), observed *m/z* 770.6979 ($[M+H]^+$); **R$_f$** 0.35 (10% MeOH in CH_2Cl_2).

N1-(2,3-Bis(hexadecyloxy)propyl)-N4-(2-(2-(2-(3-(4-(((2R,3R,4S,5S,6R)-3,4,5-trihydroxy-6-(hydroxymethyl)tetrahydro-2H-pyran-2-yl)oxy)phenyl)thioureido)ethoxy)ethoxy)ethyl)succinamide, **GlcEG3SLc (11)**

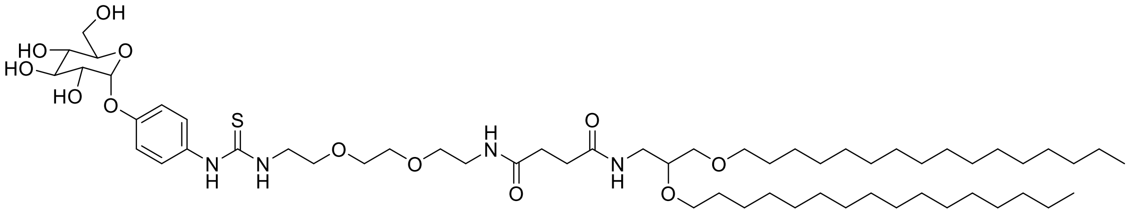

Amine **9** (0.384 g, 0.434 mmol) and *p*-isothiocyanatophenyl-α-D-glucopyranoside **10** (0.092 g, 0.29 mmol) were dissolved in MeOH (15 mL). NEt_3 (0.20 mL, 0.145 g, 1.43 mmol) was added and the reaction mixture was stirred at RT for 21 h. After this time, TLC showed the reaction to be incomplete so the reaction mixture was heated at reflux for 48 h. The crude was dry loaded onto a column and purified *via* FCC (on silica gel eluting with 1% NEt_3 and 2-8% MeOH in CH_2Cl_2). The desired fractions were combined to give 0.489 g of impure product which was dry loaded onto a second column and purified by FCC (on silica gel eluting 5-9% MeOH in CH_2Cl_2) to give 0.260 g of product that was still not 100% clean. This material was dissolved in CH_2Cl_2 and washed with 1 M HCl (3 × 15 mL) and saturated $NaHCO_3$ solution (3 × 15 mL). The aqueous layers were extracted with CH_2Cl_2 (4 × 50 mL) and the organic layers were combined, dried ($MgSO_4$) and concentrated under reduced pressure to give GlcEG3SLc **11** (0.212 g, 67%) as a white solid.

^{1}H NMR (600 MHz; CD_3OD) δ_H 0.90 (6H, apparent t, *J* = 7.0, 2 × C$\mathbf{H_3}$), 1.29-1.36 (52 H, m, cetyl chain), 1.53-1.57 (4H, m, 2 × $OCH_2C\mathbf{H_2}CH_2$), 2.47 (4H, s, C(O)C$\mathbf{H_2}$C$\mathbf{H_2}$C(O)), 3.21-3.24 (1H, m, NHC**H**HCH), 3.29-3.76 (25H, m, 6 × OC$\mathbf{H_2}$, C**H**, 3 × NHC$\mathbf{H_2}$, NHCH**H**CH, 3 × C**H**OH, C$\mathbf{H_2}$OH), 3.84 (1H, apparent t, *J* = 9.3, C**H**OH), 5.47 (1H, d, *J* = 3.6, anomeric C**H**), 7.18 (2H, d, *J* = 8.9, 2 × ArH), 7.24 (2H, d, *J* = 8.9, 2 × ArH), 7.91 (1H, bt, *J* = 5.7, N**H**), 7.99 (1H, br s, N**H**); **^{13}C NMR** (150 MHz; CD_3OD) δ_c 14.5 (**C**H_3, signals superimposed), 23.8 (cetyl chain **C**H_2), 27.3 (cetyl chain **C**H_2), 27.3 (cetyl chain **C**H_2), 30.5 (cetyl chain **C**H_2), 30.6 (cetyl chain **C**H_2), 30.7 (cetyl chain **C**H_2), 30.8-30.9 (6 × cetyl chain **C**H_2, signals superimposed), 31.2 (cetyl chain **C**H_2), 32.2 (C(O)**C**H_2**C**H_2C(O)), 33.1 (cetyl chain **C**H_2), 40.4 (**C**H_2), 41.6 (NH**C**H_2CH), 45.5 (**C**H_2), 57.5 (NH**C**(S)NH, thiourea), 62.4 (CH**C**H_2O), 70.6 (**C**H_2), 71.3 (**C**H_2, signals superimposed), 71.5 (**C**H), 72.4 (**C**H_2), 72.6 (**C**H_2), 73.3 (**C**H), 74.5 (**C**H), 74.9 (**C**H), 78.6 (CH_2**C**HCH_2), 99.6 (O**C**HO), 118.9 (Ar**C**), 127.6 (Ar**C**), 174.7 (**C**(O)), 174.8 (**C**(O)); **IR** ν_{max}/cm^{-1} 3291 (O-H), 2913 (C-H), 2846 (C-H), 1672 (C=O), 1641 (C=O), 1124 (C=S);

MP 183-189 °C; **LRMS** (LC-MS ES+) *m/z* 1083.9 (100%, $[M+H]^+$); **HRMS** (TOF MS ES+) calculated mass 1083.7601 g.mol^{-1} ($[C_{58}H_{107}N_4O_{12}S]^+$), observed *m/z* 1083.7599 ($[M+H]^+$); **R_f** 0.48 (10% MeOH in CH_2Cl_2).

7.3.2 Synthesis associated with paraCEST strategies (Section 3)

Dy-DOTA (12)[272]

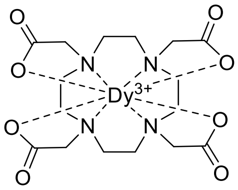

DOTA (0.996 g, 2.46 mmol) and dysprosium(III) chloride hexahydrate (0.933 g, 2.48 mmol) were dissolved in distilled water (35 mL) and stirred at RT, while ammonium hydroxide solution (1 M) was added dropwise until pH 7 was achieved. The reaction was left to stir overnight. After this time, the pH was increased to 13 *via* dropwise addition of ammonium hydroxide and the solution was stirred for 15 min and then filtered through a 0.22 μm syringe filter. The filtrate was concentrated under reduced pressure and dried on the freeze-drier to give Dy-DOTA **12** (1.36 g, 98%) as a white powder. Total Dy chelation was confirmed by the Xylenol Orange assay.[206]

^{1}H NMR (300 MHz; d_6-DMSO) 0.59-1.16 (br s); **MP** > 250 °C; **IR** ν_{max}/cm^{-1} 3124 (O-H), 3032 (O-H), 2961 (C-H), 2838 (C-H), 1587 (C=O); **LRMS** (LC-MS ES-) *m/z* 560.5 (15%, Dy^{160}-DOTA, M$^-$), 561.3 (55%, Dy^{161}-DOTA, M$^-$), 562.3 (80%, Dy^{162}-DOTA, M$^-$), 653.3 (90% Dy^{163}-DOTA, M$^-$), 564.3 (100%, Dy^{164}-DOTA, M$^-$). Data corresponds with the literature.[272]

Tm-DOTA (13)[211]

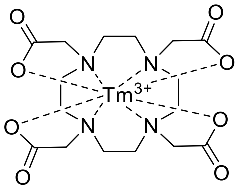

DOTA (0.198 g, 0.490 mmol) and thulium(III) chloride hexahydrate (0.189 g, 0.493 mmol) were dissolved in distilled water (15 mL) and stirred at RT, while ammonium hydroxide solution (1 M) was added dropwise until pH 7 was achieved. The reaction was left to stir overnight. After this time, the pH was increased to 13 *via* dropwise addition of ammonium hydroxide and the solution was stirred for 20 min and then filtered through a 0.22 μm syringe filter. The filtrate was concentrated under reduced pressure and dried on the freeze drier to give Tm-DOTA **13** (0.277 g, 99%) as a white powder. Total Tm chelation was confirmed by the Xylenol Orange assay.[206]

^{1}H NMR (300 MHz; d_6-DMSO) 7.28 (br s); **MP** > 250 °C; **IR** ν_{max}/cm^{-1} 3133 (O-H), 3013 (O-H), 2891 (C-H), 1648 (C=O), 1603 (C=O); **LRMS** (LC-MS ES+) *m/z* 571.3 (100%, $[M+H]^+$). Data corresponds with the literature.[211]

(1,4,7,10-Tetraaza-cyclododec-1-yl)-acetic acid benzyl ester (15)[213]

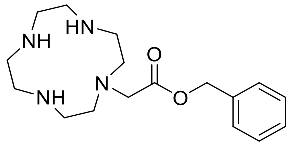

To a solution of cyclen (2.91 g, 16.9 mmol) at 0 °C in CH_2Cl_2 (20 mL) was added benzyl bromoacetate (1.34 mL, 1.94 g, 8.46 mmol) in CH_2Cl_2 (10 mL) dropwise over 2 h. The reaction mixture was stirred for 1 h at 0 °C and then for 2 h at RT. After this time, the unreacted cyclen was filtered off and the solvent was removed under reduced pressure. The crude was purified by FCC (on silica gel eluting DCM:EtOH:28% aq. NH_3 (1:0.8:0.2)) to give (1,4,7,10-tetraaza-cyclododec-1-yl)-acetic acid benzyl ester **15** (2.14 g, 79 %) as a cloudy white oil.

^{1}H NMR (600 MHz; $CDCl_3$) δ_H 2.67-2.97 (16H, m, 8 × ring C**H$_2$**), 3.49 (2H, s, C**H$_2$**C(O)), 5.13 (2H, s, OC**H$_2$**), 7.34-7.36 (5H, m, 5 × Ar**H**); **^{13}C NMR** (150 MHz; $CDCl_3$) δ_c 43.8 (**C**H$_2$), 45.6 (**C**H$_2$), 45.7 (**C**H$_2$), 46.4 (**C**H$_2$), 47.2 (**C**H$_2$), 47.3 (**C**H$_2$), 50.7 (**C**H$_2$), 51.8 (**C**H$_2$), 56.0 (**C**H$_2$C(O)), 65.1 (O**C**H$_2$), 127.0 (2 × Ar**C**H), 127.5 (Ar**C**H), 128.5 (Ar**C**), 128.6 (2 × Ar**C**H), 171.6 (**C**(O)); **IR** ν_{max}/cm^{-1} 3290 (N-H), 2843 (C-H), 1732 (C=O), 1621 (C=C); **LRMS** (ESI+) *m/z* 213.2 (100%, $[M-OBn]^+$), 321.2 (100%, $[M+H]^+$); **R$_f$** 0.40 (CH_2Cl_2:EtOH:$NH_{3(aq)}$ 1:0.8:0.2). Data corresponds with the literature.[213]

(4,7,10-Tris-*tert*-butoxycarbonylmethyl-1,4,7,10-tetraaza-cyclododec-1-yl)-acetic acid benzyl ester (16)[213]

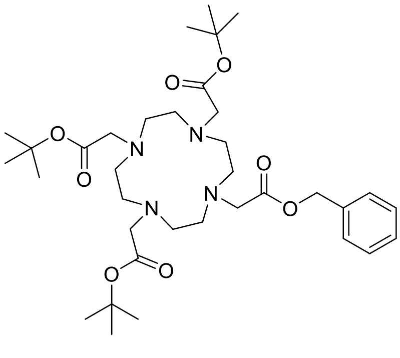

To (1,4,7,10-tetraaza-cyclododec-1-yl)-acetic acid benzyl ester **15** (2.00 g, 6.24 mmol) and K_2CO_3 (3.45 g, 25.1 mmol) in MeCN (35 mL) was added a solution of *tert*-butyl bromoacetate (3.70 mL, 4.89 g, 25.1 mmol) also in MeCN (10 mL) dropwise over a period of 45 min at RT. After 2 h another 2 eq. of *tert*-butyl bromoacetate (1.85 mL, 2.44 g, 12.5 mmol) and K_2CO_3 (1.73 g, 12.5 mmol) were added and the reaction was stirred overnight. After this period the solids were removed by filtration and the volatile components were evaporated under reduced pressure. The crude yellow oil was purified *via* FCC (on silica gel eluting 3-5% MeOH in CH_2Cl_2) to give (4,7,10-tris-*tert*-butoxycarbonylmethyl-1,4,7,10-tetraaza-cyclododec-1-yl)-acetic acid benzyl ester **16** (1.93, 47%) as a white foam.

^{1}**H NMR** (600 MHz; $CDCl_3$) δ_H 1.41-1.50 (27H, m, 3 × C(C$\mathbf{H_3}$)$_3$), 2.45-3.60 (24H, m, 8 × ring C$\mathbf{H_2}$, 4 × NC$\mathbf{H_2}$C(O)), 5.13 (2H, s, OC$\mathbf{H_2}$Ar), 7.32-7.38 (5H, m, 5 × ArH); ^{13}**C NMR** (150 MHz; $CDCl_3$) δ_c 28.0 (C(**C**H$_3$)$_3$, signals superimposed), 28.0 (C(**C**H$_3$)$_3$, signals superimposed), 28.1 (C(**C**H$_3$)$_3$), 28.2 (C(**C**H$_3$)$_3$), 28.3 (C(**C**H$_3$)$_3$), 28.3 (C(**C**H$_3$)$_3$), 48.6 (**C**H$_2$, ring), 48.6 (**C**H$_2$, ring), 48.6 (**C**H$_2$, ring), 48.7 (**C**H$_2$, ring), 52.7 (**C**H$_2$, ring), 52.8 (**C**H$_2$, ring), 52.8 (**C**H$_2$, ring), 52.9 (**C**H$_2$, ring), 55.1 (N**C**H$_2$C(O)), 55.8 (N**C**H$_2$C(O)), 55.8 (N**C**H$_2$C(O)), 55.9 (N**C**H$_2$C(O)), 67.0 (**C**H$_2$Ph), 82.0 (**C**(CH$_3$)$_3$), 82.1 (**C**(CH$_3$)$_3$, signals superimposed), 128.6 (2 × Ar**C**H), 128.7 (Ar**C**H), 128.8 (2 × Ar**C**H), 135.2 (Ar**C**), 173.1 (**C**(O)), 173.2 (2 × **C**(O)), 173.7 (**C**(O)); **IR** ν_{max}/cm^{-1} 2970 (C-H), 2937 (C-H), 2819 (C-H), 1721 (C=O), 1680 (C=O), 1468 (C=C); **LRMS** (LC-MS ES+) *m/z* 495.5 (100% [M+4H-3^{t}Bu]$^+$), 551.6 (45%, [M+3H-2^{t}Bu]$^+$), 607.6 (25%, [M+2H-^{t}Bu]$^+$), 663.7 (60%, [M+H]$^+$); **R$_f$** 0.44 (5% MeOH in CH_2Cl_2). Data corresponds with the literature.[213]

4,7,10-Tris-*tert*-butoxycarbonylmethyl-1,4,7,10-tetraaza-cyclododec-1-yl)-acetic acid (17)[213]

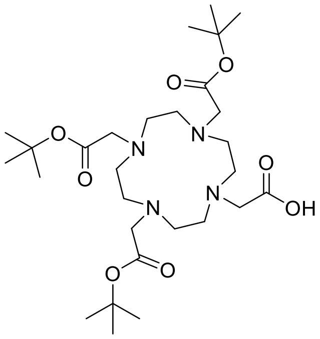

To (4,7,10-tris-*tert*-butoxycarbonylmethyl-1,4,7,10-tetraaza-cyclododec-1-yl)-acetic acid benzyl ester **16** (0.886 g g, 1.34 mmol) in MeOH (25 mL) was added 10 wt% Pd/C (86 mg, 0.081 mmol Pd). The flask was evacuated and purged with H_2 three times and the solution was vigorously stirred under a H_2 atmosphere for 4 h. After this time, a TLC was taken and the H_2 balloon replaced. After a further 3 h, a second portion of 10 wt% Pd/C (50 mg, 0.047 mmol Pd) was added to the reaction mixture, the H_2 balloon was replaced and the reaction mixture was stirred overnight. The solution was then filtered through celite® and the solvent of the filtrate was removed under reduced pressure. The oil was dried under high vacuum to give 4,7,10-Tris-*tert*-butoxycarbonylmethyl-1,4,7,10-tetraaza-cyclododec-1-yl)-acetic acid **17** (0.764 g, 99%) as a cream foam.

^{1}H NMR (300 MHz; $CDCl_3$, 60 °C) δ_H 1.47-1.50 (27H, m, 3 × $C(C\mathbf{H_3})_3$), 2.36-3.30 (22H, m, 8 × ring C$\mathbf{H_2}$ and NC$\mathbf{H_2}$Boc), 3.58 (2H, s, C$\mathbf{H_2}$COOH); **^{13}C NMR** (75 MHz; $CDCl_3$) δ_C 28.0 ($C(\mathbf{C}H_3)_3$, signals superimposed), 28.1 ($C(\mathbf{C}H_3)_3$), 28.2 ($C(\mathbf{C}H_3)_3$, signals superimposed), 28.2 ($C(\mathbf{C}H_3)_3$), 28.3 ($C(\mathbf{C}H_3)_3$), 28.3 ($C(\mathbf{C}H_3)_3$), 28.3 ($C(\mathbf{C}H_3)_3$), 48.4 (ring **C**H_2), 48.5 (ring **C**H_2), 48.6 (ring **C**H_2), 48.7 (ring **C**H_2), 52.6 (ring **C**H_2), 52.6 (ring **C**H_2), 52.6 (ring **C**H_2), 52.8 (ring **C**H_2), 55.7 (N**C**H_2C(O)), 56.0 (2 × N**C**H_2C(O)), 56.3 (N**C**H_2C(O)), 82.2 (2 × **C**$(CH_3)_3$), 82.5 (**C**$(CH_3)_3$), 172.4 (**C**(O)), 174.8 (**C**(O)); **MP** 84-88 °C; **IR** ν_{max}/cm^{-1} 3428 (O-H), 2971 (C-H), 2820 (C-H), 1722 (C=O), 1626 (C=O); **LRMS** (LC-MS ES+) m/z 405.4 (100%, $[M+4H-3^tBu]^+$), 461.3 (95%, $[M+3H-2^tBu]^+$), 517.5 (90%, $[M+2H-^tBu]^+$), 573.5 (100%, $[M+H]^+$); **R_f** 0.46 (5% MeOH in CH_2Cl_2). Data corresponds with the literature.[213]

***Tri-tert-butyl 2,2',2''-(10-(19-(hexadecyloxy)-2,13,16-trioxo-6,9,21-trioxa-3,12,17-triazaheptatriacontyl)-1,4,7,10-tetraazacyclododecane-1,4,7-triyl)triacetate* (18)**

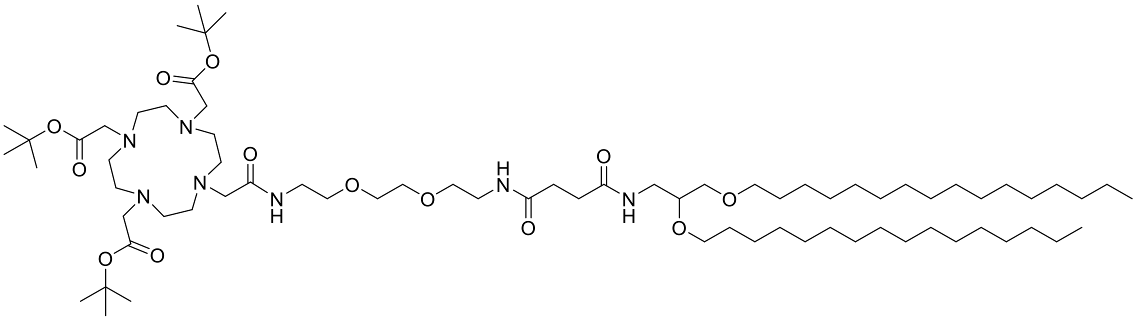

To tri-protected DOTA **17** (0.288 g, 0.503 mmol) in anhydrous CH_2Cl_2 (20 mL) under $Ar_{(g)}$ was added HBTU (0.192 g, 0.506 mmol), DIPEA (0.134 g, 0.18 mL, 1.03 mmol) and *16-(Hexadecyloxy)-10,13-dioxo-3,6,18-trioxa-9,14-diazatetratriacontan-1-aminium 2,2,2-trifluoroacetate* **9** (0.405 g, 0.509 mmol). The reaction mixture was stirred at RT under $Ar_{(g)}$ for 4.5 h. The solvent was removed under reduced pressure and the crude was purified by FCC (dry loaded on silica gel eluting 0-6% MeOH in CH_2Cl_2). The resulting residue was washed with saturated $NaHCO_3$ solution (3 × 40 mL) and distilled water (3 × 40 mL), extracted with CH_2Cl_2 (3 × 100 mL), dried ($MgSO_4$) and concentrated under reduced pressure to *give tert-butyl (16-(hexadecyloxy)-10,13-dioxo-3,6,18-trioxa-9,14-diazatetratriacontyl)carbamate* **18** (0.202 g, 30%) as a pale yellow solid.

^{1}H NMR (600 MHz; CDCl$_3$) δ_H 0.88 (6H, apparent t, *J* = 7.0, 2 × C**H$_3$**), 1.25-1.31 (52H, m, cetyl chain), 1.45-1.47 (27H, m, 3 × C(C**H$_3$**)$_3$), 1.52-1.57 (4H, m, 2 × OCH$_2$C**H$_2$**CH$_2$), 1.90-3.05 (28H, m, C(O)C**H$_2$**C**H$_2$**C(O), 8 × ring C**H$_2$** and 4 × NC**H$_2$**C(O)), 3.38-3.62 (21H, m, 7 × OC**H$_2$**, C**H**, 3 × NHC**H$_2$**), 6.98 (1H, bt, *J* = 5.6, N**H**), 7.42 (1H, br s, N**H**), 8.14 (1H, br s, N**H**); **^{13}C NMR** (150 MHz; CD$_3$OD) δ_c 14.3 (**C**H$_3$, signals superimposed), 22.8 (**C**H$_2$CH$_3$, signals superimposed), 26.2 (**C**H$_2$), 28.0 (C(**C**H$_3$)), 28.1 (C(**C**H$_3$)), 28.3 (C(**C**H$_3$)), 29.5 (**C**H$_2$), 29.6 (**C**H$_2$), 29.7 (**C**H$_2$), 29.8 (**C**H$_2$), 29.8 (**C**H$_2$), 29.8 (**C**H$_2$, signals superimposed), 30.2 (**C**H$_2$), 30.2 (**C**H$_2$), 31.6 (**C**H$_2$), 32.0 (**C**H$_2$), 32.2 (**C**H$_2$), 32.5 (**C**H$_2$), 39.3 (**C**H$_2$), 39.4 (**C**H$_2$), 39.5 (**C**H$_2$), 39.5 (**C**H$_2$), 40.7 (**C**H$_2$), 40.9 (**C**H$_2$), 52.1 (**C**H$_2$), 52.6 (**C**H$_2$), 53.6 (**C**H$_2$), 55.8 (**C**H$_2$), 56.2 (**C**H$_2$), 56.3 (**C**H$_2$), 69.6 (**C**H$_2$), 69.9 (**C**H$_2$), 70.1 (**C**H$_2$), 70.3 (**C**H$_2$), 70.4 (**C**H$_2$), 70.4 (**C**H$_2$), 70.5 (**C**H$_2$), 71.6 (**C**H$_2$), 71.7 (**C**H$_2$), 71.8 (**C**H$_2$), 71.9 (**C**H$_2$), 77.3 (**C**H), 81.1 (**C**(CH$_3$)$_3$), 81.9 (**C**(CH$_3$)$_3$), 82.0 (**C**(CH$_3$)$_3$), 170.9 (**C**(O)), 172.0 (**C**(O)CH$_2$CH$_2$), 172.3 (**C**(O)), 172.5 (**C**(O)), 172.7 (**C**(O)), 172.9 (**C**(O)CH$_2$CH$_2$); **MP** 158-162 °C; **IR** ν_{max}/cm^{-1} 3203 (N-H), 2992 (C-H), 2914 (C-H), 2847 (C-H), 1735 (C=O), 1673 (NHC=O), 1648 (NHC=O); **LRMS** (LC-MS ES+) m/z 663.0 (100%, [M+2H]$^{2+}$), 1325.2 (25%, [M+H]$^+$); **HRMS** (TOF MS ES+) calculated mass 1325.0666 g.mol^{-1} ([C$_{73}$H$_{142}$N$_7$O$_{13}$]$^+$), observed *m/z* 1325.0674 ([M+H]$^+$); **R$_f$** 0.25 (7% MeOH in CH$_2$Cl$_2$).

2,2',2''-(10-(19-(Hexadecyloxy)-2,13,16-trioxo-6,9,21-trioxa-3,12,17-triazaheptatriacontyl)-1,4,7,10-tetraazacyclododecane-1,4,7-triyl)triacetic acid, DEG3SLc (19)

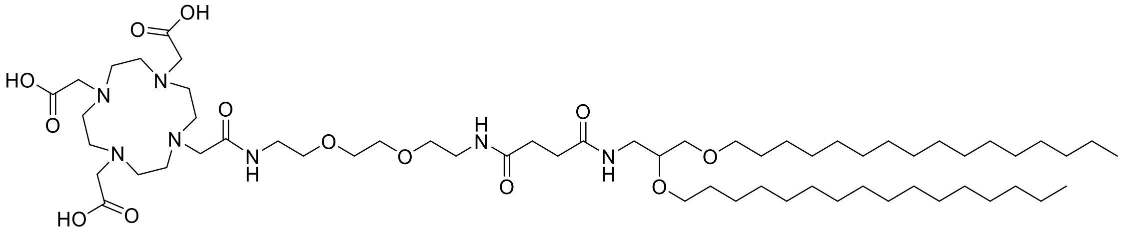

Tri-tert-butyl 2,2',2''-(10-(19-(hexadecyloxy)-2,13,16-trioxo-6,9,21-trioxa-3,12,17-triazaheptatriacontyl)-1,4,7,10-tetraazacyclododecane-1,4,7-triyl)triacetate **18** (0.174 g, 0.131 mmol) was stirred in 1:1 (v/v) solution of TFA:CH$_2$Cl$_2$ at RT for 3.5 h. After this period the solvent was removed under reduced pressure and the resulting residue dried under high vacuum. ^{1}H NMR and LC-MS analysis showed the reaction to be incomplete so the residue was stirred in a 1:1 (v/v) solution of TFA:CH$_2$Cl$_2$ at RT for a further 3 h. The solvent was removed under reduced pressure and dried under high vacuum to give *2,2',2''-(10-(19-(hexadecyloxy)-2,13,16-trioxo-6,9,21-trioxa-3,12,17-*

triazaheptatriacontyl)-1,4,7,10-tetraazacyclododecane-1,4,7-triyl)triacetic acid **19** (0.098 g, 65%) as a pale yellow amorphous solid.

^{1}H NMR (600 MHz; 3:1 $CDCl_3$: CD_3OD) 0.90 (6H, apparent t, J = 7.1, 2 × CH_3), 1.29-1.38 (52H, m, cetyl chain), 1.53-1.58 (4H, m, 2 × $OCH_2C\mathbf{H_2}CH_2$), 2.31 (4H, s, $C(O)C\mathbf{H_2}C\mathbf{H_2}C(O)$), 2.27-4.18 (45H, m, 8 × ring $C\mathbf{H_2}$, 4 × $NCH_2C(O)$, 7 × $OC\mathbf{H_2}$, $C\mathbf{H}$, 3 × $NHC\mathbf{H_2}$); **^{13}C NMR** (150 MHz; 3:1 $CDCl_3$:CD_3OD) δ_c 14.5 ($\mathbf{C}H_3$, signals superimposed), 23.8 ($\mathbf{C}H_2$, signals superimposed), 24.7 ($\mathbf{C}H_2$), 27.3 ($\mathbf{C}H_2$), 27.3 ($\mathbf{C}H_2$), 30.5 ($\mathbf{C}H_2$, signals superimposed), 30.6 ($\mathbf{C}H_2$), 30.6 ($\mathbf{C}H_2$), 30.6 ($\mathbf{C}H_2$), 30.8 ($\mathbf{C}H_2$), 30.8 ($\mathbf{C}H_2$), 30.8 ($\mathbf{C}H_2$, signals superimposed), 31.2 ($\mathbf{C}H_2$), 32.1 ($\mathbf{C}H_2$), 32.2 ($\mathbf{C}H_2$), 33.1 ($\mathbf{C}H_2$, signals superimposed), 40.2 ($\mathbf{C}H_2$), 40.2 ($\mathbf{C}H_2$), 40.3 ($\mathbf{C}H_2$), 40.4 ($\mathbf{C}H_2$), 40.8 ($\mathbf{C}H_2$), 41.6 ($\mathbf{C}H_2$), 70.1 ($\mathbf{C}H_2$), 70.4 ($\mathbf{C}H_2$), 70.5 ($\mathbf{C}H_2$), 71.2 ($\mathbf{C}H_2$), 71.2 ($\mathbf{C}H_2$), 71.3 ($\mathbf{C}H_2$), 71.3 ($\mathbf{C}H_2$), 71.3 ($\mathbf{C}H_2$, signals superimposed), 72.4 ($\mathbf{C}H_2$), 72.6 ($\mathbf{C}H_2$), 78.6 ($\mathbf{C}H$), 118.0 (q, $^1J_{C,F}$ = 292.5, $\mathbf{C}F_3$), 162.5 (q, $^2J_{C,F}$ = 35.3 , $\mathbf{C}(O)CF_3$), 174.7 ($\mathbf{C}(O)$), 174.7 ($\mathbf{C}(O)$, signals superimposed), 175.2 ($\mathbf{C}(O)$); **IR** ν_{max}/cm^{-1} 3299 (N-H), 3087 (O-H), 2913 (C-H), 2846 (C-H),1662 (C=O); **LRMS** (ESI+) *m/z* 579.0 ($[M+2H]^{2+}$), 1156.9 ($[M+H]^+$); **HRMS** (TOF MS ES+) calculated mass 1156.8788 g.mol^{-1} ($[C_{61}H_{117}N_7O_{13}]^+$), observed *m/z* 1156.8790 ($[M+H]^+$); **R$_f$** 0.30 (20% MeOH in CH_2Cl_2).

***Tri-tert-butyl 2,2',2''-(10-(2-oxo-2-(((3R,4R,5S,6R)-2,4,5-trihydroxy-6-(hydroxymethyl)tetrahydro-2H-pyran-3-yl)amino)ethyl)-1,4,7,10-tetraazacyclododecane-1,4,7-triyl)triacetate* (20)**

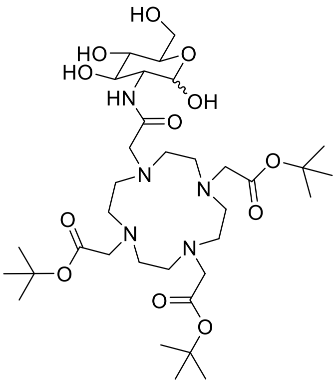

To a solution of D-(+)-glucosamine hydrochloride (0.198 g, 0.918 mmol) in DMF (20 mL) at 0 °C sodium methoxide (0.051 g, 0.94 mmol) was added and stirred for 15 min. After this period, tri-protected DOTA **17** (0.435 g, 0.760 mmol), HOBt hydrate (0.206 g, 1.52 mmol) and DCC (0.176 g, 0.853 mmol) were added and the reaction was stirred at 40 °C for 19 h. After this time, the reaction mixture was heated to 60 °C and DCC (0.5 eq.) was added and the mixture was stirred for a further 6 h. LC-MS analysis showed the presence of unreacted **17**, another 0.5 eq. of DCC were added to the reaction mixture which was stirred at 60 °C for a further 1.5 h. After this time, the reaction mixture was kept in the refrigerator overnight. Precipitated DCU was filtered off and the filtrate was poured into diethyl ether (600 mL) and left in the refrigerator over the weekend. Precipitated product was collected *via* filtration and purified by reverse-phase FCC (on C_{18}-reversed phase silica gel eluting 40-55% MeOH in H_2O with 1% TFA) to give 130 mg of impure product. This material was purified again by reverse-phase FCC (on C_{18}-reversed phase silica gel eluting 50-70% MeOH in H_2O) to give *tri-tert-butyl 2,2',2''-(10-(2-oxo-2-(((3R,4R,5S,6R)-2,4,5-trihydroxy-6-(hydroxymethyl)tetrahydro-2H-pyran-3-yl)amino)ethyl)-1,4,7,10-tetraazacyclododecane-1,4,7-triyl)triacetate* **20** (0.075 g, 13%) as a pale yellow glass.

^{1}H NMR (400 MHz; CD_3OD, 60 °C) δ_H 1.49-1.57 (27H, m, 3 × C(C**H$_3$**)$_3$), 3.07-4.16 (30 H, m, 12 × DOTA C**H$_2$**, 4 × C**H** and glucose C**H$_2$**), 5.12 (1H, d, *J* = 2.7, anomeric C**H**); **^{13}C NMR** (150 MHz; CD_3OD) δ_c 28.2 (**C**H$_3$), 28.2 (**C**H$_3$), 28.3 (**C**H$_3$), 28.3 (**C**H$_3$), 28.4 (**C**H$_3$), 28.4 (**C**H$_3$), 28.4 (**C**H$_3$), 28.4 (**C**H$_3$), 28.5 (**C**H$_3$), 28.6 (**C**H$_3$), 52.4 (**C**H$_2$), 52.5 (**C**H$_2$), 52.6 (**C**H$_2$), 52.7 (**C**H$_2$), 54.8 (**C**H$_2$), 54.8 (**C**H$_2$), 54.9 (**C**H$_2$), 55.0 (**C**H$_2$), 55.0 (**C**H$_2$), 55.0 (**C**H$_2$), 55.9 (**C**H$_2$), 55.9 (**C**H$_2$), 62.8 (glucose **C**H$_2$, α or β anomer), 62.9 (glucose **C**H$_2$, α or β anomer), 72.2 (**C**H), 72.6 (**C**H), 72.7 (**C**H), 72.8 (**C**H), 72.9 (**C**H), 73.1 (**C**H), 75.8 (**C**H), 78.1 (**C**H), 83.0 (**C**(CH$_3$)$_3$), 83.1 (**C**(CH$_3$)$_3$), 86.0 (**C**(CH$_3$)$_3$), 92.8 (α-anomeric **C**H), 96.8 (β-anomeric **C**H), 162.6 (**C**(O)), 166.7 (**C**(O)), 172.1 (**C**(O)), 172.6 (**C**(O)), approximately 3:1 α:β anomers; **IR** ν_{max}/cm^{-1} 3244 (O-H), 3082 (N-H), 2979 (C-H), 1725 (OC=O), 1667 (NHC=O); **LRMS** (TOF MS ES+) *m/z* 368.5 (45%, $[M+2H]^{2+}$), 734.5 (100%, $[M+H]^+$), 757.0 (40%, $[M+Na]^+$); **HRMS** (TOF MS ES+) calculated mass 734.4551 g.mol^{-1} ($[C_{34}H_{64}N_5O_{12}]^+$), observed *m/z* 734.4560 ($[M+H]^+$); **R$_f$** 0.31 (70% MeOH in H_2O).

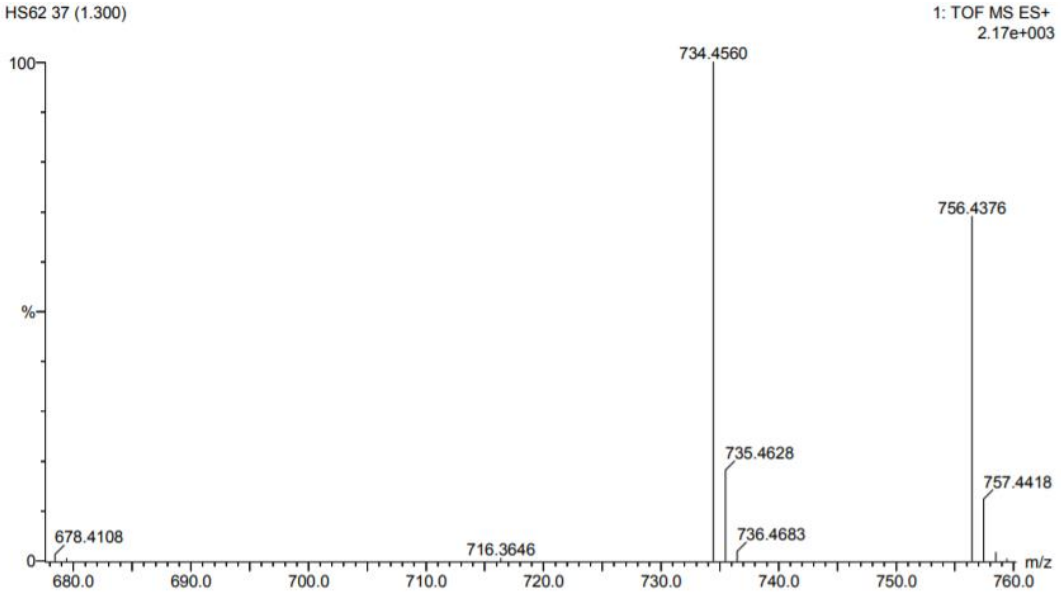

2,2',2''-(10-(2-Oxo-2-(((3R,4R,5S,6R)-2,4,5-trihydroxy-6-(hydroxymethyl)tetrahydro-2H-pyran-3-yl)amino)ethyl)-1,4,7,10-tetraazacyclododecane-1,4,7-triyl)triacetic acid **(21)**

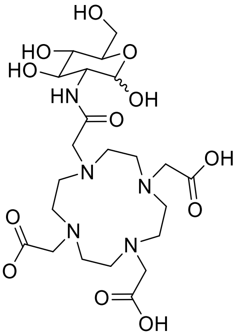

Tri-tert-butyl 2,2',2''-(10-(2-oxo-2-(((3R,4R,5S,6R)-2,4,5-trihydroxy-6-(hydroxymethyl)-tetrahydro-2H-pyran-3-yl)amino)ethyl)-1,4,7,10-tetraazacyclododecane-1,4,7-triyl)triacetate **20** (69 mg, 0.094 mmol) was stirred in a 1:1 (v/v) solution of TFA:CH_2Cl_2 (5 mL/5 mL) at RT for 6 h. The solvent was removed under reduced pressure and the remaining TFA was diluted with toluene to aid removal *via* azeotrope formation. The crude was purified by reverse-phase FCC (on C_{18}-reversed phase silica gel eluting 5-10% MeCN in H_2O) to give **21** contaminated with m/z 548 by LC-MS analysis, this mass was hypothesised to be due to internal ester formation. The residue was stirred in 1M NaOH for 1 h and purified using a size exclusion column to give *2,2',2''-(10-(2-oxo-2-(((3R,4R,5S,6R)-2,4,5-trihydroxy-6-(hydroxymethyl)tetrahydro-2H-pyran-3-yl)amino)ethyl)-1,4,7,10-tetraazacyclododecane-1,4,7-triyl)triacetic acid* **21** (25 mg, 47%) as a pale yellow glass.

^{1}H NMR (600 MHz; D_2O) δ_H 3.10-3.96 (30H, m, 12 × DOTA C**H$_2$**, 4 × C**H** and glucose C**H$_2$**), 4.80 (1H, d, *J* = 7.9, β-anomeric C**H**), 5.24 (1H, d, *J* = 3.5, α-anomeric C**H**); **^{13}C NMR** (150 MHz; D_2O) δ_c 48.7 (**C**H$_2$), 48.8 (**C**H$_2$), 48.8 (**C**H$_2$), 49.0 (**C**H$_2$), 52.0 (**C**H$_2$), 52.1 (**C**H$_2$), 54.5 (**C**H$_2$), 54.5 (**C**H), 54.7 (**C**H$_2$), 54.8 (**C**H$_2$), 55.6 (**C**H$_2$), 57.1 (**C**H$_2$), 57.1 (**C**H$_2$), 57.5 (**C**H), 61.2 (glucose **C**H$_2$, α or β anomer), 61.4 (glucose **C**H$_2$, α or β anomer), 70.4 (**C**H), 70.6 (**C**H), 71.4 (**C**H), 72.3 (**C**H), 74.0 (**C**H), 76.6 (**C**H), 91.5 (α-anomeric C**H**), 95.3 (β-anomeric C**H**), 171.1 (**C**(O)), 175.9 (**C**(O)), 176.1 (**C**(O)), 180.8 (**C**(O)); **IR** ν_{max}/cm^{-1} 3271 (O-H), 2971 (C-H), 2849 (C-H), 1677 (C=O), 1668 (C=O); **LRMS** (LC-MS ES+) *m/z* 283.8 (100%, [M+2H]$^{2+}$), 566.5 (60%, [M+H]$^+$)**;** **HRMS** (ESI+) calculated mass 566.2673 g.mol^{-1} ([$C_{22}H_{40}N_5O_{12}$]$^+$), observed *m/z* 566.2679 ([M+H]$^+$); **R$_f$** 0.71 (5% MeCN, 1% TFA in H_2O).

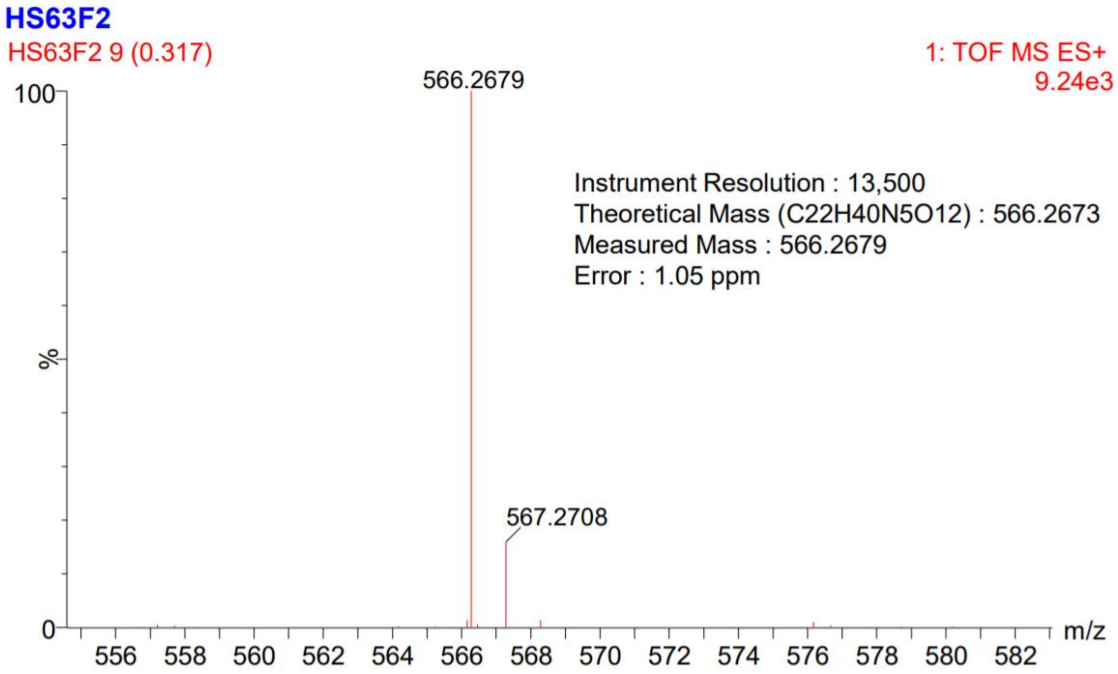

Instrument Resolution : 13,500
Theoretical Mass (C22H40N5O12) : 566.2673
Measured Mass : 566.2679
Error : 1.05 ppm

2,2',2''-(10-(2-oxo-2-(((3R,4R,5S,6R)-2,4,5-trihydroxy-6-(hydroxymethyl)tetrahydro-2H-pyran-3-yl)amino)ethyl)-1,4,7,10-tetraazacyclododecane-1,4,7-triyl)triacetic acid complexed to thulium **(22)**

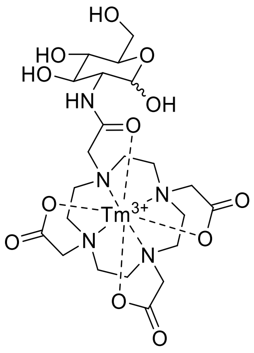

2,2',2''-(10-(2-oxo-2-(((3R,4R,5S,6R)-2,4,5-trihydroxy-6-(hydroxymethyl)tetrahydro-2H-pyran-3-yl)amino)ethyl)-1,4,7,10-tetraazacyclododecane-1,4,7-triyl)triacetic acid **21** (25 mg, 0.044 mmol) and thulium(III) chloride hexahydrate (17 mg, 0.045 mmol) were dissolved in H_2O (1.5 mL) and stirred while the pH was adjusted to pH 7 *via* addition of ammonium hydroxide solution (1M, ~ 0.1 mL). The reaction mixture was stirred at RT for 18 h. After this time, the pH was increased to pH 13 *via* addition of 1M ammonium hydroxide solution, stirred for 30 min the filtered through a 22 µm syringe filter. LC-MS analysis showed incomplete co-ordination (mass of starting material was still observable at m/z 566.54). Thulium(III) chloride hexahydrate (16 mg, 0.042 mmol) was added to the mixture and the pH was adjusted to pH 7. A precipitate was observed which was assumed to be a thulium salt thus the solution was filtered again and thulium(III) chloride hexahydrate (8.2 mg, 0.021 mmol) was added and stirred at pH 6 and 50 °C for 19 h. The pH was increased to pH 13 and the precipitated salt was filtered off using a 22 µm syringe filter. LC-MS analysis still showed incomplete co-ordination. Thulium(III) chloride hexahydrate (11 mg, 0.029 mmol) was added to the solution, the pH was adjusted to pH 6 with 1M HCl solution and heated to reflux for 16 h. The pH of the solution was adjusted to pH 8 with ammonium hydroxide solution (until precipitate formed), filtered and concentrated under reduced pressure to give **22** (25 mg, 77%) as a pale yellow glass. The product was a mixture of cyclised and uncyclised product.

^{1}**H NMR** (600 MHz; d_6-DMSO, 12.5 mM) 7.56 (br s, chelated **H_2**O), see Figure 36; **LRMS** (LC-MS ES+) *m/z* 731.5 ([M+H]$^+$).

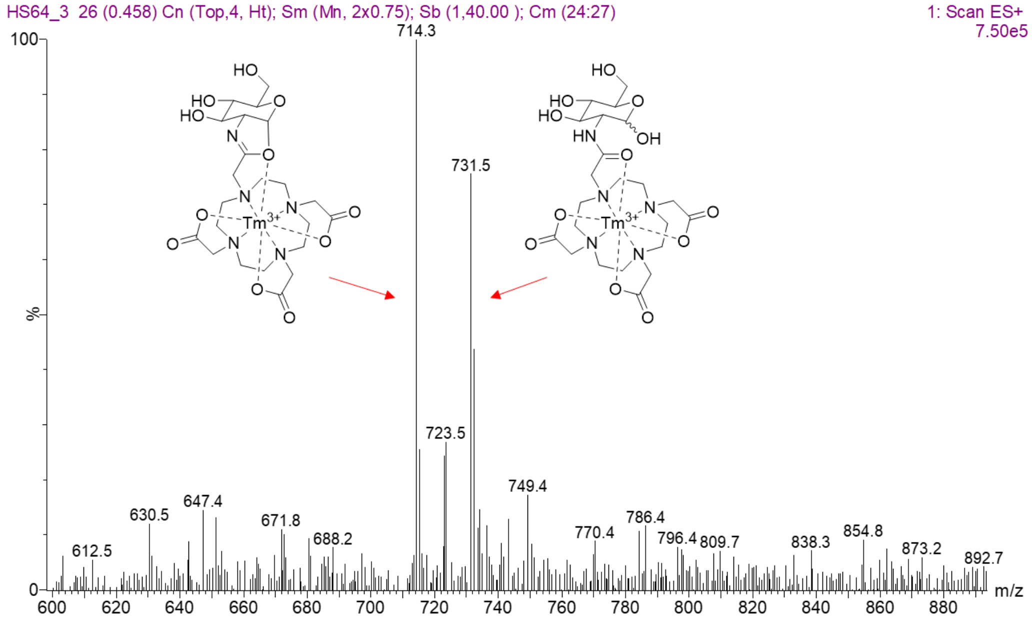

2-Deoxy-2-[*p*-methoxybenzylidene(amino)]-D-glucopyranose (23)[214]

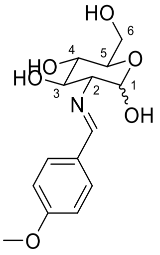

D-(+)-Glucosamine hydrochloride (2.01 g, 9.32 mmol) was dissolved in freshly prepared 1 M NaOH solution (10 mL) and *p*-anisaldehyde (1.52 g, 1.36 mL, 11.2 mmol) was added whilst stirring at RT. Crystallisation began immediately. The mixture was stirred for 5 min at RT then refrigerated for 2 h. After this time, ice-cooled distilled water (30 mL) was added and the precipitate was filtered off, washed with ice-cooled distilled water (3 × 20 mL) and a 1:1 mixture of EtOH:Et_2O (3 × 20 mL) and dried under vacuum to give 2-deoxy-2-[*p*-methoxybenzylidene(amino)]-D-glucopyranose **23** (1.21 g, 44%) as a white powder.

^{1}H NMR (600 MHz; CD_3OD) Primarily (> 90%) β anomer, when left in CD_3OD overnight, the proportion of α anomer increased to 20%, the NMR data provided is for the β anomer: δ_H 2.96 (1H, dd, *J* = 9.4, 7.8, C^2**H**), 3.37 (1H, m, C^4**H**), 3.41 (1H, dd, *J* = 5.8, 2.2, C^5**H**), 3.66 (1H, dd, *J* = 9.4, 8.7, C^3**H**), 3.72 (1H, dd, *J* = 11.8, 5.8, C^6**H**H), 3.84 (3H, s, OC**H$_3$**), 3.91 (1H, dd, J = 11.8, 2.2, C^{6}H**H**), 4.89 (1H, d, *J* = 7.8, C^1**H**), 6.99 (2H, d, *J* = 8.9, 2 × Ar**H**), 7.74 (2H, d, *J* = 8.9, 2 × Ar**H**), 8.23 (1H, s, NC**H**Ar); **^{13}C NMR** (150 MHz; CD_3OD) δ_c 55.9 (O**C**H$_3$), 62.9 (**C6**), 71.8 (**C4**), 76.1 (**C3**), 78.2 (**C5**), 79.4 (**C2**), 96.9 (**C1**), 115.1 (Ar**C**H), 129.8 (Ar**C**), 131.4 (Ar**C**H), 163.7 (Ar**C**), 166.3 (N**C**HAr); **IR** ν_{max}/cm^{-1} 3456 (O-H), 3309 (O-H), 3228 (O-H), 2920 (C-H), 1638 (C=N), 1604 (C=C); **LRMS** (LC-MS ES+) *m/z* 298.3 (100%, $[M+H]^+$)**;** **MP** 161-162 °C, lit. 163-164 °C. Data corresponds with the literature.[214]

1,3,4,6-Tetra-*O*-acetyl-2-deoxy-2-[*p*-methoxybenzylidene(amino)]-β-D-glucopyranose (24)[214]

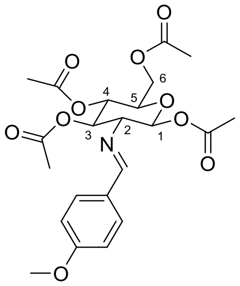

2-Deoxy-2-[*p*-methoxybenzylidene(amino)]-D-glucopyranose **23** (1.06 g, 3.58 mmol) was added to an ice-cooled solution of pyridine (7.2 mL) and Ac_2O (4 mL). The mixture was stirred in an ice bath for 1.5 h and then at RT for 16 h. After this time, the mixture was poured into ice-cooled water (100 mL). The precipitated product was filtered, washed with ice-cooled water (8 × 20 mL) and dried in the vacuum oven at 50 °C for 4 h to give 1,3,4,6-tetra-*O*-acetyl-2-deoxy-2-[*p*-methoxybenzylidene(amino)]-β-D-glucopyranose **24** (1.10 g, 66%) as a white powder.

^{1}H NMR (400 MHz; CD_3OD) Only β anomer obtained: δ_H 1.86 (3H, s, C(O)C**H$_3$**), 2.00 (3H, s, C(O)C**H$_3$**), 2.02 (3H, s, C(O)C**H$_3$**), 2.06 (3H, s, C(O)C**H$_3$**), 3.50 (1H, dd, *J* = 9.6, 8.3, C^2**H**), 3.84 (3H, s, OMe), 4.08 (1H, ddd, *J* = 9.9, 4.4, 2.3, C^5**H**), 4.13 (1H, dd, *J* = 12.4, 2.3, C^6**H**H), 4.34 (1H, dd, *J* = 12.4, 4.4, C^{6}H**H**), 5.10 (1H, dd, *J* = 9.9, 9.6, C^4**H**), 5.43 (1H, dd, *J* = 9.6, 9.6, C^3**H**), 5.96 (1H, d, *J* = 8.3, C^1**H**), 6.98 (2H, d, *J* = 8.9, 2 × Ar**H**), 7.69 (2H, d, *J* = 8.9, 2 × Ar**H**), 8.28 (1H, s, NC**H**Ar); **^{13}C NMR** (100 MHz; CD$_3$OD) δ_c 20.4 (C(O)**C**H$_3$), 20.5 (C(O)**C**H$_3$), 20.6 (C(O)**C**H$_3$), 20.6 (C(O)**C**H$_3$), 55.9 (O**C**H$_3$), 63.0 (**C6**), 69.0 (**C4**), 73.9 (**C5**), 74.1 (**C2**), 74.4 (**C3**), 94.3 (**C1**), 115.2 (Ar**C**H), 129.4 (Ar**C**), 131.4 (Ar**C**H), 164.2 (Ar**C**), 167.3 (N**C**HAr), 170.4 (**C**(O)), 171.2 (**C**(O)), 171.5 (**C**(O)), 172.3 (**C**(O)); **IR** ν_{max}/cm^{-1} 2961 (C-H), 2930 (C-H), 1747 (C=O), 1736 (C=O), 1648 (C=N), 1605 (C=C); **LRMS** (LC-MS ES+) *m/z* 466.4 (100%, [M+H]$^+$); **HRMS** (ESI+) calculated mass 466.1708 g.mol^{-1} ([C$_{22}$H$_{28}$NO$_{10}$]$^+$), observed *m/z* 466.1710 ([M+H]$^+$); **MP** 180-181 °C, lit. 180-182 °C. Data corresponds with the literature.[214]

1,3,4,6-Tetra-*O*-acetyl-β-D-glucosamine hydrochloride (25)[214]

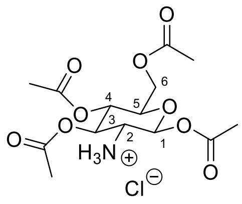

1,3,4,6-Tetra-*O*-acetyl-2-deoxy-2-[*p*-methoxybenzylidene(amino)]-β-D-glucopyranose **24** (0.85 g, 1.8 mmol) was dissolved in warm acetone (15 mL). Aqueous HCl solution (6 M, 0.63 mL) was added with the immediate formation of precipitate. The mixture was allowed to cool to RT, then Et$_2$O (20 mL) was added and the mixture was stirred for 2 h before being refrigerated overnight. The precipitated product was washed with Et$_2$O (3 × 20 mL) and dried under vacuum for 3 h to give 1,3,4,6-tetra-*O*-acetyl-β-D-glucosamine hydrochloride **25** (0.65 g, 93%) as a white powder.

^{1}H NMR (400 MHz; CD$_3$OD) Only β anomer obtained: δ_H 2.03 (3H, s, C(O)C**H$_3$**), 2.04 (3H, s, C(O)C**H$_3$**), 2.10 (3H, s, C(O)C**H$_3$**), 2.20 (3H, s, C(O)C**H$_3$**), 3.64 (1H, dd, *J* = 10.6, 8.8, C^2**H**), 4.04 (1H, ddd, *J* = 10.1, 4.6, 2.3, C^5**H**), 4.12 (1H, dd, *J* = 12.6, 2.3, C^{6}C**H**H), 4.31 (1H, dd, *J* = 12.6, 4.6, C^{6}H**H**), 5.10 (1H, dd, *J* = 10.1, 9.1, C^4**H**), (1H, dd, *J* = 10.6, 9.1, C^3**H**), 5.89 (1H, d, *J* = 8.8, C^1**H**); **^{13}C NMR** (150 MHz; CD$_3$OD) δ_c 20.5 (C(O)**C**H$_3$), 20.5 (C(O)**C**H$_3$), 20.7 (C(O)**C**H$_3$), 20.8 (C(O)**C**H$_3$), 54.3 (**C2**), 62.6 (**C**H$_2$), 69.2 (**C4**), 72.1 (**C3**), 74.0 (**C5**), 91.6 (**C1**), 170.1 (**C**(O)), 171.1 (**C**(O)), 171.9 (**C**(O)), 172.1 (**C**(O)); **IR** ν_{max}/cm^{-1} 2843 (C-H), 1756 (C=O), 1745 (C=O); **LRMS** (LC-MS ES+) *m/z* 348.3 (100%, [M+H]$^+$); **HRMS** (ESI+) calculated mass 348.1295 g.mol^{-1} ([C$_{14}$H$_{22}$NO$_9$]$^+$), observed *m/z* 348.1287 ([M+H]$^+$); **MP** at 233 °C this compound decomposed, lit. 235 °C. Data corresponds with the literature.[214]

(2S,3R,4R,5S,6R)-6-(Acetoxymethyl)-3-((6-hydroxyhexyl)amino)tetrahydro-2H-pyran-2,4,5-triyl triacetate **(27)**

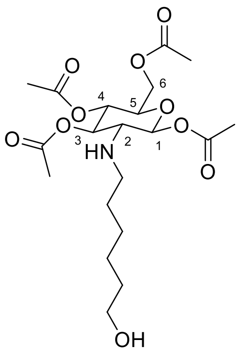

A 1 M DIBAL-H solution in toluene (8.3 mL, 8.3 mmol) was added slowly to a solution of ε-caprolactone (0.80 g, 0.78 mL, 7.0 mmol) in dry CH_2Cl_2 (5 mL) at -78 °C under $Ar_{(g)}$. The reaction mixture was stirred at -78 °C under $Ar_{(g)}$ for 1.5 h, until TLC analysis showed the reaction to be complete. Degassed and ice-cooled 0.5 M HCl solution was added dropwise to the mixture at -78 °C. The mixture was then poured into 0.5 M HCl solution (200 mL) at RT. After being stirred for 45 min, the organic layer was separated and the aqueous layer was extracted with CH_2Cl_2 (3 × 20 mL). The combined organic layers were dried ($MgSO_4$) and concentrated to give crude 6-hydroxyhexanal **26** (0.24 g) which was used without purification in the next step. ^1H NMR confirmed the presence of an aldehyde peak at 9.76 ppm.

1,3,4,6-Tetra-*O*-acetyl-β-D-glucosamine hydrochloride **25** (0.20 g, 0.52 mmol) and crude 6-hydroxyhexanal **26** (0.24 g, estimated 2.0 mmol) were stirred in a mixture of MeCN and H_2O (3:1, 20 mL) at RT for 30 min. After this time, $NaCNBH_3$ (0.10 g, 1.6 mmol) was added and stirred for 1 h at RT. The mixture was diluted with H_2O (25 mL) and extracted with $CHCl_3$ (3 × 30 mL). The organic extracts were combined, dried ($MgSO_4$) and purified by FCC (on silica gel eluting 0-5% MeOH in CH_2Cl_2). The fractions containing product were combined, concentrated and purified for a second time *via* FCC (on silica gel eluting 0-3% MeOH in CH_2Cl_2) to give *(2S,3R,4R,5S,6R)-6-(acetoxymethyl)-3-((6-hydroxyhexyl)amino)tetrahydro-2H-pyran-2,4,5-triyl triacetate* **27** (62 mg, 27%) as a clear viscous oil.

^{1}H NMR (600 MHz; $CDCl_3$) δ_H 1.28-1.42 (6H, m, $C\mathbf{H_2}C\mathbf{H_2}C\mathbf{H_2}CH_2CH_2OH$), 1.54 (2H, apparent quint, *J* = 6.8, $C\mathbf{H_2}CH_2OH$), 2.02 ($C\mathbf{H_3}$), 2.07 ($C\mathbf{H_3}$), 2.08 ($C\mathbf{H_3}$), 2.15 ($C\mathbf{H_3}$), 2.59 (1H, dt, *J* = 12.2, 6.2, $NHC\mathbf{H}H$), 2.68 (1H, dt, *J* = 12.2, 6.2, $NHCH\mathbf{H}$), 2.84 (1H, m, $C^2\mathbf{H}$), 3.63 (2H, t, *J* = 6.8, $C\mathbf{H_2}OH$), 3.77 (1H, m, $C^5\mathbf{H}$), 4.06 (1H, dd, *J* =12.4, 2.1, $C^6\mathbf{H}H$), 4.30 (1H, dd, *J* =12.4, 4.6, $C^6H\mathbf{H}$), 5.03-5.08 (2H, m, $C^3\mathbf{H}$ and $C^4\mathbf{H}$), 5.56 (1H, d, *J* = 8.4, $C^1\mathbf{H}$); **^{13}C NMR** (150 MHz; $CDCl_3$) δ_c 20.8 ($\mathbf{C}H_3$), 20.9 ($\mathbf{C}H_3$), 21.0 ($\mathbf{C}H_3$), 21.2 ($\mathbf{C}H_3$), 25.7

(**C**H_2), 26.8 (**C**H_2), 30.6 (**C**H_2), 32.8 (**C**H_2CH_2OH), 47.9 (NH**C**H_2), 61.0 (**C2**), 61.9 (**C6**), 62.9 (**C**H_2OH), 68.4 (**C4**), 72.6 (**C5**), 73.9 (**C3**), 94.7 (**C1**), 169.3 (**C**(O)), 169.8 (**C**(O)), 170.9 (**C**(O)), 171.0 (**C**(O)); **IR** v_{max}/cm^{-1} 3347 (O-H), 2931 (C-H), 2858 (C-H), 1742 (C=O); **LRMS** (LC-MS ES+) *m/z* 448.4 (100%, $[M+H]^+$)**; HRMS** (ESI+) calculated mass 448.2177 $g.mol^{-1}$ ($[C_{20}H_{34}NO_{10}]^+$), observed *m/z* 448.2180 ($[M+H]^+$); $\mathbf{R_f}$ 0.32 (3% MeOH in CH_2Cl_2).

***(2S,3R,4R,5S,6R)-6-(Acetoxymethyl)-3-((6-((methylsulfonyl)oxy)hexyl)amino)-tetrahydro-2H-pyran-2,4,5-triyl triacetate* (28)**

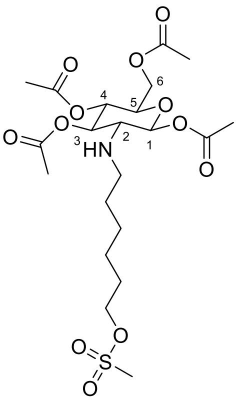

(2S,3R,4R,5S,6R)-6-(Acetoxymethyl)-3-((6-hydroxyhexyl)amino)tetrahydro-2H-pyran-2,4,5-triyl triacetate **27** (61 mg, 0.14 mmol) and NEt_3 (29 mg, 39 µL, 0.28 mmol) were dissolved in anhydrous CH_2Cl_2 (3 mL) at 0 **°**C. Methanesulfonyl chloride (19 mg, 13 µL, 0.17 mmol) in anhydrous CH_2Cl_2 (2 mL) was added dropwise over 10 min and the mixture was allowed to warm to RT and stirred for 18 h. After this time, the reaction mixture was diluted with CH_2Cl_2 (10 mL) and washed with 5% citric acid (3 × 15 mL), saturated $NaHCO_3$ solution (3 × 15 mL) and brine (3 × 15 mL). The combined aqueous layers were adjusted to pH 7 and extracted with CH_2Cl_2 (3 × 15 mL). The combined organic layers were dried ($MgSO_4$) and concentrated under reduced pressure to give *(2S,3R,4R,5S,6R)-6-(acetoxymethyl)-3-((6-((methylsulfonyl)oxy)hexyl)amino)-tetrahydro-2H-pyran-2,4,5-triyl triacetate* **28** (51 mg, 71%) as a clear viscous oil. NMR analysis showed that no further purification was necessary.

^{1}**H NMR** (600 MHz; $CDCl_3$) δ_H 1.25-1.41 (6H, m, , 3 × C$\mathbf{H_2}$), 1.73 (2H, apparent quint, *J* = 6.7, C$\mathbf{H_2}$$CH_2OH$), 2.03 (3H, s, C(O)C$\mathbf{H_3}$), 2.08 (6H, s, 2 × C(O)**C**H_3), 2.16 (3H, s, C(O)C$\mathbf{H_3}$), 2.61 (1H, br s, NHC**H**H), 2.69 (1H, br s, NHCH**H**), 2.84 (1H, br s, C^2**H**), 3.01 (SC$\mathbf{H_3}$), 3.77 (1H, br s, C^5**H**), 4.07 (1H, dd, *J* = 12.4, 2.1, C^6**H**H), 4.21 (2H, t, *J* = 6.7, C$\mathbf{H_2}$OMs), 4.30 (1H, dd, *J* = 12.4, 4.5, C^6H**H**), 5.04-5.06 (2H, m, C^3**H** and C^4**H**), 5.56 (1H, br s, C^1**H**); ^{13}**C NMR** (150 MHz; $CDCl_3$) δ_c 20.8 (C(O)**C**H_3), 20.9 (C(O)**C**H_3), 21.0 (C(O)**C**H_3), 21.2 (C(O)**C**H_3), 25.4 (**C**H_2), 26.5 (**C**H_2), 29.2 (**C**H_2), 29.8 (**C**H_2), 37.5 (S**C**H_3), 47.9 (**C**H_2NH), 61.0 (**C2**), 61.8 (**C6**), 68.4 (**C5**), 70.0 (**C**H_2OMs), 72.5 (**C4**), 73.8 (**C3**), 94.7 (**C1**), 169.3 (**C**(O)), 169.8 (**C**(O)), 170.8 (**C**(O)), 170.9 (**C**(O)); **IR** ν_{max}/cm^{-1} 3364 (N-H), 2937 (C-H), 2859 (C-H), 1742 (C=O), 1351 (S=O), 1215 (S=O); **LRMS** (LC-MS ES+) *m/z* 526.3 (100%, $[M+H]^+$)**;** **HRMS** (ESI+) calculated mass 526.1958 g.mol^{-1} ($[C_{21}H_{36}NO_{12}S]^+$), observed *m/z* 526.1960 ($[M+H]^+$); R_f 0.61 (5% MeOH in CH_2Cl_2).

***Tri-tert-butyl 2,2',2''-(10-(6-(((2S,3R,4R,5S,6R)-2,4,5-triacetoxy-6-(acetoxymethyl)-tetrahydro-2H-pyran-3-yl)amino)hexyl)-1,4,7,10-tetraazacyclododecane-1,4,7-triyl)triacetate* (30)**

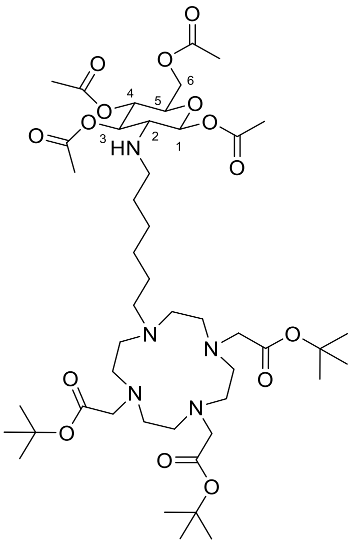

(2S,3R,4R,5S,6R)-6-(Acetoxymethyl)-3-((6-((methylsulfonyl)oxy)hexyl)amino)-tetrahydro-2H-pyran-2,4,5-triyl triacetate **28** (41 mg, 0.078 mmol) and tri-*tert*-butyl 1,4,7,10-tetraazacyclododecane-1,4,7-triacetate **29** (79 mg, 0.15 mmol) were dissolved in $CHCl_3$ (4 mL) and cooled to 0 °C. NEt_3 (28 mg, 38 μL, 0.27 mmol) in $CHCl_3$ (1 mL) was added gradually over 10 min. The reaction mixture was allowed to warm to RT and stirred for 2 h. LC-MS analysis showed a tiny conversion to product so the reaction mixture was heated to 40 °C and stirred for a further 3 h. No further conversion was observed by LC-MS analysis so the reaction was heated at reflux for 16 h. LC-MS analysis showed better conversion so the reaction mixture was heated at reflux for a further 24 h. After this period, the reaction mixture was allowed to cool to RT, diluted with $CHCl_3$ (15 mL) and washed with saturated $NaHCO_3$ solution (3 × 20 mL) and brine (3 × 20 mL). The aqueous layers were combined and extracted with $CHCl_3$ (3 × 15 mL). The organic layers were combined, dried ($MgSO_4$) and concentrated under reduced pressure. The crude orange residue was purified by FCC (on silica gel eluting 0-6% MeOH in CH_2Cl_2) to give *tri-tert-butyl 2,2',2''-(10-(6-(((2S,3R,4R,5S,6R)-2,4,5-triacetoxy-6-(acetoxymethyl)tetrahydro-2H-pyran-3-yl)amino)hexyl)-1,4,7,10-*

tetraazacyclododecane-1,4,7-triyl)triacetate **30** (25 mg, 34%) as a pale yellow glass.

^{1}H NMR (400 MHz; $CDCl_3$, 60 °C) δ_H 1.22-1.34 (8H, m, $NHCH_2C\mathbf{H_2}C\mathbf{H_2}C\mathbf{H_2}C\mathbf{H_2}$), 1.43-1.48 (27H, m, 3 × $C(CH_3)_3$), 2.01 (3H, s, $C(O)C\mathbf{H_3}$), 2.04 (3H, s, $C(O)C\mathbf{H_3}$), 2.05 (3H, s, $C(O)C\mathbf{H_3}$), 2.12 (3H, s, $C(O)C\mathbf{H_3}$), 2.27-3.40 (27H, m, 8 × DOTA ring $C\mathbf{H_2}$, 3 × $C(O)C\mathbf{H_2}N$, 2 × $NC\mathbf{H_2}CH_2$, $C^2\mathbf{H}$), 3.73-3.78 (1H, m, $C^5\mathbf{H}$), 4.09 (1H, dd, *J* = 12.3, 2.5, $C^6\mathbf{H}H$), 4.27 (1H, dd, *J* = 12.3, 4.9, $C^6H\mathbf{H}$), 4.99-5.06 (2H, m, $C^3\mathbf{H}$ and $C^4\mathbf{H}$), 5.54 (1H, d, *J* = 8.4, $C^1\mathbf{H}$); **^{13}C NMR** (150 MHz; $CDCl_3$) δ_C 20.8 ($C(O)\mathbf{C}H_3$), 20.9 ($C(O)\mathbf{C}H_3$), 20.9 ($C(O)\mathbf{C}H_3$), 21.2 ($C(O)\mathbf{C}H_3$), 29.5 (linker $\mathbf{C}H_2$), 27.1 (linker $\mathbf{C}H_2$), 27.7 (linker $\mathbf{C}H_2$), 27.9 (2 × $C(\mathbf{C}H_3)$), 28.1 (3 × $C(\mathbf{C}H_3)$), 28.3 ($C(\mathbf{C}H_3)$), 28.3 ($C(\mathbf{C}H_3)$), 28.3 ($C(\mathbf{C}H_3)$), 28.4 ($C(\mathbf{C}H_3)$), 31.0 (linker $\mathbf{C}H_2$), 47.9 ($CHNH\mathbf{C}H_2$), 50.3 (ring $C\mathbf{H_2}$), 50.4 (ring $C\mathbf{H_2}$), 50.4 (ring $C\mathbf{H_2}$), 50.5 (ring $C\mathbf{H_2}$), 52.5 (ring $C\mathbf{H_2}$), 52.6 (ring $C\mathbf{H_2}$), 53.1 (ring $C\mathbf{H_2}$), 53.1 (ring $C\mathbf{H_2}$), 55.9 ($N\mathbf{C}H_2CH_2$), 56.5 ($N\mathbf{C}H_2C(O)$), 56.6 ($N\mathbf{C}H_2C(O)$), 56.7 ($N\mathbf{C}H_2C(O)$), 61.1 (**C2**), 61.9 (**C6**), 68.4 (**C4**), 72.6 (**C5**), 73.9 (**C3**), 81.9 ($\mathbf{C}(CH_3)_3$), 82.4 ($\mathbf{C}(CH_3)_3$), 82.7 ($\mathbf{C}(CH_3)_3$), 94.7 (**C1**), 169.2 ($\mathbf{C}(O)CH_3$), 169.8 ($\mathbf{C}(O)CH_3$), 170.1 ($NCH_2\mathbf{C}(O)$), 170.8 ($\mathbf{C}(O)CH_3$), 170.9 ($\mathbf{C}(O)CH_3$), 172.8 (2 × $NCH_2\mathbf{C}(O)$); **IR** ν_{max}/cm^{-1} 3372 (N-H), 2927 (C-H), 2852 (C-H), 1721 (C=O); **LRMS** (LC-MS ES+) *m/z* 472.8 (100%, $[M+2H]^{2+}$), 944.5 (7%, $[M+H]^+$); **HRMS** (ESI+) calculated mass 944.5807 g.mol^{-1} ($[C_{46}H_{82}N_5O_{15}]^+$), observed *m/z* 944.5809 ($[M+H]^+$); **R_f** 0.27 (8% MeOH in CH_2Cl_2).

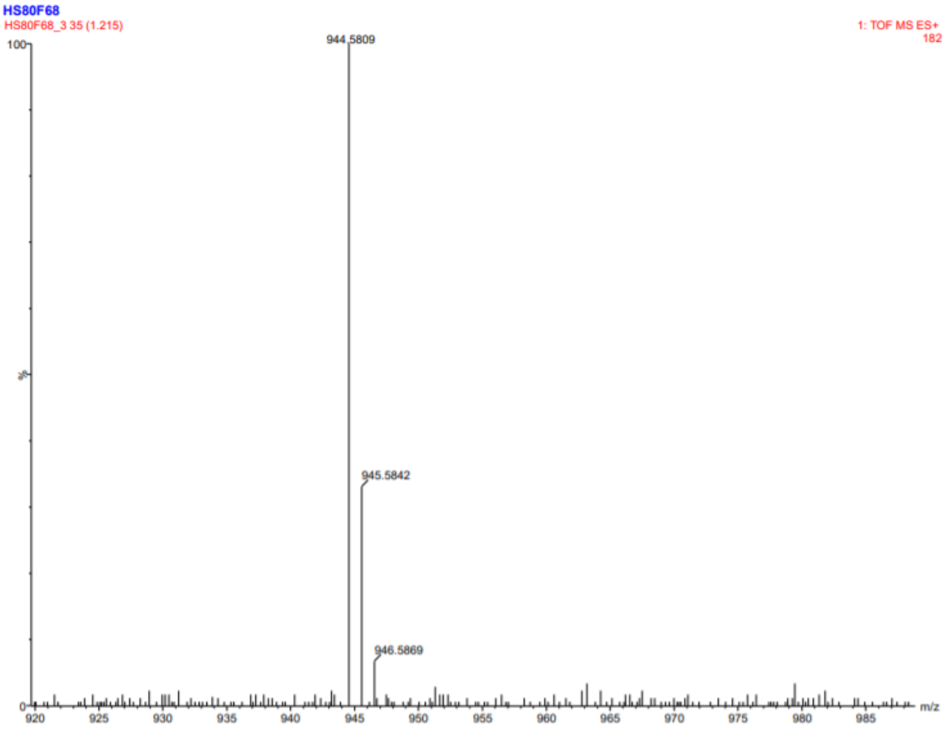

7.3.3 Short-chain PEG lipid synthesis

Ethyl 2,5,8,11,14-pentaoxahexadecan-16-oate (32)[238]

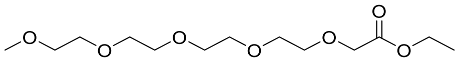

To a solution of tetraethylene glycol monomethyl ether (2.00 g, 9.60 mmol) in THF (96 mL) was added potassium *tert*-butoxide (0.592 g, 5.28 mmol) in small portions over 25 min. The reaction mixture was stirred for an additional 1 h. Ethyl bromoacetate (0.885 g, 5.30 mmol) in THF (20 mL) was added dropwise over a 25 min period and the reaction mixture was stirred overnight. The reaction mixture was concentrated under reduced pressure and TLC and LC-MS analysis showed poor conversion to product. The residue was re-dissolved in THF (50 mL) and NaH (0.300 g, 12.5 mmol; dry 95%) was added portion-wise over 10 min, the reaction mixture was stirred at RT for 20 min. Ethyl bromoacetate (0.800 g, 4.79 mmol) in THF (10 mL) was added dropwise over 15 min. The reaction mixture was stirred at RT overnight. After this time, a portion of NaH (0.113 g, 4.71 mmol; dry 95%) was added and stirred for 5 min before ethyl bromoacetate (0.790 g, 4.73 mmol) in THF (5 mL) was added dropwise. After an additional 5 h stirring, no further conversion to the product was observed by TLC, so the reaction mixture was quenched with saturated NH_4Cl solution (30 mL) and the aqueous layer was extracted with EtOAc (3 × 50 mL). The combined organic layers were dried ($MgSO_4$) and concentrated to give a crude yellow oil. The crude was purified by FCC (on silica gel eluting 0-1% MeOH in CH_2Cl_2) to give ethyl 2,5,8,11,14-pentaoxahexadecan-16-oate **32** (0.514 g, 33%) as a clear oil.

^{1}H NMR (600 MHz, $CDCl_3$) δ_H 1.27 (3H, t, *J* = 7.2, $CH_2C\mathbf{H_3}$), 3.36 (3H, s, $OC\mathbf{H_3}$), 3.52-3.54 (2H, m, $OC\mathbf{H_2}CH_2O$), 3.62-3.72 (14H, m, 7 × $OC\mathbf{H_2}CH_2O$), 4.13 (2H, s, $OC\mathbf{H_2}C(O)$), 4.20 (2H, q, *J* = 7.2, $OC\mathbf{H_2}CH_3$); **^{13}C NMR** (150 MHz, $CDCl_3$) δ_c 14.4 ($CH_2\mathbf{C}H_3$), 59.2 ($O\mathbf{C}H_3$), 61.8 ($O\mathbf{C}H_2CH_3$), 68.8 ($O\mathbf{C}H_2C(O)$), 70.3 ($O\mathbf{C}H_2$), 70.6 ($O\mathbf{C}H_2$), 70.6 ($O\mathbf{C}H_2$), 70.7 ($O\mathbf{C}H_2$), 70.7 ($O\mathbf{C}H_2$), 70.7 ($O\mathbf{C}H_2$), 70.7 ($O\mathbf{C}H_2$), 72.0 ($O\mathbf{C}H_2$), 170.7 ($\mathbf{C}(O)O$); **IR** ν_{max}/cm^{-1} 2926 (C-H), 1753 (C=O); **LRMS** (LC-MS ES+) *m/z* 295.3 (100%, $[M+H]^+$); **R_f** 0.4 (2% MeOH in CH_2Cl_2). Data corresponds with the literature.[238]

2,5,8,11,14-Pentaoxahexadecan-16-oic acid (33)[238]

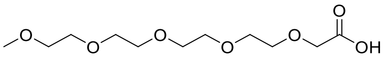

To a solution of ethyl 2,5,8,11,14-pentaoxahexadecan-16-oate **32** (185 mg, 0.629 mmol) in alcohol (1:1, MeOH:EtOH, 8 mL) was added 1 M NaOH (8 mL) and the reaction mixture was stirred overnight. After this time, the reaction mixture was acidified to pH 2 *via* dropwise addition of 1 M HCl solution, saturated with NaCl and extracted with CH_2Cl_2 (4 × 20 mL). The combined organic layers were washed with brine (20 mL), dried ($MgSO_4$) and concentrated under reduced pressure to give 2,5,8,11,14-pentaoxahexadecan-16-oic acid **33** (143 mg, 86%) as a clear oil.

^{1}H NMR (600 MHz, $CDCl_3$) δ_H 3.31 (3H, s, OC**H$_3$**), 3.48-3.50 (2H, m, C**H$_2$**), 3.57-3.63 (12H, m, 6 × C**H$_2$**), 3.65-3.67 (2H, m, C**H$_2$**), 4.08 (2H, s, OC**H$_2$**C(O)); **^{13}C NMR** (150 MHz, $CDCl_3$) δ_c 59.0 (**C**H$_3$), 69.0 (**C**H$_2$), 70.3 (**C**H$_2$), 70.4 (**C**H$_2$), 70.4 (**C**H$_2$), 70.4 (**C**H$_2$), 70.6 (**C**H$_2$), 70.6 (**C**H$_2$), 70.9 (**C**H$_2$), 71.8 (**C**H$_2$), 172.3 (**C**(O)); **IR** ν_{max}/cm^{-1} 3274 (O-H), 2922 (C-H), 1730 (C=O); **LRMS** (LC-MS ES+) *m/z* 267.1 (10%, $[M+H]^+$), 289.0 (100%, $[M+Na]^+$); **R$_f$** 0.28 (16% MeOH in CH_2Cl_2). Data corresponds with the literature.[238]

2,5-Dioxopyrrolidin-1-yl 2,5,8,11,14-pentaoxahexadecan-16-oate (34)

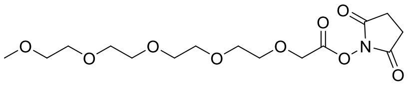

2,5,8,11,14-Pentaoxahexadecan-16-oic acid **33** (121 mg, 0.454 mmol) and NHS (60.0 mg, 0.521 mmol) were dissolved in anhydrous CH_2Cl_2 (2.3 mL). EDC (72.0 mg, 0.464 mmol) was added and the reaction was stirred overnight at RT under $N_{2(g)}$. After this time, the reaction mixture was diluted with CH_2Cl_2 (15 mL), washed with H_2O (2 × 15 mL), dried ($MgSO_4$) and concentrated to give *2,5-dioxopyrrolidin-1-yl 2,5,8,11,14-pentaoxahexadecan-16-oate* **34** (100 mg, 60%) as a cloudy oil.

^{1}H NMR (600 MHz, $CDCl_3$) δ_H 2.84 (4H, br s, C(O)C**H$_2$**C**H$_2$**C(O)), 3.37 (3H, s, OC**H$_3$**), 3.53-3.55 (2H, m C**H$_2$**), 3.63-3.66 (10H, m, 5 × C**H$_2$**), 3.69-3.70 (2H, m, C**H$_2$**), 3.78-3.80 (2H, m, C**H$_2$**), 4.52 (2H, s, OC**H$_2$**C(O)); **^{13}C NMR** (150 MHz, $CDCl_3$) δ_c 25.7 C(O)**C**H$_2$**C**H$_2$C(O)), 59.1 (O**C**H$_3$), 66.6 (O**C**H$_2$C(O)), 70.6 (**C**H$_2$), 70.7 (2 × **C**H$_2$), 70.7 (**C**H$_2$), 70.7 (**C**H$_2$), 70.7 (**C**H$_2$), 71.5 (**C**H$_2$), 72.0 (**C**H$_2$), 166.1 (**C**(O)O), 168.9 (**C**(O)CH$_2$CH$_2$**C**(O)); **IR** ν_{max}/cm^{-1} 2923 (C-H), 1733 (C=O), 1624 (C=O); **LRMS** (TOF MS ES+) *m/z* 364.2 (100%, $[M+H]^+$), 382.2 (20%, $[M+H_2O+H]^+$); **HRMS** (TOF MS ES+) calculated mass 364.1602 g.mol^{-1} ($[C_{15}H_{26}NO_9]^+$), observed *m/z* 364.1609 ($[M+H]^+$); **R$_f$** degrades on TLC.

3-((Hydroxy((16-oxo-2,5,8,11,14-pentaoxa-17-azanonadecan-19-yl)oxy)-phosphoryl)oxy)propane-1,2-diyl dipalmitate (35)

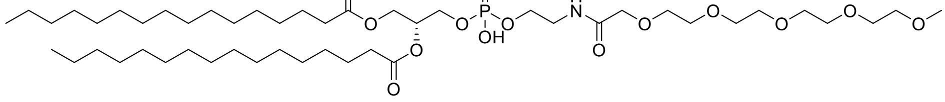

A solution of *2,5-dioxopyrrolidin-1-yl 2,5,8,11,14-pentaoxahexadecan-16-oate* **34** (105 mg, 0.289 mmol), DPPE (167 mg,0.241 mmol) and dry NEt_3 (121 µL, 0.867 mmol) in dry CH_2Cl_2 (7 mL) was stirred at RT under $Ar_{(g)}$ overnight. After this time, the reaction mixture was diluted with CH_2Cl_2 (20 mL) and washed with 0.1 M HCl solution (3 × 25 mL). The combined aqueous layers were extracted with CH_2Cl_2 (20 mL). The combined organic layers were dried ($MgSO_4$) and concentrated under reduced pressure to give *3-((hydroxy((16-oxo-2,5,8,11,14-pentaoxa-17-azanonadecan-19-yl)oxy)phosphoryl)oxy)-propane-1,2-diyl dipalmitate* **35** (217 mg, 96%) as a sticky white solid.

^{1}H NMR (600 MHz, $CDCl_3$) δ_H 0.86 (6H, t, J = 7.0, 2 × $C\mathbf{H_3}$), 1.23-1.29 (48H, palmitoyl chain), 1.57-1.60 (4H, m, 2 × $C(O)CH_2C\mathbf{H_2}$), 2.26-2.32 (4H, m, 2 × $C(O)C\mathbf{H_2}$), 3.36 (3H, s, $OC\mathbf{H_3}$), 3.53-3.54 (2H, m, $C\mathbf{H_2}OCH_3$), 3.58 (2H, apparent q, J = 5.5, $C\mathbf{H_2}NH$), 3.61-3.70 (14H, m, 7 × $OC\mathbf{H_2}CH_2O$), 4.01 (2H, s, $C(O)C\mathbf{H_2}O$), 4.10-4.16 (5H, m, $C\mathbf{H}HCHC\mathbf{HH}OPOC\mathbf{H_2}$), 4.34 (1H, dd, J = 12.0, 3.9, $C(O)OCH\mathbf{H}$), 5.21 (1H, m, $C\mathbf{H}$), 7.65 (1H, bt, J = 6.0, $N\mathbf{H}$), 7.71 (1H, br s, $O\mathbf{H}$); **^{13}C NMR** (150 MHz, $CDCl_3$) δ_c 14.2 (2 × $\mathbf{C}H_3$), 22.8 (2 × $\mathbf{C}H_2CH_3$), 25.0 (2 × $C(O)CH_2\mathbf{C}H_2$), 29.2 ($\mathbf{C}H_2$), 29.3 ($\mathbf{C}H_2$), 29.4 ($\mathbf{C}H_2$), 29.4 ($\mathbf{C}H_2$), 29.5 ($\mathbf{C}H_2$), 29.6 ($\mathbf{C}H_2$), 29.6 ($\mathbf{C}H_2$), 29.8 ($\mathbf{C}H_2$), 29.8 ($\mathbf{C}H_2$), 32.0 ($\mathbf{C}H_2$), 34.1 ($C(O)\mathbf{C}H_2$), 34.3 ($C(O)\mathbf{C}H_2$), 39.5 (d, $^3J_{CP}$ = 5.5, $POCH_2\mathbf{C}H_2$), 59.1 ($O\mathbf{C}H_3$), 62.0 ($C(O)O\mathbf{C}HH$), 65.1 (d, $^2J_{CP}$ = 5.5, $\mathbf{C}HHOP$), 66.3 (d, $^2J_{CP}$ = 5.5, $PO\mathbf{C}H_2$), 69.6 (d, $^3J_{CP}$ = 8.3, $\mathbf{C}H$), 70.3 ($C(O)\mathbf{C}H_2O$), 70.3 ($O\mathbf{C}H_2CH_2O$), 70.5 (4 × $O\mathbf{C}H_2CH_2O$), 70.6 ($O\mathbf{C}H_2CH_2O$), 71.0 ($O\mathbf{C}H_2CH_2O$), 72.0 ($\mathbf{C}H_2OCH_3$), 171.3 ($NH\mathbf{C}(O)$), 173.0 ($\mathbf{C}(O)O$), 173.4 ($\mathbf{C}(O)O$); **IR** ν_{max}/cm^{-1} 3320 (N-H), 2955 (C-H), 2916 (C-H), 2872 (C-H), 2849 (C-H), 1738 (C=O), 1669 (C=O); **LRMS** (TOF MS ES+) *m/z* 940.6 (100%, $[M+H]^+$); **HRMS** (TOF MS ES+) calculated mass 940.6490 $g.mol^{-1}$ ($[C_{48}H_{95}NO_{14}P]^+$), observed *m/z* 940.6485 ($[M+H]^+$); **R_f** 0.33 (5% MeOH in CH_2Cl_2); **$[\alpha]_D^{20}$** +2.5 (*c* 2 mg/mL, 1% $CHCl_3$ in MeOH).

3,3-Diisopropyl-2-methyl-4,7,10,13-tetraoxa-3-silapentadecan-15-ol (38)[273]

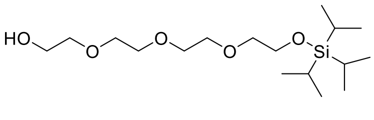

To a solution of tetraethylene glycol (4.28 g, 22.0 mmol) and imidazole (1.09 g, 16.0 mmol) in dry THF (70 mL) at 0 °C under $Ar_{(g)}$ was added TIPSCl (2.00 g, 10.4 mmol) in dry THF (10 mL) dropwise over 10 min. The reaction was allowed to warm to RT and stirred for 4 h. After this time, the solid was removed by filtration and the remaining solution was concentrated. The crude oil was purified by FCC (on silica gel eluting 0-2%

MeOH in CH_2Cl_2) to give 3,3-diisopropyl-2-methyl-4,7,10,13-tetraoxa-3-silapentadecan-15-ol **38** (2.22 g, 61%) as a clear oil.

^{1}H NMR (600 MHz, $CDCl_3$) δ_H 1.02-1.10 (21H, m, 3 × C**H**(C**H**$_3$)$_2$)), 3.56-3.59 (4H, m, C**H**$_2$CH$_2$OH, C**H**$_2$CH$_2$OTIPS), 3.63-3.68 (8H, m, 2 × OC**H**$_2$C**H**$_2$O), 3.70-3.71 (2H, m, C**H**$_2$OH), 3.82 (2H, t, J = 5.5, C**H**$_2$OTIPS); **^{13}C NMR** (150 MHz, $CDCl_3$) δ_C 12.0 (3 × **C**H), 18.1 (6 × **C**H$_3$), 61.8 (**C**H$_2$OH), 63.1 (**C**H$_2$OTIPS), 70.4 (O**C**H$_2$CH$_2$O), 70.7 (O**C**H$_2$CH$_2$O), 70.7 (O**C**H$_2$CH$_2$O), 70.9 (O**C**H$_2$CH$_2$O), 72.7 (O**C**H$_2$), 72.8 (O**C**H$_2$); **IR** ν_{max}/cm^{-1} 3435 (O-H), 2940 (C-H), 2864 (C-H); **LRMS** (LC-MS ES+) m/z 351.3 (100%, $[M+H]^+$), 373.3 (80%, $[M+Na]^+$); **R$_f$** 0.35 (4% MeOH in CH_2Cl_2). Data corresponds with the literature.[273]

3,3-Diisopropyl-2-methyl-4,7,10,13,16,19-hexaoxa-3-silahenicosan-21-ol (39)

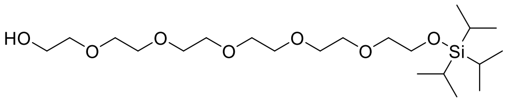

To a solution of hexaethylene glycol (5.80 g, 20.5 mmol) and imidazole (1.15 g, 16.9 mmol) in dry THF (50 mL) at 0 °C under $N_{2(g)}$ was added TIPSCl (1.92 g, 9.96 mmol) in dry THF (10 mL) dropwise over 20 min. The reaction was allowed to warm to RT and stirred overnight. After this time, the solid was removed by filtration and the remaining solution was concentrated. The crude oil was purified by FCC (on silica gel eluting 0-4% MeOH in CH_2Cl_2) to give **39** *3,3-diisopropyl-2-methyl-4,7,10,13,16,19-hexaoxa-3-silahenicosan-21-ol* (2.23 g, 51%) as a yellow oil.

^{1}H NMR (600 MHz, $CDCl_3$) δ_H 0.97-1.12 (21H, m, C**H**(C**H**$_3$)$_2$)), 3.55-3.74 (22H, m, 11 × C**H**$_2$), 3.83 (2H, t, J = 5.7, C**H**$_2$OTIPS); **^{13}C NMR** (150 MHz, $CDCl_3$) δ_C 12.0 (3 × **C**H), 18.1 (6 × **C**H$_3$), 61.9 (**C**H$_2$), 63.0 (**C**H$_2$OTIPS), 70.5 (**C**H$_2$), 70.7 (**C**H$_2$), 70.7 (**C**H$_2$), 70.7 (**C**H$_2$), 70.7 (**C**H$_2$), 70.7 (**C**H$_2$), 70.8 (**C**H$_2$), 70.9 (**C**H$_2$), 72.7 (**C**H$_2$), 72.8 (**C**H$_2$); **IR** ν_{max}/cm^{-1} 3447 (O-H), 2941 (C-H), 2865 (C-H); **LRMS** (LC-MS ES+) m/z 439.7 (80%, $[M+H]^+$), 461.6 (100%, $[M+Na]^+$); **HRMS** (TOF MS ES+) calculated mass 461.2905 g.mol^{-1} ($[C_{21}H_{46}O_7SiNa]^+$), observed m/z 461.2900 ($[M+Na]^+$); **R$_f$** 0.3 (3% MeOH in CH_2Cl_2).

Ethyl 3,3-diisopropyl-2-methyl-4,7,10,13,16-pentaoxa-3-silaoctadecan-18-oate (40)

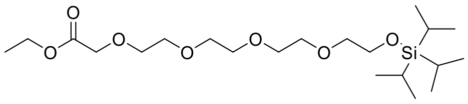

To a solution of 3,3-diisopropyl-2-methyl-4,7,10,13-tetraoxa-3-silapentadecan-15-ol **38** (2.22 g, 6.34 mmol) in anhydrous THF (30 mL) was added NaH (0.37 g, 15 mmol; dry 95%) at 0 °C. The reaction mixture was allowed to warm to RT and stirred for 30 min.

After this time, ethyl bromoacetate (1.30 mL, 11.8 mmol) in anhydrous THF (5 mL) was added dropwise over a 5 min period and the reaction mixture was stirred at RT for 2 h. After this time, another portion of NaH (0.37 g, 15 mmol; dry 95%) and ethyl bromoacetate (1.30 mL, 11.8 mmol) in dry THF (5 mL) were added and the reaction mixture was stirred overnight. After this time, the reaction mixture was quenched with saturated NH_4Cl solution (70 mL) and extracted with EtOAc (4 × 40 mL), dried ($MgSO_4$) and concentrated to give a crude yellow oil. This was purified by FCC (on silica gel eluting 0-1% MeOH in CH_2Cl_2) to give *ethyl 3,3-diisopropyl-2-methyl-4,7,10,13,16-pentaoxa-3-silaoctadecan-18-oate* **40** (1.41 g, 51%) as a clear oil.

^{1}**H NMR** (600 MHz, $CDCl_3$) δ_H 1.02-1.10 (21H, m, $C\mathbf{H}(C\mathbf{H_3})_2$)), 1.27 (3H, t, *J* = 7.2, $OCH_2C\mathbf{H_3}$), 3.58 (2H, t, *J* = 5.6, $C\mathbf{H_2}CH_2OTIPS$), 3.63-3.73 (12H, m, 3 × $OC\mathbf{H_2}C\mathbf{H_2}O$), 3.83 (2H, t, *J* = 5.6, $C\mathbf{H_2}OTIPS$), 4.14 (2H, s, $C(O)C\mathbf{H_2}O$), 4.20 (2H, q, *J* = 7.2, $OC\mathbf{H_2}CH_3$); ^{13}**C NMR** (150 MHz, $CDCl_3$) δ_c 12.0 (3 × **C**H), 14.3 ($OCH_2\mathbf{C}H_3$) 18.1 (6 × $\mathbf{C}H_3$), 61.0 ($O\mathbf{C}H_2CH_3$), 63.0 ($\mathbf{C}H_2OTIPS$), 68.8 ($C(O)\mathbf{C}H_2O$), 70.7 ($O\mathbf{C}H_2CH_2O$), 70.7 ($O\mathbf{C}H_2CH_2O$), 70.7 ($O\mathbf{C}H_2CH_2O$), 70.8 ($O\mathbf{C}H_2CH_2O$), 70.9 ($O\mathbf{C}H_2CH_2O$), 71.0 ($O\mathbf{C}H_2CH_2O$), 72.8 ($\mathbf{C}H_2CH_2OTIPS$), 170.6 ($O\mathbf{C}(O)$); **IR** ν_{max}/cm^{-1} 2941 (C-H), 2865 (C-H), 1754 (C=O); **LRMS** (LC-MS ES+) *m/z* 437.4 (75%, $[M+H]^+$), 459.4 (100%, $[M+Na]^+$); **HRMS** (TOF MS ES+) calculated mass 437.2935 $g.mol^{-1}$ ($[C_{21}H_{45}O_7Si]^+$), observed *m/z* 437.2934 ($[M+H]^+$); $\mathbf{R_f}$ 0.6 (2% MeOH in CH_2Cl_2).

3,3-Diisopropyl-2-methyl-4,7,10,13,16-pentaoxa-3-silaoctadecan-18-oic acid (42)

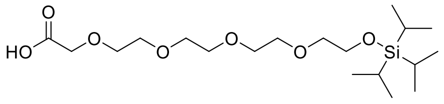

To a solution of *ethyl 3,3-diisopropyl-2-methyl-4,7,10,13,16-pentaoxa-3-silaoctadecan-18-oate* **40** (0.84 g, 0.92 mmol) in alcohol (1:1, MeOH:EtOH, 24 mL) was added 1 M NaOH solution (24 mL) and the reaction mixture was stirred at RT overnight. After this time, the reaction mixture was acidified to pH 2 using 1 M HCl solution (~ 25 mL) and saturated with NaCl. The product was extracted with CH_2Cl_2 (4 × 30 mL), dried ($MgSO_4$) and concentrated to give *3,3-diisopropyl-2-methyl-4,7,10,13bn,16-pentaoxa-3-silaoctadecan-18-oic acid* **42** (0.59 g, 76%) as a clear oil.

^{1}**H NMR** (600 MHz, $CDCl_3$) δ_H 1.03-1.12 (21H, m, $C\mathbf{H}(C\mathbf{H_3})_2$)), 3.59-3.76 (14H, m, 7 × $OC\mathbf{H_2}CH_2O$), 3.84 (2H, t, *J* = 5.5, $C\mathbf{H_2}OTIPS$), 4.14 ($C(O)C\mathbf{H_2}O$); ^{13}**C NMR** (150 MHz, $CDCl_3$) δ_c 12.0 (3 × **C**H), 18.1 (6 × $\mathbf{C}H_3$), 63.0 ($\mathbf{C}H_2OTIPS$), 69.3 ($C(O)\mathbf{C}H_2O$), 70.4 ($O\mathbf{C}H_2CH_2O$), 70.4 ($O\mathbf{C}H_2CH_2O$), 70.6 ($O\mathbf{C}H_2CH_2O$), 70.8 ($O\mathbf{C}H_2CH_2O$), 71.0 ($O\mathbf{C}H_2CH_2O$), 71.5 ($O\mathbf{C}H_2CH_2O$), 72.8 ($\mathbf{C}H_2CH_2OTIPS$), 172.1 ($\mathbf{C}(O)$); **IR** ν_{max}/cm^{-1} 3262

(O-H), 2916 (C-H), 2850 (C-H), 1737 (C=O); **LRMS** (LC-MS ES+) *m/z* 409.4 (30%, $[M+H]^+$), 431.4 (100%, $[M+Na]^+$); **HRMS** (TOF MS ES+) calculated mass 409.2616 g.mol^{-1} ($[C_{21}H_{41}O_7Si]^+$), observed *m/z* 409.2615 ($[M+H]^+$); **R$_f$** 0.33 (2% MeOH and 1% formic acid in CH_2Cl_2).

***3,3-Diisopropyl-2-methyl-4,7,10,13,16,19,22-heptaoxa-3-silatetracosan-24-oic acid* (43)**

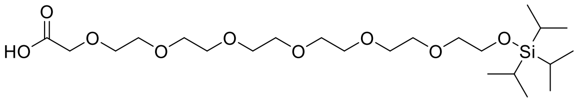

To a solution of *3,3-diisopropyl-2-methyl-4,7,10,13,16,19-hexaoxa-3-silahenicosan-21-ol* **39** (2.05 g, 4.68 mmol) in anhydrous THF (20 mL) was added NaH (0.468 g, 60 wt%, 11.7 mmol) at 0 °C. The reaction mixture was stirred under $Ar_{(g)}$ for 30 min. After this time, ethyl bromoacetate (0.78 mL, 1.2 g, 7.2 mmol) in dry THF (5 mL) was added dropwise over 10 min. The resulting solution was stirred at RT under $Ar_{(g)}$ for 4 h. After this time, the reaction was quenched with saturated NH_4Cl solution (30 mL) and extracted with EtOAc (4 × 40 mL). The organic layers were dried ($MgSO_4$) and concentrated under reduced pressure to give a yellow oil which was re-dissolved in alcohol (1:1, MeOH:EtOH, 30 mL). A 1 M solution of NaOH (30 mL) was added and the reaction mixture was stirred overnight. After this time, the reaction mixture was acidified with 1 M HCl solution and saturated with NaCl. The reaction mixture was extracted with CH_2Cl_2 (5 × 40 mL), dried ($MgSO_4$) and concentrated. The crude was purified by FCC (on silica gel eluting 0-15% MeOH in CH_2Cl_2) to give *3,3-diisopropyl-2-methyl-4,7,10,13,16,19,22-heptaoxa-3-silatetracosan-24-oic* acid **43** (180 mg, 31%) as a clear oil.

^{1}H NMR (600 MHz, $CDCl_3$) δ_H 1.00-1.09 (21H, m, C**H**(C**H$_3$**)$_2$)), 3.59-3.62 (2H, m, C**H$_2$**), 3.63-3.70 (18H, m, 9 × C**H$_2$**), 3.72-3.76 (4H, m, 2 × C**H$_2$**), 4.15 (2H, s, C(O)C**H$_2$**O); **^{13}C NMR** (150 MHz, $CDCl_3$) δ_C 12.4 (**C**H), 17.8 (**C**H$_3$), 61.65 (**C**H$_2$), 69.2 (C(O)**C**H$_2$O), 70.2 (**C**H$_2$), 70.4 (**C**H$_2$), 70.5 (2 × **C**H$_2$), 70.5 (**C**H$_2$), 70.5 (2 × **C**H$_2$), 70.6 (**C**H$_2$), 70.6 (**C**H$_2$), 71.1 (**C**H$_2$), 72.67 (**C**H$_2$), 172.39 (**C**(O)); **IR** ν_{max}/cm^{-1} 3390 (O-H), 2918 (C-H), 2862 (C-H), 1718 (C=O); **LRMS** (LC-MS ES+) *m/z* 497.4 (100%, $[M+H]^+$), 519.4 (95%, $[M+Na]^+$); **HRMS** (TOF MS ES+) calculated mass 497.3140 g.mol^{-1} ($[C_{23}H_{49}O_9Si]^+$), observed *m/z* 497.3134 ($[M+H]^+$); **R$_f$** 0.3 (10% MeOH in CH_2Cl_2).

2,5-Dioxopyrrolidin-1-yl 3,3-diisopropyl-2-methyl-4,7,10,13,16-pentaoxa-3-silaoctadecan-18-oate **(44)**

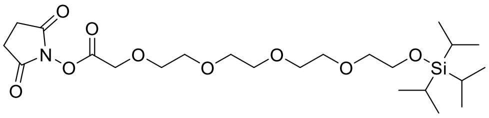

3,3-Diisopropyl-2-methyl-4,7,10,13,16-pentaoxa-3-silaoctadecan-18-oic acid **42** (0.592 g, 1.45 mmol) and NHS (0.201 g, 1.74 mmol) were dissolved in dry CH_2Cl_2 (7 mL). EDC.HCl (0.306 g, 1.59 mmol) was added and the reaction mixture was stirred at RT under $Ar_{(g)}$ overnight. After this time, the reaction mixture was diluted with CH_2Cl_2 (25 mL) and washed with brine (3 × 20 mL). The aqueous layers were combined and extracted with CH_2Cl_2 (2 × 15 mL). The combined organic layers were dried ($MgSO_4$) and concentrated to give *2,5-dioxopyrrolidin-1-yl 3,3-diisopropyl-2-methyl-4,7,10,13,16-pentaoxa-3-silaoctadecan-18-oate* **44** (0.694 g, 94%) as a pale yellow oil.

^{1}**H NMR** (600 MHz, $CDCl_3$) δ_H 1.04-1.11 (21H, m, C**H**(C**H**$_3$)$_2$)), 2.85 (4H, br s, C(O)C**H**$_2$C**H**$_2$C(O)), 3.58 (2H, t, *J* = 5.6, C**H**$_2$CH$_2$OTIPS), 3.3-3.71 (10H, m, 5 × OC**H**$_2$CH$_2$O), 3.79-3.80 (2H, m, C(O)CH$_2$OC**H**$_2$), 3.83 (2H, t, *J* = 5.6, C**H**$_2$OTIPS), 4.52 (2H, s, C(O)C**H**$_2$O); ^{13}**C NMR** (150 MHz, $CDCl_3$) δ_c 12.0 (3 × **C**H), 18.1 (6 × **C**H$_3$), 25.7 (C(O)**C**H$_2$**C**H$_2$C(O)), 63.0 (**C**H$_2$OTIPS), 66.6 (C(O)**C**H$_2$O), 70.7 (O**C**H$_2$CH$_2$O), 70.7 (O**C**H$_2$CH$_2$O), 70.8 (O**C**H$_2$CH$_2$O), 70.8 (O**C**H$_2$CH$_2$O), 70.9 (O**C**H$_2$CH$_2$O), 71.5 (O**C**H$_2$CH$_2$O), 72.8 (**C**H$_2$CH$_2$OTIPS), 166.1 (O**C**(O)), 168.9 7 (**C**(O)CH$_2$CH$_2$**C**(O)); **IR** ν_{max}/cm^{-1} 2941 (C-H), 2891 (C-H), 2865 (C-H), 1736 (C=O), 1652 (C=O); **LRMS** (LC-MS ES+) *m/z* 506.3 (100%, $[M+H]^+$), 528.2 (50%, $[M+Na]^+$); **HRMS** (TOF MS ES+) calculated mass 506.2785 g.mol^{-1} ($[C_{23}H_{44}NO_9Si]^+$), observed *m/z* 506.2785 ($[M+H]^+$); $\mathbf{R_f}$ degrades on TLC.

2,5-dioxopyrrolidin-1-yl 3,3-diisopropyl-2-methyl-4,7,10,13,16,19,22-heptaoxa-3-silatetracosan-24-oate **(45)**

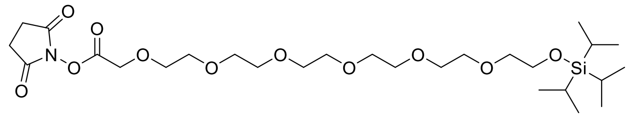

3,3-Diisopropyl-2-methyl-4,7,10,13,16,19,22-heptaoxa-3-silatetracosan-24-oic acid **43** (0.541 g, 1.09 mmol), NHS (0.150 g, 1.31 mmol) and EDC.HCl (0.250 g, 1.31 mmol) were dissolved in CH_2Cl_2 (10 mL) and stirred under $Ar_{(g)}$ for 6 h. After this time, the reaction mixture was diluted with CH_2Cl_2 (20 mL) and washed with brine (3 × 30 mL), dried ($MgSO_4$) and concentrated to *give 2,5-dioxopyrrolidin-1-yl 3,3-diisopropyl-2-*

methyl-4,7,10,13,16,19,22-heptaoxa-3-silatetracosan-24-oate **45** (0.584 g, 90%) as an orange oil.

^{1}H NMR (600 MHz, $\mathrm{CDCl_3}$) δ_H 1.01-1.15 (21H, m, $\mathrm{C\mathbf{H}(C\mathbf{H_3})_2)}$), 2.85 (4H, broad s, $\mathrm{C(O)C\mathbf{H_2}C\mathbf{H_2}C(O)}$), 3.58 (2H, t, J = 5.7, $\mathrm{C\mathbf{H_2}CH_2OTIPS}$), 3.61-3.72 (18H, m, 9 × $\mathrm{C\mathbf{H_2}}$), 3.77-3.81 (2H, m, $\mathrm{C\mathbf{H_2}}$), 3.83 (2H, t, J = 5.7, $\mathrm{C\mathbf{H_2}OTIPS}$), 4.52 (2H, s, $\mathrm{C(O)C\mathbf{H_2}O}$); **^{13}C NMR** (150 MHz, $\mathrm{CDCl_3}$) δ_C 12.1 (3 × $\mathrm{\mathbf{C}H}$), 18.1 (6 × $\mathrm{\mathbf{C}H_3}$), 25.7 ($\mathrm{C(O)\mathbf{C}H_2\mathbf{C}H_2C(O)}$), 63.1 ($\mathrm{\mathbf{C}H_2}$), 66.7 ($\mathrm{C(O)\mathbf{C}H_2O}$), 70.7 (2 × $\mathrm{\mathbf{C}H_2}$), 70.7 (2 × $\mathrm{\mathbf{C}H_2}$), 70.7 (2 × $\mathrm{\mathbf{C}H_2}$), 70.8 ($\mathrm{\mathbf{C}H_2}$), 70.8 ($\mathrm{\mathbf{C}H_2}$), 70.9 ($\mathrm{\mathbf{C}H_2}$), 71.5 ($\mathrm{\mathbf{C}H_2}$), 72.9 ($\mathrm{\mathbf{C}H_2}$), 166.10 ($\mathrm{\mathbf{C}(O)O}$), 168.79 ($\mathrm{\mathbf{C}(O)CH_2CH_2\mathbf{C}(O)}$); **IR** ν_{max}/cm^{-1} 2941 (C-H), 2865 (C-H), 1782 (C=O), 1737 (C=O); **LRMS** (LC-MS ES+) *m/z* 594.4 (100%, [M+H]$^+$), 616.4 (60%, [M+Na]$^+$); **HRMS** (TOF MS ES+) calculated mass 594.3310 g.mol^{-1} ([$\mathrm{C_{27}H_{52}NO_{11}Si}$]$^+$), observed *m/z* 594.3308 ([M+H]$^+$); **R_f** degrades on TLC.

3-((((3,3-Diisopropyl-2-methyl-18-oxo-4,7,10,13,16-pentaoxa-19-aza-3-silahenicosan-21-yl)oxy)(hydroxy)phosphoryl)oxy)propane-1,2-diyl dipalmitate (46)

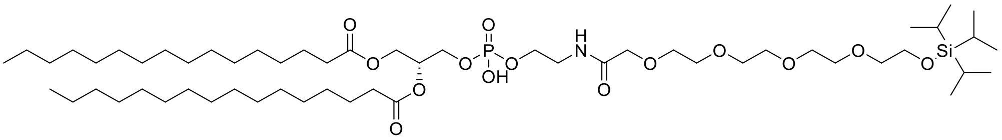

A solution of *2,5-dioxopyrrolidin-1-yl 3,3-diisopropyl-2-methyl-4,7,10,13,16-pentaoxa-3-silaoctadecan-18-oate* **44** (0.239 g, 0.473 mmol) and DPPE (0.273 g, 0.394 mmol) and $\mathrm{NEt_3}$ (165 µL, 1.18 mmol) in dry $\mathrm{CH_2Cl_2}$ (15 mL) were stirred at RT under $\mathrm{Ar_{(g)}}$ for 6 h. After this time, the reaction mixture was diluted with $\mathrm{CH_2Cl_2}$ (20 mL) and washed with 0.1 M HCl solution (3 × 20 mL). The combined aqueous layers were extracted with $\mathrm{CH_2Cl_2}$ (15 mL). The combined organic layers were dried ($\mathrm{MgSO_4}$) and concentrated to give *3-((((3,3-diisopropyl-2-methyl-18-oxo-4,7,10,13,16-pentaoxa-19-aza-3-silahenicosan-21-yl)oxy)-(hydroxy)phosphoryl)oxy)propane-1,2-diyl dipalmitate* **46** (0.421 g, 99%) as a white thin film.

^{1}H NMR (600 MHz, $\mathrm{CDCl_3}$) δ_H 0.88 (6H, t, J = 7.0, 2 × $\mathrm{C\mathbf{H_3}}$), 1.04-1.12 (21H, m, $\mathrm{C\mathbf{H}(C\mathbf{H_3})_2)}$), 1.25-1.31 (48H, m, palmitoyl chain), 1.58-1.62 (4H, m, 2 × $\mathrm{C(O)CH_2C\mathbf{H_2}}$), 2.29-2.33 (4H, m, 2 × $\mathrm{C(O)C\mathbf{H_2}}$), 3.57-3.78 (16H, m, $\mathrm{C\mathbf{H_2}NH}$, 7 × $\mathrm{OC\mathbf{H_2}CH_2O}$), 3.82-3.85 (2H, m, $\mathrm{C\mathbf{H_2}OTIPS}$), 4.03 (2H, s, $\mathrm{C(O)C\mathbf{H_2}O}$), 4.07-4.18 (5H, m, $\mathrm{C\mathbf{H}HCHC\mathbf{HH}OPOC\mathbf{H_2}}$), 4.33-4.36 (1H, m, $\mathrm{CH\mathbf{H}CHCHHOP}$), 5.22 (1H, m, $\mathrm{C\mathbf{H}}$), 7.75 (1H, bt, J = 5.9, $\mathrm{N\mathbf{H}}$); **^{13}C NMR** (150 MHz, $\mathrm{CDCl_3}$) δ_C 12.0 (3 × $\mathrm{Si\mathbf{C}H}$), 14.3 (2 × $\mathrm{CH_2\mathbf{C}H_3}$), 18.1 ($\mathrm{Si(CH(\mathbf{C}H_3)_2)_3}$), 22.8 (2 × $\mathrm{\mathbf{C}H_2CH_3}$), 25.0 (2 × $\mathrm{C(O)CH_2\mathbf{C}H_2}$), 29.2 ($\mathrm{\mathbf{C}H_2}$), 29.3 ($\mathrm{\mathbf{C}H_2}$), 29.4 ($\mathrm{\mathbf{C}H_2}$), 29.5

(**C**H$_2$), 29.5 (**C**H$_2$), 29.6 (**C**H$_2$), 29.8 (**C**H$_2$), 29.8 (**C**H$_2$), 29.8 (**C**H$_2$), 32.1 (**C**H$_2$), 34.2 (C(O)**C**H$_2$CH$_2$), 34.3 (C(O)**C**H$_2$CH$_2$), 39.3 (d, $^3J_{CP}$ = 8.3, POCH$_2$**C**H$_2$NH), 62.0 (**C**HHCHCHHOP), 63.1 (**C**H$_2$OTIPS), 65.0 (d, $^2J_{CP}$ = 4.4, CH**C**HHOP), 66.4 (d, $^2J_{CP}$ = 6.1, PO**C**H$_2$CH$_2$), 69.6 (d, $^3J_{CP}$ = 8.3, **C**H), 70.4 (C(O)**C**H$_2$O), 70.5 (O**C**H$_2$CH$_2$O), 70.5 (O**C**H$_2$CH$_2$O), 70.7 (O**C**H$_2$CH$_2$O), 70.8 (O**C**H$_2$CH$_2$O), 70.8 (O**C**H$_2$CH$_2$O), 70.9 (O**C**H$_2$CH$_2$O), 72.9 (**C**H$_2$CH$_2$OTIPS), 171.3 (NH**C**(O)), 173. 1 (**C**(O)O), 173.5 (**C**(O)O); **IR** ν_{max}/cm^{-1} 3336 (N-H), 2920 (C-H), 2851 (C-H), 1740 (OC=O), 1675 (NHC=O); **LRMS** (LC-MS ES+) *m/z* 1082.9 (100%, [M+H]$^+$), 1104.9 (70%, [M+Na]$^+$); **HRMS** (TOF MS ES+) calculated mass 1082.7668 g.mol^{-1} ([$C_{56}H_{113}NO_{14}PSi$]$^+$), observed *m/z* 1082.7668 ([M+H]+); **R$_f$** 0.32 (5% MeOH in CH$_2$Cl$_2$).

***3-((((3,3-Diisopropyl-2-methyl-24-oxo-4,7,10,13,16,19,22-heptaoxa-25-aza-3-silaheptacosan-27-yl)oxy)(hydroxy)phosphoryl)oxy)propane-1,2-diyl dipalmitate* (47)**

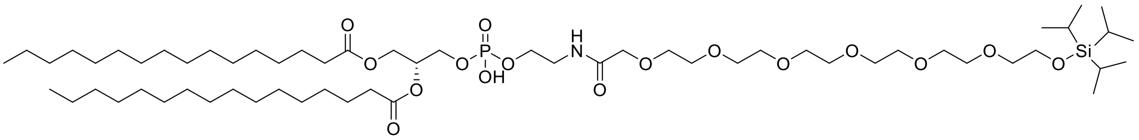

To a solution of *3-((((3,3-diisopropyl-2-methyl-24-oxo-4,7,10,13,16,19,22-heptaoxa-25-aza-3-silaheptacosan-27-yl)oxy)(hydroxy)phosphoryl)oxy)propane-1,2-diyl dipalmitate* **45** (0.583 g, 0.982 mmol) and DPPE (0.568 g, 0.821 mmol) in dry CH$_2$Cl$_2$ (26 mL) under Ar$_{(g)}$ was added NEt$_3$ (0.250 g, 344 µL, 2.45 mmol). The reaction mixture was stirred under Ar$_{(g)}$ overnight. After this time, the reaction mixture was diluted with CH$_2$Cl$_2$ (25 mL), washed with 0.1 M HCl solution (4 × 50 mL), dried (MgSO$_4$) and concentrated. The crude was purified by FCC (on silica gel eluting 0-8% MeOH in CH$_2$Cl$_2$) to give *3-((((3,3-diisopropyl-2-methyl-24-oxo-4,7,10,13,16,19,22-heptaoxa-25-aza-3-silaheptacosan-27-yl)oxy)(hydroxy)-phosphoryl)oxy)-propane-1,2-diyl dipalmitate* **47** (0.258 g, 27%) as a white amorphous solid.

^{1}H NMR (600 MHz, CDCl$_3$) δ_H 0.86 (6H, t, J = 7.0, 2 × C**H**$_3$), 1.02-1.09 (21H, m, C**H**(C**H**$_3$)$_2$)), 1.23-1.29 (48H, m, palmitoyl chain), 1.54-1.57 (4H, m, 2 × C(O)CH$_2$C**H**$_2$), 2.26 (4H, apparent quartet, J = 7.1, 2 × C(O)C**H**$_2$), 3.45-3.46 (2H, m, C**H**$_2$NH), 3.58-3.71 (22H, m, 11 × OC**H**$_2$), 3.82 (2H, t, J = 5.4, C**H**$_2$OTIPS), 3.94 3.99 (4H, m, CHC**HH**OPOC**H**$_2$), 4.01 (2H, s, C(O)C**H**$_2$O)), 4.14 (1H, dd, J = 12.0, 6.9, C(O)OC**H**H), 4.36 (1H, dd, J = 12.0, 3.0, C(O)OCH**H**CH), 5.18-5.22 (1H, m, C**H**); **^{13}C NMR** (150 MHz, CDCl$_3$) δ_c 12.0 (3 × Si**C**H), 14.2 (2 × CH$_2$**C**H$_3$), 18.1 (Si(CH(**C**H$_3$)$_2$)$_3$), 22.8 (2 × **C**H$_2$CH$_3$), 25.0 (**C**H$_2$CH$_2$C(O)), 25.1 (**C**H$_2$CH$_2$C(O)), 29.3 (**C**H$_2$), 29.3 (**C**H$_2$) 29.5 (**C**H$_2$), 29.5 (**C**H$_2$), 29.5 (**C**H$_2$), 29.7 (**C**H$_2$), 29.7 (**C**H$_2$), 29.8 (**C**H$_2$), 29.8 (**C**H$_2$), 29.8 (**C**H$_2$), 32.0 (**C**H$_2$), 34.2 (**C**H$_2$C(O)), 34.4 (**C**H$_2$C(O)), 40.9 (**C**H$_2$NH), 62.9 (C(O)O**C**HH), 63.1 (**C**H$_2$OTIPS), 63.6-63.7 (**C**HHOPO**C**H$_2$, two overlapping carbon peaks split by $^2J_{CP}$ couplings), 69.2 (O**C**H$_2$), 69.6 (O**C**H$_2$), 69.8 (O**C**H$_2$), 69.9 (O**C**H$_2$), 70.0 (O**C**H$_2$), 70.2 (O**C**H$_2$), 70.6 (d, $^3J_{CP}$ = 8.3, **C**H), 70.8 (O**C**H$_2$), 71.3 (C(O)**C**H$_2$O), 72.6 (**C**H$_2$CH$_2$OTIPS), 170.1 (**C**(O)NH), 173.2 (**C**(O)O), 173.6 (**C**(O)O); **IR** ν_{max}/cm^{-1} 3292 (N-H), 2917 (C-H), 2850 (C-H), 1737 (OC=O), 1669 (NHC=O); **LRMS** (LC-MS ES+) *m/z* 1171.1 (100%, [M+H]$^+$), 1193.1 (50%, [M+Na]$^+$); **HRMS** (MALDI TOF) calculated mass 1214.7831 g.mol^{-1} ([$C_{60}H_{119}NO_{16}PSiNa_2$]$^+$), observed *m/z* 1214.7866 ([M-H+2Na]$^+$); **R$_f$** 0.33 (5% MeOH in CH$_2$Cl$_2$).

3-((Hydroxy((17-hydroxy-4-oxo-6,9,12,15-tetraoxa-3-azaheptadecyl)oxy)-phosphoryl)-oxy)propane-1,2-diyl dipalmitate (48)

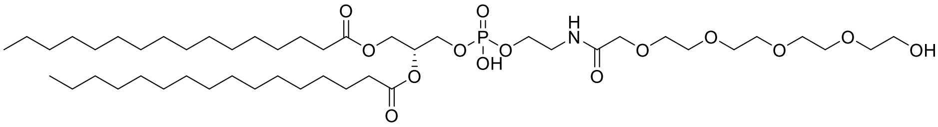

To an ice-cooled solution of *3-((((3,3-diisopropyl-2-methyl-18-oxo-4,7,10,13,16-pentaoxa-19-aza-3-silahenicosan-21-yl)oxy)(hydroxy)phosphoryl)oxy)propane-1,2-diyl dipalmitate* **46** (0.47 g, 0.43 mmol) in dry CH$_2$Cl$_2$ (5 mL) under Ar$_{(g)}$ was added TBAF (0.86 mL, 1 M solution in THF, 0.86 mmol) dropwise over 5 min, the reaction mixture was allowed to warm to RT and stirred for 2 h. After this time, a further 2 eq. of TBAF (0.86 mL, 1 M solution in THF, 0.86 mmol) were added and the reaction mixture was stirred at RT under Ar$_{(g)}$ overnight. After this time, the solvent was removed under reduced pressure and the residue was re-dissolved in 7.5% CH$_2$Cl$_2$ in MeOH, passed through a cation exchange resin (Dowex® 50WX8 200-400 (H)) and the desired fractions were pooled and concentrated (determined by LC-MS). The resulting residue was purified by FCC (on silica gel eluting 6-14% MeOH in CH$_2$Cl$_2$) to give *3-((hydroxy((17-hydroxy-4-oxo-6,9,12,15-tetraoxa-3-azaheptadecyl)oxy)phosphoryl)oxy)-propane-1,2-diyl dipalmitate* **48** (0.15 g, 38%). The product was freeze dried to give a white powder.

^{1}H NMR (600 MHz, CDCl$_3$) δ_H 0.88 (6H, t, *J* = 7.0, 2 × C**H$_3$**), 1.26-1.31 (48H, m, palmitoyl chain), 1.57-1.61 (4H, m, 2 × C(O)CH$_2$C**H$_2$**), 2.27-2.32 (4H, m, 2 × C(O)C**H$_2$**), 3.52-3.53 (2H, m, C**H$_2$**NH), 3.65-3.77 (16H, m, 4 × OC**H$_2$**C**H$_2$**O), 3.97-4.10 (6H, m, C**HH**OPOC**H$_2$**, C(O)C**H$_2$**O), 4.20 (1H, dd, *J* = 12.0, 6.5, C(O)OC**H**HCH), 4.41 (1H, dd, *J* = 12.0, 3.2, C(O)OCH**H**CH), 5.24-5.28 (1H, m, C**H**), 8.59 (1H, br s, N**H**); **^{13}C NMR** (150 MHz, CDCl$_3$) δ_C 14.2 (2 × **C**H$_3$), 22.8 (2 × **C**H$_2$CH$_3$), 25.1 (2 × C(O)CH$_2$**C**H$_2$), 29.3 (**C**H$_2$), 29.3 (**C**H$_2$), 29.4 (**C**H_2), 29.5 (**C**H_2), 29.5 (**C**H_2), 29.6 (**C**H_2), 29.8 (**C**H_2), 29.8 (**C**H_2), 29.8 (**C**H_2), 32.0 (**C**H_2), 34.3 (C(O)**C**H_2), 34.4 (C(O)**C**H_2), 40.8 (POCH_2**C**H_2NH), 60.6 (O**C**H_2CH_2O), 62.9 (**C**HHCHCHHOP), 63.7 (d, $^2J_{CP}$ = 5.5, CHHCH**C**HHOP), 65.0 (d, $^2J_{CP}$ = 5.5, CHCHHOPO**C**H_2), 69.0 (O**C**H_2CH_2O), 69.2 (O**C**H_2CH_2O), 69.3 (O**C**H_2CH_2O), 69.5 (O**C**H_2CH_2O), 69.6 (O**C**H_2CH_2O), 70.3 (O**C**H_2CH_2O), 70.5 (d, $^3J_{CP}$ = 7.2, **C**H), 71.4 (C(O)**C**H_2O), 72.2 (O**C**H_2CH_2O), 169.3 (NH**C**(O)), 173.2 (**C**(O)O), 173.6 (**C**(O)O); **IR** ν_{max}/cm^{-1} 3304 (N-H), 2916 (C-H), 2849 (C-H), 1738 (OC=O), 1670 (NHC=O); **LRMS** (LC-MS ES+) *m/z* 926.7 (100%, [M+H]$^+$), 948.7 (45%, [M+Na]$^+$); **HRMS** (TOF MS ES+) calculated mass 926.6334 g.mol^{-1} ([$C_{47}H_{93}NO_{14}P$]$^+$), observed *m/z* 926.6329 ([M+H]$^+$); **R$_f$** 0.40 (10% MeOH in CH_2Cl_2); **[α]$_D^{20}$** +9.0 (*c* 2 mg/mL, 1% $CHCl_3$ in MeOH).

***3-((Hydroxy((23-hydroxy-4-oxo-6,9,12,15,18,21-hexaoxa-3-azatricosyl)oxy)-phosphoryl)oxy)propane-1,2-diyl dipalmitate* (49)**

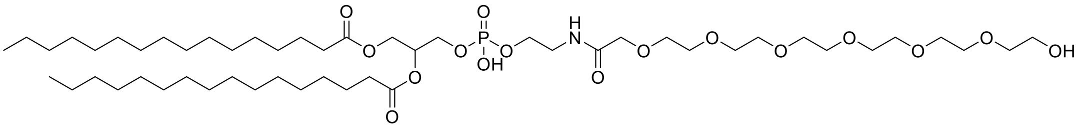

To an ice-cooled solution of *3-((((3,3-diisopropyl-2-methyl-24-oxo-4,7,10,13,16,19,22-heptaoxa-25-aza-3-silaheptacosan-27-yl)oxy)(hydroxy)phosphoryl)oxy)propane-1,2-diyl dipalmitate* **47** (0.258 g, 0.220 mmol) in dry CH_2Cl_2 (4 mL) was dropwise added TBAF (0.44 mL, 1 M solution in THF, 0.44 mmol) under $Ar_{(g)}$. The reaction mixture was stirred for 2 h then another 2 eq. of TBAF (0.44 mL, 1 M solution in THF, 0.44 mmol) were added and stirred for 5 h. After this time, another 2 eq. of TBAF (0.44 mL, 1 M solution in THF, 0.44 mmol) and dry CH_2Cl_2 (1 mL) were added and the reaction mixture was stirred under $Ar_{(g)}$ overnight. After this time, the solvent was removed under reduced pressure and the crude yellow oil was re-dissolved in 7.5% CH_2Cl_2 in MeOH. The solution was passed through a cation exchange resin (Dowex® 50WX8 100-200 (H)), the desired fractions were concentrated (determined by LC-MS), re-dissolved in CH_2Cl_2, washed with brine (1 × 20 mL), dried ($MgSO_4$) and concentrated again. The resulting yellow oil was purified by FCC (on silica gel eluting 3-12% MeOH in CH_2Cl_2) to give *3-((hydroxy((23-hydroxy-4-oxo-6,9,12,15,18,21-hexaoxa-3-azatricosyl)oxy)-phosphoryl)oxy)propane-1,2-diyl dipalmitate* **49** (0.142 g, 64%) as a white powder.

^{1}H NMR (600 MHz, $CDCl_3$) δ_H 0.87 (6H, t, *J* = 7.0, 2 × C$\mathbf{H_3}$), 1.24-1.30 (48H, m, palmitoyl chain), 1.55-1.62 (4H, m, 2 × C(O)CH_2C$\mathbf{H_2}$), 2.26-2.30 (4H, m, 2 × C(O)C$\mathbf{H_2}$), 3.52-3.55 (2H, m, C$\mathbf{H_2}$NH), 3.62-3.75 (24H, m, 6 × OC$\mathbf{H_2}$C$\mathbf{H_2}$O), 3.94-4.00 (4H, m, C**HH**OPOC$\mathbf{H_2}$), 4.01 (2H, s, C(O)C$\mathbf{H_2}$O), 4.17 (1H, dd, *J* = 12.0, 6.6, C(O)OC**H**H), 4.39 (1H, dd, *J* = 12.0, 3.2, C(O)OCH**H**), 5.21-5.24 (1H, m, C**H**), 8.25 (1H, br s, N**H**); **^{13}C NMR** (150 MHz, $CDCl_3$)

δ_C 14.3 (2 × $\mathbf{C}H_3$), 22.8 (2 × $\mathbf{C}H_2CH_3$), 25.0 ($\mathbf{C}H_2CH_2C(O)$), 25.0 ($\mathbf{C}H_2CH_2C(O)$), 29.3 ($\mathbf{C}H_2$), 29.3 ($\mathbf{C}H_2$), 29.4 ($\mathbf{C}H_2$), 29.5 ($\mathbf{C}H_2$), 29.5 ($\mathbf{C}H_2$), 29.6 ($\mathbf{C}H_2$), 29.8 ($\mathbf{C}H_2$), 29.8 ($\mathbf{C}H_2$), 29.8 ($\mathbf{C}H_2$), 32.0 ($\mathbf{C}H_2$), 34.2 ($\mathbf{C}H_2C(O)$), 34.4 ($\mathbf{C}H_2C(O)$), 40.5 (d, $^3J_{CP}$ = 3.9, $\mathbf{C}H_2NH$), 60.5 ($O\mathbf{C}H_2CH_2O$), 62.9 ($C(O)O\mathbf{C}HH$), 63.5 (d, $^2J_{CP}$ = 5.0, $CH\mathbf{C}HHOP$), 64.1 (d, $^2J_{CP}$ = 4.4, $PO\mathbf{C}H_2CH_2NH$), 68.9 ($O\mathbf{C}H_2CH_2O$), 69.1 ($O\mathbf{C}H_2CH_2O$), 69.1 ($O\mathbf{C}H_2CH_2O$), 69.4 ($O\mathbf{C}H_2CH_2O$), 69.5 ($O\mathbf{C}H_2CH_2O$), 69.6 ($O\mathbf{C}H_2CH_2O$), 69.8 ($O\mathbf{C}H_2CH_2O$), 69.9 ($O\mathbf{C}H_2CH_2O$), 70.1 ($O\mathbf{C}H_2CH_2O$), 70.6 (d, $^3J_{CP}$ = 8.3, $\mathbf{C}H$), 71.0 ($C(O)\mathbf{C}H_2O$), 71.1 ($O\mathbf{C}H_2CH_2O$), 72.2 ($O\mathbf{C}H_2CH_2O$), 170.2 ($NH\mathbf{C}(O)$), 173.2 ($\mathbf{C}(O)O$), 173.6 ($\mathbf{C}(O)O$); **IR** ν_{max}/cm^{-1} 3370 (O-H), 2916 (C-H), 2849 (C-H), 1737 (OC=O), 1665 (NHC=O); **LRMS** (LC-MS ES+) *m/z* 1014.9 (85%, $[M+H]^+$), 1036.9 (100%, $M+Na^+$); **HRMS** (QTOF) calculated 1014.6853 mass g.mol^{-1} ($[C_{51}H_{101}NO_{16}P]^+$), observed *m/z* 1014.6857 ($[M+H]^+$); **R$_f$** 0.24 (8% MeOH in CH_2Cl_2).

2,5-Dioxopyrrolidin-1-yl 1-(9H-fluoren-9-yl)-3-oxo-2,7,10,13,16-pentaoxa-4-azanonadecan-19-oate **(51)**

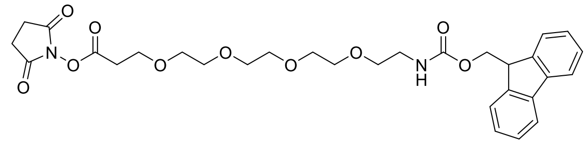

15-(9-Fluorenyloxycarbonyl)amino-4,7,10,13-tetraoxa-pentadecanoic acid **50** (138 mg, 0.283 mmol) and NHS (48.0 mg, 0.417 mmol) were dissolved in dry CH_2Cl_2 (1.5 mL). EDC (60.0 mg, 0.313 mmol) was added and the reaction mixture was stirred at RT under $Ar_{(g)}$ overnight. After this time, the reaction mixture was diluted with CH_2Cl_2 (15 mL) and washed with brine (3 × 15 mL). The combined aqueous layers were extracted with CH_2Cl_2 (2 × 10 mL). The combined organic layers were dried ($MgSO_4$) and concentrated to give *2,5-dioxopyrrolidin-1-yl 1-(9H-fluoren-9-yl)-3-oxo-2,7,10,13,16-pentaoxa-4-azanonadecan-19-oate* **51** (123 mg, 75%) as a clear oil.

^{1}H NMR (600 MHz, $CDCl_3$) δ_H 2.79 (4H, br s, $C(O)C\mathbf{H_2}C\mathbf{H_2}C(O)$), 2.86 (2H, t, *J* = 6.4, $C(O)C\mathbf{H_2}$), 3.39 (2H, apparent q, *J* = 5.4, $C\mathbf{H_2}NH$), 3.56-3.67 (14H, 7 × $OC\mathbf{H_2}$), 3.80 (2H, t, *J* = 6.4, $C(O)CH_2C\mathbf{H_2}$), 4.22 (1H, t, *J* = 7.0, $ArC\mathbf{H}$), 4.40 (2H, d, *J* = 7.0, $ArCHC\mathbf{H_2}$), 5.55 (1H, t, *J* = 5.4, $N\mathbf{H}$), 7.31 (2H, apparent td, *J* = 7.5, 1.1, 2 × $Ar\mathbf{H}$), 7.39 (2H, apparent t, *J* = 7.4, 2 × $Ar\mathbf{H}$), 7.61 (2H, d, *J* = 7.4, 2 × $Ar\mathbf{H}$), 7.76 (2H, d, *J* = 7.5, 2 × $Ar\mathbf{H}$); **^{13}C NMR** (150 MHz, $CDCl_3$) δ_C 25.7 ($C(O)\mathbf{C}H_2\mathbf{C}H_2C(O)$), 32.2 ($C(O)\mathbf{C}H_2$), 41.0 ($N\mathbf{C}H_2$), 47.4 (Fmoc $\mathbf{C}H$), 65.8 ($C(O)CH_2\mathbf{C}H_2$), 66.6 (Fmoc $\mathbf{C}H_2$), 70.1 ($O\mathbf{C}H_2$), 70.4 ($O\mathbf{C}H_2$), 70.6 ($O\mathbf{C}H_2$), 70.6 ($O\mathbf{C}H_2$), 70.7 ($O\mathbf{C}H_2$), 70.7 ($O\mathbf{C}H_2$), 70.8 ($O\mathbf{C}H_2$), 120.0 ($Ar\mathbf{C}H$), 125.2 ($Ar\mathbf{C}H$), 127.2 ($Ar\mathbf{C}H$), 127.8 ($Ar\mathbf{C}H$), 141.4 ($Ar\mathbf{C}$), 144.1 ($Ar\mathbf{C}$), 156.7 ($NH\mathbf{C}(O)$), 166.9 ($O\mathbf{C}(O)$), 169.1

(**C**(O)CH_2CH_2**C**(O)); **IR** ν_{max}/cm^{-1} 3341 (N-H), 2872 (C-H), 1781 (C=O), 1733 (C=O), 1525 (C=C); **LRMS** (LC-MS ES+) *m/z* 585.3 (100%, [M+H]$^+$), 607.3 (65%, [M+Na]$^+$); **HRMS** (TOF MS ES+) calculated mass 585.2443 g.mol^{-1} ([$C_{30}H_{37}N_2O_{10}$]$^+$), observed *m/z* 585.2445 ([M+H]$^+$); **R$_f$** 0.5 (4% MeOH in CH_2Cl_2).

3-((((1-(9H-Fluoren-9-yl)-3,19-dioxo-2,7,10,13,16-pentaoxa-4,20-diazadocosan-22-yl)oxy)(hydroxy)phosphoryl)oxy)propane-1,2-diyl dipalmitate **(52)**

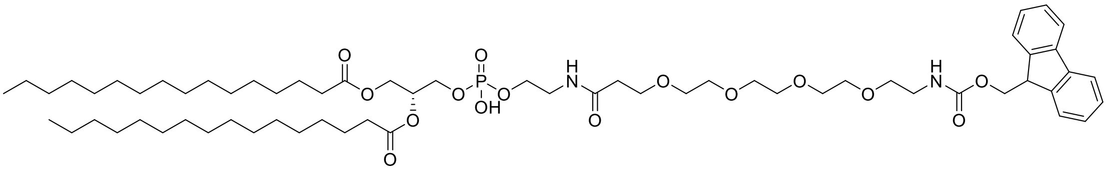

A solution of *2,5-Dioxopyrrolidin-1-yl 1-(9H-fluoren-9-yl)-3-oxo-2,7,10,13,16-pentaoxa-4-azanonadecan-19-oate* **51** (0.118 g, 0.202 mmol), DPPE (0.116 g, 0.168 mmol) and NEt_3 (71 µL, 0.505 mmol) in dry CH_2Cl_2 (6.5 mL) was stirred overnight at RT under $Ar_{(g)}$. After this time, the reaction mixture was diluted with CH_2Cl_2 (25 mL), washed with 0.1 M HCl solution (3 × 20 mL) and extracted with CH_2Cl_2 (20 mL). The combined organic layers were dried ($MgSO_4$) and concentrated to give *3-((((1-(9H-fluoren-9-yl)-3,19-dioxo-2,7,10,13,16-pentaoxa-4,20-diazadocosan-22-yl)oxy)(hydroxy)phosphoryl)oxy)-propane-1,2-diyl dipalmitate* **52** (0.195 g, 100%) as a white solid.

^{1}H NMR (600 MHz, $CDCl_3$) δ_H 0.87 (6H, t, *J* = 7.1, 2 × C**H$_3$**), 1.24-1.29 (48H, m, palmitoyl chain), 1.57-1.58 (4H, m, 2 × C(O)CH_2C**H$_2$**), 2.26-2.31 (4H, m, 2 × C(O)C**H$_2$**), 2.48-2.49 (2H, m, NHC(O)C**H$_2$**), 3.39 (2H, t, *J* = 4.5, C**H$_2$**NHC(O)O), 3.50 (2H, br s, C**H$_2$**NHC(O)CH_2), 3.57-3.65 (14H, m, 7 × OC**H$_2$**), 3.70-3.72 (2H, m, NHC(O)CH_2C**H$_2$**), 4.05-4.16 (5H, m, C**H**HCHC**HH**OPOC**H$_2$**), 4.20-4.22 (1H, m, Fmoc C**H**), 4.34 (1H, dd, *J* = 12, 3.7, CH**H**CHCHHOP), 4.38 (2H, d, *J* = 7.2, Fmoc C**H$_2$**), 5.21 (1H, m, C**H**), 7.29-7.31 (2H, m, 2 × Ar**H**), 7.37-7.39 (2H, m, 2 × Ar**H**), 7.61 (2H, d, *J* = 7.3, 2 × Ar**H**), 7.75 (2H, d, *J* = 7.5, 2 × Ar**H**); **^{13}C NMR** (150 MHz, $CDCl_3$) δ_c 14.3 (2 × **C**H_3), 22.8 (2 × **C**H_2CH_3), 25.0 (2 × C(O)CH_2**C**H_2), 29.2 (**C**H_2), 29.3 (**C**H_2), 29.4 (**C**H_2), 29.5 (**C**H_2), 29.5 (**C**H_2), 29.6 (**C**H_2), 29.7 (**C**H_2), 29.8 (**C**H_2), 29.8 (**C**H_2), 32.1 (**C**H_2), 34.1 (C(O)**C**H_2), 34.3 (C(O)**C**H_2), 36.6 (NHC(O)**C**H_2), 40.0 (d, $^3J_{CP}$ = 5.5, POCH_2**C**H_2), 40.9 (**C**H_2NHC(O)O), 47.4 (Fmoc **C**H), 62.08 (C(O)O**C**HH), 65.0 (d, $^2J_{CP}$ = 4.4, **C**HHOP), 66.3 (d, $^2J_{CP}$ = 5.0, PO**C**H_2), 66.7 (Fmoc **C**H_2), 67.2 (NHC(O)CH_2**C**H_2), 69.6 (d, $^3J_{CP}$ = 8.3, **C**H), 70.2 (O**C**H_2), 70.3 (O**C**H_2), 70.4 (O**C**H_2), 70.5 (O**C**H_2), 70.5 (O**C**H_2), 70.6 (O**C**H_2), 70.7 (O**C**H_2), 120.1 (Ar**C**H), 125.2 (Ar**C**H), 127.2 (Ar**C**H), 127.8 (Ar**C**H), 141.4 (Ar**C**), 144.1 (Ar**C**), 156.8 (NH**C**(O)O), 172.5 (NH**C**(O)CH_2), 173.1 (O**C**(O)CH_2), 173.5 (O**C**(O)CH_2); **IR** ν_{max}/cm^{-1} 3318 (N-H), 2956 (C-H), 2916 (C-H), 2849 (C-H), 1736 (OC=O), 1655 (NHC=O), 1537

(C=C); **LRMS** (LC-MS ES+) *m/z* 1161.9 (100%, $[M+H]^+$), 1183.9 (75%, $M+Na^+$); **HRMS** (TOF MS ES+) calculated mass 1159.7180 $g.mol^-$ ($[C_{63}H_{104}N_2O_{15}P]^-$), observed *m/z* 1159.7174 ($[M-H]^-$); $\mathbf{R_f}$ 0.31 (4% MeOH in CH_2Cl_2).

3-((((1-Amino-15-oxo-3,6,9,12-tetraoxa-16-azaoctadecan-18-yl)oxy)(hydroxy)-phosphoryl)oxy)propane-1,2-diyl dipalmitate **(53)**

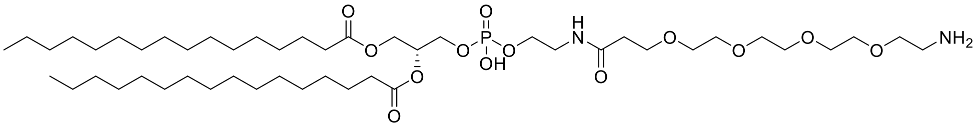

A solution of 3-((((1-(9H-fluoren-9-yl)-3,19-dioxo-2,7,10,13,16-pentaoxa-4,20-diazadocosan-22-yl)oxy)(hydroxy)phosphoryl)oxy)-propane-1,2-diyl dipalmitate **52** (198 mg, 0.170 mmol) in 20% piperidine in CH_2Cl_2 (5.6 mL) was stirred at RT under $Ar_{(g)}$ for 50 min. After this time, the reaction mixture was diluted with CH_2Cl_2 (25 mL) and washed with $NaHCO_3$ (2 × 20 mL) and brine (2 × 20 mL). The aqueous layers were extracted with CH_2Cl_2 (2 × 20 mL). The combined organic layers were dried ($MgSO_4$) and concentrated. The crude was purified by FCC (on silica gel eluting 6-14% MeOH and 1% NEt_3 in CH_2Cl_2) to give **53** *3-((((1-amino-15-oxo-3,6,9,12-tetraoxa-16-azaoctadecan-18-yl)oxy)(hydroxy)phosphoryl)oxy)propane-1,2-diyl dipalmitate* (53 mg, 33%) as a white solid.

^{1}H NMR (600 MHz, $CDCl_3$) δ_H 0.86 (6H, t, *J* = 7.1, 2 × C**H₃**), 1.25-1.29 (48H, m, palmitoyl chain), 1.56-1.60 (4H, m, 2 × C(O)CH₂C**H₂**), 2.27-2.31 (4H, m, 2 × C(O)C**H₂**), 2.50 (2H, t, *J* = 5.8, NHC(O)C**H₂**), 3.14 (2H, br s, C**H₂**NH₂), 3.44-3.46 (2H, m, C**H₂**NHC(O)CH₂), 3.60-3.68 (12H, m, 6 × OC**H₂**), 3.76-3.78 (2H, m, C**H₂**CH₂NH₂), 3.80 (2H, t, *J* = 5.8, NHC(O)CH₂C**H₂**), 3.94-3.98 (4H, m, C**HH**OPOC**H₂**), 4.17 (1H, dd, *J* = 12.0, 6.6, C(O)OC**H**H), 4.39 (1H, dd, *J* = 12.0, 3.3, C(O)OCH**H**), 5.21 (1H, m, C**H**), 8.32 (1H, br s, amide N**H**), 8.37 (2H, br s, N**H₂**); **^{13}C NMR** (150 MHz, $CDCl_3$) δ_C 14.3 (2 × **C**H₃), 22.8 (2 × **C**H₂CH₃), 25.0 (2 × C(O)CH₂**C**H₂), 29.3 (**C**H₂), 29.3 (**C**H₂), 29.5 (**C**H₂), 29.5 (**C**H₂), 29.5 (**C**H₂), 29.7 (**C**H₂), 29.7 (**C**H₂), 29.8 (**C**H₂), 29.8 (**C**H₂), 32.1 (**C**H₂), 34.2 (C(O)**C**H₂), 34.4 (C(O)**C**H₂), 36.3 (NHC(O)**C**H₂), 39.9 (**C**H₂NH₂), 40.8 (d, $^3J_{CP}$ = 5.0, POCH₂**C**H₂), 62.8 (**C**HHCHCHHOP), 63.7 (d, $^2J_{CP}$ = 5.5, CH**C**HHOP), 64.4 (d, $^2J_{CP}$ = 7.2, PO**C**H₂CH₂), 67.5 (NHC(O)CH₂**C**H₂), 67.5 (**C**H₂CH₂NH₂), 70.0 (O**C**H₂CH₂O), 70.0 (O**C**H₂CH₂O), 70.2 (O**C**H₂CH₂O), 70.4 (O**C**H₂CH₂O), 70.4 (O**C**H₂CH₂O), 70.4 (O**C**H₂CH₂O), 70.5 (d, $^3J_{CP}$ = 8.3, **C**H), 171.3 (NH**C**(O)), 173.2 (**C**(O)O), 173.6 (**C**(O)O); **IR** ν_{max}/cm^{-1} 3265 (N-H), 2955 (C-H), 2916 (C-H), 2849 (C-H), 1738 (C=O), 1650 (C=O); **LRMS** (LC-MS ES+) *m/z* 939.7 (100%, $[M+H]^+$), 961.6 (15%, $[M+Na]^+$); **HRMS** (TOF MS ES+) calculated mass 939.6650 g.mol^{-1} ([$C_{48}H_{96}N_2O_{13}P$]$^+$), observed *m/z* 939.6639 ([M+H]$^+$); $\mathbf{R_f}$ 0.55 (14% MeOH and 1% TEA in CH_2Cl_2); $\mathbf{[\alpha]_D^{20}}$ +1 (*c* 2 mg/mL, 1% $CHCl_3$ in MeOH).

7.3.4 Maleimide-lipid synthesis

N1-(2,3-Bis(hexadecyloxy)propyl)-N4-(2-(2-(2-(3-(2,5-dioxo-2,5-dihydro-1H-pyrrol-1-yl)propanamido)ethoxy)ethoxy)ethyl)succinamide **(54)**

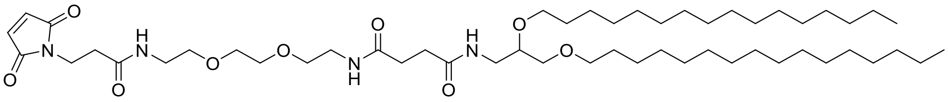

3-Maleimidopropionic acid (30.0 mg, 0.177 mmol) in DMF (2 mL) was added to a solution of *16-(Hexadecyloxy)-10,13-dioxo-3,6,18-trioxa-9,14-diazatetratriacontan-1-aminium 2,2,2-trifluoroacetate* **9** (127 mg, 0.144 mmol), HBTU (97.0 mg, 0.256 mmol) and DIPEA (50.0 µL, 0.287 mmol) in CH_2Cl_2 (2.5 mL). The reaction mixture was stirred at RT overnight. After this time, the solvent was removed under reduced pressure and the crude was purified by FCC (dry loaded on silica gel eluting 0-4% MeOH in CH_2Cl_2) to give *N1-(2,3-bis(hexadecyloxy)propyl)-N4-(2-(2-(2-(3-(2,5-dioxo-2,5-dihydro-1H-pyrrol-1-yl)propanamido)-ethoxy)ethoxy)ethyl)succinamide* **54** (74.0 mg, 56%) as a white solid.

^{1}H NMR (600 MHz, $CDCl_3$) δ_H 0.88 (6H, t, *J* = 7.0, 2 × $CH_2C\mathbf{H_3}$), 1.25-1.29 (52H, m, cetyl chain), 1.54 (4H, quint, *J* = 6.8, 2 × $C(O)CH_2C\mathbf{H_2}$), 2.52 (4H, s, $C(O)C\mathbf{H_2}C\mathbf{H_2}C(O)$), 2.54 (2H, t, *J* = 7.2, mal-$CH_2C\mathbf{H_2}C(O)$), 3.25-3.28 (1H, m, $C(O)NHC\mathbf{H}H$), 3.38-3.57 (16H, m, 2 × $NHC\mathbf{H_2}C\mathbf{H_2}O$, $NHCH\mathbf{H}C\mathbf{H}C\mathbf{HH}$, 2 × $OC\mathbf{H_2}CH_2$), 3.60 (4H, s, $OC\mathbf{H_2}C\mathbf{H_2}O$), 3.84 (2H, t, *J* = 7.2, mal-$C\mathbf{H_2}$), 6.20 (1H, br s, N**H**), 6.55 (1H, br s, N**H**), 6.61 (1H, br s, N**H**), 6.70 (2H, s, C**H**C**H**); **^{13}C NMR** (150 MHz, $CDCl_3$) δ_C 14.3 (2 × $\mathbf{C}H_3$), 22.8 (2 × $\mathbf{C}H_2CH_3$), 26.2 ($\mathbf{C}H_2$), 29.5 ($\mathbf{C}H_2$), 29.6 ($\mathbf{C}H_2$), 29.8 ($\mathbf{C}H_2$), 29.8 ($\mathbf{C}H_2$), 29.8 ($\mathbf{C}H_2$), 29.8 ($\mathbf{C}H_2$), 30.2 ($\mathbf{C}H_2$), 31.8 ($C(O)\mathbf{C}H_2CH_2C(O)$), 31.8 ($C(O)CH_2\mathbf{C}H_2C(O)$), 32.1 ($\mathbf{C}H_2$), 34.5 (mal-$\mathbf{C}H_2$), 34.7 (mal-$CH_2\mathbf{C}H_2$), 39.4 ($NH\mathbf{C}H_2$), 39.4 ($NH\mathbf{C}H_2$), 41.1 ($NH\mathbf{C}HHCH$), 70.0 ($O\mathbf{C}H_2$), 70.1 ($O\mathbf{C}H_2$), 70.3 ($O\mathbf{C}H_2$), 70.3 ($O\mathbf{C}H_2$), 70.4 ($O\mathbf{C}H_2$), 71.5 ($O\mathbf{C}H_2$), 72.0 ($O\mathbf{C}H_2$), 76.7 ($\mathbf{C}H$), 134.3 ($\mathbf{C}H\mathbf{C}H$), 170.3 ($NCH_2CH_2\mathbf{C}(O)NH$), 170.7 ($\mathbf{C}(O)CHCH\mathbf{C}(O)$), 172.3 ($NHC(O)CH_2CH_2\mathbf{C}(O)NH$), 172.5 ($NH\mathbf{C}(O)CH_2CH_2C(O)NH$); **IR** ν_{max}/cm^{-1} 3293 (N-H), 2916 (C-H), 2849 (C-H), 1701 (C=O), 1636 (C=O), 1550 (C=C); **LRMS** (LC-MS ES+) *m/z* 921.8 (100%, [M+H]$^+$), 943.7 (30%, [M+Na]$^+$); **HRMS** (TOF MS ES+) calculated mass 921.7256 g.mol^{-1} ([$C_{52}H_{97}N_4O_9$]$^+$), observed *m/z* 921.7255 ([M+H]$^+$); $\mathbf{R_f}$ 0.42 (7% MeOH in CH_2Cl_2).

***tert*-Butyl (3-bromopropyl)carbamate (56)**[274]

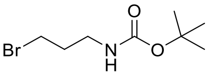

3-Brompropylamine hydrobromide (2.00 g, 9.14 mmol) was dispersed in CH_2Cl_2 (40 mL) and Boc_2O (3.80 g, 17.4 mmol) in CH_2Cl_2 (30 mL) was added. The solution was made basic with TEA (1.5 mL). The reaction mixture was stirred at RT for 3 h then washed with saturated $NaHCO_3$ solution (2 × 40 mL) and brine (40 mL), dried ($MgSO_4$) and concentrated under reduced pressure. The crude was purified by FCC (on silica gel eluting 0-25% EtOAc in petroleum ether) to give *tert*-butyl (3-bromopropyl)carbamate **56** (2.01 g, 92%) as a clear oil.

^{1}H NMR (600 MHz, $CDCl_3$) δ_H 1.42 (9H, s, C(C**H$_3$**)$_3$), 2.04 (2H, quint, *J* = 6.5, CH_2C**H$_2$**CH_2), 3.25 (2H, apparent q, *J* = 6.5, C**H$_2$**NH), 3.43 (2H, t, *J* = 6.5, BrC**H$_2$**), 4.72 (1H, br s, N**H**); **^{13}C NMR** (150 MHz, $CDCl_3$) δ_c 28.5 (C(**C**H$_3$)$_3$), 31.0 (Br**C**H$_2$), 32.8 (CH$_2$**C**H$_2$CH$_2$), 39.1 (**C**H$_2$NH), 79.5 (**C**(CH$_3$)$_3$), 156.1 (**C**(O)); **IR** ν_{max}/cm^{-1} 3374 (N-H), 2978 (C-H), 2934 (C-H), 1685 (C=O); **LRMS** (LC-MS ES+) *m/z* 238.2 (80%, $[M+H]^+$), 240.1 (80%, $[M+H]^+$), 475.1 (50%, $[2M+H]^+$), 477.1 (100%, $[2M+H]^+$), 479.2 (50%, $[2M+H]^+$); **R$_f$** 0.5 (15% EtOAc in petroleum ether). Data corresponds with the literature.[274]

2,3-Bis(hexadecyloxy)-*N*,*N*-dimethylpropan-1-amine (58)[275]

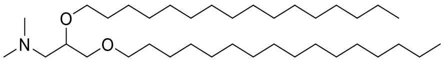

NaH (1.20 g, 50.0 mmol; dry 95%) was placed in an oven dried RBF and purged with $Ar_{(g)}$. Anhydrous THF (30 mL) was added followed by dropwise addition of 3-(dimethylamino)-1,2-propanediol (1.87 g, 15.7 mmol) in anhydrous THF (20 mL). The reaction mixture stirred for 40 min and hexadecyl methanesulfonate **5** (14.9 g, 46.5 mmol) in anhydrous THF (40 mL) was added slowly and the reaction mixture was heated to reflux overnight. After this time, 150 mL distilled H_2O was added to the reaction mixture and the product was extracted into EtOAc (4 × 100 mL). The combined organic phases were washed with brine (3 × 200 mL), dried ($MgSO_4$) and concentrated under reduced pressure. The product was purified by FCC (on silica gel eluting 0-5% MeOH in CH_2Cl_2) to give the product **58** (901 mg, 10%) and a mixture of single alkylation products (1.46 g) as orange oils. NaH (0.31 g, 12.9 mmol; dry 95%) was placed in an oven dried RBF and purged with $Ar_{(g)}$. Anhydrous toluene (20 mL) was added followed by dropwise addition the mixture of singly alkylated product (1.46 g, 4.26 mmol) in anhydrous toluene (20 mL). The reaction mixture stirred for 40 min and hexadecyl methanesulfonate **5** (2.73

g, 8.52 mmol) in anhydrous toluene (20 mL) was added slowly and the reaction mixture was heated to reflux overnight. After this time, 100 mL distilled H_2O was added to the reaction mixture and the product extracted into EtOAc (4 × 80 mL). The combined organic phases were washed with brine (3 × 100 mL), dried ($MgSO_4$) and concentrated under reduced pressure. The product was purified by FCC (on silica gel eluting 0-5% MeOH in CH_2Cl_2) to give **58** (1.022 g). The products from the two alkylation reactions gave **58** 2,3-bis(hexadecyloxy)-*N*,*N*-dimethylpropan-1-amine (1.92 g, 22%) as a cloudy white oil.

^{1}H NMR (600 MHz, $CDCl_3$) δ_H 0.88 (6H, t, J = 7.0, 2 × $CH_2C\mathbf{H_3}$), 1.25-1.32 (52H, m, cetyl chain), 1.56 (4H, quint, J = 6.6, 2 × $C(O)CH_2C\mathbf{H_2}$), 2.26 (6H, s, $N(C\mathbf{H_3})_2$), 2.34-2.42 (2H, m, $NC\mathbf{H_2}CH$), 3.42-3.53 (6H, m, $C\mathbf{H}C\mathbf{H}HO$, 2 × $OC\mathbf{H_2}$), 3.57-3.61 (1H, m, $CHCH\mathbf{H}O$); **^{13}C NMR** (150 MHz, $CDCl_3$) δ_C 14.3 (2 × $CH_2\mathbf{C}H_3$), 22.8 (2 × $\mathbf{C}H_2CH_3$), 26.3 (2 × $\mathbf{C}H_2$), 29.5 ($\mathbf{C}H_2$), 29.6 ($\mathbf{C}H_2$), 29.7 ($\mathbf{C}H_2$), 29.8 ($\mathbf{C}H_2$), 29.8 ($\mathbf{C}H_2$), 29.8 ($\mathbf{C}H_2$), 30.3 ($\mathbf{C}H_2$), 32.1 ($\mathbf{C}H_2$), 46.5 ($N(\mathbf{C}H_3)_2$), 61.2 ($N\mathbf{C}HH$), 70.4 ($CH\mathbf{C}HHO$), 71.7 ($O\mathbf{C}H_2$), 72.3 ($O\mathbf{C}H_2$), 77.3 ($\mathbf{C}H$); **IR** ν_{max}/cm^{-1} 2920 (C-H), 2850 (C-H); **LRMS** (LC-MS ES+) *m/z* 568.5 (100%, $[M+H]^+$); **R_f** 0.4 (6% MeOH in CH_2Cl_2). Data corresponds with the literature.[275]

N-(3-Aminopropyl)-2,3-bis(hexadecyloxy)-N,N-dimethylpropan-1-aminium **(60)**

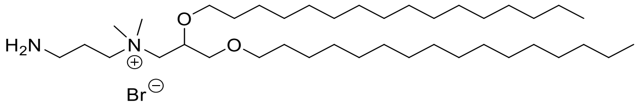

tert-Butyl (3-bromopropyl)carbamate **56** (0.768 g, 3.23 mmol), 2,3-bis-(hexadecyloxy)-*N*,*N*-dimethylpropan-1-amine **58** (0.900 g, 1.58 mmol) and acetone (5 mL) were heated to 80 °C in a sealed tube and stirred for 48 h. and then. After this time, the solvent was removed under reduced pressure. The residue was dissolved in TFA (3 mL) and CH_2Cl_2 (3 mL) and the reaction mixture was stirred at RT for 3 h. The solvent was removed under reduced pressure and the crude purified by FCC (on silica gel eluting 5-12% MeOH in CH_2Cl_2) to *give N-(3-aminopropyl)-2,3-bis(hexadecyloxy)-N,N-dimethylpropan-1-aminium* **60** (0.527 g, 45%) as a cream foam.

^{1}H NMR (600 MHz, CD_3OD) δ_H 0.90 (6H, t, J = 7.0, 2 × $CH_2C\mathbf{H_3}$), 1.29-1.36 (52H, cetyl chain), 1.59 (4H, m, 2 × $C(O)CH_2C\mathbf{H_2}$), 2.15-2.25 (2H, m, $NH_2CH_2C\mathbf{H_2}$), 3.05 (2H, t, J = 7.6, $NH_2C\mathbf{H_2}$), 3.21 (3H, s, $NC\mathbf{H_3}$), 3.23 (3H, s, $NC\mathbf{H_3}$), 3.46-3.62 (9H, m, $C\mathbf{H_2}N(CH_3)_2C\mathbf{HH}CHC\mathbf{H}HO$, 2 × $OC\mathbf{H_2}$), 3.69-3.73 (1H, m, $CHCH\mathbf{H}O$), 4.08-4.10 (1H, m, $C\mathbf{H}$); **^{13}C NMR** (150 MHz, CD_3OD) δ_C 14.5 (2 × $CH_2\mathbf{C}H_3$), 22.3 ($NH_2CH_2\mathbf{C}H_2$), 23.8 (2 × $\mathbf{C}H_2$), 27.3 ($\mathbf{C}H_2$), 27.4 ($\mathbf{C}H_2$), 30.5 ($\mathbf{C}H_2$), 30.6 ($\mathbf{C}H_2$), 30.7 ($\mathbf{C}H_2$), 30.7 ($\mathbf{C}H_2$), 30.8 ($\mathbf{C}H_2$), 30.8 ($\mathbf{C}H_2$), 30.9 ($\mathbf{C}H_2$), 31.2 ($\mathbf{C}H_2$), 33.1 ($\mathbf{C}H_2$), 37.7 ($\mathbf{C}H_2NH_2$), 52.4 ($N\mathbf{C}H_3$), 52.9 ($N\mathbf{C}H_3$), 63.5 ($\mathbf{C}H_2N(CH_3)_2$), 67.4 ($N(CH_3)_2\mathbf{C}HHCH$), 70.1 ($O\mathbf{C}H_2CH_2$), 70.2 ($CH\mathbf{C}HHO$), 72.9 ($O\mathbf{C}H_2CH_2$), 74.2 ($\mathbf{C}H$); **IR** ν_{max}/cm^{-1} 3416 (N-H), 2916 (C-H), 2849 (C-H); **LRMS** (TOF MS ES+) *m/z* 625.5 (100%, M^+), 313.3 (60%, $(M^++H)^{2+}$); **HRMS** (TOF MS ES+) calculated mass 625.6606 g.mol^{-1} ($[C_{40}H_{85}N_2O_2]^+$), observed *m/z* 625.6611 (M^+); **R_f** 0.2 (10% MeOH in CH_2Cl_2).

***N-(3-(3-(2,5-Dioxo-2,5-dihydro-1H-pyrrol-1-yl)propanamido)propyl)-2,3-bis(hexadecyloxy)-N,N-dimethylpropan-1-aminium* (61)**

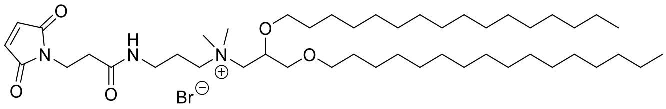

N-(3-Aminopropyl)-2,3-bis(hexadecyloxy)-N,N-dimethylpropan-1-aminium **60** (0.410 g, 0.554 mmol), 3-maleimidopropionic acid (0.135 g, 0.798 mmol) and HBTU (0.440 g, 1.16 mmol) were dissolved in a 1:1 mixture of CH_2Cl_2:DMF then made basic with DIPEA (0.380 mL, 2.18 mmol). The reaction mixture was stirred overnight, evaporated to dryness and the crude was purified by FCC (on silica gel eluting 0-8% MeOH in CH_2Cl_2) to give 140 mg of impure product which was purified again by FCC (on silica gel eluting 3-6% MeOH in CH_2Cl_2) to give *N-(3-(3-(2,5-dioxo-2,5-dihydro-1H-pyrrol-1-yl)propanamido)-propyl)-2,3-bis(hexadecyloxy)-N,N-dimethylpropan-1-aminium* **61** (50 mg, 11%) as a white solid.

^{1}H NMR (600 MHz, CD_3OD) δ_H 0.90 (6H, t, *J* = 7.0, 2 × $CH_2C\mathbf{H_3}$), 1.29-1.37 (52H, cetyl chain), 1.55-1.62 (4H, m, 2 × $C(O)CH_2C\mathbf{H_2}$), 1.92-2.04 (2H, m, $NHCH_2C\mathbf{H_2}$), 2.45 (2H, t, *J* = 6.6, $C\mathbf{H_2}C(O)$), 3.17 (3H, s, $NC\mathbf{H_3}$), 3.18 (3H, s, $NC\mathbf{H_3}$), 3.23 (2H, t, *J* = 6.8, $NHC\mathbf{H_2}$), 3.38-3.58 (9H, m, $C\mathbf{H_2}N(CH_3)_2C\mathbf{HH}CHC\mathbf{H}H$, 2 × $OC\mathbf{H_2}$), 3.72 (1H, apparent dt, *J* = 8.9, 6.8, $CHCH\mathbf{H}O$), 3.79 (2H, t, *J* = 6.6, mal-$C\mathbf{H_2}$), 4.03-4.05 (1H, m, $C\mathbf{H}$), 6.84 (2H, s, $C\mathbf{H}C\mathbf{H}$); **^{13}C NMR** (150 MHz, CD_3OD) δ_C 14.5 (2 × $CH_2\mathbf{C}H_3$), 23.8 ($NHCH_2\mathbf{C}H_2$), 24.3 (2 × $\mathbf{C}H_2$), 27.3 ($\mathbf{C}H_2$), 27.4 ($\mathbf{C}H_2$), 30.5 ($\mathbf{C}H_2$), 30.6 ($\mathbf{C}H_2$), 30.6 ($\mathbf{C}H_2$), 30.7 ($\mathbf{C}H_2$), 30.8 ($\mathbf{C}H_2$), 30.8 ($\mathbf{C}H_2$), 30.8 ($\mathbf{C}H_2$), 31.2 ($\mathbf{C}H_2$), 33.1 ($\mathbf{C}H_2$), 35.6 (mal-$\mathbf{C}H_2$), 36.0 ($C\mathbf{H_2}C(O)$)), 37.2 ($NH\mathbf{C}H_2$), 52.4 ($N\mathbf{C}H_3$), 52.7 ($N\mathbf{C}H_3$), 64.8 ($N^+(CH_3)_2\mathbf{C}H_2CH_2$), 67.1 (($N^+(CH_3)_2\mathbf{C}HHCH$), 70.1 ($O\mathbf{C}H_2CH_2$), 70.1 ($CH\mathbf{C}HHO$), 72.8 ($O\mathbf{C}H_2CH_2$), 74.2 ($\mathbf{C}H$), 135.6 ($\mathbf{C}H\mathbf{C}H$), 172.3 ($\mathbf{C}(O)CHCH\mathbf{C}(O)$)), 173.7 ($\mathbf{C}(O)NH$); **IR** ν_{max}/cm^{-1} 3401 (N-H), 2916 (C-H), 2849 (C-H), 1705 (C=O), 1656 (C=O), 1549 (C=C); **LRMS** (LC-MS ES+) *m/z* 776.6 (100%, M^+); **HRMS** (TOF MS ES+) calculated mass 776.6880 g.mol^{-1} ($[C_{47}H_{90}N_3O_5]^+$), observed *m/z* 776.6876 (M^+); **R_f** 0.3 (8% MeOH in CH_2Cl_2).

7.3.5 Peptide synthesis

7.3.5.1 General peptide synthesis procedures

Fmoc-protected amino acids were sourced from Merck Millipore Ltd. and used without further purification: Fmoc-Ala-OH, Fmoc-Cys(Trt)-OH, Fmoc-Glu(O^{t}Bu)-OH, Fmoc-Gly-OH, Fmoc-His(Trt)-OH, Fmoc-Leu-OH, Fmoc-Lys(Boc)-OH, Fmoc-Asn(Trt)-OH, Fmoc-Pro-OH, Fmoc-Gln(Trt)-OH, Fmoc-Arg(Pbf)-OH, Fmoc-Thr(^{t}Bu)-OH, Fmoc-Val-OH, Fmoc-Trp(Boc)-OH, Fmoc-Tyr(^{t}Bu)-OH. Amino acid and reagent concentrations were calculated based on the quantity of the resin used. All reagents were dissolved in HPLC-grade DMF and reactions were carried out in a 5 mL polypropylene reaction syringe with a frit.

7.3.5.1.1 Automated synthesis

Automated synthesis of peptides was carried out on a MultiSynTech Syro Peptide Synthesiser (Model MP-60) using preloaded Wang resins (detailed for each peptide). The resin was swollen *via* addition of 1.5 mL DMF and agitated for 10 min.

Fmoc deprotection steps were carried out using a solution of 40% piperidine in DMF (1.5 mL), which was added to the syringe containing the resin. The mixture was agitated for 20 sec every minute for a total of 3 min before removal of reagent by filtration under vacuum. The resin was washed with DMF (4 x 1.5 mL) before addition of a second portion of piperidine in DMF solution (40% v/v, 0.75 mL), followed by DMF (0.75 mL) to make an overall 20% v/v solution of piperidine in DMF. This mixture was agitated for 20 sec every minute for a total of 10 min. The reagents were removed by filtration under vacuum and the resin washed with DMF (6 x 1.5 mL). Washing refers to the addition of solvent to the resin followed by 20 sec agitation and evacuation.

Amino acid coupling steps were carried out by the addition of the required Fmoc-protected amino acid (5 eq.) to the reaction syringe with HBTU (5 eq.) and DIPEA (10 eq.). The mixture was agitated for 20 seconds every 3 min for a total of 40 min. The reagents were removed by filtration under vacuum and the resin washed with DMF (4 x 1.5 mL).

7.3.5.1.2 Peptide synthesis by hand

Peptides that were synthesised by hand were made using the Fmoc solid-phase synthesis strategy and preloaded Wang resins (detailed for each peptide). The resin was consistently agitated during coupling, deprotection and cleavage steps *via* shaking on an IKA KS130 basic platform shaker at 480 rpm. The resin was thoroughly washed with DMF following each coupling or deprotection step. Washing refers to addition of DMF (~ 2 mL) to the resin followed by swirling and immediate evacuation.

1. Swelling:
   DMF (2 mL) was added to the resin in a syringe and agitated for 30 min. After this time, DMF was evacuated and the resin washed with DMF (2 x 2 mL).
2. Fmoc Deprotection:
   Piperidine in DMF (40% v/v, 1.5 mL) was added to the resin and agitated for 3 min. The syringe was evacuated and another portion of piperidine in DMF (20% v/v, 1.5 mL) was added to the resin and agitated for 10 min. This was evacuated and the resin washed with DMF (6 x 2 mL).
3. Coupling:
   The desired Fmoc-protected amino acid (5 eq.), HBTU (5 eq.) and DIPEA (10 eq.) were dissolved in DMF (2 mL). This solution was left to activate for 2 min and then added to the resin and agitated for 40 min. The solution was evacuated and the resin was washed with DMF (4 x 2 mL).
   Steps 2 and 3 were repeated until all amino acids had been coupled and Fmoc-deprotected.

7.3.5.1.3 Cleavage

Irrespective of whether the peptide was synthesised by automated synthesis or by hand, the resin-bound peptide was washed by hand with CH_2Cl_2 (3 x 2 mL), MeOH (2 x 2 mL) and diethyl ether (2 x 2 mL) then dried under vacuum for 30 min before cleavage from the resin and the amino acid sidechain protecting groups. Cleavage solution (TFA/TIPS/H_2O/EDT, 94:1:2.5:2) was added to the resin and agitated, the volume and agitation time are detailed for specific peptides. After this time, the solution was ejected into a 15 mL Falcon tube containing cold ether (7 mL), to precipitate the peptide. Another portion of fresh cleavage solution was added to the reaction syringe and agitated, the volume and agitation time are detailed for specific peptides. The solution was ejected into the same Falcon tube containing ice-cold diethyl ether. The volume was made up to 14 mL with refrigerated diethyl ether and the Falcon tube was placed in the freezer for 30 min.

The mixture was centrifuged at 4000 rpm at 5 °C for 15 min. The ether was poured off and fresh refrigerated diethyl ether was added to resuspend the pellet followed by a further round of centrifugation (4000 rpm, 5 °C, 15 min). This resuspension/centrifugation process was repeated for a third time. The resultant pellet was resuspended in water (~ 4 mL) and lyophilised to yield the crude peptide.

7.3.5.1.4 Purification

Peptide purification was performed using a Teledyne Isco Combiflash Companion automated chromatography system or by high-performance liquid chromatography

(HPLC), or both. Preparative reverse-phase HPLC was carried out on a Varian Prostar HPLC System with a ProStar 335 UV-Vis Variable Wavelength Diode Array Detector (detection was at 214 nm and 254 nm), two Varian ProStar 210 Pumps, a Varian ProStar 410 AutoSampler and a Varian ProStar 701 X-Y Fraction Collector. Methods are detailed for specific peptides.

Peptide purity was assessed *via* LC-MS, HRMS and analytical HPLC. Analytic HPLCs were obtained using an Agilent 1260 Infinity Preparative Scale Purification System and a C18 Hichrom column (150 × 4.6 mm) with a linear solvent gradient of 5-95% MeCN (0.1% TFA) in H_2O (0.1% TFA) over 17 min and a flow rate of 1 mL/min and detection at 214 nm and 254 nm.

7.3.5.2 Synthesis of EGFR-targeting peptides

CYHWYGYTPQNVI

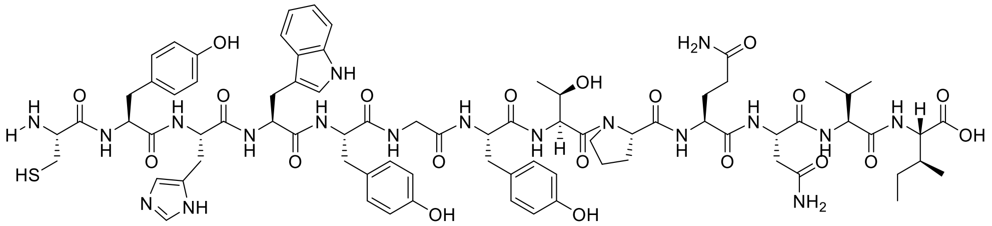

CYHWYGYTPQNVI was synthesised by automated synthesis using an Fmoc-Ile-Wang resin (150 mg) from Merck Millipore Ltd. Two portions of cleavage solution were used (2 × 1.5 mL), which were agitated for 1 h and 40 min respectively.

The crude was purified on a Teledyne Isco Combiflash Companion automated chromatography system using a Biotage SNAP cartridge (KP-C18-HS, 12 g) with a gradient of 5-95% MeCN (0.1 % TFA) in H_2O (0.1% TFA) over 80 min and a flow rate of 6 mL/min. Two fractions containing product were identified by LC-MS analysis and further purified by HLPC.

Purification by reverse-phase preparative HPLC was performed using a Vydac (preparative, 10 µm, 300 Å, 22 mm ID x 250 mm L) C18 reverse-phase column. The first fraction was purified using a flat gradient of 23% H_2O with 0.1% TFA (A) and 77% MeCN with 0.1% TFA (B) with a flow rate of 8 mL/min and run length of 40 min. The second fraction was purified with a gradient of 23-27% of solvent system A in B over 35 min with a flow rate of 8 mL/min. The desired fractions (determined by LC-MS) were pooled and lyophilised to give CYHWYGYTPQNVI (6.6 mg, 2%).

LRMS (TOF MS ES+) *m/z* 329.3 (100%, $[M+5H]^{5+}$), 822.3 (20%, $[M+2H]^{2+}$); **HRMS** (TOF MS ES+) calculated mass 1643.7311 g.mol^{-1} ($[C_{78}H_{103}N_{18}O_{20}S]^{+}$), observed m/z 1643.7324 ($[M+H]^{+}$); **R$_T$** 6.785.

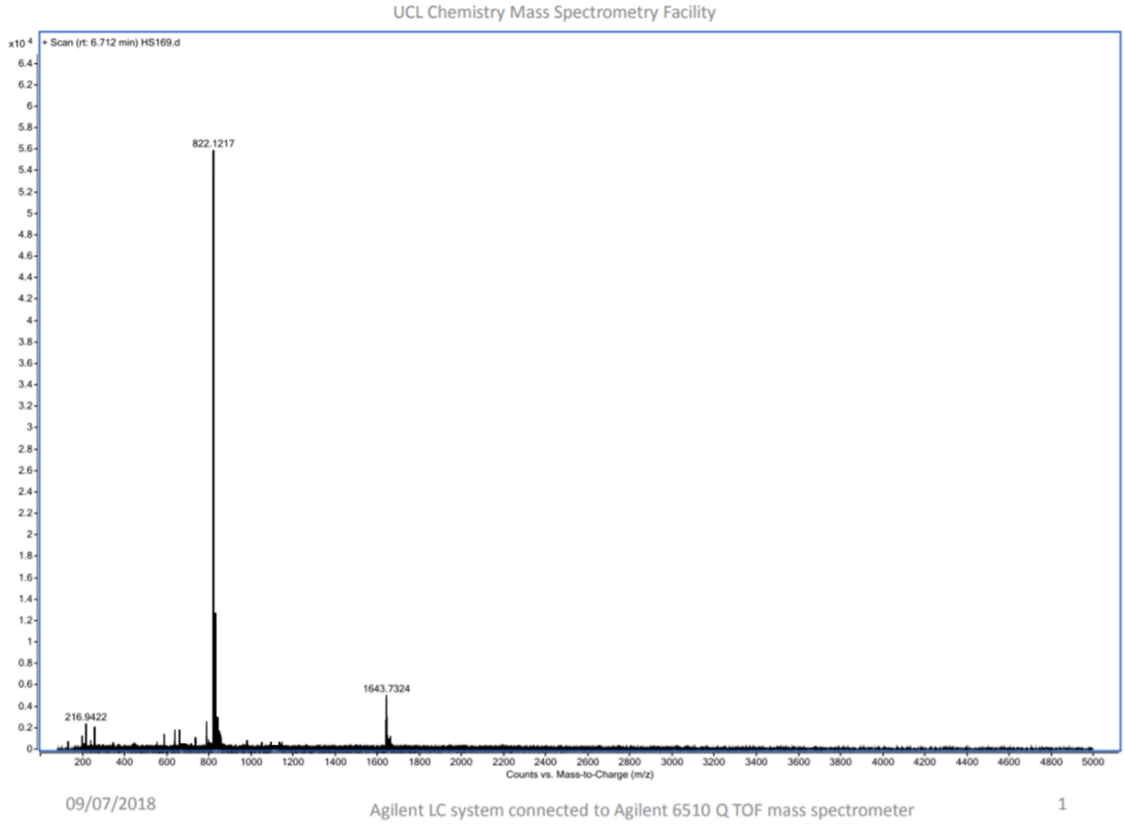

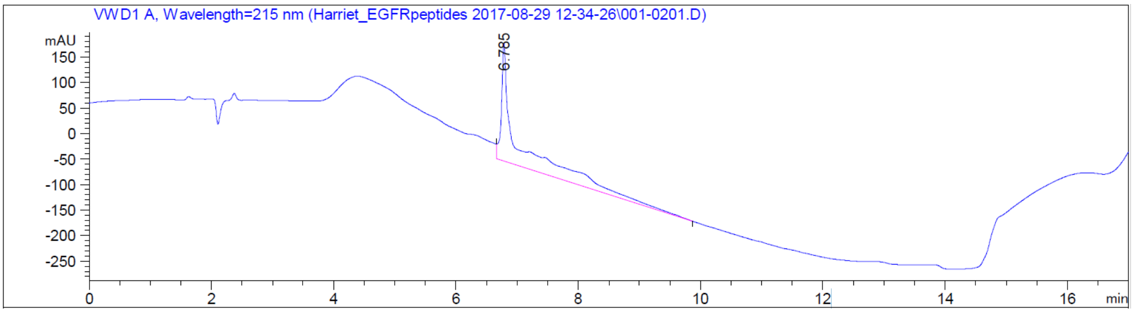

CLARLLT

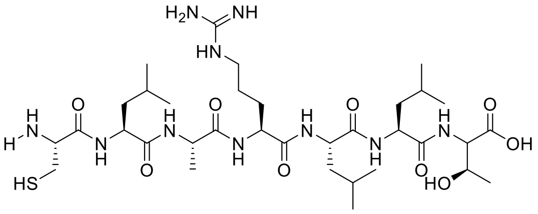

CLARLLT was synthesised by automated synthesis using an Fmoc-Thr(tBu)-Wang resin (150 mg) from Merck Millipore Ltd. Two portions of cleavage solution were used (2 × 1.5 mL), which were agitated for 1 h and 40 min respectively.

Purification was performed on a Teledyne Isco Combiflash Companion automated chromatography system using a Biotage SNAP cartridge (KP-C18-HS, 12 g) with a gradient of 5-95% MeCN (0.1 % TFA) in H_2O (0.1% TFA) over 80 min and a flow rate of 8 mL/min. Fractions containing pure peptide were pooled and lyophilised to give CLARLLT (17 mg, 11%).

LRMS (LC-MS ES+) *m/z* 395.1 (55%, $[M+2H]^{2+}$), 789.2 (100%, $[M+H]^+$); **HRMS** (TOF MS ES+) calculated mass 789.4657 g.mol^{-1} ($[C_{34}H_{65}N_{10}O_9S]^+$), observed m/z 789.4627 ($[M+H]^+$); **R$_T$** 6.603.

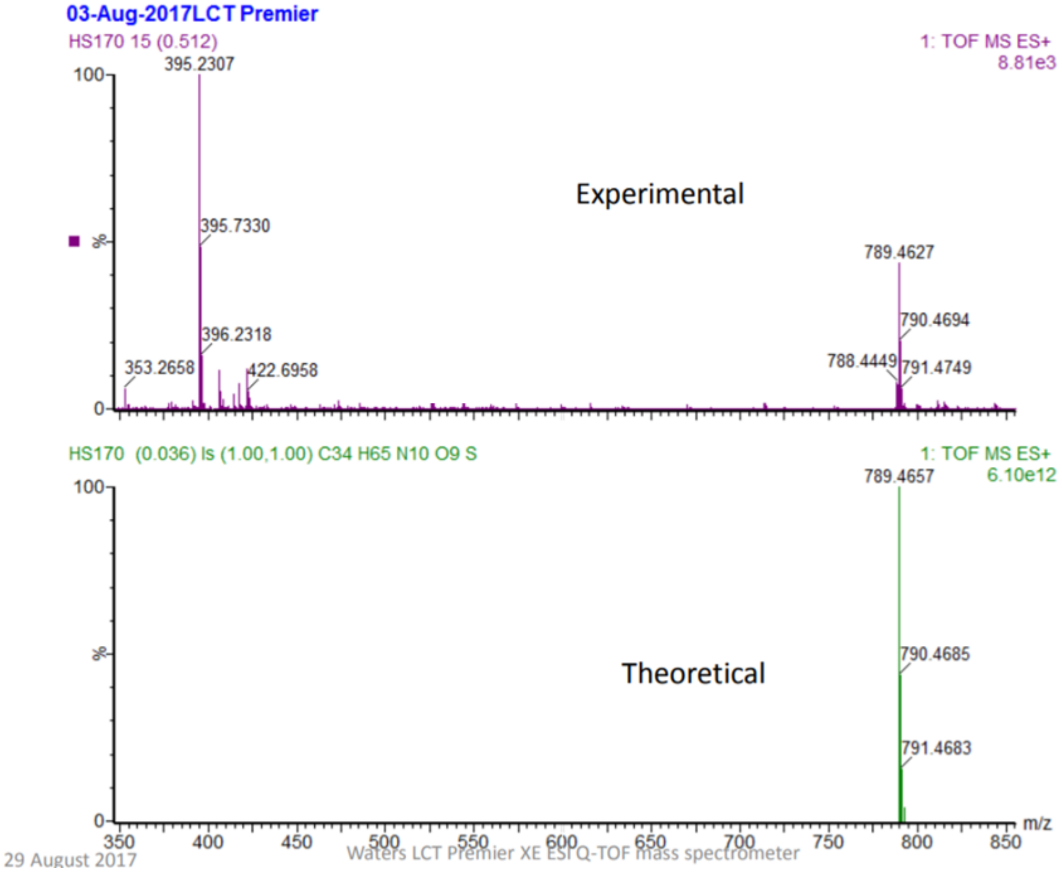

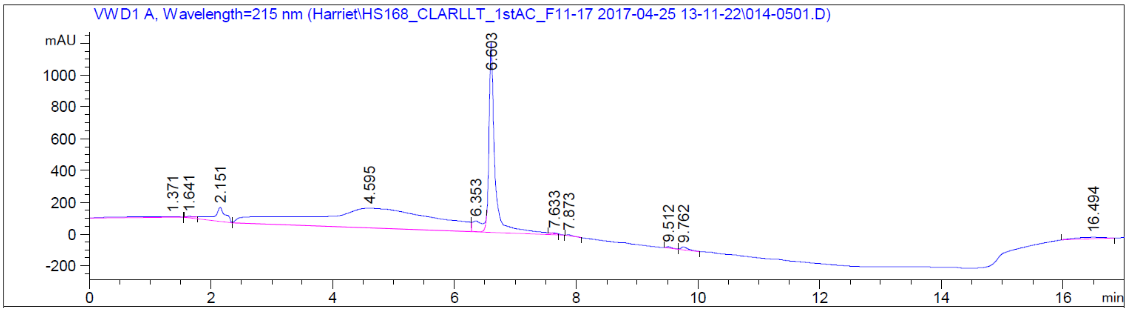

CAEYLR

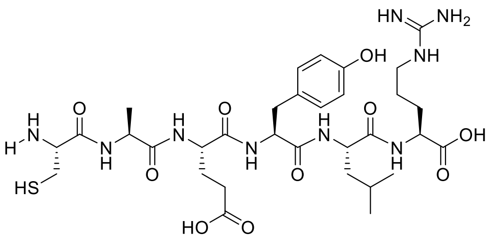

CAEYLR was synthesised by hand using an Fmoc-Arg(Pbf)-Wang resin (150 mg) from Merck Millipore Ltd. Two portions of cleavage solution were used (2 × 2 mL), which were agitated for 1 h and 40 min respectively.

Purification was performed on a Teledyne Isco Combiflash Companion automated chromatography system using a Biotage SNAP cartridge (KP-C18-HS, 12 g) with a gradient of 5-95% MeCN (0.1 % TFA) in H_2O (0.1% TFA) over 40 min and a flow rate of 8 mL/min. Fractions containing pure peptide were pooled and lyophilised to give CAEYLR (33 mg, 46%).

LRMS (LC-MS ES+) *m/z* 377.6 (100%, $[M+2H]^{2+}$), 754.3 (100%, $[M+H]^+$); **HRMS** (TOF MS ES+) calculated mass 754.3558 g.mol^{-1} ($[C_{32}H_{52}N_9O_{10}S]^+$), observed m/z 754.3541 ($[M+H]^+$); $\mathbf{R_T}$ 6.450.

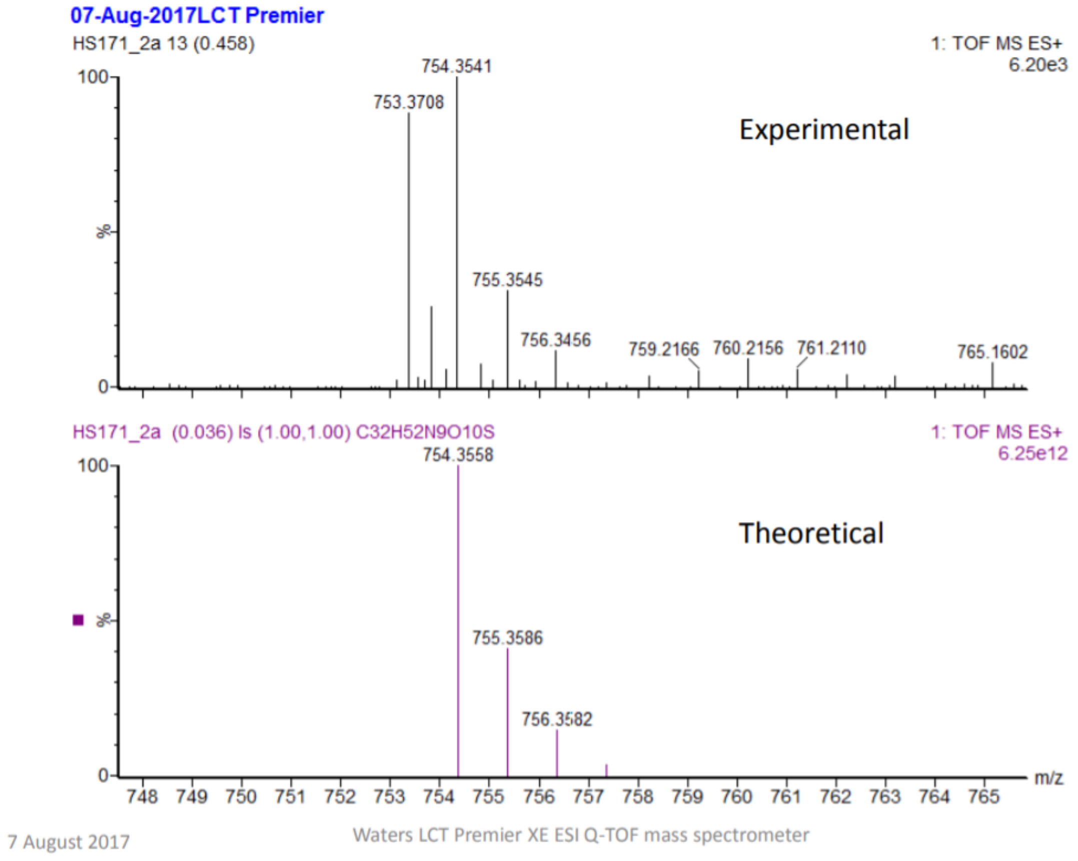

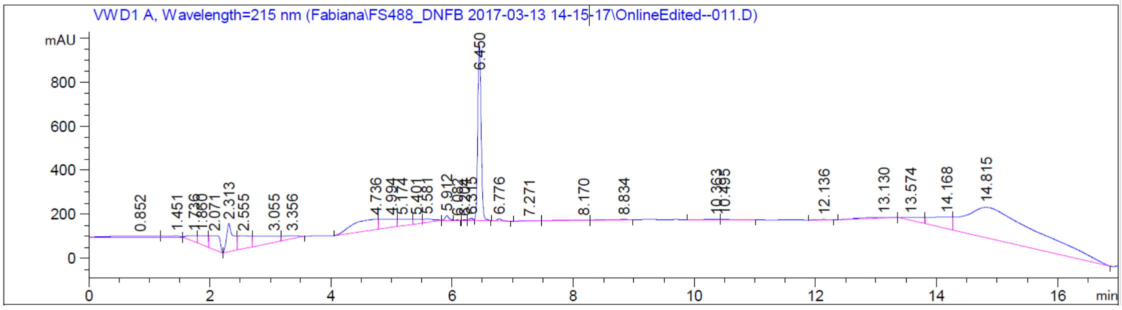

7.4 *In vitro* experiments

All assays in this Section were carried out in triplicate by Adam Westhorpe (UCL Cancer Institute).

7.4.1 Resazurin cell viability assay procedure

Day 1: Cells were plated onto 96 well plates and allowed to adhere for 24 h in 25 mM glucose media.

Day 2: After this time and 2 h before drugging, cell media was replaced with low (2 mM) glucose media. Following these 2 h of starvation, free or liposomal 2-DG was added to the wells to produce an overall 2-DG concentration of 5 mM and where 2-DG was absent, equal volumes of empty liposomes were added. To create a concentration of 1.6 × PBS in wells, 32 µL of the 200 mL cell media volume of each well was removed and replaced with 32 µL of 10 × PBS stock solution.

For the radiosensitisation experiments in Figure 70, after 4 h of 2-DG exposure, plates were irradiated at 4 Gy, or mock irradiated for controls (this means that they were treated in exactly the same way but without irradiation; taken out of the incubator at the same time, taken down to the irradiation room in the same box etc.).

Day 3-5: 24 h after drugging, all media was replaced with 25 mM glucose and cells were allowed to grow for 48 h at which point a resazurin cell viability assay was run on the plates. Statistical significance was determined *via* the One-Way ANOVA method with Tukey's multiple comparisons test.

The results are shown in Figure 69 and Figure 70.

7.4.2 Classical clonogenic assay procedure

Day 1: Cells were plated in appropriate cell numbers (200/2000/20,000/200,000 cells per well for radiation doses of 0/4/8/10 Gy, respectively), onto 6 well plates and allowed to adhere for 4 h. After this time, the cells were drugged with free or liposomal 2-DG at 5 mM and 10 mM concentrations.

Day 2: Plates were irradiated 16-18 h after drugging to allow time for the 2-DG to interact with cells.

Day 3: 24 h after irradiation, the media was replaced and the cells were incubated at 37 °C to allow colony formation.

Day 10-14: Colonies were fixed, stained with methylene blue and counted (Stuart™ Scientific SC6 colony counter).

The results are shown in Figure 71.

7.4.3 Clonogenic assay procedure from the literature

The following procedure was reported by Sinthupibulyakit *et al.*[137]

Day 1: A549 cells were plated at 200 or 500 cells per well and allowed to adhere for 4 h. After this time, cells were treated with 2-DG to give new concentrations in each well of 0 mM, 5 mM,10 mM or 20 mM.

Day 2: 24 h after treatment with 2-DG, cells were mock irradiated or irradiated at 2, 4 or 6 Gy.

Day 3-21: 24 h after treatment with 2-DG, all media was aspirated and replaced. Colonies were allowed to grow up for up to 21 days. After colonies reached ~ 50 cells, they were washed, fixed, stained and counted.

The results are shown in Figure 72.

7.5 NMR of novel compounds

tert-butyl (16-(hexadecyloxy)-10,13-dioxo-3,6,18-trioxa-9,14-diazatetratriacontyl)carbamate **8**

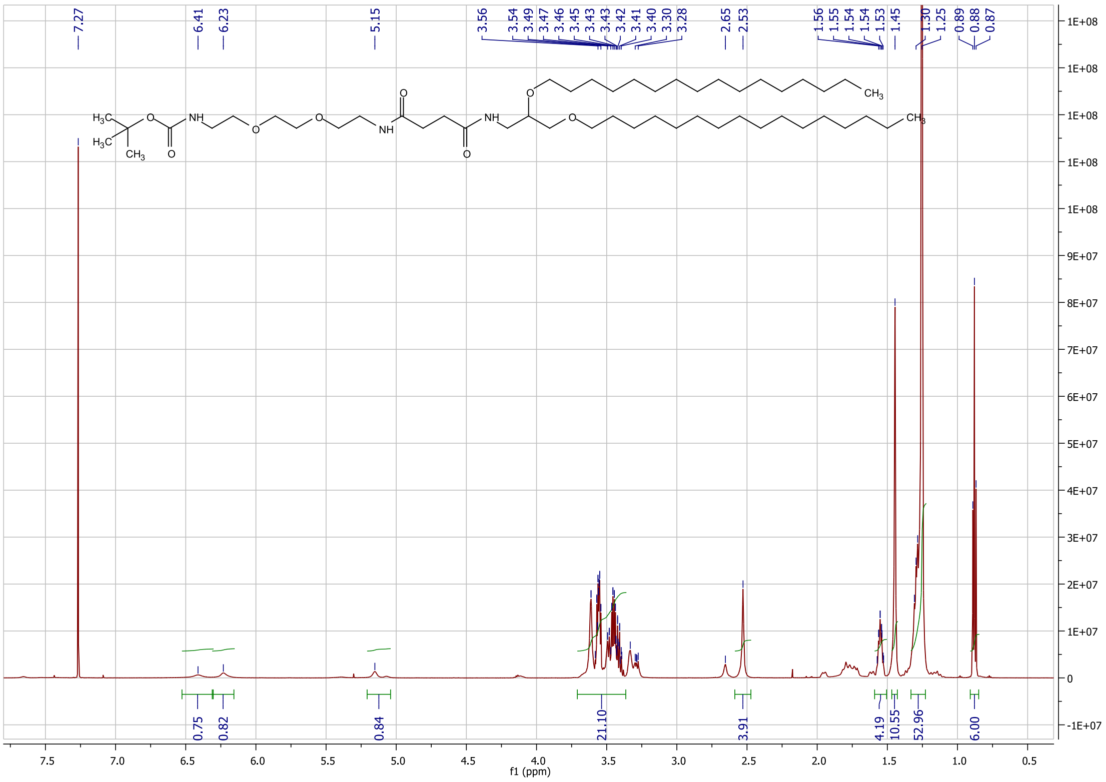

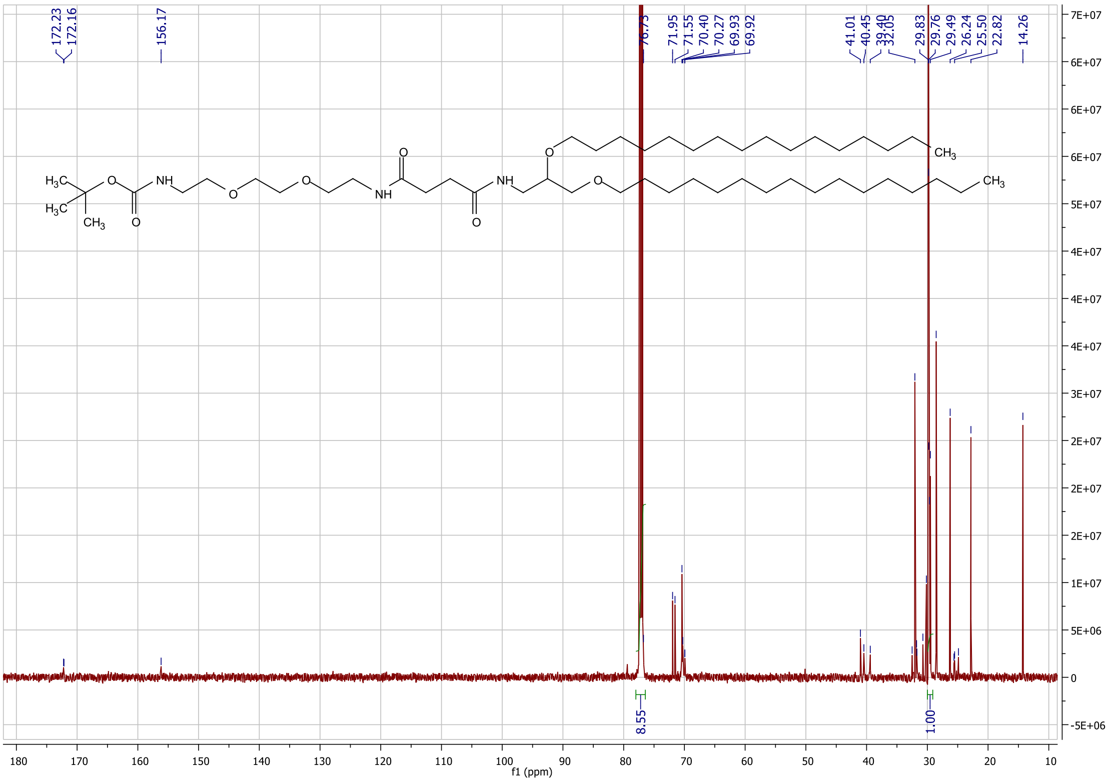

16-(hexadecyloxy)-10,13-dioxo-3,6,18-trioxa-9,14-diazatetratriacontan-1-aminium 2,2,2-trifluoroacetate **9**

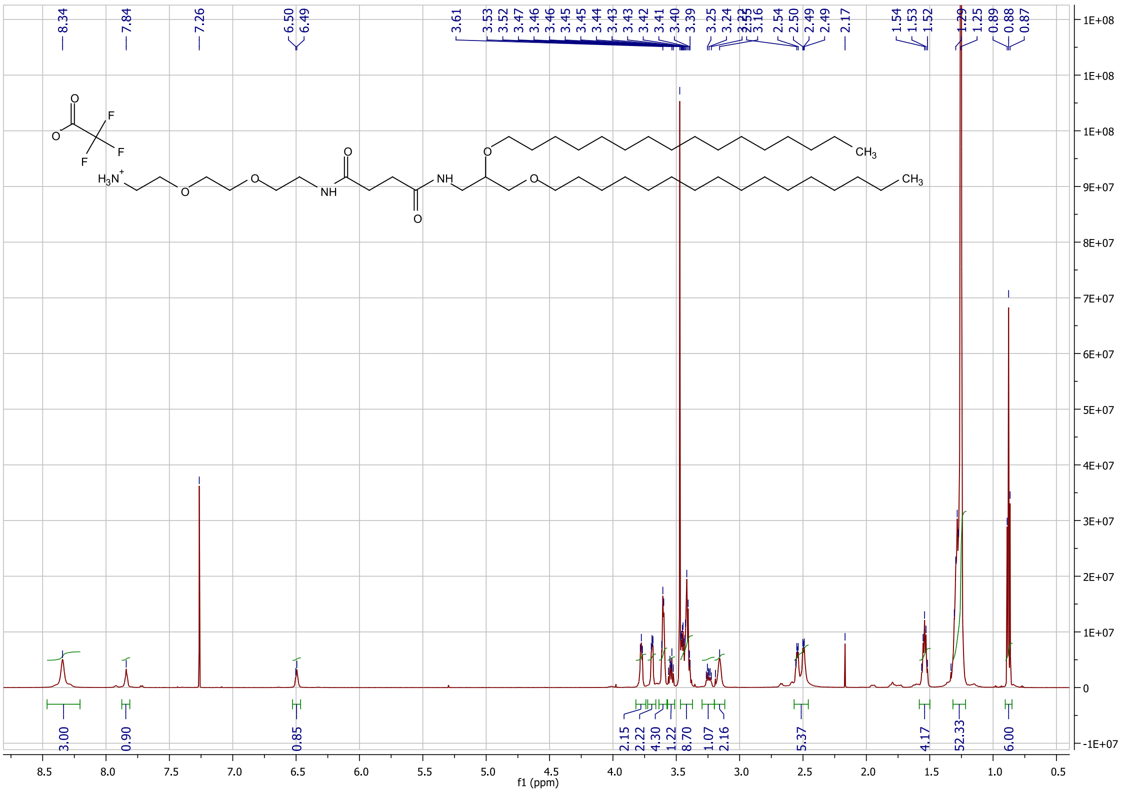

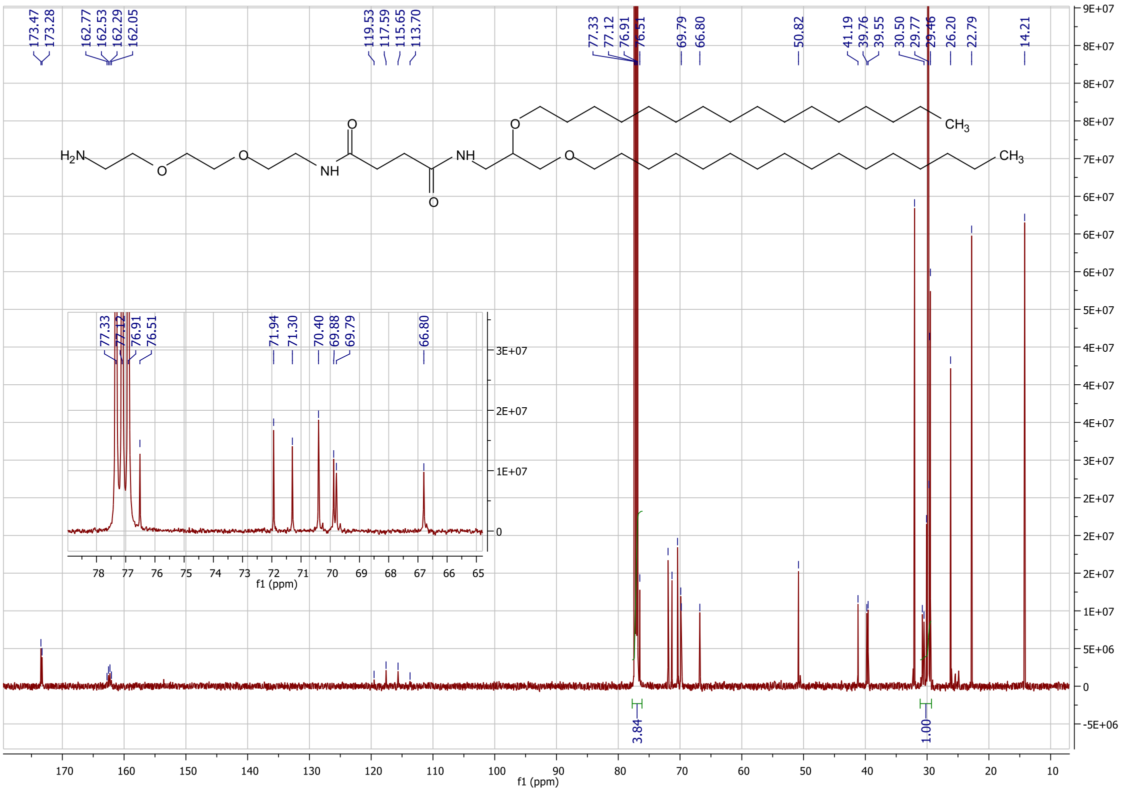

GlcEG3SLc **11**

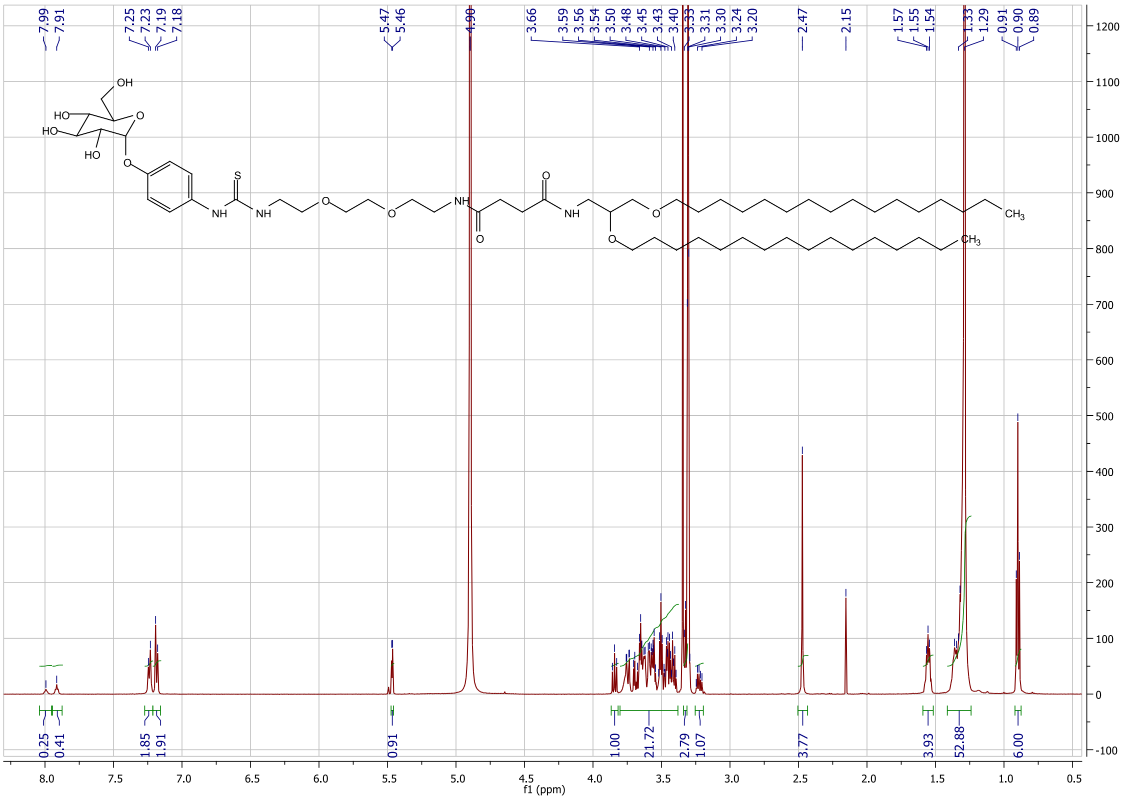

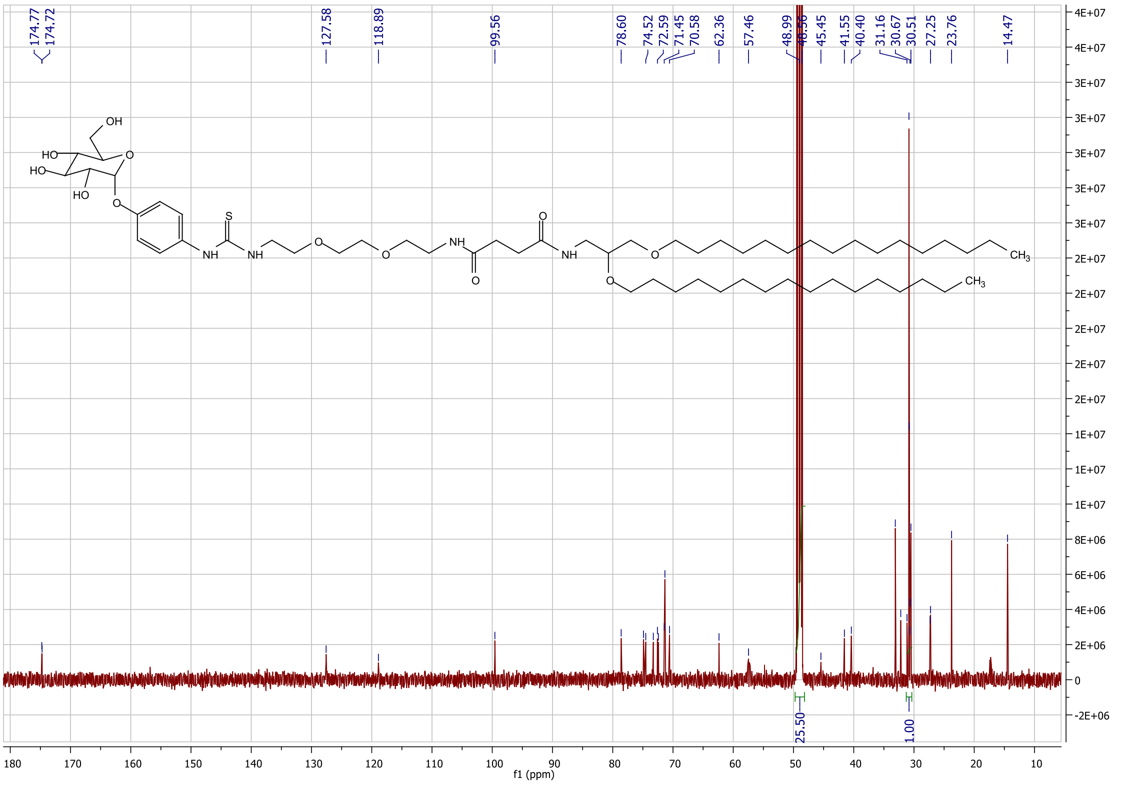

tri-tert-butyl 2,2',2''-(10-(19-(hexadecyloxy)-2,13,16-trioxo-6,9,21-trioxa-3,12,17-triazaheptatriacontyl)-1,4,7,10-tetraazacyclododecane-1,4,7-triyl)triacetate **18**

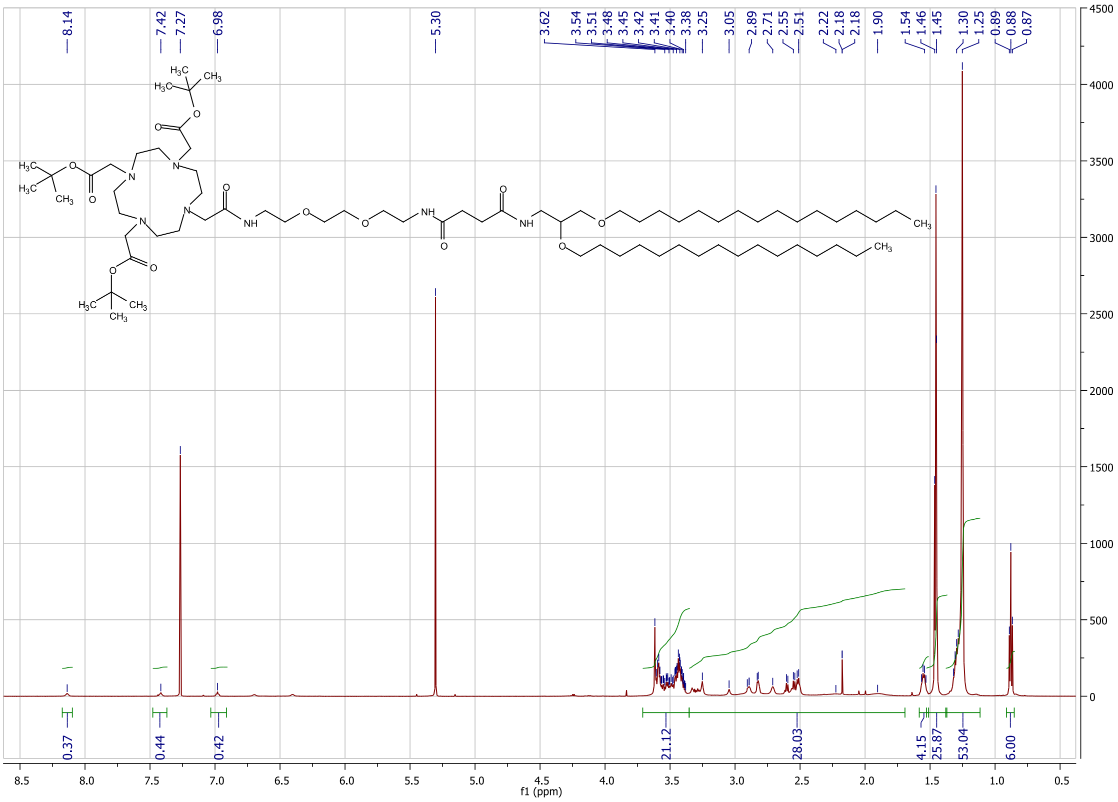

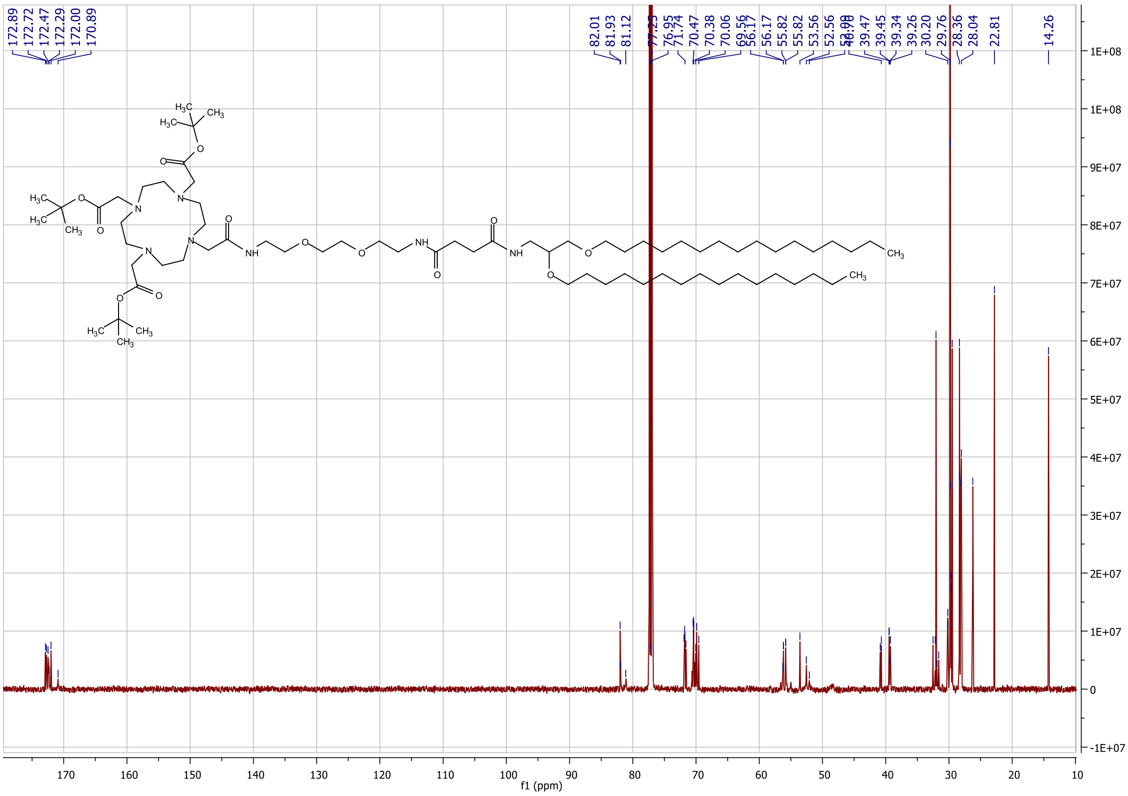

DEG3SLc **19**

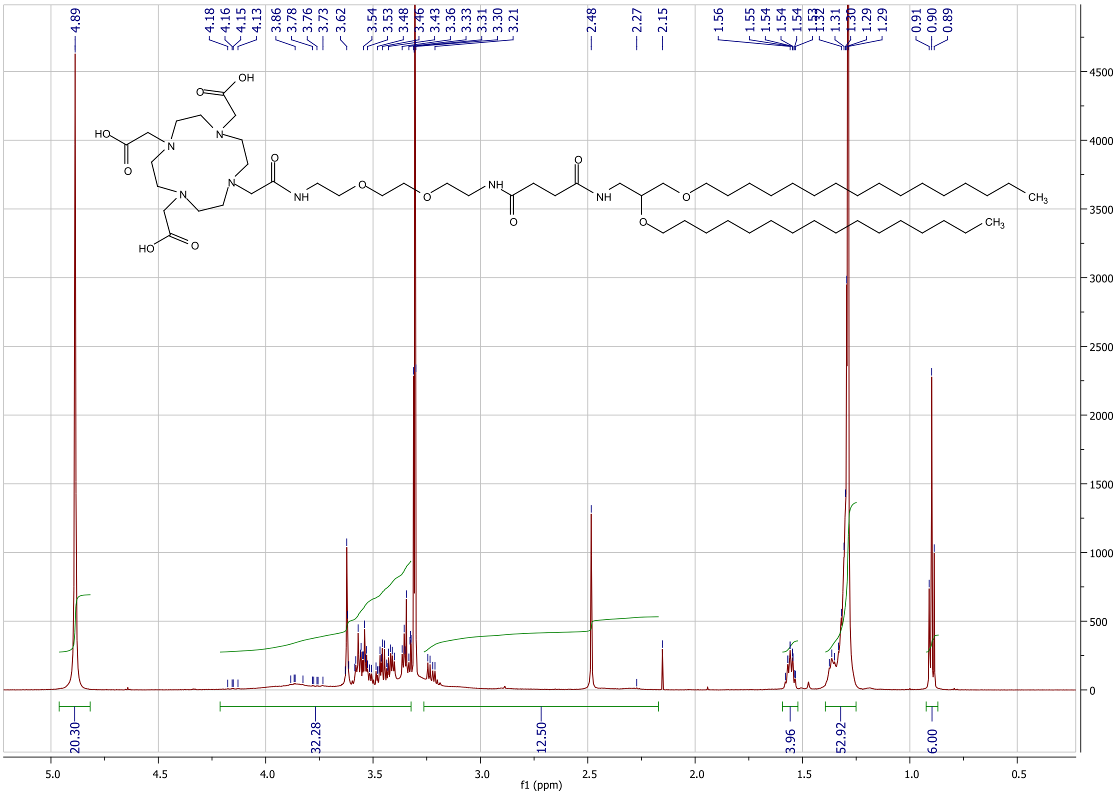
4.89
4.18
4.16
4.15
4.13
3.86
3.78
3.76
3.73
3.62
3.54
3.53
3.48
3.46
3.43
3.36
3.33
3.31
3.30
3.21
2.48
2.27
2.15
1.56
1.55
1.54
1.54
1.54
1.53
1.32
1.31
1.30
1.29
1.29
0.91
0.90
0.89
OH
O
HO
N
N
N
N
O
HO
O
O
NH
O
O
NH
O
O
NH
O
O
CH3
CH3
4500
4000
3500
3000
2500
2000
1500
1000
500
0
20.30
32.28
12.50
3.96
52.92
6.00
5.0
4.5
4.0
3.5
3.0
2.5
2.0
1.5
1.0
0.5
f1 (ppm)

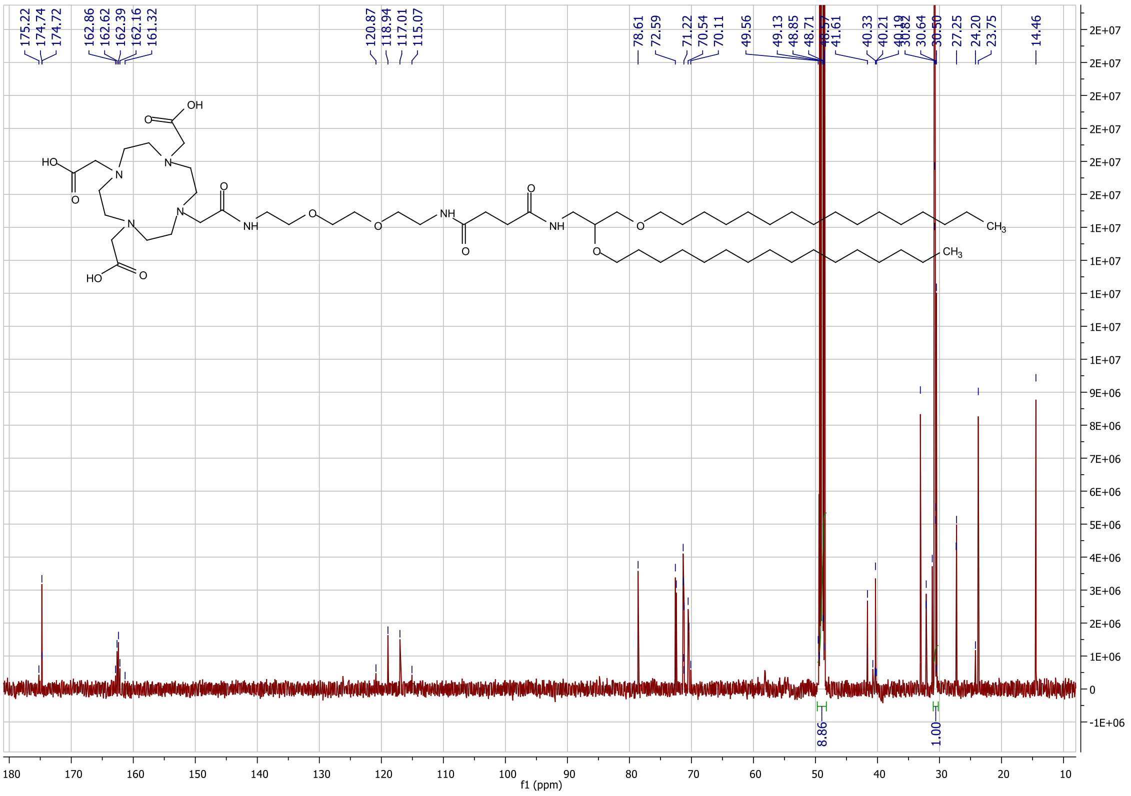
175.22
174.74
174.72
162.86
162.62
162.39
162.16
161.32
120.87
118.94
117.01
115.07
78.61
72.59
71.22
70.54
70.11
49.56
49.13
48.85
48.71
48.57
41.61
40.33
40.21
40.19
32.82
30.64
30.50
27.25
24.20
23.75
14.46
OH
O
HO
N
N
N
N
O
HO
O
O
NH
O
O
NH
O
O
NH
O
O
CH3
CH3
2E+07
2E+07
2E+07
2E+07
2E+07
2E+07
1E+07
1E+07
1E+07
1E+07
1E+07
9E+06
8E+06
7E+06
6E+06
5E+06
4E+06
3E+06
2E+06
1E+06
0
-1E+06
8.86
1.00
180
170
160
150
140
130
120
110
100
90
80
70
60
50
40
30
20
10
f1 (ppm)

tri-tert-butyl 2,2',2''-(10-(2-oxo-2-(((3R,4R,5S,6R)-2,4,5-trihydroxy-6-(hydroxymethyl)tetrahydro-2H-pyran-3-yl)amino)ethyl)-1,4,7,10-tetraazacyclododecane-1,4,7-triyl)triacetate **20**

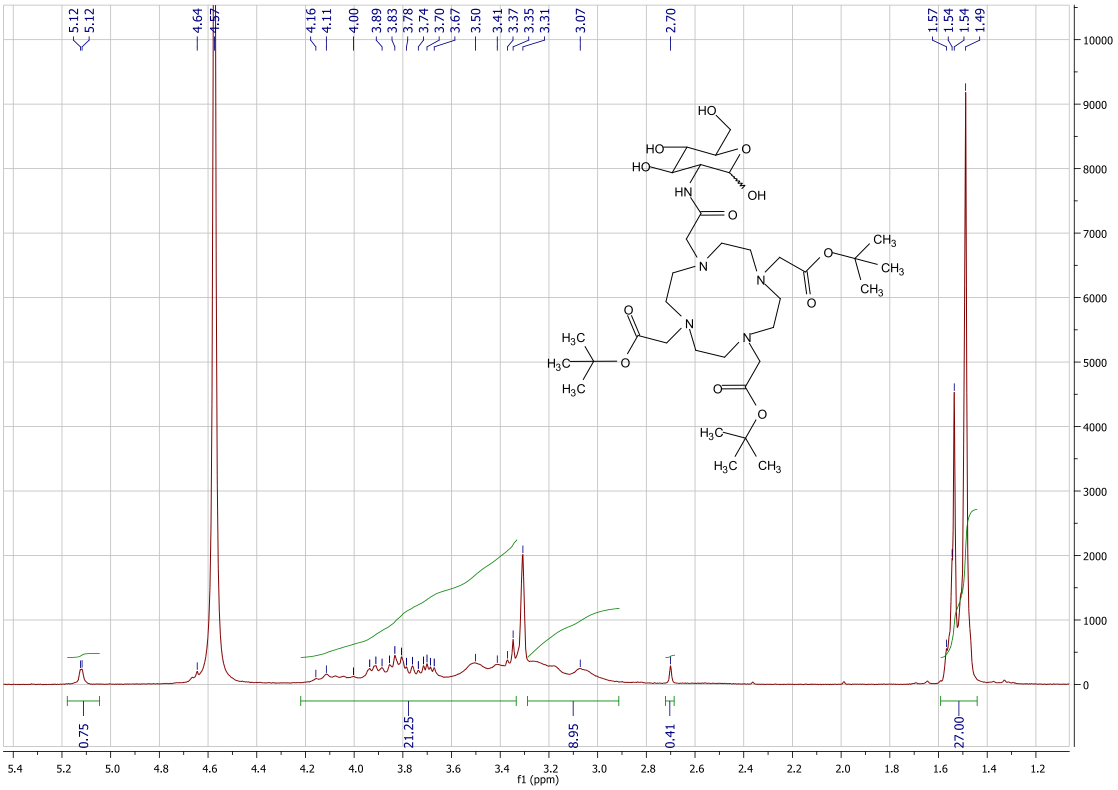

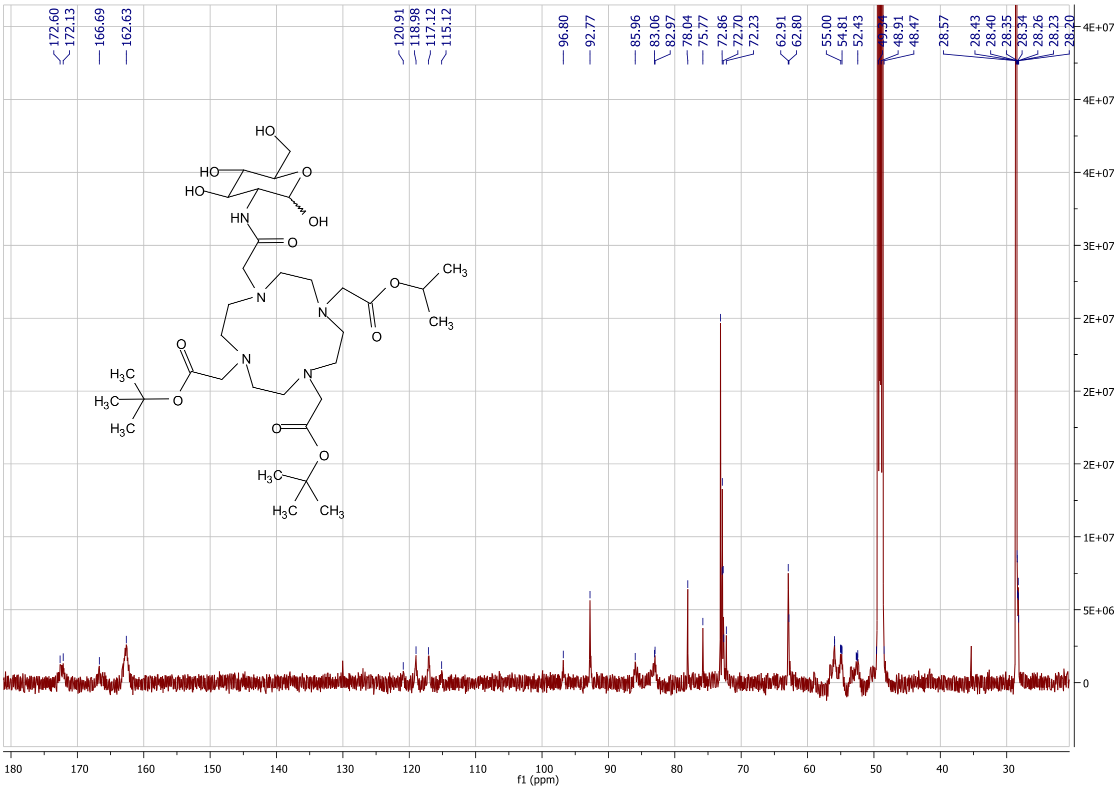

2,2',2''-(10-(2-oxo-2-(((3R,4R,5S,6R)-2,4,5-trihydroxy-6-(hydroxymethyl)tetrahydro-2H-pyran-3-yl)amino)ethyl)-1,4,7,10-tetraazacyclododecane-1,4,7-triyl)triacetic acid **21**

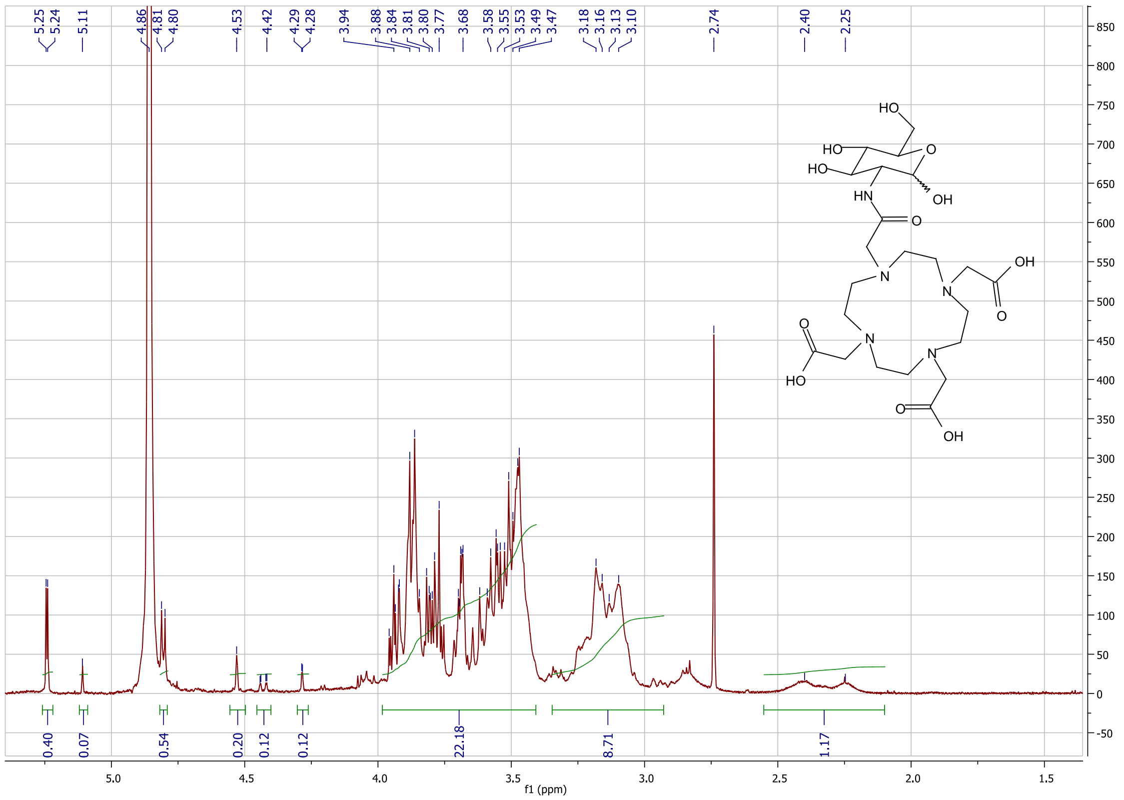

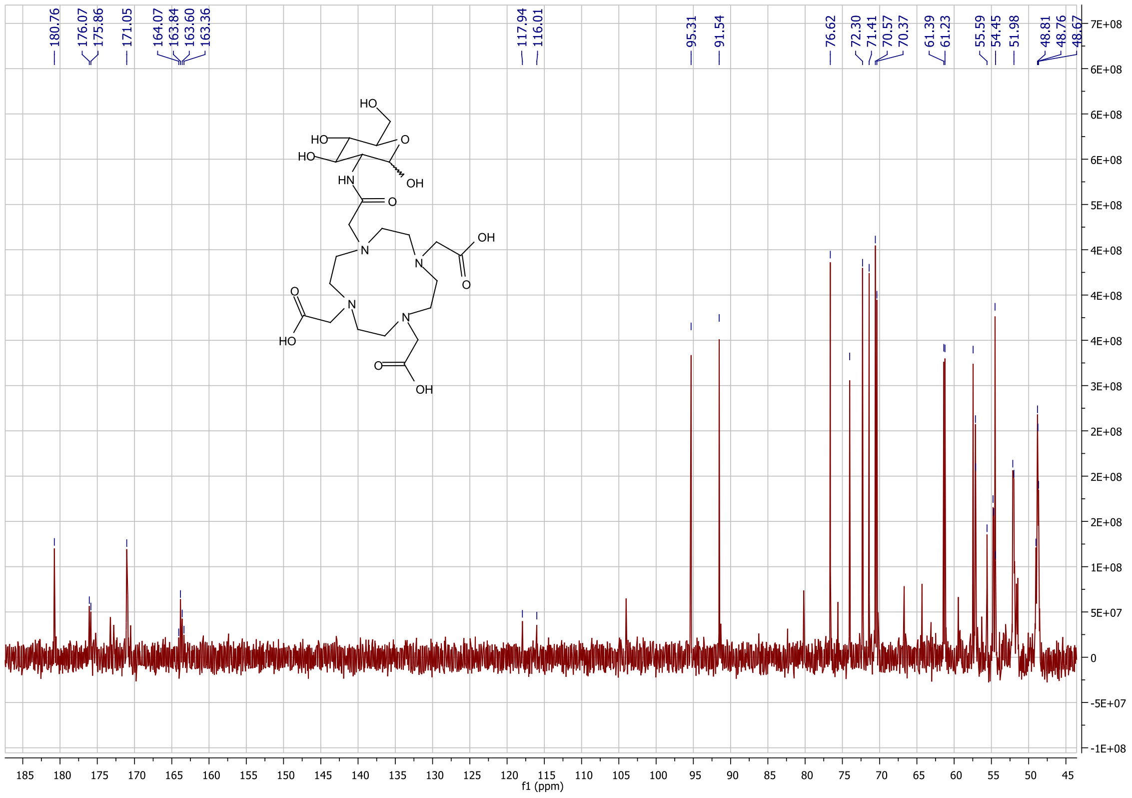

(2S,3R,4R,5S,6R)-6-(acetoxymethyl)-3-((6-hydroxyhexyl)amino)tetrahydro-2H-pyran-2,4,5-triyl triacetate **27**

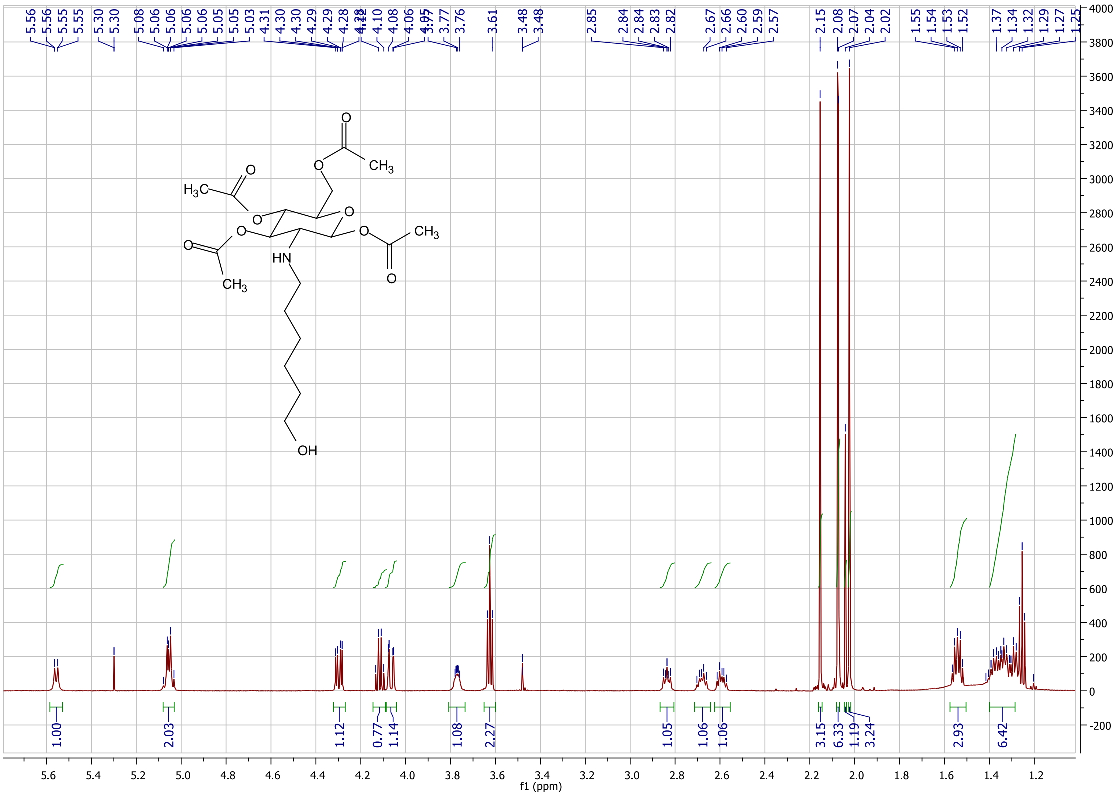

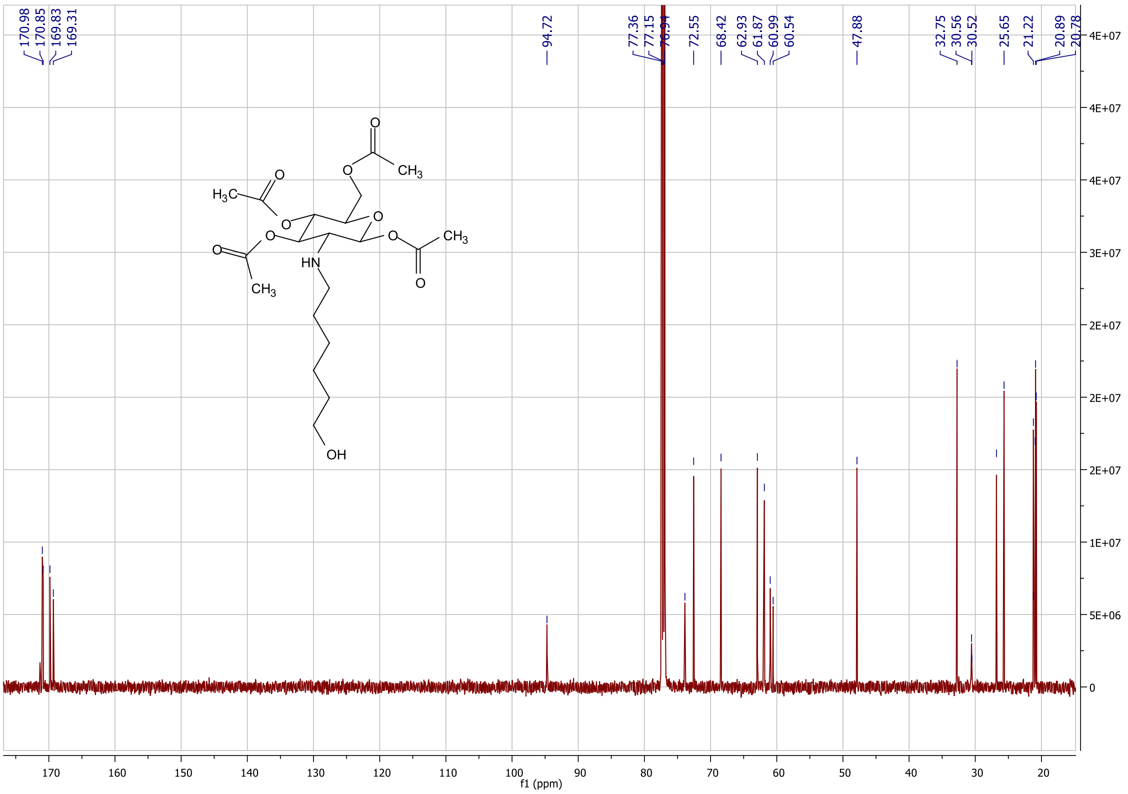

(2S,3R,4R,5S,6R)-6-(acetoxymethyl)-3-((6-((methylsulfonyl)oxy)hexyl)amino)tetrahydro-2H-pyran-2,4,5-triyl triacetate **28**

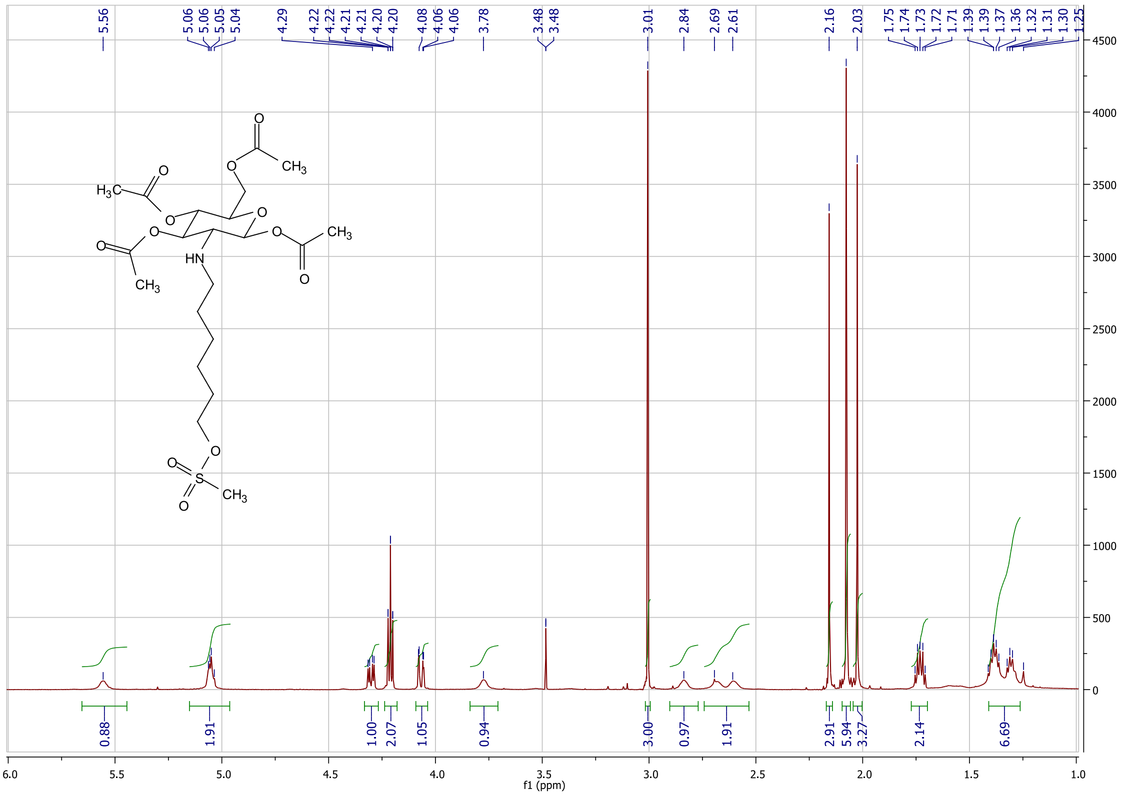

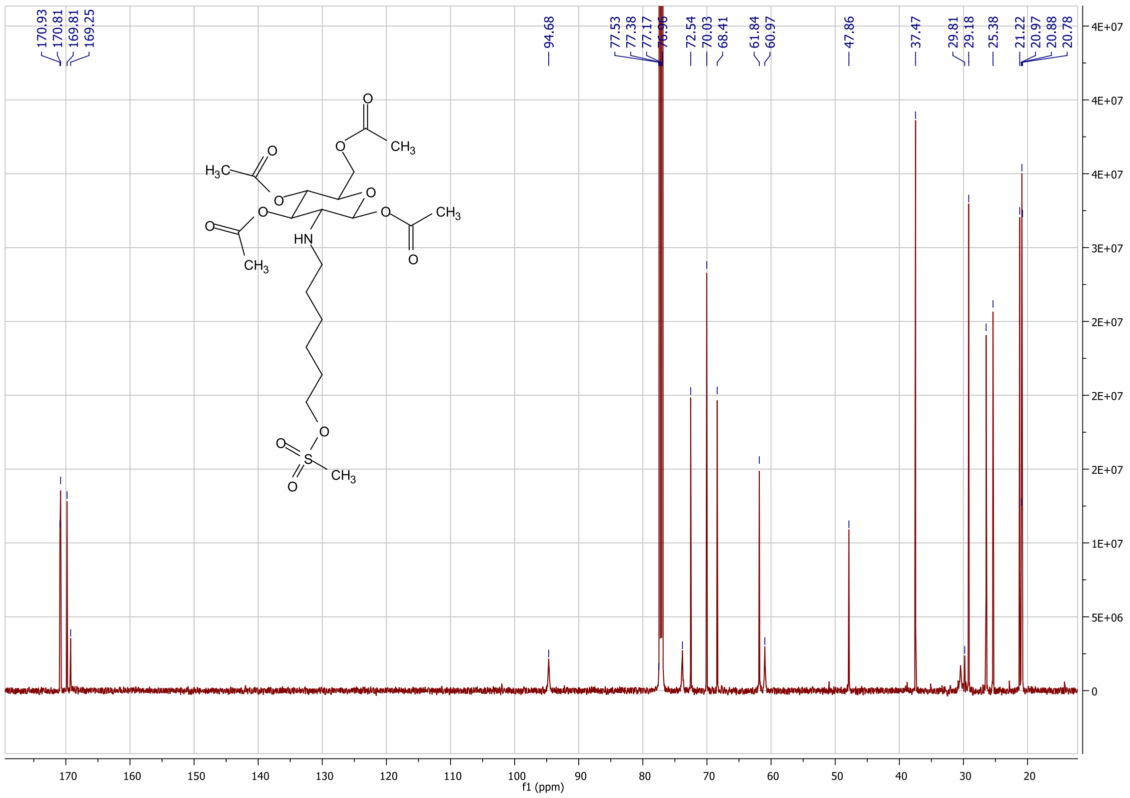

tri-tert-butyl 2,2',2''-(10-(6-(((2S,3R,4R,5S,6R)-2,4,5-triacetoxy-6-(acetoxymethyl)-tetrahydro-2H-pyran-3-yl)amino)hexyl)-1,4,7,10-tetraazacyclododecane-1,4,7-triyl)triacetate **30**

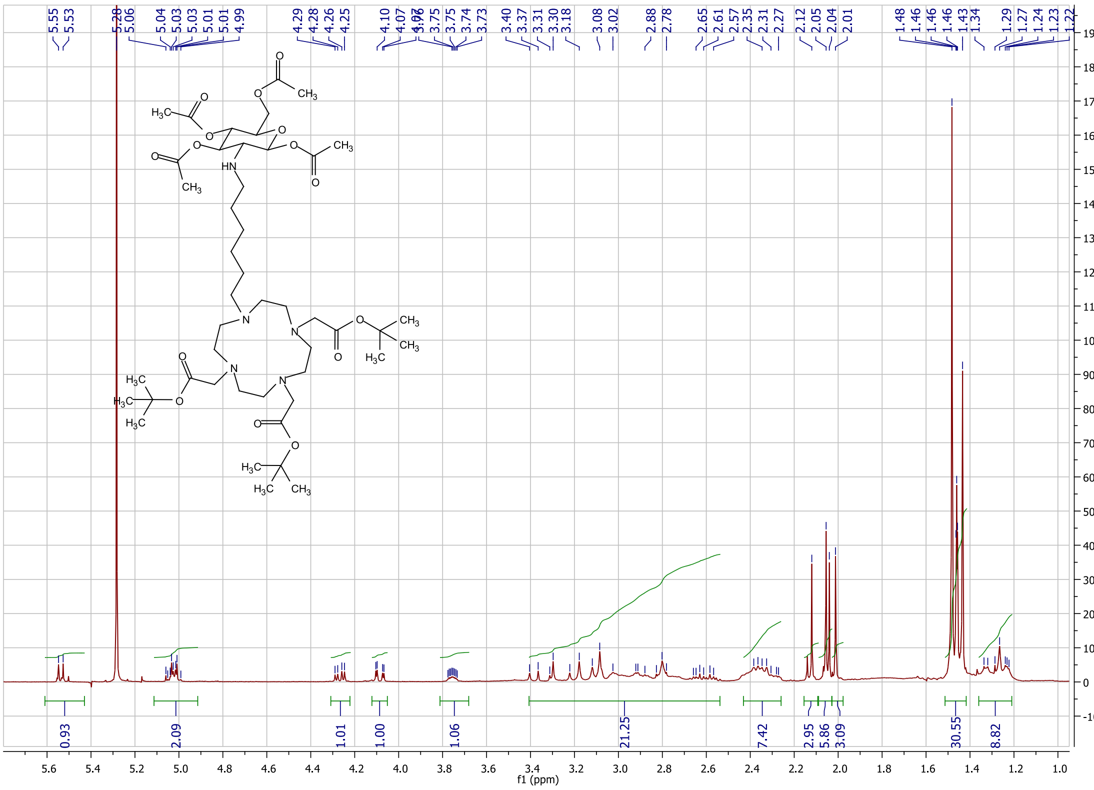

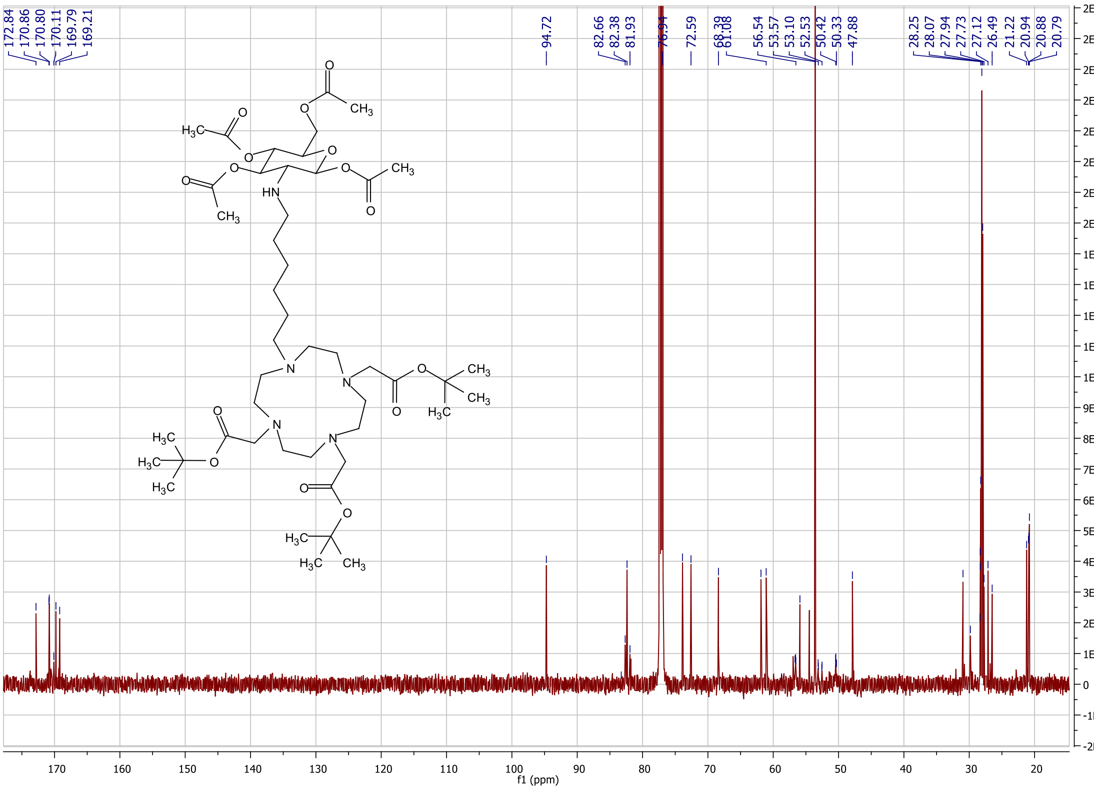

2,5-Dioxopyrrolidin-1-yl 2,5,8,11,14-pentaoxahexadecan-16-oate **34**

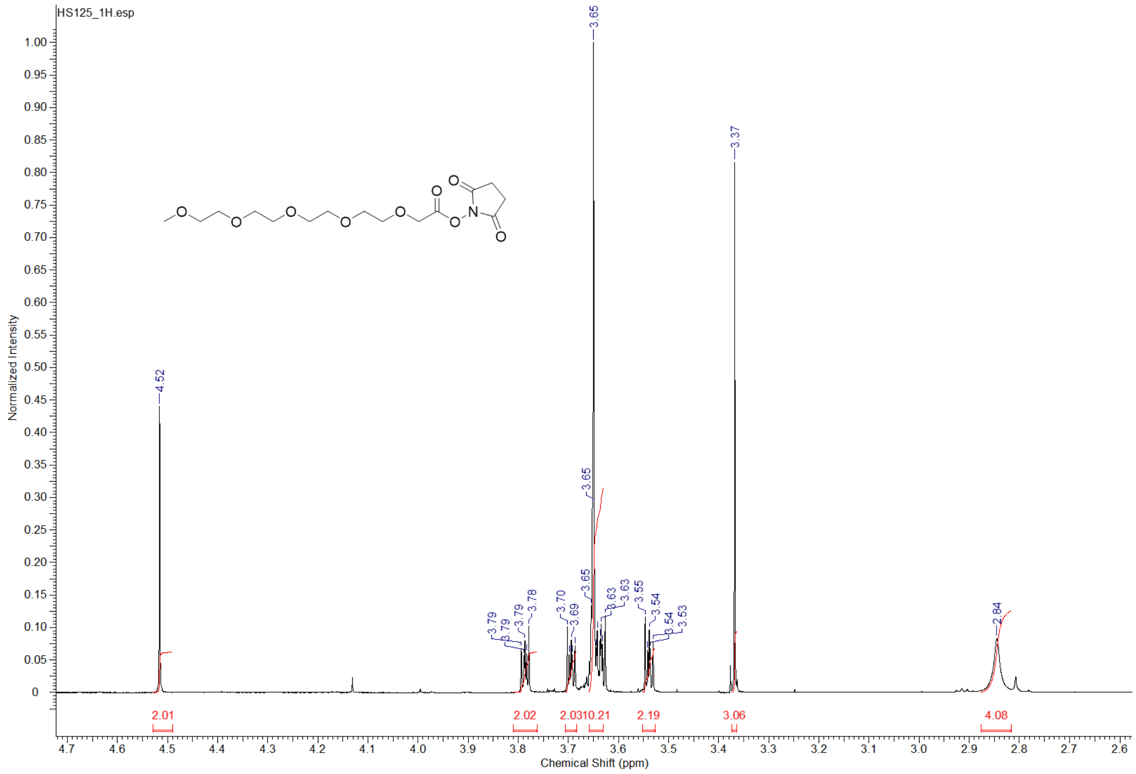

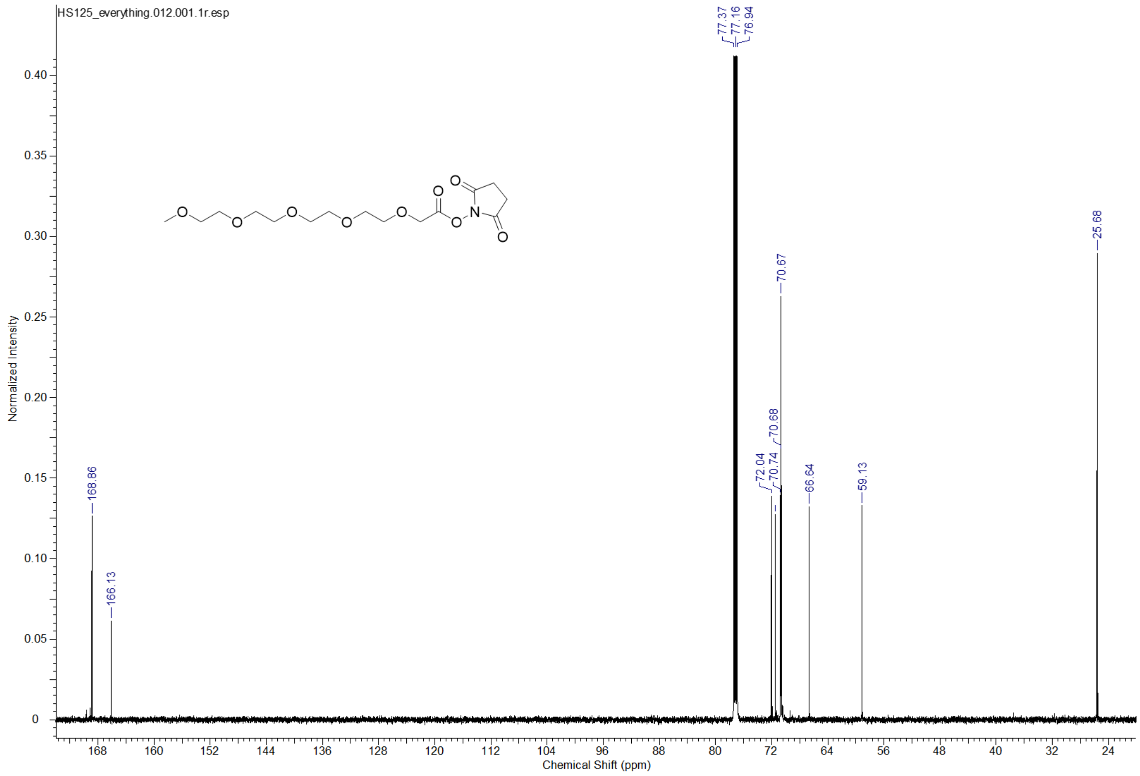

DPPE-EG4-OMe **35**

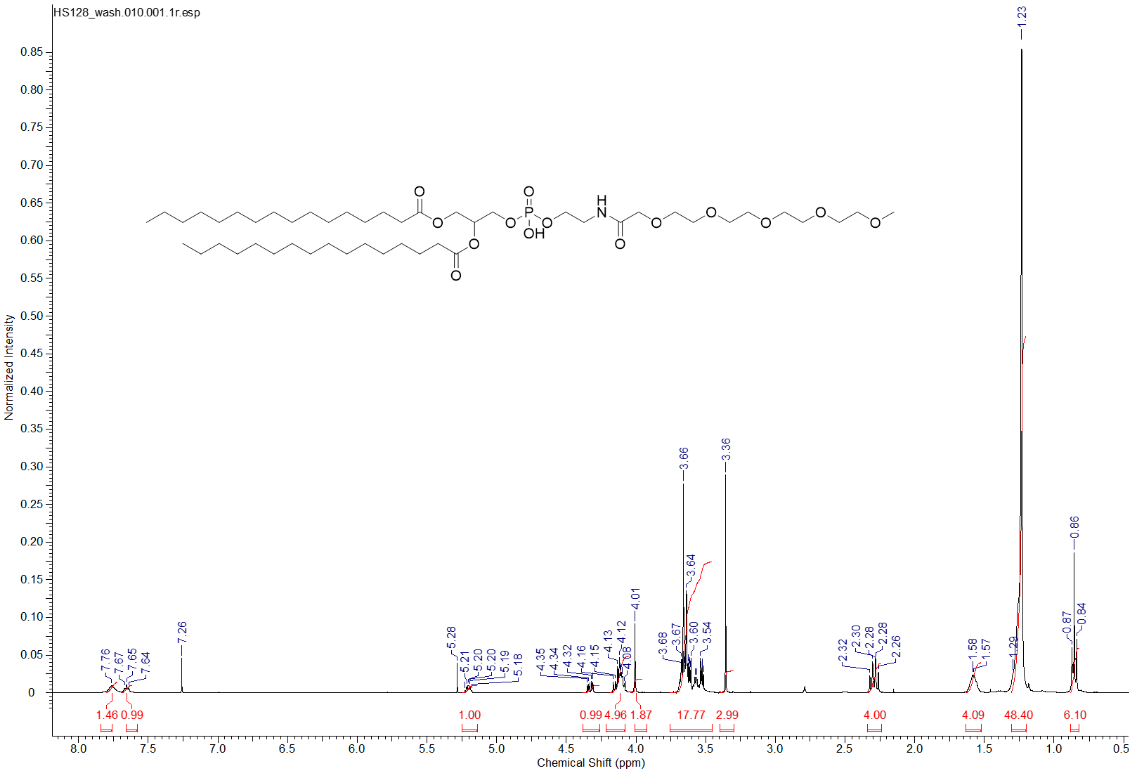

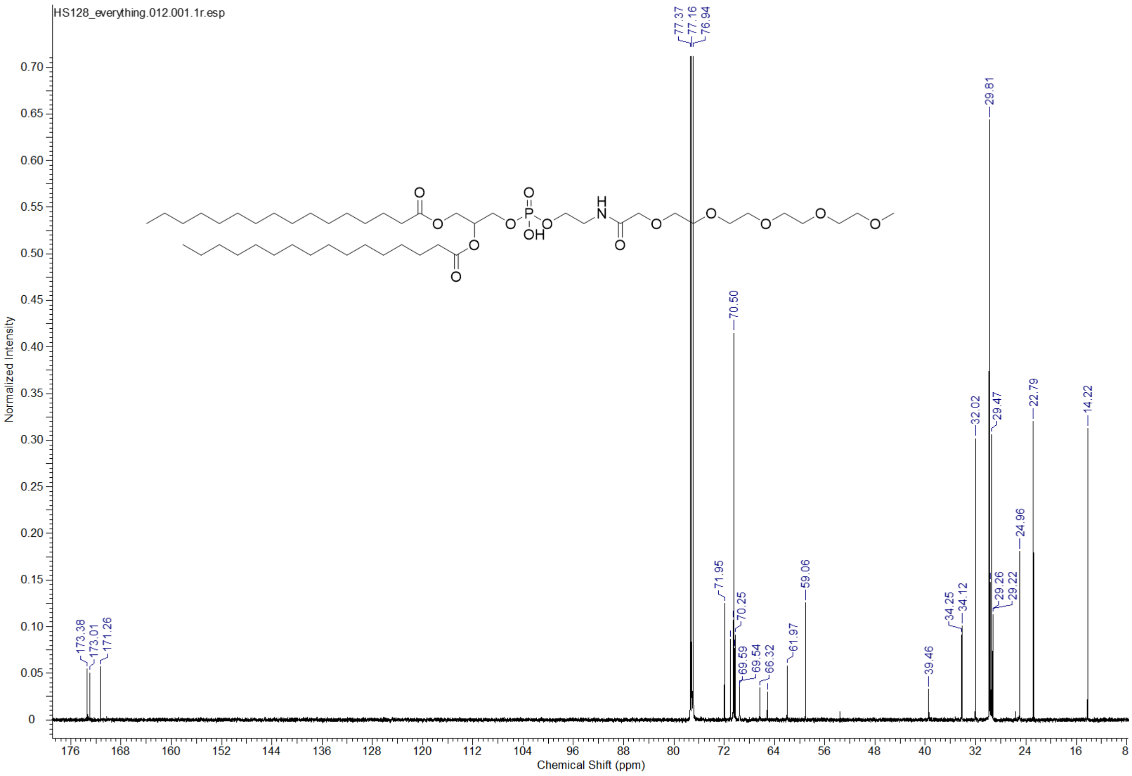

3,3-diisopropyl-2-methyl-4,7,10,13,16,19-hexaoxa-3-silahenicosan-21-ol **39**

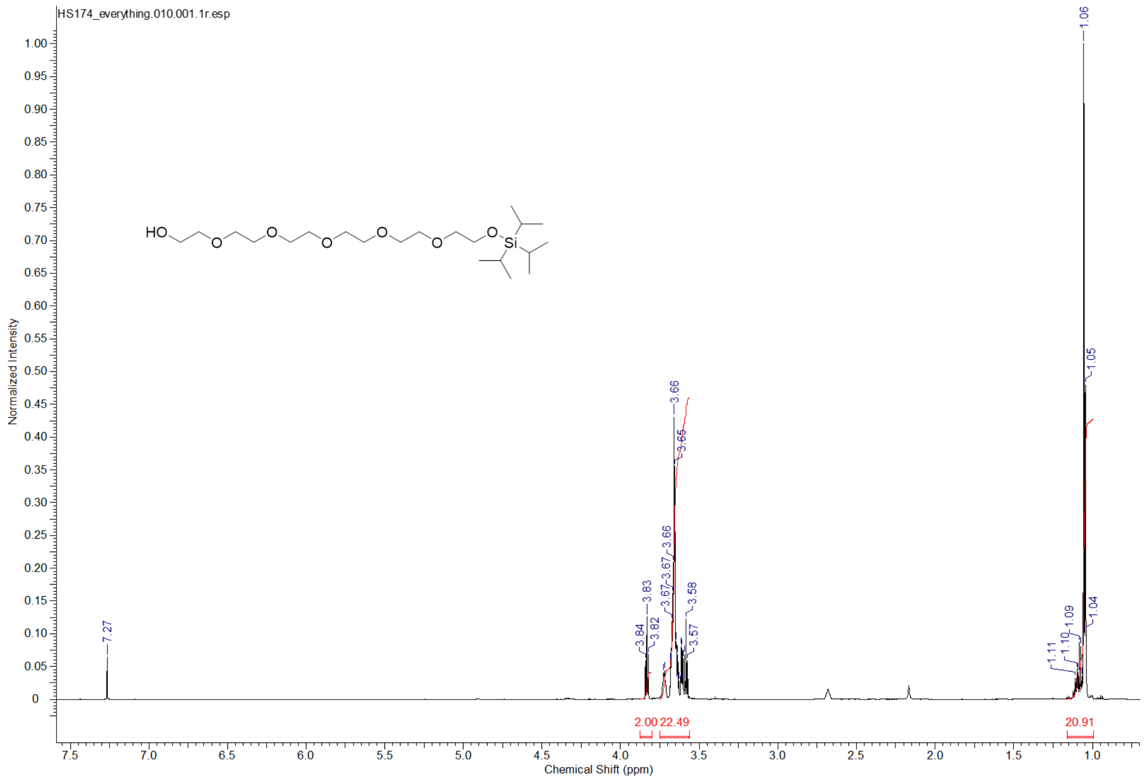

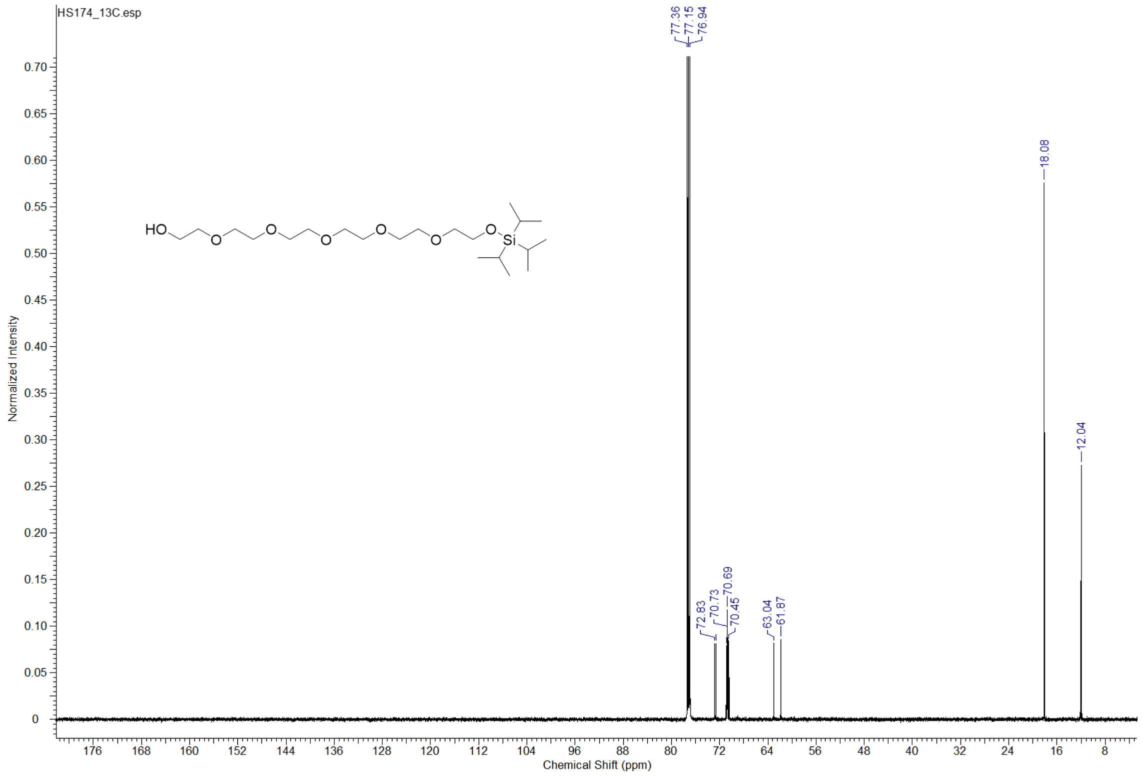

Ethyl 3,3-diisopropyl-2-methyl-4,7,10,13,16-pentaoxa-3-silaoctadecan-18-oate **40**

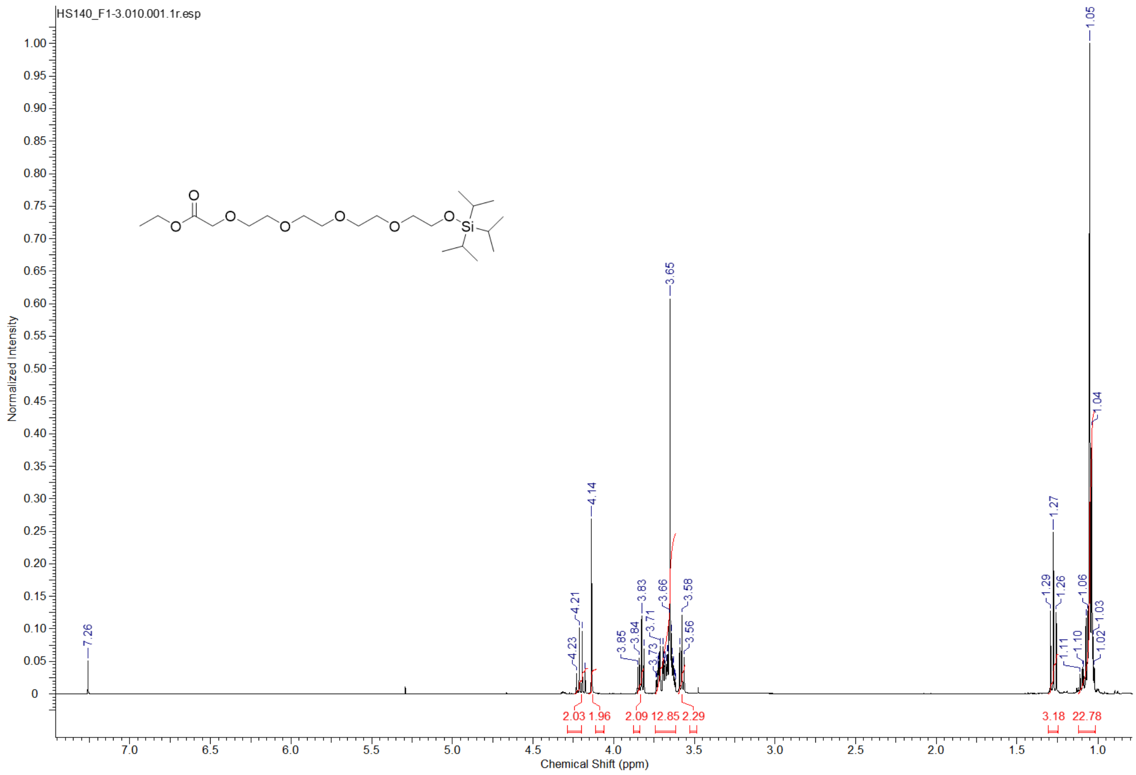

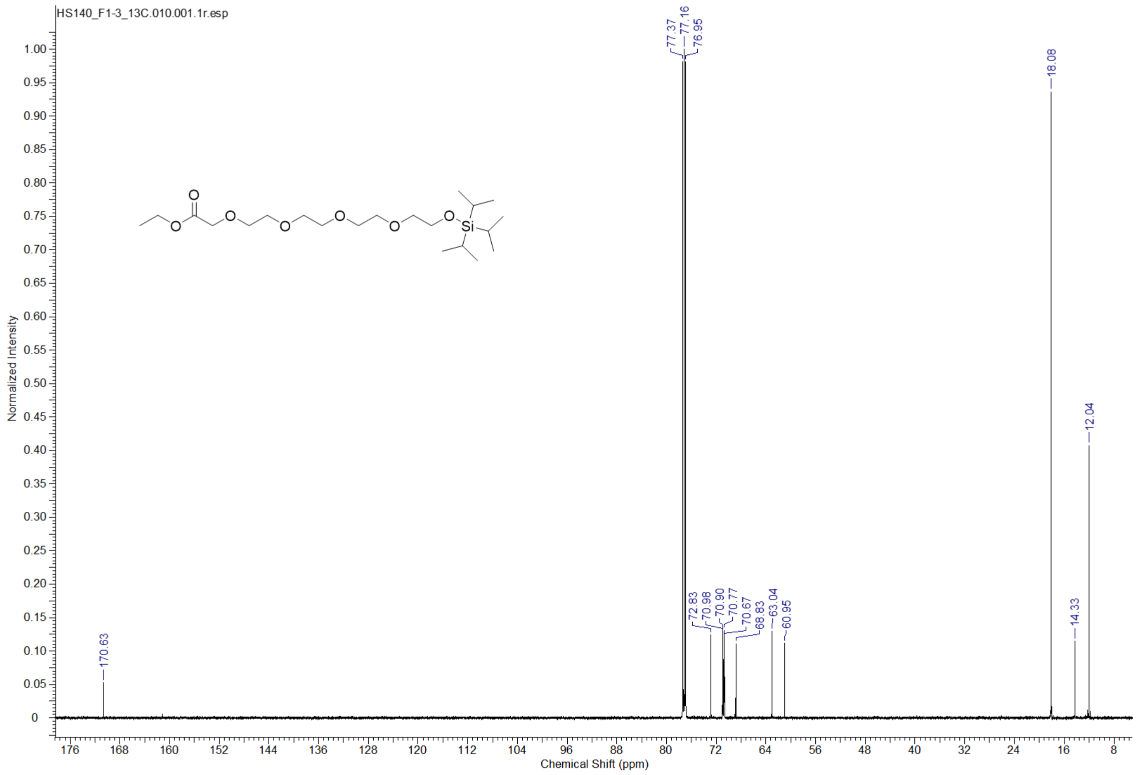

3,3-Diisopropyl-2-methyl-4,7,10,13,16-pentaoxa-3-silaoctadecan-18-oic acid **42**

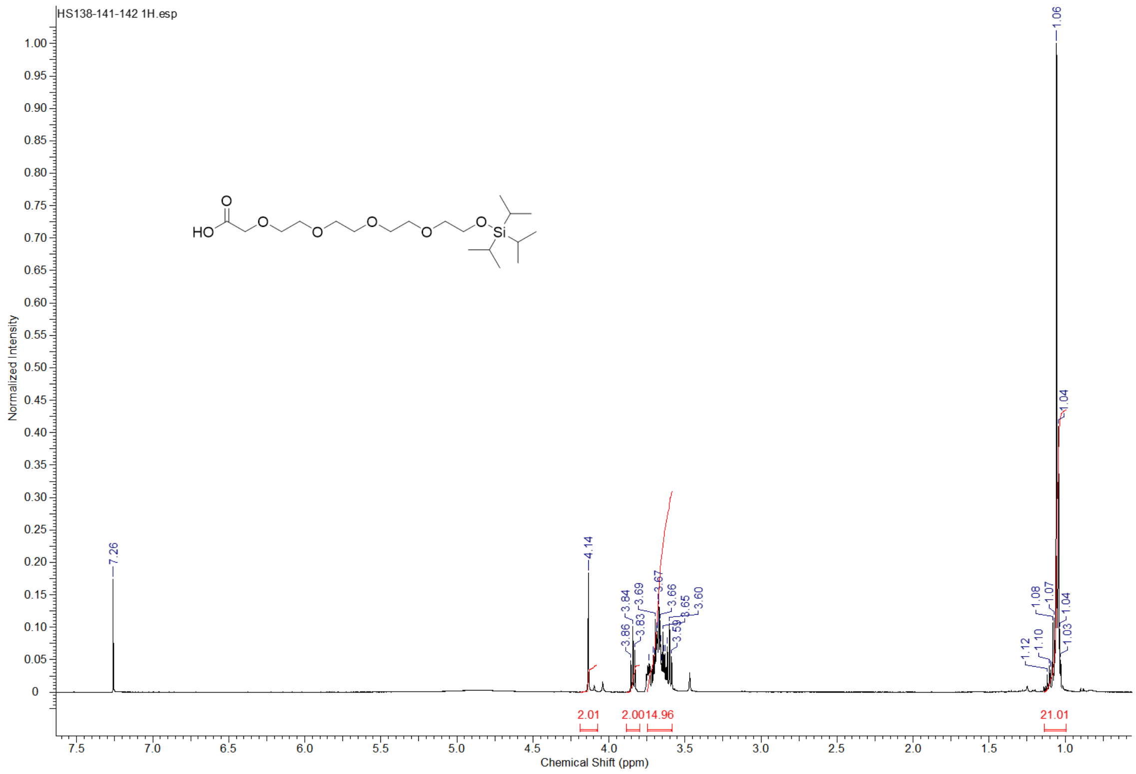

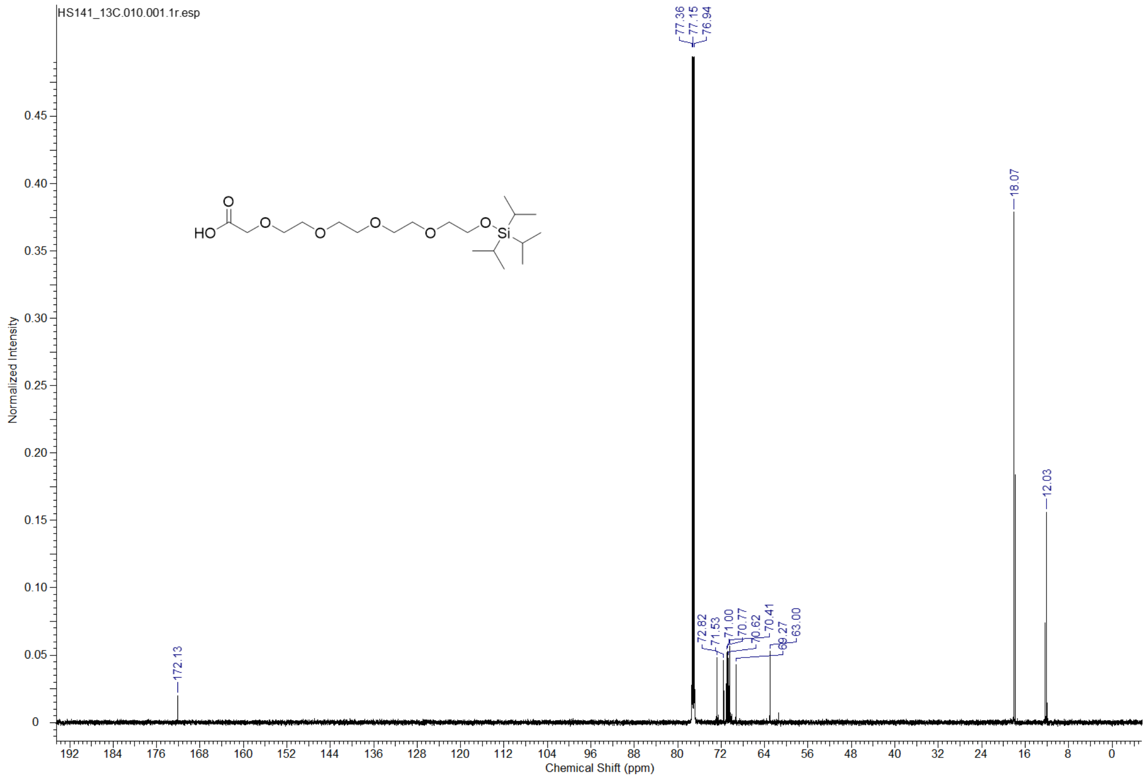

3,3-diisopropyl-2-methyl-4,7,10,13,16,19,22-heptaoxa-3-silatetracosan-24-oic acid **43**

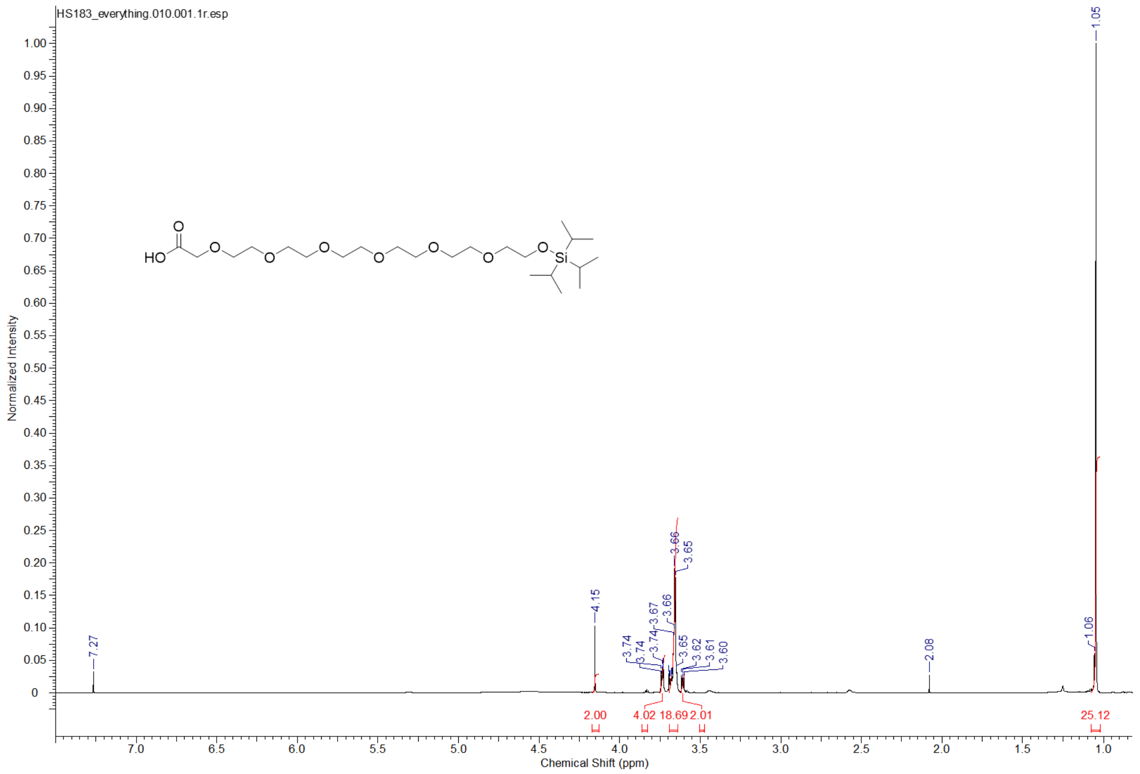

2,5-Dioxopyrrolidin-1-yl 3,3-diisopropyl-2-methyl-4,7,10,13,16-pentaoxa-3-silaoctadecan-18-oate **44**

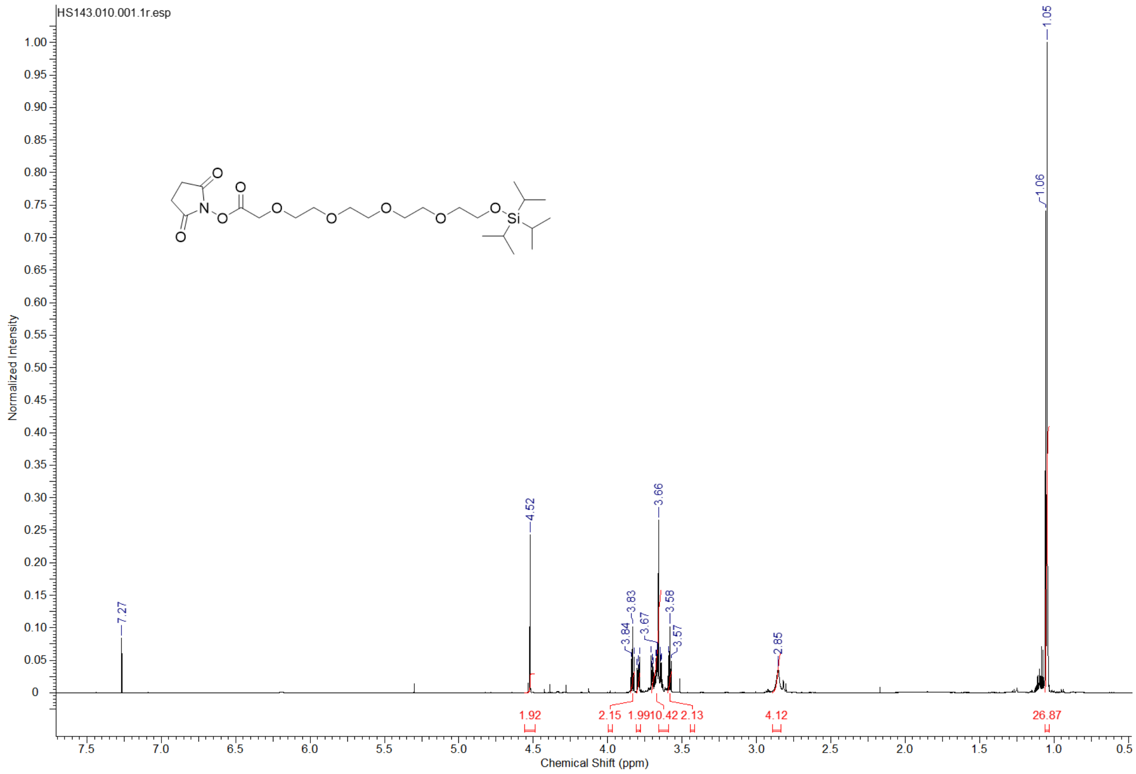

2,5-dioxopyrrolidin-1-yl 3,3-diisopropyl-2-methyl-4,7,10,13,16,19,22-heptaoxa-3-silatetracosan-24-oate **45**

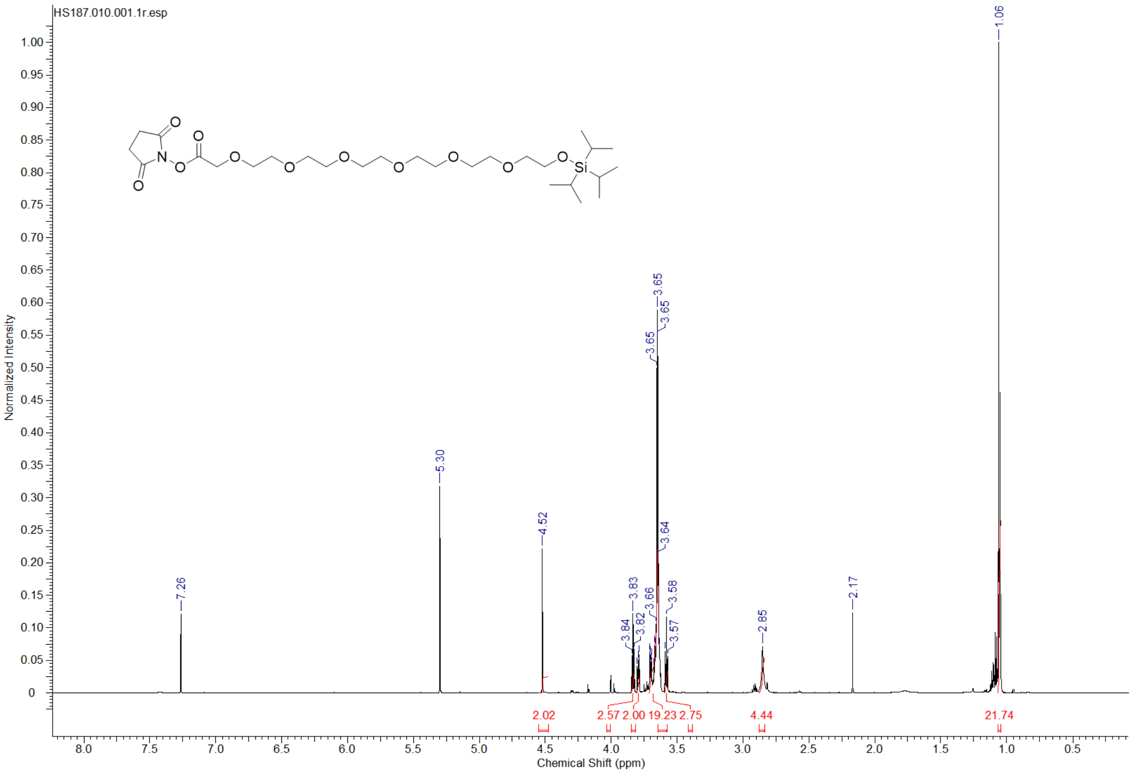

3-((((3,3-Diisopropyl-2-methyl-18-oxo-4,7,10,13,16-pentaoxa-19-aza-3-silahenicosan-21-yl)oxy)(hydroxy)phosphoryl)oxy)propane-1,2-diyl dipalmitate **46**

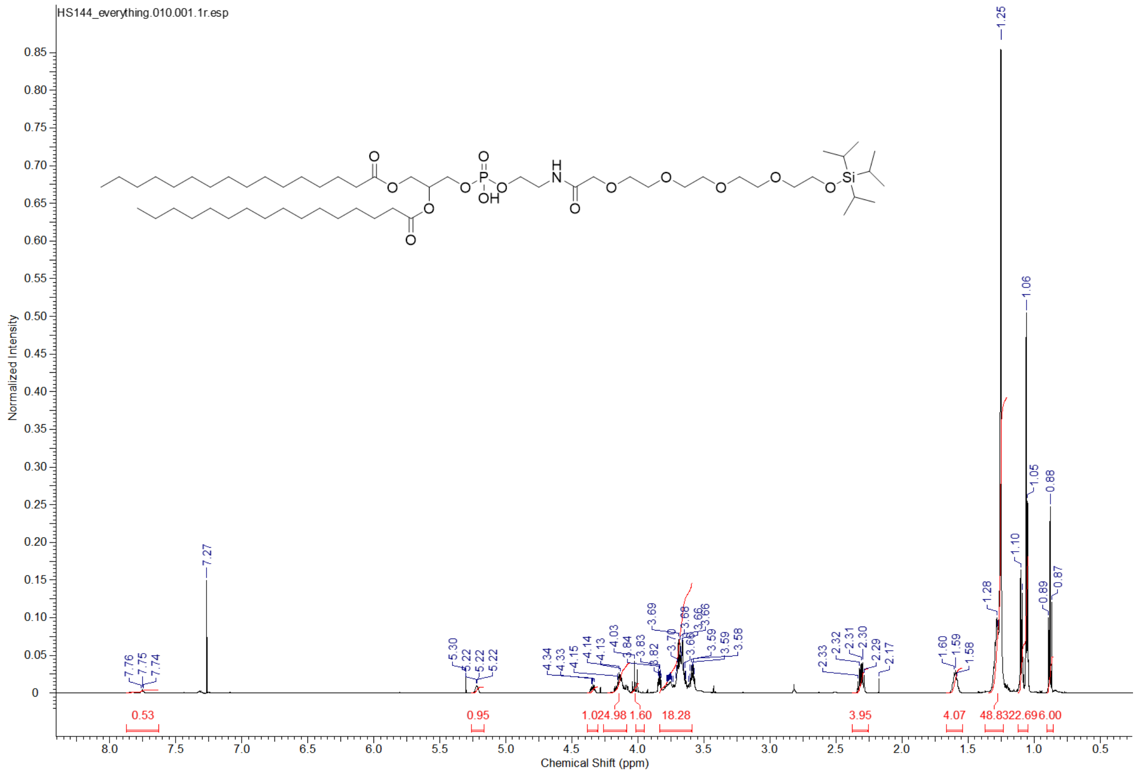

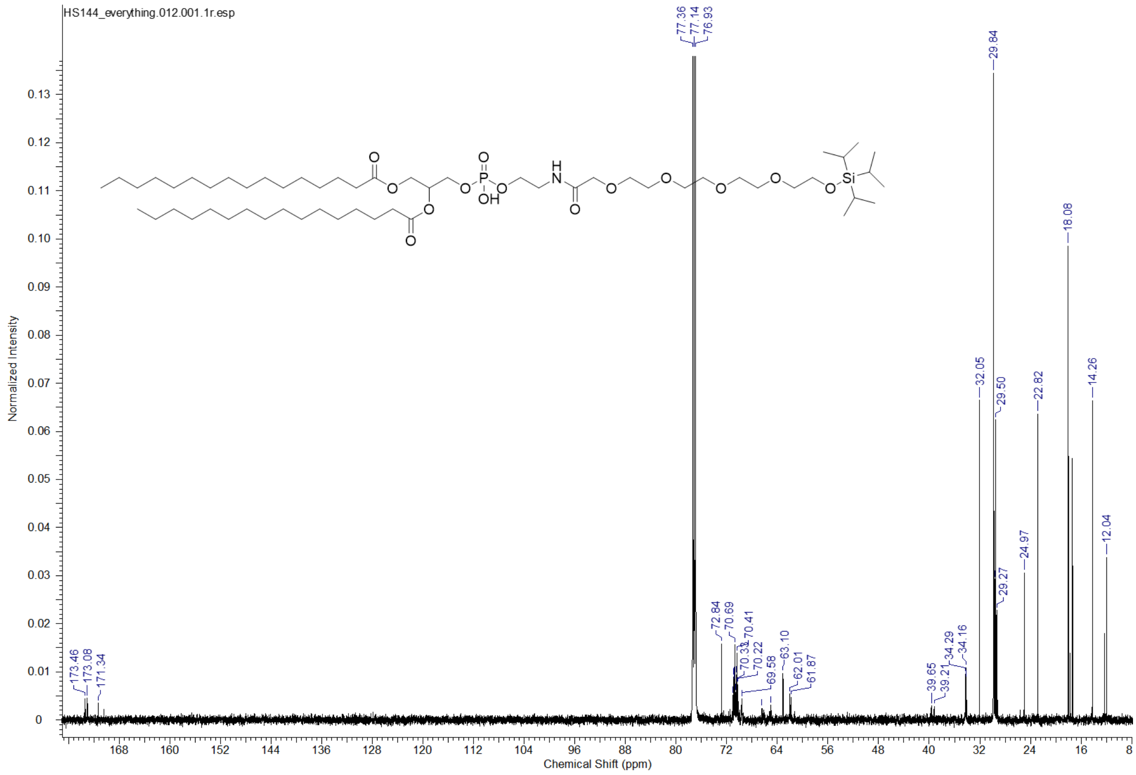

3-((((3,3-diisopropyl-2-methyl-24-oxo-4,7,10,13,16,19,22-heptaoxa-25-aza-3-silaheptacosan-27-yl)oxy)(hydroxy)phosphoryl)oxy)propane-1,2-diyl dipalmitate **47**

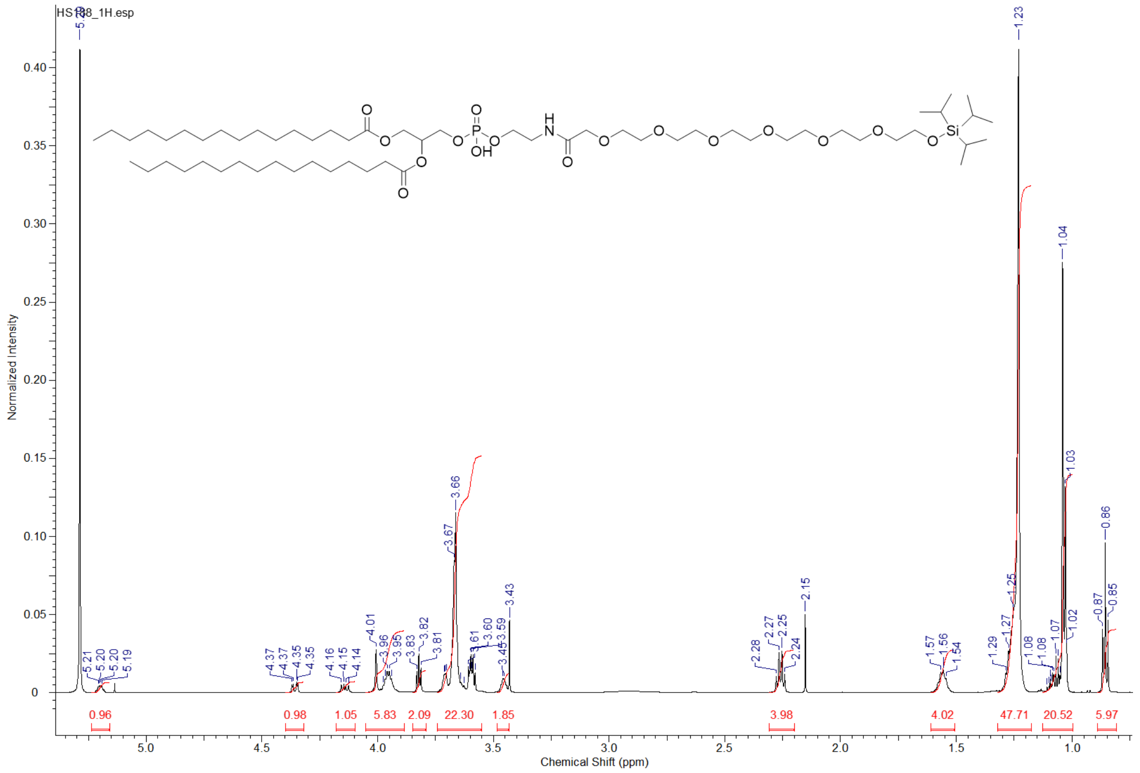

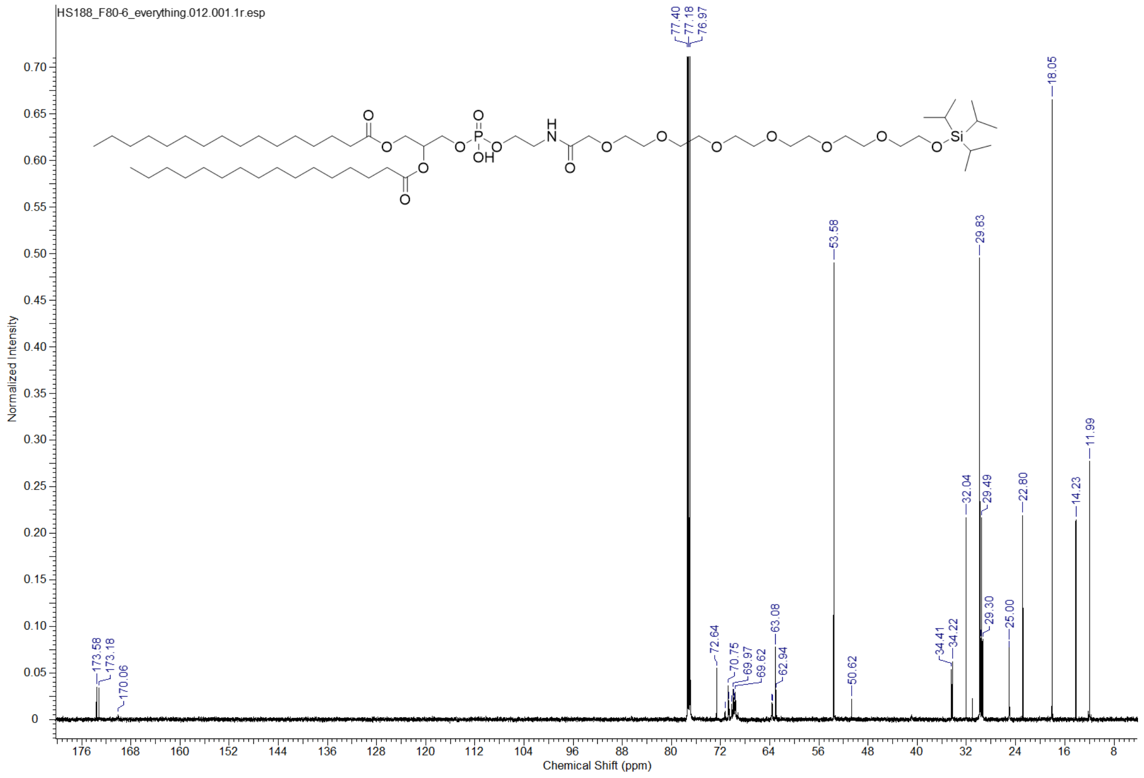

DPPE-EG4-OH **48**

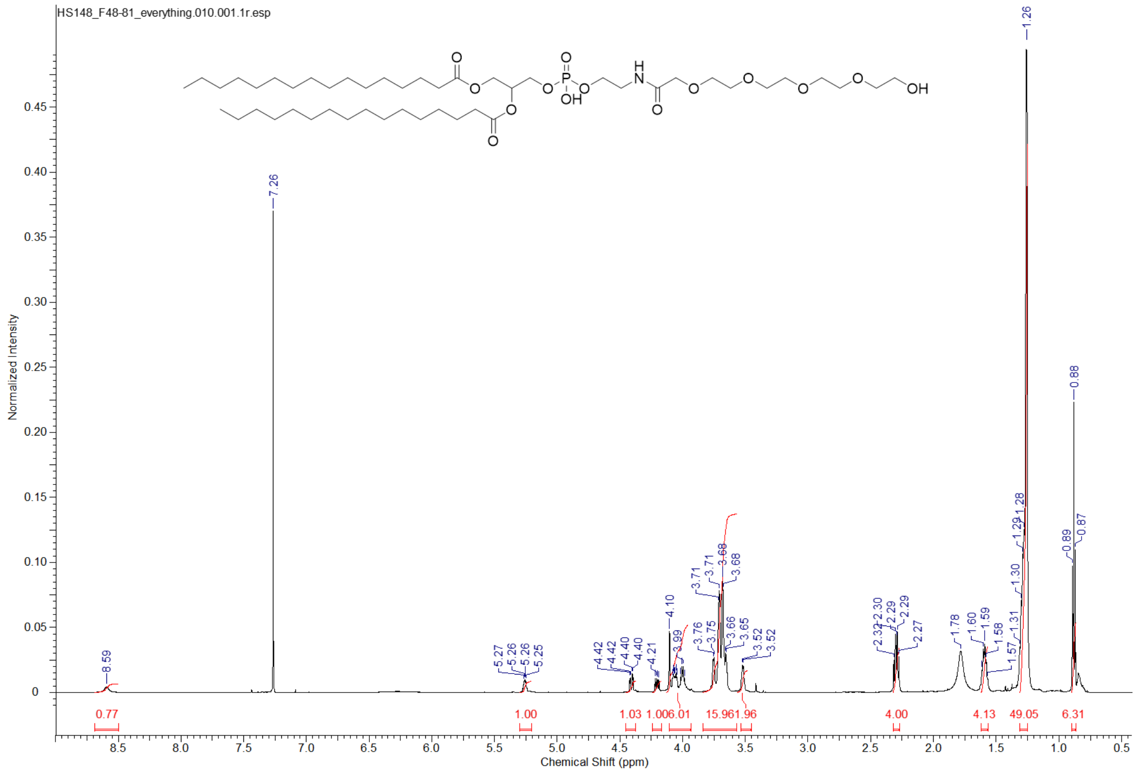

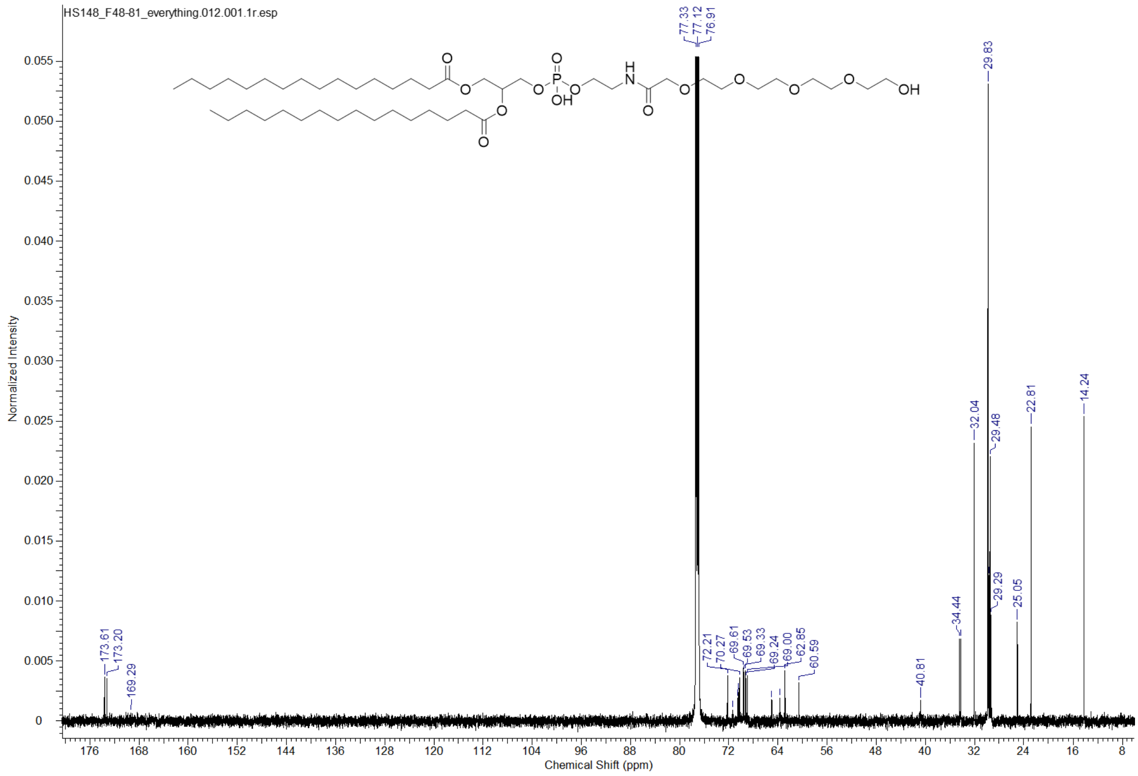

DPPE-EG6-OH **49**

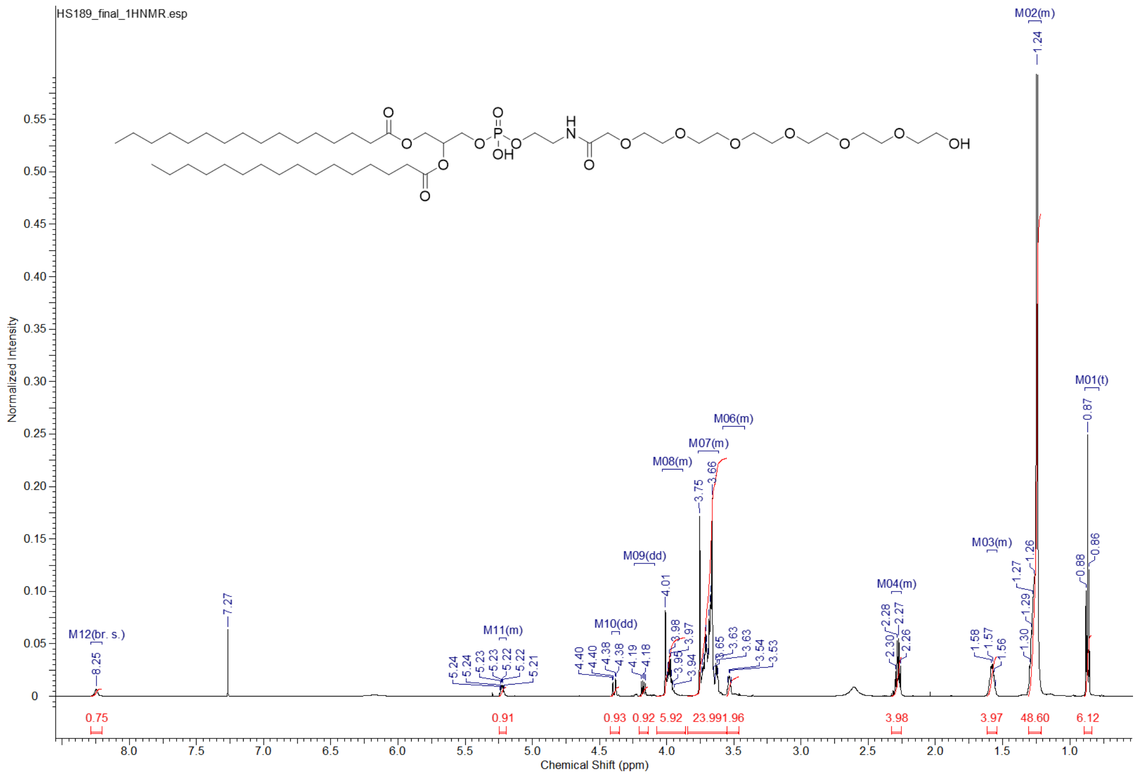

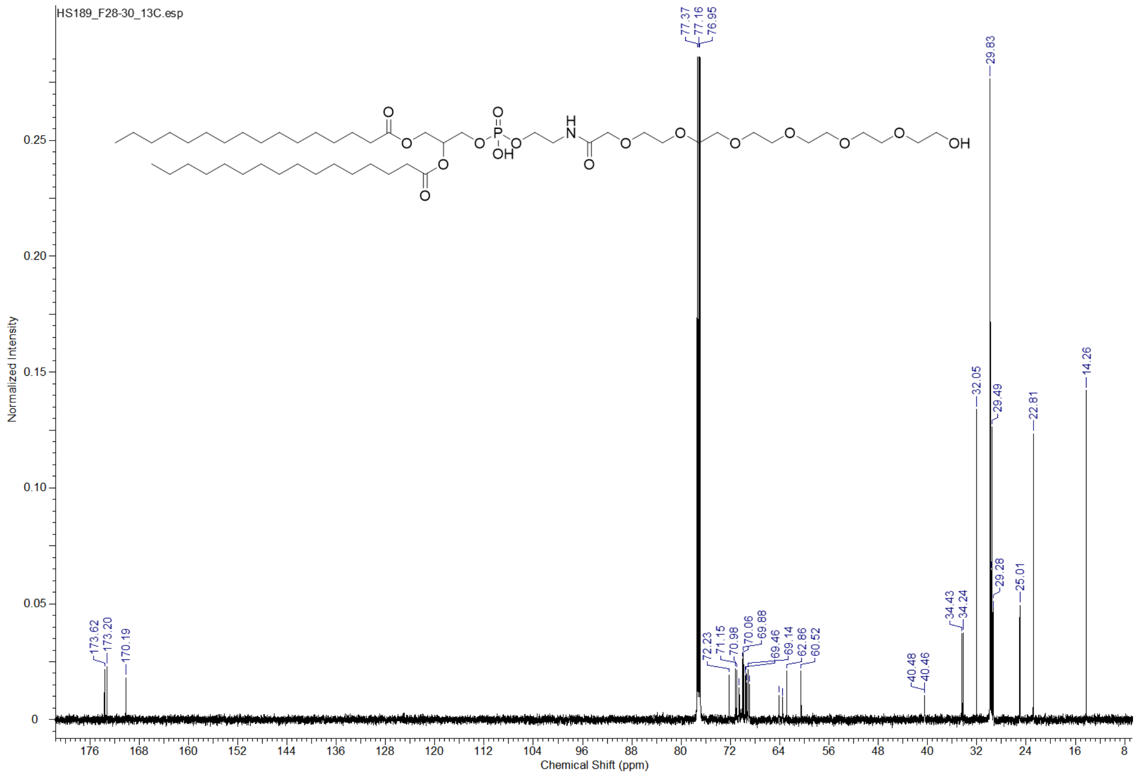

2,5-Dioxopyrrolidin-1-yl 1-(9H-fluoren-9-yl)-3-oxo-2,7,10,13,16-pentaoxa-4-azanonadecan-19-oate **51**

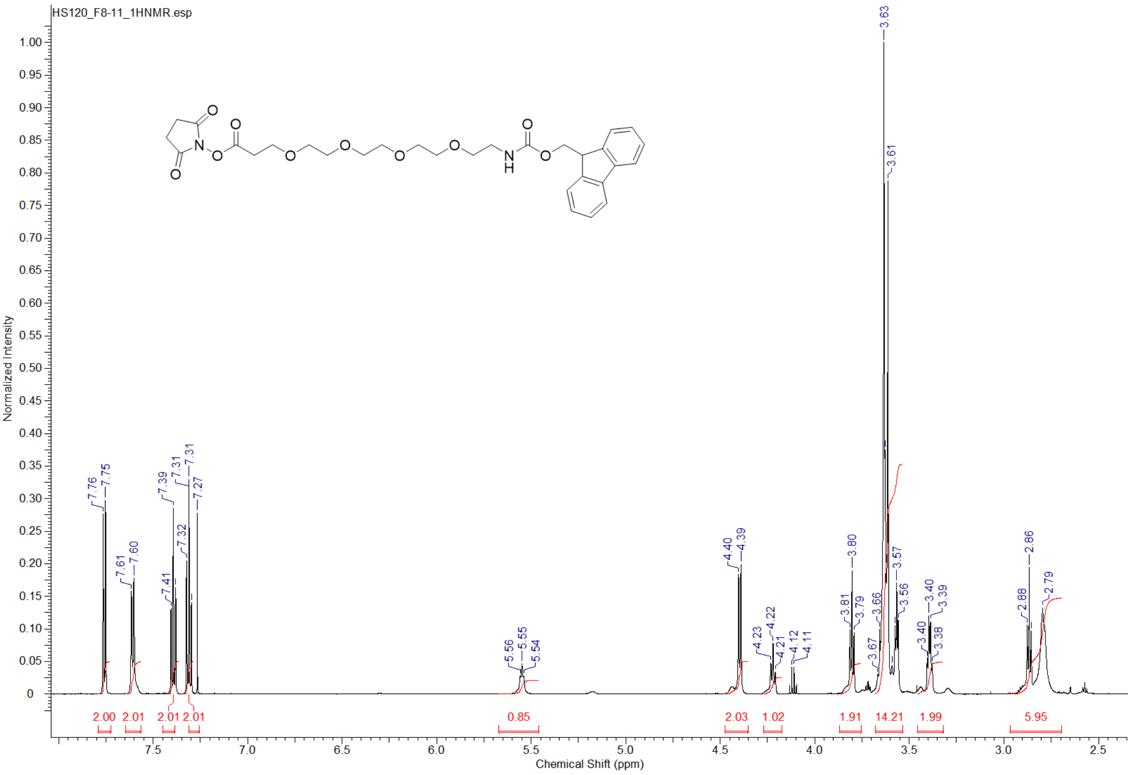

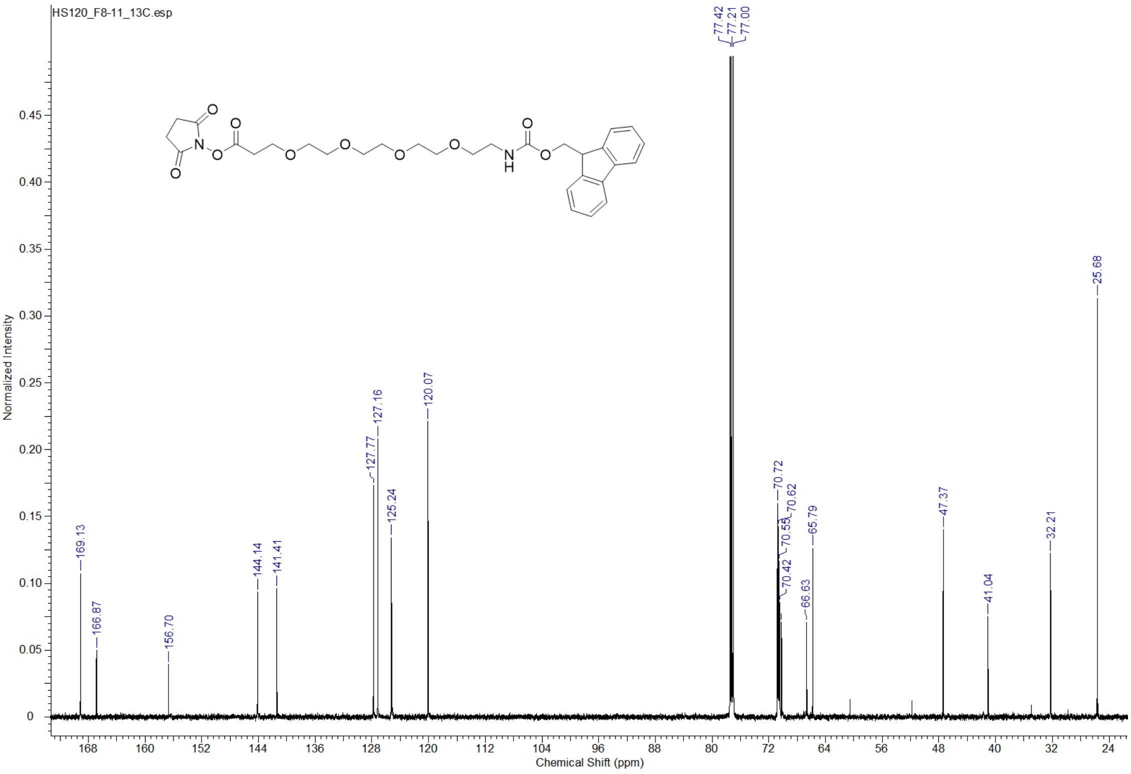

3-((((1-(9H-fluoren-9-yl)-3,19-dioxo-2,7,10,13,16-pentaoxa-4,20-diazadocosan-22-yl)oxy)(hydroxy)phosphoryl)oxy)propane-1,2-diyl dipalmitate **52**

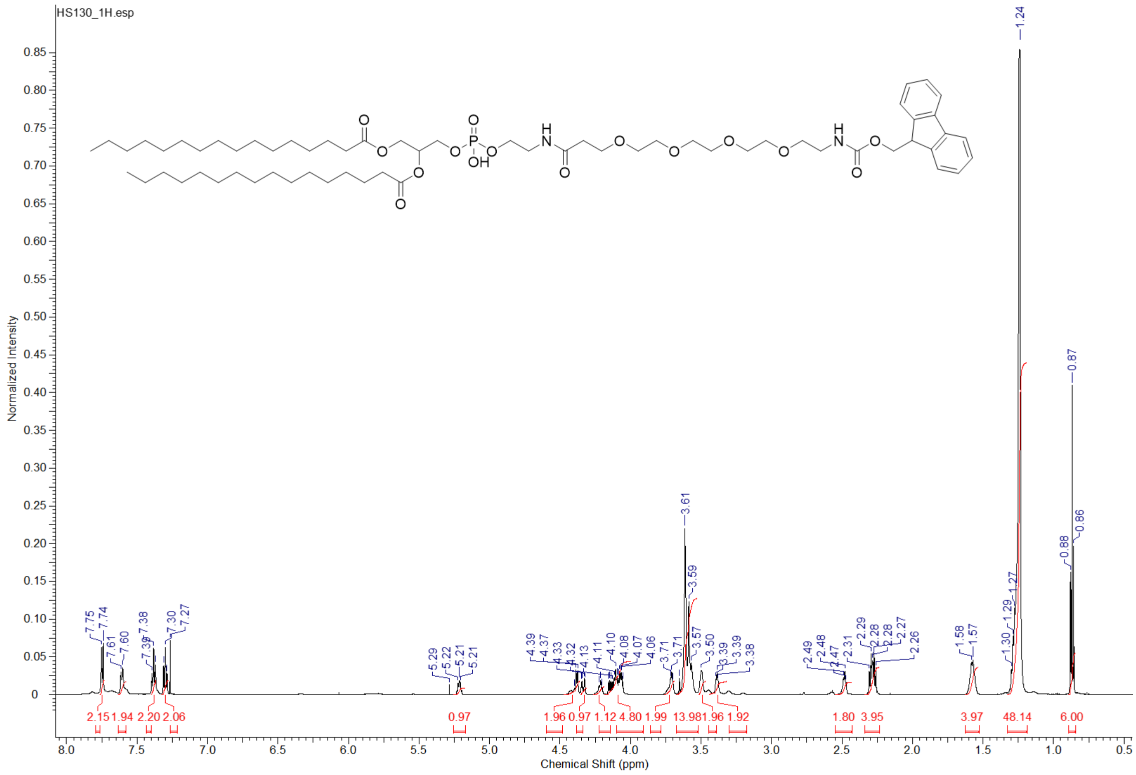

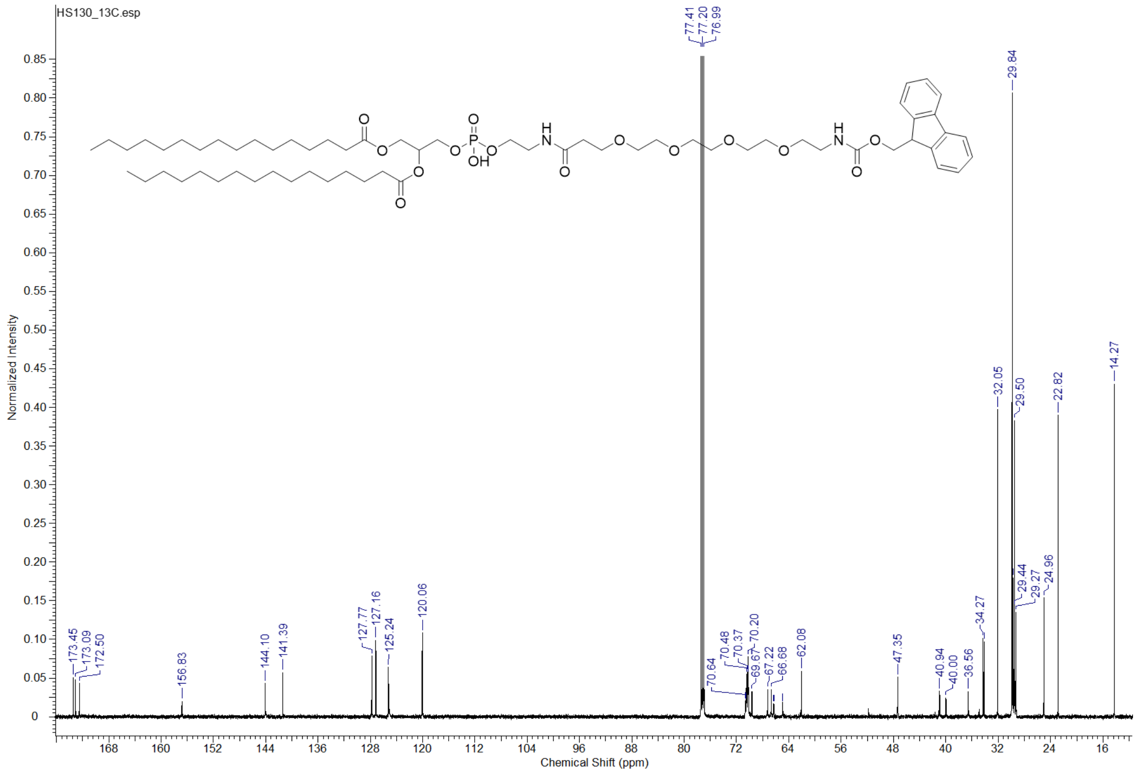

DPPE-EG4-NH$_2$ **53**

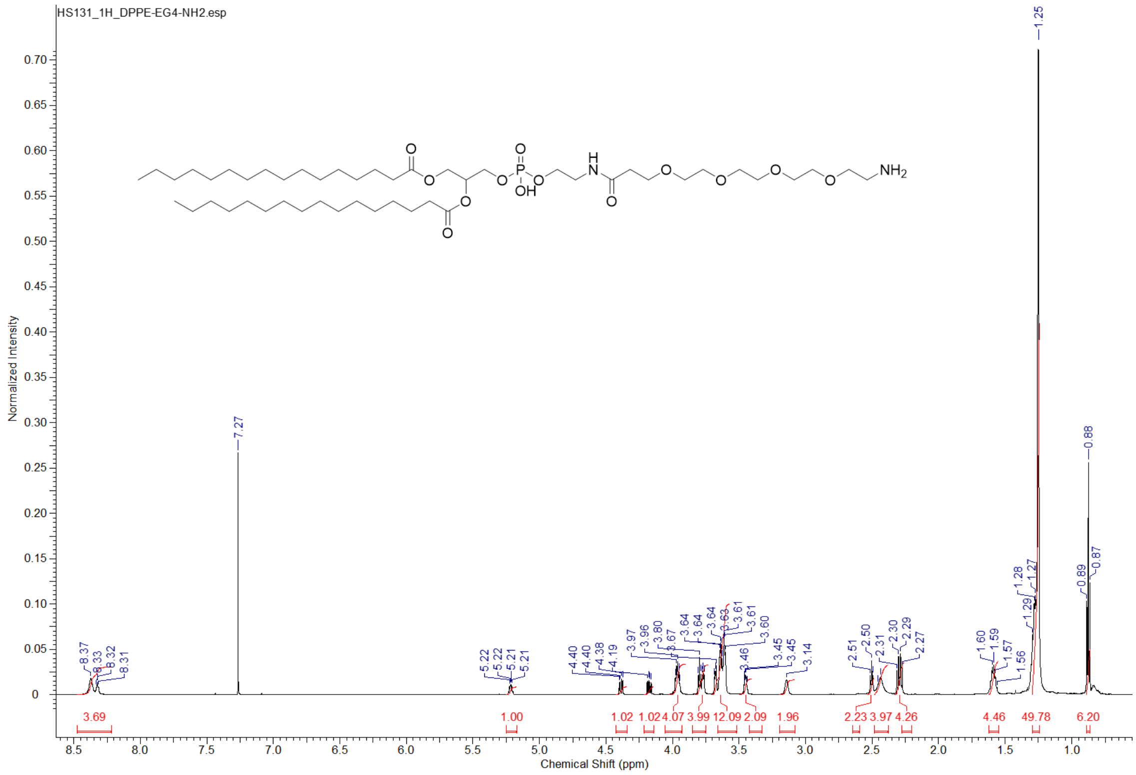

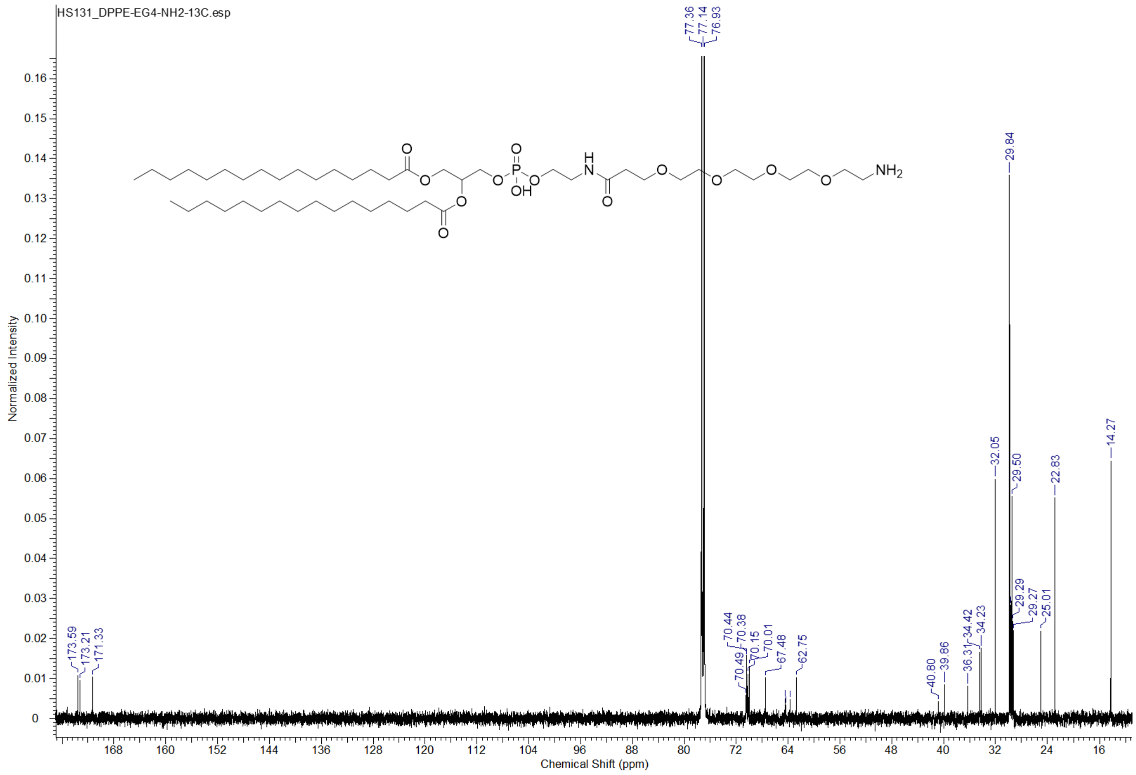

Mal1 **54**

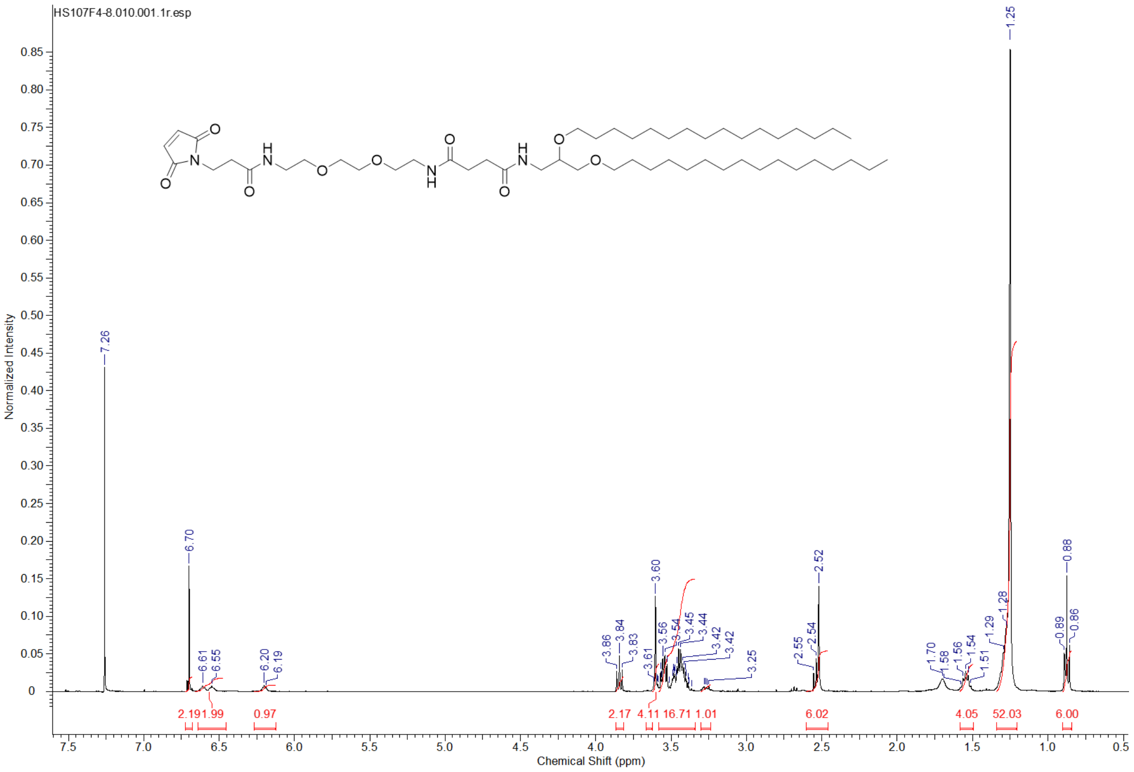
HS107F4-8.010.001.1r.esp
Normalized Intensity
Chemical Shift (ppm)
7.26
6.70
6.61
6.55
6.20
6.19
3.86
3.84
3.83
3.61
3.60
3.56
3.54
3.45
3.44
3.42
3.42
3.25
2.55
2.54
2.52
1.70
1.58
1.56
1.54
1.51
1.29
1.28
1.25
0.89
0.88
0.86
2.19
1.99
0.97
2.17
4.11
16.71
1.01
6.02
4.05
52.03
6.00
O
N
H
O
O
N
H
O
O
N
H
O
O
O

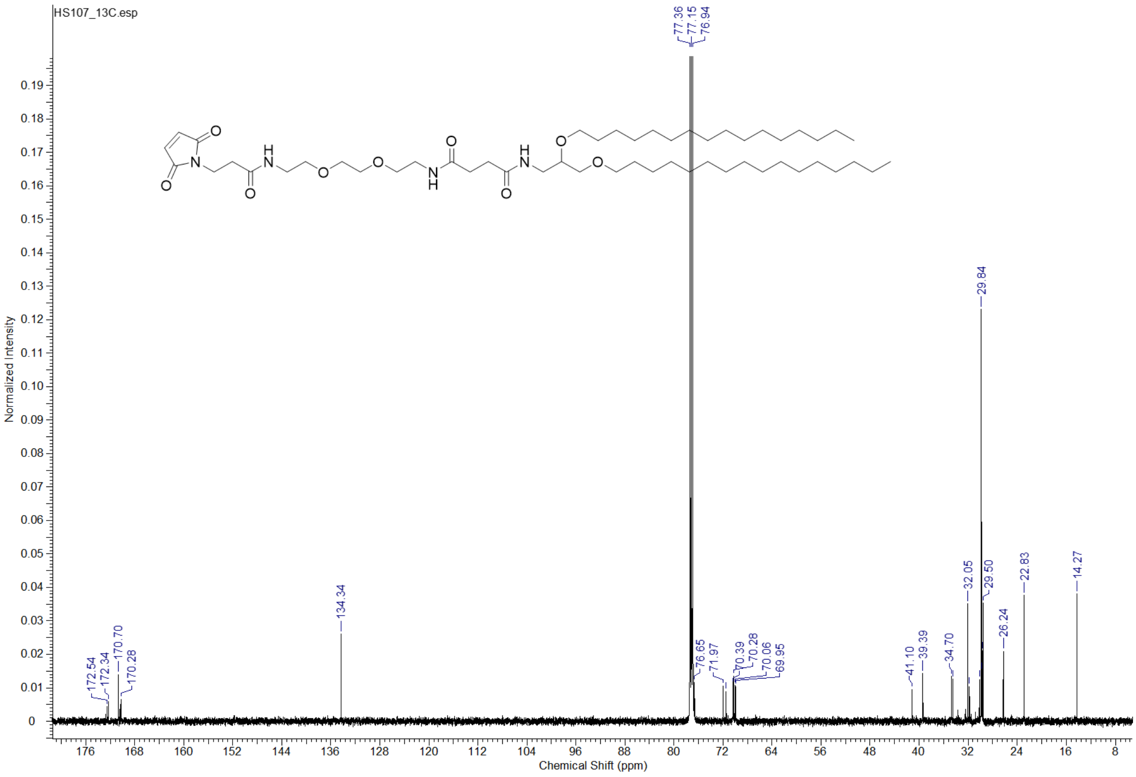
HS107_13C.esp
Normalized Intensity
Chemical Shift (ppm)
77.36
77.15
76.94
172.54
172.34
170.70
170.28
134.34
76.65
71.97
70.39
70.28
70.06
69.95
41.10
39.39
34.70
32.05
29.84
29.50
26.24
22.83
14.27
O
N
H
O
O
N
H
O
O
N
H
O
O
O

N-(3-Aminopropyl)-2,3-bis(hexadecyloxy)-N,N-dimethylpropan-1-aminium **60**

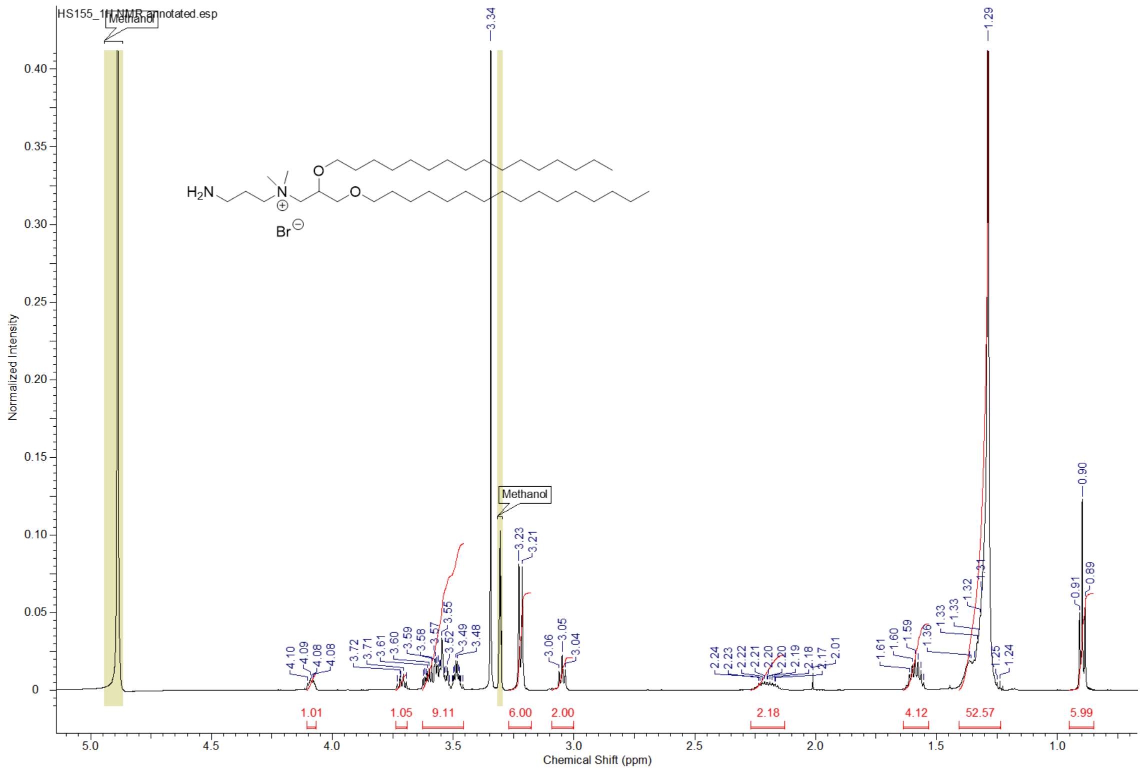

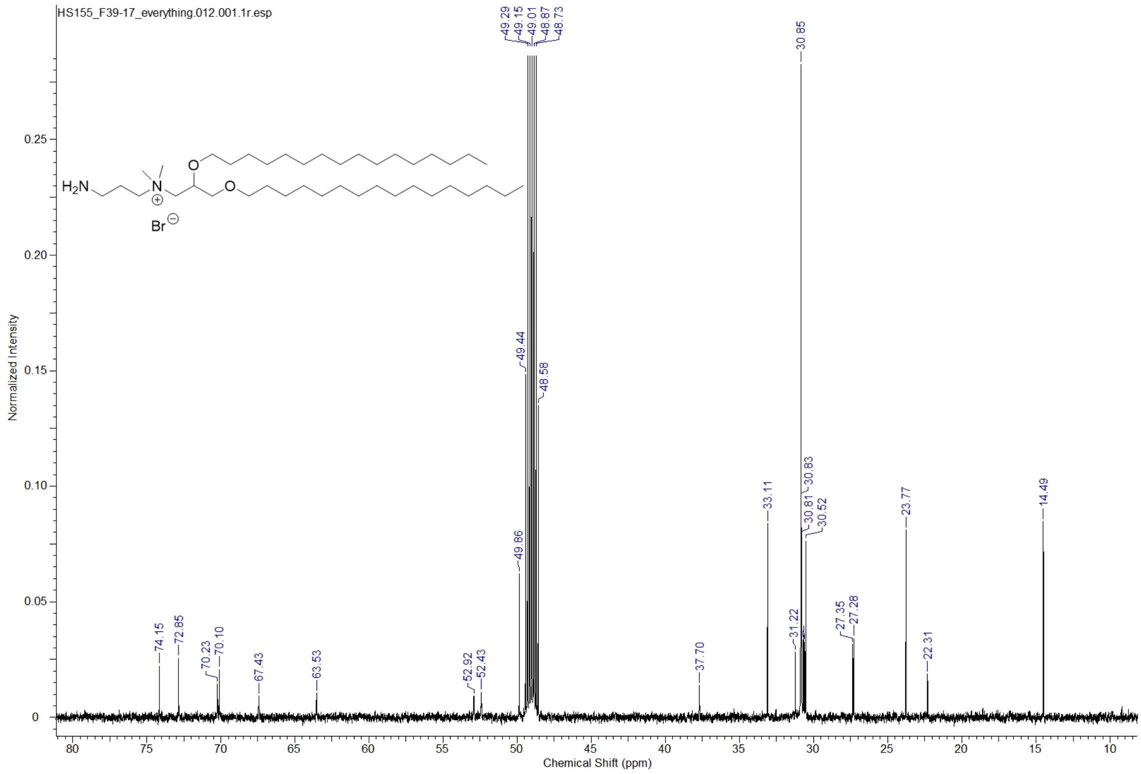

Mal2 **61**

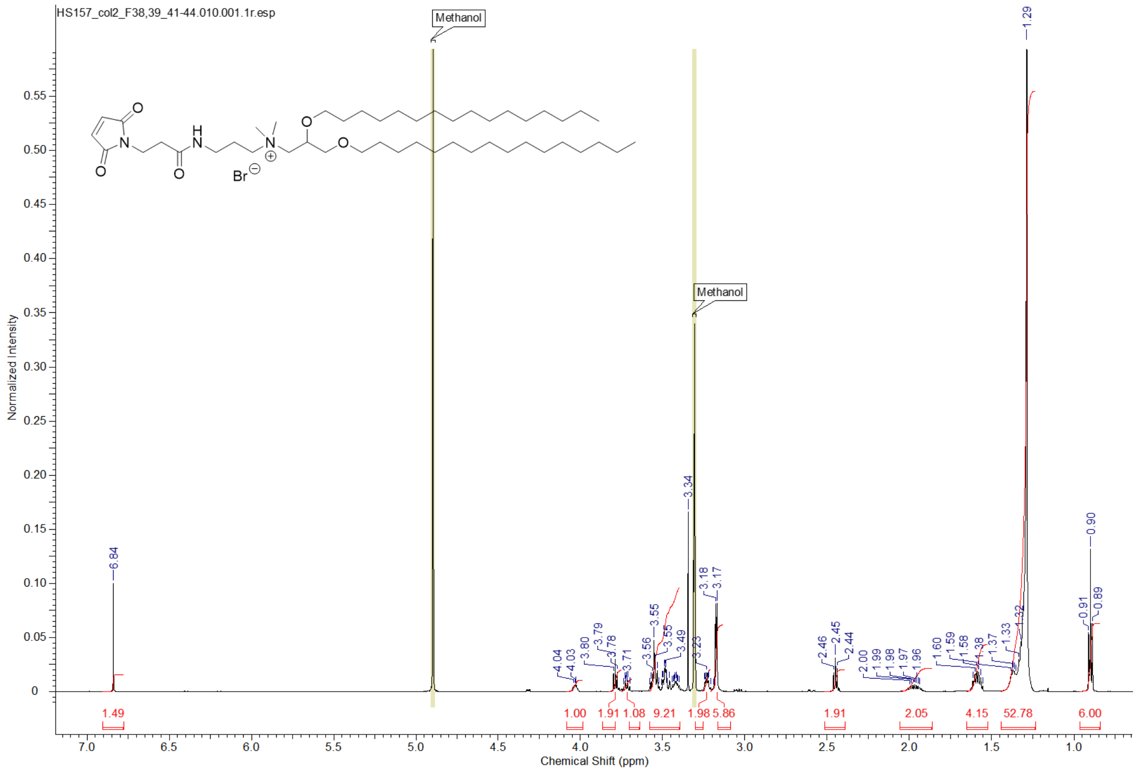
HS157_col2_F38,39_41-44.010.001.1r.esp
Methanol
Methanol
Br⊖
Normalized Intensity
Chemical Shift (ppm)
6.84
4.04
4.03
3.80
3.79
3.78
3.71
3.56
3.55
3.55
3.49
3.34
3.23
3.18
3.17
2.46
2.45
2.44
2.00
1.99
1.98
1.97
1.96
1.60
1.59
1.58
1.38
1.37
1.33
1.32
1.29
0.91
0.90
0.89
1.49
1.00
1.91
1.08
9.21
1.98
5.86
1.91
2.05
4.15
52.78
6.00

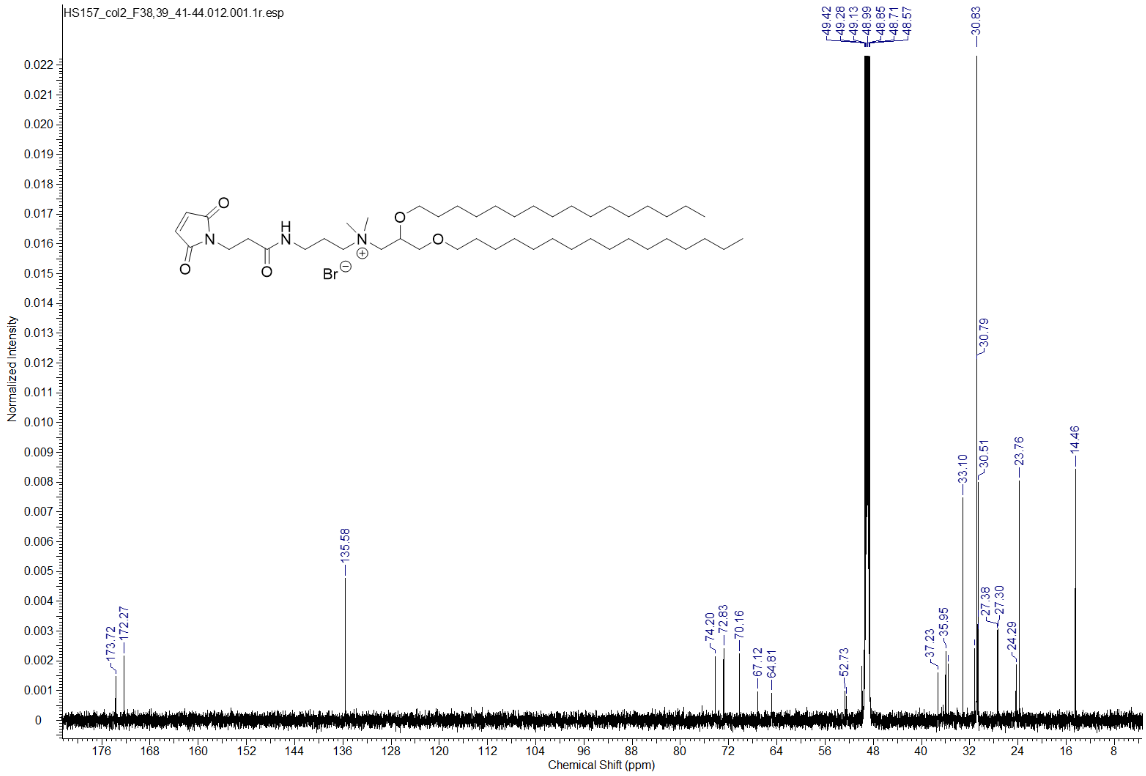
HS157_col2_F38,39_41-44.012.001.1r.esp
Br⊖
Normalized Intensity
Chemical Shift (ppm)
173.72
172.27
135.58
74.20
72.83
70.16
67.12
64.81
52.73
49.42
49.28
49.13
48.99
48.85
48.71
48.57
37.23
35.95
33.10
30.83
30.79
30.51
27.38
27.30
24.29
23.76
14.46